UNIVERSITY OF BIRMINGHAM

THE IMMOBILISATION OF CAESIUM AND STRONTIUM FROM NUCLEAR WASTE CAPTURED BY IONSIV

by

GEORGE DAY

Supervisor: Dr Joseph A. Hriljac

A thesis submitted to The University of Birmingham for the degree of Doctor of Philosophy

The School of Chemistry
College of Engineering and Physical Sciences
University of Birmingham
December 2017

Abstract

A previous study revealed $Cs_2TiNb_6O_{18}$ to be the major Cs-containing phase after hot isostatic pressing Cs-loaded IONSIV (a commercial exchanger) which demonstrated excellent wasteform properties. Both experimental and theoretical studies have been carried out in order to assess if $Cs_2TiNb_6O_{18}$ is able to retain $^{137}Ba^{2+}$, the transmutation product of $^{137}Cs^{+}$. A series of samples with different charge compensation mechanisms have been synthesised including $Cs_{2-x}Ba_xTi^{(4+)}_{1+x}Nb^{(5+)}_{6-x}O_{18}$, $Cs_{2-x}Ba_xTi^{(3+)}_xTi^{(4+)}_{1-x}Nb_6O_{18}$ and $Cs_{2-x}Ba_xTiNb^{(4+)}_xNb^{(5+)}_{6-x}O_{18}$. Analysis suggested that Ba incorporation was not successful because of the identification of Ba impurities in the X-ray diffraction patterns. A series of atomistic simulations have also been performed to support the experimental work, using the General Utility Lattice Program code which suggested that Ba incorporation is not energetically favourable.

Sr-loaded IOSNIV has also been thermally converted via calcination (in air) and hot isostatic pressing. The removal and immobilisation of Sr is an important process on account of ^{90}Sr being one of the more problematic radionuclides produced from the fission process. Both thermal conversion methods produced crystalline phase assembles which were analysed by X-ray diffraction, X-ray fluorescence and microscopy studies. The HIPed materials performed well in aqueous durability tests, suggesting these wasteforms will be suitable for final disposal in a geological disposal facility.

Acknowledgements

` I would like to thank Dr Joe Hriljac for his incredible support throughout this PhD. I would also like to thank Dr Tzu-Yu Chen and Dr Geoffrey Cutts for their invaluable help in my studies and without their input, this work would not have been possible. I would like to thank the School of Chemistry at the University of Birmingham for financial sponsorship and I would also like to thank the DISTINCTIVE program (EPSRC funded) for the opportunity to be an associate member of a fantastic Nuclear consortium.

A big thank you will have to go out to Floor 5 members past and present. To name a few Geoff Cutts, Matt Howard, Tzu-Yu Chen, Ryan George, Laura Driscoll, Ben de Laune, Rachel Bill and my old pal Dean Fletcher. All of these people have made my time on floor 5 unforgettable and I count myself fortunate to have worked alongside such fantastic people and formed great friendships. I would also like to thank the members of staff on floor 5 including Professor Frank Berry, Dr Paul Anderson, Professor Colin Greeves and Dr Adrian Wright for their inciteful conversations about chemistry and most importantly, football banter! I would also like to thank Dr Jackie Deans for all her help over the years with the analytical instruments, your help will not be forgotten.

A special mention must go to Dr Yina Guo (University of Limerick) for carrying out TEM analysis on my materials and Dr Tzu-Yu Chen (University of Birmingham) for assisting with all my microscopy work. Mr Mike Glynn (University of Birmingham) for all his help with HIPing, including can preparation and running the HIP unit. Thank you to Dr Geoff Cutts (University of Birmingham) for all his help with my computational studies and allowing me use of two of his fantastic codes and lastly Mr Steve Baker (University of Birmingham) for the ICP analyses.

I would like to thank my Mum, Dad and Sister for all their support throughout my PhD, I could not have done it without them. Lastly and most importantly I would like to thank Jessica, my steady rock, who has managed to keep me on track for the last four years and provided me with the encouragement I needed in the most difficult of times. Thank you so much.

Abbreviations

VLLW Very Low-Level waste

LLW Low-Level waste

ILW Intermediate-Level waste

HLW High-Level waste

HLLW High-Level Liquid waste

FP's Fission Products

AMP Ammonium Molybdophosphate

GDF Geological Disposal Facility

DF Decontamination Factors

PXRD Powder X-ray Diffraction

XRD X-ray Diffraction

XRF X-ray Fluorescence

SEM Scanning Electron Microscopy

BSE Back Scattered Electrons

EDX Energy Dispersive X-ray

TEM Transmission Electron Microscopy

TGA Thermogravimetric Analysis

DTA Differential Thermal Analysis

MS Mass Spectrum

GSAS General Structure Analysis Software

GULP General Utility Lattice Program

RMC Reverse Monte-Carlo

MCMC Markov Chain Monte-Carlo

HIP Hot Isostatic Pressing

ASTM American Society for Testing and Materials

MCC Materials Characterisation Centre

PCT Product Consistency Test

Table of Contents

Contents

List of Figures

1 INTRODUCTION

1.1 Background

It is reported that around 14% of the world's electricity is supplied from nuclear power and as the drive for low-carbon energy sources increases, it is thought that this percentage will increase in the coming decades.[1,2] The relatively recent Fukushima disaster has caused confidence to be lost in nuclear power and as a result there have been some substantial setbacks in many nuclear programs.[1,3,4] As an example Germany plan to close all of their nuclear reactors by 2022 following the accident in Japan.[5,6] However with rising energy demands and fossil fuels depleting it seems unlikely that nuclear power will be disregarded in the long term and there are as many as 64 new reactors being currently constructed across the globe.[2,7]

The nuclear process itself is a relatively clean way of producing electricity with almost no CO_2 production. The majority of CO_2 is produced at the beginning of the nuclear fuel cycle where the uranium is mined. [7,8] Despite this, a small amount of highly radioactive waste is produced, commonly labelled the 'Achillies heel' of nuclear power.[1,9] Thousands of tonnes of waste has been produced over the last six decades and not only from power generation but also from the defence, research and medical industries. [1,9] The composition of the waste depends on a number of factors including the type of reactor, the type of cladding materials, the nature of the source and also how the waste has been stored before final processing and disposal.[9] The majority of waste around the globe is stored in stainless steel tanks in alkaline or acidic media at intermediate depositories.[9]

Nuclear waste is classed differently according to characteristics such as heat output, concentration and length of half-life. The categories include very low level waste (VLLW), low level wastes (LLW), intermediate level waste (ILW) and high level waste (HLW).[7,9,10]

The regulation for disposal of wastes follows the obvious, with VLLW being the easiest to dispose of and HLW being the most difficult. HLW is often a complex mixture and may contain over 90 fission products (FPs) of 35 different elements making processing and final disposal challaneging.[11] To add to the FPs, HLW waste may also contain varying concentrations of corrosion products from cladding materials and storage containers which further complicates the mixture.[9,11]

Certain components of nuclear waste are more 'active' than others and their presence may class waste in a higher category, equally their removal could lower the category of the waste; such radionuclides include ^{137}Cs and ^{90}Sr.[12] These radionuclides are thought to be the primary heat generating radionuclides in nuclear waste and also contribute to most of the radioactivity.[13,14] Both are considered to be extremely hazardous and highly mobile in the environment and therefore are often the main radionuclides accidently released into the biopshere.[15] ^{137}Cs is a strong beta-gamma emitter and is highly volatile, highly soluble and has a reasonably long half-life of 30.17 years.[16,17] ^{90}Sr, a beta emitter, is similar to ^{137}Cs with a half-life of 28.8 years.[12,13] Both ^{137}Cs and ^{90}Sr are harmful to humans due to their chemical similarities to K^+ and Ca^{2+} respectively,[18,19] therefore their removal from waste and subsequent immobilisation is preferential and many nuclear waste processing sites across the world implement separation or exchange steps to remove ^{137}Cs and ^{90}Sr such as the SIXEP process at Sellafield. [14,16,20–22]

A number of different processing methods have been researched and developed for the separation of ^{137}Cs and ^{90}Sr from waste streams. These include precipitation, volatilisation, solvent extraction, the membrane process and ion exchange.[15,17] Ion exchange seems to offer the most advantages of all these technologies, [15,17] as it can be used in both batch and column systems, be very efficient (i.e. high decontamination factors), requires

only simple equipment which can be adapted to be stationary or mobile and lastly no harmful solvents are introduced to the waste which could further complicate the processing.[15,17] A number of ion exchangers have been studied, both inorganic and organic and sometimes a combination of the two.[15,17]

1.2 Inorganic Exchangers

Inorganic ion exchangers are reported to be somewhat superior to their organic counterparts. They have a much higher resistance to chemical, thermal and radiation damage and tend to be more selective which is largely due to their ordered crystalline frameworks.[17,23,24] Such materials include zeolites (natural and synthetic), transition metal hexacyanoferrates, heteropolyacid salts of molybdenum and tungsten and silicotitanates.

1.2.1 Zeolites

Zeolites were the first generation of inorganic ion exchangers used for the remediation of nuclear wastes.[20] They are made up of connecting SiO_4/AlO_4 tetrahedral units which give a net negative aluminosilicate framework system (Si^{4+}/Al^{3+}). The charge is balanced by cations such as Na^+ and K^+ which sit in the aluminosilicate cages which can be exchanged for other positively charged species, such as Cs^+ and Sr^{2+}..[25] For the past 24 years clinoptilolite, a natural zeolite, has been employed at the Sellafield ion exchange effluent plant (SIXEP) in Cumbria to remove Cs and Sr from nuclear waste.[21,22] Clinoptilolite is one of the most abundant natural zeolites and is used at SIXEP because of its relative cheapness, and like many zeolites, its ease of use, high cation exchange capacity, radiation stability and compatibility with final immobilisation.[15,20,21,26–28] Other zeolites such as Na-Zeolite-A and Na-Zeolite-Y have also been studied for the removal of harmful radionuclides.[15,29] Despite their advantages zeolites can only really be effective in a limited pH range and the efficiency rapidly decreases as the concentration of competitive ions increases. [17,20,30,31]

1.2.2 Cs-treat®

Cs-treat® is a highly selective transition metal hexacyanoferrate with the formula $K_2CoFe(CN)_6$.[32] Unlike zeolites, this material is operational over a much larger pH range (1-13) and the decontamination factors are excellent. [24,33] Its high selectivity allows for much faster flow rates than other exchangers and is able to operate in both batch and column exchange systems. However, there are limitations which include low operating temperatures and decreased efficiency in the presence of competing ions.[24,33,34]

1.2.3 Ammonium Molybdophosphate (AMP)

Ammonium molybdophosphate (AMP), has been the centre of much study since its exchange properties for Cs^+ were first discovered over 50 years ago.[35] It can also work in both batch and column systems and is resistant to radiation. Despite being extremely selective for Cs^+ and possessing exceptional sorption rates, like zeolites, the effective operational pH range is narrow and also the presence of interfering anions can have some detrimental effect on the overall performance of AMP.[36]

1.2.4 Sodium Nonatitanate ($Na_4Ti_9O_{20}$)

Sodium nonatitanate with formula $Na_4Ti_9O_{20}$, is an exchange material that is highly selective for Sr^{2+}. It was developed by a joint team that is now known as Honeywell International and Texas A&M University.[25,37] Sodium nonatitanate is a semi crystalline layered material which was found to be radiation resistant, have a high exchange capacity and be able to function in highly alkaline environments in the presence of competing cations. [37,38] A previous study reports that sodium nonatitanate outperforms many other ion exchange materials such as Sr-treat®, pharmacosiderites and IONSIV IE-911 in terms of Sr exchange coefficients using many different waste simulants.[37]

1.2.5 Sr-treat®

Sr-treat® is a titanium oxide Sr exchanger which has been developed by Fortum Nuclear Services Ltd. [39] This material has already proved its ability to remove Sr from waste effluents after being used on an industrial scale in Murmansk, Russia demonstrating average decontamination factors (DF) of 7400.[33,39] This material can remove Sr from both dilute and aqueous solutions and performs particularly well in alkaline media. With this material, Sr exchange is not affected by high concentrations of Na^+ but a high Ca^{2+} content does reduce Sr^{2+} take up. [33,39]

1.2.6 Crystalline Silicotitanates (CST)

In 1989, following some initial work on amorphous hydrous titanium oxides, a new inorganic exchanger known as Crystalline Silicotitanate (CST) was developed by the Sandia National laboratory and Texas A&M University.[17,40,41] In the early 1990s a number of different CST phases were synthesised and the material with the highest Cs selectivity was labelled TAM-5 by Anthony et al. (1993).[41] CST displayed exceptional properties, possessing excellent exchange coefficients and selectivity for Cs^+ and Sr^{2+} over a wide pH range and in the presence of a number of competing ions, particularly Na^+.[12,13,17,41] CST also demonstrated excellent radiation stability and furthermore it was found to be compatible with final immobilised wasteforms such as glasses and ceramics.[17,14,41,42]

CST's have a 'zeolite like' open framework system.[31] It is composed of Ti-O octahedra which connect to form Ti_4O_{16} cubane-like clusters (see **Figure 1.1**) which corner share with Si-O tetrahedra.[43] This forms to create ideally sized channels or pores which are occupied by water and exchangeable cations, such as sodium, to balance the charge.[12,43] The synthetic material Na-CST crystallises with the sitinakite topology and has tetragonal crystal

structure.[43] The pores are highly selective for Cs^+ and Sr^{2+} which can be seen in **Figure 1.1**.[12,13,43–45]

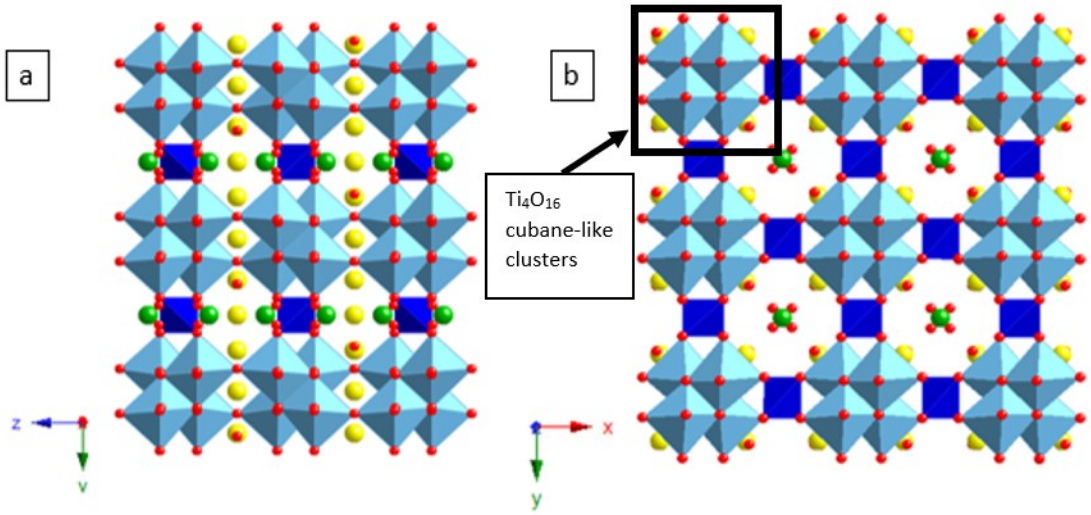

Figure 1.1 *Crystal Structure of CST, view down [100] (a) and [001] (b). Light blue octahedra represent: [(Ti/Nb)O_6], dark blue tetrahedra: SiO_4, green spheres: Cs, yellow spheres: Na and red spheres: O. CIF file adapted from Thorogood et al.*[46]

The ideal formula for CST is $Na_2Ti_2O_3(SiO_4)\cdot 2H_2O$ but it has been found that by varying the composition, the exchange capability can be enhanced. By doping Nb^{5+} cations for some Ti^{4+} ions, the Cs^+ exchange properties are improved.[13,34] The difference in charge of the Nb^{5+} and Ti^{4+}, means that less Na^+ is needed to balance the charge and it is thought the less crowded the tunnels allow more Cs^+ uptake.[42] UOP (Universal Oil Products) and Sandia in a joint collaboration started to produce niobium substituted CST on a commercial level. UOP first made IE-910 (now labelled R9120-P) commercially available which was then developed to IONSIV IE-911 (now R9120-B). IE-911 possessed important improved mechanical properties which made it easier to use in industrial applications which later satisfied a range of test conditions.[17] Essentially it combines the powder form (R9120-P) with a $Zr(OH)_4$ binder to form beads of approximately 400 to 600 µm in size which improves the overall performance in column systems.[17]

1.3 Immobilisation and Final Disposal of Nuclear Waste

For decades thousands of tonnes of nuclear waste has been produced from a number of industries and most awaits final storage.[1,9] Some 56 000 tonnes of HLW is stored in intermediate depositories in the USA alone.[7,47] This has become a huge concern within the nuclear industry due to the vast volumes of wastes being stored in 'interim facilities' with ambiguity regarding the condition of the storage tanks.[13] Wastes stored on an intermediate basis are usually stored as liquids in alkaline or acidic media and it is in this form where the radionuclides are most likely to leach out. The idea behind immobilisation is to create a safer, more durable solid wasteform that will prevent harmful nuclides leaching into the biosphere. [9,48,11,20] When waste is immobilised it is either encapsulated within an inert matrix or incorporated into the lattice on an atomic scale.[9]

Most countries plan to bury the immobilised waste several hundred meters below the ground in 'geological disposal facilities' (GDFs).[1,7,9] The rock formations have or will be carefully selected on their ability to ensure radionuclides do not leach out into the biosphere even if the waste package containers fail, creating a 'multi-barrier' system [1,9]

Ideally immobilised waste must; ensure the safety of radioactive species, achieve a high waste loading, be chemically durable, resistant to radiation, thermodynamically stable, and be compatible with the geological environment.[11,49] Furthermore the production technology to immobilise waste used must be economical, practical and safe.[11,49] Unfortunately no current wasteform satisfies all these requirements although it is accepted that glass and ceramic wasteforms satisfy the majority of these.[11,49] Due to their superior properties, ceramics and glasses are the most appropriate wasteforms for immobilising HLW, whereas cements and concretes are generally used for ILW and LLW. [9]

1.3.1 Glass Hosts

At this time the accepted 1st generation wasteform for HLW are glasses, processed via vitrification. Vitrification technology is well implemented within industry and for the past 50 years vitrification plants in the UK, Germany, Italy, Canada, USA, India, Japan and the former USSR have been immobilising HLW into glasses.[9] Glasses dissolve the majority of HLW at waste loadings of up 30 % and the final wasteform usually demonstrates excellent chemical, thermal and radiation resistance and is also mechanically stable making it an ideal wasteform. [9,11] Furthermore the glass matrix can mostly accommodate the varied composition that is HLW and the subsequent fission products that will be produced over time. [9,11]A number of glasses have been studied including silicate glasses, borosilicate glasses, phosphate glasses and rare earth oxide glasses.

In early work with silicate glasses in the 1950s, the processing temperatures were very high,[9,11] causing problems with the more volatile species found in nuclear waste such as caesium. To rectify this, the silicate composition was changed with the addition of boron oxide giving the system Na_2O-B_2O_3-SiO_2, known as borosilicate glass.[11] This lowered the processing temperature and it was also found that adding Li_2O further decreased the temperature. [11]

Despite glasses being selected as primary HLW forms, in particular borosilicate glasses, there are some issues regarding the solubility of some sulphates, molybdates and other constituents of nuclear waste.[11] These species do not fully dissolve into the glass matrix and their presence may cause the formation of a 'yellow phase' which consists of a mixture of metal molybdates, sulphates and chromates.[11] This can concentrate elements such as Cs and Sr and can have a dramatic effect on the leach rates.[11]

As well as borosilicate glasses, other glass formations such as phosphate glasses have been studied. It was discovered that phosphate glasses are able to dissolve such substituents as sulphates and molybdates, however it was later found to have low thermal stability and poor chemical durability.[9,11] Rare earth oxide glasses have also been studied as a result of their increased solubility for Pu and U compared to borosilicate glasses.[9]

Despite glass being the current selected wasteform for the immobilisation of HLW, it is accepted by geochemists that on exposure to ground waters in depositaries, waste glasses will likely disintegrate especially at elevated temperatures.[48] This would no doubt cause the leaching of harmful substances into the biosphere. As a result, a number of other wasteforms have also been studied which may possess more suitable properties for geological disposal.

1.3.2 Ceramic Hosts

Ceramic wasteforms have also been recommended for HLW immobilisation on account of being extremely chemically durable.[11] Despite this, there is no current infrastructure built within industry for this kind of immobilisation.[9] Ceramic hosts can be in the form of single phase or multiphase systems.[11] Titanate ceramics have received the most attention of all the ceramic hosts, the most well-known example is the multi-phase titanate ceramic known as SYNROC (SYNthetic ROCk). If borosilicate glass is considered the first generation wasteform, SYNROC is certainly the second.[9]

SYNROC was first developed by Ringwood and others in Australia in the 1970s.[48] It was envisaged that SYNROC could be a much improved wasteform compared to borosilicate glass due to its superior leach rate properties.[48] Different types of SYNROC have been tailored to immobilise particular HLW depending on the source of the waste.[48,50] For example SYNROC-C is the chosen formulation for the immobilisation of spent fuel

from commercial power reactors whereas SYNROC-D is selected for defence waste immobilisation.[48] Normally the phases include titanium oxide (rutile), hollandite, zirconolite and perovskite.[9,11,31,48,50]

Each individual phase in SYNROC is designed to incorporate different components of HLW.[48] Hollandite with the formula $BaAl_2Ti_6O_{16}$ can host Cs^+, Ba^{2+}, Rb^+, K^+, $Cr^{3+}$and Sr^{2+}. The Ba^{2+} can be replaced by Cs^+, Rb^+ and K^+. The Al^{3+} can be replaced by other trivalent cations such as Cr^{3+} and Ga^{3+} or by a combination with other tetravalent and divalent cations.[51–53] ^{137}Cs is one of the most problematic radionuclides produced from the fission process and hollandite is the primary candidate for a ceramic host for ^{137}Cs. Importantly, studies have shown that hollandite can retain $^{137}Ba^{2+}$, the decay product of ^{137}Cs which is crucial for the long term mechanical integrity of the wasteform.[48,54–56] It is reported that hollandite is chemically durable and therefore it is expected that it will perform well within an GDF.[48,50]

The zirconolite phase has the formula $CaZrTi_2O_7$ and can incorporate Th, Pu and U and also other tetravalent actinides. U^{4+} and Th^{4+} can substitute for either Ca^{2+} or Zr^{4+}, where U^{4+} favours the Zr^{4+} site and Th^{4+} heavily favours the Ca^{2+} site, a preference dictated by ionic radius. Like hollandite, zirconolite has demonstrated the ability to retain fission products and be highly stable in GDFs.[48,57,58]

The perovskite phase ($CaTiO_3$) is able to play host to a number of elements from radioactive waste including a number of rare earth metals and trivalent actinides. Evidence in nature suggests perovskite phases have remained stable in the environment for millions of years.[48]

Overall SYNROC demonstrates to be an excellent final waste for the immobilisation of HLW. Its credentials are somewhat enhanced through simply observing how the phases

or analogues of the phases have naturally immobilised radioactive species for thousands years in the environemnt.[48] It also offers high wt. % loadings, high radiation and thermal resistance and clear improved leach rate performance in hydrothermal conditions over borosilicate glasses.[31,48,50]

1.3.3 Ceramic-glass Hosts

Processing ceramic wasteforms is generally more expensive than that of glasses however ceramics do more often give more chemically durable wasteforms.[9] A glass-ceramic composite could therefore have a number of advantages as an intermediate between glasses and ceramics. The manufacturing process of glass-ceramics is far simpler compared to traditional ceramics, and the cost is lowered as a result.[9] The negative properties that are associated borosilicate glass are improved giving increased thermal stability and better mechanical properties.[9] With a glass-ceramic host, a more diverse HLW composition can be accommodated which would widen the possible application for this type of wasteform.[9]

1.3.4 Cement and Concrete Hosts

Cement and concrete hosts are normally only used for LLW and ILW.[59] This is mainly because of the amount of water present in the host material. Waste of a more 'active' nature can cause the radiolysis of the hydroxyl groups in the cement and concrete, producing H_2. This would eventually cause the mechanical breakdown of the wasteform decreasing the chemical durability dramatically. Furthermore, some constituents of nuclear waste can prevent the cement from hardening sufficiently. Despite the issues, the processing can be done at low temperatures, it is cheap and is readily available.[9]

1.4 Processing Techniques

Currently the two suggested waste immobilisation techniques are vitrification into glass for HLW and cementation for ILW.[14] Vitrification plants are immobilising waste

worldwide such as the Sellafield site (Cumbria, UK) and the Savannah River Plant in (South Carolina, USA).[9,14,60] Immobilisation into glasses has dominated industry thus far, with borosilicate glass and phosphate the preferred wasteforms, [49] however more recently processing glass-ceramic and ceramic wasteforms have become increasing popular due to the superior properties over glass wasteforms.[9,11,14,48] Methods of immobilising glasses, ceramic and glass-ceramic wastes include traditional vitrification, sintering and powder methods, sol-gel processing, microwave processing and HIP (Hot Isostatic Pressing).[9,10,14,61–63]

Vitrification and melting plants are well implemented in industry have been used extensively to process HLW into glasses. [9,10,14,60] Vitrification can be carried out in many ways including pot processing, continuous melting processes using both induction furnaces and joule-heated ceramic melters and cold crucible induction processes.[10] The process essentially involves firstly calcining the HLW to oxides, adding the waste to a glass frit and then heating. Swirling and repeated melting techniques are often used to ensure the waste is homogenous. Melting and vitrification has only really used to produce glass wasteforms rather than ceramics.[9,10]

Powder processing and sintering methods have been useful where lower temperature processing methods are required. Sintering can reduce the processing temperature which can be advantageous especially when dealing with volatile fission products such as Tc and Cs.[9,10,64] Sintering methods can be used to process glass, glass-ceramic and ceramic wasteforms.[9,10,64]

Sol-gel methods can be used to process glass, glass-ceramic and ceramic wasteforms.[9,65] These alternative ‘wet’ chemistry routes offer a number of advantages over conventional sintering methods. This method yields well reacted and homogenous products

and the choice of reactants may mean the processing temperatures can be lowered which may assist where volatile fission products are involved. [9]

Microwave processing has been a familiar technology for over 65 years, but it has only really been studied for immobilisation purposes in the last 25 years.[9,10,66] This method has been used for a number of different materials including ceramics, glasses and glass-ceramics.[67–69] Advantages of this technique over traditional powder methods is that heat is generated throughout the bulk of the material meaning quicker processing times with uniform heating which in turn creates homogenous wasteforms.[9,10,66]

Hot isostatic pressing (HIP) is able to immobilise a variety of nuclear waste into dense, robust wasteforms.[9,10,14] HIP is a fairly new technology for the nuclear waste industry and it is likely that this process will play a supplementary role to the more established immobilisation techniques already implemented in the industry, such as vitrification and cementation.[14] HIPing for the time being will most likely be used for the immobilisation of waste that currently falls outside the remit of conventional processing techniques, however there can be no doubt that HIP will play an important role for future nuclear cycles.[14]

HIPing operates through the application of both temperature and pressure through the use of an inert gas on a feed that is in a hermetically sealed metal can.[14] The HIP process offers a number of advantages making it suitable for processing to final wasteforms. There is minimal secondary waste, a near 100 % dense monolith is produced, there are usually large associated volume reductions, the process is insensitive to the particular properties of the wasteform and the closed nature of system means no volatile species are lost in the process.[14,63] This could be particularly important in this study due to highly volatile caesium at elevated temperatures.[54] There is some doubt however to how and to what extent the wasteform interacts with the container under HIPing conditions.[14,63] HIPing has already

been studied for the immobilisation of spent exchangers such as clinoptilolite [28] and Cs-IONSIV [34,70], a range of Pu containing wastes at the Sellafield site [71–73], other volatile wastes such as Tc [54] and also HLW from wastes at ANSTO produced from the production of Mo^{99}.[74]

1.5 Scope of Study

The separation and immobilisation of ^{137}Cs is a crucial process as it is one of the most problematic radionuclides produced from the fission process. Not surprisingly, there has been much incentive to develop suitable host materials for Cs immobilisation, particularly ones that can withstand the high heat and radiation output from ^{137}Cs and also accommodate for the decay product, $^{137}Ba^{2+}$. In this work experimental and computational studies have been carried out to determine if there is any Ba solubility in a new Cs-wasteform, $Cs_2TiNb_6O_{18}$. A previous study discovered that this phase was major Cs-containing phase after Cs-loaded IONSIV was HIPed. Following this, a series of Sr-loaded IONSIV materials have been thermally converted via calcination (in air) and HIPing. ^{90}Sr like ^{137}Cs, is often separated and immobilised to make it safe on account of its harmful properties. In this work, two processing methods have been carried out and the products have been analysed and subjected to aqueous chemical durability tests.

2 EXPERIMENTAL

2.1 Synthesis

Four different synthesis methods have been used in this study including solid-state, sol-gel, hydrothermal and a modified solid-state synthesis method. All niobium doped CST systems were synthesised via the hydrothermal method and the preferential synthesis for $Cs_2TiNb_6O_{18}$ and the related Ba doped systems was the conventional solid state and the modified solid-state methods.

2.1.1 Solid-state and sol-gel reactions

For the majority of this study, the main synthesis method has been the solid-state (ceramic) method. This method is one of the more traditional methods and likely the oldest form of synthesis in the solid-state field. The process is simple and is a direct method to form the desired materials. The process involves mixing two or more stoichiometric powders followed by heating to high temperatures, usually between 500-2000°C. The solids require high temperatures to provide enough energy to drive them to react, as they will not react at low temperatures, even if it is thermodynamically favourable. Inhomogeneity and getting starting materials to fully react can often be an issue, therefore multiple firings and intermittent grinding/mixing are required.[75]

Sol-gel synthesis provides an alternative method to solid-state synthesis and has been used expansively in materials science to make a range of different materials, including ceramics. The basic process involves sol preparation, sol gelation, solvent and then a final high temperature firing step.[76] The ‘sol’ is a colloidal suspension of particles in a liquid and the precursors to a sol are usually hydrolysed metal oxides in a solvent. The gel is then formed in an aging step from a series of hydrolysis and condensation reactions. The solvent is then removed via an evaporation step and a final high temperature firing step yields the

final product.[76] Sol-gel offers a number of advantages over the solid-state method including better homogeneity, highly pure products and also the firing temperatures are often lower.

2.1.2 Solid-state sealed tube method

Where Ba-doped $Cs_2TiNb_6O_{18}$ samples containing Nb^{4+} and Ti^{3+} were concerned, a modified solid-state synthesis had to be devised due to difficulties controlling oxidation in the standard solid-state synthesis method described in **section 2.1.1**. This new method allowed the high temperature heating required for the synthesis but also prevented Nb^{4+} and Ti^{3+} from oxidising. This method is outlined in a schematic presented in **Figure 2.1** and to begin with the starting materials (stochiometric powders) were well ground and placed in inside an alumina (Al_2O_3, open one end tube) crucible which was then placed in a quartz (SiO_2) tube (open one end) **(Step 1 and 2).** The alumina crucible was crucial to prevent Cs contacting the quartz tube during the reaction. Following this, a Young's tap was placed on the end of the quartz tube and the tap opened. The tap was then attached to a high-vacuum pump and the whole system was evacuated for 2-3 hours **(step 3)**, the tap was then shut (leaving the tube under vacuum). Then the tap and tube were then removed from the vacuum pump **(step 4)** and the quartz tube sealed (just above the sample) using a oxyacetylene gas torch. The tube (still under vacuum) was then placed in the furnace and fired without any concern of oxidation **(step 5)**.

Where the Cs and Ba sources for reactions were $CsNO_3$ and $Ba(NO_3)_2$ respectively, the method described in **Figure 2.1** had to be changed slightly. As these nitrates decompose, (550°C for $Ba(NO_3)_2$ and 555°C for $CsNO_3$) oxygen and nitrogen dioxide are released (**Equation 2.1** and **Equation 2.2)**. [77] Therefore when inside a sealed tube (which has a relatively small internal volume), the decomposition products will cause the tube to explode at high temperatures.

$$Ba(NO_3)_2 \rightarrow BaO + 2NO_2 + \frac{1}{2} O_2$$

Equation 2.1 *Thermal decomposition of Barium Nitrate*

$$CsNO_3 \rightarrow CsO + NO_2$$

Equation 2.2 *Thermal decomposition of Caesium Nitrate*

To solve this issue, the nitrates, along with the other starting materials in the desired ratio, (except NbO_2 and Ti_2O_3) were put in an alumina crucible and placed in a sealed tube much like **steps 1** and **2** in **Figure 2.1**. Then, the powders were subjected to a prior decomposition step at 800°C for 2 hours also under vacuum. The omission of NbO_2 and Ti_2O_3 from this step was vital, as it meant there was no possibility of any in-situ oxidation, as the small amount of oxygen released from the nitrate decomposition could cause Nb^{4+} or Ti^{3+} to oxidise. After decomposition, the quartz tube was unloaded in a glove box and the decomposed powder removed. NbO_2 and Ti_2O_3 were then added, meaning all the starting materials were present in the correct stochiometric ratio, these were then ground together. The material was then added back into an alumina crucible and placed in a fresh quartz tube and removed from the glove box. It was then evacuated and sealed as described previously (**Steps 3** to **5**, **Figure 2.1**). Once the heating step had been carried out (1200°C, for 2 hours) the sample was removed from the tube and the resulting powders appeared dark blue in colour which was a potential indication of Nb^{4+} or Ti^{3+} suggesting that this method is successful in preventing oxidation.

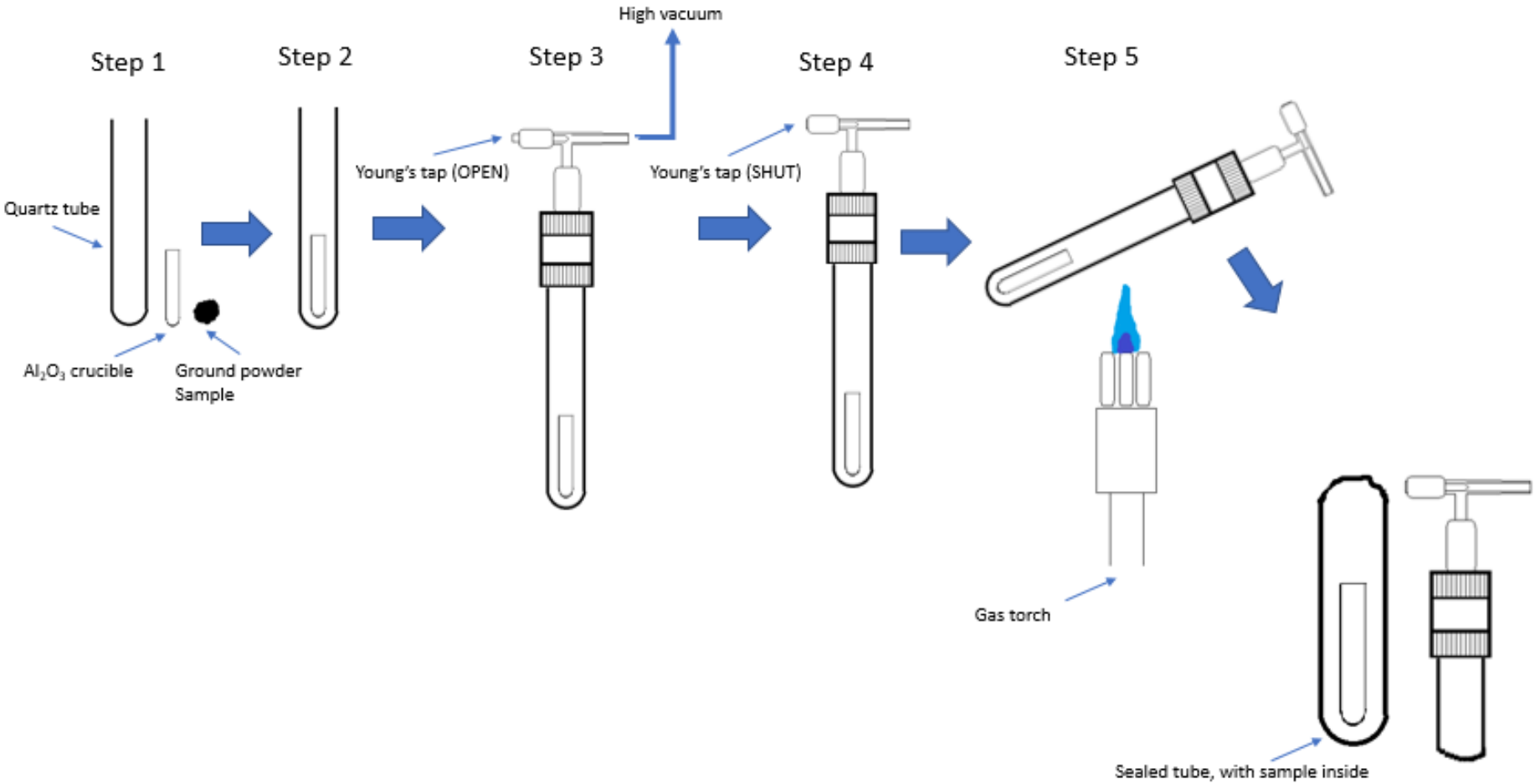

Figure 2.1 *Sealed quartz tube synthesis schematic*

2.1.3 Hydrothermal synthesis

Hydrothermal synthesis has been used in this study to synthesise niobium doped CST. Stainless steel autoclaves (45 and 125 mL) lined with Teflon^{TM} reaction pots were used for synthesis. Traditionally the process involved heating previously mixed and aged aqueous solutions to temperatures up to 270°C for up to 3 days. The sealed reaction environment creates high autogenous pressure at these temperatures which results in highly pure products which are usually of small particle size.

2.2 Crystallography and X-ray Diffraction

X-ray diffraction is one of, if not the most important technique for the analysis of crystalline materials. Crystals are solids that possess a regular periodic arrangement. They consist of a three-dimensional lattice built up with an infinite array of unit cells (repeating units). X-ray diffraction can elucidate much information about such materials, including details of the unit cell, atomic positions, phase identification, phase purity, and particle size.

Seven crystal systems have been derived based on the shape and symmetry of unit cells which are listed in **Table 2.1**. Unit cells are defined by their lattice parameters which includes the lengths of the edges of the unit cell *a*, *b* and *c* and the angles between them: α, β and γ (**Table 2.1**). Combining lattice centrings with the seven crystal systems produces 14 Bravais lattices. The Bravais lattices combined with the 32 crystallographic point groups (set of symmetry operations) produces 230 crystallographic space groups. All three-dimensional crystals must belong to one of the 230 space groups.[78]

Table 2.1 *Seven crystal systems*

System	Unit Cell
Cubic	$a=b=c,\ \alpha=\beta=\gamma=90^o$
Hexagonal	$a=b\neq c,\ \alpha=\beta=90^o, \gamma=120^o$
Trigonal	$a=b=c,\ \alpha=\beta=\gamma\neq90^o$
Tetragonal	$a=b\neq c,\ \alpha=\beta=\gamma=90^o$
Orthorhombic	$a\neq b\neq c,\ \alpha=\beta=\gamma=90^o$
Triclinic	$a\neq b\neq c,\ \alpha\neq\beta\neq\gamma\neq90^o$
Monoclinic	$a\neq b\neq c,\ \alpha=\gamma=90^o\ \beta\neq90^o$

Crystals can be defined as a series of lattice planes known as Miller indices. These planes are labelled (*hkl*). The *h* value cuts the *a* axis at 1/h, the *k* value cuts the *b* axis at 1/*k* and the *l* value cuts the *c* axis at 1/*l*; for example the (222) plane cuts each axis at ½ way along each axis. A set of the same planes are separated by a value denoted 'd' and is usually measured in Å.

X-rays for the diffraction experiment are usually sourced from sealed tubes or rotating anodes. To produce X-rays electrons are released from a hot cathode material (thermionic emission process) and are accelerated through a strong electronic potential under vacuum within the tube. They then collide with a metal anode (such as copper) ionising core electrons. X-rays are emitted when high energy electrons relax to lower orbitals in the copper material. Beryllium windows allow the X-rays to radiate out of the sealed tube.

The X-rays are then monochromated to produced single wavelength X-rays. β-filters (Ni foil in the case of Cu radiation) remove and reduce the intensity of unwanted radiation. Alternatively, single crystals such as germanium can also be used to yield single wavelength X-rays. The X-ray beam is then focused using optics onto the sample which for powder X-ray diffraction will be randomly orientated crystallites which act like an atomic diffraction grating. The X-rays interact with atoms (electrons) of the solid and scatter (diffract) in

different directions. It is assumed for powder samples, that one or more crystallites will be aligned so that their (*hkl*) planes adhere to Bragg's law **(Equation 2.3)**. When diffracted X-rays interfere with one another constructively their intensity increases **(Figure 2.2).** For this to happen the beams must reach the detector (usually scintillation counters or positron sensitive detectors (PSD's)) in-phase as shown in **Equation 2.3** and **Figure 2.2**:

$$n \cdot \lambda = 2d_{hkl} \cdot sin\theta$$

Equation 2.3 *Bragg's Law* [79]

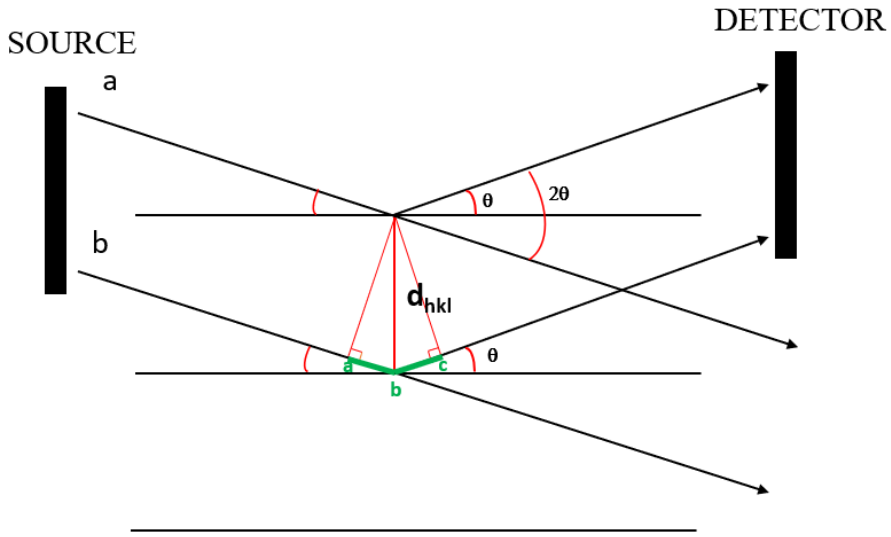

Figure 2.2 *Schematic showing requirements of Bragg's Law being satisfied*

Where there is constructive interference, the intensity of the reflected beam increases and is detected as a function of 2θ. There are many different sets of planes (Miller indices) in a given crystal and therefore a number of reflections are observed from one crystal as Bragg's Law [79] can be satisfied many times. Each set of planes within a crystal contributes one peak to the pattern. For powder samples, each crystallite scatters X-rays individually and diffracted beams with identical *d* values are distributed over cones (Debye-Scherrer cones). These are detected by scintillation counters and will give a series of peaks. Studying the peak position, shape and intensity can allow characterisation of the crystalline material.

2.2.1 Laboratory Diffractometers

In this work the in-house diffraction experiment was carried out on Bruker D8 diffractometer set up in transmission mode. The X-rays are produced from a copper X-ray source and the beam was monochromated using a germanium crystal, delivering Cu $K_{\alpha 1}$ radiation of wavelength of 1.5406 Å. On account of the transmission geometry, absorption corrections were carried out on the data for Rietveld refinements. Variable temperature XRD data were collected in two ways, firstly using a Bruker D8 Diffractometer capable of heating samples to over 1000^{o}C courtesy of a MRI heating stage. This diffractometer is also fitted with a germanium crystal monochromator. Secondly variable temperature XRD experiments were also carried out on a PANalytical Empyrean diffractometer equipped with a Pixcel 2D detector and a Ni filter producing Cu $K_{\alpha 1}$ and $K_{\alpha 2}$ radiation (1.54188 Å). Bruker EVA search match software has been in this study to match phases to the XRD data.

2.2.2 Synchrotron Radiation

When electrons are accelerated at a velocity approaching the speed of light around a ring several hundred meters in circumference, electromagnetic radiation is emitted. The radiation is diverted into booths or hutches where the high energy beam can be used to analyse samples. The use of undulators (or wigglers) and magnets allow varied types of radiation to reach the booths which can be used for many different types of analysis. Synchrotron radiation possess a number of advantages over conventional X-ray sources such as improved signal to noise ratio, have tunable wavelengths and less sample is generally required to carry out the experiments and much better-quality data can be collected over shorter experiment times. In this work, synchrotron data were collected at the Diamond Light Source (Oxford) at the high-resolution powder diffraction beam line (I11). Samples

were loaded into 0.5 mm borosilicate glass capillaries and sealed. The wavelength for this work was set at 0.8257 Å.

2.3 Rietveld Refinement

The Rietveld refinement is a 'whole pattern fitting' method used to analyse powder diffraction data.[80–83] Essentially Rietveld exploits a least squares approach to refine a calculated pattern until it reaches the best possible match or 'be more like' the experimental (observed) pattern. The method allows calculation across a whole pattern using a number of different tuneable parameters. To start a refinement, a relevant crystallographic model including atomic positions, lattice constants and space group is needed so a theoretical model can be calculated. The wavelength and instrument parameters must also be known. By refining a number of parameters such as thermal motion, absorption, peak shape and occupancy the difference can be calculated between the theoretical data and the observed data which is minimised by the least squares method, shown in (Equation 2.4) [80–83]:

$$S_y = \sum_{\mathrm{j}} \mathrm{w_j} \left(\mathrm{y_i} - \mathrm{y_{ic}}\right)^2$$

$$where\ w_j is\ \frac{1}{y_{io}}$$

Equation 2.4 *Residual*

The calculated intensity (Y_{ic}) of any point (i) in the pattern is the sum of contributions from any Bragg peak plus the background. It can be determined using **Equation 2.5:** [80–83]

$$y_{ic} = \sum_{n} \left(S \sum_{K} LM_k |F_k|^2 \phi(2\theta_i - 2\theta_k)\, P_K A \right) + y_{ib}$$

Equation 2.5 *Calculation of intensity. (n: number of phases, S: Scale Factor, L: Lorentz Polarisation correction, M_k: Multiplicity, F_k: Structure factor corrected for thermal motion, ϕ : Peak shape, P_k: Preferred orientation and A: Absorption caused by sample.*

There are a number of ways the 'goodness' of fit can be quantified. These include R_p (R-pattern), R_e (R-expected) and R_{wp} (weighted profile R-factor). R_e and R_{wp} are calculated via **Equation 2.6** and **Equation 2.7** respectively [80–83]:

$$R_p = \frac{\sum |y_i - y_{ci}|}{\sum y_i}$$

Equation 2.6 *Calculation of* R_p

$$R_{wp} = \left(\frac{\sum w_j (y_i - y_{ci})^2}{\sum w_j (y_i)^2} \right)^{1/2}$$

Equation 2.7 *Calculation of* R_{wp}

R_e (R-expected) is defined by **Equation 2.8** [80–83]**:**

$$R_e = \left(\frac{N}{\sum w_i (y_i)^2} \right)^{1/2}$$

$$where\ N\ is\ (N - P - C)$$

Equation 2.8 *Calculation of* R_e

Where w_i is weight factor, y_i is the observed intensity, y_{ci} is the calculated intensity, N is number of observables, P is number of refined parameters and C is the number of constraints used. Using **Equation 2.9** [80–83] we can relate R_{wp} and R_e to give χ^2:

$$\chi^2 = \left(R_{wp} / R_e \right)^2$$

Equation 2.9 *Calculation of* χ^2

The goodness of fit can also be determined by scrutinising the difference curve between the observed and calculated data. Difference curves are standard output on programmes such as GSAS (General structure analysis system). To summarise the Rietveld method is able to provide accurate lattice parameters, atomic positions and can quantify thermal motion behaviour. Furthermore, in samples where more than one phase are present

weight fractions can be calculated from the relative intensities. All refinements were performed using EXPGUI GSAS (General structure analysis system) software. The references for all the crystallographic models used in this study for Rietveld refinement are listed in the **Table 2.2**;

Table 2.2 *References for Rietveld Starting Models*

Phase	Reference
$Cs_2TiNb_6O_{18}$	Desgardin et al (1977) [84]
$Ba_2Ti_3Nb_4O_{18}$	Gasperin (1994) [85]
$Ba_3Nb_4Ti_4O_{21}$	Groult et al. (1976) [86]
$BaTi_3Nb_4O_{17}$	Mezaoui et al. (1986) [87]
$BaTiNb_4O_{13}$	Awadalla (1978) [88]
$Ti_2Nb_{10}O_{29}$	Von Dreele and Cheetham (1974) [89]
$TiNb_2O_7$	Von Dreele and Cheetham (1974) [89]
$BaNb_2O_6$ (Space group 20)	Galasso et al. (1968) [90]
$BaNb_2O_6$ (Space group 14)	Sirotinkin et al. (1974) [91]
$Ba_4Nb_5O_{28}$	Vanderah et al. (1974) [92]
$Ba_{1.24}Al_{2.48}Ti_{5.52}O_{16}$	Aubin-Chevaldonnet et al. (2007) [93]
$Ba_{0.62}Cs_{0.62}Al_{1.86}Ti_{6.14}O_{16}$	Cheary (1987) [94]
$Ba_4Al_2Ti_{10}O_{27}$	Kaduk et al. (1998) [95]
$H_{0.5}Na(Nb_{0.5}Ti_{1.5})O_3(SiO_4)(H_2O)_2$	Tripathi et al. (2003) [96]
$Sr_{0.25}Na(Nb_{0.5}Ti_{1.5})O_3(SiO_4)(H_2O)_3$	Tripathi et al. (2003) [96]
TiO_2 (Rutile)	Baur and Khan (1971) [97]
$(Na_{0.3}Sr_{0.7})(Ti_{0.7}Nb_{0.3})O_3$	Chung and Kim (1995) [98]
$ZrTiO_4$	Troitzsch et al. (2005) [99]
$Zr_5Ti_7O_{24}$	Bordet et al. (1986) [100]
$SrZrO_3$	Ahtee et al. (1976) [101]
SiO_2 (Space group 92)	Kim et al. (2005) [102]
SiO_2 (Space group 154)	Kihara (1990) [103]
SiO_2 (Space group 19)	Barth (1932) [104]
$Na_{13}Nb_{35}O_{94}$	Craig and Stephenson (1971) [105]
$NaNbO_3$ (Space group 59)	Peel et al. (2012) [106]
$NaNbO_3$ (Space group 57)	Hewat (1974) [107]
TiO_2 (Anatase)	Horn (1972) [108]
$Ti_{0.912}Nb_{0.088}O_2$	Okrusch et al. (2003) [109]
$Ti_{0.69}Nb_{0.24}O_2$	Okrusch et al. (2003) * [109]
$Sr_6Nb_{34}O_{91}$	Schueckel and Buschbaum (1986) [110]
$Sr_{0.3}Na_{0.7}NbO_3$	Istomin et al. (2002) [111]
$NaSr_2Nb_5O_{15}$	Lanfredi et al. (2011) [112]
$ZrSiO_4$	Finger (1974) [113]
$SrNb_2O_6$	Marinder et al. (1986) [114]
$Cs_2ZrSi_6O_{15}$	Jolicart et al. (1996) [115]

2.4 X-ray Fluorescence (XRF)

X-ray fluorescence (XRF) was the primary method for elemental analysis in this study. Effectively the principles of XRF are the same to how the X-rays are generated for XRD. Electrons are again accelerated by an applied voltage which strikes a target (such as Rhodium) and when the core electrons of the target are ionised by these electrons, higher energy electrons drop down to a lower energy level emitting X-ray radiation. This radiation is then fired into a sample which can take many forms including pressed pellets, loose powders and fused beads. The X-ray source removes an electron from core orbitals of the elements in the sample and the phenomenon of a higher energy electron dropping to a lower energy orbital gives off characteristic radiation (fluorescent X-rays) of the element involved which is subsequently detected. This allows the quantitative and qualitative analysis of the elements in the sample. The XRF experiments were carried out with a Bruker S8 Tiger X-ray Fluorescence Spectrometer with a Rhodium tube operating at 3 kW. The majority of the samples were measured as fused beads. The data were analysed using Spectra Plus software.

Fused beads were prepared in this study by firstly ensuring all elements were in their highest oxidation states by firing at 800ºC in air. For most samples in this study, the elements were already in the highest oxidation states and therefore did not require the pre-oxidation step. 0.35 g of sample were mixed/ground with 3.5 g of a lithium metaborate (Li_2BO_2):Lithium tetraborate ($Li_2B_4O_7$) mix at a 2:1 ratio. This was then placed in a platinum crucible and heated for 7 minutes at 1050ºC. Ammonium iodide (NH_4I) was then added as the releasing agent and then heated again for a further 7 minutes at 1050ºC. Finally, the mixture was swirled to expel any bubbles and then heated again for 2 minutes at the same temperature. The crucible was removed and allowed to cool. The bead was subsequently removed and analysed using a Bruker S8 Tiger spectrometer.

2.5 Electron Microscopy

Both Scanning electron microscopy (SEM) and Transmission electron microscopy (TEM) studies have been carried out to examine the microstructure of synthesised materials and HIPed wasteforms. As well as studying the microstructure, elemental analysis was also carried out.

2.5.1 SEM/EDX

Scanning electron microscopy (SEM) works by an electron beam striking a sample. The interaction between the sample and incident electron beam gives off many signals which can be detected, and this gives a wealth of information about the material. For SEM, the signals detected are primarily released from the sample surface. Some of the signals are listed in the **Table 2.3** below:

Table 2.3 *Signals irradiated when electron beam strikes sample (SEM)*

Signals from SEM	Information
Secondary electrons	Topographical information
Backscattered electrons	Atomic Number and Topographical information
Auger Electrons	Surface sensitive compositional information
Characteristic X-rays	Compositional Information
Cathodoluminescence (CL)	Electrical information

Topology information of the surface can be gained via the release and subsequent detection of secondary electrons. In this phenomenon, loosely held electrons of the atoms in the specimen are released as the beam scans the surface. The detection is extremely surface sensitive, and the roughness of the specimen surface will alter the number of electrons released i.e. when the beam catches ‘mounds’ or ‘bumps’ on the surface, more electrons will be released, which gives the information about the surface texture. As the signal is weak, the samples in this study have been coated with Au powder.

Topological information can also be acquired from detecting back scattered electrons (BSEs). This signal is produced from elastic interactions and the signal is somewhat stronger than secondary electrons. With BSE, the heavier atoms appear brighter than lighter elements in the image as the atoms with larger atomic number are more likely to produce back scattered electrons. For BSE images, the samples must be polished as irregularity in the surface will cause additional back scattered electrons and distort the image.

Elemental analysis, similar to XRF can also be carried out in the SEM experiment using an energy dispersive X-ray (EDX) detector. When the incident beam strikes the sample, an electron is removed from the inner shells of the atoms in the sample. As an electron from an higher energy electron drops into the vacant shell, characteristic X-rays are released which are subsequently detected.

2.5.2 TEM/EDX

Transmission electron microscopy (TEM) is associated with signals that are transmitted through the specimen. The signals emitted in TEM are listen in **Table 2.4**. Four main interactions are listed, and all contribute to help analyse the microstructure and crystallography of a specimen.

Table 2.4 *Signals produced from TEM and relevant information*

Signals from TEM	Information
Elastically scattered electrons	SAD Point Diagram and Dark Field imaging
Transmitted electrons	Bright field imaging
Inelastically scattered electrons	Kikuchi Diagrams
X-rays	Chemical analysis

The high energy incident beam associated with TEM passes through the specimen and the number of electrons that pass through are inversely proportional to the thickness of the specimen. As the electron beam passes through the sample, the electrons are scattered by

atoms and heavier atoms will scatter electrons more than lighter atoms and as a result, less electrons will get through to the detector and the area will appear darker in a bright field image. Crystallographic information can also be acquired from elastically scattered electrons which yield electron diffractions patterns. Elemental composition information can also be gained from the X-rays released from the atoms in the sample. This works in the same way as EDX in SEM. One advantage of TEM/EDX over SEM/EDX is the area of analysis when detecting X-rays for compositional information is much smaller in TEM, so individual particles can be targeted rather than larger areas encompassing multiple particles.

2.6 Hot Isostatic Pressing (HIPing) and Calcining (air)

As discussed in the introduction section there are a number of techniques and processes used to convert spent ion exchange materials into robust immobilised forms suitable for final disposal. Examples including cementation, vitrification, microwave processing, calcination and HIPing. In this work, calcination and HIPing methods for immobilising spent ion exchange IONSIV has been studied.

HIPing as a process was first used in the 1950s for diffusion bonding of nuclear fuels. [116] It has since found application in a number of different areas including manufacturing of ceramic and metal components. HIPing has also been extensively studied for waste immobilisation and consolidation at ANSTO. [57] It is clear from these studies that HIPing can offer a number of advantages over traditional processing methods. Firstly, in HIP, the can is hermetically sealed, so the process is carried out in a closed environment. As a result, any volatile species that may escape in other processes are not able to. This is especially relevant in this study considering Cs is very volatile. Furthermore, the HIPing process results in a significant volume reduction which is advantageous when considering the size of waste packages for long term disposal facilities. Also, the HIP can itself that contains the

wasteform provides an additional layer to the 'multi-barrier' system, of which the GDF model is based. The HIP can (usually copper or steel) will encase the wasteform which will enhance the chemically durability of the wasteform. In this study the HIPing process was carried out with mild steel HIP cans formed from two different sized tubes. The process is described below:

1. **Can Preparation:** Mild steel tubes were firstly cut into specific lengths. Each can consist of two sections. The bottom part of the can was a wider section of tube (roughly 4 cm length and 1.2 cm inner diameter). A narrow tube (roughly 12 cm in length and 0.6 cm inner diameter) made up the top part.
2. **Tube fabrication:** The two different sized tubes were cleaned up and TIG-welded together. The can was also closed off at one end (bottom section) by welding a plate mild steel plate to the bottom tube.
3. **Sample loading: I**n this study, the powders to be HIPed were subjected to a pre-heating step (heated to 800°C at 10°/min for 12 hours) in order to remove any moisture or organic components. The powder was then added to the HIP can and carefully compacted. Approximately 10 g of sample was placed in each tube and glass wool was placed down the can to prevent sample being lost in the evacuation step.
4. **Evacuation and crimping:** Each tube was attached individually to a high vacuum line and evacuated. Whilst attached to the line, the samples in the tube was heated with a butane gas torch to help remove any residual moisture after the loading stage. The tubes were then crimped twice at the top of tube with a hydraulic clamp and TIG-welded to seal the HIP can.

5. **HIPing step:** The tubes were then placed in the HIP unit. The HIP vessel with cans inside was purged with high purity argon until and compressed until the required pressure was reached. Once the required pressure was achieved the vessel was heated to the required temperature.
6. **Cooling:** At the end of the heating program, the vessel was cooled at rate of approximately 5-10 °C/min.
7. **Cutting and pickling:** Once the HIPing process was complete the cans were cut using a cutting machine equipped with a Al_2O_3 blade. The thickness of cut was dependant on the type of analysis carried out. Once cut, to remove the can, the sections were added to 0.1 M HNO_3 which removed the mild steel leaving the ceramic monolith.

In this study the HIP process operated at 1100ºC, 190 MPa for two hours under argon gas. It was found that a nearly 100 % dense monolithic ceramic sample was produced from HIPing. Once the samples were removed from the HIP unit, the samples were cut and pickled (HIP can removed) and analysed using XRD, XRF, SEM and TEM. Furthermore, specifically cut HIP samples were subjected to MCC-1 chemical durability tests.

As well as HIPing Cs and Sr loaded IONSIV, samples were thermally decomposed in air in a standard muffle furnace at 900, 1000 and 1100ºC for 12 hours. Samples were heated up to temperature at a heating rate of 10ºC/min but no specific cooling rate was set. Alumina crucibles were used as vessels and analysis suggested there was no interaction between sample and crucible on account of no Al impurity peaks being observed in the XRD pattern nor any Al present in XRF analysis. Samples were heated in a fume hood in anticipation of some volatiles and gasses being released in the process.

2.7 TGA / DTA

Thermal gravimetric analysis (TGA) and differential thermal analysis (DTA) are powerful tools to help characterise materials. TGA essentially measures the change in mass of a material as it is heated as a function of time. TGA experiments can be carried out under different gases such as nitrogen, argon and oxygen and run up to temperatures of 1500°C which can help gain an understanding of the thermal properties of a material, such as its thermal stability and water content. TGA can also be coupled with a Mass Spectrometer (MS) which can help identify any gasses released in the heating process. Furthermore, if the conditions are considered, TGA can also be used to understand the oxidation/reduction behaviour of a material. DTA can be used to record exothermic and endothermic events as a function of time. In this study all TGA experiments were carried out using a Netzsch STA 449F1 Jupiter (TGA).

2.8 Computational Techniques

In this work, a series of static atomistic simulations have been carried out to assess the Ba solubility of Ba in $Cs_2TiNb_6O_{18}$. These simulations were carried out using the General Utility Lattice Program (GULP) code [117] and the ions were set to be rigid. Two codes have been used in this study including a Reverse Monte Carlo pair potential fitting code and also a Markov-Chain Monte-Carlo code both of which have been written and developed by a previous group member, Dr Geoffrey Cutts.[118]

2.8.1 Atomic Interactions

Calculations performed in this study are constructed around the Born model of ionic solids in which the lattice is described as an infinite arrangement of non-overlapping point charges. [119] The energy of a system can therefore be described as a sum of contributions from all ions which are dependent on distance. The interactions between all the ions in the

lattice can be complex, but it can be approximated with a number of assumptions which yields **Equation 2.10**, where the contributions of ions to the total energy are decreasing with increasing distance [120]:

$$U = \sum_{i=1}^{N} U_i + \frac{1}{2}\sum_{i=1}^{n}\sum_{j=1}^{n} U_{ij} + \frac{1}{6}\sum_{i=1}^{n}\sum_{j=1}^{n}\sum_{k=1}^{n} U_{ijk}$$

Equation 2.10 *Total energy of the system*

Interactions between pairs of ions in the lattice can be described in two ways, long-range electrostatic interaction Φ_{LR} and short-range interactions Φ_{SR}. These components combine to give **Equation 2.11**[120]:

$$U_{ij}(r_{ij}) = \Phi_{long}(r_{ij}) + \Phi_{short}(r_{ij})$$

Equation 2.11 *Total energy of the system of a pair of ions (i and j), long and short-range energy added together*

The short-range component of **Equation 2.11** almost entirely represents a repulsive interaction, to stop the ions from getting too close together. The long-term component of **Equation 2.11** represents the electrostatic interactions between the ions which can be described by Coulomb's law, shown in **Equation 2.12** [120]:

$$\emptyset_{long}(r_{ij}) = \frac{q_i q_j}{4\pi\varepsilon_o r_{ij}}$$

Equation 2.12 *Long-range interactions, Coulomb's law*

Where q_i and q_j represent the charge of two ions i and j, r_{ij} is the distance between ion i and j and ε_o is the permittivity of free space. Whilst this equation is relatively simple, calculating interactions this way would be computationally expensive as there are a huge number of interactions that must be considered for each ion in the lattice. However, using Ewald's summation [121], the model can be approximated such that there is a short-range interaction and a long-range reciprocal space component. [121–124]

When describing interactions at short-range between a pair of ions, the interactions can either be completely repulsive if the pair of ions being described are either both positive or both negative, or there can be a repulsive component and an attractive component if the ions are oppositely charged (ions that are highly polarizable will have stronger attractions). The repulsive force at short-range is a result of overlap of electron clouds and nuclear-nuclear interactions at very small distances and as atoms move closer together the repulsive forces increase.[120] The attractive component is on account of van der Waals forces (instantaneous dipoles) and has a r_{ij}^{-6} dependence (for atoms *i* and *j)*. In this study, Buckingham pair potentials (**Equation 2.13**), where A, ρ and C are the parameters that are varied, have been used to model the interactions of ions at short-range and this method has been used in many previous studies to describe the interactions of solids. [120,125]

$$\emptyset_{short}(r_{ij}) = A_{ij} exp\left(\frac{-r_{ij}}{\rho_{ij}}\right) - \frac{C_{ij}}{r_{ij}^6}$$

Equation 2.13 *Buckingham Potential*

To reduce computational times, cut-off values have been set to set a distance where the short-range interaction will no longer have any effect. At increased distance, the contribution to the interaction at short-range will be almost zero, therefore calculating these energies is redundant. In this study cut of distances have been set to 10 Å for every interaction accept the oxygen – oxygen interaction which was set at 12 Å.

2.8.2 Pair Potential Derivation

The Buckingham potentials in this work have been derived using code developed by a group member.[118] The derivation was thought necessary instead of using published potentials, in order to better simulate the range of phases required to carry out this study. Further details of pair potential derivation can be found in the computational results section **3.2.9**.

2.8.3 Energy Minimisation

The pair potentials described only approximate the actual material and therefore there will be a number of differences such as atomic positions in the unit cell. As a result, when using the potentials, the structure must be able to move (or relax) to allow the system to reach the lowest energy configuration with respect to the potentials. Each ion is moved iteratively in order to minimise the total force on the system. All the geometry optimisation processes carried out in this study were carried out at constant pressure, but the unit cell values where allowed to vary (i.e. not at constant volume) which helped reduce the overall strain on the system.[120]

2.8.4 Defect Calculations

Having optimised the geometry, defect calculations can be carried out. Once a defect is incorporated into the lattice, the ions closest to the defect will relax and the extent of the relaxation will reduce on increasing distance to the defect i.e. the further an ion is away from the defect, the smaller the perturbation. The Mott-Littleton [126] approximation (often known as the two region approach) has been used in this study to calculate defect calculations. The Mott-Littleton approximation relies on a defect centre being assigned which usually will be the centre point of an impurity or the centre point between two defect sites (defect clusters).[126] From this, two regions are defined, region I and region II. Ions within region I, are said to be strongly perturbed by the defect and the ions in region II are said to be weakly affected by the defect.[126] Region II is split into two distant components, region IIa and region IIb. Region IIb extends to infinity and will not be affected by the defect. The size of the region I and IIa are important, the larger the size of the region, the better the approximation of defect energy, however, large regions will be computationally expensive and timely therefore convergence testing is carried out before hand to calculate suitable region sizes. In

this work, region I (14 Å) is half the size of region IIa (28 Å). Defect calculations are calculated via **Equation 2.14** where $U^{d}_{total}\ (x, \xi)$ is energy of defect region and $U^{p}_{total}(x, \xi)$ is energy of a perfect system.[120]

$$U_{defect}(x, \xi) = U^{d}_{total}\ (x, \xi) - U^{p}_{total}(x, \xi)$$

Equation 2.14 *Calculation of defect energy*

In these studies, defect calculations have been carried out using supercells via the Mott-Littleton method. The defects were incorporated as impurities using the GULP software at infinite dilution and as clusters. Defects have also been incorporated into supercells using a Markov Chain Monte Carlo method of which more details can be found in section **3.2.9.**

3 THE SOLUBILITY OF BARIUM IN A NEW CAESIUM WASTEFORM, $Cs_2TiNb_6O_{18}$

3.1 Introduction

Crystalline silicotitanates (CST) are a group of inorganic ion exchangers that have been used for the removal of Cs and Sr from nuclear waste streams.[12,13,17,41] Since early studies in the 1990s, CST has been developed and engineered by Honeywell UOP (formally Universal Oil Products) into a commercially available ion exchanger known as IONSIV IE-911 (now known as R9120-B).[17] IONSIV has proven to be an excellent exchanger and is highly selective for Cs over a wide pH range and in the presence of a number of other competing ions, such as Na^+.[12,13,17,31] IONSIV is also selective for Sr, but only at neutral to high pH.[127] IONSIV has been utilised all around the globe (mainly for the removal of Cs) and much of this 'spent' material is being stored in specially designed containers across many nuclear sites and awaits final processing and storage. The consolidation and immobilisation of spent IONSIV into a safe and durable wasteform suitable for long term geological disposal is a crucial process. The processing method must be safe, economical, reduce the waste volume and produce a robust wasteform suitable for final disposal.[14] A number of methods have been studied including vitrification, encapsulation in cement and hot isostatic pressing (HIPing).[34,128–130]

It was found in a recent study that HIPing Cs-loaded IONSIV produces a robust wasteform suitable for long term geological storage.[34,130] Not only is the final wasteform chemically durable, but there are a number of advantages associated with the HIPing process. There is a large volume reduction (up to 40%) after HIPing and also the mild steel HIP can forms part of the final wasteform container and therefore contributes to the 'multi barrier system'. Furthermore, the heating process itself is carried out in a closed system, therefore there are no issues with volatile Cs.

The major Cs-containing phase was identified as $Cs_2TiNb_6O_{18}$, a pyrochlore analogue.[84] $Cs_2TiNb_6O_{18}$ has the potential to be an excellent wasteform for the immobilisation of Cs, demonstrating excellent Cs leach rates and thermal stability, a vital requirement for any wasteform.[34] The Cs leach rates proved far superior to glass wasteforms and compared well to other ceramic Cs-containing wasteforms such as the hollandite phase found in SYNROC.[34,48,50,54–56] The structure of $Cs_2TiNb_6O_{18}$ is shown in **Figure 3.1** and it was thought that the excellent Cs leach rate are a result of the high coordination number (9) of Cs to oxygen (**Figure 3.2**).[34] In the $Cs_2TiNb_6O_{18}$ structure, Ti and Nb are split across two sites, one of which is a special position which are listed in **Table 3.1**.

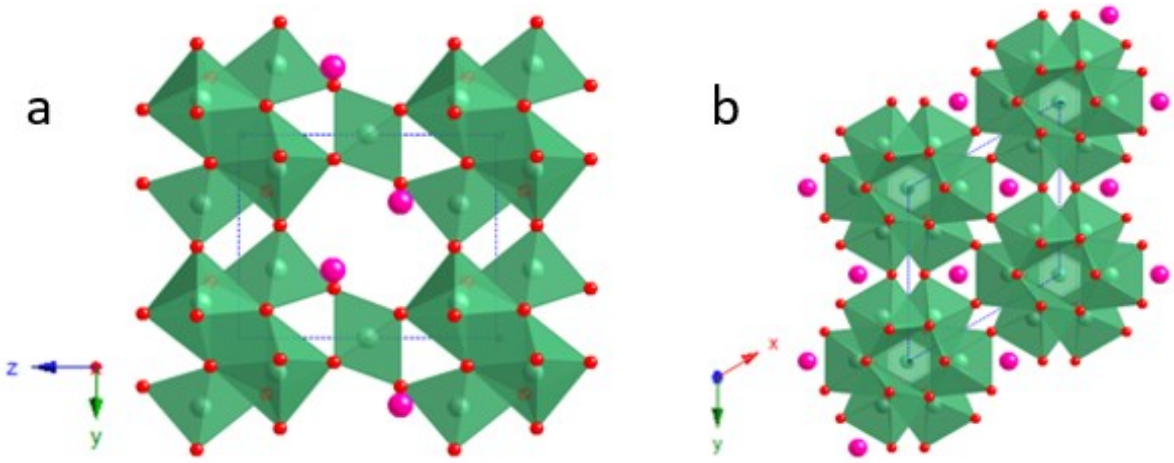

Figure 3.1 *Crystal structure of $Cs_2TiNb_6O_{18}$. Sourced from Desgardin et al.[84] a: View down [100] direction. b: View down [001] direction.*

Table 3.1 *Crystal structure of $Cs_2TiNb_6O_{18}$. Taken from reference* [84]

$Cs_2TiNb_6O_{18}$					
			Atomic Coordinates		
Atom	Multiplicity	Occupancy	x	y	z
Cs	2	1	0.3333	0.6667	0.632
Ti (Site 1)	1	0.143	0	0	0.5
Nb (Site 1)	1	0.857	0	0	0.5
Ti (Site 2)	6	0.143	0.17	-0.17	0.1457
Nb (Site 2)	6	0.857	0.17	-0.17	0.1457
O 1	6	1	0.447	-0.447	0.16
O 2	6	1	0.861	-0.861	0.11
O 3	6	1	0.12	-0.12	0.37

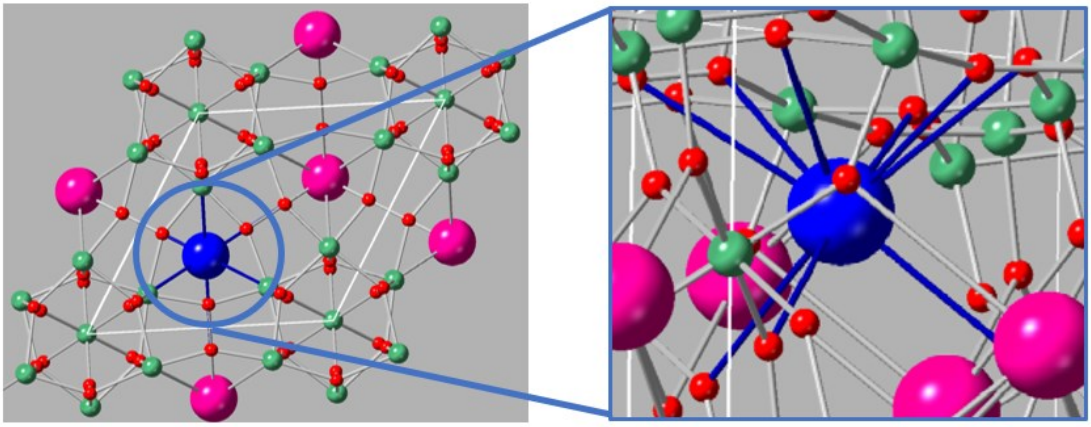

Figure 3.2 *Cs site (blue sphere) (9 coordinate) close-up in $Cs_2TiNb_6O_{18}$, taken from reference* [84]

Due to the nature of radioactive waste, it must be considered how any wasteform will respond to the decay of radionuclides. It is well understood that glass wasteforms are able to accommodate a wide range of fission products due to their versatile matrices.[9,11] In ceramics the issue of transmutation is less clear. For these types of wasteforms, radionuclides are usually immobilised into a host phase on an atomic scale, on specific crystallographic sites. Therefore, the transmutation product of any radioisotope may not be suitable for the same crystallographic site. If the transmutation product, in this case $^{137}Ba^{2+}$, cannot be retained in the structure it may cause fracturing and affect the overall mechanical stability of the wasteform which may ultimately cause an increase in the Cs leach rates.

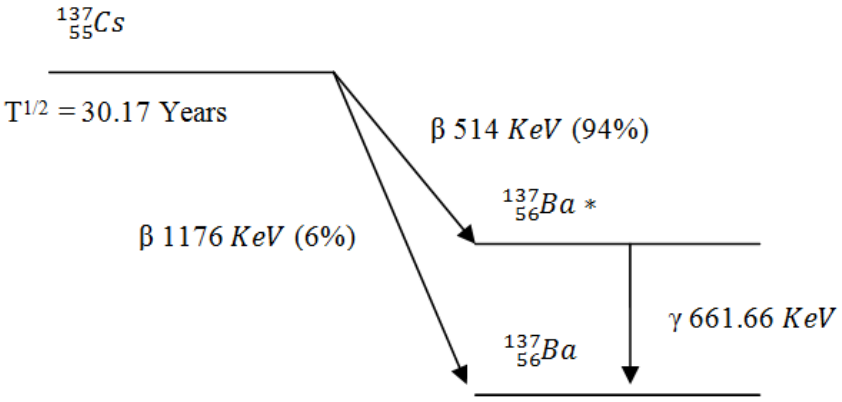

Figure 3.3 *Transmutation of ^{137}Cs. Adapted from reference* [131]

The transmutation of ^{137}Cs is shown in **Figure 3.3**, it is a beta-gamma decay process and has a half-life of 30.17 years.[131] Around 94% decomposes by beta decay to the short lived ^{137m}Ba which finally decays to $^{137}Ba^{2+}$ via gamma emission, the other 6% directly decays to non-radioactive $^{137}Ba^{2+}$ via beta decay.[131] Therefore, for Ba^{2+} to remain incorporated in the host phase, there must be a charge compensating mechanism within the wasteform itself. This process has been reported successful in a number of other Cs containing wasteforms including hollandite (one of the main components of SYNROC) and pollucite.[55,56,132,133]

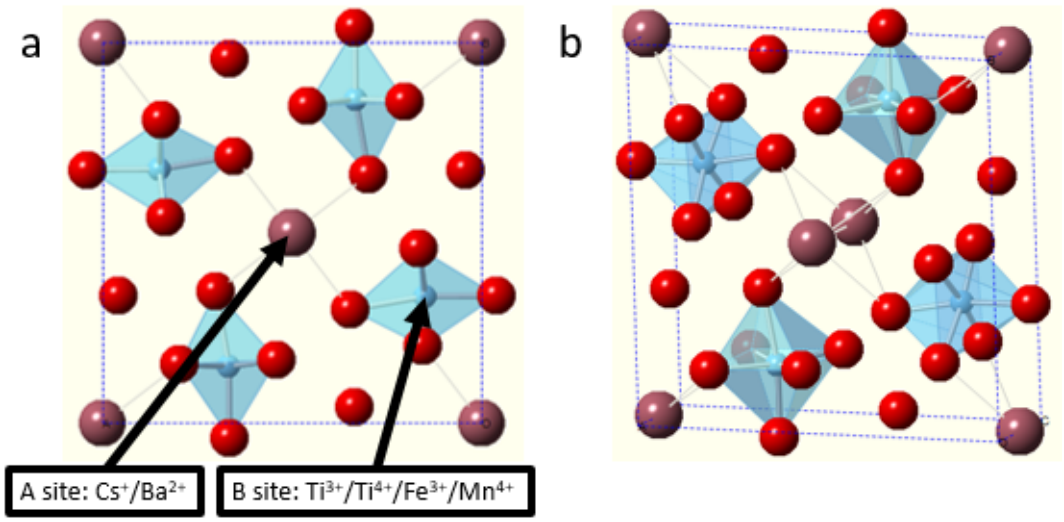

Figure 3.4 *Structure of Hollandite. Sourced from Leinekugel-le-Cocq-Errien et al (2007).*[56] *a: view down [100] direction. b: angled view*

Hollandite, with formula $Ba(Mn^{3+},Mn^{4+})_8O_{16}$ has been extensively studied as a host phase for radioactive Cs and it is reported to be able to accommodate the transmutation product of ^{137}Cs, mainly owing to the fact that the hollandite mineral is a Ba containing phase. **Figure 3.4** shows the structure of hollandite, it is tetragonal and crystallises in the space group *I*4/*m*. The Cs^+/Ba^{2+} cations are found on the A site and Mn^{3+},Mn^{4+}, Ti^{4+}, Ti^{3+} and Fe^{3+} can be found on the B site (labelled in **Figure 3.4**). Charge balance can be achieved after transmutation by the β^- particle released in the decay process simultaneously reducing another species in the structure such as Ti^{4+} to Ti^{3+} or Fe^{3+} to Fe^{2+}. [9,11,31,48,50,55,56]

Caesium titanium silicate ($CsTiSi_2O_{6.5}$) is a titanium analogue of pollucite ($CsAlSi_2O_6$), a naturally occurring mineral (structure shown in **Figure 3.5**).[132,133] It has a zeolite like framework with small pore openings and the material demonstrates excellent durability demonstrating good leach rates and thermal stability, therefore a potential candidate for the Cs immobilisation. [132,133] Whilst $BaTiSi_2O_{6.5}$ does not exist, it has been reported that Ba can be incorporated into the $CsTiSi_2O_{6.5}$ structure through a charge compensating vacancy mechanism giving the formula $Cs_{0.5}Ba_{0.25}\square_{0.25}TiSi_2O_{6.5}$ (where □ is a vacancy) . [132]

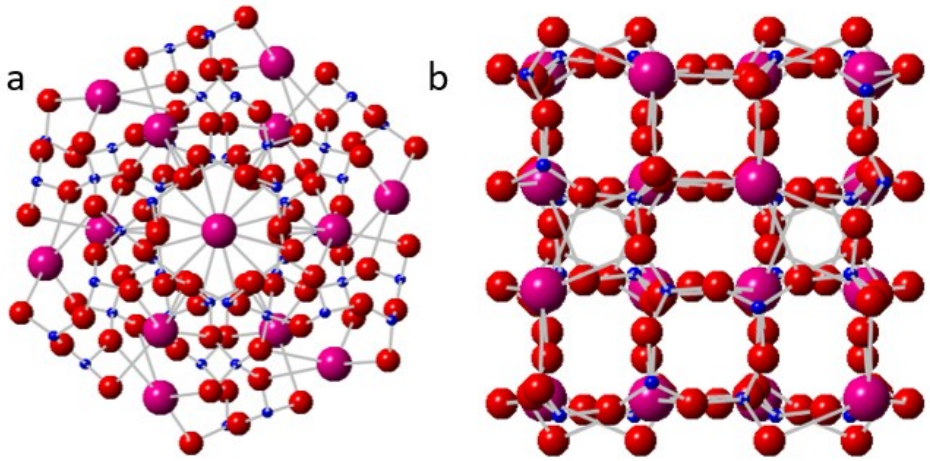

Figure 3.5 *Structure of Pollucite. Sourced from Yanase et al (2005)* [134]*. a: View down [111] direction. b: View down [100] direction.*

It was thought that a similar process that occurs in hollandite could take place in the $Cs_2TiNb_6O_{18}$ phase. As $^{137}Cs^{+}$ decays to $^{137}Ba^{2+}$ and releases a β^- particle, Nb^{5+} or Ti^{4+} in the structure, could reduce to Nb^{4+} or Ti^{3+} respectively acting as 'electron traps' and balance the overall charge which may keep Ba in the structure.[34] To try and determine whether Ba could be incorporated this way, experimental and computational studies of Ba doped $Cs_2TiNb_6O_{18}$ materials have been carried out. Four co-substituted mechanisms (simultaneous metal reduction for charge balance of Ba^{2+} for Cs^{+}) have been tested and materials based on these synthesised and analysed: Ti^{4+} for Nb^{5+}, Ti^{3+} for Ti^{4+}, Nb^{4+} for $Nb^{5+}$and a mix of both Ti^{3+} for $Ti^{4+}$and Nb^{4+} for Nb^{5+}. As well as these samples, attempts have also been carried out by doping Al^{3+} and Ga^{3+} for Ti^{4+} to balance the charge when Ba is doped into the structure. A number of techniques including X-ray diffraction (XRD), X-ray fluorescence (XRF) and transmission electron microscopy (TEM) experiments were used to confirm whether Ba had substituted into the target phase. Furthermore, atomistic modelling was then carried out using the General Utility Lattice Program (GULP) to assess the energetic feasibility of each scheme.

3.2 Experimental

3.2.1 Synthesis of $Cs_2TiNb_6O_{18}$ and Ba derivatives

Both sol-gel and solid-state (ceramic) methods based on techniques outlined by Balmer et al. [135] and Desgardin et al. [84] respectively to synthesise $Cs_2TiNb_6O_{18}$. For the solid-state method the correct ratio of Nb_2O_5 (or NbO_2 for a Nb^{4+} source), $CsNO_3$, TiO_2 (Ti_2O_3 for a Ti^{3+} source) and $Ba(NO_3)_2$ (for the barium samples) were weighed out and ground together for 10 minutes. For the trivalent doped samples, Ga_2O_3 and Al_2O_3 oxides were used as Ga^{3+} and Al^{3+} sources respectively. The powder was then placed in an alumina crucible and heated in a furnace to 1200ºC at 10ºC/min and held for 12 hours. Multiple firings with subsequent grinding were carried out to encourage particle integration as mobility in the solid-state is low and after the first firing the powder were pressed into 13 mm pellets to help with particle integration, 4 to 5 firings were required to get the starting materials to fully react. However, the high temperatures used for the synthesis of $Cs_2TiNb_6O_{18}$ is less than ideal due to the volatility of Cs.

For the synthesis of oxygen sensitive samples (i.e. samples containing Ti^{3+} and Nb^{4+}) a modified solid-state method was used which is described in section **2.1.2**. $CsNO_3$ (or Cs_2TiO_3, $Ba(NO_3)_2$ (or $BaNb_2O_6$), (or Cs_2TiO_3 and $BaNb_2O_6$), Nb_2O_5 and TiO_2 were added together at the desired ratio, ground and then loaded into an alumina tube crucible and placed inside a quartz tube. The material was then heated under vacuum to 800°C at 2°C/min and held for 2 hours to fully decompose the nitrates. Once this decomposition step had been completed, NbO_2 and/or Ti_2O_3 (Nb^{4+} and Ti^{3+} sources) were added to the mixture at the correct stoichiometric ratio in an inert environment. The powder was then ground and added to an alumina tube crucible and placed in a new quartz tube. The tube was then evacuated and sealed and heated in a furnace to 1200ºC at a heating rates of 10ºC min^{-1} and held for 2

hours. The pre-decomposition step to decompose the nitrates was not necessary when Cs_2TiO_3 and $BaNb_2O_6$ were used as starting materials. More details of this synthesis method are discussed section **2.1.2**.

The sol-gel method was also used to synthesise $Cs_2TiNb_6O_{18}$. Better element mixing in the sol-gel method results in the need for less firings and grinding and therefore this method would be better suited for this work due to the volatility of Cs. To create the sol, $Nb(OEt)_5$, $Ti(_iOC_3H_6)_4$ and $Ba(NO_3)_2$ (for the barium doped samples) were added to a small amount of ethanol. Then, 0.5mL measures of CsOH/EtOH were added at 15 minute intervals. Once all the CsOH/EtOH was added a final 1mL portion of distilled water was added. The solution was then aged at room temperature overnight. Following aging, the mixture was filtered and washed with a generous portion of distilled water and dried overnight at 100ºC. The resulting powder was then pressed into a 13 mm pellet and fired in air in an alumina crucible at 1200ºC at a 10ºC/min heating rate for 12 hours.

3.2.2 Synthesis of Ba hollandites

A series of Ba and Cs/Ba hollandites have been synthesised via a metal citrate combustion method. [136,137] The citrate solutions were made by mixing $Ba(NO_3)_2$, ($CsNO_3$ for Ba/Cs mixed sample) and $Al(NO_3)_3.9H_2O$ with citric acid in a molar ratio of one metal cation to 4 citric acid giving (Ba^{2+} or Cs^+) : 4 citric acid and Al^{3+} : 4 citric acid. A Ti^{4+} / citrate solution was prepared by dissolving $Ti(iOC_3H_6)_4$ in a solution of citric acid and hydrogen peroxide in the molar ratios Ti^{4+}: 3 citric acid : 10 H_2O_2. The resulting solutions were then mixed in the required ratios and heated to 50 ºC to remove the majority of the water. Then the precursors were fired at 900 ºC for 30 minutes followed by quick cooling in air. The calcined powders were then ground and pressed into pellets. The resulting pellets were then fired in a Al_2O_3 crucible at 1250 ºC for 3 hours.

3.2.3 X-ray diffraction (XRD) and Rietveld Analysis

In this work the in-house diffraction experiments were carried out on two different diffractometers. Firstly, a Bruker D8 Advance (X-ray) diffractometer using Cu $K_{\alpha 1}$ (1.5406 Å) radiation in transmission mode, fitted with a Lynx Eye Si-strip detector was used. Data were collected in the 2θ range 5° to 90° or 20° to 38° at a step size of 0.0198°. The transmission geometry meant that for each sample where Rietveld analysis was required, an absorption correction was applied to the data before refinements could be carried out. Secondly a Bruker D2 PHASER diffractometer operating in reflection mode equipped with a Co tube ($K_{\alpha 1}$ 1.7890 Å, $K_{\alpha 1}$ 1.7928 Å) was used. Rietveld analysis of XRD data was performed using EXPGUI GSAS suite. [138,139] Details of each Rietveld refinement can be found in the appendices including the live plots for each sample. When phases existed in low concentrations (particularly Ba impurities) the atomic positions, thermal parameters and occupancies were not refined.

3.2.4 Variable Temperature X-ray diffraction (XRD) Studies

Variable temperature XRD was carried out on two different diffractometers. Firstly, on a Bruker D8 diffractometer (reflection mode) equipped with a MRI heating stage and germanium crystal monochromator, producing Cu $K_{\alpha 1}$ radiation (1.5406 Å). Experiments were also carried out on a PANalytical Empyrean diffractometer equipped with a Pixcel 2D detector and a Ni filter producing Cu $K_{\alpha 1}$ and $K_{\alpha 2}$ radiation (1.54188 Å).

3.2.5 X-ray Fluorescence (XRF)

Elemental analysis was carried out using a Bruker S8 Tiger Wavelength Dispersive X-ray Fluorescence (XRF) spectrometer. All samples in this chapter accept the hollandite materials and the Al^{3+}/Ga^{3+} doped $Cs_2TiNb_6O_{18}$ samples were made into fused Li – borate

glass beads prior to analysis. The hollandites and Al^{3+}/Ga^{3+} doped $Cs_2TiNb_6O_{18}$ materials were well ground and pressed into pellets using a cellulose binder.

3.2.6 Thermogravimetric Analysis / Differential Thermal Analysis (TGA/DTA)

In these studies, thermogravimetric analysis experiments were carried out on a Netzsch STA 449F1 Jupiter Thermal Analyser. Samples (30-60 mg) were heated to 1000 °C at of 5 °C/min under an oxygen atmosphere.

3.2.7 Scanning Electron Microscopy (SEM)

Secondary electron (SE) imaging and back scattered electron (BSE) imaging were carried out using a Philips XL30 ESEM-FEG with an Oxford Inca 300 EDX system operating at 10 kV. SE image samples were well ground and placed on conductive carbon film and coated with Au. BSE samples were mounted and polished. All SEM work in this chapter was carried out with the assistance of Dr Tzu-Yu Chen (University of Birmingham).

3.2.8 Transmission Electron Microscopy (TEM)

TEM data were collected using a JEOL JEM-2100F equipped with a SEI/BSE detector, operating at 200 kV in STEM mode. Samples were placed in ethanol and dispersed on conductive carbon grids. All TEM work in this chapter were carried at the University of Limerick by Dr Yina Guo (University of Limerick) and Dr Tzu-Yu Chen (University of Birmingham).

3.2.9 Computational Techniques

All atomistic modelling in this work has been carried out using the General Utility Lattice Program (GULP) code. Buckingham potentials were empirically derived using a code that integrates with GULP, previously developed by a group member based on Reverse Monte Carlo (RMC) methodology.[118] Defect calculations have been performed in two ways, firstly using the Mott-Littleton approximation in-built in GULP and secondly using a

Markov Chain Monte Carlo (MCMC) code that also integrates with GULP which was also written and developed by a group member.[118]

3.3 Results

3.3.1 $Cs_2TiNb_6O_{18}$

$Cs_2TiNb_6O_{18}$ is trigonal, a = 7.53 Å, c = 8.18 Å, space group $P\bar{3}m1$. [84] It was synthesised using both solid-state and sol-gel methods. For the solid-state method multiple firings were required to ensure all the starting materials had fully reacted to achieve a pure product **(Figure 3.6).** The XRD pattern for the final product from solid-state synthesis is shown in **Figure 3.7**.

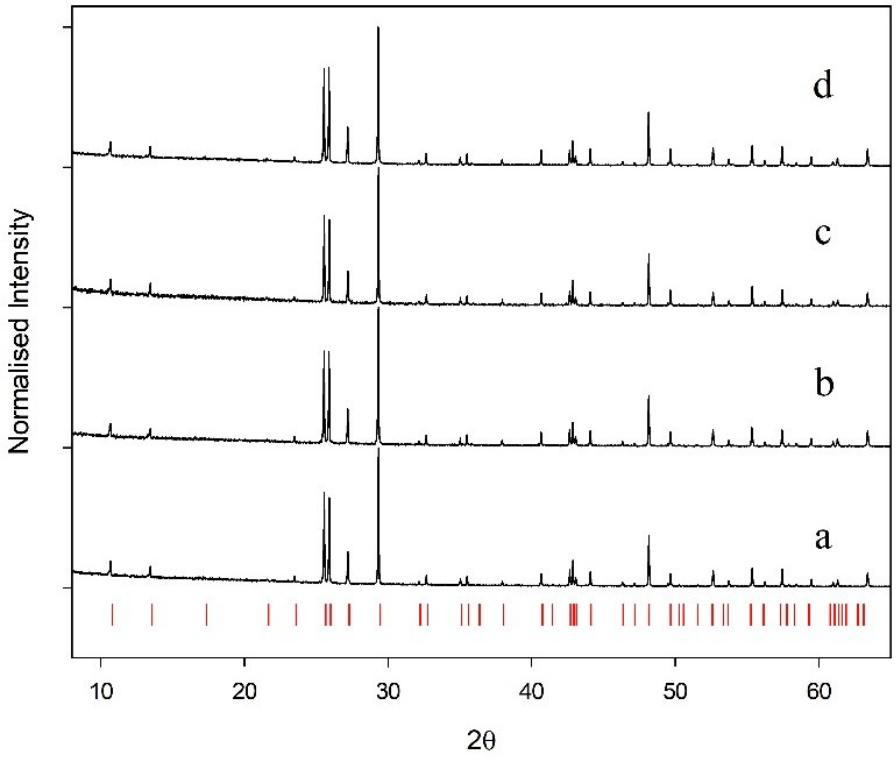

Figure 3.6 *Powder XRD patterns of multiple $Cs_2TiNb_6O_{18}$ firings. Solid-state method. a: 1st firing, b: 2nd firing, c: 3rd firing and d: 4th firing. Red ticks are indexed peaks from the ICDD PDF: 01-070-0674 ($Cs_2TiNb_6O_{18}$)*

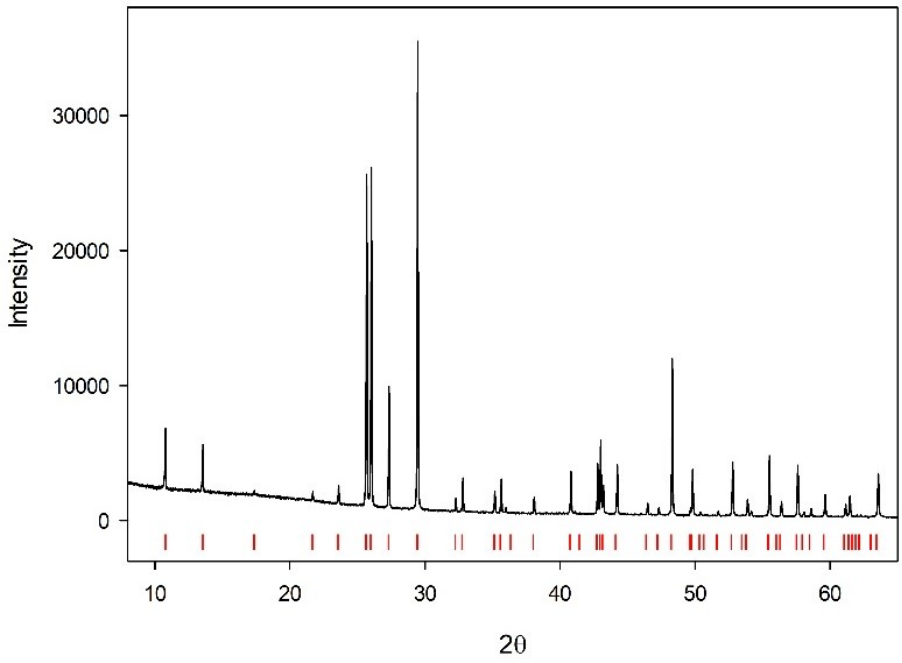

Figure 3.7 *Powder XRD pattern of $Cs_2TiNb_6O_{18}$ (solid-state method). Red ticks: $Cs_2TiNb_6O_{18}$*

Due to the volatility of caesium, it was thought that a multi-firing solid-state synthesis might not be a suitable method. Sol-gel synthesis was therefore also carried out, as this method only required a single firing step, hence less Cs is likely to be lost. However, on inspection of the XRD pattern **(Figure 3.8)**, the product appeared to be less crystalline than the solid-state method, with fewer counts observed for each reflection in the sol-gel pattern (**Figure 3.8**) compared to the solid-state pattern (**Figure 3.7**). Furthermore, the reflections are slightly broader in the sol-gel pattern which is likely because the sample has only been fired once resulting in smaller particles than those produced from solid-state methods, where the samples have been fired multiple times. Rietveld refinement of $Cs_2TiNb_6O_{18}$ synthesised from solid-state sample yielded a better fit than the sol-gel method which was reflected in the R_p and R_{wp} values in **Table 3.2**.

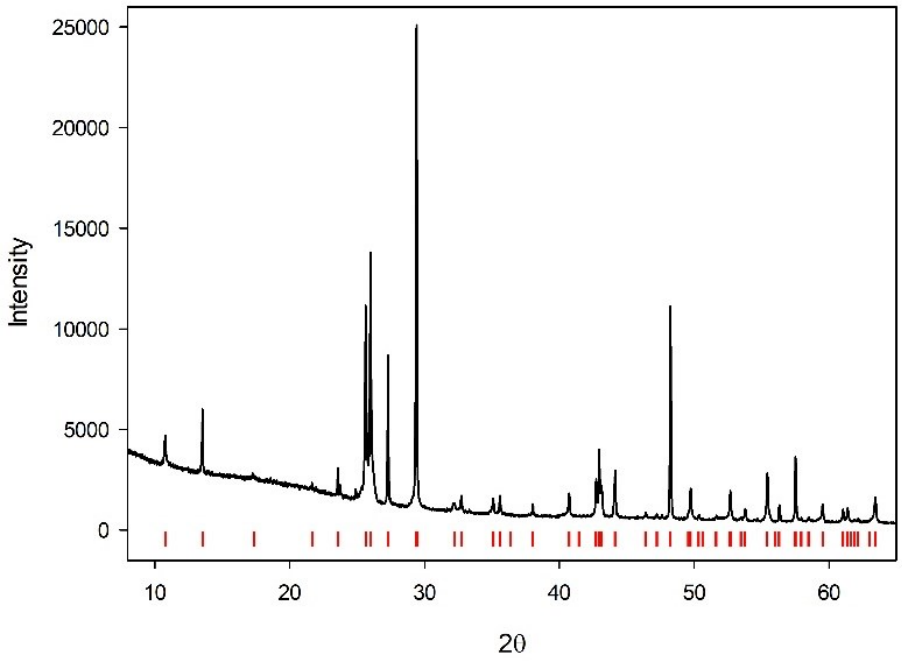

Figure 3.8 *Powder XRD pattern of $Cs_2TiNb_6O_{18}$ (sol-gel method). Red ticks: $Cs_2TiNb_6O_{18}$*

Rietveld refinement confirmed that $Cs_2TiNb_6O_{18}$ crystallises in the trigonal structure with space group $P\bar{3}m1$. The refined parameters and refinement details are shown in **Table 3.2**.

Table 3.2 *Rietveld refinement details for $Cs_2TiNb_6O_{18}$ solid-state and sol-gel*

	Lattice Parameters (Å)		Refinement Details		
	a	*c*	χ^2	R_{wp}	R_p
$Cs_2TiNb_6O_{18}$ (Solid-state)	7.52862(5)	8.18147(7)	3.841	5.85%	3.91%
$Cs_2TiNb_6O_{18}$ (Sol-gel)	7.53707(16)	8.19577(25)	12.78	9.93%	6.01%

Table 3.3 *XRF details for $Cs_2TiNb_6O_{18}$ Solid-state and sol-gel*

	Sol-gel - $Cs_2TiNb_6O_{18}$		
Element	wt. %	at. %	Molar ratio (Normalised to Nb)
Cs	23.2	6.9	2.2
Ti	3.50	2.9	0.9
Nb	44.5	18.9	6
O	28.8	71.3	22.6

	Solid-state - $Cs_2TiNb_6O_{18}$		
Element	wt. %	at. %	Molar ratio (Normalised to Nb)
Cs	22.4	6.5	2.2
Ti	5.3	4.3	1.4
Nb	42.6	17.7	6
O	29.7	71.6	24.3

Elemental analysis was carried out on both $Cs_2TiNb_6O_{18}$ samples. **Table 3.3** shows the weight percent and atomic percentage for each element and the molar ratio normalised to Nb. The values for both samples are in reasonable agreement with the expected formula. The Cs content for both samples appear consistent when normalised to Nb suggesting that Cs is not lost in the multiple firing process carried out in the solid-state method. The Ti content for the solid-state sample are higher than expected whereas the Ti content in the sol gel value is close to the proposed formula. The oxygen content for both is higher than calculated. The differences may be a result of the associated errors with the instrument and preparation method of the fusion beads. There also may be some error in the synthesis process, particularly for the sol-gel preparation, as for mentioned there was difficulty weighing out small volumes of liquids accurately. Due to the lack of crystallinity and expense of niobium ethoxide, it was thought best from this point on, to synthesise samples via the solid-state method only, rather than the sol-gel method.

Having successfully synthesised the parent material, a series of Ba-doped $Cs_2TiNb_6O_{18}$ materials have been considered. Successful synthesis would provide excellent

evidence to suggest that the material could retain $^{137}Ba^{2+}$, the transmutation product of $^{137}Cs^{+}$ **(Figure 3.3)**. To incorporate divalent Ba^{2+} for monovalent Cs^{+}, there would have to be a charge compensation mechanism, similar to that observed in hollandite and pollucite.[9,11,31,48,50,55,56,133,140] It was thought that in a 'real life scenario', the β^{-} particle released when $^{137}Cs^{2+}$ decays into $^{137}Ba^{+}$, would simultaneously reduce either Nb^{5+} to Nb^{4+} or Ti^{4+} to Ti^{3+} giving the formulas $Cs_{2-x}Ba_xNb^{(5+)}_{6-x}Nb^{(4+)}_xTiO_{18}$ and $Cs_{2-x}Ba_xTi^{(4+)}_{1-x}Ti^{(3+)}_xNb_6O_{18}$ respectively thus retaining Ba^{2+}.

For successful co-substitution, Ba would have to be compatible with the Cs site (9 coordinate) in $Cs_2TiNb_6O_{18}$ (shown in **Figure 3.2** and **Table 3.1**), along with there being some flexibility across the Ti^{4+}/Nb^{5+} sites. In $Cs_2TiNb_6O_{18}$, the Ti/Nb cations are split across two different octahedral sites, suggesting there must be some tolerance in the size of cations compatible for these sites. Nb^{5+} (6 coordinate) is 0.640 Å and Ti^{4+} (6 coordinate) is 0.605 Å and the two reduced cations for these species are only marginally larger, $Nb^{(4+)}$ (6 coordinate) is 0.680 Å and Ti^{3+} (6 coordinate) is 0.670 Å (**Table 3.4**)[141]. Therefore, it was expected that the reduced versions (Nb^{4+}/Ti^{3+}) would be compatible with the (Nb^{5+}/Ti^{4+}) sites and therefore it is possible that co-substitution could be achieved.

Table 3.4 *Comparison of ionic radii.* [141]

Cation	Ionic Radii / (Å)
Cs^{+}	1.780 (9-coord)
Ba^{2+}	1.610 (9-coord)
Ti^{4+}	0.605 (6-coord)
Ti^{3+}	0.670 (6-coord)
Nb^{5+}	0.640 (6-coord)
Nb^{4+}	0.680 (6-coord)

As a starting point in this work, samples were synthesised to the formula $Cs_{2-x}Ba_xTi^{(4+)}_{1+x}Nb^{(5+)}_{6-x}O_{18}$. In this example, excess Ti^{4+} was doped in for Nb^{5+} which would charge compensate for the incorporation of divalent Ba. There is flexibility across the Ti/Nb

sites as Ti and Nb are disordered across the two sites, suggesting that incorporating excess Ti^{4+} for Nb^{5+} would be feasible. The synthesis for these samples was relatively straight forward in comparison to the $Cs_{2-x}Ba_xNb^{(5+)}_{6-x}Nb^{(4+)}_xTiO_{18}$ and $Cs_{2-x}Ba_xTi^{(4+)}_{1-x}Ti^{(3+)}_xNb_6O_{18}$ mechanisms, as all the cations in this example would be in their highest oxidation states. Although this does not represent a 'realistic' mechanism, the results could hint whether it is possible to incorporate Ba in to the target phase and then following this, the more complex samples which rely on air sensitive Nb^{4+} and Ti^{3+} for charge compensation could be synthesised.

3.3.2 $Cs_{2-x}Ba_xTi^{(4+)}_{1+x}Nb^{(5+)}_{6-x}O_{18}$, x = 2 ($Ba_2Ti_3Nb_4O_{18}$)

A previous study [85] has reported the successful synthesis of $Ba_2Ti_3Nb_4O_{18}$, the stochiometric end member of the Ba-doped $Cs_2TiNb_6O_{18}$ series. Before a co-substituted $Ba/Cs_2TiNb_6O_{18}$ material was synthesised in this work, an attempt was made to prepare $Ba_2Ti_3Nb_4O_{18}$ via the solid-state method and the material was analysed using XRD and XRF. It was hoped these techniques would confirm the presence of pure $Ba_2Ti_3Nb_4O_{18}$.

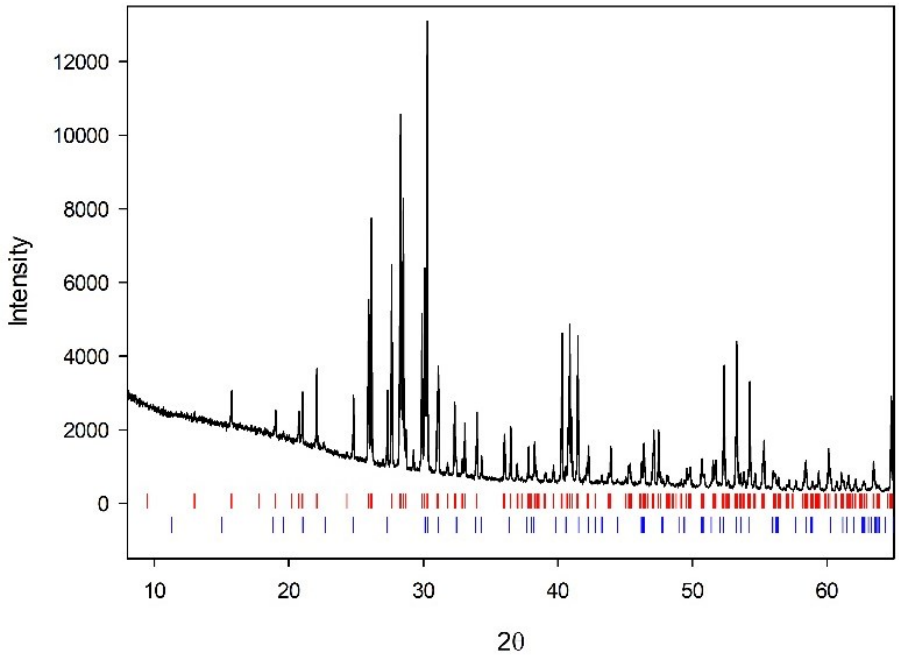

Figure 3.9 *Powder XRD pattern of $Ba_2Ti_3Nb_4O_{18}$ (solid-state method). Red ticks are indexed peaks from the ICDD PDF: 01-073-6191 ($Ba_2Ti_3Nb_4O_{18}$) Blue ticks are indexed peaks from the ICDD PDF: 01-070-1150 ($Ba_3Ti_4Nb_4O_{21}$)*

Table 3.5 *XRF details for $Ba_2Ti_3Nb_4O_{18}$ (solid-state method)*

	Solid-state - $Ba_2Ti_3Nb_4O_{18}$		
Element	wt. %	at. %	Molar ratio (Normalised to Nb)
Ti	12.8	10.1	3.1
Nb	31.7	12.9	4
Ba	25.7	7.0	2.2
O	29.8	70.0	21.8

XRF **(Table 3.5)** confirmed the expected amount of Ba and the normalised molar ratio agree reasonably well with the expected formula. Despite the correct elemental composition, the XRD pattern in **Figure 3.9** shows that a pure product was not achieved. At least two phases are present which were identified as the target phase, $Ba_2Ti_3Nb_4O_{18}$ and an impurity phase $Ba_3Nb_4Ti_4O_{21}$. Rietveld refinement suggested that the weight fraction of the target phase is 90 % and the impurity 10 wt. %. Attempts were made to synthesise a pure sample, but even after increasing firing steps and temperature, it still proved difficult to eradicate the $Ba_3Nb_4Ti_4O_{21}$ impurity. It was still possible however to recognise that the $Ba_2Ti_3Nb_4O_{18}$ end member does exist but does not have any structural similarity to

$Cs_2TiNb_6O_{18}$.

Table 3.6 *Rietveld refinement details for $Ba_2Ti_3Nb_4O_{18}$ (solid-state method)*

	Lattice Parameters (Å)				
	a / Å	*b* / Å	*c* / Å	*β*/°	wt. %
$Ba_2Ti_3Nb_4O_{18}$	10.00113(11)	9.96209(11)	7.31243(8)	111.3007(7)	89.838(5)
$Ba_3Nb_4Ti_4O_{21}$	9.03753(19)	/	11.7716(4)	/	10.162(2)
Refinement Details					
χ^2	R_{wp}	R_p			
3.006	5.28 %	3.66 %			

The crystal structure from Rietveld analysis **(Table 3.6)** for $Ba_2Ti_3Nb_4O_{18}$ is displayed in **Figure 3.10** which confirmed that, $Ba_2Ti_3Nb_4O_{18}$ crystallises in the monoclinic structure with space group $P2_1/c$ and is not isostructural with trigonal, $Cs_2TiNb_6O_{18}$. Despite this, attempts were made to synthesise lower content Ba substituted $Cs_2TiNb_6O_{18}$ phases.

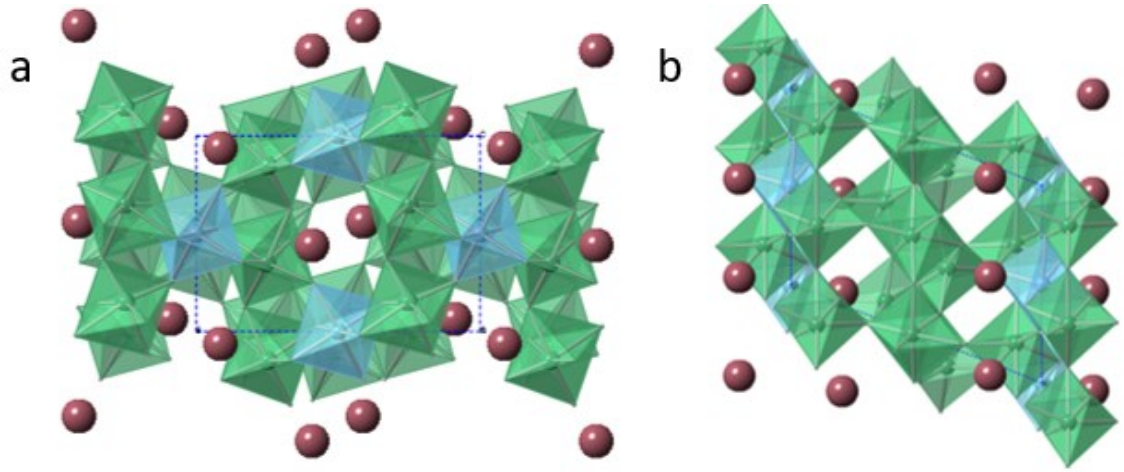

Figure 3.10 *Crystal structure of $Ba_2Ti_3Nb_4O_{18}$. a: View down [100] direction and b: View down [001] direction. Brown spheres: Barium and green octahedra: Ti/NbO_6.*[85]

3.3.3 $Cs_{2-x}Ba_xTi^{(4+)}_{1+x}Nb^{(5+)}_{6-x}O_{18}$, x = 1 ($CsBaTi_2Nb_5O_{18}$)

An attempt was made to make $CsBaTi_2Nb_5O_{18}$ using the solid-state method and the resulting product was analysed using XRD and XRF. This formula represents a 50 % conversion of Cs to Ba which equates to around 12 wt. % Ba in the final product. The

incorporation of Ba^{2+} in this example would be achieved by doping excess Ti^{4+} for Nb^{5+} giving the formula $CsBaTi^{(4+)}_2Nb^{(5+)}_5O_{18}$. Despite this not being a 'realistic mechanism' this charge balancing scheme poised to be the easiest method synthetically in comparison with the other schemes which involved Nb^{4+} and Ti^{3+} where the conditions for reaction would have be more carefully considered to prevent oxidation.

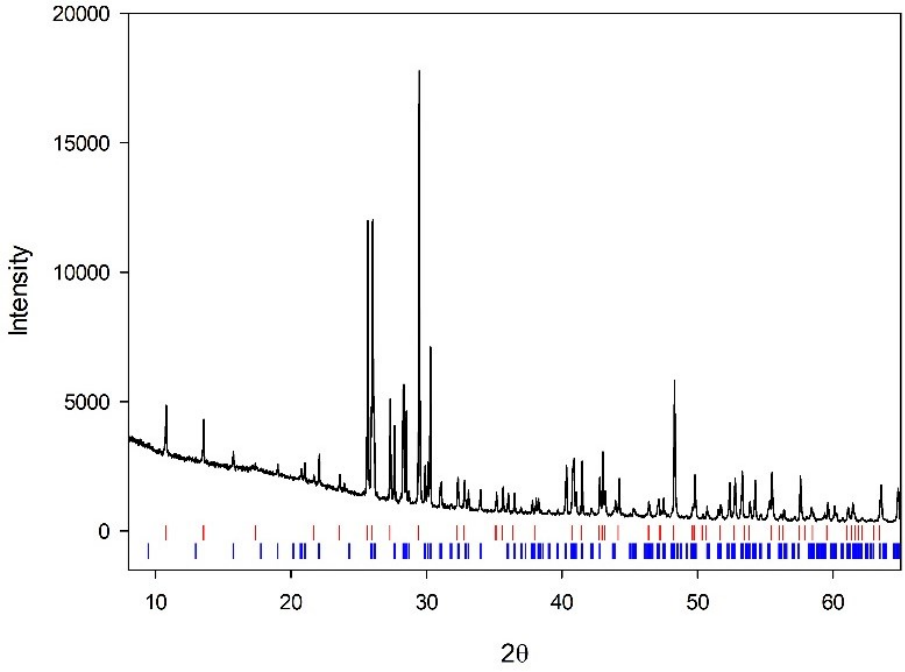

Figure 3.11 *Powder XRD Pattern $CsBaTi_2Nb_5O_{18}$ (solid-state method). Red lines: $Cs_2TiNb_6O_{18}$. Blue lines are indexed peaks from the ICDD PDF 01-073-6191 $Ba_2Ti_3Nb_4O_{18}$*

The XRD pattern in **Figure 3.11** revealed many additional peaks to what was expected. It was thought if Ba doping was successful in the $Cs_2TiNb_6O_{18}$ phase there would be a shift in unit cell size, but not a change in symmetry, therefore additional reflections were not expected. Search match using EVA software identified that both $Cs_2TiNb_6O_{18}$ and $Ba_2Ti_3Nb_4O_{18}$ (the stoichiometric end member studied in section **3.3.2**) were present. XRF confirmed the expected ratio of Cs and Ba in the sample (**Table 3.7**).

Table 3.7 *XRF details for $CsBaTi_2Nb_5O_{18}$ (Solid-state method)*

	Solid-state - $CsBaTi_2Nb_5O_{18}$		
Element	wt. %	at. %	Molar ratio (Normalised to Nb)
Cs	11.5	3.3	1.0
Ti	8.5	6.9	2.2
Nb	38.4	15.9	5
Ba	12.4	3.5	1.1
O	29.1	70.3	22.0

Table 3.8 *Rietveld refinement details for $CsBaTi_2Nb_5O_{18}$ (Solid-state method)*

	Lattice Parameters (Å)				
	a / Å	*b* / Å	*c* / Å	*β*/°	wt. %
$Cs_2TiNb_6O_{18}$	7.52798(8)	/	8.18296(12)	/	50.953(2)
$Ba_2Ti_3Nb_4O_{18}$	10.00074(15)	9.96186(16)	7.31464(12)	111.3042(12)	49.047(2)
Refinement Details					
χ^2	R_{wp}	R_p			
3.264	5.05%	3.58%			

Rietveld analysis of the attempted synthesis of $CsBaTi_2Nb_5O_{18}$ **(Table 3.8)** suggested that the two phases identified from XRD exist in a near 50:50 mix hinting that all the Ba resides in the $Ba_2Ti_3Nb_4O_{18}$ impurity phase rather than the target $CsBaTi_2Nb_5O_{18}$. This is a fairly high level of doping and therefore it may be no surprise the Ba doping was unsuccessful. Considering this, attempts were made to synthesise samples with lower Ba content using the same charge compensation method (substituting Ti^{4+} for Nb^{5+}), to determine if there is any Ba solubility in the target phase.

3.3.4 $Cs_{2-x}Ba_xTi^{(4+)}_{1+x}Nb^{(5+)}_{6-x}O_{18}$, Mid-level Ba doping

Attempts have been made to synthesise a series of four Ba doped samples by substituting excess Ti^{4+} for Nb^{5+} via the solid-state method to the formula $Cs_{2-x}Ba_xTi^{(4+)}_{1+x}Nb^{(5+)}_{6-x}O_{18}$ (x = 0.6, 0.5, 0.4 and 0.3) and each material has been analysed using XRD and XRF. The values from XRF analysis **(Table 3.9)** suggest the expected increase in

Ba and Ti content and decrease Nb content as the Ba doping (x) increase from x= 0.3, 0.4, 0.5 to 0.6.

Table 3.9 *XRF for* $Cs_{2-x}Ba_xTi^{(4+)}{}_{1+x}Nb^{(5+)}{}_{6-x}O_{18}$ *(x=0.6, 0.5, 0.4 and 0.3) solid-state method*

$Cs_{2-x}Ba_xTi^{(4+)}{}_{1+x}Nb^{(5+)}{}_{6-x}O_{18}$, x = 0.6			
Element	wt. %	at. %	Molar ratio (Normalised to Nb)
Cs	16.9	5.2	1.5
Ti	6.8	5.8	1.7
Nb	41.7	18.2	5.4
Ba	7.5	2.2	0.7
O	27.1	88.6	20.4
$Cs_{2-x}Ba_xTi^{(4+)}{}_{1+x}Nb^{(5+)}{}_{6-x}O_{18}$, x = 0.5			
Element	wt. %	at. %	Molar ratio (Normalised to Nb)
Cs	18.0	5.4	1.7
Ti	6.4	5.3	1.6
Nb	41.4	17.8	5.5
Ba	6.2	1.8	0.6
O	28.0	69.7	21.6
$Cs_{2-x}Ba_xTi^{(4+)}{}_{1+x}Nb^{(5+)}{}_{6-x}O_{18}$, x = 0.4			
Element	wt. %	at. %	Molar ratio (Normalised to Nb)
Cs	19.0	5.9	1.7
Ti	6.1	5.2	1.5
Nb	43.3	19.2	5.6
Ba	5.1	1.5	0.4
O	26.6	68.2	19.9
$Cs_{2-x}Ba_xTi^{(4+)}{}_{1+x}Nb^{(5+)}{}_{6-x}O_{18}$, x = 0.3			
Element	wt. %	at. %	Molar ratio (Normalised to Nb)
Cs	19.6	6.0	1.8
Ti	5.5	4.6	1.4
Nb	43.7	19.0	5.7
Ba	3.8	1.1	0.3
O	27.4	69.2	20.7

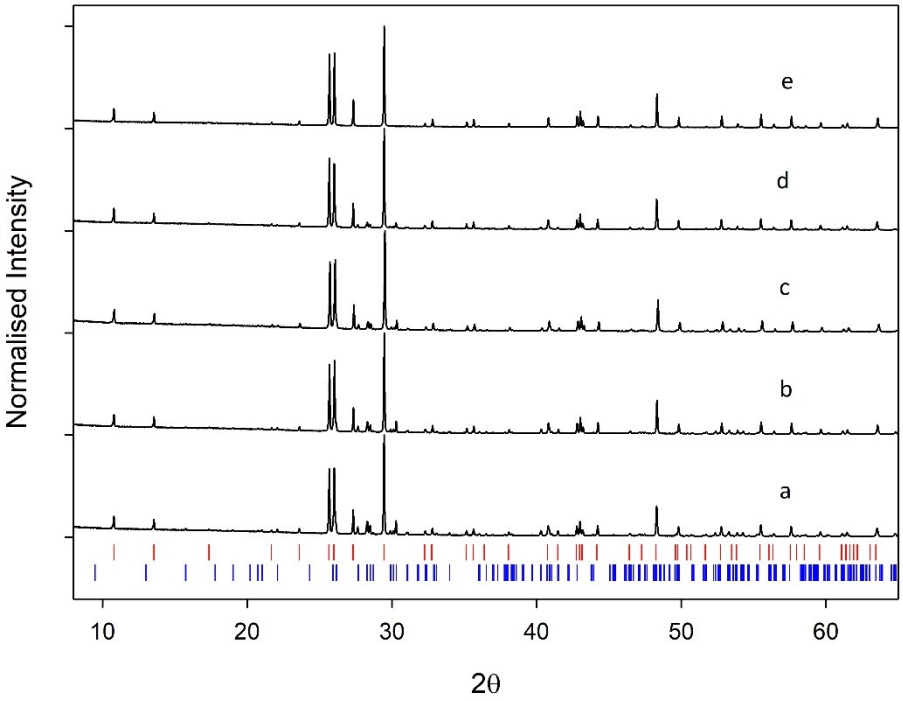

Figure 3.12 *Powder XRD pattern* $Cs_{2-x}Ba_xTi^{(4+)}_{1+x}Nb^{(5+)}_{6-x}O_{18}$ *(solid-state method), (a: x = 0.6, b: x = 0.5, c: x=0.4, d: x=0.3 and e: x=0.0), Red lines:* $Cs_2TiNb_6O_{18}$ *and Blue lines:* $Ba_2Ti_3Nb_4O_{18}$

The powder XRD patterns in **Figure 3.12** show that as these levels of Ba doping, additional impurity peaks are observed, like the previous sample, $CsBaTi_2Nb_5O_{18}$, the impurity peaks again have been identified as $Ba_2Ti_3Nb_4O_{18}$.

Table 3.10 *Rietveld refinement details for $Cs_{2-x}Ba_xTi^{(4+)}_{1+x}Nb^{(5+)}_{6-x}O_{18}$ (x = 0.6, 0.5, 0.4 and 0.3)*

x= 0.6	Lattice Parameters (Å)				
	a / Å	*b* / Å	*c* / Å	*β*/°	wt. %
$Cs_2TiNb_6O_{18}$	7.52921(6)	/	8.18432(8)	/	71.610(9)
$Ba_2Ti_3Nb_4O_{18}$	10.00397(18)	9.96445(19)	7.31424(14)	111.3049(16)	28.39(2)
Refinement Details					
χ^2	R_{wp}	R_p			
2.756	5.13%	3.60%			

x = 0.5	Lattice Parameters (Å)				
	a / Å	*b* / Å	*c* / Å	*β*/°	wt. %
$Cs_2TiNb_6O_{18}$	7.52622(5)	/	8.18054(7)	/	76.724(7)
$Ba_2Ti_3Nb_4O_{18}$	10.00037(21)	9.96140(22)	7.31017(17)	111.3038(19)	23.28(2)
Refinement Details					
χ^2	R_{wp}	R_p			
2.959	5.20%	3.63%			

x = 0.4	Lattice Parameters (Å)				
	a / Å	*b* / Å	*c* / Å	*β*/°	wt. %
$Cs_2TiNb_6O_{18}$	7.51870(7)	/	8.17232(10)	/	80.181(7)
$Ba_2Ti_3Nb_4O_{18}$	9.98936(33)	9.9508(4)	7.30418(26)	111.3043(31)	19.82(2)
Refinement Details					
χ^2	R_{wp}	R_p			
3.066	5.36%	3.57%			

x = 0.3	Lattice Parameters (Å)				
	a / Å	*b* / Å	*c* / Å	*β*/°	wt. %
$Cs_2TiNb_6O_{18}$	7.52815(5)	/	8.18430(7)	/	85.530(5)
$Ba_2Ti_3Nb_4O_{18}$	10.0053(4)	9.9655(5)	7.31398(33)	111.311(4)	14.47(2)
Refinement Details					
χ^2	R_{wp}	R_p			
2.438	5.29 %	3.74 %			

Table 3.11 *Ba content expected and experimental values, $Cs_{2-x}Ba_xTi^{(4+)}_{1+x}Nb^{(5+)}_{6-x}O_{18}$ (a: x = 0.6, b: x = 0.5, c: x=0.4 and d=0.3)*

Sample / x	Ba content expected / wt. %	Ba content in impurity phase / wt. %
0.6	7.26 %	7.23 %
0.5	6.03 %	5.93 %
0.4	4.81 %	5.05 %
0.3	3.60 %	3.68 %

Rietveld analysis **(Table 3.10)** of the four Ba doped samples indicated that as the Ba content increases, the weight fraction of the impurity increases. **Table 3.11** shows that the expected amount of Ba coincides with the exact amount found in in the impurity phases, which was calculated from Rietveld refinement. Thus far XRD and XRF studies have suggested no incorporation of Ba at high and mid-levels of doping via the proposed excess Ti^{4+} for Nb^{5+} mechanism. As a results attempts have been made to synthesise samples of much lower level of Ba doping following the same scheme. This may indicate if the $Cs_2TiNb_6O_{18}$ unit cell is able to tolerate smaller amounts of Ba doping.

3.3.5 $Cs_{2-x}Ba_xTi^{(4+)}_{1+x}Nb^{(5+)}_{6-x}O_{18}$, Low-level Ba doping

To investigate lower levels of Ba doping in the $Cs_2TiNb_6O_{18}$ phase, another series of samples have been synthesised to the same charge compensation method with the formula $Cs_{2-x}Ba_xTi^{(4+)}_{1+x}Nb^{(5+)}_{6-x}O_{18,}$ x = 0.15, 0.1 and 0.05. XRF suggested the expected amount of Ba has been incorporated **Table 3.12.**

Table 3.12 *XRF for* $Cs_{2-x}Ba_xTi^{(4+)}{}_{1+x}Nb^{(5+)}{}_{6-x}O_{18}$ *x = 0.15, 0.1 and 0.05*

	$Cs_{2-x}Ba_xTi^{(4+)}{}_{1+x}Nb^{(5+)}{}_{6-x}O_{18}$ (x = 0.15)		
Element	wt. %	at. %	Molar ratio (Normalised to Nb)
Cs	20.4	5.9	1.9
Ti	4.8	3.9	1.3
Nb	43.5	18.1	5.85
Ba	1.7	0.5	0.15
O	29.6	71.6	23.1
	$Cs_{2-x}Ba_xTi^{(4+)}{}_{1+x}Nb^{(5+)}{}_{6-x}O_{18}$ (x = 0.1)		
Element	wt. %	at. %	Molar ratio (Normalised to Nb)
Cs	21.2	6.4	1.9
Ti	4.5	3.8	1.1
Nb	45.4	19.7	5.9
Ba	1.1	0.3	0.1
O	27.7	69.8	21.0
	$Cs_{2-x}Ba_xTi^{(4+)}{}_{1+x}Nb^{(5+)}{}_{6-x}O_{18}$ (x = 0.05)		
Element	wt. %	at. %	Molar ratio (Normalised to Nb)
Cs	22.8	7.3	2.0
Ti	4.6	4.1	1.1
Nb	46.6	21.3	5.95
Ba	0.6	0.2	0.05
O	25.3	67.1	18.8

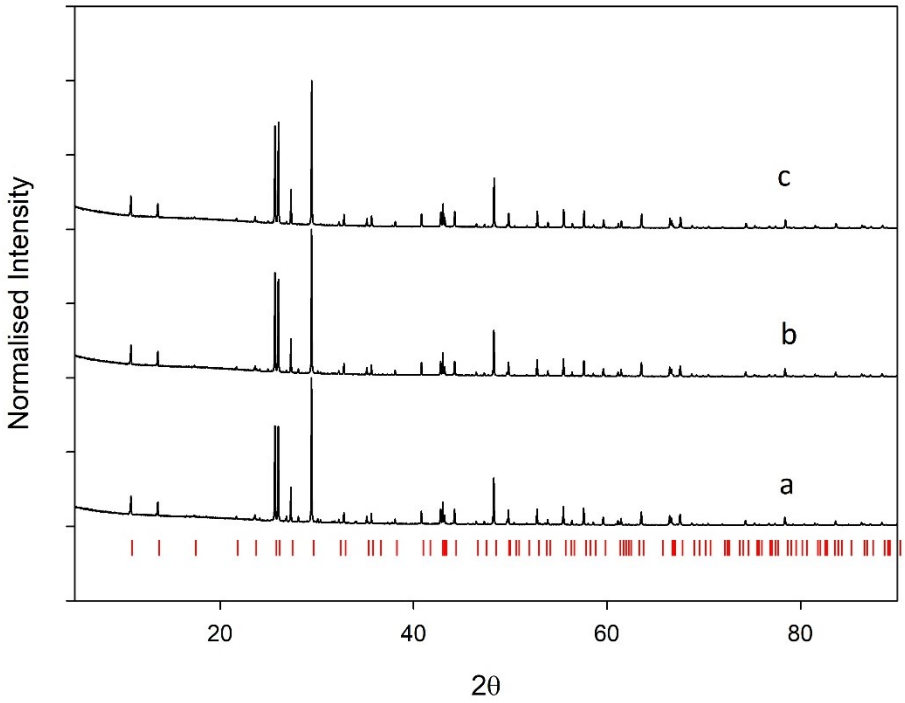

Figure 3.13 *Powder XRD Pattern* $Cs_{2-x}Ba_xTi^{(4+)}_{1+x}Nb^{(5+)}_{6-x}O_{18}$ *solid-state method, (a: x = 0.15, b: x = 0.1 and c: x=0.05). Red ticks:* $Cs_2TiNb_6O_{18}$

Initial inspection of the XRD patterns in **Figure 3.13** suggested that there may have been some level of Ba doping at levels where x = 0.05, as no impurity peaks appeared to be present. However, after collecting better quality data between over a shorter 2θ range (20-38°) small impurity peaks were again identified. **Figure 3.14** displays the better quality XRD patterns and compared to pure $Cs_2TINb_6O_{18}$ (**Figure 3.14, d**) it is clear there are small impurity peaks in the Ba x = 0.05 sample, marked *. The impurities in the x = 0.10 and 0.15 samples are more obvious. The Ba impurity phases identified in these samples differ to the $Ba_2Ti_3Nb_4O_{18}$ impurity found in the higher doped Ba samples, in this case the Ba impurities were identified as $BaTi_3Nb_4O_{17}$ and $BaTiNb_4O_{13}$.

$BaTi_3Nb_4O_{17}$ and $BaTiNb_4O_{13}$ are materials more commonly studied for their dielectric properties for microwave applications.[142] $BaTi_3Nb_4O_{17}$ crystallises in the orthorhombic structure with space group $Cmcm$ and $BaTiNb_4O_{13}$ crystallises in the orthorhombic system with space group *Pbcm*. The crystal structure for $BaTiNb_4O_{13}$ used in

this work for Rietveld refinement been modified from KTa_5O_{13}. [88]

Table 3.13 shows the refinement details for the three lower Ba doped samples. The calculated weight fractions from Rietveld analysis suggest there is some discrepancy in the calculated Ba values and the actual amount of Ba present in the impurity phases (**Table 3.14**). The Ba content in the impurity phases is slightly lower than expected amount which opens the question to whether there is any Ba doping in the target phase. However, this discrepancy is most likely due to the error in the weight fraction calculation as the intensity of the Ba impurity peaks relative to the main phase are very small and therefore the error in the weight fraction calculation is likely to be significant. For the x = 0.15 sample there is also a small amount of $Ti_2Nb_{10}O_{29}$ present which is most likely a result of errors in the stoichiometry in the starting materials.

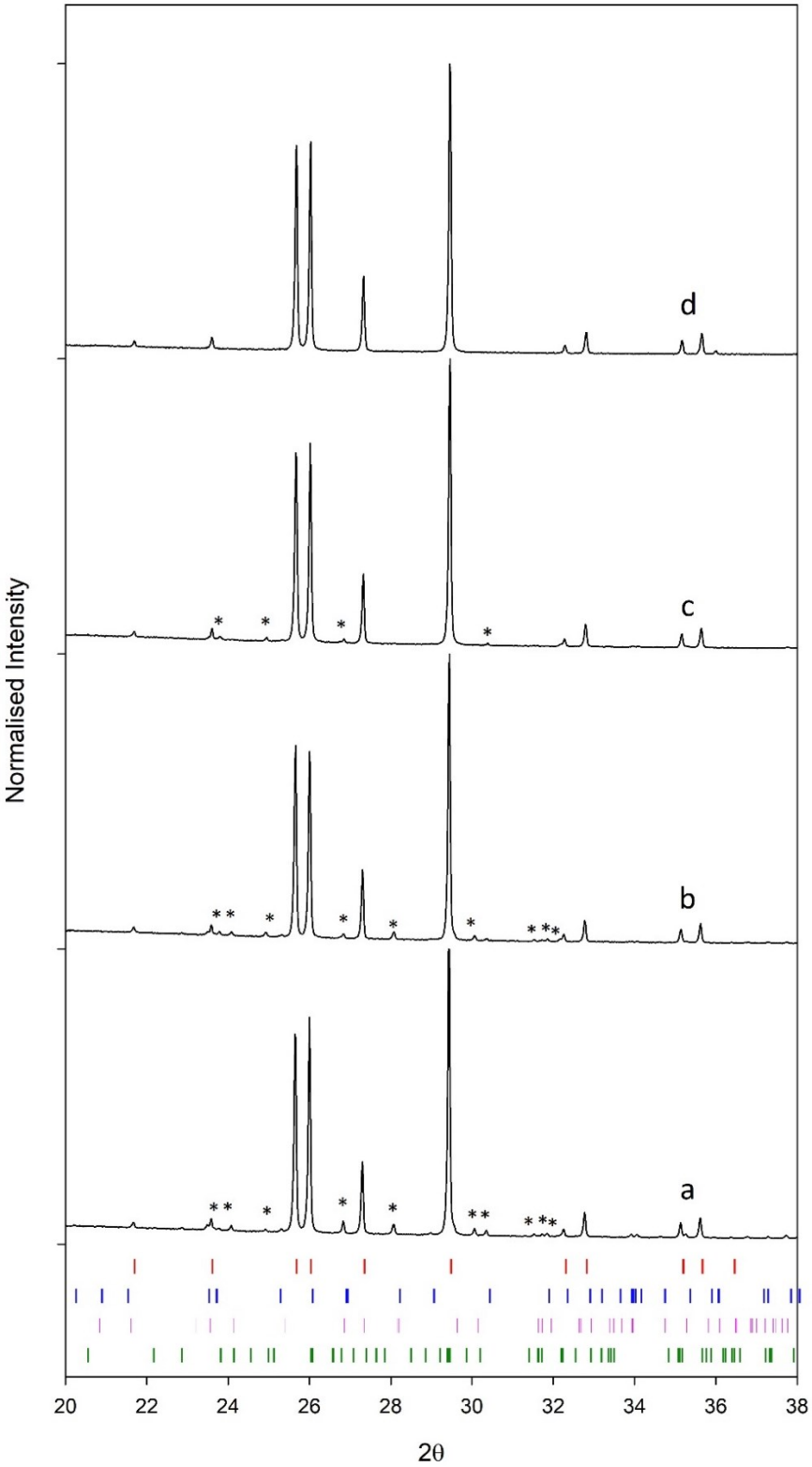

Figure 3.14 *Powder XRD Pattern, high quality scans between 20 – 38° $Cs_{2-x}Ba_xTi^{(4+)}_{1+x}Nb^{(5+)}_{6-x}O_{18}$ (a: x = 0.15, b: x = 0.1, c: x=0.05 and d=0) (solid-state method) Red lines: $Cs_2TiNb_6O_{18}$. Blue lines are indexed peaks from the ICDD PDF:00-038-1483 ($BaTi_3Nb_4O_{17}$), pink lines are indexed peaks from the ICDD PDF: 00-084-1102 ($BaTiNb_4O_{13}$) and green lines are indexed peaks from the ICDD PDF: 00-040-0039 ($Ti_2Nb_{10}O_{29}$).*

Table 3.13 *Rietveld refinement details* $Cs_{2-x}Ba_xTi^{(4+)}_{1+x}Nb^{(5+)}_{6-x}O_{18}$ *x = 0.15, 0.1 and 0.05*

x = 0.15	Lattice Parameters (Å)				
	a / Å	*b* / Å	*c* / Å	*β*/°	wt. %
$Cs_2TiNb_6O_{18}$	7.52979(4)	/	8.18412(6)	/	88.831(4)
$BaTi_3Nb_4O_{17}$	6.63262(31)	8.9647(7)	21.1380(14)	/	4.98(2)
$BaTiNb_4O_{13}$	5.6306(5)	10.7171(8)	16.4567(11)	/	5.28(2)
$Ti_2Nb_{10}O_{29}$	15.557(4)	3.8109(8)	20.519(5)	113.526(23)	0.92(1)
Refinement Details					
χ^2	R_{wp}	R_p			
2.977	4.99%	3.35%			

x = 0.1	Lattice Parameters (Å)				
	a / Å	*b* / Å	*c* / Å	*β*/°	wt. %
$Cs_2TiNb_6O_{18}$	7.529004(29)	/	8.18402(5)	/	91.462(4)
$BaTi_3Nb_4O_{17}$	6.6323(10)	8.9685(19)	21.138(4)	/	1.74(2)
$BaTiNb_4O_{13}$	5.6299(8)	10.7187(13)	16.4553(19)	/	4.03(2)
$Ti_2Nb_{10}O_{29}$	15.571(4)	3.8088(6)	20.543(4)	113.649(22)	2.77(2)
Refinement Details					
χ^2	R_{wp}	R_p			
4.113	5.80%	3.87%			

x = 0.05	Lattice Parameters (Å)				
	a / Å	*b* / Å	*c* / Å	*β*/°	wt. %
$Cs_2TiNb_6O_{18}$	7.52469(5)	/	8.17920(7)	/	95.637(2)
$BaTi_3Nb_4O_{17}$	6.6286(15)	8.9585(31)	21.122(6)	/	2.16(2)
$Ti_2Nb_{10}O_{29}$	15.547(5)	3.8065(8)	20.512(5)	113.552(28)	2.21(2)
Refinement Details					
χ^2	R_{wp}	R_p			
3.118	5.05%	3.43%			

Table 3.14 *$Cs_{2-x}Ba_xTi^{(4+)}_{1+x}Nb^{(5+)}_{6-x}O_{18}$ x = 0.15, 0.1 and 0.05 expected Ba (Calculated) and actual Ba in sample from Rietveld refinement weight fractions*

Sample / x	Expected Ba / wt. %	Ba in sample
0.15	1.79	1.69
0.1	1.19	0.98
0.05	0.59	0.32

3.3.6 SEM $Cs_{2-x}Ba_xTi^{(4+)}_{1+x}Nb^{(5+)}_{6-x}O_{18}$, x = 0.1

To further examine Ba doped $Cs_2TiNb_6O_{18}$, scanning electron microscopy (SEM) experiments have been carried out as it was thought elemental analysis by SEM/EDS could locate Ba and reveal whether there is any incorporation in the target phase or confirm if all

the Ba resides in the impurity phases. A previous study carried out by Park et al.[132] on Ba substituted Caesium titanium silicate used SEM/EDS mapping techniques in order to determine whether Ba is isolated or well distributed throughout the sample. The findings found that Ba was uniform across the sample, suggesting successful Ba incorporation.

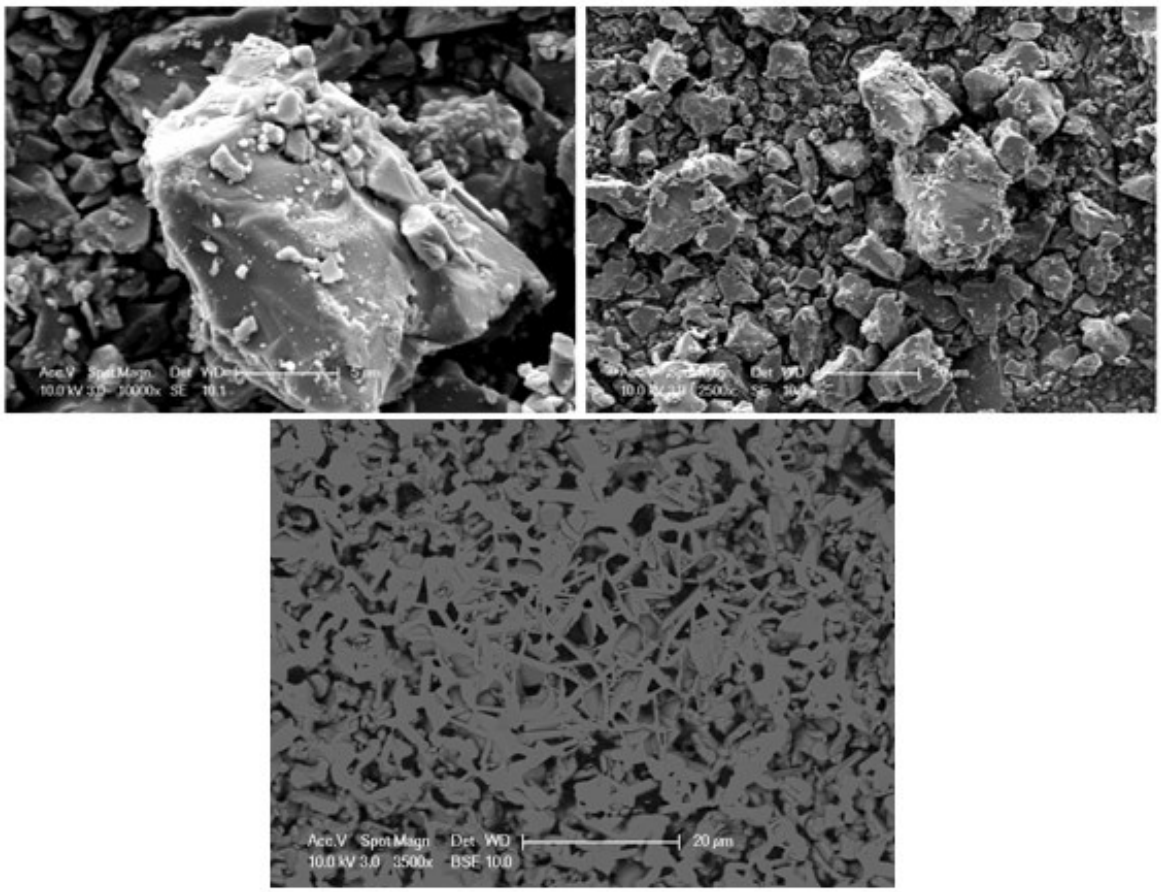

Figure 3.15 *Top left and right: Secondary electron (SE) images of* $Cs_{2-x}Ba_xTi^{(4+)}{}_{1+x}Nb^{(5+)}{}_{6-x}O_{18}$*, x = 0.1. Bottom image: Back scattered electron (BSE) image* $Cs_{2-x}Ba_xTi^{(4+)}{}_{1+x}Nb^{(5+)}{}_{6-x}O_{18}$*, x = 0.1.*

SEM **(Figure 3.15)** experiments did give an idea of the sample morphology; but it was quickly realised that SEM/EDX experiments would not be able to locate Ba in the sample. The spot size associated with SEM is large and therefore it proved difficult to target individual particles, furthermore there is emission line overlap with Ba and Ti making qualitative analysis difficult. The Ti K_α lines overlap with the Ba L_α lines **(Table 3.15)** and the Oxford Inca 300 EDX system does not have the required resolution to distinguish

between these energies. As a result of this mapping experiments to study the distribution of Ba were not carried out.

Table 3.15 *Emission lines Cs, Ba, Ti and Nb* [143]

Element	$K_{\alpha1}$	$K_{\alpha2}$	$K_{\beta1}$	$L_{\alpha1}$	$L_{\alpha2}$	$L_{\beta1}$	$L_{\beta2}$
Cs	30.9728	30.6251	34.9869	4.2865	4.2722	4.6198	4.9359
Ba	32.1936	31.8171	36.3782	**4.46626**	**4.4509**	4.82753	5.1565
Ti	**4.51084**	**4.50486**	4.93181	0.4522	0.4522	0.584	/
Nb	16.6151	16.521	18.6225	2.16589	2.163	2.2574	2.367

*** N.B. Values are in KeV**

As a result of the issues with SEM, a series of TEM experiments have been carried out. TEM has a higher energy beam with a much smaller spot size meaning individual particles can be targeted and also Ti and Ba can be distinguished as the higher energy K_{α} emission lines of Ba are accessible in TEM.

3.3.7 TEM $Cs_{2-x}Ba_xTi^{(4+)}_{1+x}Nb^{(5+)}_{6-x}O_{18}$, x = 0.1

TEM/EDS elemental studies were carried out at the University of Limerick using a JEOL JEM-2100F equipped with a SEI/BSE detector, operating at 200 kV in STEM mode by Dr Yina Guo (University of Limerick) and Dr Tzu-Yu Chen (University of Birmingham). TEM is cable of producing higher magnification images **(Figure 3.16)** allowing the examination of individual particles and also the higher energy beam allowed both Ti and Ba to be quantified in EDS. The dark-field TEM image **(Figure 3.17)** and EDS results suggest that points A and C are representative of the same phase, $Cs_2TiNb_6O_{18}$. Point B shows a particle on top of the $Cs_2TiNb_6O_{18}$ crystal which EDS suggests is rich in Ba. Considering the EDS results for points A, B and C the Ba content of point B can be estimated by subtracting an average of the values from points A and C from that of B. The residual suggests that all the Ba is located in the top particle, in this case likely a barium titanium niobate impurity phase. These results, coupled with the X-ray data strongly indicates that in Ba does not incorporate into the target phase $Cs_{2-x}Ba_xTi^{(4+)}_{1+x}Nb^{(5+)}_{6-x}O_{18}$, x = 0.1.

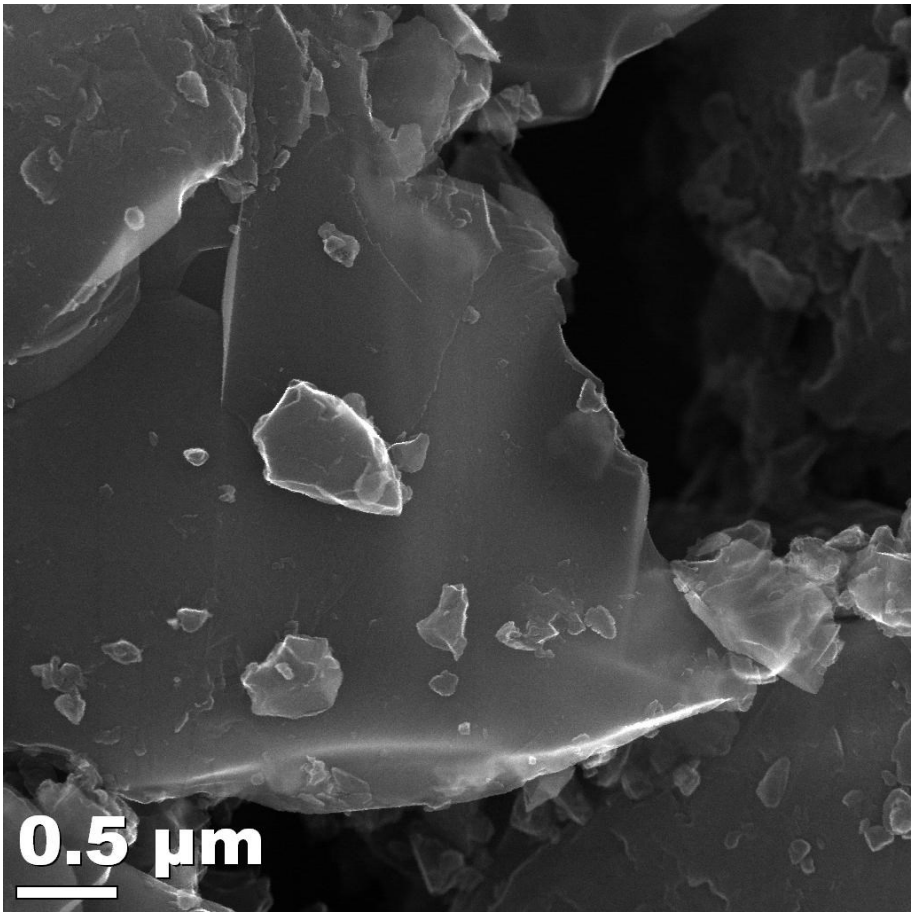

Figure 3.16 *TEM Secondary electron image of* $Cs_{2-x}Ba_xTi^{(4+)}_{1+x}Nb^{(5+)}_{6-x}O_{18}$, $x = 0.1$[144]

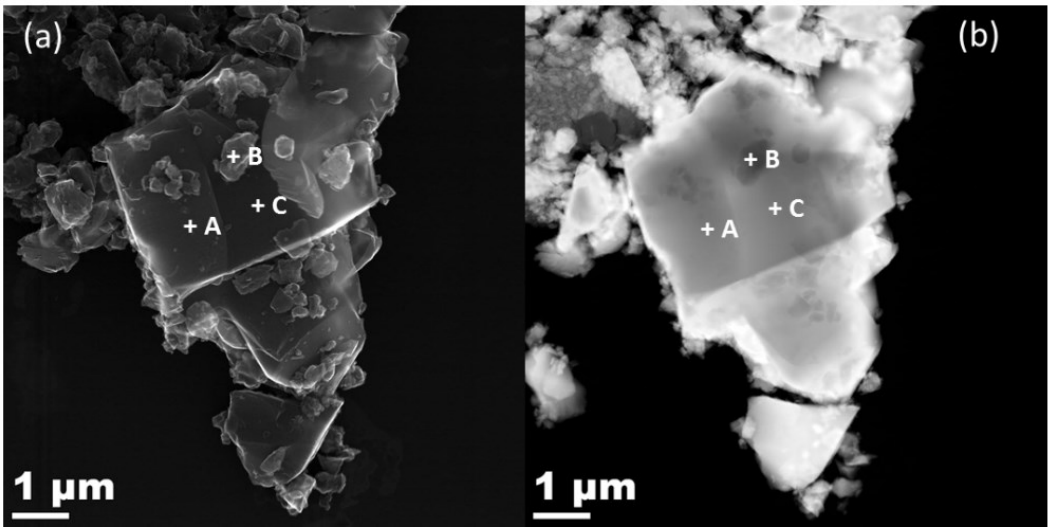

Figure 3.17 *TEM image of* $Cs_{2-x}Ba_xTi^{(4+)}_{1+x}Nb^{(5+)}_{6-x}O_{18}$, $x = 0.1$ *(a) secondary electron image (b) dark-field image. + marks the points for EDS analysis.* [144]

Table 3.16 *Multi-point analysis of* $Cs_{1.9}Ba_{0.1}Ti^{(4+)}_{1.1}Nb^{(5+)}_{5.9}O_{18}$ *using TEM/EDS.* [144]

	CsL	BaL		TiK		NbK	
	at%	**at%**	**At. Ratio (to Cs)**	**at%**	**At. Ratio (to Cs)**	**at%**	**At. Ratio (to Cs)**
Point A	22.8	1.9	0.08	8.1	0.35	46.3	2.03
Point B	8.0	**28.8**	**3.61**	13.0	1.63	37.3	4.68
Point C	24.8	2.0	0.08	9.2	0.37	49.7	2.00
Residual*			3.53		2.03		2.47

*** Residual elements after subtracting equal amount of those of average point A and C.**

Thus far analysis of XRD, XRF and microscopy data suggests that Ba resides in an impurity phase rather than doping into the target phase. However, the samples synthesised and analysed so far have been concerned with doping excess Ti^{4+} for Nb^{5+} giving the formula $Cs_{2-x}Ba_xTi^{(4+)}_{1+x}Nb^{(5+)}_{6-x}O_{18}$ which is not representative of a realistic scenario. Therefore a series of samples have been synthesised to represent realistic mechanisms such as Nb^{5+} reducing to Nb^{4+} or Ti^{4+} reducing to Ti^{3+} as $^{137}Cs^{+}$ decays to $^{137}Ba^{2+}$, giving the formulas; $Cs_{2-x}Ba_xNb^{(5+)}_{6-x}Nb^{(4+)}_{x}TiO_{18}$ and $Cs_{2-x}Ba_xTi^{(4+)}_{1-x}Ti^{(3+)}_{x}Nb_6O_{18}$ respectively.

3.3.8 $Cs_{2-x}Ba_xTiNb^{(4+)}_{x}Nb^{(5+)}_{6-x}O_{18}$ and $Cs_{2-x}Ba_xNbTi^{(3+)}_{x}Ti^{(4+)}_{1-x}O_{18}$ (Realistic mechanisms)

For samples where the charge compensation mechanism concerns excess Ti^{4+} for Nb^{5+}, no consideration was required for the high-temperature synthesis to keep these cations in their oxidation states as they are stable. However, where Nb^{4+} and Ti^{3+} are used for charge compensation, the synthesis method must be modified in order to avoid oxidation of Nb^{4+} and Ti^{3+} to Nb^{5+} and Ti^{4+} respectively. The traditional solid-state methods discussed previously would be an inadequate synthesis method for Nb^{4+} and Ti^{3+} doped samples. To better understand the stability of Nb^{4+} and Ti^{3+}, variable temperature X-ray diffraction (VT-XRD) experiments were carried out. These experiments were able to determine at what

temperatures NbO_2 **(Figure 3.18)** and Ti_2O_3 **(Figure 3.19)** oxidise into Nb_2O_5 and TiO_2 which would help devise a new suitable synthesis method.

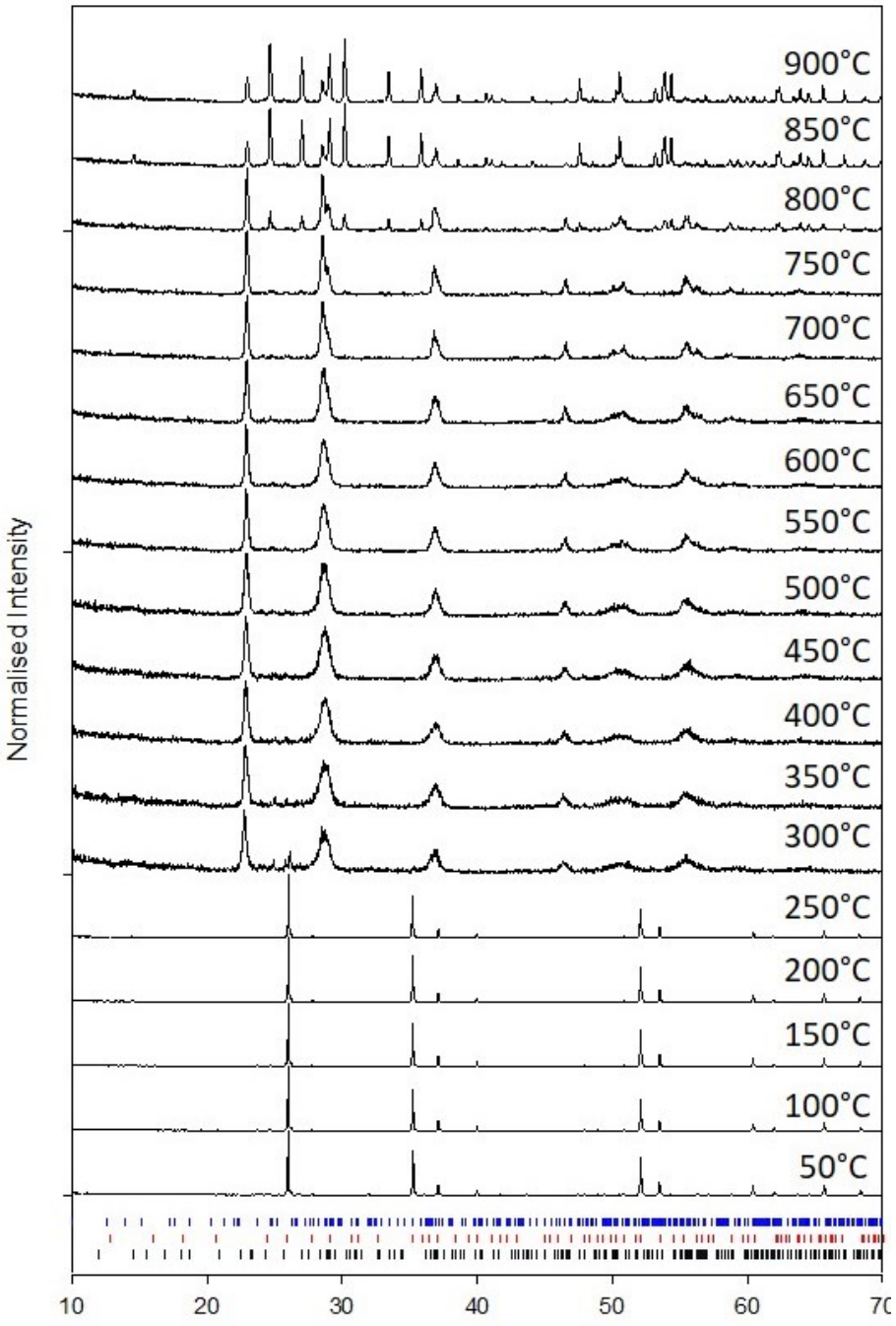

Figure 3.18 *Powder XRD (Variable-Temperature 50-900°C) NbO_2. Red ticks are indexed peaks from the ICDD PDF: 01-071-0020 NbO_2, blue ticks are indexed peaks from the ICDD PDF 01-071-0005 (Nb_2O_5, Monoclinic) and black ticks are indexed peaks from the ICDD PDF: 01-071-0336 (Nb_2O_5, Orthorhombic)*

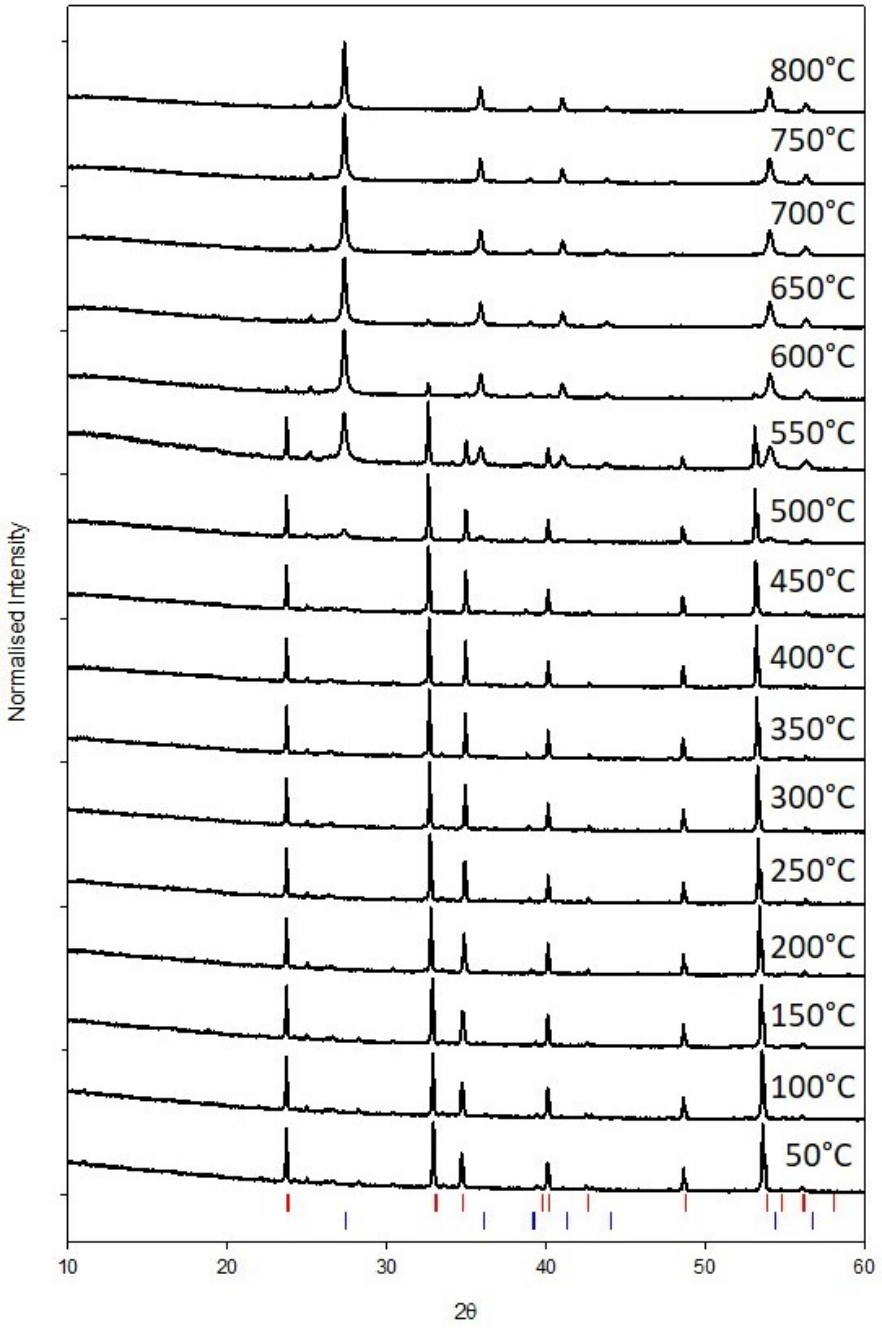

Figure 3.19 *Powder XRD (Variable-Temperature) Ti_2O_3. Red ticks are indexed peaks from the ICDD PDF: 01-071-0269 Ti_2O_3 and blue ticks are indexed peaks from the ICDD PDF: 01-072-1148 TiO_2 (rutile)*

Figure 3.18 is a stack plot of VT-XRD of NbO_2 from 50 to 900°C. NbO_2 crystallises in the tetragonal crystal system with space group $I4_1/a$. As the temperature reaches around 250 – 300 °C Nb^{4+} begins to oxidise to Nb^{5+} and an orthorhombic Nb_2O_5 (*Pbam*) phase is formed. At around 850°C, a different Nb_2O_5 (monoclinic, *P*2/*m*) phase is formed. **Figure**

3.19 is a stack plot of VT-XRD data of Ti_2O_3 from 50 - 800°C. Ti_2O_3 is trigonal with space group $R\bar{3}c$ and at temperatures of around 450 – 500°C Ti^{3+} begins to oxidise to Ti^{4+} and TiO_2 starts to form. At 600°C and above, TiO_2 (rutile) is the only phase present which is tetragonal with space group $P4_2/mnm$. These studies proved essential as it is known that to synthesis $Cs_2TiNb_6O_{18}$, temperatures in excess of 1100 °C are required. Therefore, alternative synthesis methods to heating in air had to be explored.

Initially it was thought that solid-state type reactions could be carried out in a tube furnace under an inert atmosphere such as nitrogen or argon. Some tests were carried out where NbO_2 alone was heated to 1100°C in a tube furnace under a nitrogen atmosphere. This would determine whether the tube furnace could provide the correct conditions to prevent oxidation when synthesising $Cs_{2-x}Ba_xTiNb^{(4+)}{}_xNb^{(5+)}{}_{6-x}O_{18}$ materials.

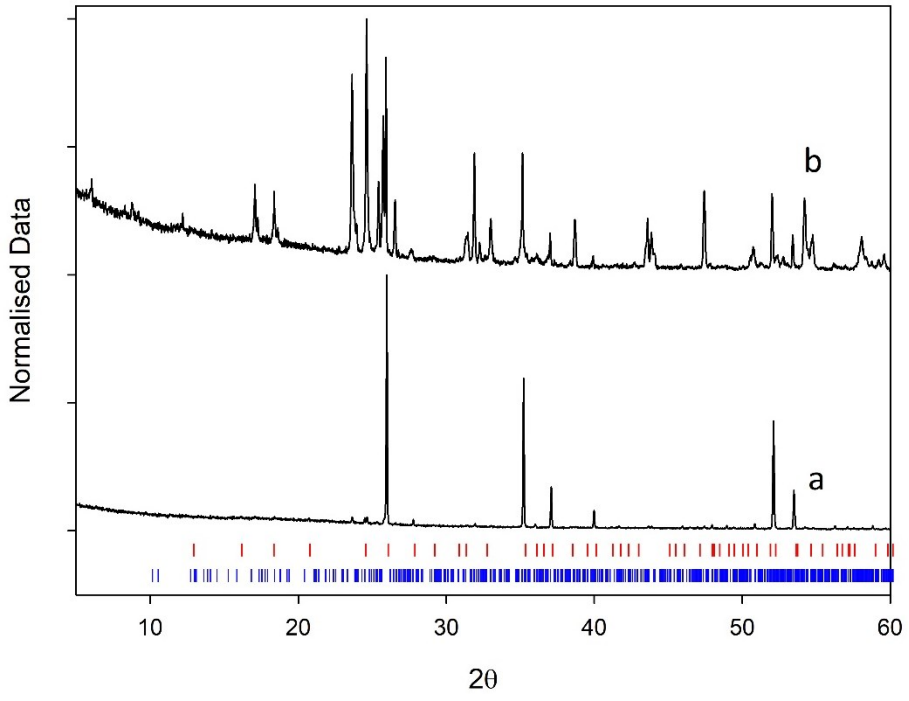

Figure 3.20 *Powder XRD of NbO_2 nitrogen tube furnace tests. a: NbO_2 from bottle and b: NbO_2 heated at 1100°C in tube furnace under nitrogen. Red ticks: NbO_2 and blue ticks: Nb_2O_5*

The XRD pattern in **Figure 3.20** labelled (a) is NbO_2 directly from the bottle which is bench top stable and the peaks match well to the expected tetragonal ($I4_1/a$) NbO_2 phase.

NbO_2 was then heated in the tube furnace under flowing Nitrogen to 1100°C at a rate of 10°C/minute and held for 12 hours. Following this heating step, XRD data were collected and additional peaks were clearly visible in the pattern, labelled (b) in **Figure 3.20**, which were identified as monoclinic Nb_2O_5. The tests proved that solid-state synthesis in a tube furnace under nitrogen is an insufficient method to prevent Nb^{4+} from oxidising to Nb^{5+} at these high temperatures. It was thought this may have been down to insufficient purging of the system before heating which could leave some oxygen in the system, so longer purge times were initiated, however the same result was observed after another test. As well as nitrogen, other inert gases such as argon were used. It was hoped that argon, being a heavier inert gas, would better displace any oxygen in the system and prevent oxidation of Nb^{4+} but this also failed. It was assumed that if Nb^{4+} oxidised under these conditions, Ti^{3+} would also oxidise.

Following these tests, it was clear that heating in a tube furnace under an inert atmosphere would not be an adequate method for synthesising either $Cs_{2-x}Ba_xNb^{(5+)}_{6-x}Nb^{(4+)}_xTiO_{18}$ or $Cs_{2-x}Ba_xTi^{(4+)}_{1-x}Ti^{(3+)}_xNb_6O_{18}$. As a result, a new method was developed where it could be guaranteed that Nb^{4+} and Ti^{3+} would not oxidise in the heating step. This new method essentially follows the basic principles of a solid-state reaction except that the heating step would be carried out in a sealed quartz tube that has previously been evacuated using a high vacuum pump. Full details of this synthesis can be found in the experimental section (**2.1.2**).

To ensure this new modified method worked, similar tests were carried out as before with NbO_2 and the tube furnace. NbO_2 fresh from the bottle was placed in the tube, evacuated, sealed and heated to 1100°C for 2 hours. The resulting powder was analysed using XRD (**Figure 3.21**) labelled (b). The pattern labelled in (a) in **Figure 3.21** is pure

NbO_2 and a comparison of the two patterns clearly show that both samples are same, suggesting NbO_2 has not oxidised to Nb_2O_5, where it did in the tube furnace example (**Figure 3.21**).

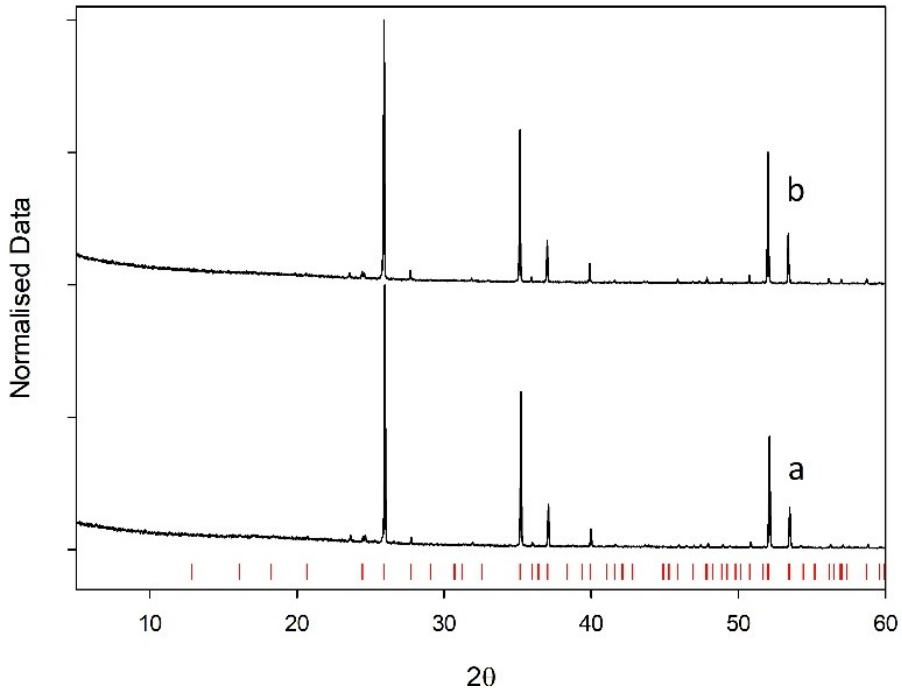

Figure 3.21 *Powder XRD of NbO_2 N_2 quartz tube furnace tests. a: NbO_2 from bottle and b: NbO_2 heated at 900°C in a sealed quartz tube. Red ticks: NbO_2.*

For reasons discussed in the experimental **section 2.1.2**, to start with $CsNO_3$ and $Ba(NO_3)_2$ were not used as starting materials for the sealed tube synthesis. Decomposition of these materials in a sealed tube would cause the tube to explode as oxygen and nitrogen dioxide released as the nitrates are heated. As a result, new sources for Ba and Cs were used which included Cs_2TiO_3 and $BaNb_2O_6$. These materials were ideal as they did not release any gases upon decomposition.

To test the new starting materials, pure $Cs_2TiNb_6O_{18}$ was synthesised using Cs_2TiO_3 and Nb_2O_5. **Figure 3.22** shows two XRD patterns, the bottom pattern, labelled (a), is the product from a stoichiometric mix of Cs_2TiO_3 and Nb_2O_5. There are obvious impurity peaks present in this pattern which have predominantly been assigned to a monoclinic Nb_2O_5 phase meaning that it is likely there is a lack of Cs and Ti in the starting mixture. The synthesis was repeated in the same ratio in case there was a mistake with the first attempt, but the Nb_2O_5 peaks remained in the sample. Therefore, a second sample was synthesised where a 20 mol % excess of Cs_2TiO_3 was added to the starting mixture. This new ratio between Cs_2TiO_3 and Nb_2O_5 proved successful and the pattern labelled (b) in **Figure 3.22** suggests a pure sample as all peaks were assigned to $Cs_2TiNb_6O_{18}$.

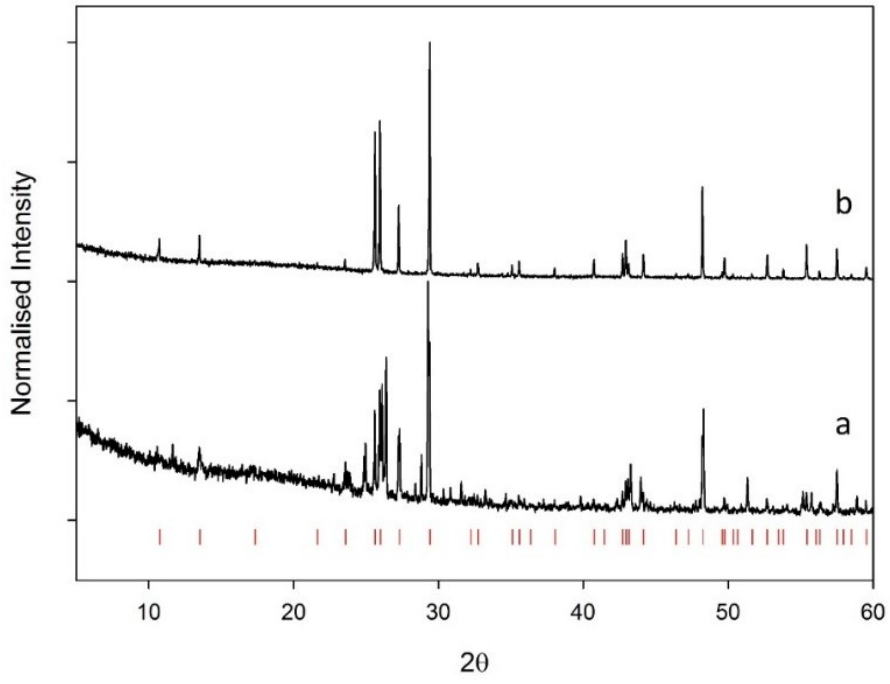

Figure 3.22 *Powder XRD of $Cs_2TiNb_6O_{18}$ synthesis from Cs_2TiO_3 and Nb_2O_5. a = from a stoichiometric Cs_2TiO_3 + 3 Nb_2O_5 mix. b = 20 mol % extra Cs_2TiO_3 + 3Nb_2O_5, Red ticks: $Cs_2TiNb_6O_{18}$*

Having discovered that an excess of Cs_2TiO_3 was required to achieve a pure $Cs_2TiNb_6O_{18}$ product, further investigations into the Cs_2TiO_3 starting material was carried out. XRD data for Cs_2TiO_3 were collected and search match revealed that the actual material

is a mixture of $Cs_2CO_3 \cdot H_2O$ and TiO_2 (**Figure 3.23**). Cs_2CO_3 is extremely hygroscopic, which is likely why the stoichiometric example shown in **Figure 3.22 (a)**, did not work and the 20 mol % excess Cs_2TiO_3 was needed to make pure $Cs_2TiNb_6O_{18}$. The findings here and fact there is no known structure in the database suggests that Cs_2TiO_3 does not exist.

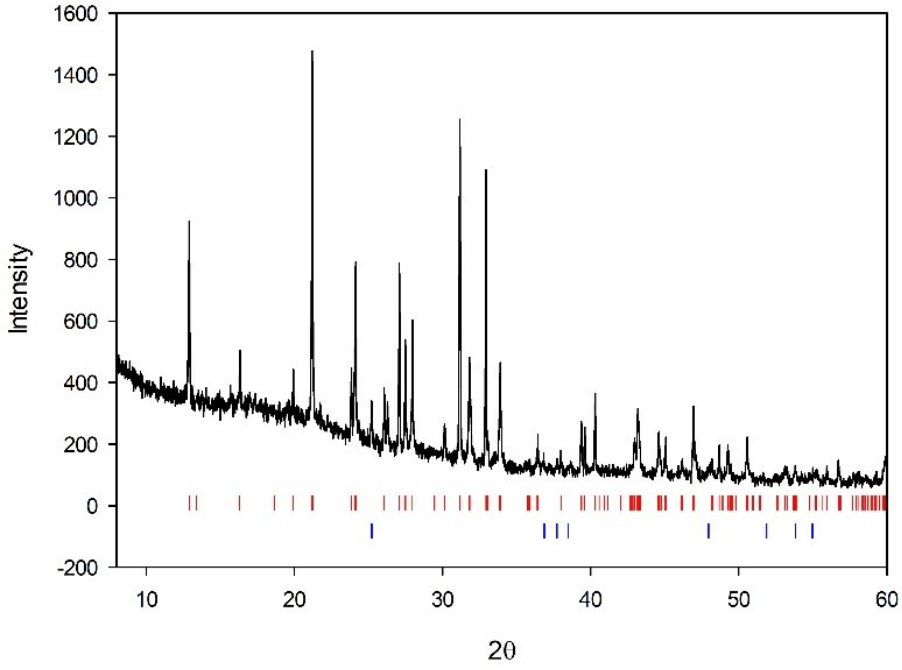

Figure 3.23 *Powder XRD of Cs_2TiO_3. Red ticks are indexed peaks from the ICDD PDF 01-071-3032 $Cs_2CO_3 \cdot 3H_2O$ Blue ticks are indexed peaks from ICDD PDF 01-075-2545 TiO_2 (anatase).*

$BaNb_2O_6$ was also characterised via XRD (**Figure 3.24**) and it was found that two polymorphs of $BaNb_2O_6$ (monoclinic and trigonal) as well as a $Ba_5Nb_4O_{15}$ (trigonal) impurity phase were present in the starting material. The presence of the $Ba_5Nb_4O_{15}$ impurity in the starting material meant that the amounts of starting materials had to be adjusted wherever $BaNb_2O_6$ is used. This was calculated using the weight fractions from Rietveld refinement (**Table 3.17**).

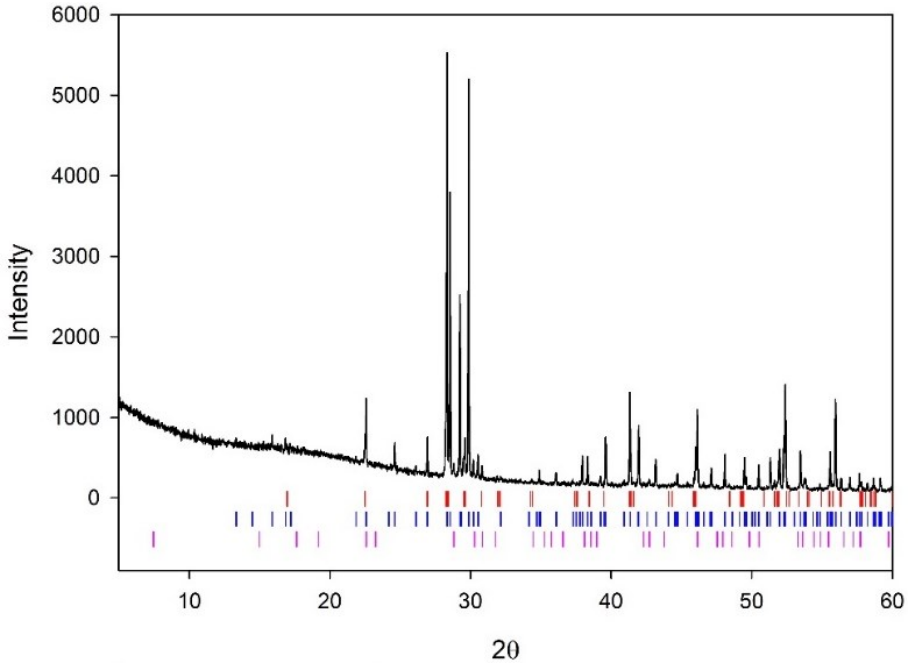

Figure 3.24 *Powder XRD of $BaNb_2O_6$. Red ticks are indexed peaks from the ICDD PDF 04-077-0541 ($BaNb_2O_6$, Monoclinic). Blue ticks are indexed peaks from ICDD PDF 01-077-0589 ($BaNb_2O_6$, Orthorhombic) and pink ticks are indexed peaks from the ICDD PDF 01-070-9002 ($Ba_5Nb_4O_{15}$)*

Table 3.17 *Rietveld refinement details for $BaNb_2O_6$ from bottle*

$BaNb_2O_6$	Lattice Parameters (Å)				
	a / Å	*b* / Å	*c* / Å	*β*/°	wt. %
$BaNb_2O_6$	3.9461(4)	6.0396(7)	10.4157(9)	89.636(10)	10.58(3)
$BaNb_2O_6$	7.85631(14)	12.18796(26)	10.26735(11)	/	87.24(7)
$Ba_4Nb_5O_{28}$	5.7887(12)	5.7887	11.782(4)	/	2.18(2)
Refinement Details					
χ^2	R_{wp}	R_p			
2.405	7.75%	5.09%			

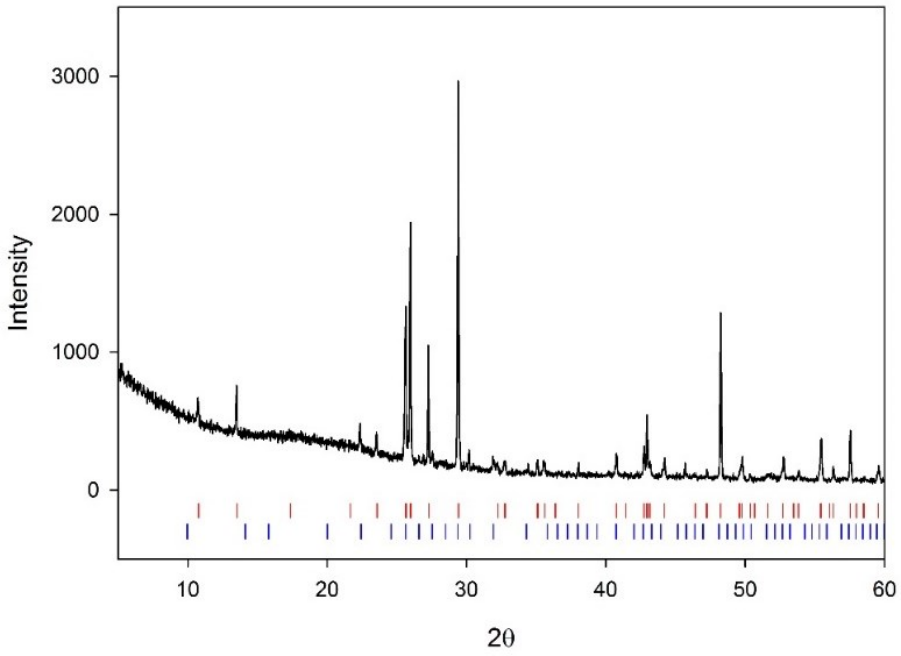

Figure 3.25 *Powder XRD of Ba-doped $Cs_2TiNb_6O_{18}$ ($Cs_{2-x}Ba_xNb^{(5+)}_{6-x}Nb^{(4+)}_xTiO_{18}$, x = 0.3) Red lines: $Cs_2TiNb_6O_{18}$ and blue lines indexed peaks from ICDD PDF: 01-070-9006 ($Ba_3Nb_{10}O_{28}$)*

One attempt was made to synthesise a Ba doped $Cs_2TiNb_6O_{18}$ material where Nb^{4+} was the charge compensating cation with Cs_2TiO_3 and $BaNb_2O_6$ as the sources for Cs and Ba respectively. This sample was synthesised in a sealed tube as discussed, to prevent Nb^{4+} from oxidising. XRD (**Figure 3.25**) revealed a number of peaks that were identified as $Cs_2TiNb_6O_{18}$ and $Ba_3Nb_{10}O_{28}$ (tetragonal, space group *P*4*bm*), a Ba impurity, indicating that Ba had again failed to incorporate into the target phase. Due to the complications with Cs_2TiO_3 (hygroscopic) and $BaNb_2O_6$ (impure) as starting materials, $CsNO_3$ and $Ba(NO_3)_2$ were reverted back to being the sources for Cs and Ba for the synthesis of $Cs_{2-x}Ba_xNb^{(5+)}_{6-x}Nb^{(4+)}_xTiO_{18}$ and $Cs_{2-x}Ba_xTi^{(4+)}_{1-x}Ti^{(3+)}_xNb_6O_{18}$ samples.

To get around the issue of nitrate decomposition at high temperatures inside a sealed tube where $CsNO_3$ and $Ba(NO_3)_2$ were used as starting materials the method was once again altered, this time with a pre-decomposition (under vacuum) step to break down the nitrates before other starting materials were added. This prevented the sealed tube from exploding

at high temperature in the synthesis step. Furthermore, all of the loading and grinding of starting materials were carried out in an inert environment. Details of this modification are found in the experimental **section 2.1.2**.

TGA experiments were carried out to confirm whether the sealed quartz tube solid-state method had prevented Nb^{4+} and Ti^{3+} from oxidising. The measurement was run under an oxygen atmosphere and it was expected that if Nb^{4+} or Ti^{3+} are present in the sample, as the temperature increases, a weight gain would be observed as Nb^{4+} or Ti^{3+} oxidise to Nb^{5+} and Ti^{4+} respectively. **Figure 3.27** ($Cs_{2-x}Ba_xNb^{(5+)}_{6-x}Nb^{(4+)}_xTiO_{18}$) and **Figure 3.27** ($Cs_{2-x}Ba_xTi^{(4+)}_{1-x}Ti^{(3+)}_xNb_6O_{18}$) show a mass increase (green line) as the sample heats up in oxygen, suggesting that Nb^{4+} and Ti^{3+} had oxidised in the thermal analysis, hinting that the sealed quartz tube solid-state synthesis method is successful. For the $Cs_{2-x}Ba_xNb^{(5+)}_{6-x}Nb^{(4+)}_xTiO_{18}$ sample there is an overall weight gain (**Figure 3.26**) of about 0.13 mg as Nb^{4+} oxidises to Nb^{5+} and for $Cs_{2-x}Ba_xTi^{(4+)}_{1-x}Ti^{(3+)}_xNb_6O_{18}$ sample there is a weight gain (**Figure 3.27**) of around 0.18 mg as Ti^{3+} oxidises to Ti^{4+}.

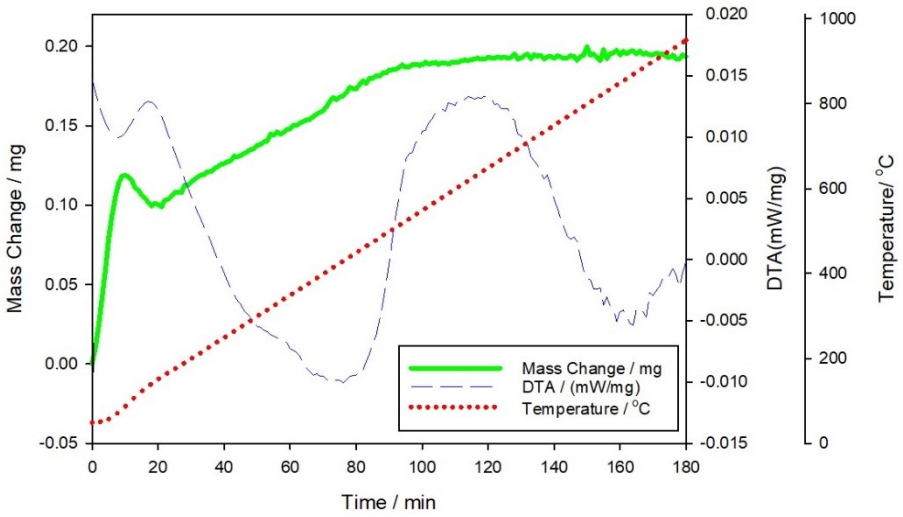

Figure 3.26 *TGA/ DTA for* $Cs_{2-x}Ba_xNb^{(5+)}_{6-x}Nb^{(4+)}_xTiO_{18}$, $x = 0.2$

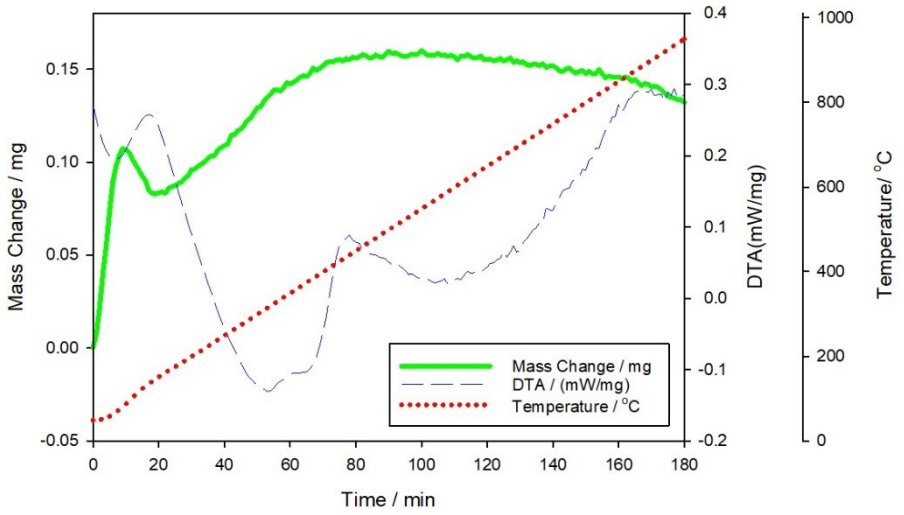

Figure 3.27 *TGA/DTA for* $Cs_{2-x}Ba_xTi^{(4+)}{}_{1-x}Ti^{(3+)}{}_xNb_6O_{18}$, *x = 0.2*

Having confirmed that oxidation had not occurred in synthesis via TGA studies, XRD and XRF analysis of $Cs_{2-x}Ba_xNb^{(5+)}{}_{6-x}Nb^{(4+)}{}_xTiO_{18}$ and $Cs_{2-x}Ba_xTi^{(4+)}{}_{1-x}Ti^{(3+)}{}_xNb_6O_{18}$ (x=0.2) samples synthesised using the sealed quartz tube solid-state synthesis were carried out. XRF (**Table 3.18**) suggested the expected Ba content and other elements agree reasonably well with the calculated values for both samples. XRD analysis of both $Cs_{2-x}Ba_xNb^{(5+)}{}_{6-x}Nb^{(4+)}{}_xTiO_{18}$ and $Cs_{2-x}Ba_xTi^{(4+)}{}_{1-x}Ti^{(3+)}xNb_6O_{18}$ (x=0.2) revealed Ba impurity peaks (**Figure 3.28** and **Figure 3.29**). These impurities were identified as $BaTiNb_4O_{13}$ and $BaTi_3Nb_4O_{17}$ for the $Nb^{(4+)}$ sample and $BaTiNb_4O_{13}$ in addition to another impurity $TiNb_2O_7$ (monoclinic, *C*2/*m*) for the Ti^{3+} sample. **Table 3.19** shows the refinement details for these samples. For the Nb^{4+} doped sample, the weight fractions suggest that the Ba fully resides in the impurity phases. The Ti^{3+} doped sample proved more difficult to refine, with unexpected differences with the intensities on some peaks. This was thought to be on account of preferred orientation rather than any Ba doping as the presence of the $BaTiNb_4O_{13}$ impurity strongly suggested that Ba had not incorporated in to the target phase despite the weight fractions. The March-Dollase preferred orientation correction was applied and the zero point was refined, but this did not rectify the issues fully.[138,145,146]

Table 3.18 *XRF $Cs_{2-x}Ba_xNb^{(5+)}{}_{6-x}Nb^{(4+)}{}_xTiO_{18}$ and $Cs_{2-x}Ba_xTi^{(4+)}{}_{1-x}Ti^{(3+)}xNb_6O_{18}$, x = 0.2*

	$Cs_{2-x}Ba_xNb^{(5+)}{}_{6-x}Nb^{(4+)}{}_xTiO_{18}$ (x = 0.2)		
Element	wt. %	at. %	Molar ratio (Normalised to Nb)
Cs	18.9	5.4	1.8
Ti	4.2	3.3	1.1
Nb	44.2	18.2	6.2
Ba	2.6	0.7	0.24
O	30.2	72.3	23.8
	$Cs_{2-x}Ba_xTi^{(4+)}{}_{1-x}Ti^{(3+)}xNb_6O_{18}$ (x = 0.2)		
Element	wt. %	at. %	Molar ratio (Normalised to Nb)
Cs	16.8	5.3	1.4
Ti	4.1	3.6	0.9
Nb	51.0	22.9	6
Ba	2.2	0.7	0.2
O	26.0	67.7	17.7

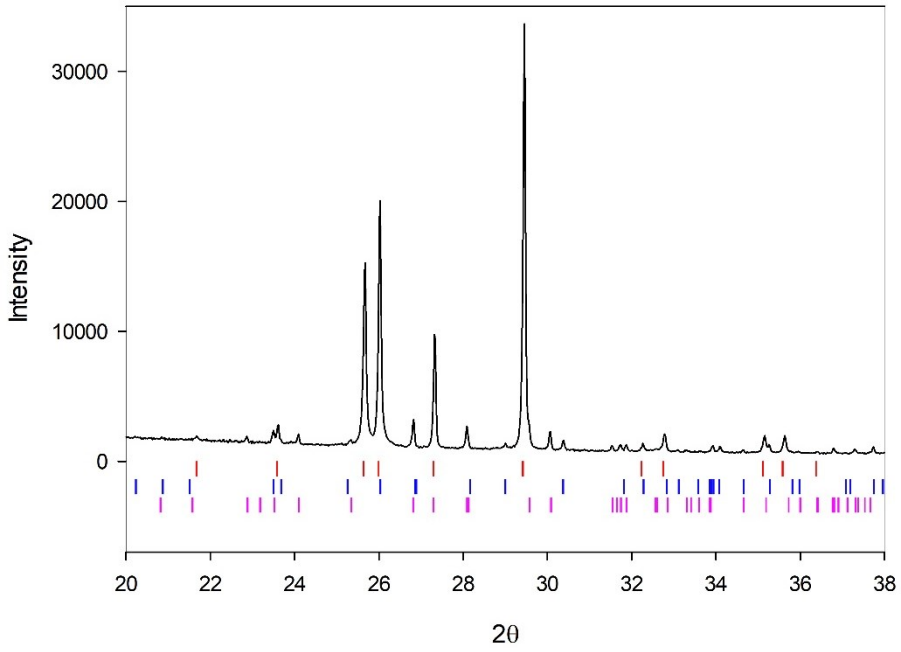

Figure 3.28 *Powder XRD of sealed quartz tube synthesis $Cs_{2-x}Ba_xNb^{(5+)}{}_{6-x}Nb^{(4+)}{}_xTiO_{18}$, x = 0.2. Red ticks: $Cs_2TiNb_6O_{18}$, blue ticks: $BaTiNb_4O_{13}$ and pink ticks: $BaTi_3Nb_4O_{17}$*

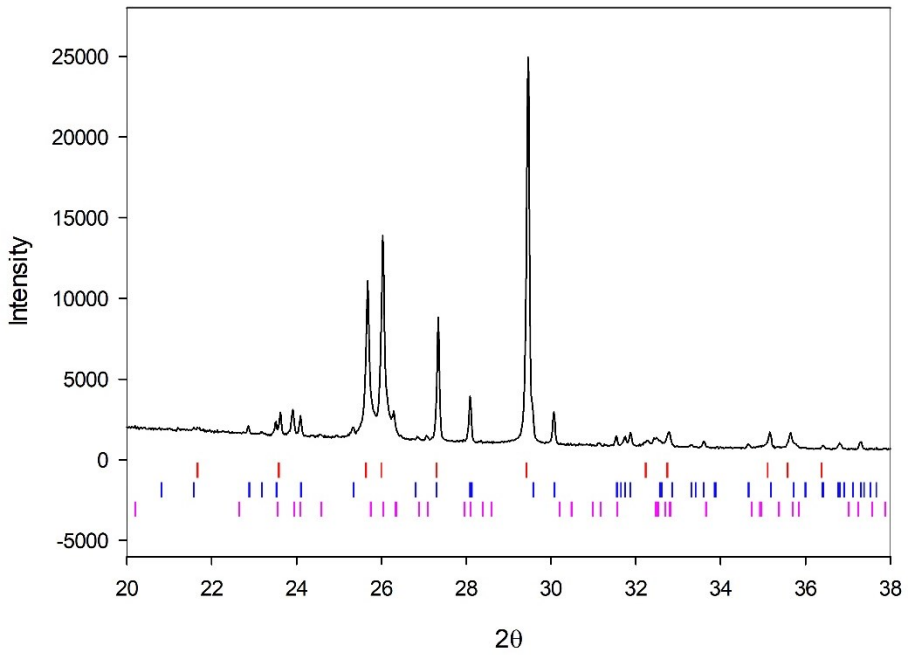

Figure 3.29 *Powder XRD of sealed quart tube synthesis $Cs_{2-x}Ba_xTi^{(4+)}{}_{1-x}Ti^{(3+)}xNb_6O_{18}$, x = 0.2. Red ticks: $Cs_2TiNb_6O_{18}$, blue ticks: $BaTiNb_4O_{13}$ and pink ticks are indexed peaks from ICDD PDF:01-077-1374 ($TiNb_2O_7$)*

Table 3.19 *Rietveld refinement details for $Cs_{2-x}Ba_xNb^{(5+)}{}_{6-x}Nb^{(4+)}{}_xTiO_{18}$ and $Cs_{2-x}Ba_xTi^{(4+)}{}_{1-x}Ti^{(3+)}xNb_6O_{18}$ (x=0.2)*

$Nb^{(4+)}$	Lattice Parameters (Å)				
	a / Å	*b* / Å	*c* / Å	*β*/°	wt. %
$Cs_2TiNb_6O_{18}$	7.52859(8)	7.52859	8.18712(12)	/	84.73(8)
$BaTiNb_4O_{13}$	5.6346(4)	10.7248(7)	16.4530(10)	/	7.6(2)
$BaTi_3Nb_4O_{17}$	6.6406(4)	8.9688(7)	21.1200(16)	/	7.6(3)
Refinement Details					
χ^2	R_{wp}	R_p	Expected Ba (wt. %):		2.37%
6.075	7.41%	4.80%	Ba in sample:		2.49%

$Ti^{(3+)}$	Lattice Parameters (Å)				
	a / Å	*b* / Å	*c* / Å	*β*/°	wt. %
$Cs_2TiNb_6O_{18}$	7.50619(19)	7.50619	8.16354(31)	/	74.8(2)
$BaTiNb_4O_{13}$	5.6182(6)	10.6987(10)	16.4099(15)	/	11.4(4)
$TiNb_2O_7$	17.565(6)	3.7921(6)	11.846(4)	94.959(21)	13.8(6)
Refinement Details					
χ^2	R_{wp}	R_p	Expected Ba (wt. %):		2.36%
12.77	10.39%	6.20%	Ba in sample:		2.05%

3.3.9 $Cs_{2-x}Ba_xNb^{(5+)}_{6-(x/2)}Ti^{(3+)}_{x/2}Ti^{(4+)}_{1-(x/2)}Nb^{(4+)}_{x/2}O_{18}$ ($Ti^{(3+)}$ and $Nb^{(4+)}$ mix)

So far two samples have been synthesised where either Nb^{4+} or Ti^{3+} have been used as the charge compensation cations as Ba is doped into $Cs_2TiNb_6O_{18}$. In this example, an attempt was made for both Nb^{4+} and Ti^{3+} to be incorporated into the same phase to charge balance for Ba^{2+} giving the formula $Cs_{2-x}Ba_xNb^{(5+)}_{6-(x/2)}Ti^{(3+)}_{x/2}Ti^{(4+)}_{1-(x/2)}Nb^{(4+)}_{x/2}O_{18}$. The method used for synthesis was again the modified quartz tube method previously discussed, which was used to make the other air sensitive samples. XRF analysis for this material (**Table 3.20**) suggested the expected amount of Ba and roughly the correct ratios of the other elements including Nb, Ti and Cs.

Table 3.20 *XRF $Cs_{2-x}Ba_xNb^{(5+)}_{6-(x/2)}Ti^{(3+)}_{x/2}Ti^{(4+)}_{1-(x/2)}Nb^{(4+)}_{x/2}O_{18}$ ($Ti^{(3+)}$ and $Nb^{(4+)}$ mix, x = 0.2)*

	$Cs_{2-x}Ba_xNb^{(5+)}_{6-(x/2)}Ti^{(3+)}_{x/2}Ti^{(4+)}_{1-(x/2)}Nb^{(4+)}_{x/2}O_{18}$ (x = 0.2)		
Element	/ wt. %	/ at. %	Molar ratio (Normalised to Nb)
Cs	20.9	6.1	2.0
Ti	4.0	3.2	1.1
Nb	43.2	18.1	6
Ba	2.3	0.7	0.2
O	29.5	71.8	23.9

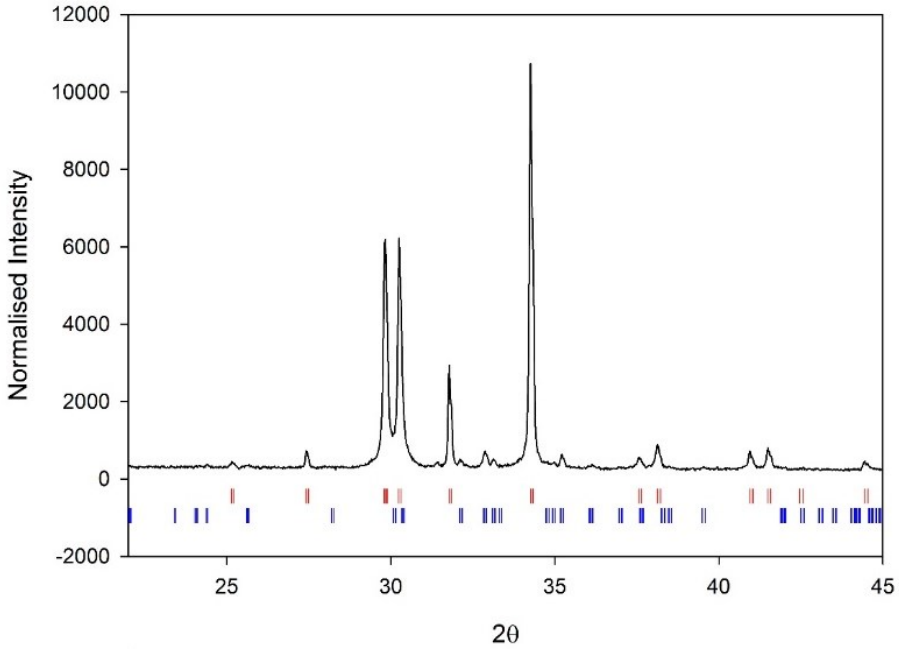

Figure 3.30 *Powder XRD $Cs_{2-x}Ba_xNb^{(5+)}_{6-(x/2)}Ti^{(3+)}_{x/2}Ti^{(4+)}_{1-(x/2)}Nb^{(4+)}_{x/2}O_{18}$ (Ti^{3+} and Nb^{4+} mix, x = 0.2). Red ticks: $Cs_2TiNb_6O_{18}$ and blue ticks: $Ba_2Ti_3Nb_4O_{18}$*

However, XRD (**Figure 3.30**) again revealed Ba impurity peaks which were identified as $Ba_2Ti_3Nb_4O_{18}$ (the stoichiometric end member). Weight fractions from Rietveld analysis hinted that Ba again resides in the impurity and not in the target phase.

Table 3.21 *$Cs_{2-x}Ba_xNb^{(5+)}_{6-(x/2)}Ti^{(3+)}_{x/2}Ti^{(4+)}_{1-(x/2)}Nb^{(4+)}_{x/2}O_{18}$ ($Ti^{(3+)}$ and $Nb^{(4+)}$ mix, x = 0.2) Rietveld refinement details*

$Ti^{(3+)}$ / $Nb^{(4+)}$	Lattice Parameters (Å)				
	a / Å	*b* / Å	*c* / Å	*β*/°	wt. %
$Cs_2TiNb_6O_{18}$	7.54249(21)	7.54249	8.21052	/	88.882(9)
$Ba_2Ti_3Nb_4O_{18}$	10.0414(22)	9.9931(21)	7.3318(17)	111.332(23)	11.11(3)
Refinement Details					
χ^2	R_{wp}	R_p	Expected Ba (wt. %):		2.36%
4.054	9.99%	7.55%	Ba in sample:		2.83%

3.3.10 $Cs_{2-x}Ba_xTi^{(4+)}_{1-x}E^{(3+)}_xNb^{(5+)}_6O_{18}$, E = $Ga^{(3+)}$ or $Al^{(3+)}$ x = 0.1

So far, a number of co-substituted mechanisms have been explored for Ba incorporation for Cs inducing excess Ti^{4+} for Nb^{5+}, Nb^{4+} for Nb^{5+}, Ti^{3+} for Ti^{4+} and also a mixed Nb^{4+} for Nb^{5+} and Ti^{3+} for Ti^{4+}. XRD and TEM studies suggested that whatever the charge compensation method, Ba does not reside in the target phase. Considering this, another charge compensation method was studied where a trivalent cation is used instead of Ti^{3+} as has been studied in the much discussed hollandite systems.[51,53] Ga^{3+} and Al^{3+} cations were selected according to their ionic radii which is shown in **Table 3.22**. Although this does not represent a realistic mechanism, it may give some indication of Ba can remain in the target phase. XRF (**Table 3.23**) confirmed the presence of both the trivalent cations (Ga^{3+} and Al^{3+}) and Ba in each sample.

Table 3.22 *Ionic radii of charge compensation cations including trivalent cations Gallium and Aluminium* [141]

Cation	Ionic radii / Å
Ti^{4+} (6 coordinate)	0.605
Nb^{5+} (6 coordinate)	0.64
Ti^{3+} (6 coordinate)	0.67
Nb^{4+} (6 coordinate)	0.68
Ga^{3+} (6 coordinate)	**0.62**
Al^{3+} (6 coordinate)	**0.535**

Table 3.23 *XRF details for $Cs_{2-x}Ba_xTi^{(4+)}{}_{1-x}Ga^{(3+)}{}_xNb^{(5+)}{}_6O_{18}$ and $Cs_{2-x}Ba_xTi^{(4+)}{}_{1-x}Al^{(3+)}{}_xNb^{(5+)}{}_6O_{18}$ (x=0.1)*

	$Cs_{2-x}Ba_xTi^{(4+)}{}_{1-x}Ga^{(3+)}{}_xNb^{(5+)}{}_6O_{18}$ (x=0.1)		
Element	wt. %	at. %	Molar ratio (Normalised to Nb)
Cs	20.8	6.1	1.9
Ti	3.4	2.8	0.9
Nb	45.0	18.9	6
Ba	0.9	0.2	0.1
Ga	0.6	0.3	0.1
O	29.4	71.6	22.8
	$Cs_{2-x}Ba_xTi^{(4+)}{}_{1-x}Al^{(3+)}{}_xNb^{(5+)}{}_6O_{18}$ (x=0.1)		
Element	wt. %	at. %	Molar ratio (Normalised to Nb)
Cs	22.3	6.8	2.0
Ti	3.6	3.1	0.9
Nb	45.7	20.1	6
Ba	1.0	0.3	0.1
Al	0.3	0.4	0.1
O	27.1	69.3	20.7

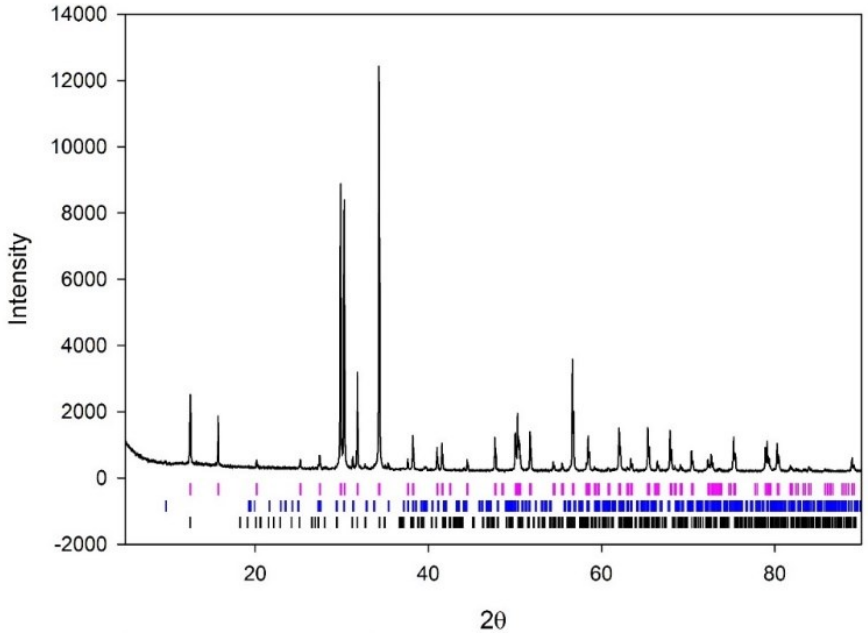

Figure 3.31 *Powder XRD pattern $Cs_{2-x}Ba_xTi^{(4+)}{}_{1-x}Ga^{(3+)}{}_xNb^{(5+)}{}_6O_{18}$ (x=0.1). Pink ticks: $Cs_2TiNb_6O_{18}$, blue ticks: $BaTi_3Nb_4O_{17}$ and black ticks: $BaTiNb_4O_{13}$.*

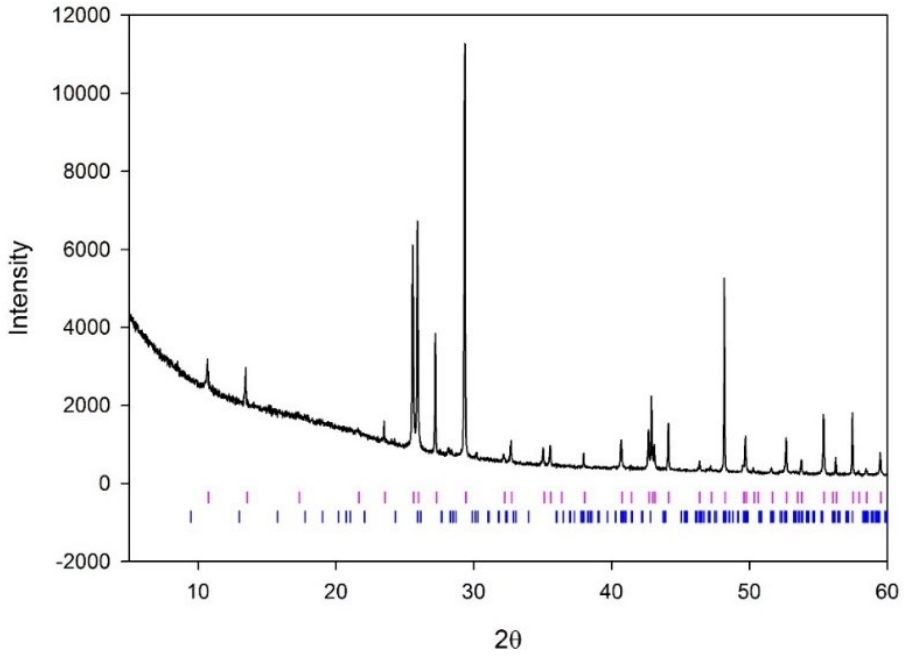

Figure 3.32 *Powder XRD pattern* $Cs_{2-x}Ba_xTi^{(4+)}{}_{1-x}Al^{(3+)}{}_xNb^{(5+)}{}_6O_{18}$ *(x=0.1). Pink ticks:* $Cs_2TiNb_6O_{18}$ *and blue ticks:* $Ba_2Ti_3Nb_4O_{18}$

Powder XRD patterns (**Figure 3.31** and **Figure 3.32**) of $Cs_{2-x}Ba_xTi^{(4+)}{}_{1-x}Ga^{(3+)}{}_xNb^{(5+)}{}_6O_{18}$ (x=0.1) and $Cs_{2-x}Ba_xTi^{(4+)}{}_{1-x}Al^{(3+)}{}_xNb^{(5+)}{}_6O_{18}$ (x=0.1) revealed several impurity peaks. For the Ga^{3+} doped sample, two Ba impurities were present including $BaTi_3Nb_4O_{17}$ and $BaTiNb_4O_{13}$. For the Al^{3+} sample, only one impurity phase was present which was identified as $Ba_2Ti_3Nb_4O_{18}$. No peaks could be assigned for phases containing either Ga^{3+}or Al^{3+}which is likely because the Ga and Al are in such low concentration they cannot be easily seen via XRD. However, it may be either Ga^{3+} or Al^{3+} has replaced some Nb^{5+} or Ti^{4+} in either the target phase or indeed any of the impurity phases which would be difficult to detect via this type of analysis. It's clear from Rietveld analysis that despite possible Ga^{3+}/Al^{3+} incorporation, Ba resides in the impurity phase, not $Cs_2TiNb_6O_{18}$.

Table 3.24 *Rietveld refinement details for $Cs_{2-x}Ba_xTi^{(4+)}_{1-x}Ga^{(3+)}_xNb^{(5+)}_6O_{18}$ (x=0.1) and $Cs_{2-x}Ba_xTi^{(4+)}_{1-x}Al^{(3+)}_xNb^{(5+)}_6O_{18}$ (x=0.1)*

$Ga^{(3+)}$	Lattice Parameters (Å)				
	a / Å	*b* / Å	*c* / Å	*β*/°	wt. %
$Cs_2TiNb_6O_{18}$	7.54182(5)	7.54182	8.19872(8)	/	92.508(2)
$BaTi_3Nb_4O_{17}$	6.6429(16)	8.9926(28)	21.182(6)	/	4.71(2)
$BaTiNb_4O_{13}$	5.6503(32)	10.790(5)	16.487(8)	/	2.78(2)
Refinement Details					
χ^2	R_{wp}	R_p	Expected Ba (wt. %):		1.18%
3.294	9.14%	7.21%	Ba in sample:		1.20%

$Al^{(3+)}$	Lattice Parameters (Å)				
	a / Å	*b* / Å	*c* / Å	*β*/°	wt. %
$Cs_2TiNb_6O_{18}$	7.53223(15)	7.53223(15)	8.18280(23)	/	94.129(3)
$Ba_2Ti_3Nb_4O_{18}$	10.0094(30)	9.965(4)	7.3143(24)	111.291(31)	5.87(44)
Refinement Details					
χ^2	R_{wp}	R_p	Expected Ba (wt. %):		1.19%
3.722	5.75%	3.58%	Ba in sample:		1.50%

3.3.11 Cs/Ba Hollandites

Hollandite, a key component of the multi-phase SYNROC formation, is an extremely durable phase and therefore is a potential candidate for radioactive Cs immobilisation.[48,50,55,56] It is reported in several studies that hollandite can retain Ba, the product after ^{137}Cs decays.[55,56] XRD and microscopy studies have suggested that Ba and Cs can coexist in the same phase via a charge compensation mechanism that involves reduced species such as Ti^{3+} and Fe^{2+}.[9,11,31,48,50,55,56] To support the study of Ba substitution into $Cs_2TiNb_6O_{18}$, both a pure hollandite (Ti/Al formation) and a Cs/Ba co-substituted hollandite (Ti/Al formation) have been synthesised and analysed. Both samples were synthesised via a citrate combustion method of which details can be found in **section 3.2.2**.

Two hollandite materials have been synthesised with formulas $Ba_{1.24}Al_{2.48}Ti_{5.52}O_{16}$ and $Ba_{0.62}Cs_{0.62}Al_{1.86}Ti_{6.14}O_{16}$. The charge compensation for the Cs incorporation has been

achieved by doping excess Ti^{4+} for Al^{3+}. Once synthesised, XRD and XRF studies have been carried out to confirm the incorporation of Ba and Cs in the same hollandite structure. No samples in this work due to time constraints have been synthesised to represent a realistic mechanism where for example Ti^{3+} or Fe^{2+} are used for charge compensation.

XRF (**Table 3.25**) analysis for the Ba pure example suggested the expected amount of Ti is present, however there is a small discrepancy in the Al and Ba values which is likely a result of the stoichiometry being incorrect from the starting materials and instrument errors. XRF did confirm the presence of both Cs and Ba in the mixed Cs/Ba hollandite. However, it suggested that there is less Cs and more Ba present and an excess of Ti. Again, this may be a result of the starting materials not being in the correct ratio.

Table 3.25 *XRF analysis of Ba hollandite ($Ba_{1.24}Al_{2.48}Ti_{5.52}O_{16}$) and Cs/Ba hollandite ($Ba_{0.62}Cs_{0.62}Al_{1.86}Ti_{6.14}O_{16}$)*

	$Ba_{1.24}Al_{2.48}Ti_{5.52}O_{16}$		
Element	wt. %	at. %	Molar ratio (Normalised to Ti)
Ti	32.8	20.0	5.5
Al	7.2	7.8	2.1
Ba	22.9	4.9	1.3
O	37.0	67.4	18.6
	$Ba_{0.62}Cs_{0.62}Al_{1.86}Ti_{6.14}O_{16}$		
Element	wt. %	at. %	Molar ratio (Normalised to Ti)
Ti	39.1	24.2	6.1
Al	6.4	7.0	1.8
Ba	11.7	2.5	0.6
Cs	7.8	1.7	0.4
O	35.0	64.6	16.4

XRD (**Figure 3.33** and **Figure 3.34**) and subsequent Rietveld analysis (**Table 3.26** and **Table 3.27**) confirmed that both hollandite materials crystallise in the *I*4/*m* space group. Both have small impurity phases present. The Ba pure hollandite phase contained an

impurity identified as $Ba_4Al_2Ti_{10}O_{27}$ and the Cs/Ba hollandite contained a small amount of TiO_2 (anatase).

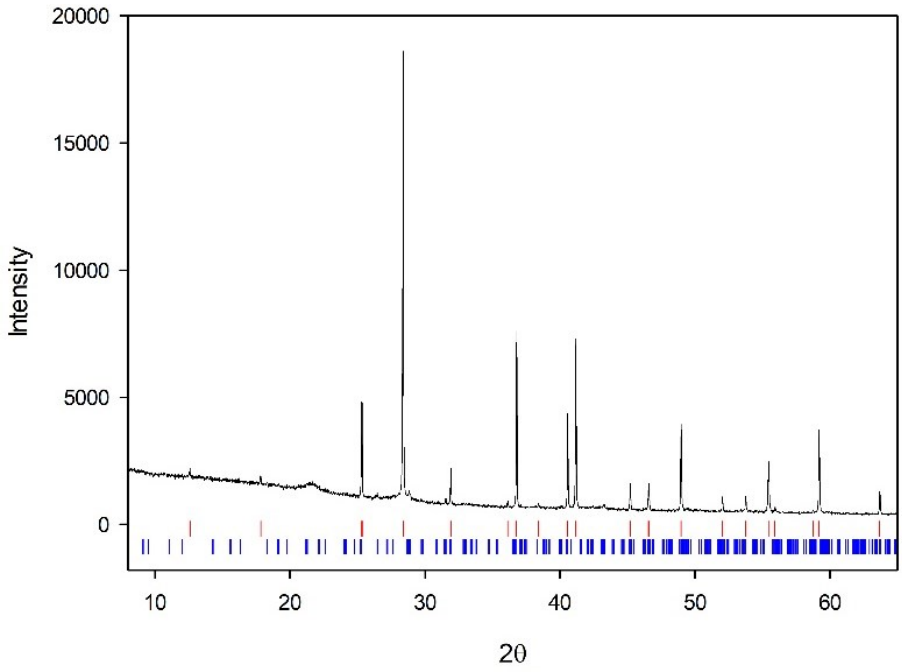

Figure 3.33 *Powder XRD $BaAl_2Ti_6O_{16}$, Ba-hollandite. Red ticks are indexed from ICDD PDF: 01-078-0013 ($Ba_{1.24}Al_{2.48}Ti_{5.52}O_{16}$) and Blue ticks are indexed from ICDD PDF: 01-089-5859 ($Ba_4Al_2Ti_{10}O_{27}$).*

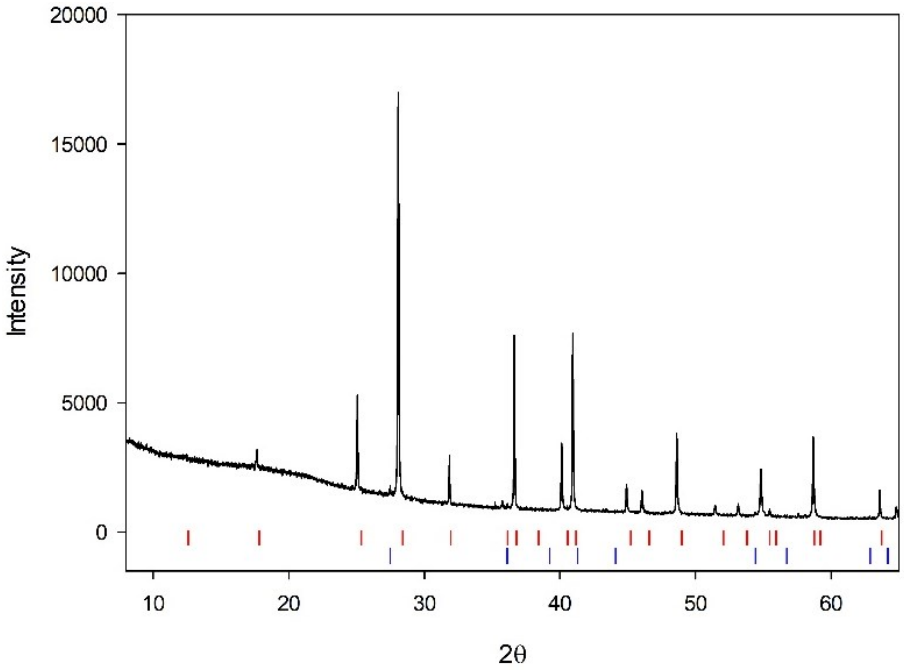

Figure 3.34 *Powder XRD $BaCsAl_2Ti_6O_{16}$, Cs/Ba- hollandite. Red ticks are indexed from ICDD PDF: 01-078-0013 $Ba_{0.965}Cs_{0.187}Al_{2.115}Ti_{5.885}O_{16}$. Blue ticks are indexed from ICDD PDF:01-071-1166 (TiO_2, anatase)*

Table 3.26 *Refinement details Ba – hollandite ($Ba_{1.24}Al_{2.48}Ti_{5.52}O_{16}$)*

Ba-Hollandite	Lattice Parameters (Å)				
	a / Å	*b* / Å	*c* / Å	*β*/°	wt. %
$Ba_{1.24}Al_{2.48}Ti_{5.52}O_{16}$	9.93202(11)	9.93202	2.9191 (33)	/	96.861(3)
$Ba_4Al_2Ti_{10}O_{27}$	19.671(5)	11.3355(26)	9.8122(24)	109.241(16)	3.14(2)
Refinement Details					
χ^2	R_{wp}	R_p			
2.367	5.14%	3.71%			

Table 3.27 *Rietveld refinement details for Cs/Ba – Hollandite $Ba_{0.62}Cs_{0.62}Al_{1.86}Ti_{6.14}O_{16}$*

Cs/Ba- hollandite	Lattice Parameters (Å)			
	a / Å	b / Å	c / Å	*wt. %*
$Ba_{0.62}Cs_{0.62}Al_{1.86}Ti_{6.14}O_{16}$	10.03715(13)	10.03715	2.92299(4)	98.645(1)
TiO_2	4.5842(9)	4.5842	2.9537(11)	1.36(1)
Refinement Details				
χ^2	R_{wp}	R_p		
2.144	4.04%	2.97%		

The lattice parameters refined from Rietveld refinement suggest that the Cs/Ba hollandite unit cell size in comparison to the Ba pure Hollandite increases as Cs is doped into the structure suggesting that a co-substituted Cs/Ba hollandite had been successfully synthesised. The *a* parameter increased from 9.93202(11) to 10.03715(13) Å and the *c* parameter 2.91911(33) to 2.92299(4) Å. The occupancies (**Table 3.28**) were also refined for the co-substituted Ba/Cs hollandite giving the approximate formula $Ba_{0.49}Cs_{0.91}Ti_{5.70}Al_{2.3}O_{16}$. This formula agrees with the XRF analysis where the co-substituted sample suggested more Ba and less Cs that what was expected from the original calculated stoichiometry.

Table 3.28 *Refined occupancy for Cs/Ba-hollandite (*Not refined)*

Atom	Occupancy	Multiplicity	Formula
Cs	0.112(15)	4	0.488
Ba	0.228(15)	4	0.912
Ti	0.712(15)	8	5.696
Al	0.288(15)	8	2.304
O1*	8	8	8
O2*	8	8	8

3.3.12 Computational studies of Ba – doped $Cs_2TiNb_6O_{18}$

Having been unable to confirm any level of Ba doping experimentally, a series of static calculations have been carried out using the GULP (general utility lattice program code)[117] to investigate the energetics of different mechanisms associated with Ba incorporation into $Cs_2TiNb_6O_{18}$. Initially this study was carried out using Buckingham potentials taken from the literature of which the references can be found in **Table 3.29**. It quickly became clear that these potentials would not prove sufficient for this study as even basic simulations of relatively simple unit cells (BaO, $BaTiO_3$) failed to produce acceptable results compared to empirical data, therefore a set of new potentials have been derived.

3.3.13 Fitting Buckingham Potentials

A set of novel Buckingham potentials, listed in **Table 3.30** have been empirically derived using a code based on Reverse Monte Carlo (RMC) methodology developed by another group member.[118,147] Details of the code are outside the remit of this study but details can be found in the reference.[118] Briefly, the RMC fitting code integrates with the GULP code and samples the potential surface. The quality of fit was determined by a weighted least-squares method which compared the simulated data with empirical data which included lattice parameters, bond lengths and bulk modulus.[148] The starting points for each fit have been taken from literature and are listed in **Table 3.29**.

Table 3.29 *Starting Potentials from the GULP Library*

Interaction	Reference	A / eV	ρ /Å	C / eV·Å^6	R_{cut} / Å
O core O core	Woodley et al. [149]	25.41	32.32	0	12
Ba core O core	Bush et al. [150]	4818.416	0.3067	0	10
Cs core O core	Jackson et al.[151]	15085.4788	0.2549	0	10
Ti^{4+} core O core	Woodley et al. [149]	4545.823	0.261	0	10
Ti^{3+} core O core	**Same starting point as Ti^{4+}**				
Nb^{5+} core O core	Woodley et al. [149]	3023.184	0.3	0	10
Nb^{4+} core O core	**Same starting point as Nb^{4+}**				
Si core O core	Catlow et al [152]	1283.907	0.32052	0	10
Al core O core	Baram et al. [153]	1142.6775	0.29912	0	10
Ga core O core	Girard et al. [154]	1950.797	0.287	0	10
Fe core O core	Catlow et al. [155]	862.08	0.3299	0	10

Table 3.30 *Buckingham Potentials* [144]

Interaction	A / eV	ρ /Å	C / eV·Å^6	R_{cut} / Å
$Cs^{0.66}$ core $O^{-1.32}$ core	48865.058	0.24566	178.45697	10
$Ti^{2.64}$ core $O^{-1.32}$ core	5910.0299	0.24483	70.37101	10
$Nb^{3.3}$ core $O^{-1.32}$ core	7627.351	0.22762	2.14322	10
$Ba^{1.32}$ core $O^{-1.32}$ core	14978.099	0.25091	9.44896	10
$Ti^{1.98}$ core $O^{-1.32}$ core	1325.8973	0.29404	96.85703	10
$Nb^{2.64}$ core $O^{-1.32}$ core	7882.4242	0.24021	120.97084	10
$Ga^{1.98}$ core $O^{-1.32}$ core	1373.712	0.26213	1.51743	10
$Al^{1.98}$ core $O^{-1.32}$ core	1095.4966	0.26653	7.41994	10
$O^{-1.32}$ core $O^{-1.32}$ core	2065.0236	0.31729	110.89703	12

In general, the lattice parameters were the main focus in terms of fitting and therefore the lattice parameters were weighted heavily in terms of least-squares fitting. In terms of acceptable differences, any parameter simulated to within 3% error of the original experimental lattice constant was considered a satisfactory fit. Where applicable, the bulk modulus of the material has also been fit. This is the case for simple oxides such as TiO_2, Nb_2O_5, BaO and $BaTiO_3$ but no high-pressure data could be acquired for the more complex oxides. The general method for fitting was an iterative process. To start with, simple oxides such as BaO, Nb_2O_5 and TiO_2 were fit. Once a reasonable set of potentials had been derived for the first few phases, additional polymorphs of Nb_2O_5 and TiO_2 were added to ensure the potentials were robust. When the fitting process included Cs_2O, there were difficulties. Cs_2O is an unstable material and the Cs-O bonds are extremely polarized compared with the other phases containing Cs-O bonds. In effect this meant that the same Cs-O potential could not describe the short-range interactions in both Cs_2O and $Cs_2TiNb_6O_{18}$ and therefore, Cs_2O was omitted from the fitting process and hence the simulated data does not match the experimental data well (Phase 12, **Table 3.31**). Additional Cs containing phases have been included in the fit as well as $Cs_2TiNb_6O_{18}$ in order to ensure the Cs-O potential is robust and transferable. These included $CsNbO_3$, $CsAlO_2$, $CsBaAlTi_7O_{16}$ (Hollandite) and $CsAlSi_2O_{6.5}$ (pollucite). As more complex phases such as $Cs_2TiNb_6O_{18}$, $BaTiNb_4O_{13}$ and $BaTi_3Nb_4O_{18}$ were included to the fitting process it proved impossible to fit phases at full formal charge to within a 3% error. Therefore, the model was scaled to partial charges (66%) which improved the overall fit of all phases. **Table 3.31** shows the simulated outputs from GULP compared to the experimental data.

Table 3.31 *Phases, simulated values versus experimental values GULP*

	Phase and Space Group	**Lattice Constants**							
1	**BaO,** *Fm*-3*m*	*a* / Å	*b* / Å	*c* / Å	*V* / Å	*α* / °	*β* / °	*γ* / °	Bulk Modulus / GPa
	Experimental Value [156]	5.517	/	/	167.922523	90	90	90	66 [157]
	Simulated Value	5.488509	/	/	165.334329				65.80065
	Error / %	**-0.52**	**/**	**/**	**-1.54**				0.3 %
2	**TiO_2 (Rutile) ,** $P4_2/mnm$	*a* / Å	*b* / Å	*c* / Å	*V* / Å	*α* / °	*β* / °	*γ* / °	Bulk Modulus / GPa
	Experimental Value [97]	4.5941	/	2.9589	62.449818	90	90	90	244 [158]
	Simulated Value	4.502819	/	3.038329	61.603281				266.35561
	Error / %	**-1.99**	**/**	**2.68**	**-1.36**				9.16 %
3	**TiO_2 (Anatase),** $I4_1/amd$	*a* / Å	*b* / Å	*c* / Å	*V* / Å	*α* / °	*β* / °	*γ* / °	Bulk Modulus / GPa
	Experimental Value [108]	3.7842	/	9.5146	136.250686	90	90	90	190 [158]
	Simulated Value	3.75907	/	9.723438	137.398089				203.62069
	Error / %	**-0.66**	**/**	**2.19**	**0.84**				-6.69 %
4	**TiO_2 (Brookite),** *Pbca*	*a* / Å	*b* / Å	*c* / Å	*V* / Å	*α* / °	*β* / °	*γ* / °	Bulk Modulus / GPa
	Experimental Value [159]	9.174	5.449	5.138	256.844129	90	90	90	220 [158]
	Simulated Value	9.16031	5.398402	5.191133	256.706893				235.51013
	Error / %	**-0.15**	**-0.93**	**1.03**	**-0.05**				-6.59 %

5	**$BaTiO_3$,** *Pm*-3*m*	*a* / Å	*b* / Å	*c* / Å	*V* / Å	*α* / °	*β* / °	*γ* / °	Bulk Modulus / GPa
	Experimental Value [160]	4.006	/	/	64.288432	90	90	90	195 [161]
	Simulated Value	3.992481	/	/	63.9762	90	90	90	184.72216
	Error / %	**-0.34**			**-1.01**				-5.27 %

6	**Nb_2O_5,** *C*2/*c*	*a* / Å	*b* / Å	*c* / Å	*V* / Å	*α* / °	*β* / °	*γ* / °	Bulk Modulus / GPa
	Experimental Value [162]	12.74	4.883	5.5609	334.121457	90	105.02	90	109 [163]
	Simulated Value	12.950446	4.757537	5.52567	329.835944	90	104.343785	90	146.25671
	Error / %	**1.65**	**-2.57**	**-0.63**	**-1.28**		0.64		25.47 %

7	**$Cs_2TiNb_6O_{18}$,** *P*-3*m*1	*a* / Å	*b* / Å	*c* / Å	*V* / Å	*α* / °	*β* / °	*γ* / °	Bulk Modulus / GPa
	Experimental Value [84]	7.533	/	8.189	402.436569	90	90	120	/
	Simulated Value	7.381081	/	8.433568	397.907287				/
	Error / %	**-2.02**	/	**2.99**	**-1.13**				/

8	**$BaTi_3Nb_4O_{17}$,** *Cmcm*	*a* / Å	*b* / Å	*c* / Å	*V* / Å	*α* / °	*β* / °	*γ* / °	Bulk Modulus / GPa
	Experimental Value [164]	6.639	8.957	21.145	1257.398484	90	90	90	/
	Simulated Value	6.550625	8.971175	21.365655	1255.591118				/
	Error / %	**-1.33**	**0.16**	**1.04**	**-0.14**				/

9	**$BaTiNb_4O_{13}$,** *Pbcm*	*a* / Å	*b* / Å	*c* / Å	*V* / Å	*α* / °	*β* / °	*γ* / °	Bulk Modulus / GPa
	Experimental Value [88]	5.64	10.37	16.488	965.074297	90	90	90	/
	Simulated Value	5.567257	10.699497	16.801124	1000.790064				/
	Error / %	**-1.29**	**3.1**	**1.9**	**3.7**				/

10	**Nb_2O_5,** *P*2/*m*	*a* / Å	*b* / Å	*c* / Å	*V* / Å	*α* / °	*β* / °	*γ* / °	Bulk Modulus / GPa
	Experimental Value [165]	21.153	3.823	19.356	1358.295423	90	90	90	157 [163]
	Simulated Value	20.89881	3.853089	18.998762	1333.292595				194.68148
	Error / %	**-1.2**	**0.79**	**-1.85**	**-1.84**				27.39 %

11	**$Ba_2Ti_3Nb_4O_{18}$,** *P*2_1/*c*	*a* / Å	*b* / Å	*c* / Å	*V* / Å	*α* / °	*β* / °	*γ* / °	Bulk Modulus / GPa
	Experimental Value [85]	10	9.959	7.315	678.784027	90	111.29	90	/
	Simulated Value	10.196174	10.098802	7.25356	697.61138	90	110.929913	90	/
	Error / %	**1.96**	**1.4**	**-0.84**	**2.77**		-0.32		/

12	**Cs_2O,** *R*-3*m*	*a* / Å	*b* / Å	*c* / Å	*V* / Å	*α* / °	*β* / °	*γ* / °	Bulk Modulus / GPa
	Experimental Value [166]	4.256	/	18.99	297.891996	90	90	120	/
	Simulated Value	4.905276	/	12.015766	250.385447	90	90	120	/
	Error / %	**15.26**		**-36.73**	**-47.506549**				/

13	**NbO_2,** *I*4$_1$/*a*	*a* / Å	*b* / Å	*c* / Å	*V* / Å	*α* / °	*β* / °	*γ* / °	Bulk Modulus / GPa
	Experimental Value [167]	13.696		5.981	1121.918468	90	90	90	235 [168]
	Simulated Value	13.639484		5.963715	1109.462818	90	90	90	231
	Error / %	**-0.41**		**-0.29**	**-1.11**				1.70 %

14	**$CsNbO_3$,** *P*2_1/*c*	*a* / Å	*b* / Å	*c* / Å	*V* / Å	*α* / °	*β* / °	*γ* / °	Bulk Modulus / GPa
	Experimental Value [169]	5.148	15.89	9.143	747.902874	90	90.3	90	/
	Simulated Value	5.149934	16.10438	9.0263	748.20413	90	91.885905	90	/
	Error / %	**0.04**	**1.35**	**-1.28**	**0.04**				/

15	**Ti_2O_3,** *R*-3*m*	*a* / Å	*b* / Å	*c* / Å	*V* / Å	*α* / °	*β* / °	*γ* / °	Bulk Modulus / GPa
	Experimental Value [170]	5.158		13.611	313.605262	90	90	120	206 [171]
	Simulated Value	5.1587808	/	13.737406	320.186605	90	90	120	212
	Error / %	**0.58**	/	**0.93**	**2.1**				2.91%

16	**$CsAlSi_2O_6$,** *Im*-3*m*	*a* / Å	*b* / Å	*c* / Å	*V* / Å	*α* / °	*β* / °	*γ* / °	Bulk Modulus / GPa
	Experimental Value [172]	13.74	/	/	2593.941624	90	90	90	/
	Simulated Value	13.557441	/	/	2491.914872				/
	Error / %	**-1.33**			**-3.93**				/

17	**Al_2O_3 ,** *R*-3*m*	*a* / Å	*b* / Å	*c* / Å	*V* / Å	*α* / °	*β* / °	*γ* / °	Bulk Modulus / GPa
	Experimental Value [173]	4.7617	/	12.999	255.249345	90	90	120	186 [174]
	Simulated Value	4.823013	/	13.311196	268.154191				250
	Error / %	**1.29**		**2.4**	5.06				34.41%

18	**$BaAl_2Ti_6O_{16}$,** *I*4/*m*	*a* / Å	*b* / Å	*c* / Å	*V* / Å	*α* / °	*β* / °	*γ* / °	Bulk Modulus / GPa
	Experimental Value [175]	9.9485	/	2.9242	289.415	90	90	90	/
	Simulated Value	10.01745	/	3.025763	303.633191				/
	Error / %	**0.69**		**3.47**	4.91				/

19	**SiO_2,** *C*2/*m*	*a* / Å	*b* / Å	*c* / Å	*V* / Å	*α* / °	*β* / °	*γ* / °	Bulk Modulus / GPa
	Experimental Value [176]	7.173	12.328	7.175	549.47254	90	120	90	/
	Simulated Value	7.086469	12.359716	7.184865	545.126663		119.9745895		/
	Error / %	**-1.21**	**0.26**	**0.14**	-0.79		-0.02		/

20	**$Ti_2Nb_{10}O_{29}$,** *C*2/*m*	*a* / Å	*b* / Å	*c* / Å	*V* / Å	*α* / °	*β* / °	*γ* / °	Bulk Modulus / GPa
	Experimental Value [177]	7.173	12.328	7.175	549.47254	90	120	90	/
	Simulated Value	7.086469	12.359716	7.184865	545.126663		119.9745895		/
	Error / %	**-1.21**	**0.26**	**0.14**	**-0.79**		-0.02		/

21	**$BaNb_2O_6$,** *Cmmm*	*a* / Å	*b* / Å	*c* / Å	*V* / Å	*α* / °	*β* / °	*γ* / °	Bulk Modulus / GPa
	Experimental Value [178]	7.88	12.215	10.292	990.648266	90	90	90	/
	Simulated Value	7.702374	12.538552	10.508875	1014.911609	90	90	90	/
	Error / %	**-2.25**	**2.65**	**2.11**	**2.45**				/

22	**$(Ti,Nb)O_2$ (Rutile),** *P*4/*mmm*	*a* / Å	*b* / Å	*c* / Å	*V* / Å	*α* / °	*β* / °	*γ* / °	Bulk Modulus / GPa
	Experimental Value [179]	4.6392	4.6329	2.9902	64.355613	90	90	90	/
	Simulated Value	4.619738	4.619738	3.134927	66.905532	90	90	90	/
	Error / %	**-0.42**	**-0.42**	**4.84**	**3.96**				/

23	**$CsTi_3AlO_8$,** *I*4/*m*	*a* / Å	*b* / Å	*c* / Å	*V* / Å	*α* / °	*β* / °	*γ* / °	Bulk Modulus / GPa
	Experimental Value [180]	10.18477	10.18477	2.94607	305.594486	90	90	90	/
	Simulated Value	10.166712	10.166715	3.019796	312.132278	90	90	90	/
	Error / %	**-0.18**	**-0.18**	**2.5**	**2.14**				/

24	**Ga_2O_3,** *R*-3*m*	*a* / Å	*b* / Å	*c* / Å	*V* / Å	*α* / °	*β* / °	*γ* / °	Bulk Modulus / GPa
	Experimental Value [181]	4.9825	4.9825	13.433	288.800713	90	90	120	/
	Simulated Value	4.981598	4.981598	13.595837	292.195767	90	90	120	/
	Error / %	**-0.02**	**-0.02**	**1.21**	**1.18**				/

25	**Ga_2O_3,** *C*2/*m*	*a* / Å	*b* / Å	*c* / Å	*V* / Å	*α* / °	*β* / °	*γ* / °	Bulk Modulus / GPa
	Experimental Value [182]	12.23	3.04	5.8	209.50423	90	103.7	90	/
	Simulated Value	12.062604	3.06021	5.879958	210.10988	90	104.531424	90	/
	Error / %	-1.37	0.66	1.38	0.29				/

26	**Fe_2O_3,** *R*-3*m*	*a* / Å	*b* / Å	*c* / Å	*V* / Å	*α* / °	*β* / °	*γ* / °	Bulk Modulus / GPa
	Experimental Value [183]	5.038	5.038	13.772	302.721992	90	90	120	/
	Simulated Value	4.997052	4.997052	13.575915	293.580702	90	90	120	/
	Error / %	**-0.81**	**-0.81**	**-1.42**	**-3.02**				/

27	**$Ba_{0.6}Cs_{0.14}Ti_{2.684}Al_{0.9}Fe_{0.408}O_8$,** *I*4/*m*	*a* / Å	*b* / Å	*c* / Å	*V* / Å	*α* / °	*β* / °	*γ* / °	Bulk Modulus / GPa
	Experimental Value [56]	10.048	10.048	2.94246	297.077541	90	90	90	/
	Simulated Value	10.058269	10.058269	3.033345	306.879835	90	90	90	/
	Error / %	**0.1**	**0.1**	**3.09**	**303**				/

28	**$CsAlO_2$,** *Fm*-3*m*	*a* / Å	*b* / Å	*c* / Å	*V* / Å	*α* / °	*β* / °	*γ* / °	Bulk Modulus / GPa
	Experimental Value [184]	8.098	8.098	8.098	531.047437	90	90	90	/
	Simulated Value	7.837911	7.837911	7.837911	481.5052225	90	90	90	/
	Error / %	**-3.21**	**-3.21**	**-3.21**	**-9.33**				/

29	**$BaAl_2O_4$,** $P6_322$	*a* / Å	*b* / Å	*c* / Å	*V* / Å	*α* / °	*β* / °	*γ* / °	Bulk Modulus / GPa
	Experimental Value [185]	5.227	5.227	8.802	208.265338	90	90	120	/
	Simulated Value	5.225036	5.225036	8.835831	208.908749	90	90	120	/
	Error / %	**-0.04**	**-0.04**	**0.38**	**0.31**				/

3.3.14 Defect calculations

To compliment the experimental studies, a number of mechanisms have been investigated for the doping of Ba into $Cs_2TiNb_6O_{18}$. This included scheme 1 (**Equation 3.1**), where the simulation represents Ba incorporation via Ti^{4+} reducing to Ti^{3+}, scheme 2 (**Equation 3.2**) where Nb^{5+} reduced to Nb^{4+}, scheme 3 (**Equation 3.3**) where excess Ti^{4+} is doped for Nb^{5+} and also scheme 4 (**Equation 3.4**), where a mixture of Ti^{3+} and Nb^{4+} is used for charge compensation.

$$BaO + \frac{1}{2}Ti_2O_3 + Cs_{Cs}^{X} + Ti_{Ti}^{X} \rightarrow Ba_{Cs}^{\bullet} + Ti_{Ti}' + TiO_2 + \frac{1}{2}Cs_2O$$

Equation 3.1 *Kröger-Vink [186] charge compensating mechanism, scheme 1 (Ti^{4+}/Ti^{3+})*

$$BaO + NbO_2 + Cs_{Cs}^{X} + Nb_{Nb}^{X} \rightarrow Ba_{Cs}^{\bullet} + Nb_{Nb}' + \frac{1}{2}Nb_2O_5 + \frac{1}{2}Cs_2O$$

Equation 3.2 *Kröger-Vink charge compensating mechanism, scheme 2 (Nb^{5+}/Nb^{4+})*

$$BaO + TiO_2 + Cs_{Cs}^{X} + Nb_{Nb}^{X} \rightarrow Ba_{Cs}^{\bullet} + Ti_{Nb}' + \frac{1}{2}Nb_2O_5 + \frac{1}{2}Cs_2O$$

Equation 3.3 *Kröger-Vink charge compensating mechanism, scheme 3 (Nb^{5+}/Ti^{4+})*

$$2BaO + NbO_2 + \frac{1}{2}Ti_2O_3 + 2Cs_{Cs}^{X} + Nb_{Nb}^{X} + Ti_{Ti}^{X}$$
$$\rightarrow 2Ba_{Cs}^{\bullet} + Nb_{Nb}' + Ti_{Ti}' + TiO_2 + \frac{1}{2}Nb_2O_5 + Cs_2O$$

Equation 3.4 *Kröger-Vink charge compensating mechanism, scheme 4 ($Ti^{4+}/Ti^{3+}/Nb^{5+}/Nb^{4+}$)*

As well as these mechanisms, two other schemes have also been investigated where trivalent cations have been doped in to balance the charge for Ba incorporation. These included Al^{3+} (**Equation 3.5**) and Ga^{3+} (**Equation 3.6)** which again complements the experimental study.

$$BaO + \frac{1}{2}Ga_2O_3 + Cs_{Cs}^{X} + Ti_{Nb}^{X} \rightarrow Ba_{Cs}^{\bullet} + Ga_{Ti}' + TiO_2 + \frac{1}{2}Cs_2O$$

Equation 3.5 *Kröger-Vink charge compensating mechanisms, scheme 5 (Ti^{4+}/Ga^{3+})*

$$BaO + \frac{1}{2}Al_2O_3 + Cs_{Cs}^{X} + Ti_{Ti}^{X} \rightarrow Ba_{Cs}^{\bullet} + Al_{Ti}' + TiO_2 + \frac{1}{2}Cs_2O$$

Equation 3.6 *Kröger-Vink charge compensating mechanisms, scheme 6 (Ti^{4+}/Al^{3+})*

Defect calculations have been carried out in 3x3x3 $Cs_2TiNb_6O_{18}$ supercells **(Figure 3.35)** generated using the GULP [117] code. It was deemed that this supercell (729 atom) would be of sufficient size to achieve convergence and also not and be too computationally expensive. Defect calculations have been carried out at infinite dilution (**Figure 3.35, a**) and as clusters (**Figure 3.35, b**) using the Mott-Littleton approximation (two-region approach) [126]. Combining the results yielded a binding energy, which indicated whether the defects preferred to cluster or not. In this approach the defect sites were simply selected as near to the centre of the supercell as possible.

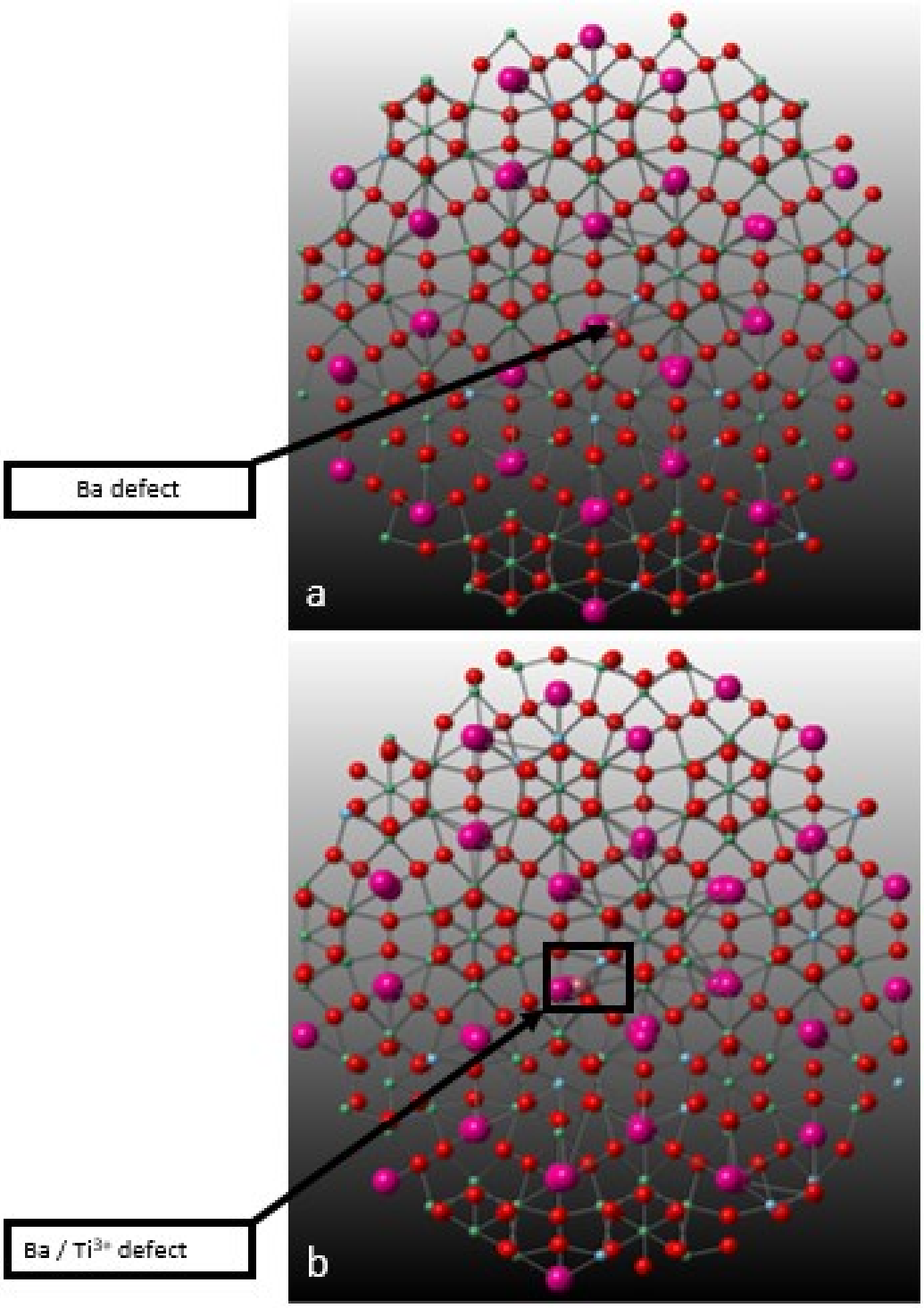

Figure 3.35 *(a) Ba defect in 3x3x3 $Cs_2TiNb_6O_{18}$ supercell at infinite dilution and (b) Ba / Ti^{3+} defect in 3x3x3 $Cs_2TiNb_6O_{18}$ supercell as clusters*

Table 3.32 *Defect energies (Mott-Littleton) at infinite dilution*

		Region sizes / Å			
		13/26	14/28	15/30	
Defect schemes		Defect energy / eV			Combined Energy (at region size 14/28 Å) / eV
Cs/Ba	Site	-4.687	-4.687	-4.687	/
1 $Ti^{(4+)}/Ti^{(3+)}$	1	15.014	15.013	15.014	10.326
1 $Ti^{(4+)}/Ti^{(3+)}$	2	14.890	14.888	14.882	10.201
2 $Nb^{(5+)}/Nb^{(4+)}$	1	14.746	14.746	14.745	10.059
2 $Nb^{(5+)}/Nb^{(4+)}$	2	13.515	13.514	13.513	8.827
3 $Nb^{(5+)}/Ti^{(4+)}$	1	18.754	18.753	18.753	14.067
3 $Nb^{(5+)}/Ti^{(4+)}$	2	17.609	17.610	17.608	12.923

For defects at infinite dilution simulations have been performed with three different region sizes (Region I/Region IIa). This was done to ensure convergence was achieved i.e. ensure the regions were large enough, which they were as all the defect values for region sizes 13/26, 14/28 and 15/30 Å have very similar energies (**Table 3.32**). For the Mott-Littleton calculations, defect energies at region sizes of 14/28 Å were used for all calculations from this point forward. A single Ba defect, on a Cs site, had a negative defect energy of around -4.68 eV. For the $Ti^{4+}/Ti^{3+}/Nb^{4+}$ defects, the site selection was more complex. In the $Cs_2TiNb_6O_{18}$ structure, there are two possible crystallographic sites for Ti/Nb (**Table 3.33**), labelled site 1 which is a special position with cell coordinates of (0, 0, 0.5) and site 2 which has cell coordinates of (0.17, 0.17, 0.1457) (**Figure 3.36**). Both Ti and Nb can occupy either site 1 or site 2 in the unit cell. Therefore, two defect calculations were carried out for each mechanism to cover the two different sites. The defect energies for $Ti^{4+}/Ti^{3+}/Nb^{4+}$ are all of lower energy on site 2 compared to site 1. The defect energies range from 13.5 to 18.8 eV. In order to get a defect pair energy at infinite dilution, the defect energy for Cs/Ba was combined with each of the $Ti^{4+}/Ti^{3+}/Nb^{4+}$ defects on each site (**Table 3.32**).

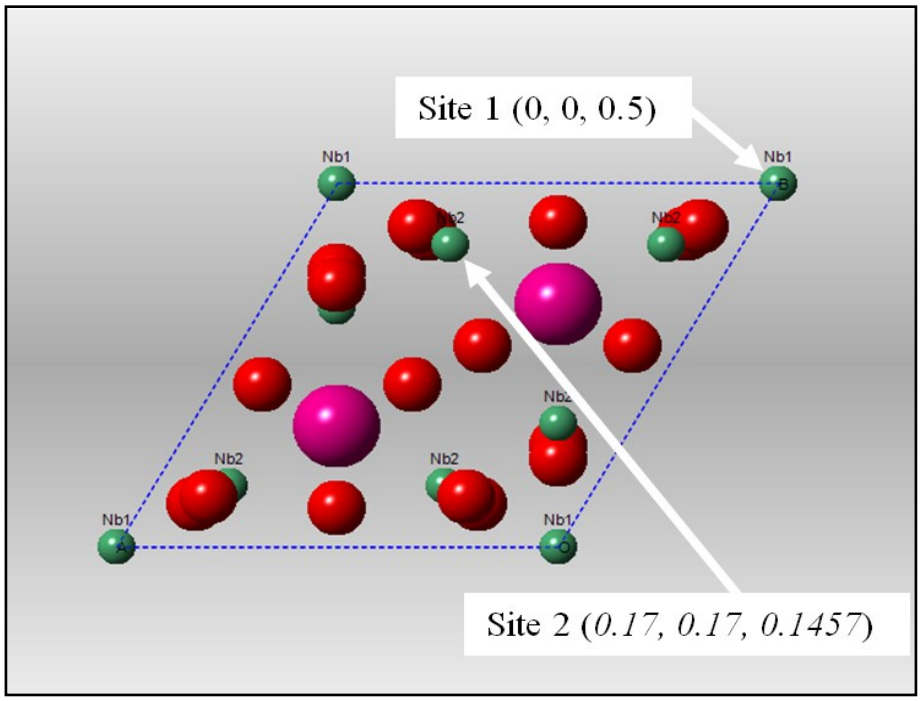

Figure 3.36 *Crystal structure of $Cs_2TiNb_6O_{18}$, site 1 and site 2 Ti/Nb*

Table 3.33 *Site coordinates of Ti and Nb in $Cs_2TiNb_6O_{18}$. Taken from reference* [84]

	Site Coordinates		
Atom	x	y	z
Ti (Site 1)	0	0	0.5
Nb (Site 1)	0	0	0.5
Ti (Site 2)	0.17	-0.17	0.1457
Nb (Site 2)	0.17	-0.17	0.1457

Calculations have also been carried out as clusters (**Table 3.34**). In this instance the defect calculation was carried out with a Cs/Ba defect and either a Nb^{4+}/Nb^{5+} defect, Ti^{3+}/Ti^{4+} defect or Ti^{4+}/Nb^{5+} defect at the same time, rather than running the two defects separately (infinite dilution). Again, for these calculations, 3 different region sizes were calculated in order to confirm convergence had been achieved (**Table 3.32**). As observed at infinite dilution, site 2 was again the favoured defect site for $Ti^{4+}/Ti^{3+}/Nb^{4+}$ when calculations were performed as clusters. Having calculated defects as clusters and at infinite dilution binding energies have been calculated to determine whether the defects prefer to cluster **(Equation 3.7**). A negative binding energy means that the defects prefer to cluster

which has been observed in all of the mechanisms (**Table 3.34**).

$$Defect\ Energy\ (clusters) - \ Defect\ Energy\ (infinite\ dilution) = Binding\ Energy$$

Equation 3.7 *Binding Energy*

Table 3.34 *Defect calculations (Mott-Littleton) as clusters*

		Region sizes / Å			
		13	14	15	
Defect schemes	Site	Defect energy / eV			Binding Energy (at region size 14/28 Å)
1 Cs/Ba , $Ti^{(4+)}/Ti^{(3+)}$	1	10.045	10.048	10.053	-0.2726
1 Cs/Ba , $Ti^{(4+)}/Ti^{(3+)}$	2	9.932	9.900	9.895	-0.3060
2 Cs/Ba , $Nb^{(5+)}/Nb^{(4+)}$	1	9.501	9.507	9.501	-0.5573
2 Cs/Ba , $Nb^{(5+)}/Nb^{(4+)}$	2	8.493	8.498	8.501	-0.3262
3 Cs/Ba , $Nb^{(5+)}/Ti^{(4+)}$	1	13.504	13.511	13.507	-0.5595
3 Cs/Ba , $Nb^{(5+)}/Ti^{(4+)}$	2	12.609	12.615	12.618	-0.3044

Using the energies from cluster defect calculations it has been possible to calculate solution energies to determine whether it is thermodynamically favourable to dope Ba into $Cs_2TiNb_6O_{18}$ via the three charge compensation mechanisms. There are a number of ways the solution energy can be calculated and usually it is done through using the simple oxides. In this study, it proved difficult to successfully model Cs_2O, so using simple oxides was not an option. Therefore, the solution energies had to be calculated using the other oxides listed in **Table 3.31**.

$$Cs_2TiNb_6O_{18} + BaNb_2O_6 + \frac{1}{2}\,Ti_2O_3 \rightarrow \mathbf{CsBaTi^{3+}Nb_6^{5+}O_{18}} + \ CsNbO_3 + \frac{1}{2}Nb_2O_5 + \ TiO_2$$

Equation 3.8 *Solution Energies (Mott-Littleton), scheme 1 (Cs/Ba, Ti^{4+}/Ti^{3+})*

$$Cs_2TiNb_6O_{18} + BaNb_2O_6 + NbO_2 \rightarrow \mathbf{CsBaTi^{4+}Nb^{4+}Nb_5^{5+}O_{18}} + \ CsNbO_3 + Nb_2O_5$$

Equation 3.9 *Solution Energies (Mott-Littleton) s, scheme 2 (Cs/Ba, Nb^{5+}/Nb^{4+})*

$$Cs_2TiNb_6O_{18} + BaNb_2O_6 + TiO_2 \rightarrow \mathbf{CsBaTi_2^{4+}Nb_5^{5+}O_{18}} + \ CsNbO_3 + Nb_2O_5$$

Equation 3.10 *Solution Energies (Mott-Littleton), scheme 3 (Cs/Ba, Nb^{5+}/Ti^{4+})*

Table 3.35 *Solution energies using the Mott-Littleton approximation (at region size 14/28 Å)* [144]

Scheme	Site	Energy of Reactants / eV	Defect Energy / eV (Clusters)	Energy of Products / eV	**Solution Energy / eV**
1 Cs/Ba , $Ti^{(4+)}/Ti^{(3+)}$	2	-741.095	9.89	-740.048	**1.047**
2 Cs/Ba , $Nb^{(5+)}/Nb^{(4+)}$	2	-757.837	8.498	-761.294	**-3.456**
3 Cs/Ba , $Nb^{(5+)}/Ti^{(4+)}$	2	-761.129	12.615	-757.176	**3.953**

The calculated solution energies from the cluster defects (Mott-Littleton) suggest that Ba incorporation is only favourable via scheme 2 (Cs/Ba, Nb^{5+}/Nb^{4+}) with a negative energy of -3.456 eV (**Table 3.35**). Scheme 1 and 3 both proved unfavourable, scheme 3 (Cs/Ba, Nb^{5+}/Ti^{4+}) with a solution energy of 3.953 eV is the most unfavourable followed by scheme 1 (Cs/Ba, Ti^{4+}/Ti^{3+}), 1.047 eV.

To support the main bulk of calculations and experimental work, a series of simulations have been carried out where Ba is incorporated into the $Cs_2TiNb_6O_{18}$ structure with a trivalent cation acting as the charge balancing cation. The experimental work indicated that it is unlikely Ba would incorporate into the structure via a trivalent (Ga^{3+}, Al^{3+}) mechanism as Ba impurities were observed in the synthesis process. Despite this, the calculations were carried out in the same way the first set of calculations were, at infinite dilution and as clusters via the Mott-Littleton approximation.

$$Cs_2TiNb_6O_{18} + BaNb_2O_6 + \frac{1}{2}\,Ga_2O_3 \rightarrow \mathbf{CsBaGa^{3+}Nb_6^{5+}O_{18}} + CsNbO_3 + \frac{1}{2}Nb_2O_5 + TiO_2$$

Equation 3.11 *Solution Energies, Ga^{3+} (Mott-Littleton) scheme 5 (Cs/Ba, Ga^{3+}/Ti^{4+})*

$$Cs_2TiNb_6O_{18} + BaNb_2O_6 + \frac{1}{2}\,Al_2O_3 \rightarrow \mathbf{CsBaAl^{3+}Nb_6^{5+}O_{18}} + CsNbO_3 + \frac{1}{2}Nb_2O_5 + TiO_2$$

Equation 3.12 *Solution Energies, Al^{3+} (Mott-Littleton), scheme 6 (Cs/Ba, Al^{3+}/Ti^{4+})*

Table 3.36 *Defect calculations (Mott-Littleton) at infinite dilution*

		Region sizes / Å			
		13 / 26	14 / 28	15/ 30	
Defect schemes		Defect energy / eV			
Cs/Ba	Site	-4.687	-4.687	-4.687	Combined Energy (at region size 14/28 Å)
5 $Ga^{(3+)}/Ti^{(4+)}$	1	20.227	20.227	20.226	15.540
5 $Ga^{(3+)}/Ti^{(4+)}$	2	19.857	19.856	19.853	15.169
6 $Al^{(3+)}/Ti^{(4+)}$	1	19.297	19.297	19.297	14.610
6 $Al^{(3+)}/Ti^{(4+)}$	2	18.783	18.783	18.780	14.096

For the trivalent defects, at infinite dilution, site 2 was again the preferred defect site **(Table 3.36)**. The binding energy was again calculated and the defects in these examples preferred to cluster as the binding energies were all negative (**Table 3.37**).

Table 3.37 *Defect calculations (Mott-Littleton) as clusters, Trivalent defects,* Ga^{3+} *and* Al^{3+}

		Region sizes / Å			
Defect schemes		13 / 26	14 / 28	15/ 30	Binding Energy (at region size 14/28 Å)
	Site	Defect energy / eV			
5 $Ga^{(3+)}/Ti^{(4+)}$	1	15.256	15.263	15.271	-0.277
5 $Ga^{(3+)}/Ti^{(4+)}$	2	14.772	14.757	14.759	-0.411
6 $Al^{(3+)}/Ti^{(4+)}$	1	14.326	14.333	14.341	-0.269
6 $Al^{(3+)}/Ti^{(4+)}$	2	13.669	13.656	13.669	-0.427

Table 3.38 *Solution energies using the Mott-Littleton approximation,* $Ga^{(3+)}$ *and* $Al^{(3+)}$ *(at region size 14/28 Å)*

Defect schemes	Site	Energy Reactants / eV	Defect Energy / eV (Clusters)	Energy Products / eV	**Solution Energy / eV**
5 $Ga^{(3+)}/Ti^{(4+)}$	2	-739.484	15.170	-735.203	**4.281**
6 $Al^{(3+)}/Ti^{(4+)}$	2	-740.604	14.010	-736.276	**4.327**

The Ba defects in $Cs_2TiNb_6O_{18}$ with Ga^{3+} and Al^{3+} as the charge compensating cations again proved unfavourable. Both scheme 5 (Ga^{3+}) and scheme 6 (Al^{3+}) have positive solution energies (**Table 3.38**) of around 4.3 eV. This is in agreement with experimental work where rather than Ba incorporating into the target phase, it resides in impurity phases

(**Figure 3.31** and **Figure 3.32**).

The defect calculations carried out thus far have been a useful indicator to whether Ba is likely to incorporate in the $Cs_2TiNb_6O_{18}$ structure. However, in the Mott-Littleton defect calculations, many assumptions have been made. Firstly, the selection of the defect sites have been manually picked, i.e the defects have been selected as close to the middle of the supercell as possible. Secondly these defect calculations are single defects or a pair of defects, therefore these calculations do not take into account the interactions between multiple defects in one cell. Lastly Ti and Nb are split across two different sites in the material and thus far the distribution of Ti/Nb (and the defects) in the supercell have been fixed, which may affect the overall energy of the system. Therefore a series of more robust calculations have been carried out using a Markov Chain Mote Carlo (MCMC) method which is based on the Metropolis–Hastings algorithm which again integrates with GULP.[187–190] This method, developed by a previous group member, works by starting off with an initial configuration of atoms of which the energy is calculated.[118] A random move of a single atom is then carried out and the new energy is calculated. The new energy is then compared to the old configurational energy and the move is either accepted or refused based the difference between the two the two moves creating the Markov Chain. If the move is not accepted, the configuration returns to the original distribution. Bad moves can be accepted which is dependent on the acceptability probability criteria weighted by the Boltzmann constant.[187–190] Moves or cycles are repeated to reach equilibrium but there can be issues working out exactly how many cycles are required for this but the more cycles, the higher the probability that convergence is reached. In this study, an initial simulated annealing step was performed so that more of the energy surface can be explored. Once simulated annealing had been carried out. The distribution with the lowest energy was used as a starting point for the real

simulation. The energy distributions are shown in histograms below for $Cs_2TiNb_6O_{18}$, two sampling areas were discovered and are shown below in **Figure 3.37.** The sample distributions for the other materials can be found in the appendix.

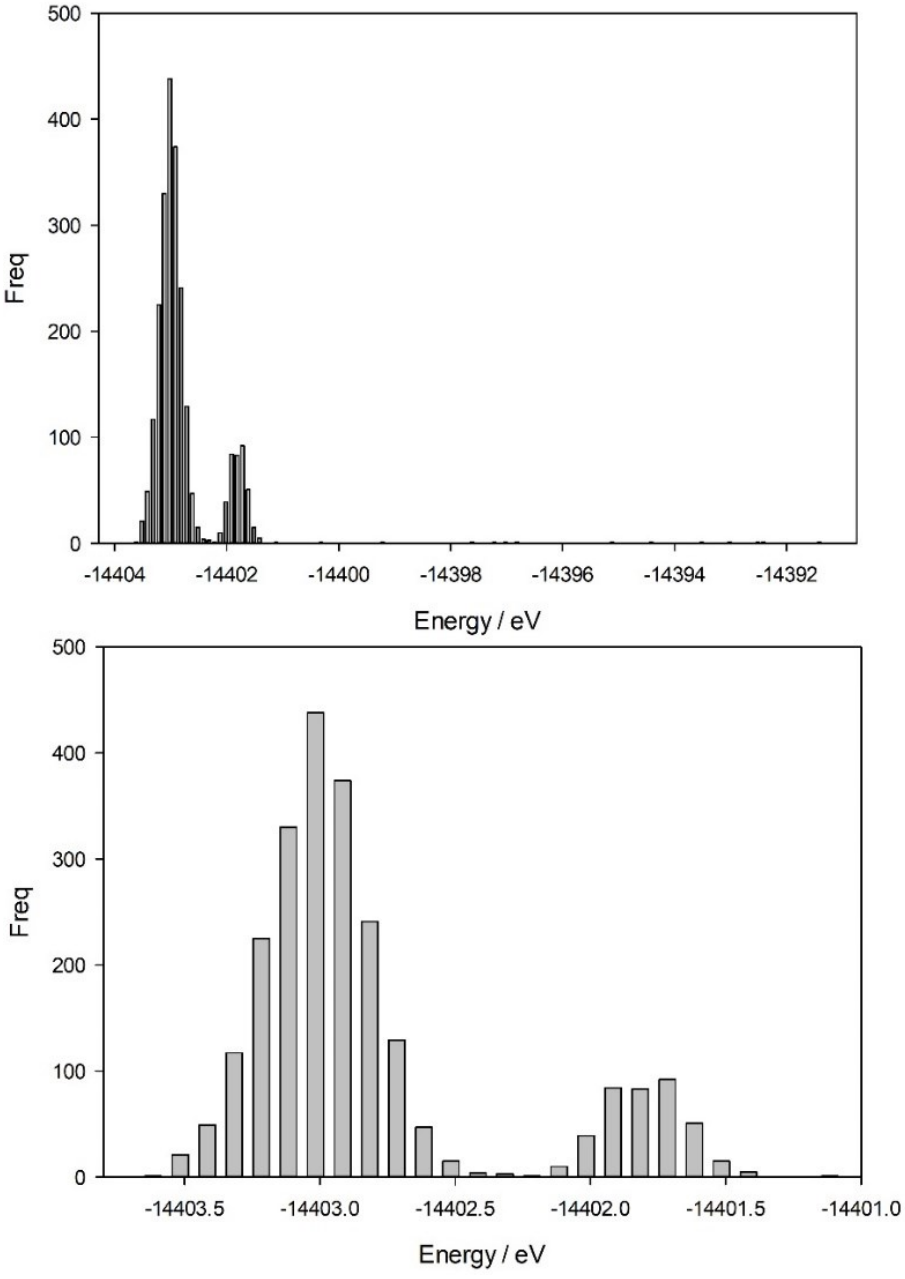

Figure 3.37 *Energy distributions, histograms for MCMC* $Cs_2TiNb_6O_{18}$

Table 3.39 *MCMC defect calculations site preference, schemes 1, 2, 3 and 4*

Material / Scheme	Ti / Site / %	Ti^{3+} / Site / %	Nb^{4+} / Site / %
$Cs_2TiNb_6O_{18}$ (Parent)	Site 2 100 %	/	/
1 (20 % Cs → Ba)	Site 2 100 %	/	/
1 (30 % Cs → Ba)	Site 2 100 %	/	/
2 (20 % Cs →Ba)	Site 2 100 %	/	Site 2 100 %
2 (30 % Cs → Ba)	Site 2 100 %	/	Site 2 100 %
3 (20 % Cs → Ba)	Site 2 100 %	Site 2 100 %	/
3 (30 % Cs → Ba)	Site 2 100 %	Site 2 100 %	/
4 (20 % Cs → Ba)	Site 2 100 %	Site 2 100 %	Site 2 100 %
4 (30 % Cs → Ba)	Site 2 100 %	Site 2 100 %	Site 2 100 %

With the MCMC swap code calculations, the cations such (Ti^{3+}, Nb^{4+}, Ti^{4+} and Nb^{5+}) are able to move freely between sites 1 and 2 all around the supercell. The Ba defects are also free to move around the supercell on the Cs sites, so this is a much more considerate method in regard to the many configurations possible when calculating the feasibility of Ba incorporation. **Table 3.39** shows that for every scheme at the two levels of Ba doping (20 and 30 % conversion of Cs → Ba) the charge compensating cations, Ti^{3+}, Nb^{4+} and Ti^{4+} are always found on site 2, which is in agreement with the Mott-Littleton simulations, where the charge compensating cations all preferred to be on site 2 across all schemes.

$$Cs_{54}Ti_{27}Nb_{162}O_{486} + 11BaNb_2O_6 + 5.5Ti_2O_3 \rightarrow \mathbf{Cs_{43}Ba_{11}Ti_{16}^{4+}Ti_{11}^{3+}Nb_{162}^{5+}O_{486}} + 11CsNbO_3 + 5.5Nb_2O_5 + 11TiO_2$$

$$Cs_{54}Ti_{27}Nb_{162}O_{486} + 16BaNb_2O_6 + 8Ti_2O_3 \rightarrow \mathbf{Cs_{38}Ba_{16}Ti_{11}^{4+}Ti_{16}^{3+}Nb_{162}^{5+}O_{486}} + 16CsNbO_3 + 8Nb_2O_5 + 16TiO_2$$

Equation 3.13 Solution Energies, scheme 1 (20 and 30 % Cs → Ba) MCMC (Cs/Ba, Ti^{4+}/Ti^{3+})

$$Cs_{54}Ti_{27}Nb_{162}O_{486} + 11BaNb_2O_6 + 11NbO_2 \rightarrow \mathbf{Cs_{43}Ba_{11}Ti_{27}^{4+}Nb_{11}^{4+}Nb_{151}^{5+}O_{486}} + 11CsNbO_3 + 11Nb_2O_5$$

$$Cs_{54}Ti_{27}Nb_{162}O_{486} + 16BaNb_2O_6 + 16NbO_2 \rightarrow \mathbf{Cs_{38}Ba_{16}Ti_{27}^{4+}Nb_{16}^{4+}Nb_{146}^{5+}O_{486}} + 16CsNbO_3 + 16Nb_2O_5$$

Equation 3.14 *Solution Energies, scheme 2 (20 and 30 % Cs → Ba) MCMC (Cs/Ba, Nb^{5+}/Nb^{4+})*

$$Cs_{54}Ti_{27}Nb_{162}O_{486} + 11BaNb_2O_6 + 11TiO_2 \rightarrow \mathbf{Cs_{43}Ba_{11}Ti_{38}^{4+}Nb_{151}^{5+}O_{486}} + 11CsNbO_3 + 11Nb_2O_5$$

$$Cs_{54}Ti_{27}Nb_{162}O_{486} + 16BaNb_2O_6 + 16TiO_2 \rightarrow \mathbf{Cs_{38}Ba_{16}Ti_{43}^{4+}Nb_{146}^{5+}O_{486}} + 16CsNbO_3 + 16Nb_2O_5$$

Equation 3.15 *Solution Energies, scheme 3 (20 and 30 % Cs → Ba) MCMC (Cs/Ba, Nb^{5+}/Ti^{4+})*

$$Cs_{54}Ti_{27}Nb_{162}O_{486} + 12BaNb_2O_6 + 3Ti_2O_3 + 6NbO_2 \rightarrow \mathbf{Cs_{42}Ba_{12}Ti_6^{3+}Ti_{21}^{4+}Nb_6^{4+}Nb_{156}^{5+}O_{486}} + 12CsNbO_3 + 9Nb_2O_5 + 6TiO_2$$

$$Cs_{54}Ti_{27}Nb_{162}O_{486} + 16BaNb_2O_6 + 4Ti_2O_3 + 8NbO_2 \rightarrow \mathbf{Cs_{38}Ba_{16}Ti_8^{3+}Ti_{19}^{4+}Nb_6^{4+}Nb_{154}^{5+}O_{486}} + 16CsNbO_3 + 12Nb_2O_5 + 8TiO_2$$

Equation 3.16 *Solution Energies, scheme 4 (20 and 30 % Cs → Ba) MCMC (Cs/Ba, $Ti^{3+}/Ti^{4+}/Nb^{5+}/Nb^{4+}$)*

Table 3.40 *Solution Energies, MCMC Schemes 1, 2 and 3* [144]

Scheme	Energy Reactants / eV	Defect Energy / eV	Energy Products / eV	Solution Energy / eV
1. 20 % Cs to Ba	-16692.1255	34.3391	-16657.7864	3.12173
1. 30 % Cs to Ba	-17732.40821	49.9834	- 17682.42483	3.12396
2. 20 % Cs to Ba	-16876.29872	30.3441	-16845.9546	2.75856
2. 30 % Cs to Ba	-18000.29654	44.0498	-17956.24672	2.75311
3. 20 % Cs to Ba	-16912.50729	38.3532	-16874.1541	3.48666
3. 20 % Cs to Ba	-18052.96354	55.9019	-17997.06161	3.49387
4. 20 % Cs to Ba	-17000.64017	34.9856	-16965.65459	2.91546
4. 20 % Cs to Ba	-17866.35238	43.3604	-17819.99195	2.89753

The MCMC simulations carried out for schemes 1, 2 and 3 suggest a similar trend to the original Mott-Littleton calculations. Scheme 3 (Nb^{5+}/Ti^{4+}) with a solution energy of 3.49 eV again is the most unfavourable, followed by scheme 1 (Ti^{4+}/Ti^{3+}) with a slightly lower energy of 3.12 eV and the most favourable was scheme 2 (Nb^{5+}/Nb^{4+}) with the lowest energy of 2.75 eV. Scheme 4 ($Ti^{3+}/Ti^{4+}/Nb^{5+}/Nb^{4+}$) also proved unfavourable with a solution energy of around 2.90 eV. Interesting in these calculations, all of solution energies were positive suggesting Ba incorporation is unfavourable. In the previous Mott-Littleton calculations, scheme 2 (Nb^{5+}/Nb^{4+}) had a negative solution energy of -3.456 eV, suggesting that Ba incorporation is favourable. The MCMC calculations are much more robust and therefore are better approximations than the Mott-Littleton simulations. It can therefore be concluded that the computational work carried out for the incorporation of Ba is in agreement with the experimental work, in that Ba does not want to reside in the $Cs_2TiNb_6O_{18}$ phase via a number of different mechanisms.

3.3.15 Hollandite calculations

Defect calculations to this point have suggested that Ba incorporation into $Cs_2TiNb_6O_{18}$ is not thermodynamically favourable, which is in agreement with experimental work discussed at the start of this chapter. As discussed, a pure Ba – hollandite and a Ba/Cs – hollandite have been synthesised and analysed to support the study on Ba doped $Cs_2TiNb_6O_{18}$. Analysis of XRD and XRF data suggested that a mixed Cs/Ba – hollandite had been successfully synthesised with Cs and Ba sharing the same site in the hollandite structure which was in agreement with the literature. [9,11,31,48,50,55,56] In order to validate the potentials and support the defect simulations already carried out on Ba doped $Cs_2TiNb_6O_{18}$ a pure Ba – Hollandite and mixed Cs/Ba hollandite phase has been modelled. It was thought that if calculations using the same set of potentials as before suggested that it is favourable to have a co-substituted Cs/Ba – Hollandite (as the experimental work suggested (**Figure 3.34**)) it would authenticate the computational studies carried out on Ba doped $Cs_2TiNb_6O_{18}$.

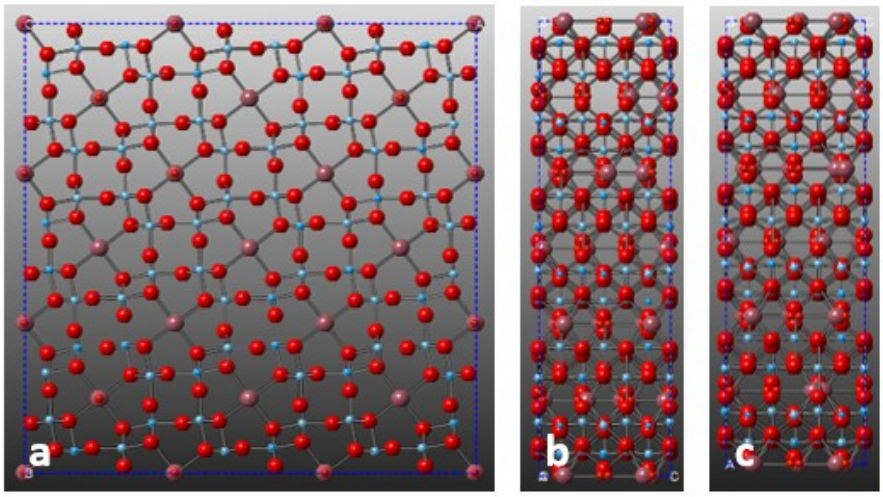

Figure 3.38 *Hollandite structure [56], view down a = [001], b =[010] c = [100]*

In order to mirror the previous study, defect calculations were carried out at infinite dilution and as clusters using the Mott-Littleton approach on supercells generated from GULP. However, these simulations proved difficult and the calculations would not optimise

in GULP. The reason for this was on account of the starting supercells. When the 3x3x3 supercell is generated using GULP from the hollandite unit cell (**Figure 3.38** and **Table 3.41**), the occupancy of each site is not taken into account and therefore all sites will be fully occupied regardless of the chemistry. In hollandite, the Ba site is only partially occupied and therefore when cell is produced with all possible Ba sites occupied, a number of Ba's will overlap and will not be in realistic positions and therefore energy minimisation in GULP is impossible. Many attempts were made to manually select the Ba sites in sensible configurations and the defect simulations carried out after, but this still failed. Therefore, defect calculations at infinite dilution and as clusters via the Mott-Littleton approximation were abandoned.

On account of the issues defect calculations were carried out via the MCMC method (used previously with Ba doped $Cs_2TiNb_6O_{18}$) with 3x3x3 supercells. This method would solve the issues of partial occupancy on the Ba/Cs site as the MCMC code would allow Ba to move around the cell and find the lowest energy configurations. If the cell did not optimise, the configuration would return to its original configuration and another Ba would be moved to a new position.

To begin with, a Ba hollandite pure supercell was edited such that only 36 Ba's were present. The code was then set such that the Ba's would be able to move on all 108 different sites (**Table 3.41**) throughout the supercell. Using this method, Ba's would not be able to occupy sites that sit too close together as the calculation would not optimise in GULP and the move would be rejected. Eventually after a number of moves a sensible a energetically favourable Ba distribution throughout the structure was achieved. As well as the Ba distribution, the Ti/Al distribution in the supercell is also taken into consideration as they

share the same site, much like before where the Ti/Nb share sites in the $Cs_2TiNb_6O_{18}$ structure.

Table 3.41 *Atomic positions and occupancy of Ba-Hollandite* [191]

Atom	x	y	z	Multiplicity	Sites in (3x3x3) supercell	Occupancy
Ba	0	0	0.094	4	108	0.28
Ti1	0.3308	0.1454	0	8	216	0.72
Al1	0.3308	0.1454	0	8	216	0.28
O1	0.2982	0.3456	0	8	216	1.00
O2	0.0414	0.3344	0	8	216	1.00

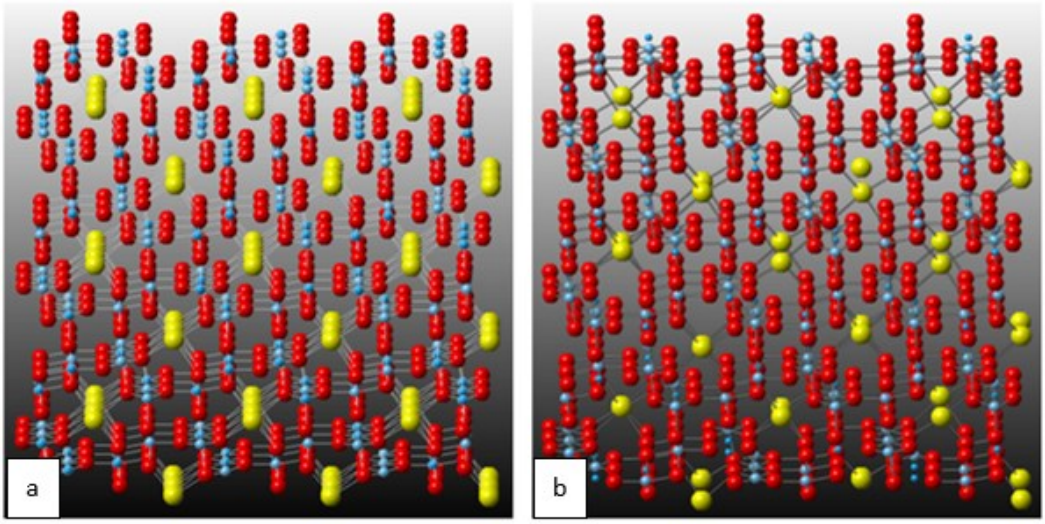

Figure 3.39 *Ba – Hollandite, MCMC code used to remove and move Ba's to most stable configuration*

Figure 3.39 (a), shows a supercell with fully occupied Ba sites which was produced directly from GULP. The structure shown in **Figure 3.39 (b)**, has the correct number of Ba spread over sites which gave the lowest energy over a number of steps (2400 cycles) via the MCMC code. The lowest energy configuration of the Ba pure hollandite was used as a start point **(Figure 3.39, (b))** for the Cs doped version. However, the Cs and Ba's in these calculations were still able to move onto the other unoccupied (vacant) sites. Charge compensation was achieved by doping excess Ti^{4+} for Al^{3+} **(Equation 3.17)**. As well as a (Ba/Cs, Al^{3+},Ti^{4+}) - Hollandite, a (Ba,Cs)/(Al^{3+},Ti^{4+},Fe^{3+}) - Hollandite has also

been doped with Cs **(Equation 3.18)** to access if there is any difference when the B site cation is varied.

$$Ba_{36}Ti_{144}Al_{72}O_{432} + 11CsNbO_3 + 11TiO_2 \rightarrow \mathbf{Cs_{11}Ba_{25}Ti^{4+}_{155}Al^{3+}_{61}O_{432}} + \mathbf{11BaAlO_4} + \mathbf{5.5Nb_2O_5}$$

Equation 3.17 *Solution Energies scheme 7, MCMC (Ba,Cs)/ (Al^{3+},Ti^{4+})*

$$Ba_{36}Ti_{144}Fe_{23}Al_{49}O_{432} + 11CsNbO_3 + 11TiO_2 \rightarrow \mathbf{Cs_{11}Ba_{25}Fe^{3+}_{23}Ti^{4+}_{155}Al^{3+}_{38}O_{432}} + \mathbf{11BaAl_2O_4} + \mathbf{5.5Nb_2O_5}$$

Equation 3.18 *Solution Energies scheme 8, MCMC (Ba,Cs)/ (Al^{3+},Ti^{4+},Fe^{3+})*

Table 3.42 *Solution energy (Ba,Cs)/ ($Al^{(3+)}$,$Ti^{(4+)}$) - Hollandite and (Ba,Cs)/ (Al^{3+},Ti^{4+},Fe^{3+}) - Hollandite*

Scheme	Energy Reactants / eV	Defect Energy / eV	Energy Products / eV	Solution Energy / eV
7 (Ba/Cs, $Al^{(3+)}$,$Ti^{(4+)}$)	-13276.073	-13.423	-13289.496	-1.220
8 (Ba/Cs, $Al^{(3+)}$,$Ti^{(4+)}$,$Fe^{(3+)}$)	-13241.434	-14.946	-13256.380	-1.359

The calculated solution energies from Ba/Cs doped hollandites suggest that it is favourable to have a co-substituted hollandite phase as the solution energies are negative. The mixed Cs/Ba hollandite containing Fe had a solution energy of **-1.359 eV** compared to **-1.220 eV** for the ((Ba/Cs, Al^{3+},Ti^{4+},Fe^{3+}) hollandite suggesting that a mixed Cs/Ba is more energetically favourable if Fe is present in the structure as the solution energy is lower.

3.3.16 Conclusions of computational work

A series of defect calculations has been carried out exploring the different mechanisms involved with doping Ba in $Cs_2TiNb_6O_{18}$. These mechanisms or 'schemes' included doping Ti^{3+} for Ti^{4+}, Nb^{4+} for Nb^{5+}, excess Ti^{4+} for Nb^{5+} and lastly a mixture of Ti^{3+} and Nb^{4+} for Ti^{4+} and Nb^{5+} all to compensate for doping divalent Ba^{2+} for monovalent Cs^{+}. Initial calculations via the Mott-Littleton suggested that Ba incorporation for all schemes were unfavourable except scheme 2 (Nb^{4+} for Nb^{5+}) which had a negative solution energy of **-3.5 eV (Table 3.35)**. More robust calculations were then carried out where all species

involved in the defect calculation could move around the supercells step by step. These MCMC calculations suggested that all mechanisms involving Ba incorporation were unfavourable, as all solution energies calculated were positive (**Table 3.40**). This supported the experimental work carried out.

To support the simulations and to help validate the potentials derived in this study, defect calculations have also been performed on the well-known hollandite system. It is widely reported that co-substituted Ba/Cs hollandites exists and that therefore Cs hollandite wasteforms will be able to retain Ba after transmutation. XRD analysis of a Ba/Cs – hollandite in this study proved that Cs/Ba can be incorporated into the same hollandite phase (**Table 3.27**, **Figure 3.34**). The defect calculations in this study agree with the literature and the experiment work and suggest that it is favourable to have mixed Ba/Cs hollandites as the solution energies are negative (**Table 3.42**).

3.3.17 Conclusions of Ba-doping into $Cs_2TiNb_6O_{18}$

A previous study suggested that $Cs_2TiNb_6O_{18}$ has the potential to be an excellent Cs wasteform suitable for final disposal. $Cs_2TiNb_6O_{18}$ is the major Cs phase produced when Cs loaded IONSIV is HIPed.[34] Aqueous durability tests suggested that this phase is extremely durable and the Cs leach rates compared well to other accepted ceramic wasteforms such as hollandite. [9,11,31,48,50,55,56] One of the major requirements of any radioactive wasteform is the ability to retain the transmutation products, failure to do so may cause mechanical instability i.e. fracturing or failing of the wasteform which could cause the increase in the release of harmful ^{137}Cs. In this study, attempts have been made to incorporate Ba in $Cs_2TiNb_6O_{18}$ via a number of charge compensation mechanisms via experimental and computational techniques.

Synthesising a Ba – doped $Cs_2TINb_6O_{18}$ would go a long way to suggest that this wasteform could retain Ba after ^{137}Cs decays. Firstly, $Cs_2TiNb_6O_{18}$ was doped to medium levels of Ba doping via a mechanism where excess Ti^{4+} is doped in for Nb^{5+} giving the formula $Cs_{2-x}Ba_xTi^{(4+)}_{1+x}Nb^{(5+)}_{6-x}O_{18}$ (x = 1, 0.6, 0.5, 0.4 and 0.3). XRD revealed impurity peaks which were indexed to a $Ba_2Ti_3Nb_4O_{18}$ phase. Subsequent Rietveld analysis suggested that all of the doped Ba favoured the impurity phase, rather than the target phase. Lower level doping (x = 0.15, 0.10 and 0.05) also suggested Ba did not incorporate and other Ba impurities were present such as $BaTiNb_4O_{13}$ and $BaTi_3Nb_4O_{17}$. SEM and TEM also confirmed the presence of the impurity phases. This mechanism did not represent a realistic scenario and was just a quick test that could be easily carried out as all the cations are in there most stable oxidation states.

From this point three other schemes were carried out which involved much more difficult synthesis routes and the traditional solid-state method had to be modified to ensure unstable species did not oxidise in the reaction process. These schemes better represented a more 'realistic scenario' than the previous attempts. Initially attempts were made with Ba doping where Ti^{3+} replaced Ti^{4+} giving the formula $Cs_{2-x}Ba_xTi^{(4+)}_{1-x}Ti^{(3+)}_xNb_6O_{18}$ and also doping Nb^{4+} for Nb^{5+} giving the formula $Cs_{2-x}Ba_xNb^{(5+)}_{6-x}Nb^{(4+)}_xTiO_{18}$. The last attempt involved a mechanism where both Ti^{3+} and Nb^{4+} were doped in to achieve charge compensation, giving the formula $Cs_{2-x}Ba_xNb^{(5+)}_{6-(x/2)}Ti^{(3+)}_{x/2}Ti^{(4+)}_{1-(x/2)}Nb^{(4+)}_{x/2}O_{18}$. All these mechanisms produced Ba impurities similar to the first examples, so from an experimental perspective, it appears that Ba is not able to incorporate into $Cs_2TINb_6O_{18}$ suggesting that the phase may not be suitable to retain Ba^{137}, the transmutation product of Cs^{137}.

Although successful synthesis of a Ba-doped $Cs_2TiNb_6O_{18}$ would have been strong evidence that the parent material could retain Ba after transmutation, synthesis this way does

not 100% confirm either way of in a 'real' scenario, Ba will be retained in the $Cs_2TiNb_6O_{18}$. Therefore, to support this work, a series of defect simulations have been carried out using the general utility lattice program (GULP). Simulations were carried out on all schemes via two main methods. Both methods used 3x3x3 supercells but the first relied on the Mott-Littleton approximation and the second, a much more robust method, was the Markov Chain Monte Carlo method. Calculations generally agreed with the experimental studies in that it is unfavourable to incorporate Ba. One scheme (Nb^{4+} for Nb^{5+}) via the Mott-Littleton calculation did suggested that this was favourable, however the MCMC method with the same scheme suggested it was unfavourable. The MCMC method is much more reliable and robust and therefore was a better approximation.

4 IMMOBILISATION OF CAESIUM AND STRONTIUM LOADED IONSIV

4.1 Introduction

The separation of radioactive ^{137}Cs and ^{90}Sr from waste streams has been an important process for the last 40/50 years. A number of different methods and materials have been used for this process including inorganic ion exchange materials in ion exchange processes. Inorganic exchangers are used because of their high selectivity, heat and radiation resistance, effectiveness in a wide pH range and compatibility to form final wasteforms. [17,23,24] These exchangers include Cs-treat® (hexacyanoferrates) [24], Sr-treat® (titanium oxide based exchanger) [33], Clinoptilolite (natural zeolite) [192,193] , zeolite-A [15] and IONSIV R9120-B (CST, $Na_2Ti_2SiO_7 \bullet 2H_2O$). [43,194–196] Many of these exchangers have been used or 'spent' in clean up processes all around the globe. For most of these spent materials, final processing into suitable robust wasteforms has not been completed and in many cases the method of processing into a final wasteform hasn't even been decided. However, consolidation of the spent exchangers is an important process to consider, Cs and Sr are two of the more problematic radionuclides produced from fission and therefore their immobilisation is critical.

IONSIV, a commercial product developed and engineered by Honeywell UOP is an exchange material, advertised for the removal of Cs and Sr from nuclear waste streams. IONSIV has already demonstrated its utility finding use in the UK, US and also at the Fukushima power plant after the disaster in 2011. IONSIV is available commercially in two forms, firstly as a powder, named IONSIV R9120-P (formally IE-910) and also as a bead, named IONSIV R9120-B (formally IE-911). Both these materials are based on an optimised version of crystalline Silicotitanate where Nb^{5+} is doped in for Ti^{4+} which improves the Cs exchange properties (structure shown in **Figure 4.1 a**). In this work the material used is

IONSIV R9120-B, which is only different to R9120-P in that it is bound into a 'bead' with $Zr(OH)_4$ (**Figure 4.1 b**) and the reason for binding was to improve the mechanical properties of the exchanger.

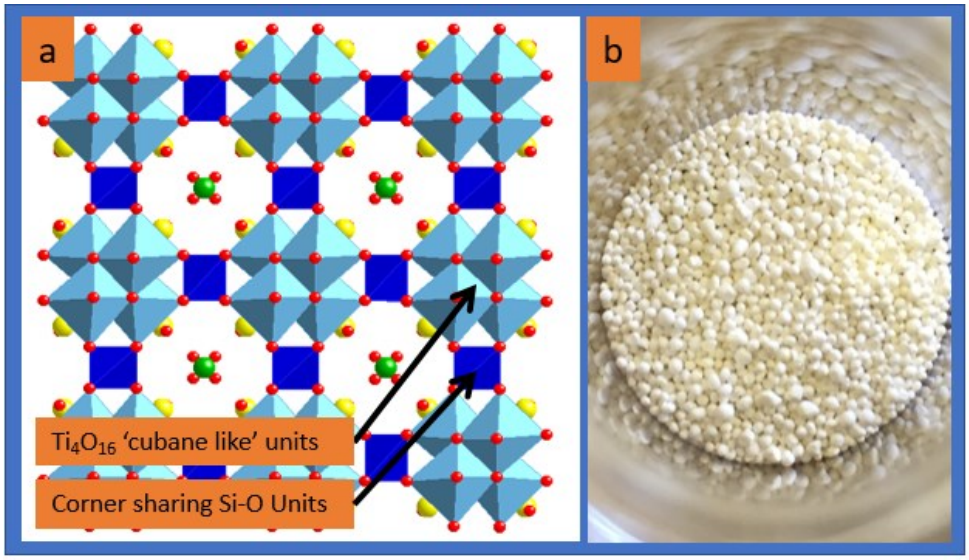

Figure 4.1 *a: Crystal Structure of CST, view down the [001] direction. CIF file adapted from Thorogood et al.* [46] *b: Picture of IONSIV R9120-B as received*

Traditionally, CST has mostly been utilised for Cs removal, but studies have shown CST it can also be selective for Sr^{2+}, particularly at neutral to alkaline pH [127]. Despite selectivity for both cations, the exchange process for each cation is slightly different.[42,43,96,197,198] It is understood that Nb doping for Ti increases the uptake of Cs as there is less Na and more H_2O in the channels allowing for increased Cs uptake but Nb substitution neither hinders or improves the uptake of Sr.[13,43,96,197] The difference in exchange for Sr^{2+} and Cs^+ is on account of the coordination sites adopted in the 8 membered ring channel.[96,197] For Cs, at levels of 4, 8 and 12 wt. % Cs loading, different Cs sites are occupied in the structure depending on the amount of Cs present, however the symmetry of the system does not change on increased Cs exchange.[96] At 4 wt. %, a Cs partially occupies a single site labelled Cs_1, in the channel which is said to be 8 coordinate, at 8 wt. % and 12 wt. % as well as the Cs_1 site (in these examples 8 to 12 coordinate), there is an additional Cs

site in the channel, labelled Cs_2 which has a coordination of 6 (**Table 4.1** and **Figure 4.2**).[96] For Sr, there is only one exchange site which is also found in the 8 membered ring channel which is 7 coordinate (**Table 4.2** and **Figure 4.3**). [96] Interestingly for Sr exchanged CST the symmetry of the system changes from the original unexchanged material, whereas is does not change when it is Nb doped CST.[197]

Table 4.1 *Crystallographic sites for Cs-Nb-CST taken from reference* [96]

Cs-Nb-CST				
		Atomic Coordinates		
Atom	Multiplicity	x	y	z
Na	1	0	0.5	0.5
Cs1	1	0.5	0.5	0.25
Cs2	1	0.5	0.5	0.1582
Ti	8	0.14	0.14	0.1531
Nb	8	0.14	0.14	0.1531
Si	4	0	0.5	0.25
O	16	0.1222	0.387	0.1662
O	8	0.1153	0.1153	0.3266
O	4	0.1494	0.1494	0
O	4	0.2451	0.2451	0.5
O	4	0.4264	0.4264	0
O	8	0.2496	0.3473	0.5

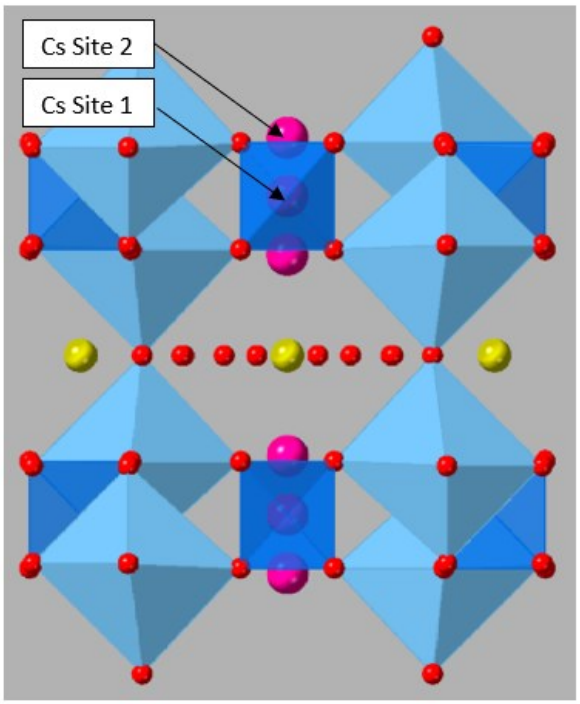

Figure 4.2 *Cs exchange sites Nb-CST view down [100] direction, crystal structure taken from reference* [96]

Table 4.2 *Crystallographic sites for Sr-Nb-CST taken from reference* [96]

Sr-Nb-CST				
		Atomic Coordinates		
Atom	Multiplicity	x	y	z
Na	4	0	0.5	0.5
Sr1	4	0.3969	0.3969	0
Ti	8	0.1435	0.1435	0.1548
Nb	8	0.1435	0.1435	0.1548
Si	4	0	0.5	0.25
O	16	0.1256	0.3978	0.1663
O	8	0.1190	0.1190	0.3234
O	4	0.1559	0.1559	0
O	4	0.2683	0.2683	0.5

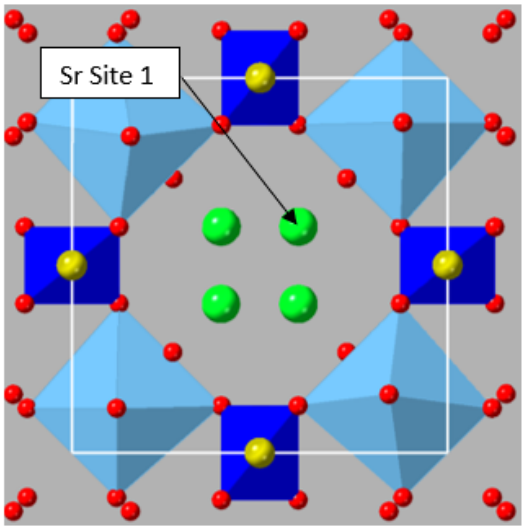

Figure 4.3 *Sr exchange sites Nb-CST view down [001] direction , crystal structure taken from reference* [96]

Currently the suggested method in literature for immobilising spent IONSIV is encapsulating into cement. [128] It's been demonstrated that IONSIV could be immobilised into a number of cement formations including a 3:1 mixture of blast furnace slag (BFS) and Ordinary Portland Cement (OPC), 9:1 BFS:OPC and 3:1 Pulverised Fly Ash (PVA) and OPC. 20 wt. % Cs-IONSIV was added to the cement formations and it was confirmed that Cs-IONSIV is stable in the cement matrix and leach tests over 91 days resulted in a 1.4 wt. % release of Cs for PVA formations and only 0.6 wt. % for the slag cement systems.[128]

Studies have also been carried out where CST has been immobilised via vitrification. Traditionally, materials that contain a high Ti content have been difficult to successfully dissolve in vitrification processes and as a result, only very small amounts of Ti can be added to large amounts of flux which results in a large volume of volume of vitrified waste. In this study loadings of 5 wt. % CST were proposed with an additional 25 wt. % sludge oxides.[199]

As well as encapsulation of Cs-IONSIV in cement and vitrification into a glass, other immobilisation methods have also been explored. A previous study demonstrated that Hot isostatic pressing (HIPing) is an excellent way to immobilise spent IONSIV.[34,200] In this

work carried out by Chen et al.[34,70,130], Cs has been exchanged into IONSIV to a number of different Cs exchange levels and then HIPed to produce dense ceramic wasteforms.[34,70]

XRD and SEM/TEM studies of these HIPed materials suggested that different Cs phases are produced dependant on the Cs loading. At Cs levels of 2-6 wt. % IONSIV, the major Cs phase is $Cs_2TiNb_6O_{18}$ and from 8-12 wt. % Cs, a second phase Cs phase, $Cs_2ZrSi_6O_{15}$, grows in and coexists with $Cs_2TiNb_6O_{18}$. Static leach tests were performed on polished monoliths cut from the HIP cans to assess the chemical durability, the results indicated extremely durable HIPed products. The normalised leach rate for Cs in the 6 wt. % Cs – IONSIV HIPed material was less than 0.16 g /m^2/day, which is far superior to glass wasteforms and compares well to hollandite, another accepted Cs wasteform.[48,50,55,56] Further leach tests were carried out on pure $Cs_2TiNb_6O_{18}$ and $Cs_2ZrSi_6O_{15}$ and this study suggested that $Cs_2TiNb_6O_{18}$ is the most durable phase with a normalised leach rate for Cs of 0.003751 g /m^2day compared to 0.1255 g /m^2day for $Cs_2ZrSi_6O_{15}$, therefore the better quality wasteform is produced when the Cs loading is around 6 wt. %, where only $Cs_2TiNb_6O_{18}$ is produced. [34,130]

To investigate Cs-IONSIV a little further, in this study a series of Cs-IONSIV samples (4, 6, 8, 10 and 12 wt. % Cs) have been calcined in air and analysed using XRD, XRF and SEM, to see what phases are formed compared to the previous HIPing study. Considering the apparent success of Cs-IONSIV immobilisation via HIPing a series of Sr loaded IONSIV materials have also been thermally converted through calcination (in air) and HIPing and the products analysed. The monoliths produced from HIPing have were subjected to static leach testing to assess how robust the HIP materials are and therefore their potential suitability for final disposal in a GDF. As well as Sr loaded materials, a mixed

Cs/Sr-IONSIV has also been studied, where the mixed sample was calcined and HIPed, again chemical durability tests were carried out.

4.2 Experimental

4.2.1 Synthesis of Nb-doped Crystalline Silicotitanate

The Niobium substituted form of Crystalline Silicotitanate was synthesised using a hydrothermal method based on one reported by Poojary et al.[201] The hydrothermal method involves the crystallisation of materials at high vapour pressures. The hydrothermal synthesis took place in a Teflon^{TM} liner secured in a high-pressure stainless-steel autoclave (45 and 125 mL). For Nb-CST, the correct ratio of $Ti(iOC_4H_7)_4$, $Si(OC_2H_5)_4$ and $Nb(OEt)_5$ were added to a solution of 3.3M NaOH. The mixture was then stirred for 45 minutes and placed in a Teflon^{TM} liner fitted inside an autoclave and heated at 200^{o}C for 3 days. The product was then filtered and washed with deionised water and dried at 65^{o}C for 12 hours.

4.2.2 Hot Isostatic Pressing (HIPing) and Calcination (Thermal Decomposition)

To remove moisture and any organics, powders for HIPing were pre-heated at 800°C for 12 hours at a heating rate of 10°C/min and then carefully loaded and compacted into mild steel HIP cans in an inert environment (to prevent the powder picking up moisture). Before HIPing, with the powder inside, the cans were evacuated, crimped and welded shut and once ready the cans were HIPed in a EPSI Lab HIP unit operating at 1100°C, 190 MPa for 2 hours under a pure argon atmosphere. The heating and cooling rates were both 5°C/min. Furthermore, samples have also been decomposed via more conventional calcination methods. Samples were ground and placed in Al_2O_3 (alumina) crucible and fired in non-specialist muffle furnaces, the conditions for each sample are listed in **Table 4.3**.

Table 4.3 *Thermal decomposition synthesis conditions*

Sample	Temperature, time, heating rate
Sr-Nb-CST	900°C, 12 hours, 10°C/min
Sr-Nb-CST + $Zr(OH)_4$	900°C, 12 hours, 10°C/min
Unloaded IONSIV	900°C, 12 hours, 10°C/min
Unloaded IONSIV	1000°C, 12 hours, 10°C/min
Unloaded IONSIV	1100°C, 12 hours, 10°C/min
Sr-IONSIV (1.5 wt. % Loading)	900°C, 6 hours, 10°C/min
Sr-IONSIV (1.5 wt. % Loading)	1000°C, 6 hours, 10°C/min
Sr-IONSIV (1.5 wt. % Loading)	1100°C, 6 hours, 10°C/min
Sr-IONSIV (3.0 wt. % Loading)	900°C, 6 hours, 10°C/min
Sr-IONSIV (3.0 wt. % Loading)	1000°C, 6 hours, 10°C/min
Sr-IONSIV (3.0 wt. % Loading)	1100°C, 6 hours, 10°C/min
Cs-IOSNIV (4.0 wt. % Loading)	900°C, 6 hours, 10°C/min
Cs-IOSNIV (4.0 wt. % Loading)	1000°C, 6 hours, 10°C/min
Cs-IOSNIV (4.0 wt. % Loading)	1100°C, 6 hours, 10°C/min
Cs-IOSNIV (6.0 wt. % Loading)	900°C, 6 hours, 10°C/min
Cs-IOSNIV (6.0 wt. % Loading)	1000°C, 6 hours, 10°C/min
Cs-IOSNIV (6.0 wt. % Loading)	1100°C, 6 hours, 10°C/min
Cs-IOSNIV (12.0 wt. % Loading)	900°C, 6 hours, 10°C/min
Cs-IOSNIV (12.0 wt. % Loading)	1000°C, 6 hours, 10°C/min
Cs-IOSNIV (12.0 wt. % Loading)	1100°C, 6 hours, 10°C/min
Cs-IONSIV (8.0 wt. % Loading)	1100°C, 6 hours, 10°C/min
Cs-IONSIV (10.0 wt. % Loading)	1100°C, 6 hours, 10°C/min
Cs/Sr-IONSIV (Cs 6.5 wt. %, Sr 1.5 wt. % loading)	1100°C, 12 hours, 10°C/min

4.2.3 Ion Exchange

Ion exchange of Cs and Sr with Nb-CST or IONSIV® was done with loading calculated following **Equation 4.1**;

$$\left[\frac{(mass\ X^{n+}(g))}{(mass\ X^{n+}\ (g) +\ mass\ CST\ (g))}\right] \times 100 = wt\%\ Loading$$

N.B. *X= Cs (n=1) or Sr (n=2)*

Equation 4.1 *Ion Exchange*

For exchange $CsNO_3$ or $Sr(NO_3)_2$ was dissolved in deionised water. IONSIV was then added and the mixture shaken or agitated for 3 days. The powder (or beads for IONSIV) was then filtered under vacuum and washed thoroughly with deionised water and dried at 60ºC overnight. The Cs or Sr (or both) content was determined via XRF. UOP advise that IONSIV should be pre-treated with acid to improve the ion exchange capacity, but a test in this study and previous studies have deemed this step unnecessary. [194]

4.2.4 XRD and Rietveld Refinements

In this chapter, in-house diffraction experiment were carried out on two different diffractometers. Firstly, a Bruker D8 Advance (X-ray) Diffractometer using Cu $K_{\alpha 1}$ (1.5406 Å) radiation in transmission mode, fitted with a Lynx Eye Si-strip detector was used. Data were collected in the 2θ range 5° to 90° at a step size of 0.0198°. As described in the experimental section, absorption corrections were carried out before Rietveld refinements because of the transmission geometry. As well as in-house XRD experiments, data were also collected at the Diamond Light Source (DLS) facility on the high-resolution powder diffraction beam line (I11). Samples were loaded into 0.5 mm borosilicate glass capillaries and sealed; data were collected using radiation of wavelength 0.8257 Å. Rietveld analysis of XRD data was performed using EXPGUI GSAS suite. [138,139] Details of each Rietveld refinement can be found in the appendices including the live plots for each sample. For the multi-phase refinements where phases existed in low concentrations the atomic positions, thermal parameters and occupancies were not refined.

4.2.5 SEM and TEM

Secondary electron (SE) imaging and back scattered electron (BSE) imaging were carried out using a Philips XL30 ESEM-FEG with an Oxford Inca 300 EDX system equipped operating at 10 kV allowing in-situ EDX experiments to be undertaken. SE image samples were well ground and placed on conductive carbon film and coated with Au. BSE samples were mounted and polished according to the procedure listed in **Table 4.4.** All SEM work in this chapter was carried out with the assistance of Dr Tzu-Yu Chen (University of Birmingham).

Table 4.4 *Polishing procedure for SEM BSE*

Step	Surface	Lubricant	rpm/Force(N)	Time(mins)
Plane grinding	MD-Primo220	water	250/15	5
Fine grinding	MD-Large	9 μm diamond paste	125/5	3
Diamond Polishing	MD-Dac	3 μm diamond paste	125/5	3
Final Polishing	MD-Nap	1 μm diamond paste	125/5	1

TEM data were collected using a JEOL JEM-2100F equipped with a SEI/BSE detector, operating at 200 kv in STEM mode. Samples were placed in ethanol and dispersed on conductive carbon grids. All TEM work in this chapter was carried at the University of Limerick by Dr Yina Guo (University of Limerick) and Dr Tzu-Yu Chen (University of Birmingham)

4.2.6 XRF

Elemental analysis was carried out using a Bruker S8 Tiger Wavelength Dispersive X-ray Fluorescence (XRF) spectrometer. All samples in this chapter samples were fused into Li – borate glass beads prior to analysis. (Full details of the procedure are found in **section 2.4**).

4.3 Results for Cs and Sr loaded IONSIV

4.3.1 Niobium-doped CST (Nb-CST) and IONSIV

Before any work was carried out on commercial IONSIV, niobium doped CST (Nb-CST) was synthesised to confirm the crystal structure. Nb-CST has the approximate formula of $H_{0.5}Na(Nb_{0.5}Ti_{1.5})O_3(Si\ O_4)(H_2O)_2$.[96] It is tetragonal, a=7.8331(4), c=12.0074(7) Å and space group $P4_2/mcm$.[96] Nb-CST was synthesised using a hydrothermal process based on a method reported previously.[201]

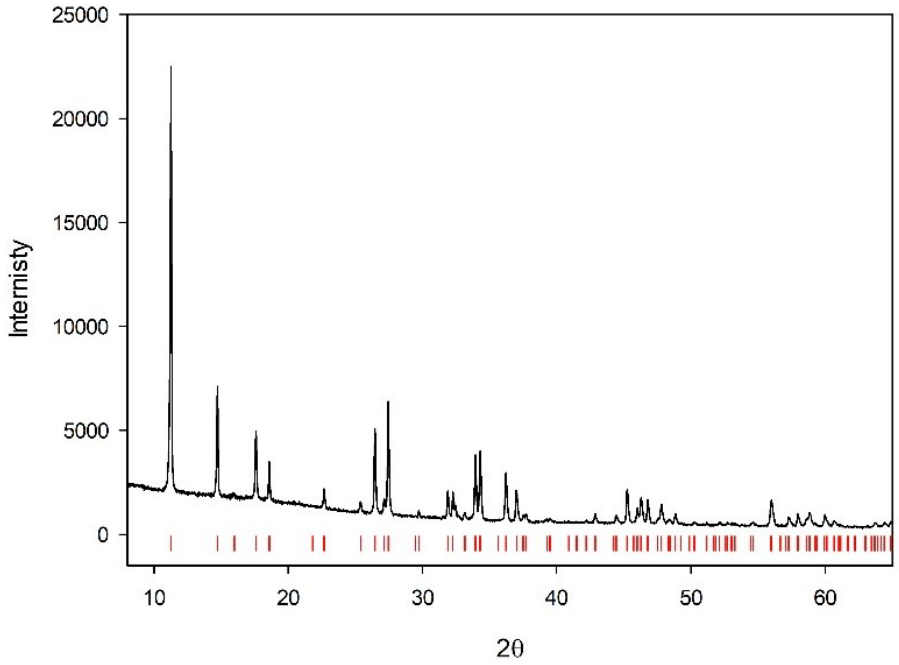

Figure 4.4 *Powder X-ray diffraction pattern of Nb doped CST synthesised via the hydrothermal method. Red Ticks are indexed peaks for ICDD PDF: 01-072-7604 Nb-CST ($H_{0.5}Na(Nb_{0.5}Ti_{1.5})O_3(SiO_4)(H_2O)_2$)*

Table 4.5 *Rietveld refinement details for Nb-CST*

	Lattice Parameters (Å)	
	a / Å	*c* / Å
Nb-CST	7.83604(15)	12.00876(29)
Refinement Details		
χ^2	R_{wp}	R_p
5.306	7.41%	4.97%

The XRD pattern (**Figure 4.4**) and subsequent Rietveld analysis (**Table 4.5**) confirms that Nb-CST is tetragonal and crystallises in the expected $P4_2/mcm$ space group. The pattern does not appear to display any impurity peaks, suggesting a clean hydrothermal synthesis of the target product. **Figure 4.5** below displays the XRD pattern for the commercially sold IONSIV (R9120-B), the beads have been well ground by hand in order to carry out this powder diffraction experiment. The $Zr(OH)_4$ binder in IONSIV (around 20 wt. %) is amorphous and therefore is not seen via XRD. The active ion exchange part of IONSIV (80 wt. %) was identified via XRD as Nb-CST, the same phase indexed in **Figure 4.4**.

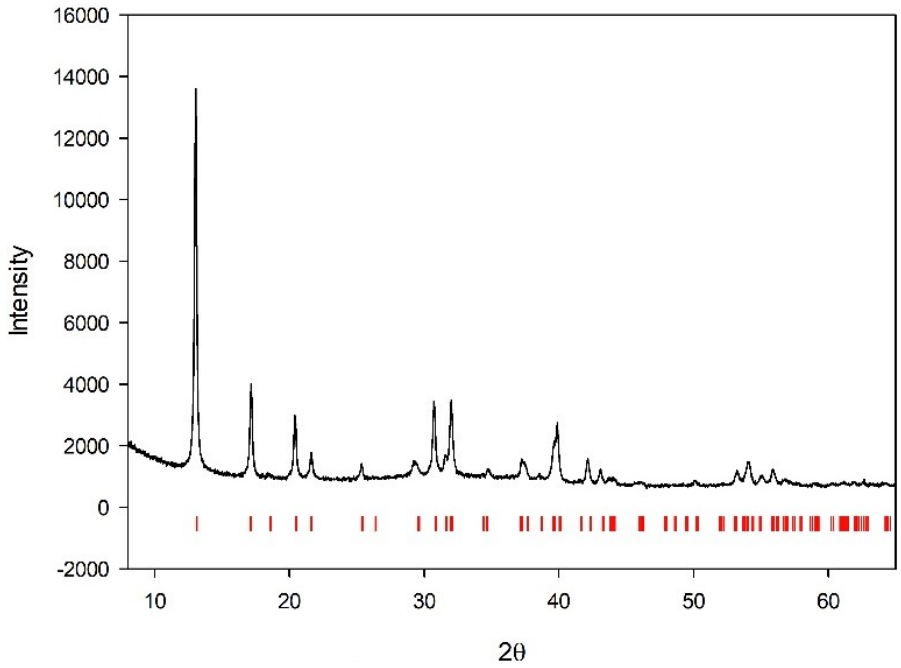

Figure 4.5 *Powder X-ray diffraction pattern of unloaded IONSIV. Red ticks in this pattern are the indexed peaks of the same phase in* ***Figure 4.4****,* $(H_{0.5}Na(Nb_{0.5}Ti_{1.5})O_3(SiO_4)(H_2O)_2)$

Table 4.6 *Rietveld refinement details for IONSIV (R9120-B, 80 wt. % $H_{0.5}Na(Nb_{0.5}Ti_{1.5})O_3(SiO_4)(H_2O)_2$ (CST) and 20 wt. % $Zr(OH)_4$)*

	Lattice Parameters (Å)	
	a / Å	*c* / Å
IONSIV (R9120-B)	7.8716(5)	11.9910(8)
Refinement Details		
χ^2	R_{wp}	R_p
3.104	5.46 %	4.17 %

Rietveld refinement (**Table 4.6**) again confirmed the space group $P4_2/mcm$. Considering the Ti/Nb occupancies can vary in Nb-doped CST, the Nb/Ti occupancies were refined. Any change in occupancy i.e, change in a Nb^{5+} for Ti^{4+} the charge was balanced by also refining the occupancy of Na in the pores. The refinements suggested that there was more Nb present in the commercially sold IONSIV giving the rough formula $H_{0.393}Na_{0.781}(Nb_{0.826}Ti_{1.174})SiO_7 \bullet xH_2O$, and therefore less Ti was present compared to hydrothermally synthesised Nb-CST which has the rough formula $H_{0.804}Na_{0.848}(Nb_{0.384}Ti_{1.652})SiO_7 \bullet xH_2O$. XRF (**Table 4.7**) also agreed with the Rietveld refinement in that there is a higher Ti/Nb ratio i.e. less Nb in the Nb-CST sample than in the IONSIV sample.

Table 4.7 *XRF of Niobium doped CST and IONSIV*

Elements	Nb-CST / wt. %	Nb-CST / at. %	Normalised to Si
Na	15.0	16.6	1.9
Ti	26.3	14.0	1.6
Nb	13.2	3.6	0.4
Si	9.8	8.9	1
O	35.7	56.8	6.4
	Ti/Nb Molar Ratio: 4		

Elements	IONSIV / wt. %	IONSIV / at. %	Normalised to Si
Na	2.5	3.1	0.3
Ti	21.5	12.8	1.4
Nb	15.7	4.8	0.5
Si	8.9	9.0	1
Zr	14.4	4.5	0.5
O	37.0	65.8	7.3
	Ti/Nb Molar Ratio: 2.8		

4.3.2 Sr exchanged Nb-CST

Figure 4.6 displays the powder XRD pattern for Sr-exchanged Nb-CST. Sr^{2+} is larger than Na^{+} and therefore it was expected that the unit cell would increase in size after Sr^{2+} is exchanged for Na^{+}, however the refined lattice parameters (**Table 4.8**) suggest that the unit cell decreases after Sr^{2+} exchange. The Na-Nb-CST form has lattice parameters *a*: 7.83604(15) and *c*: 12.00876(29) Å, the Sr-Nb-CST form *a*: 7.7804(4) and *c*: 11.9096(7) Å which overall is a decrease in cell volume of 2.3%, which was rough agreement with the findings in a previous publication, where a decrease in cell volume was also observed.[197] The refinement suggested a Ti/Nb content roughly similar to the Na-Nb-CST (unexchanged) refined earlier (**Table 4.5**). XRF analysis of the Sr-Nb-CST (**Table 4.9**) suggested the Nb content was slightly lower than expected, giving a higher Ti/Nb ratio. This may be a result of some of the Nb content being lost in the exchange process, but this seemed unlikely and was most probably an instrument error. XRF did suggest 11.6 wt. % of Sr in the sample confirming exchange was successful (**Table 4.9**).

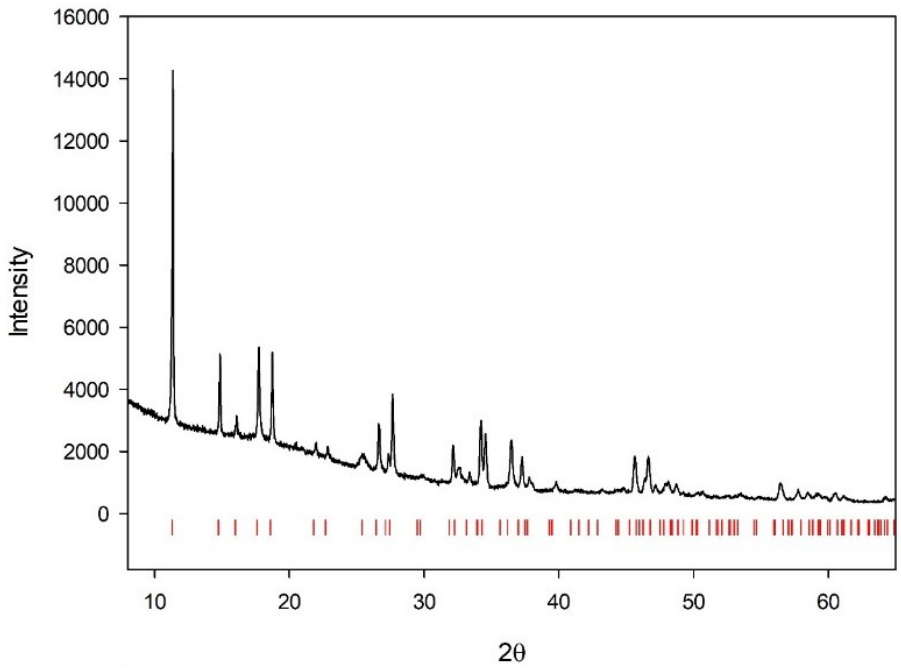

Figure 4.6 *Powder XRD Sr – Nb CST. Red ticks in this pattern are the indexed peaks of the same phase in* ***Figure 4.4****, $(H_{0.5}Na(Nb_{0.5}Ti_{1.5})O_3(SiO_4)(H_2O)_2)$*

Table 4.8 *Rietveld Refinement details for Sr-Nb-CST*

	Lattice Parameters (Å)	
	a / Å	*c* / Å
Sr-Nb-CST	7.7804(4)	11.9096(7)
Refinement Details		
χ^2	R_{wp}	R_p
6.184	7.14%	4.56%

Table 4.9 *XRF analysis of Sr-Nb-CST*

Elements	Sr-Nb-CST / wt. %	Sr-Nb-CST / at. %	Normalised to Si
Na	6.9	8.2	0.9
Ti	27.3	15.5	1.7
Nb	8.9	2.6	0.3
Si	9.4	9.1	1
Sr	11.6	3.6	0.4
O	35.9	61.0	6.7
	Ti/Nb Molar Ratio: 5.6		

4.3.3 Sr – Nb – CST Thermal Decomposition (Calcining in air)

Before carrying out HIPing, Sr-IONSIV, Sr-Nb-CST and a Sr-Nb-CST mixed with $Zr(OH)_4$ were thermally converted via calcination in air. This was done to gain an understanding of how these materials behave at high temperature. Studying the products formed after calcination at varied temperatures would help select the appropriate HIPing conditions i.e. temperature and dwelling times.

Having confirmed Sr exchange into Nb-CST via XRD and XRF, the material was calcined at both 1000°C and 1100°C (selected to mirror HIPing temperatures used in a previous study).[34,130] Once decomposed, the materials were analysed using XRD to ascertain if any crystalline phases are formed and if so identify which phase or phases, Sr resides in. Interestingly at these temperatures, Sr-Nb-CST melted into a glass and fused to the alumina crucible, making XRD analysis impossible. Nb-CST should not melt until temperatures of around 1120°C and therefore the Sr exchanged version was not expected to melt at these temperatures. The cause for the lower temperature may be a result of compositional differences between this version of CST and the one reported. As a result of this, decomposition was carried out at 900°C, to prevent melting. XRD revealed two crystalline phases for thermally converted Sr-Nb-CST (**Figure 4.7**).

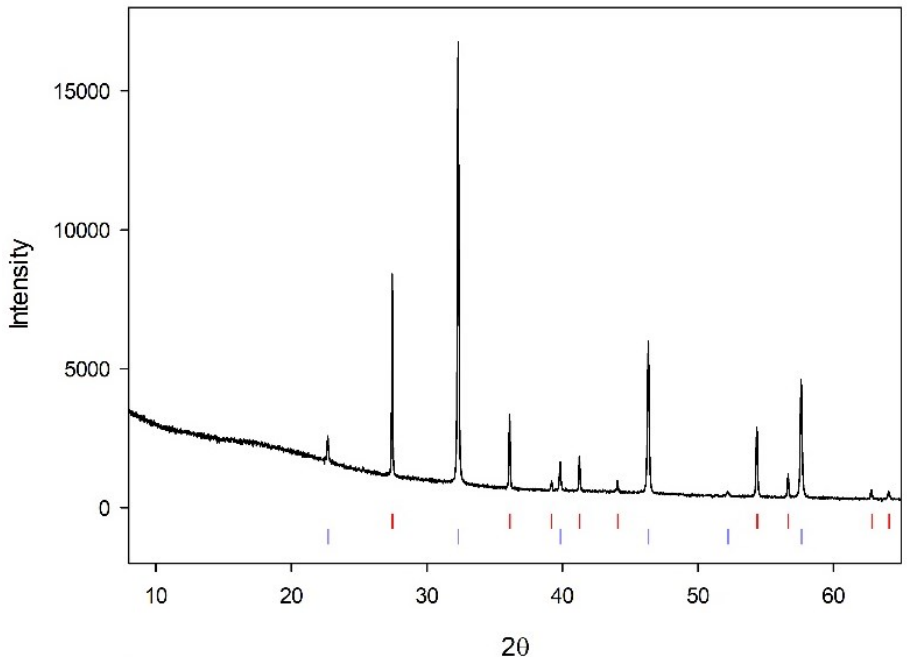

Figure 4.7 *Powder XRD of calcined (900°C) Sr-Nb-CST. Red ticks are indexed peaks from ICDD PDF: 01-089-0555 TiO_2 (Rutile) and Blue ticks are indexed peaks from ICDD PDF: 01-085-2008 ($Na_{0.3}Sr_{0.7}Ti_{0.7}Nb_{0.3}O_3$)*

Search match using EVA software revealed two main phases in Sr-Nb-CST decomposed at 900°C. These included TiO_2 (rutile) and (Sr,Na)(Ti,Nb)O_3, a perovskite-like phase. $Na_{0.3}Sr_{0.7}Ti_{0.7}Nb_{0.3}O_3$ is cubic and crystallises in the *Pm*-3*m* space group. The presence of the perovskite phase was potentially encouraging for HIPing experiments considering the major Sr phases in SYNROC is also a Sr perovskite.[48,50] In this material, no Si containing phases were observed and it is likely in this sample, Si resides in an amorphous SiO_2 phase unseen by XRD.

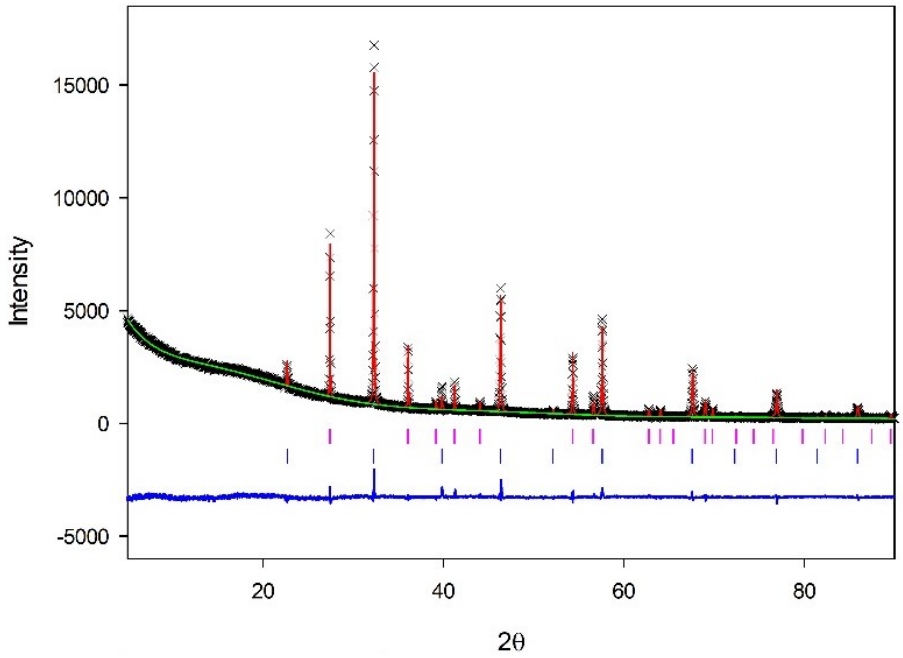

Figure 4.8 *Rietveld refinement plot (GSAS) of calcined (900°C) Sr-Nb-CST. Red line: calculated pattern, black crosses: experimental pattern, green line: background, blue line: difference curve, pink ticks: TiO_2 (rutile) and blue ticks: $Na_{0.3}Sr_{0.7}Ti_{0.7}Nb_{0.3}O_3$*

Rietveld analysis (**Figure 4.8**) indicated that the decomposed material is crystalline and the experimental and calculated patterns from the refinement match well. The refinement (**Table 4.10**) suggested that TiO_2 (rutile) makes up around 40% of the material and the strontium perovskite phase make up 60% of the phase assembly. Refinement of the Sr and Na occupancy suggested the actual formula of the perovskite phase is $Sr_{0.736}Na_{0.027}Ti_{0.5}Nb_{0.5}O_3$.

Table 4.10 *Rietveld refinement details of calcined (900°C) Sr-Nb-CST*

	Lattice Parameters (Å)		
	a / Å	*c* / Å	wt. %
TiO_2 (rutile)	4.59111(5)	2.95641(6)	40.67(2)
$(Sr,Na)(Ti,Nb)O_3$	3.914483(22)	/	59.33(1)
Refinement Details			
χ^2	R_{wp}	R_p	
2.368	4.67 %	3.35 %	

4.3.4 Sr – Nb – CST + $Zr(OH)_4$ Thermal Decomposition (Calcination in air) 900°C

As well as Sr-Nb-CST, a Sr-Nb-CST + $Zr(OH)_4$ mixed material has also been thermally decomposed. In this sample, 20 wt. % $Zr(OH)_4$ was ground with Sr-Nb-CST using a mortar and pestle. The addition of $Zr(OH)_4$ was designed to imitate the powdered commercial IONSIV (R9120-P). Initially temperatures in excess of 1000°C were used for thermal conversion but the sample melted again as it did before with Sr-Nb-CST, so as a result, thermal conversion was carried out at 900°C.

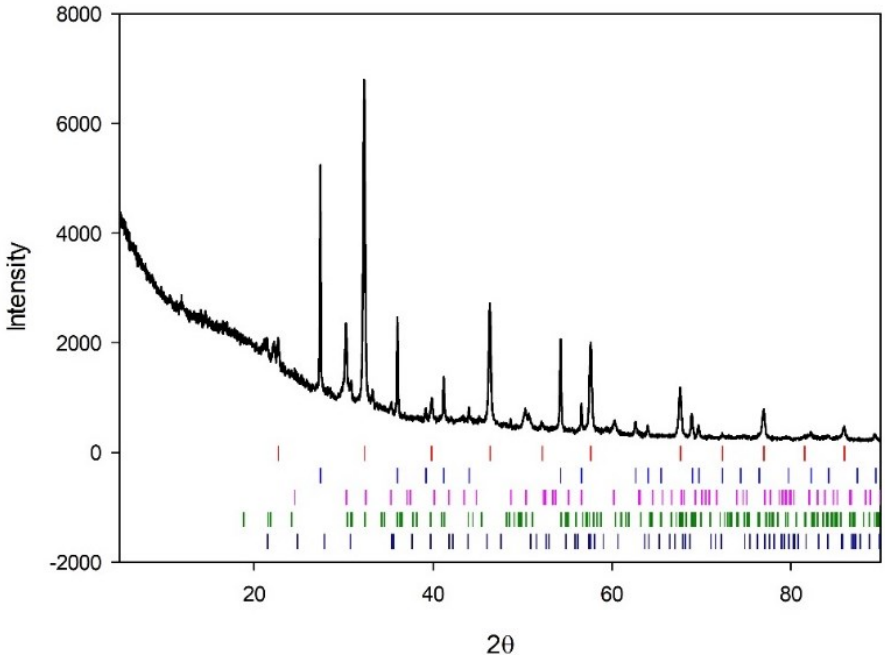

Figure 4.9 *Powder XRD of calcined (900°C) Sr-Nb-CST + $Zr(OH)_4$. Red ticks are indexed peaks from ICDD PDF: PDF: 01-085-2008 ($Na_{0.3}Sr_{0.7}Ti_{0.7}Nb_{0.3}O_3$), Blue ticks are indexed peaks from ICDD PDF: 01-089-0555 (TiO_2, rutile), Pink ticks are indexed peaks from ICDD PDF: 01-074-9431 ($ZrTiO_4$), green ticks are indexed peaks from ICDD PDF: 00-044-0161 ($SrZrO_3$) and dark blue ticks are indexed peaks from ICDD PDF: 01-077-8309 (SiO_2, cristobalite)*

Adding $Zr(OH)_4$ into the mixture complicated the phases formed after thermal decomposition compared to Sr-Nb-CST. XRD (**Figure 4.9**) and subsequent Rietveld analysis (**Figure 4.10** and **Table 4.11**) suggested the formation of an additional Sr phase as well as some other phases to what was observed in the Sr-Nb-CST sample. The $(Na,Sr)(Ti,Nb)O_3$ perovskite phase (observed earlier) makes up around 50 wt. % of the

material and Sr is also found in $SrZrO_3$. $SrZrO_3$ is orthorhombic and crystallises in the *Cmcm* space group. The Sr/Na content in the perovskite phase was not refined because of the complexity of the pattern and quality of the data. The other phases in the assembly include $ZrTiO_4$, TiO_2 (rutile) and SiO_2. Interestingly, in this example where Zr has been added, cristobalite, a crystalline form of SiO_2 was identified in the pattern. The lattice parameters were not refined for SiO_2 because of issues with peak overlap and intensities.

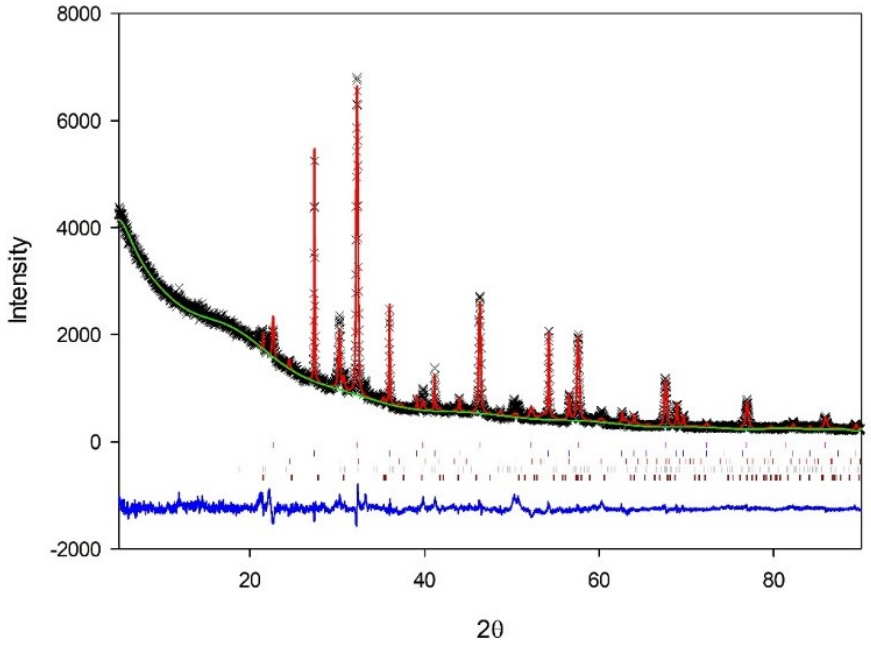

Figure 4.10 *Rietveld refinement plot (GSAS) of calcined (900°C) Sr-Nb-CST + $Zr(OH)_4$. Pink ticks: $Na_{0.3}Sr_{0.7}Ti_{0.7}Nb_{0.3}O_3$, Blue ticks: TiO_2 (Rutile), Red ticks: $ZrTiO_4$, dark grey ticks: $SrZrO_3$) and brown ticks: SiO_2 (cristobalite)*

Table 4.11 *Rietveld Refinement details for calcined (900°C) Sr-Nb-CST + $Zr(OH)_4$*

	Lattice Parameters (Å)			
	a / Å	*b* / Å	*c* / Å	wt. %
$(Na,Sr)(Ti,Nb)O_3$	3.91448(7)	/	3.91448	49.062(2)
TiO_2 (Rutile)	4.59609(11)	/	2.96316(13)	34.549(2)
$Zr_{0.5}Ti_{0.5}O_2$	4.8013(23)	5.5083(30)	5.0824(25)	13.820(3)
$SrZrO_3$	5.773(9)	5.887(11)	8.151(10)	1.270(2)
SiO_2	5.07	5.07	7.085	1.290(2)
Refinement Details				
χ^2	R_{wp}	R_p		
3.678	5.91	3.93		

The calcination of these materials suggested that exchanged Nb-CST materials would not be suitable for HIPing at temperatures above 900°C. At this point a decision was made not to carry out HIPing Sr exchanged Nb-CST. HIPing in this study was carried out in an external department and therefore the time and conditions for HIPing were limited. As a result of this, lower temperature HIP runs were not possible as far as Nb-CST samples are concerned.

4.3.5 IONSIV (unloaded) Thermal Decomposition in air (Calcination at 900, 1000 and 1100°C)

Prior to calcining Sr-IONSIV, unloaded IOSNIV has been thermally converted at three different temperatures, 900, 1000 and 1100°C. Studying the phases formed after heating unloaded IONSIV would help later identify new phases formed when Sr-IOSNIV is thermally decomposed. Having discovered that synthesised Nb-CST melted at 1000°C it was expected that IONSIV would behave in the same way. Interestingly, it was found that IONSIV did not melt when heated to temperatures as high as 1100°C.

The three XRD patterns presented in **Figure 4.11** display the thermal conversion of unloaded IONSIV at the three different temperatures. The pattern labelled (a), represents decomposition at 900°C, which proved to be the least crystalline of the three samples. The crystallinity improved as the temperature increased to 1000°C (labelled **Figure 4.11**, (b)) and 1100°C (labelled **Figure 4.11**, (c)). EVA search match software identified a number of crystalline phases and subsequent Rietveld refinements of the XRD data were used to and quantity the phases present.

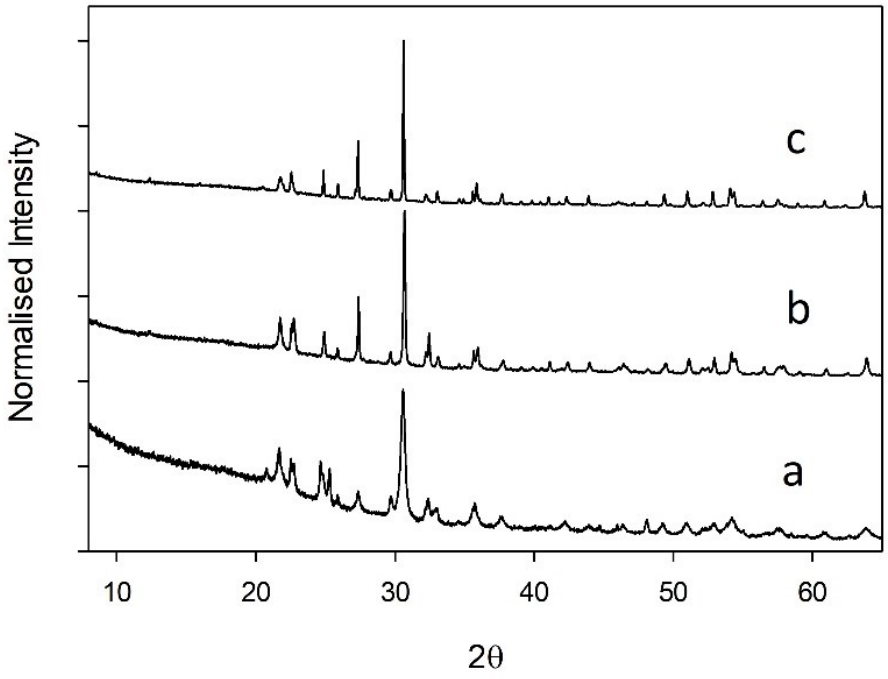

Figure 4.11 *Powder XRD Patterns of IONSIV (Unloaded) calcined at 900 (a), 1000 (b) and 1100°C (c)*

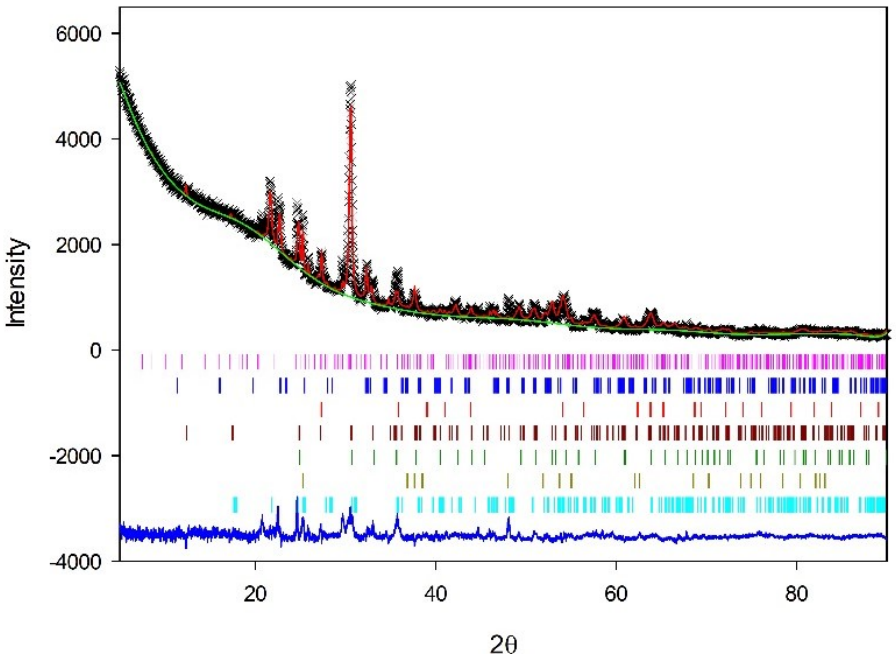

Figure 4.12 *Rietveld refinement plot (GSAS) of calcined (900°C) IONSIV (Unloaded). Pink ticks: $Na_{13}Nb_{35}O_{94}$, blue ticks: $NaNbO_3$, red ticks: TiO_2 (rutile), brown ticks: $Zr_5Ti_7O_{24}$, green ticks: $ZrTiO_4$, dark yellow ticks: TiO_2 (anatase) and cyan ticks: SiO_2 (cristobalite)*

Table 4.12 *Refinement Details for calcined (900°C) IONSIV (Unloaded)*

	Lattice Parameters (Å)			
	a / Å	*b* / Å	*c* / Å	wt. %
$Na_{13}Nb_{35}O_{94}$	12.406(6)	37.089(16)	3.9033(10)	3.42(4)
$NaNbO_3$	7.7661(22)	7.8796(22)	15.659(4)	4.85(3)
TiO_2(R)	4.5986(10)	/	2.9844(16)	7.76(5)
$Zr_5Ti_7O_{24}$	14.297(9)	5.4779(32)	5.050(4)	19.2(1)
$Zr_{0.33}Ti_{0.67}O_4$	4.7480(13)	5.4376(14)	5.0349(12)	42.39(8)
TiO_2(Anatase)	3.7828(8)	/	9.5386(28)	4.70(3)
SiO_2	7.24(4)	7.41(4)	6.661(32)	17.69(6)
Refinement Details				
χ^2	R_{wp}	R_p		
4.824	6.28%	4.11%		

At 900°C, calcination of unloaded IONSIV produced a host of crystalline phases. Rietveld analysis (**Figure 4.12**) was carried out and the weight fraction analysis results are shown in **Table 4.12**. Two orthorhombic sodium niobate phases were identified, $Na_{13}Nb_{35}O_{94}$ and $NaNbO_3$ which make up about 8 wt. % of the material. Two TiO_2 polymorphs (rutile and anatase) and two zirconium titanate phases with the formulas $Zr_5Ti_7O_{24}$ and $Zr_{0.33}Ti_{0.67}O_4$ were also present with SiO_2 making up the rest of the material.

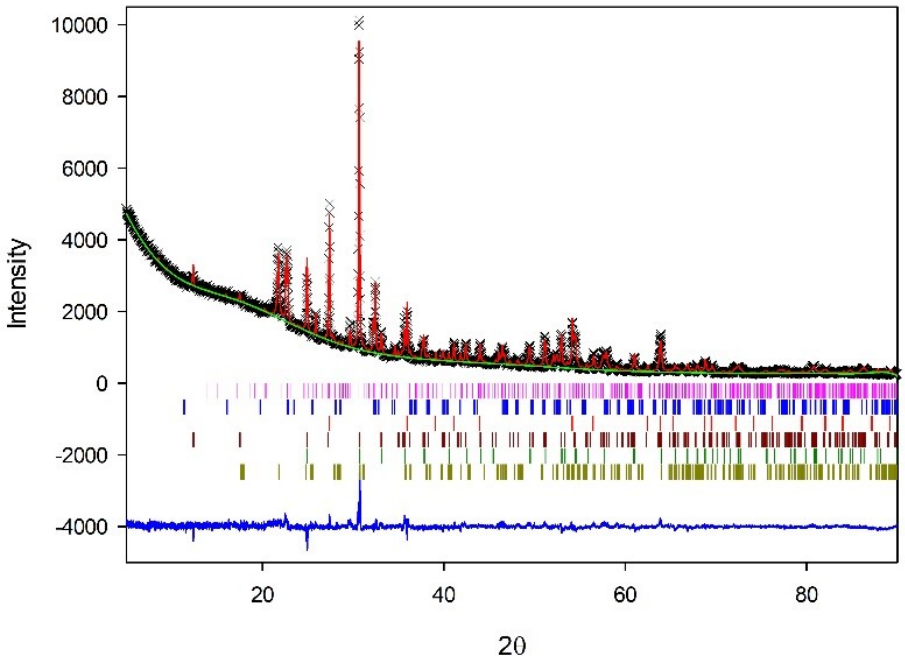

Figure 4.13 *Rietveld refinement plot (GSAS) of calcined (1000°C) IONSIV (Unloaded. Pink ticks: $Na_{13}Nb_{35}O_{94}$, blue ticks: $NaNbO_3$, red ticks: TiO_2 (rutile), brown ticks: $Zr_5Ti_7O_{24}$, green ticks: $ZrTiO_4$ and dark yellow ticks: SiO_2 (cristobalite)*

XRD and Rietveld analysis (***Figure 4.13*** and ***Table 4.13***) of the 1000°C sample revealed similar set of phases to what were observed in the sample that had been heated to 900°C. However, there were some subtle differences; firstly, this material is somewhat more crystalline, a result of the higher temperature, secondly anatase (TiO_2) was not observed and as a result more rutile is present. Furthermore, there was also an increased amount of Na phases present which again is likely because of the higher processing temperature causing more Na phases to crystallise.

Table 4.13 *Refinement details for calcined (1000°C) IONSIV (Unloaded)*

	Lattice Parameters (Å)			
	a / Å	*b* / Å	*c* / Å	wt. %
$Na_{13}Nb_{35}O_{94}$	12.4116(18)	37.156(5)	3.93621(29)	7.07(2)
$NaNbO_3$	5.5446(7)	15.5553(13)	5.5038 (7)	9.45(1)
TiO_2(R)	4.60044(14)	/	2.96823(17)	21.00(2)
$Zr_5Ti_7O_{24}$	14.2698(14)	5.4113(5)	5.0278(5)	26.63(5)
$Zr_{0.33}Ti_{0.67}O_4$	4.7501(5)	5.3967(5)	5.0267(5)	19.47(5)
SiO_2	7.184(13)	7.021(13)	6.973(15)	16.38(3)
Refinement Details				
χ^2	R_{wp}	R_p		
3.678	5.69%	3.66%		

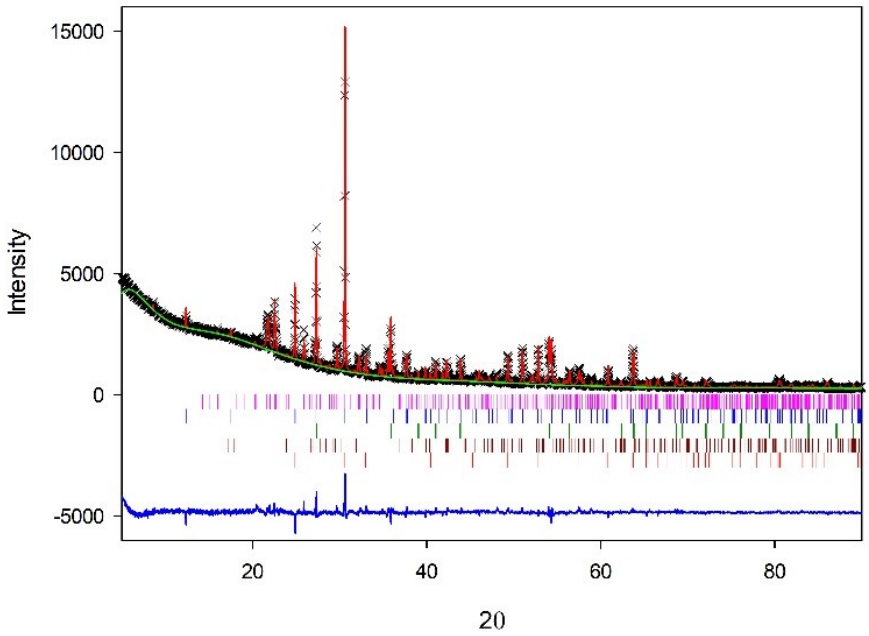

Figure 4.14 *Rietveld refinement plot (GSAS) of calcined (1100°C) IONSIV (Unloaded). Pink ticks: $Na_{13}Nb_{35}O_{94}$, blue ticks: $Zr_5Ti_7O_{24}$, green ticks: $(Ti,Nb)O_2$, brown ticks: SiO_2 (cristobalite) and dark red ticks $ZrTiO_4$*

XRD and Rietveld fits of unloaded IONSIV decomposed at 1100°C is shown in **Figure 4.14** and **Table 4.14**. This material is the most crystalline of the three samples and the phases present are much the same as the previous 1000°C sample although the weight fractions are slightly varied. At 1100°C, Rietveld refinement suggests the Na phases increase in concentration making up almost 45 wt. % of the material.

Table 4.14 *Refinement details of calcined (1100°C) IONSIV (Unloaded)*

	Lattice Parameters (Å)			
	a / Å	*b* / Å	*c* / Å	wt. %
$Na_{13}Nb_{35}O_{94}$	12.3960(15)	37.101(4)	3.93759(22)	13.66(2)
$Zr_5Ti_7O_{24}$	14.2965(6)	5.41248(22)	5.03822(21)	30.94(3)
$Ti_{0.912}Nb_{0.088}O_2$	4.60757(11)	/	2.97427(12)	23.29(2)
SiO_2	7.457(20)	7.072(19)	6.681(17)	15.29(4)
$Zr_{0.33}Ti_{0.67}O_4$	4.75975(35)	5.42305(33)	5.03850(30)	16.82(4)
Refinement Details				
χ^2	R_{wp}	R_p		
4.003	5.83%	4.04%		

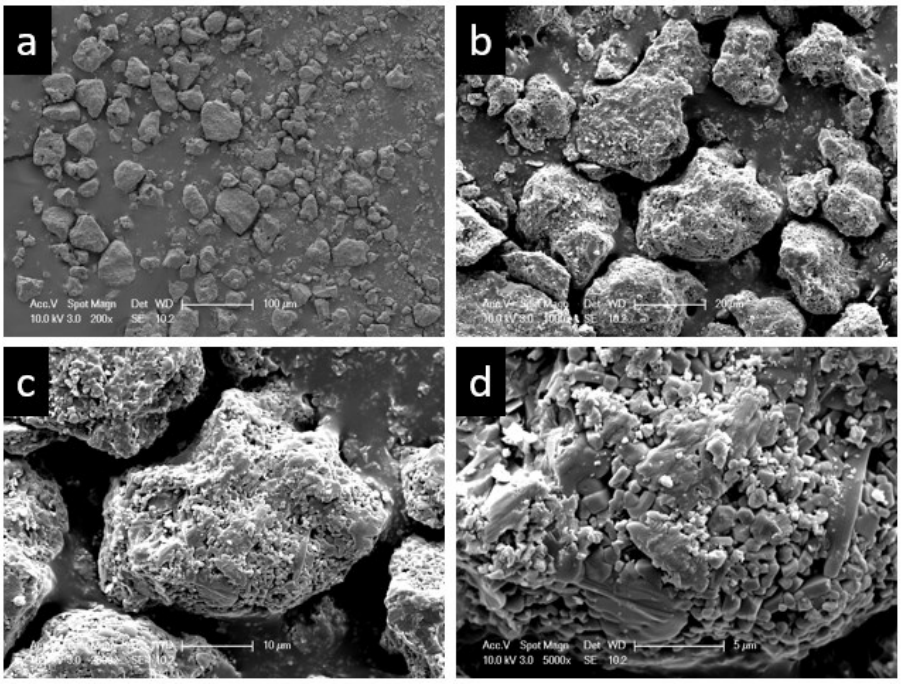

Figure 4.15 *SEM of images of IONSIV (Unloaded) after calcination at 1100°C. a:100 µm scale, b: 20 µm scale, c: 10 µm scale and d: 5 µm scale*

SEM images of unloaded IONSIV thermally decomposed at 1100°C are shown in **Figure 4.16**. Calcination at these temperatures produces reasonably uniform particles of roughly 20 µm size.

4.3.6 Sr-IONSIV (1.5 and 3 wt. %, Sr) Thermal Decomposition in air (Calcination 900, 1000 and 1100°C)

Following the decomposition studies of unloaded IOSNIV at 900, 1000 and 1100°C, Sr has been exchanged into IONSIV at two different levels, 1.5 and 3.0 wt. % and then decomposed at the same three temperatures as the unloaded IONSIV examples. Exchange levels were calculated according to **Equation 4.2**;

$$[Sr^{2+}_{(g)} / (Sr^{2+}_{(g)} / \text{Nb-CST}_{(g)})] \times 100 = \text{wt. \%}$$

Equation 4.2 *Calculation of exchange levels in IONSIV*

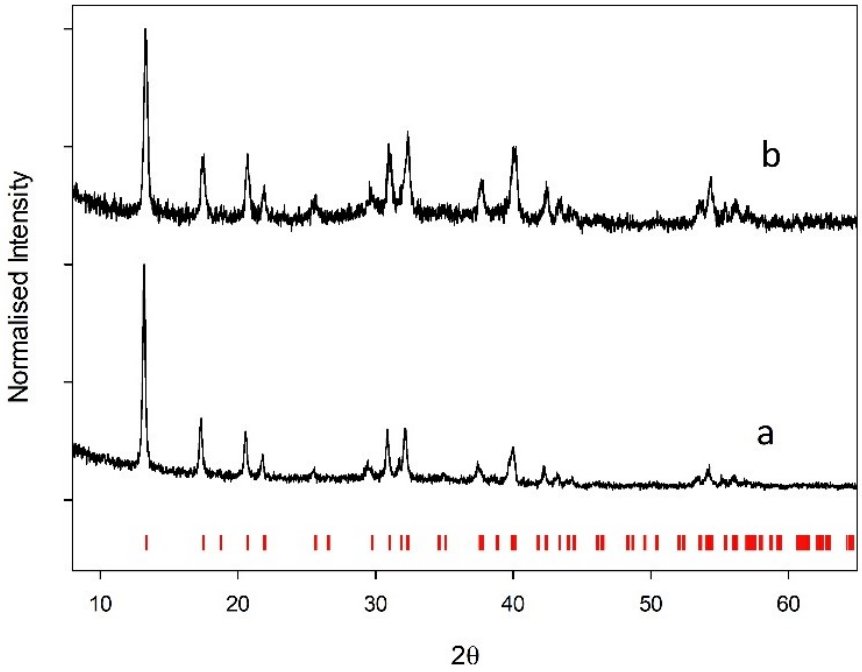

Figure 4.16 *Powder XRD of Sr-exchanged IONSIV a: 1.5 wt. % Sr b : 3.0 wt. % Sr. Red ticks: Nb-CST ($H_{0.5}Na(Nb_{0.5}Ti_{1.5})O_3(SiO_4)(H_2O)_2$)*

Powder XRD data (**Figure 4.16**) were collected for both the 1.5 and 3 wt. % Sr - IONSIV samples and refinements carried out (**Table 4.15** and **Table 4.16**). The refined lattice parameters suggest there is a tiny contraction in unit cell as Sr loading is increased from 1.5 to 3.0 wt. %. This was expected considering the results observed for Nb-CST and Sr-Nb-CST samples. There is only a small contraction in this case, with a unit cell volume reduction of 0.35% as Sr loading is increased. It was thought this contraction would be more

significant as the Sr content was doubled but XRF analysis (**Table 4.17**) of these suggested the actual levels of Sr in each sample are close in value and hence the unit cell contraction is only small.

Table 4.15 *Refinement details for Sr-IONSIV (1.5 wt. %, Sr)*

	Lattice Parameters (Å)	
	a / Å	*c* / Å
Sr-IONSIV 1.5 wt. % Sr	7.8694(14)	11.9765(25)
Refinement Details		
χ^2	R_{wp}	R_p
1.904	12.69%	9.66%

Table 4.16 *Refinement details for Sr-IONSIV (3.0 wt. %, Sr)*

	Lattice Parameters (Å)	
	a / Å	*c* / Å
Sr-IONSIV 3.0 wt. % Sr	7.8640(26)	11.952(5)
Refinement Details		
χ^2	R_{wp}	R_p
2.036	12.02%	9.45%

Table 4.17 *XRF results for Sr-IONSIV (1.5 and 3.0 wt. %, Sr)*

	Sr-IONSIV (1.5 wt. %)		
Elements	wt. %	at. %	Normalised to Si
Na	1.7	2.2	0.2
Ti	21.9	13.3	1.4
Nb	15.4	4.8	0.5
Si	9.1	9.4	1
Sr	1.3	0.4	0.04
Zr	14.5	4.6	0.5
O	36.1	65.3	7.0
	Ti/Nb Molar Ratio: 2.8		

	Sr-IONSIV (3.0 wt. %)		
Elements	wt. %	at. %	Normalised to Si
Na	1.5	1.9	0.2
Ti	21.6	13.1	1.4
Nb	15.4	4.8	0.5
Si	9.1	9.4	1
Sr	1.9	0.6	0.06
Zr	14.4	4.6	0.5
O	36.1	65.6	7.0
	Ti/Nb Molar Ratio: 2.8		

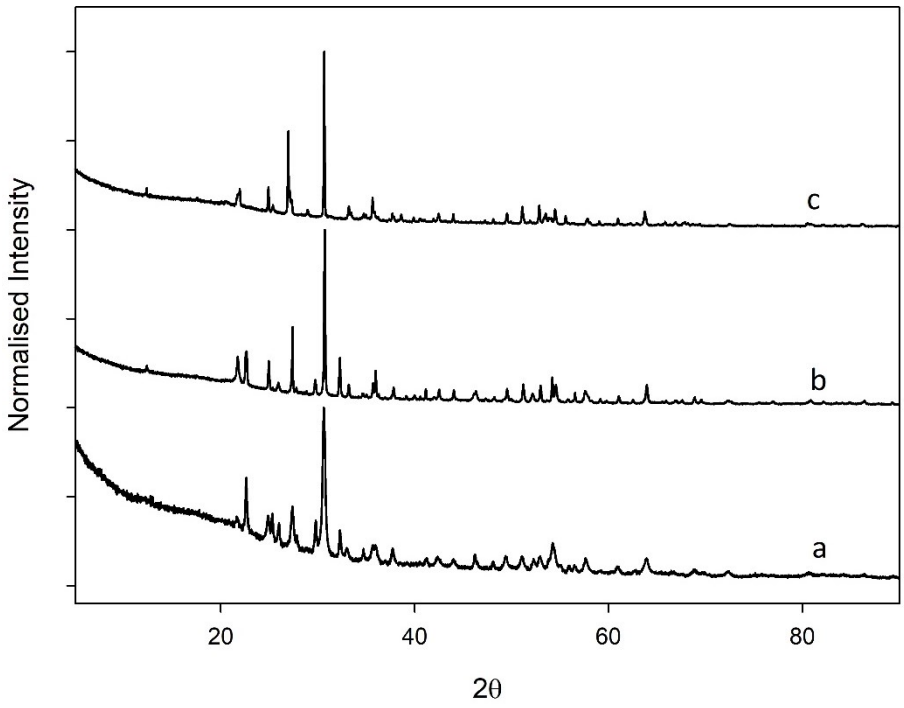

Figure 4.17 *Powder XRD stack of Sr-IONSIV (1.5 wt. %, Sr) calcined at 900 (a), 1000 (b) and 1100°C (c).*

Having confirmed Sr exchange in IONSIV via XRD and XRF Sr-IONSIV samples have been calcined in air. **Figure 4.17** displays three different XRD patterns for each temperature of decomposition for Sr-IONSIV (1.5 wt. %). As seen before in the unloaded IONSIV example, the crystallinity of the decomposition phases increases as the temperature increases. Decomposition at these temperatures results in three slightly different phase compositions which have been analysed below.

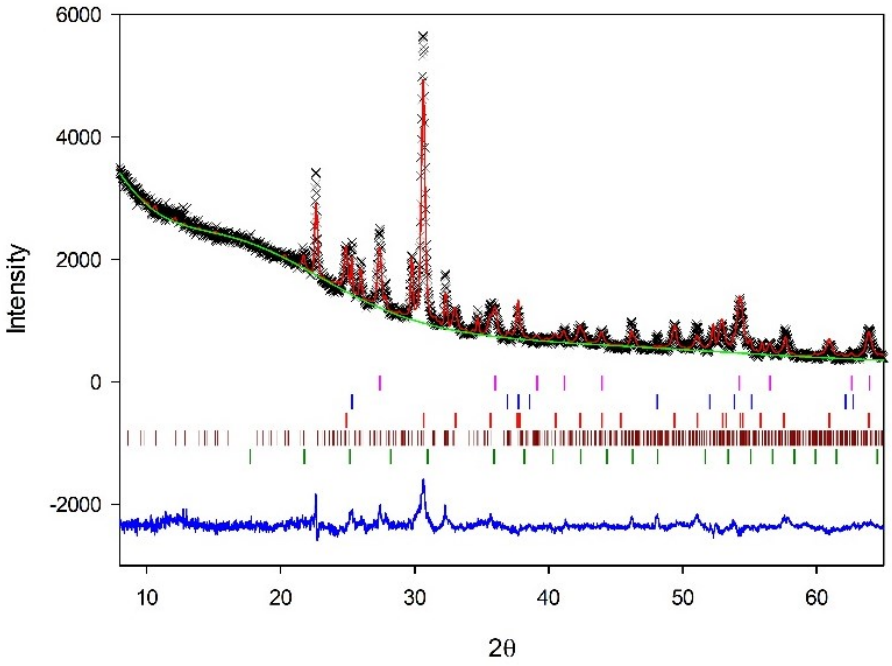

Figure 4.18 *Rietveld refinement plot (GSAS) of calcined (900°C) Sr-IONSIV (1.5 wt. %, Sr). Pink ticks: TiO_2 (rutile), blue ticks: TiO_2 (anatase), red ticks: $ZrTiO_4$, dark red ticks: $Sr_6Nb_{34}O_{91}$ and green ticks: SiO_2 (Cristobalite)*

At 900°C, five different phases have been identified including two polymorphs of TiO_2 (anatase and rutile), a $(Zr,Ti)O_4$ phase which was also observed in early decomposition samples, SiO_2 (cristobalite) and all the Sr appears to reside in a strontium niobate phase of formula $Sr_6Nb_{34}O_{91}$. $Sr_6Nb_{34}O_{91}$ is tetragonal and crystallises with the space group *P*4*bm*. Rietveld refinements quantified these phases (shown in **Table 4.18**). It was found that $Sr_6Nb_{34}O_{91}$ makes up around 16 wt. % of the overall phase assembly which suggested

approximately 1.6 wt. % Sr content in the sample which is in approximate agreement with XRF (**Table 4.17**).

Table 4.18 *Rietveld refinement details for calcined (900°C) Sr-IONSIV (1.5 wt. %, Sr)*

	Lattice Parameters (Å)			
	a / Å	*b* / Å	*c* / Å	wt. %
TiO_2 (R)	4.6014(6)	/	2.9656(7)	19.52(4)
TiO_2 (A)	3.7809(7)	/	9.5267(15)	3.86(3)
$Zr_{0.33}Ti_{0.67}O_2$	4.7512(8)	5.4188(9)	5.0344(8)	57.78(3)
$Sr_6Nb_{34}O_{91}$	37.0663(26)	/	3.9269(5)	16.27(3)
SiO_2	7.07	7.07	7.07	2.57(49)
Refinement Details				
χ^2	R_{wp}	R_p		
4.436	6.26	4.22		

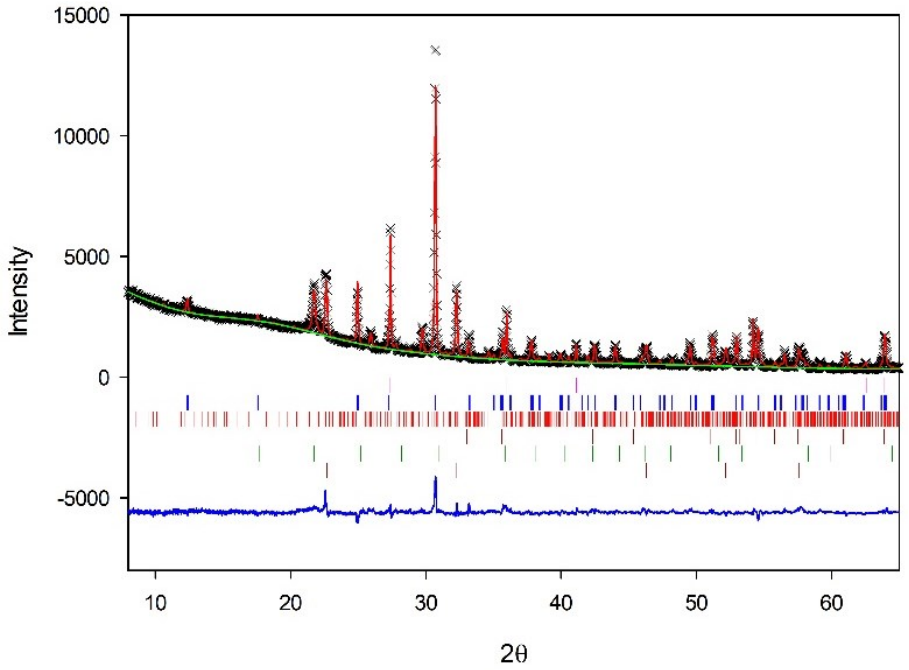

Figure 4.19 *Rietveld refinement plot (GSAS) of calcined (1000°C) Sr-IONSIV (1.5 wt. %, Sr). Pink ticks: TiO_2 (rutile), blue ticks: $Zr_5Ti_7O_{24}$, red ticks: $Sr_6Nb_{34}O_{91}$, brown ticks: $ZrTiO_4$, green ticks: SiO_2 (Cristobalite) and dark red ticks: $(Na,Sr)NbO_3$*

The sample decomposed in air at 1000°C has a slightly different phase assembly and, in this case, 6 phases are present, including TiO_2 (rutile), two orthorhombic zirconium titanate phases, $ZrTiO_4$ and $Zr_5Ti_7O_{24}$, SiO_2 and two different Sr phases. Sr resides in $Sr_6Nb_{34}O_{91}$ (present in the 900°C sample) and a $(Na_{0.5}Sr_{0.25})NbO_3$ perovskite-like phase, a

similar phase to the one observed in the Sr-Nb-CST decomposition. Rietveld analysis suggested that there is 10.55 wt. % $Sr_6Nb_{34}O_{91}$ and 6.69 wt. % of $(Na_{0.5}Sr_{0.25})NbO_3$ in the sample which equates to 1.9 wt. % Sr in the overall material which is slightly more than what XRF suggested for Sr content. This is likely a result of the occupancy not being refined on the A site of the Sr containing perovskite. Occupancy was not refined because of the complexity of phase assembly and quality of data.

Table 4.19 *Rietveld refinement details for calcined (1000°C) Sr-IONSIV (1.5 wt. %, Sr)*

	Lattice Parameters (Å)			
	a / Å	*b* / Å	*c* / Å	wt. %
TiO_2 (R)	4.59917(11)	/	2.96786(13)	21.04(2)
$Zr_5Ti_7O_{24}$	14.2665(9)	5.38519(34)	5.02545(33)	29.09(5)
$Sr_6Nb_{34}O_{91}$	37.1125(24)	/	3.9338(5)	10.55(3)
$Zr_{0.33}Ti_{0.67}O_2$	4.7488(5)	5.3985(4)	5.0233(4)	17.00(5)
SiO_2	8.163(18)	6.026(7)	7.525(16)	15.64(4)
$(Na,Sr)NbO_3$	3.91703(16)	/	/	6.69(2)
Refinement Details				
χ^2	R_{wp}	R_p		
4.554	6.21%	4.11%		

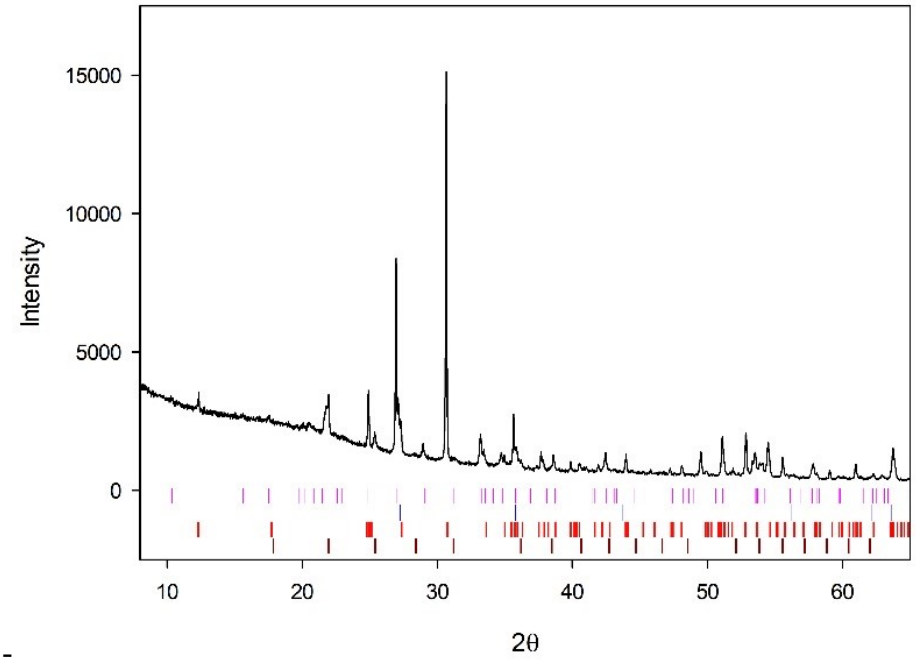

Figure 4.20 *Powder XRD of calcined (1100°C) Sr-IONSIV (1.5 wt. %, Sr). Pink ticks are indexed peaks from ICDD PDF: 00-049-0396 ($SrTi_9Nb_4O_{29}$), blue ticks are indexed peaks from ICDD PDF: 01-072-7371 ($(Ti,Nb)O_2$), red ticks: $Zr_5Ti_7O_{24}$ and brown ticks: SiO_2 (cristobalite)*

The phases produced from decomposition in air at 1100°C are again slightly different to the other compositions formed at the other two temperatures. In this case, four phases were identified from XRD including $Ti_{0.912}Nb_{0.088}O_2$, $Zr_5Ti_7O_{24}$, SiO_2 and a strontium titanium niobate phase with the formula $SrTi_9Nb_4O_{29}$. Rietveld refinement was not carried out on this sample as there is no solved structure for $SrTi_9Nb_4O_{29}$. It is known however that $SrTi_9Nb_4O_{29}$ is orthorhombic and crystallises in the *Cmcm* space group. This material is a member of a homologous series of chemically twinned rutile oxides. [202] The first member of this series is $SrTi_3Nb_4O_{17}$ which has *a*-, *b*- and *c* parameters of approximately 6.6, 8.9 and 20.8 Å (crystal structure shown in **Figure 4.21**). [164,202] As each $\{TiO_2\}_2$ unit is added to the structure the *c* parameter increases by 4.4 Å. The approximate lattice parameters for $SrTi_9Nb_4O_{29}$ are *a*: 6.589. *b*: 8.869 and *c*: 33.968 Å. [202]

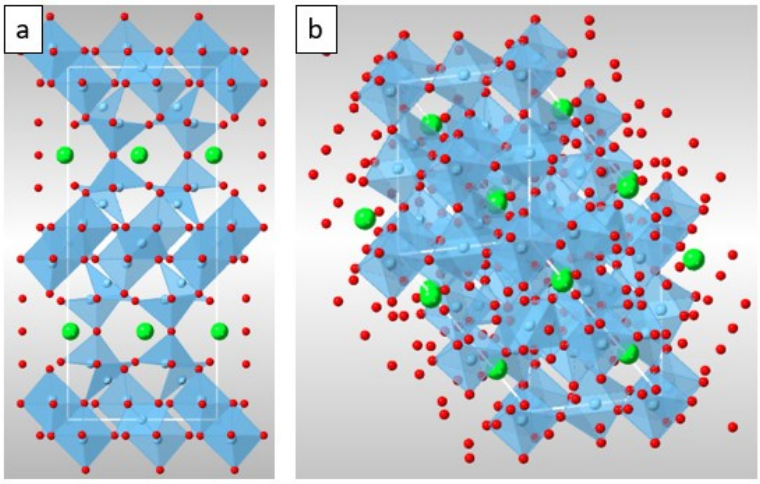

Figure 4.21 *Crystal structure of $SrTi_3Nb_4O_{17}$ modified from Mezaoui et al.* [164]

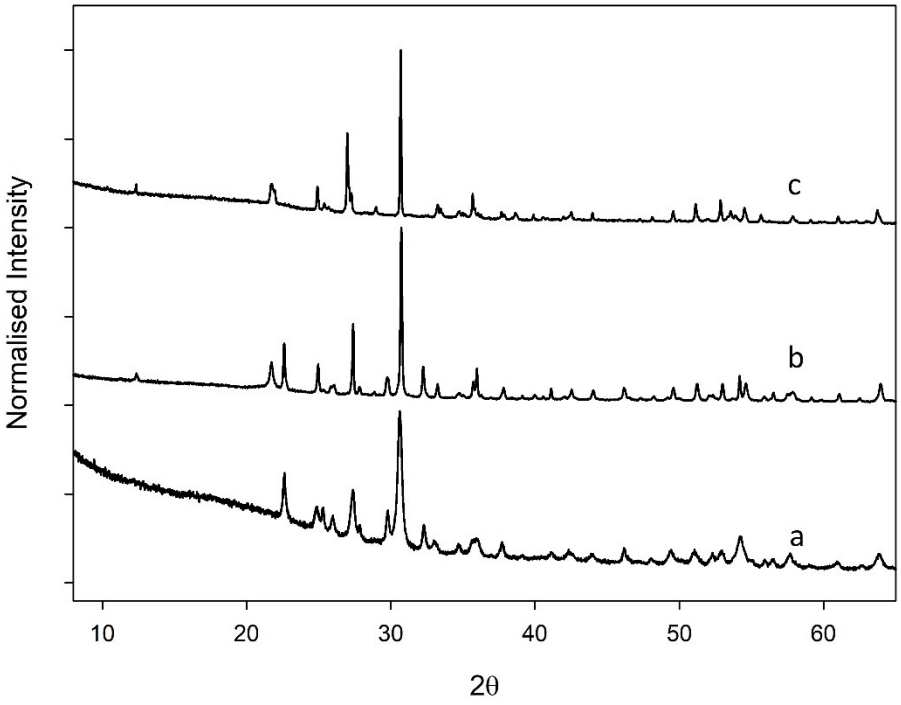

Figure 4.22 *Powder XRD Stack plots of calcined Sr-IONSIV (3.0 wt. %, Sr) at 900 (a), 1000 (b) and 1100°C (c).*

Figure 4.22 displays the three XRD patterns for each temperature of calcining the Sr-IONSIV at 3 wt. % Sr loading. Again, the crystallinity of the decomposition phases increases as the temperature increases from 900 to 1100°. Decomposition at this Sr loading results in three patterns that are fairly similar to the 1.5 wt. % Sr sample, the phase compositions have been analysed below.

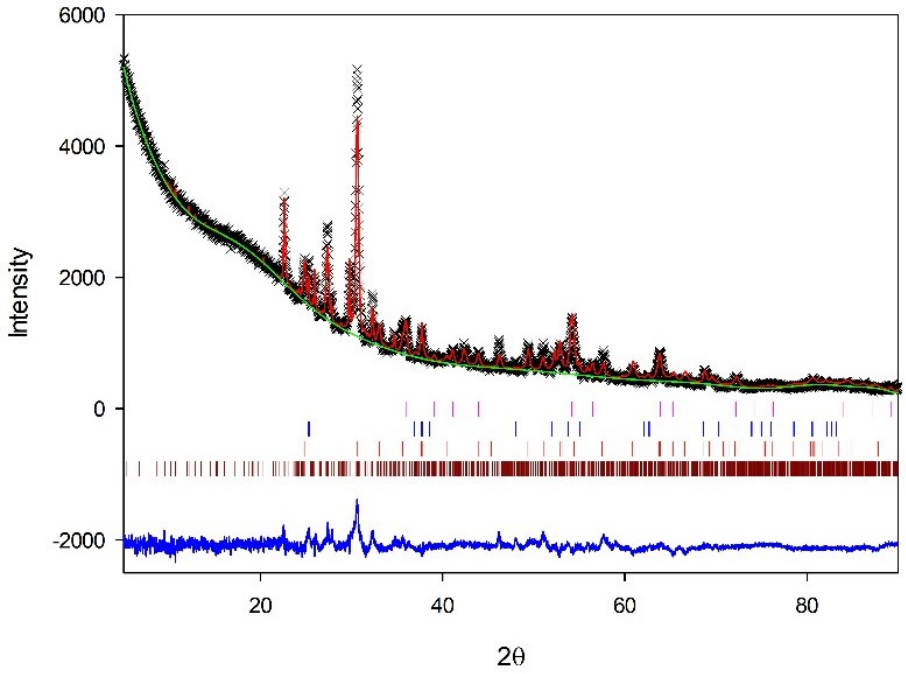

Figure 4.23 *Rietveld refinement plot (GSAS) of calcined (900°C) Sr-IONSIV (3.0 wt. %, Sr). Pink ticks: TiO_2 (R), blue ticks: TiO_2 (A), red ticks: $ZrTiO_4$ and brown ticks: $Sr_6Nb_{34}O_{91}$*

Calcining at 900°C of 3 wt. % Sr-IONSIV, produces a similar phase assembly to that observed for the 1.5 wt. % Sr – IONSIV sample. In this case XRD (**Figure 4.23**) indicate the only difference is that SiO_2 is not observed here, otherwise the phase assembly is the same. XRD identified the same two polymorphs of TiO_2, $(Zr,Ti)O_4$ and the same Sr phase, $Sr_6Nb_{34}O_{91}$. Rietveld analysis (**Table 4.20**) suggested that the decomposed material is 18.03 wt. % $Sr_6Nb_{34}O_{91}$, very slightly more than was calculated in the 1.5 wt. % Sr – IONSIV decomposition at 900°C, which was expected on account of the increased Sr content identified by XRF (**Table 4.17**).

Table 4.20 *Rietveld refinement details for calcined (900°C) Sr-IONSIV (3.0 wt. %, Sr)*

	Lattice Parameters (Å)			
	a / Å	*b* / Å	*c* / Å	wt. %
TiO_2 (R)	4.6044(6)	/	2.9663(7)	23.51(4)
TiO_2 (A)	3.7837(11)	/	9.524(4)	2.93(3)
$Zr_{0.33}Ti_{0.67}O_2$	4.7570(9)	5.4148(11)	5.0338(9)	55.53(3)
$Sr_6Nb_{34}O_{91}$	37.0499(31)	/	3.9272(5)	18.03(3)
Refinement Details				
χ^2	R_{wp}	R_p		
4.499	5.97 %	3.85 %		

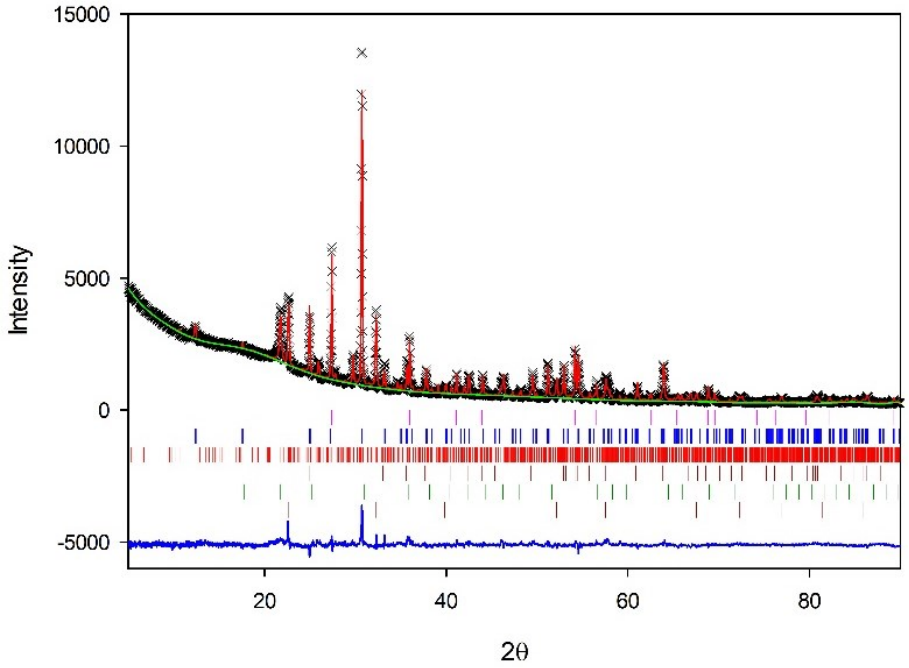

Figure 4.24 *Rietveld refinement plot (GSAS) of calcined (1000°C) Sr-IONSIV (3.0 wt. %, Sr). Pink ticks: TiO_2 (R), blue ticks: $Zr_5Ti_7O_{24}$, red ticks: $Sr_6Nb_{34}O_{91}$, brown ticks: $ZrTiO_4$, green ticks: SiO_2 (cristobalite) and dark red ticks: $Na_{0.5}Sr_{0.25}NbO_3$*

Figure 4.24 is the refinement for Sr-IONSIV at 3 wt. % Sr loading calcined at 1000°C. The phase assembly is identical to the 1.5 wt. % sample except the calculated weight fractions from Rietveld analysis (**Table 4.21**) suggest slightly different amounts of each material. There is slightly more $Sr_6Nb_{34}O_{91}$ at 13.12 wt. % present but slightly less $(Na_{0.5},Sr_{0.25})NbO_3$ at 4.21 wt. %, overall however there is still more Sr in this material which is expected considering the higher Sr content in the sample.

Table 4.21 *Rietveld refinement details for calcined (1000°C) Sr-IONSIV (3.0 wt. %, Sr)*

	Lattice Parameters (Å)			
	a / Å	*b* / Å	*c* / Å	wt. %
TiO_2 (R)	4.59999(12)	/	2.96873(14)	20.74(2)
$Zr_5Ti_7O_{24}$	14.2662(10)	5.3867(4)	5.0224(4)	31.82(5)
$Sr_6Nb_{34}O_{91}$	37.0622(26)	/	3.9301(5)	13.12(3)
$Zr_{0.33}Ti_{0.67}O_2$	4.7478(6)	5.3791(5)	5.0228(5)	14.38(6)
SiO_2	7.07	7.07	7.07	15.69(4)
(Na,Sr)NbO_3	3.92306(19)	/	/	4.21(1)
Refinement Details				
χ^2	R_{wp}	R_p		
7.298	8.58 %	5.97 %		

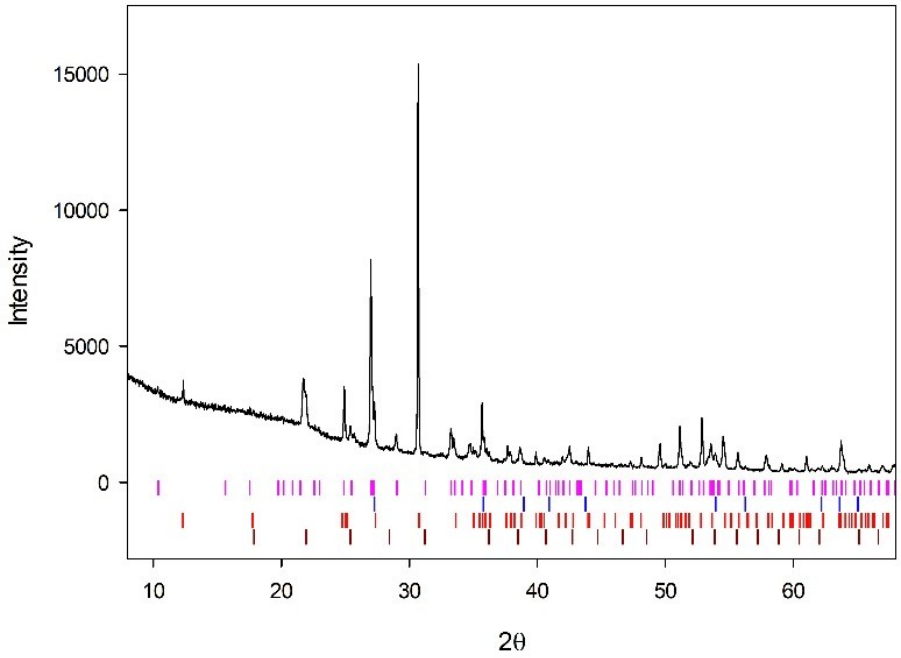

Figure 4.25 *Powder XRD of calcined (1100°C) Sr-IONSIV (3.0 wt. %, Sr). Pink ticks: $SrTi_9Nb_4O_{29}$, blue ticks: $(Ti,Nb)O_2$, red ticks: $Zr_5Ti_7O_{24}$ and brown ticks: SiO_2 (cristobalite)*

The phases identified in the Sr-IONSIV (3 wt. %) (**Figure 4.25**) calcined at 1100°C, are the same as those observed previously at 1.5 wt. % Sr loading. Again, Rietveld refinement has not been carried out on account of there not being a known crystal structure for $SrTi_9Nb_4O_{29}$. The other phases include $Ti_{0.912}Nb_{0.088}O_2$, $Zr_5Ti_7O_{24}$ and SiO_2.

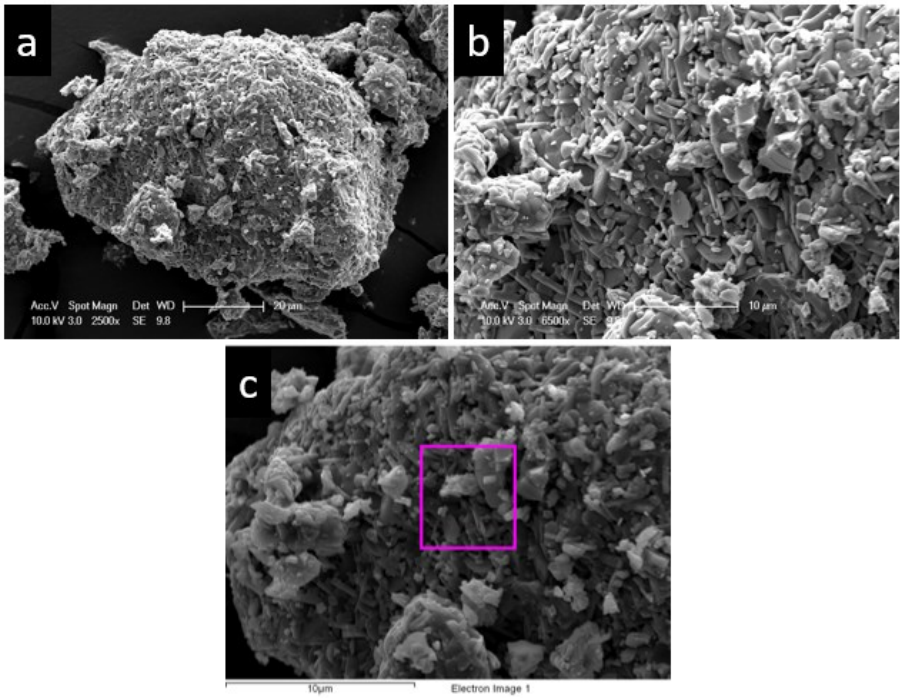

Figure 4.26 *SEM images of Sr-IONSIV (3 wt. %, Sr) calcined (in air) at 1100°C. a: SE image 10 µm. b: SE image 20 µm. c: EDX Analysis area (**Table 4.22**)*

SEM images of Sr-IONSIV (3wt. %) calcined at 1100°C are displayed in **Figure 4.26**. SEM/EDS experiments were also carried out. The SEM experiment failed to analyse individual particles as the spot size associated with SEM is too large. However, the EDX further confirm the presence of Sr in the decomposed sample. EDX (**Table 4.22**) in this case suggests around 1.41 wt. % Sr is present in this particular area of the sample.

Table 4.22 *SEM / EDS (Image C **Figure 4.26**) Sr-IONSIV (3 wt. %) calcination at 1100°C*

Element	Weight %	Atomic %
O K	27.3	60.4
Na K	0.4	0.7
Si K	3.5	4.4
Ti K	22.0	16.3
Sr L	**1.4**	**0.6**
Zr K	36.5	14.2

Calcining Sr-IONSIV at 900, 1000 and 1100°C (in air) has provided a crucial insight into what phases may be formed through HIPing Sr-loaded IONSIV. The background phases (not containing Sr) are mostly similar at the three different temperatures however the Sr phases do change at each different temperature. At 900°C, the main Sr phase is $Sr_6Nb_{34}O_{91}$ and as the temperature increase to 1000°C, a second phase, $Na_{0.5}Sr_{0.25}NbO_3$ as well as $Sr_6Nb_{34}O_{91}$ was identified. At 1100°C, a different single Sr phase is observed, which was identified as $SrTi_9Nb_4O_{29}$. The HIPing process in this study would be carried out at 1100°C, 190 MPa for 2 hours. Therefore, it was expected that the phases produced would more likely be similar to the phases identified in the sample calcined at 1100°C sample.

4.3.7 Sr-IONSIV (1.5, 3.0 and 4.0 wt. %) Thermal Decomposition through Hot Isostatic Pressing (HIPing)

Sr-IONSIV samples have been HIPed at three different loadings of Sr, 1.5, 3.0 and 4 wt. %. For these samples, XRD data has been collected using both in-house equipment (Bruker D8 Advance Diffractometer) and at the Diamond Light Source (High resolution powder XRD Beam Line: I11). Following this, Rietveld Refinements have been carried out in order to quantify the individual phases that make up the entire assembly. Furthermore, microscopy techniques including SEM and TEM have been carried out in order to confirm the phases identified from XRD.

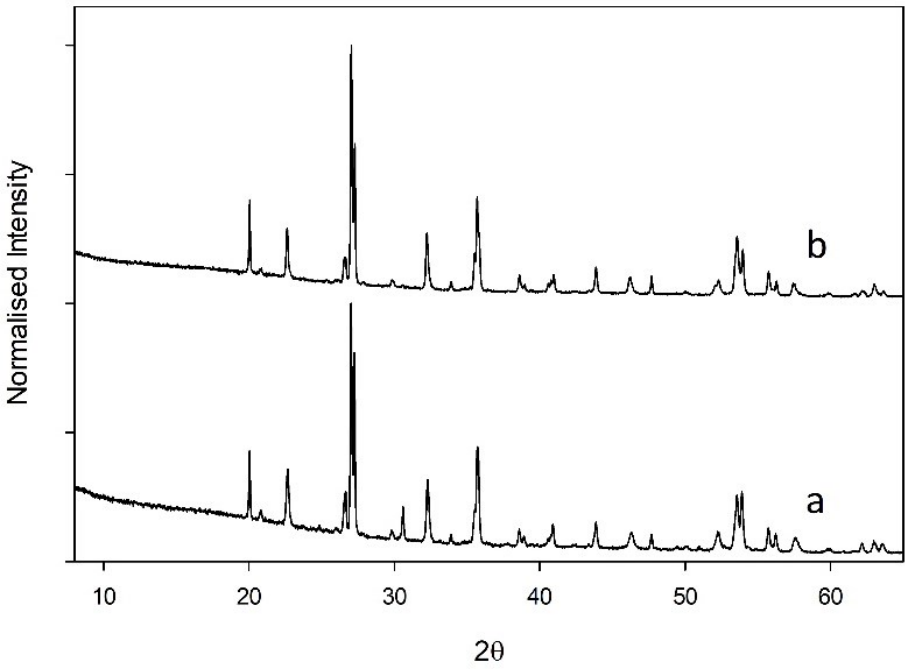

Figure 4.27 *Powder XRD patterns of HIPed (1100°C, 2 hours) Sr-IONSIV (a: 1.5 and b: 3 wt. %)*

Figure 4.27 displays two XRD patterns for the HIPed Sr-IONSIV at 1.5 wt. % (labelled a) and 3.0 wt. % (labelled b) Sr loading. Both patterns suggest crystalline products and the phases identified using EVA search match software indicate that the phase compositions are mostly the same for both Sr weight loadings.

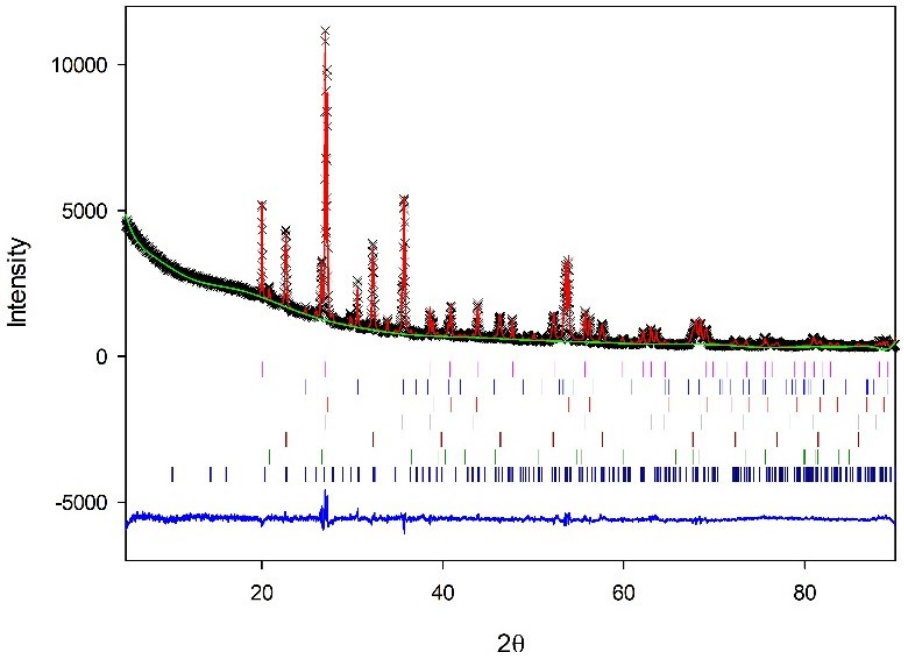

Figure 4.28 *Rietveld refinement plot (GSAS) of HIPed Sr-IONSIV (1.5 wt. %) (in-house D8 data). Pink ticks: $ZrSiO_4$, blue ticks: $ZrTiO_4$, red ticks: $Ti_{0.912}Nb_{0.088}O_2$, grey ticks: $Ti_{0.69}Nb_{0.24}O_2$, dark red ticks: $Sr_{0.056}Na_{0.889}NbO_3$, green ticks: SiO_2 (cristobalite) and dark blue ticks: $NaSr_2Nb_5O_{15}$*

For the HIPed Sr-IONSIV (1.5 wt. %) sample, seven different phases have been identified via in-house XRD experiments (**Figure 4.28**). The majority of the phases observed here were identified in the earlier calcined samples. In this case the background phases (non-Sr containing) include $ZrSiO_4$, two different titanium niobate phases with the formulas $Ti_{0.912}Nb_{0.088}O_2$ and $Ti_{0.69}Nb_{0.24}O_2$, SiO_2 and $Zr_{0.33}Ti_{0.67}O_2$. The main Sr phase is the $(Sr,Na)NbO_3$ perovskite-like phase which was also observed in the earlier. The refined formula was refined to be $Sr_{0.056}Na_{0.889}NbO_3$ and the refinement (**Table 4.23**) suggested this phase made up 11.03 wt. % of the material. As well as the Sr-perovskite like phase, some $NaSr_2Nb_5O_{15}$ (4.11 wt. %) was also present which is tetragonal and crystallises in the *P*4*bm* space group.

Table 4.23 *Rietveld refinement details for HIPed Sr-IONSIV (1.5 wt. %, Sr) (In-house D8 data)*

	Lattice Parameters (Å)				
	a / Å	*b* / Å	*c* / Å	*β*/°	wt. %
$ZrSiO_4$	6.58817(24)	/	5.96861(26)	/	25.35(2)
$Zr_{0.33}Ti_{0.67}O_2$	4.6944(14)	5.5290(20)	5.0373(15)	/	4.47(2)
$Ti_{0.912}Nb_{0.088}O_2$	4.62220(15)	/	2.98259(12)	/	33.98(2)
$Ti_{0.69}Nb_{0.24}O_2$	4.66034(35)	/	3.00588(28)	/	9.87(2)
$Sr_{0.056}Na_{0.889}NbO_3$	3.91561(17)	/	/	/	11.03(2)
SiO_2	4.9169(10)	/	5.4084(18)	113.235(23)	11.19(3)
$NaSr_2Nb_5O_{15}$	12.3279(23)	/	3.9302(11)	/	4.11(2)
Refinement Details					
χ^2	R_{wp}	R_p			
3.754	5.5%	3.88%			

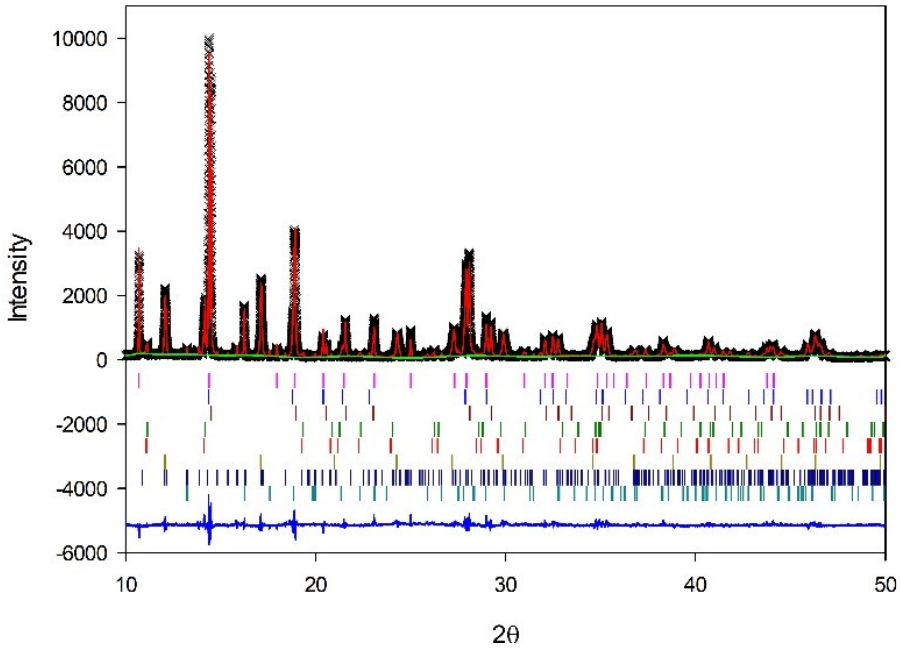

Figure 4.29 *Rietveld refinement plot (GSAS) of HIPed Sr-IONSIV (1.5 wt. %) (Beam-line data, I11). Pink ticks: $ZrSiO_4$, blue ticks: $Ti_{0.912}Nb_{0.088}O_2$, dark red ticks: $Ti_{0.69}Nb_{0.24}O_2$, green ticks: SiO_2 (1), red ticks: SiO_2 (2), yellow ticks: $Sr_{0.148}Na_{0.705}NbO_3$, dark blue ticks: $Na,Sr_2Nb_5O_{15}$ and light blue ticks: $ZrTiO_4$*

Despite being able to identify the phases using in -house XRD data it was not of sufficient quality to confidently refine occupancies of the key phases, particularly the Sr content of the perovskite phase. As a result, data were collected at the Diamond Light Source on the High-Resolution Powder diffraction beam line (I11). The difference in quality

between the in-house and synchrotron XRD data is shown in **Figure 4.30**, the two patterns show the benefits of beam line high resolution powder XRD synchrotron data over in-house data. This data (**Figure 4.29**) revealed similar phases to the in-house equipment. However, this better-quality data did suggest an additional SiO_2 phase to the one already identified which possessed the same symmetry, but different lattice parameters. Furthermore, the Sr occupancy on the A site of the main Sr perovskite phase is higher in this refinement (**Table 4.24**). The in-house refinement predicted the formula $Sr_{0.056}Na_{0.889}NbO_3$ and the beam line data $Sr_{0.148}Na_{0.705}NbO_3$.

Table 4.24 *Refinement Details for HIPed Sr-IONSIV (1.5 wt. %) (Beam line data, I11)*

	Lattice Parameters (Å)			
	a / Å	*b* / Å	*c* / Å	wt. %
$ZrSiO_4$	6.59804(7)	/	5.97785(8)	20.422(8)
$Zr_{0.33}Ti_{0.67}O_2$	4.79036(29)	5.40470(23)	5.04478(3)	5.161(7)
$Ti_{0.794}Nb_{0.206}O_2$	4.66632(11)	/	3.0187(7)	13.73(2)
$Ti_{0.964}Nb_{0.035}O_2$	4.62884(4)	/	2.987492(32)	35.97(1)
SiO_2 (1)	4.91530(17)	/	5.4078(4)	4.11(3)
SiO_2 (2)	4.9380(6)	/	5.4145(10)	6.55(3)
$Sr_{0.148}Na_{0.705}NbO_3$	3.92215(6)	/	/	10.505(4)
$(Na,Sr_2)Nb_5O_{15}$	12.33919(31)	/	3.93579(19)	3.554(7)
Refinement Details				
χ^2	R_{wp}	R_p		
8.592	13.08 %	9.81 %		

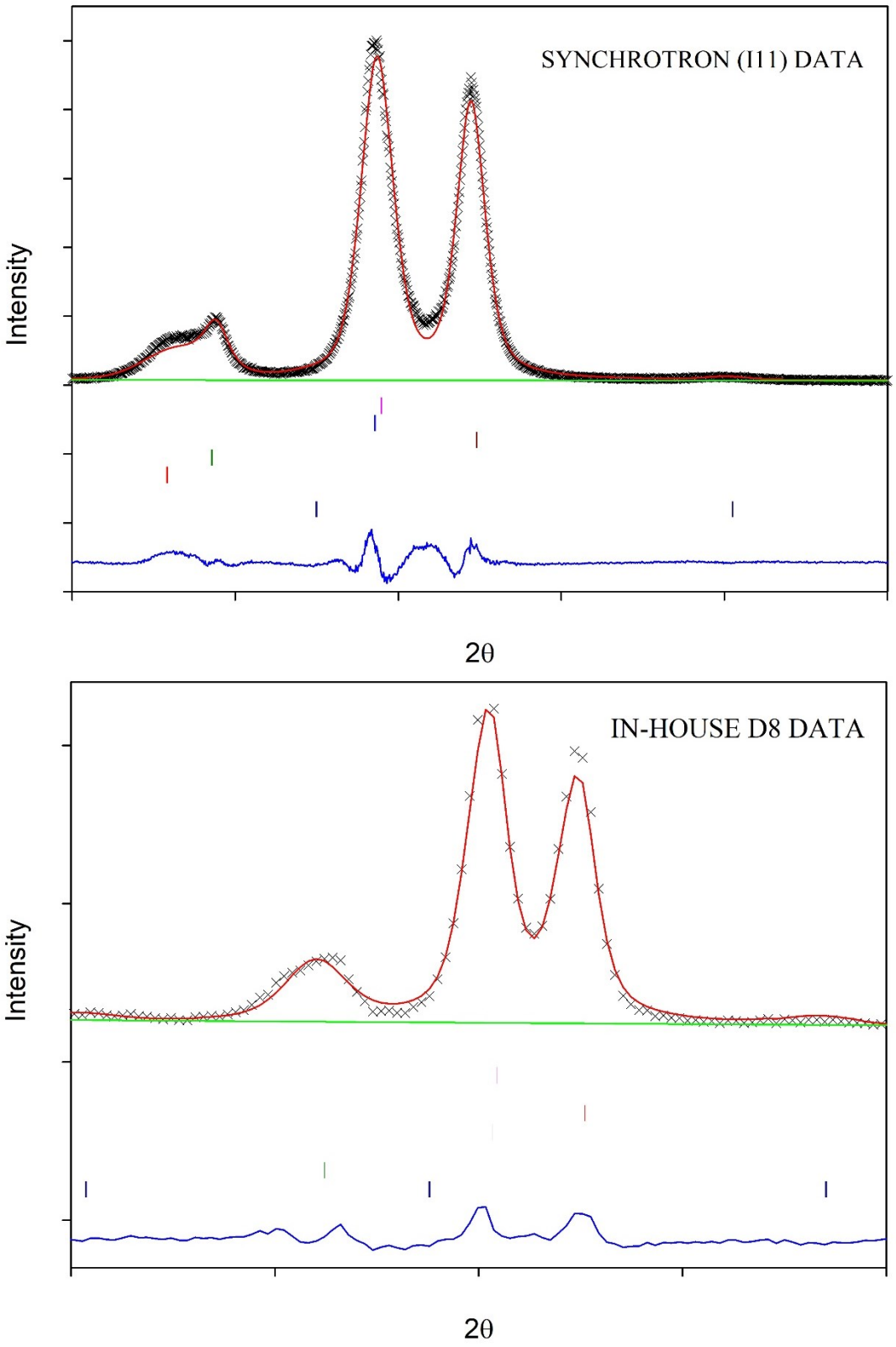

Figure 4.30 *Comparison of in-house and synchrotron XRD data of HIPed IONSIV Sr-IONSIV 1.5 wt. %*

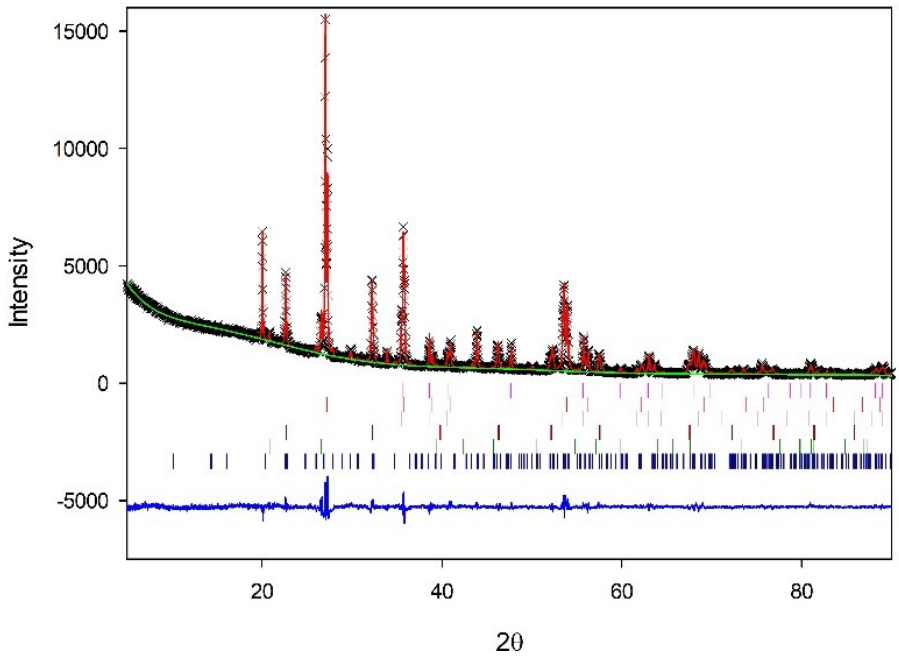

Figure 4.31 *Rietveld refinement plot (GSAS) of HIPed Sr-IONSIV (3.0 wt. %) (In-house D8 data). Pink ticks: $ZrSiO_4$, red ticks: $Ti_{0.912}Nb_{0.088}O_2$, grey ticks: $Ti_{0.69}Nb_{0.24}O_2$, dark red ticks: $Sr_{0.056}Na_{0.889}NbO_3$, green ticks: SiO_2 (Cristobalite) and dark blue ticks: $NaSr_2Nb_5O_{15}$*

XRD using in-house equipment (**Figure 4.31**) suggests that the phase assembly formed from HIPing Sr-IONSIV (3.0 wt. %) is much the same as the 1.5 wt. % Sr HIPed sample. The main difference in the two samples is that there doesn't seem to be any $(Zr,Ti)O_4$ present in this material, otherwise the only difference is the expected increase in Sr which was confirmed from the Rietveld refinement (**Table 4.25**) as there is slightly more $(Na,Sr_2)Nb_5O_{15}$ present and also more Sr present in the Sr-perovskite phase. The occupancy has been refined to give the formula $Sr_{0.132}Na_{0.74}NbO_3$. The Sr perovskite in the 1.5 wt. % sample has a formula of $Sr_{0.056}Na_{0.889}NbO_3$.

Table 4.25 *Refinement Details for Sr-IONSIV (3.0 wt. %) HIPing (1100°C, 2 hours) (D8)*

	Lattice Parameters (Å)			
	a / Å	*b* / Å	*c* / Å	wt. %
$ZrSiO_4$	6.58689(18)	/	5.96935(19)	30.34(2)
$Ti_{0.912}Nb_{0.088}O_2$	4.62055(13)	/	2.97856(11)	31.77(2)
$Ti_{0.69}Nb_{0.24}O_2$	4.66018(24)	/	3.00486(18)	14.27(3)
$Sr_{0.132}Na_{0.74}NbO_3$	3.92280(13)	/	/	10.25(1)
SiO_2	4.9203(14)	/	5.4064(26)	8.98(2)
$(Na,Sr_2)Nb_5O_{15}$	12.3200(19)	/	3.9297(10)	4.38(2)
Refinement Details				
χ^2	R_{wp}	R_p		
3.451	5.33 %	3.80 %		

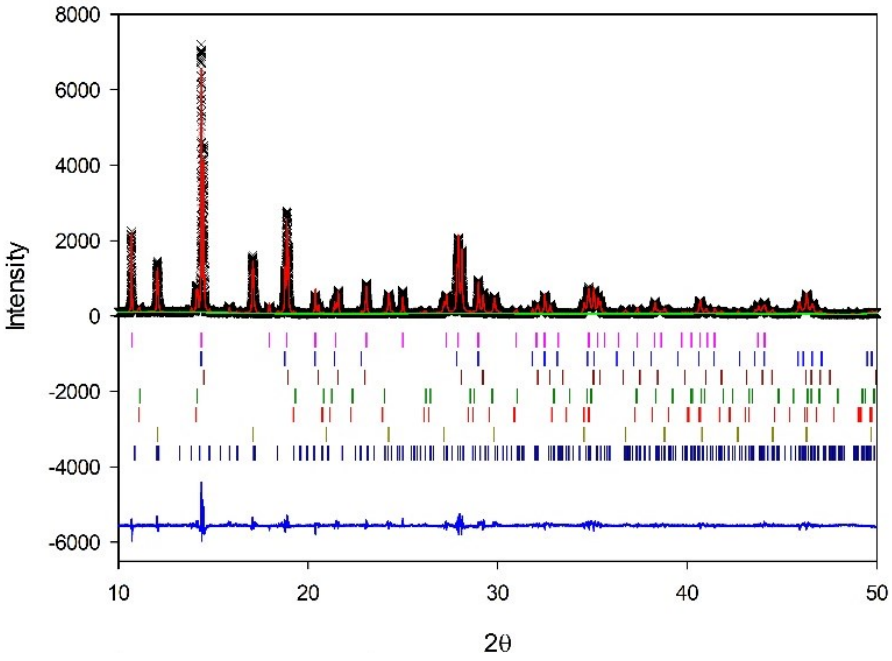

Figure 4.32 *Rietveld refinement plot (GSAS) of HIPed Sr-IONSIV (3.0 wt. %, Sr) (Beam-line data, I11). Pink ticks: $ZrSiO_4$, blue ticks: $Ti_{0.912}Nb_{0.088}O_2$, dark red ticks: $Ti_{0.69}Nb_{0.24}O_2$, green ticks: SiO_2, red ticks: SiO_2, yellow ticks: $Sr_{0.148}Na_{0.705}NbO_3$, dark blue ticks: $(Na,Sr_2)Nb_5O_{15}$ and light blue ticks: $ZrTiO_4$*

The synchrotron data (**Figure 4.32**) again revealed similar phases to the pattern collected on the in-house equipment. However, as before an additional SiO_2 phase was identified. Furthermore, the occupancy of the main Sr perovskite phase is higher in this refinement which was also observed previously in the 1.5 wt. % Sr-IONSIV sample. The in-

house refinement predicted the formula $Sr_{0.132}Na_{0.74}NbO_3$ but the refinement of synchrotron data (**Table 4.26**) $Sr_{0.189}Na_{0.662}NbO_3$.

Table 4.26 *Refinement Details for Sr-IONSIV (3.0 wt. %) HIPing (1100°C, 2 hours) (I11 data)*

	Lattice Parameters (Å)			
	a / Å	*b* / Å	*c* / Å	wt. %
$ZrSiO_4$	6.59779(4)	/	5.97961(6)	26.480(8)
$Ti_{0.911}Nb_{0.019}O_2$	4.627923(29)	/	2.98350(4)	35.58(2)
$Ti_{0.830}Nb_{0.170}O_2$	4.66843(7)	/	3.01041(5)	15.58(2)
SiO_2 (1)	4.91910(21)	/	5.4105(4)	2.865(10)
SiO_2 (2)	4.94234(31)	/	5.4241(7)	5.33(1)
$Sr_{0.189}Na_{0.662}NbO_3$	3.92997(4)	/	/	9.839(7)
$NaSr_2Nb_5O_{15}$	12.3429(6)	/	3.9340(4)	4.327(9)
Refinement Details				
χ^2	R_{wp}	R_p		
7.196	15.38%	11.67%		

For both the 1.5 and 3 wt. % Sr-IONSIV HIP samples, the I11 data is of much better quality and therefore the weight fractions and occupancies calculated from Rietveld refinement were assumed to be the more accurate figures.

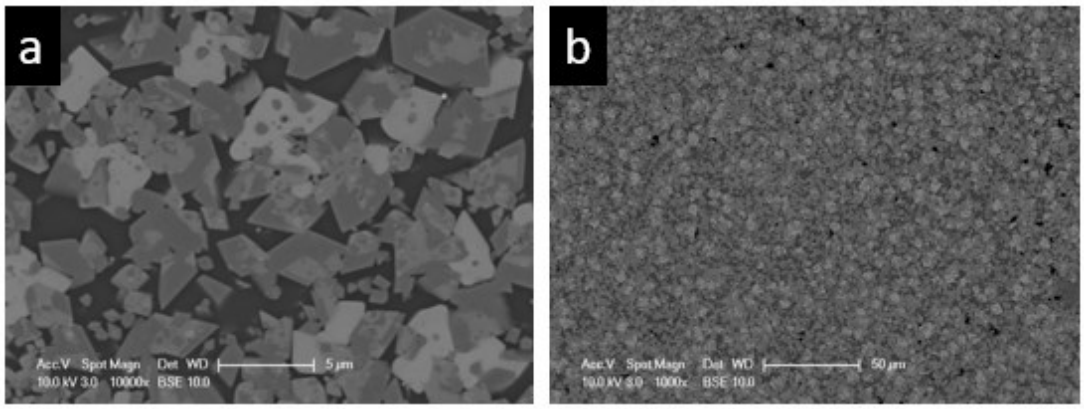

Figure 4.33 *BSE image of HIPed Sr – IONSIV (1.5 wt. %) a: 5µm scale b: bottom: 50 µm scale*

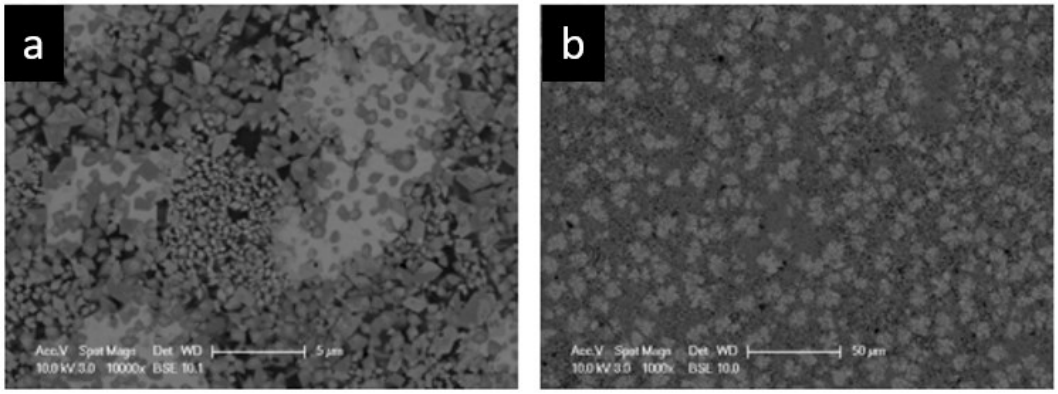

Figure 4.34 *BSE of HIPed Sr – IONSIV (3.0 wt. %) a: 5 µm scale b: bottom: 50 µm scale*

Figure 4.33 and **Figure 4.34** shows the back scattered electron images of the polished HIPed Sr-IONSIV monoliths. Similar morphologies were observed for both the 1.5 and 3 wt. % HIPed IONSIV at magnifications of 100 µm. At higher magnification slightly, different morphologies were identified. At 5 µm, the particle sizes for the 1.5 wt. % Sr-IONSIV are somewhat larger than that of the 3 wt. % sample. This theme was also observed in the previous study where the higher loaded Cs-IONSIV HIPed samples had smaller particles overall compared to the lower doped versions.[34,70] It was thought that this had something to do with the crystallisation process. EDX experiments were carried out but were unable to target individual phases as the spot size associated with SEM is too large. As a result, a series of TEM experiments including elemental mapping, line analysis and multi point EDS were performed in order to better analyse the individual phases present in the HIPed sample.

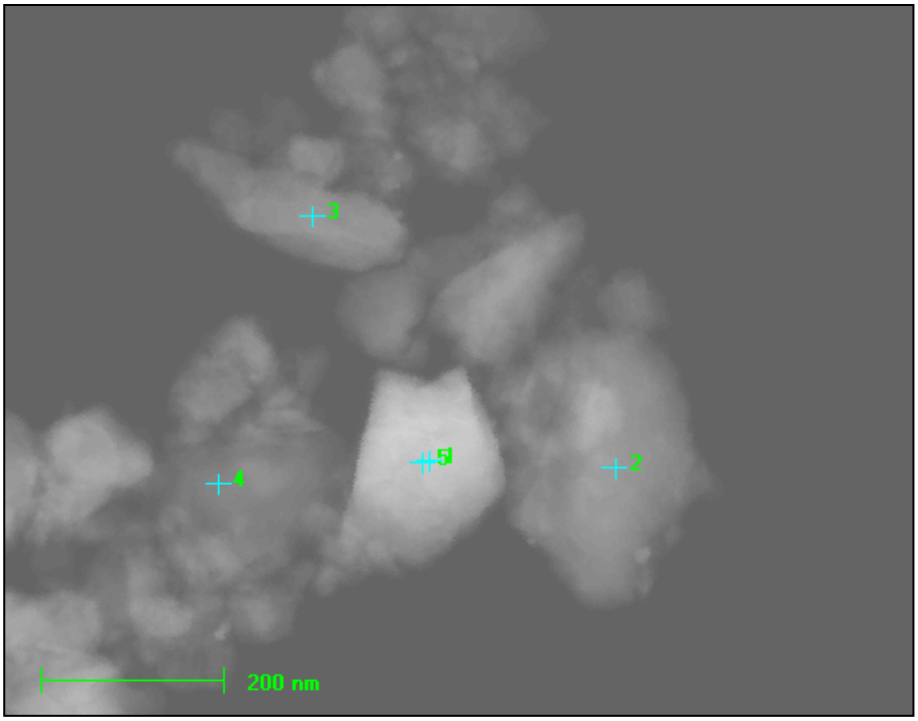

Figure 4.35 *HIPed Sr-IONSIV (3 wt. %) Multi-point analysis TEM*

Table 4.27 *HIPed Sr-IONSIV (3 wt. %) Multi-point analysis TEM data*

	wt. %						
MultiPoint	**O K**	**NaK**	**SiK**	**TiK**	**SrK**	**ZrK**	**NbK**
1	**9.1**	**3.2**	**1.4**	**1.2**	**7.3**	**1.2**	**25.7**
2	9.3	0.0	0.4	12.2	0.2	1.4	8.6
3	8.7	0.0	0.3	12.9	0.3	1.8	9.1
4	16.7	0.0	18.9	0.2	0.2	0.3	0.3
5	**6.9**	**2.5**	**1.1**	**1.0**	**5.6**	**0.8**	**20.0**

Targeting individual particles in TEM proved much easier on account of the small spot size associated with TEM. Multi point analysis of HIPed Sr-IONSIV (3 wt. %) is shown in **Figure 4.35** and **Table 4.27** and this experiment allowed elemental analysis of much more discrete areas which were labelled points 1 to 5. Multi points 2 and 3 are likely the $(Ti,Nb)O_2$ rutile phase discussed earlier as the Ti and Nb content in **Table 4.27** suggest and Si content and lack of any other in point 4 suggests that particle is SiO_2. Points 1 and 5 (in the centre of **Figure 4.35**) strongly suggest the same phase which is either the $(Sr,Na)NbO_3$ (perovskite) phase or the $NaSr_2Nb_5O_{15}$ phase identified earlier from XRD. The Sr, Nb and

Na content are in rough agreement with the proposed formula for the Sr-perovskite refined from Rietveld analysis of the synchrotron data. However, additional TEM studies are required to confirm this.

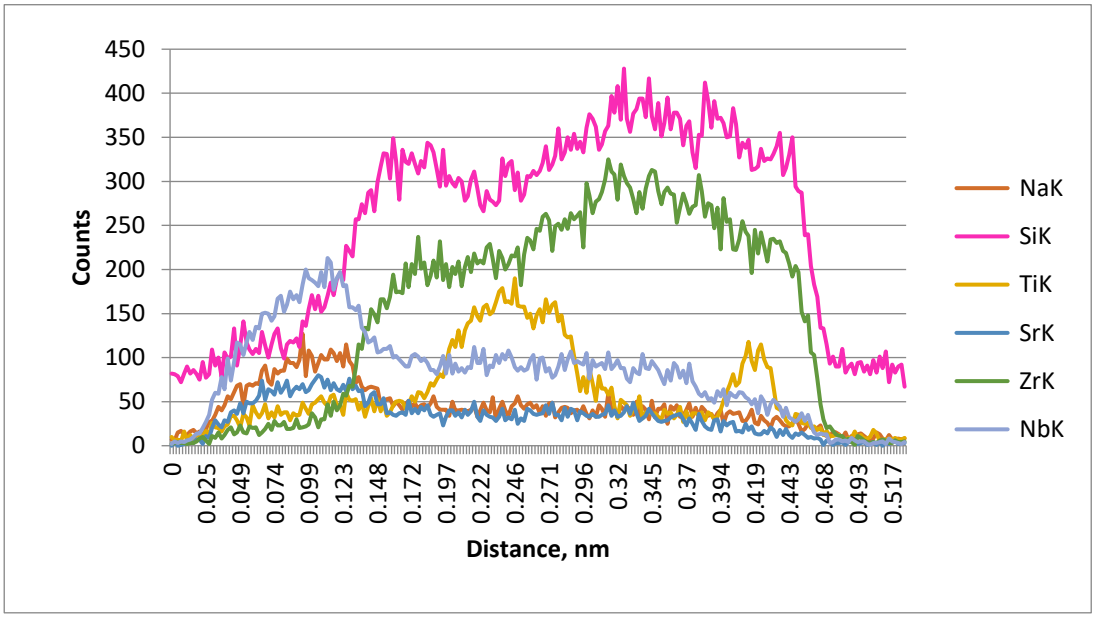

Figure 4.36 *Sr-IONSIV (3 wt. %, Sr) TEM line analysis with a Graph showing the concentration of each element versus line distance*

Line analysis of the particle shown in **Figure 4.36** suggests that $ZrSiO_4$ is the major phase present in this particular particle. As the line moves across the particle (shown by the blue line in the TEM image) the Zr and Si concentrations (counts) appear to mirror each

other and increase simultaneously as a function of line distance suggesting that Zr and Si are present in the same $ZrSiO_4$ phase. The other elements in this line analysis proved more difficult to assign to discrete phases. The beginning of line does potentially show that there may be some $(Na,Sr)NbO_3$ perovskite or $Na_2SrNb_5O_{15}$ present as the Na (orange line), Sr (dark blue line) and Nb (light blue line) concentrations are at levels that are potentially consistent with the perovskite phase.

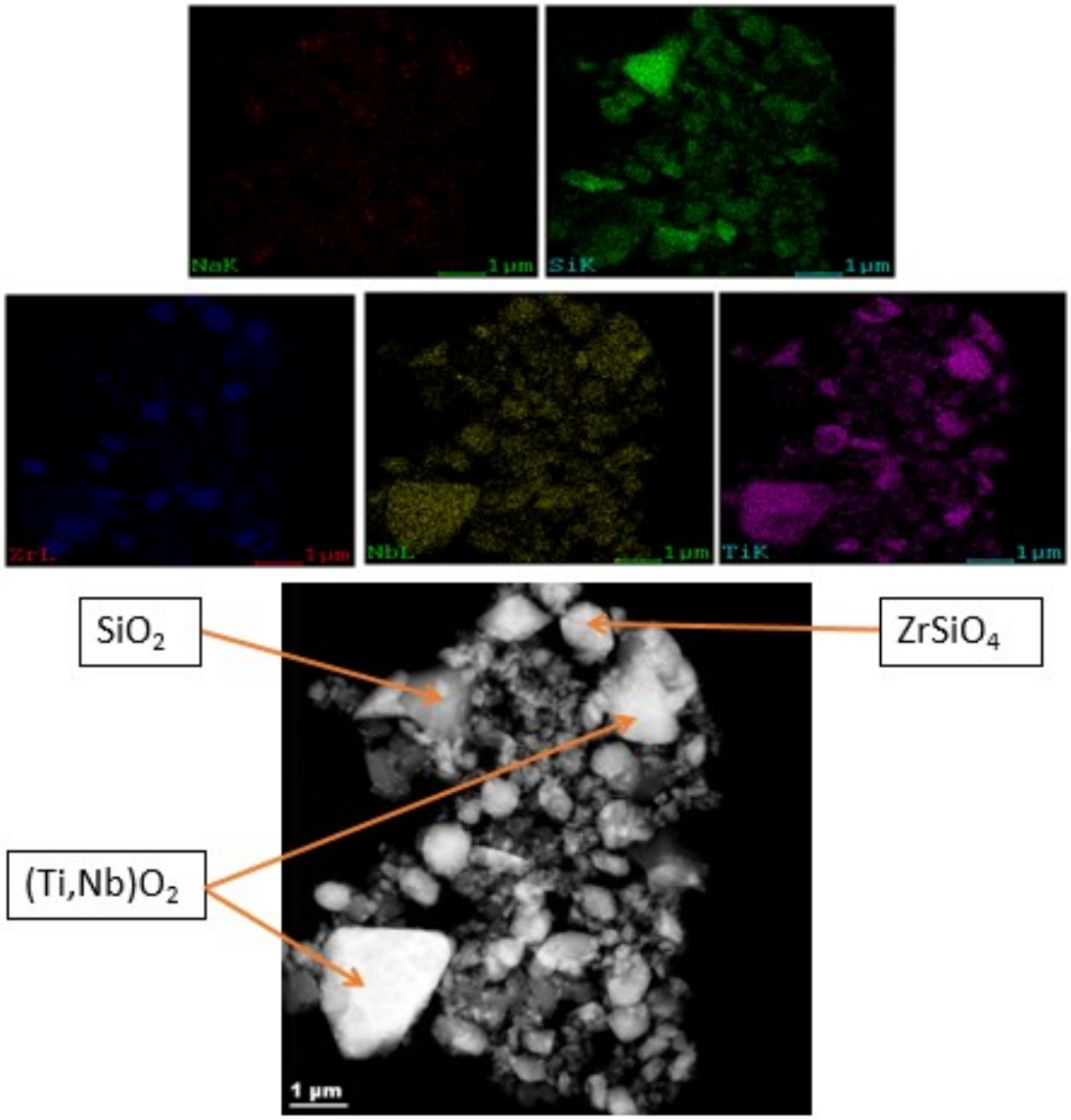

Figure 4.37 *Sr-IONSIV (3 wt. %, Sr) TEM Elemental mapping, Na K, Si k, Zr L, Nb L and Ti K*

Elemental mapping (**Figure 4.37**) of the HIPed product suggested a number of the phases which were also identified from XRD (**Figure 4.31** and **Figure 4.32**). Mapping identified $(Ti,Nb)O_2$, SiO_2 and $ZrSiO_4$. Sr could not be successfully mapped on account of the low concentration of Sr present in the material.

As well as Sr being incorporated at levels of 1.5 and 3.0 wt. %, Sr has also been incorporated at higher levels. In this case, rather than targeting a specific weight loading the exchange process carried out in an excess to force as much Sr into the channels as possible. The Sr content was confirmed via XRF (**Table 4.28**) at approximately 3.4 wt. % Sr.

Table 4.28 *XRF data for Sr-IONSIV (4.0 wt. %) HIPing (1100°C, 2 hours) (D8)*

Elements	Sr-IONSIV (4.0 wt. %) / wt. %	Sr-IONSIV (4.0 wt. %) / at. %	Normalised to Si
Na	0.7	0.8	0.1
Ti	21.2	12.8	1.4
Nb	15.0	4.7	0.5
Si	8.7	9.0	1
Sr	3.4	1.1	0.1
Zr	13.8	4.4	0.5
O	37.1	67.1	7.5
	Ti/Nb Molar Ratio: 2.8		

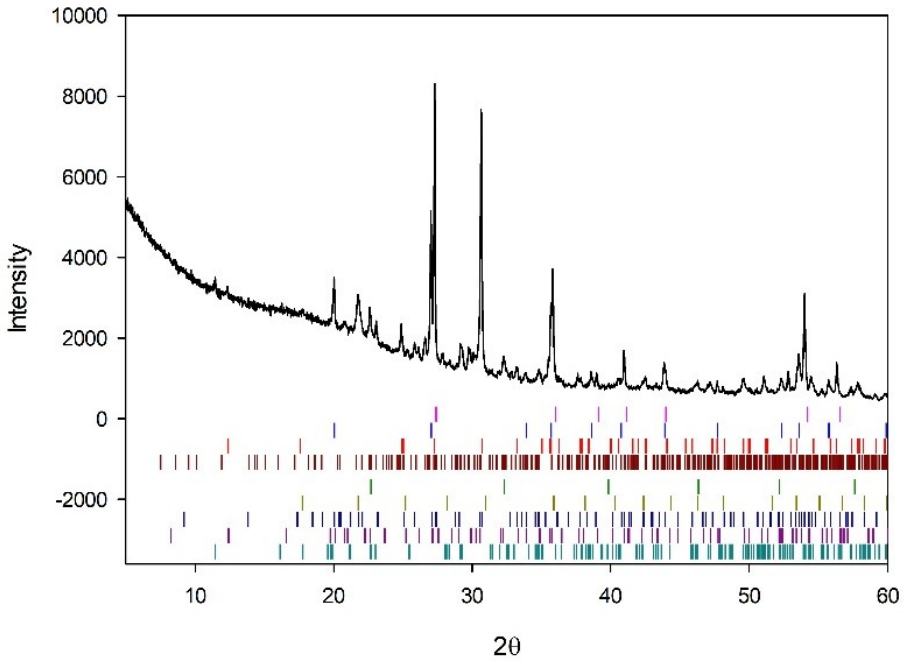

Figure 4.38 *Powder XRD of HIPed Sr-IONSIV (4.0 wt. %) (In-house D8 data). Pink ticks: TiO_2 (Rutile), blue ticks: $ZrSiO_4$, red ticks: $Zr_5Ti_7O_{24}$, dark red ticks: $Na_{13}Nb_{35}O_{94}$, dark green ticks: $(Na,Sr)NbO_3$, dark yellow ticks: SiO_2, dark blue ticks are indexed from ICDD PDF: 00-049-0397 ($SrTi_{11}Nb_4O_{33}$), dark purple ticks are indexed from ICDD PDF: 00-049-0398 ($SrTi_{13}Nb_4O_{37}$) and cyan ticks: $SrNb_2O_6$.*

When this higher Sr exchanged sample was HIPed, the phase assembly formed is somewhat different to the lower doped samples discussed previously. At least 9 different phases were identified from XRD (**Figure 4.38**) which included 4 different Sr phases. The $(Na,Sr)NbO_3$ perovskite observed earlier was identified along with a strontium niobate, $SrNb_2O_6$ and two different strontium titanium niobates. $SrNb_2O_6$ is monoclinic and crystallises in the $P2_1/c$ space group. The strontium titanium niobate phases were identified as $SrTi_{11}Nb_4O_{33}$ and $SrTi_{13}Nb_4O_{37}$. These materials are structurally related to the $SrTi_3Nb_4O_{17}$ and $SrTi_9Nb_4O_{29}$ phases discussed earlier and both crystallise in the *Cmcm* space group. Rietveld refinement was not carried out on this sample on account of not having solved crystal structures for $SrTi_{11}Nb_4O_{33}$ and $SrTi_{13}Nb_4O_{37}$.

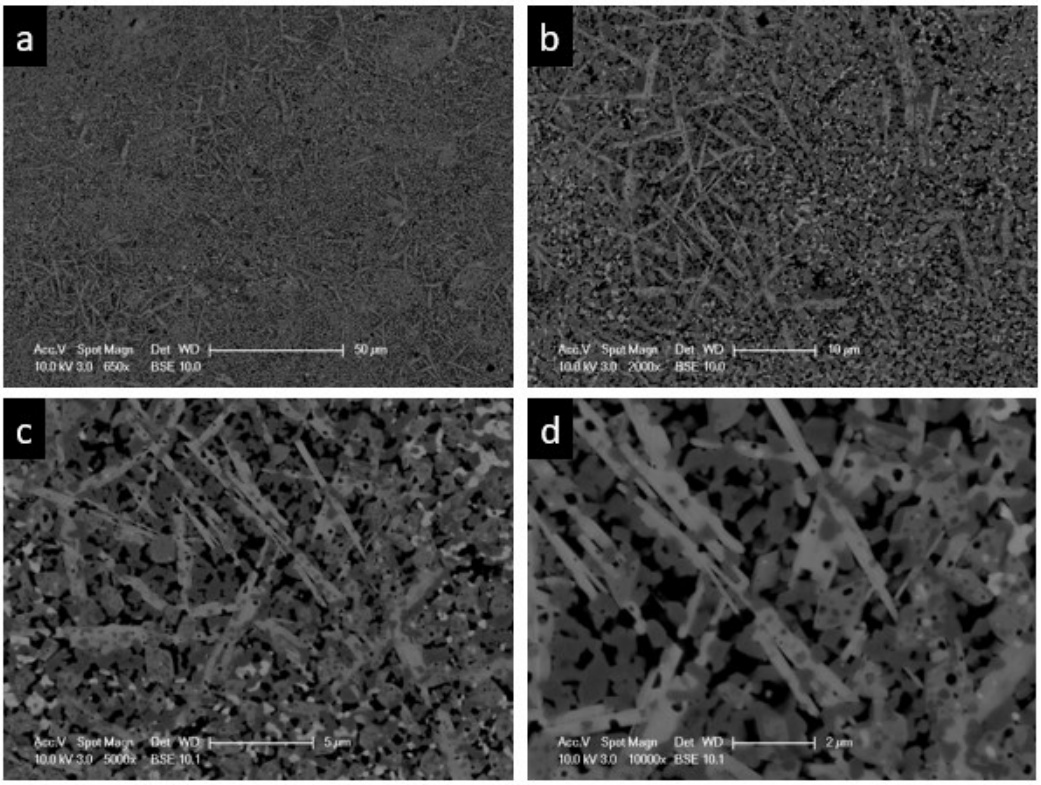

Figure 4.39 *SEM BSE images of Sr-IONSIV (4.0 wt. %) HIPing (1100°C, 2 hours) a: 50 µm b: 10 µm c: 5 µm and d: 2 µm.*

Back scattered electron images of HIPed Sr-IONSIV (4.0 wt. %) are shown in **Figure 4.39**. The crystallites are somewhat different in appearance to the Sr-IONSIV at 1.5 and 3 wt. % loading. The particles in this sample are more dendritic like amongst other more spherical particles. It has not been possible to confirm which phase is the dendritic like particle considering EDX could not discretely analyse these particles. However, considering most of the other phases are observed in the other HIP formations accept $SrTi_{11}Nb_4O_{33}$ and $SrTi_{13}Nb_4O_{37}$, it is possible it is these materials that are responsible for the dendritic particles.

4.3.8 Cs/Sr-IONSIV Thermal Decomposition and HIPing

So far, thermal conversion has been carried out on a series of Sr exchanged IOSNIV materials using both HIPing and calcination techniques. Considering waste streams are often contaminated with both ^{90}Sr and ^{137}Cs it was thought it would be a worthwhile study investigating the thermal conversion products of a mixed Cs/Sr - IONSIV sample. The exchange was carried out with two initial exchange steps with 0.1M Sr^{2+} followed by a final exchange with Cs^{+}. XRF (**Table 4.29**) confirmed the presence of approximately 7 wt. % Cs and 1.5 wt. % Sr in the material.

Table 4.29 *XRF data for Cs/Sr exchanged IONSIV*

	Cs/Sr-IONSIV		
Elements	wt. %	at. %	Molar Ratio (Normalised to Si)
Na	0.5	0.7	0.1
Ti	19.7	12.1	1.5
Nb	13.9	4.4	0.5
Si	7.8	8.1	1
Sr	1.2	0.4	0.05
Cs	6.5	1.4	0.2
Zr	12.9	4.1	0.5
O	37.5	68.8	8.5
	Ti/Nb Molar Ratio: 3.0		

Following the confirmation of Cs and Sr content from XRF, thermal conversion has been carried out via calcining in air at 1100°C or HIPing. The phase assemblies produced have been analysed using XRD and microscopy techniques.

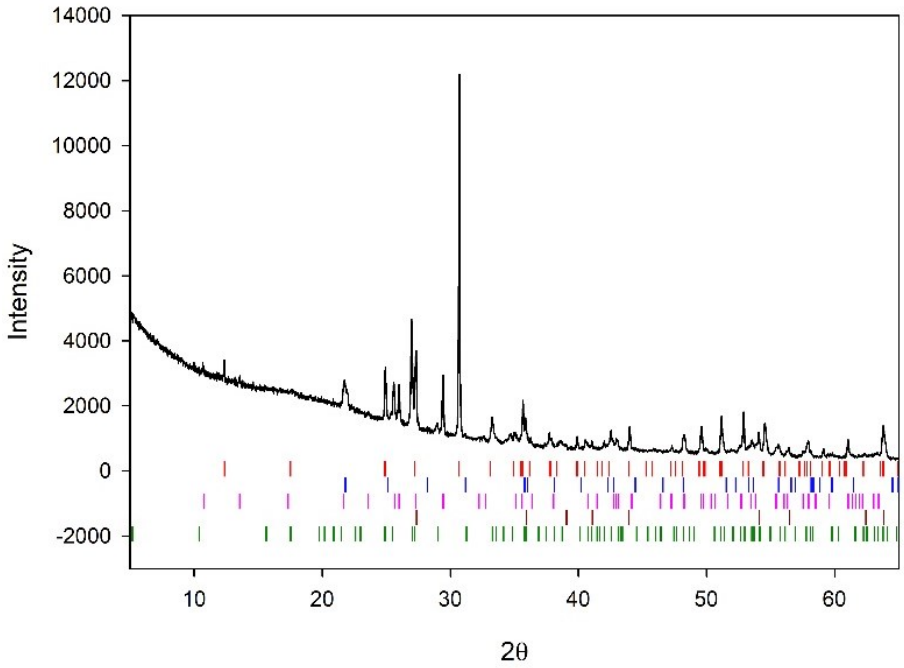

Figure 4.40 *Powder XRD Cs/Sr-IONSIV calcined at 1100°C. Red ticks: $Zr_5Ti_7O_{24}$, Blue ticks: SiO_2 (Cristobalite), Pink Ticks: $Cs_2TiNb_6O_{18}$, Brown ticks: $(Ti,Nb)O_2$ and green ticks: $SrTi_9Nb_4O_{29}$*

XRD of mixed Cs/Sr-IONSIV calcined in air at 1100°C revealed a number of phases including the already discussed $Cs_2TiNb_6O_{18}$ and $SrTi_9Nb_4O_{29}$ (**Figure 4.40**). The three additional phases include $(Zr,Ti)O_4$, SiO_2 and $(Ti,Nb)O_2$. Rietveld refinement was again not carried out as a result of there being no solved crystal structure for $SrTi_9Nb_4O_{29}$.

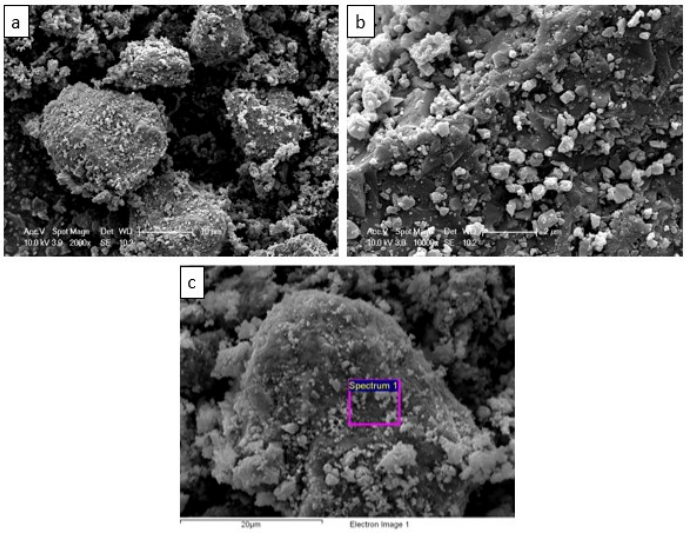

Figure 4.41 *SEM images and EDX of Cs/Sr-IONSIV calcined at 1100°C. A: SE image at 10 µm, b: SE image at 2 µm and c: EDX Spectrum Area*

Table 4.30 *SEM EDX results for Cs/Sr-IONSIV calcined at 1100°C*

Element/Line	wt. %	At. %
O K	33.6	65.9
Na K	0.6	0.8
Si K	5.9	6.6
Ti K	21.5	14.1
Sr L	2.2	0.8
Zr L	12.5	4.3
Nb L	19.9	6.7
Cs L	3.8	0.9

SEM/EDX experiments were carried out on the calcined Cs/Sr-IONSIV mixed sample and the spectrum area is displayed in **Figure 4.41** with the results listed in **Table 4.30**. EDX confirmed the presence of both Cs and Sr in the sample. The values here differ slightly to XRF (**Table 4.29**) which is most likely only because only a region of the sample is being analysed by EDX. Thermal conversion has also been carried out via HIPing which resulted in a fairly similar composition, the main difference being the Sr phase.

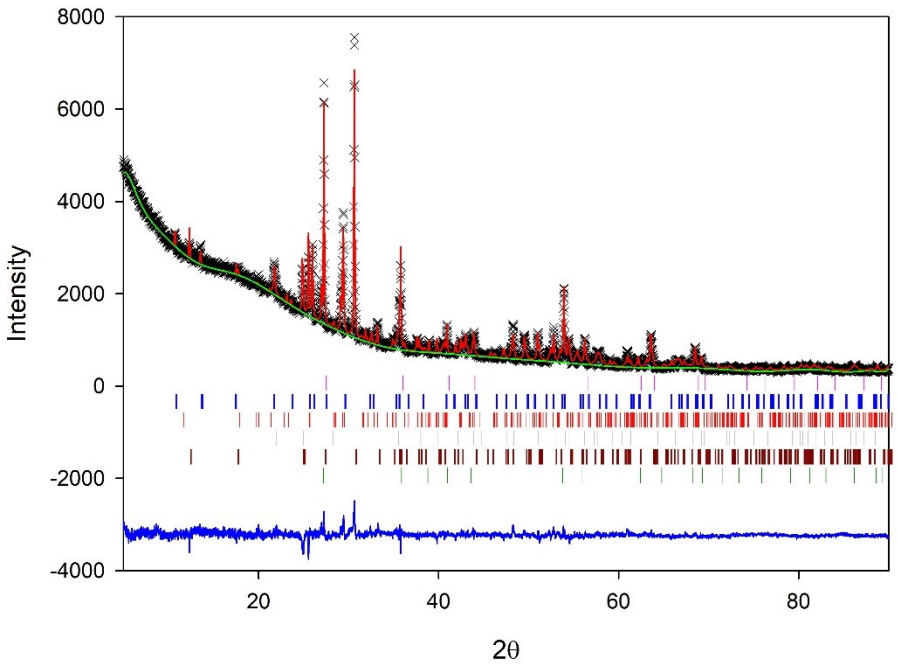

Figure 4.42 *Rietveld refinement plot (GSAS) of HIPed Cs/Sr-IONSIV. Pink ticks: $(Ti,Nb)O_2$, blue ticks: $Cs_2TiNb_6O_{18}$, red ticks: $SrNb_2O_6$, grey ticks: SiO_2, dark red ticks: $Zr_5Ti_7O_{24}$ and green ticks: $(Ti,Nb)O_2$*

When Cs/Sr – IONSIV was HIPed the main Cs and Sr phases from XRD (**Figure 4.43**) include $Cs_2TiNb_6O_{18}$ and $SrNb_2O_6$, the other phases include two different $(Ti,Nb)O_2$ with the formulas $Ti_{0.69}Nb_{0.24}O_2$ and $T_{i0.912}Nb_{0.088}O_2$ phases along with SiO_2 and $(Zr,Ti)O_4$. The presence of $Cs_2TiNb_6O_{18}$ was seen as encouraging as previous work suggests that $Cs_2TiNb_6O_{18}$ is extremely durable. $SrNb_2O_6$ was observed in the HIPed 4 wt. % Sr-IONSIV material. Rietveld analysis (**Table 4.31**) suggested 15.75 wt. % of $Cs_2TiNb_6O_{18}$ and 5.809 wt. % of $SrNb_2O_6$. These values suggest there is approximately 3.6 wt. % Cs and 1.4 wt. % Sr in the sample.

Table 4.31 *Refinement Details for HIPed Cs/Sr-IONSIV*

	Lattice Parameters (Å)			
	a / Å	*b* / Å	*c* / Å	wt. %
$Ti_{0.69}Nb_{0.24}O_2$	4.62059(11)	/	2.98206(12)	29.138(2)
$Cs_2TiNb_6O_{18}$	7.52927(33)	/	8.2399(6)	15.749(2)
$SrNb_2O_6$	7.6788(14)	5.6027(11)	10.9783(19)	5.809(2)
SiO_2	5.080(5)	5.080(5)	6.812(13)	7.366(4)
$Zr_5Ti_7O_{24}$	14.3399(8)	5.39018(31)	5.03037(31)	37.17(2)
$T_{i0.912}Nb_{0.088}O_2$	4.6668(6)	/	2.9873(9)	4.769(3)
Refinement Details				
χ^2	R_{wp}	R_p		
2.857	4.8%	3.35%		

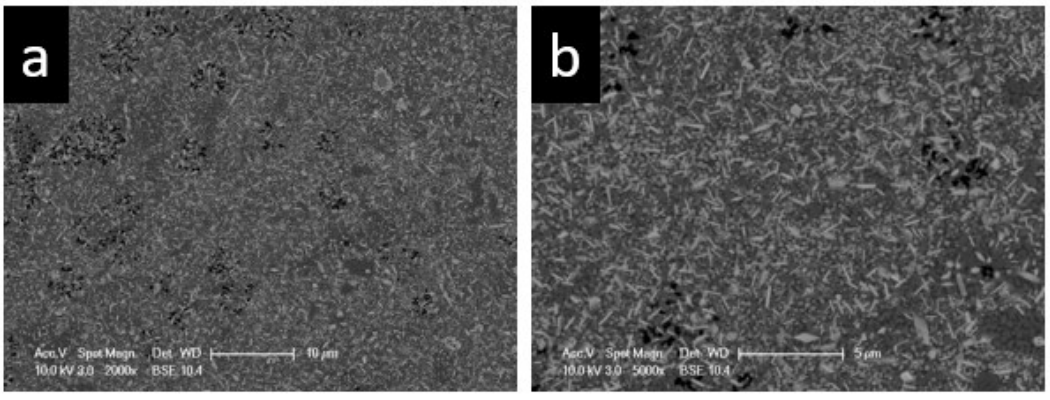

Figure 4.43 *SEM BSE images of HIPed Cs/Sr-IONSIV. a: 10 µm and b: 5 µm*

BSE images of Cs/Sr-IONSIV are shown in **Figure 4.43** and the crystallites have characteristics of both the Sr-IONSIV HIPed sample and HIPed Cs-IONSIV (in previous

study). EDX was not carried out on the Cs/Sr-IONSIV HIP material on account of the spot size being too large and not being able to target discrete particles.

4.3.9 Cs-IONSIV (4, 6 and 12 wt. %) Thermal Decomposition via calcination in air at 900, 1000 and 1100°C

Previous research demonstrated how HIPing Cs loaded-IONSIV formed robust ceramic wasteforms which would be suitable for long term disposal in a geological disposal facility (GDF).[70] One of the questions raised form this previous study is why different products were formed from HIPing compared to calcining in air. To answer this, a series of Cs-IONSIV samples (4, 6, 8, 10 and 12 wt. % Cs) have been thermally calcined in air at the same three temperatures as before. The products were then compared to the phase assemblies formed through HIPing. Firstly, the Cs content was confirmed through XRF analysis (**Table 4.32**). The expected trends were observed with the wt. % of Cs increasing and Na content decreasing (**Figure 4.44**) as a function of Cs incorporation. The other elemental compositions remain consistent for each weight loading of Cs.

Table 4.32 *XRF data for Cs-IONSIV (4, 6, 8, 10 and 12 wt. %) after calcination at 1100°C*

Cs-IONSIV (values in wt. %)							
Wt. % Cs	Na	Cs	Ti	Nb	Zr	Si	O
4	1.5	**5.1**	20.5	14.9	13.1	8.2	36.8
6	0.9	**7.9**	19.7	14.5	12.8	7.9	36.2
8	0.6	**10.1**	19.2	13.6	12.7	7.9	35.9
10	0.3	**12.5**	19.5	13.9	13.0	7.9	33.0
12	0	**12.8**	18.7	13.4	11.9	7.5	35.7

Cs-IONSIV (values in at. %)							
Wt. % Cs	Na	Cs	Ti	Nb	Zr	Si	O
4	1.9	1.1	12.5	4.7	4.2	8.5	67.1
6	1.2	1.8	12.3	4.6	4.2	8.4	67.5
8	0.8	2.3	12.1	4.4	4.2	8.5	67.7
10	0.4	3.0	12.9	4.8	4.5	8.9	65.5
12	0.0	3.0	11.9	4.4	4.0	8.2	68.5

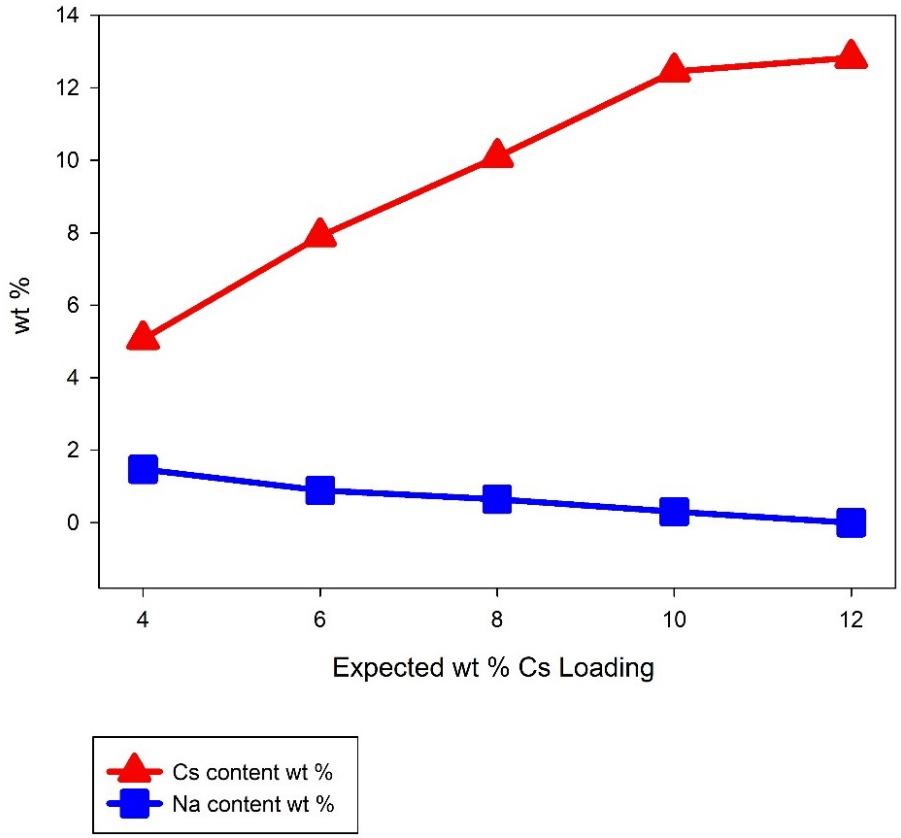

Figure 4.44 *Cs-loaded IONSIV (4, 6, 8, 10 and 12 wt. %) Cs content (red line) versus Na content (blue line)*

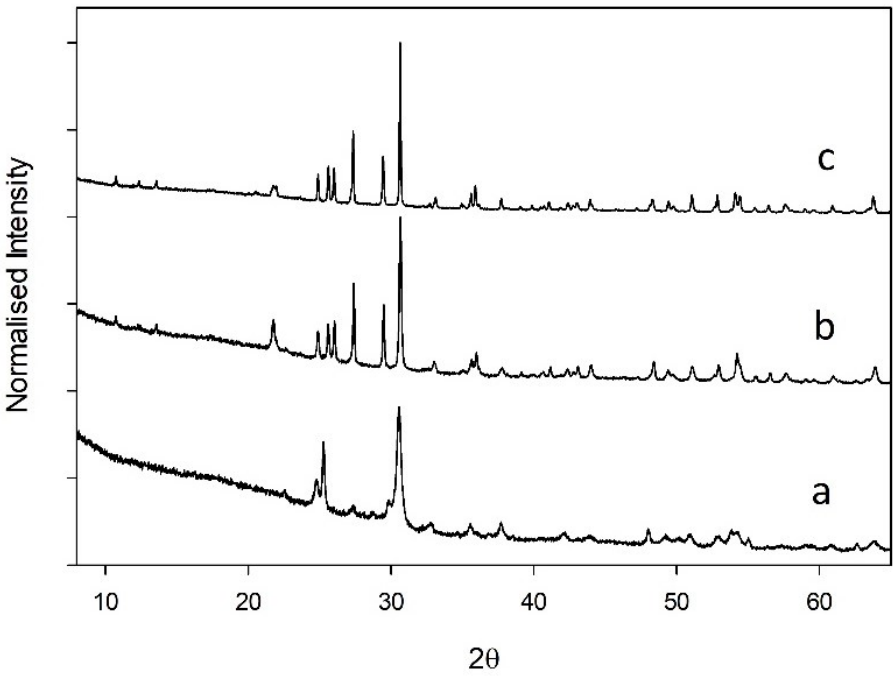

Figure 4.45 *Powder XRD for Cs-IONSIV (4wt. %, Cs) Calcined at a: 900°C, b: 1000°C and c: 1100°C*

As seen in **Figure 4.45**, much like the previous decomposition samples, thermal conversion at 900°C yields a much less crystalline group pf phases in comparison to the 1000 and 1100°C samples.

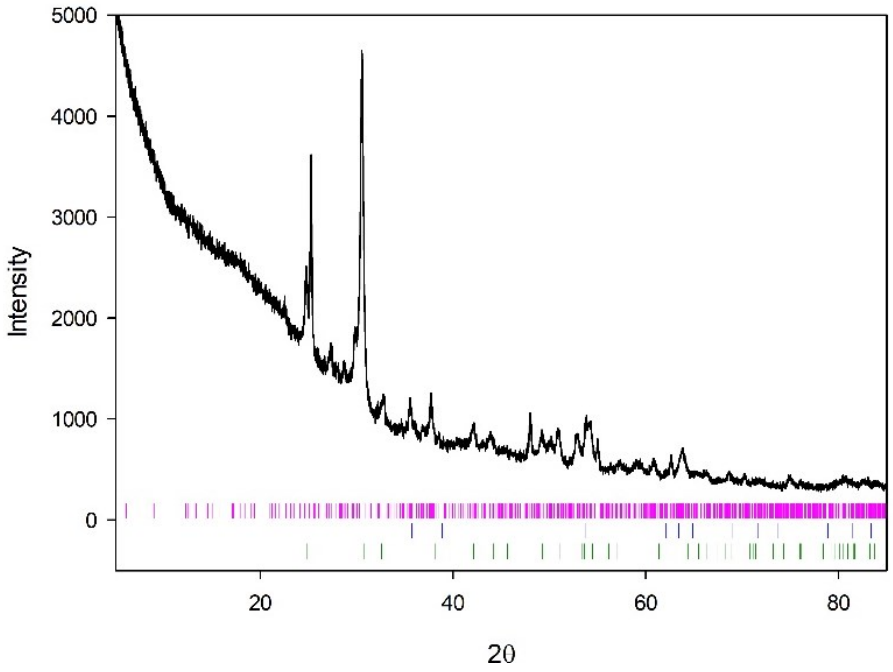

Figure 4.46 *Powder XRD for calcined (900°C) Cs-IONSIV (4 wt. %, Cs). Pink ticks are indexed peaks from ICDD PDF: PDF: 01-074-0719 ($Cs_2Nb_4O_{11}$), blue ticks: TiO_2 (anatase) and Green ticks: $ZrTiO_4$*

At 900°C, three different phases were identified using the EVA match software, including TiO_2 (anatase) and $ZrTiO_4$. The only Cs phase that could be identified was a $Cs_2Nb_4O_{11}$ phase which is orthorhombic and crystallises in the P2*nn* space group. Rietveld refinement was not carried out on this material on account of a number of peaks not being assigned a phase in the XRD pattern.

Cs-IONSIV (4 wt. %) calcined at 1000 and 1100°C produces very different XRD patterns compared to the 900°C sample. Phases have been identified using the search match EVA software and it appears Cs is found in the $Cs_2TiNb_6O_{18}$ phase. For these patterns Rietveld analysis (***Figure 4.47*** and **Figure 4.48**) has been performed and the results are shown below.

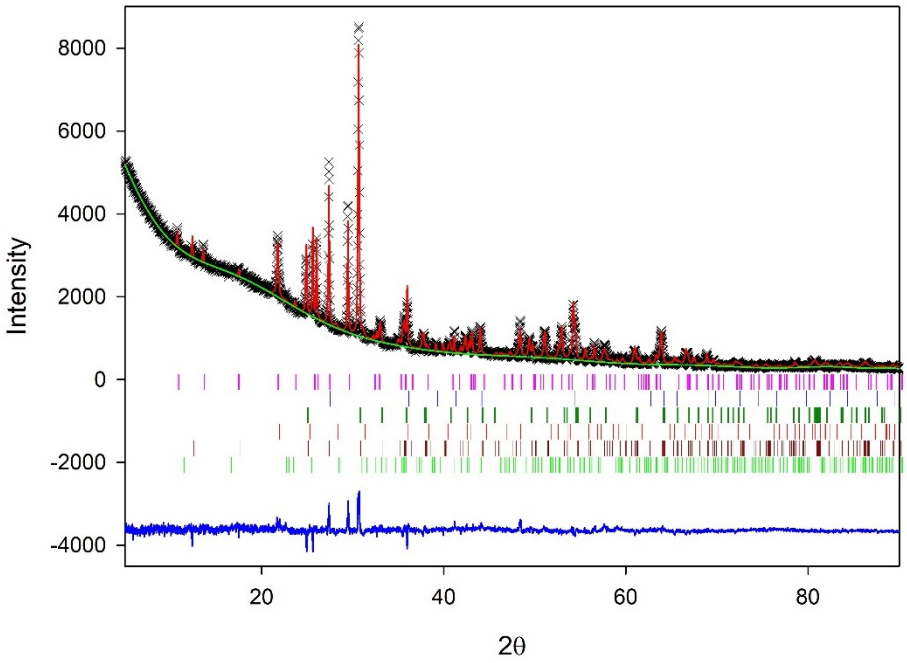

Figure 4.47 *Rietveld refinement plot (GSAS) of calcined (1000°C) Cs-IONSIV (4 wt. %, Cs). Pink ticks: $Cs_2TiNb_6O_{18}$, blue Ticks: $Ti_{0.912}Nb_{0.088}O_2$, Dark green ticks: $ZrTiO_4$, red ticks: SiO_2 (cristobalite) Brown ticks: $Zr_5Ti_7O_{24}$ and green ticks: $NaNbO_3$*

Table 4.33 *Rietveld refinement details for calcined (1000°C) Cs-IONSIV (4 wt. %, Cs)*

	Lattice Parameters (Å)			
	a / Å	*b* / Å	*c* / Å	wt. %
$Cs_2TiNb_6O_{18}$	7.5153(4)	/	8.2201(6)	15.514(2)
$Ti_{0.912}Nb_{0.088}O_2$	4.59925(25)	/	2.96636(20)	18.907(2)
$ZrTiO_4$	4.7534(8)	5.4250(8)	5.0312(7)	19.887(7)
SiO_2	5.0116(28)	/	6.996(7)	14.677(4)
$Zr_5Ti_7O_{24}$	14.2618(21)	5.4108(7)	5.0312(7)	30.66(6)
$NaNbO_3$	5.84(10)	15.65(9)	5.27(6)	0.362(3)
Refinement Details				
χ^2	R_{wp}	R_p		
3.33	5.15 %	3.38 %		

There are 6 phases (**Figure 4.47**) present after decomposing Cs-IONSIV (4 wt. %, Cs) at 1000°C, including $Cs_2TiNb_6O_{18}$, $Ti_{0.912}Nb_{0.088}O_2$, $ZrTiO_4$, SiO_2, $Zr_5Ti_7O_{24}$ and a small amount of $NaNbO_3$. In this sample, Rietveld refinement (**Table 4.33**) suggests the assembly is made up of approximately 15.5 wt. % of $Cs_2TiNb_6O_{18}$ and only 0.362 wt. % $NaNbO_3$. The decomposition at 1100°C produces a similar phase assembly (**Figure 4.48** and **Table 4.34**)

except there is no $ZrTiO_4$ or $NaNbO_3$ present. The $Cs_2TiNb_6O_{18}$ content in the case of the 1100°C sample is 19.48 wt. %, suggesting that in the 1000°C sample, Cs has not fully crystallised into $Cs_2TiNb_6O_{18}$ as there is approximately 4 wt. % more in the higher temperature sample. $NaNbO_3$ was not detected in the 1100°C which indicates that Na may be lost at the higher processing temperature of 1100°C.

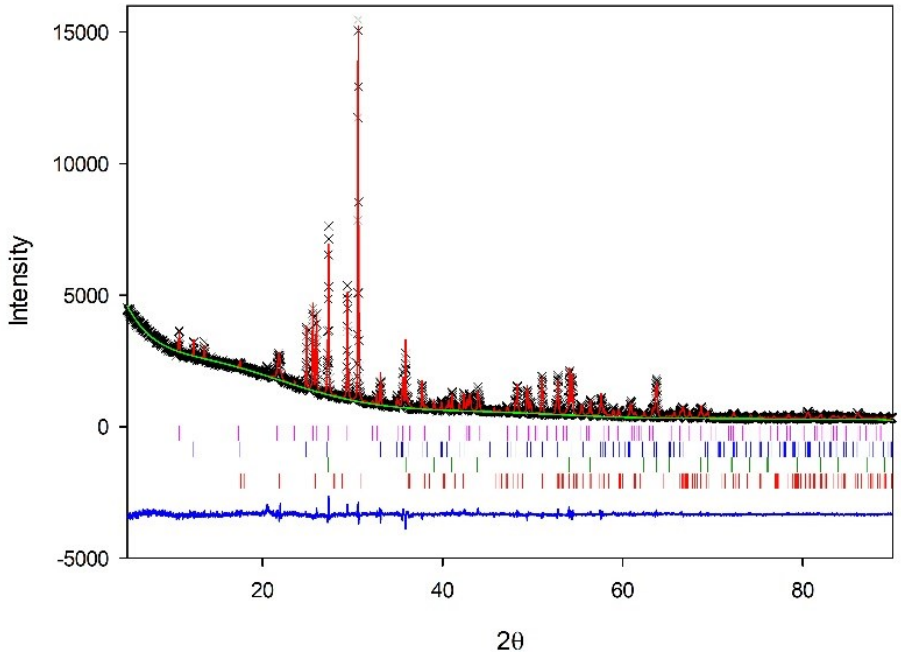

Figure 4.48 *Rietveld refinement plot (GSAS) of calcined (1100°C) Cs-IONSIV (4 wt. %, Cs). Pink ticks: $Cs_2TiNb_6O_{18}$. Blue Ticks: $Ti_{0.8}Nb_{0.2}O_2$, Dark green ticks: $Zr_5Ti_7O_{24}$, Red ticks: SiO_2 (cristobalite)*

Table 4.34 *Rietveld refinement details for calcined (1100°C) Cs-IONSIV (4 wt. %, Cs)*

	Lattice Parameters (Å)			
	a / Å	*b* / Å	*c* / Å	wt. %
$Cs_2TiNb_6O_{18}$	7.52785(21)	/	8.20863(34)	19.48(2)
$Zr_5Ti_7O_{24}$	14.2940(5)	5.40375(17)	5.03624(16)	47.12(2)
$Ti_{0.8}Nb_{0.2}O_2$	4.60635(12)	/	2.97211(10)	21.84(3)
SiO_2	7.150(24)	7.046(23)	6.908(16)	11.56(4)
Refinement Details				
χ^2	R_{wp}	R_p		
2.373	4.53 %	3.27 %		

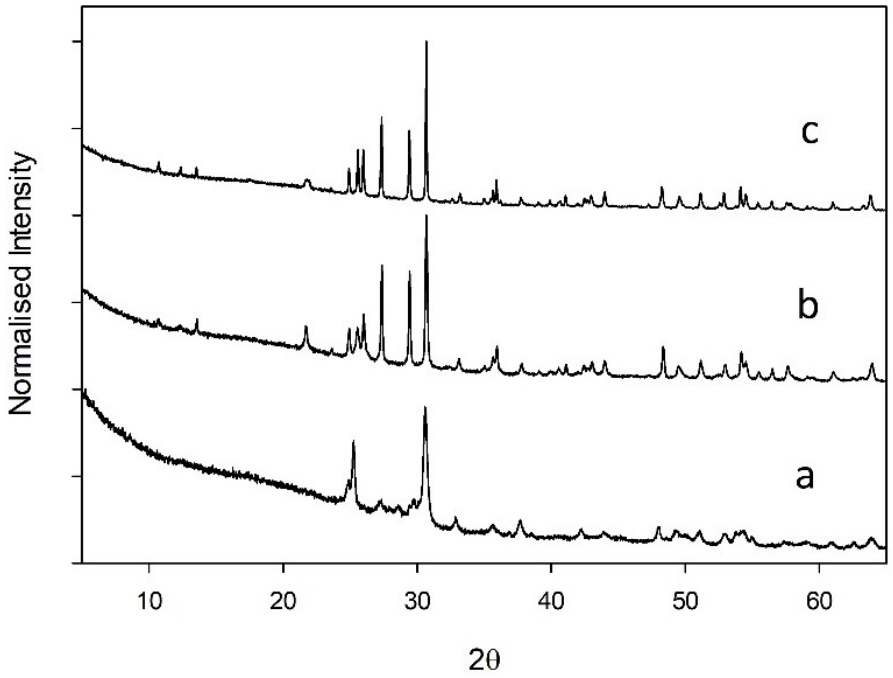

Figure 4.49 *Powder XRD of calcined Cs-IONSIV (6 wt. %, Cs) Stack a: 900°C, b: 1000°C and c: 1100°C*

At 6 wt. % Cs-loading the calcined products at 900, 1000 and 1100°C (**Figure 4.49**), display much the same trend as with the samples at 4 wt. % loading. The crystallinity improves greatly as the temperature increases and the phases identified at each temperature mirror the 4 wt. % samples closely.

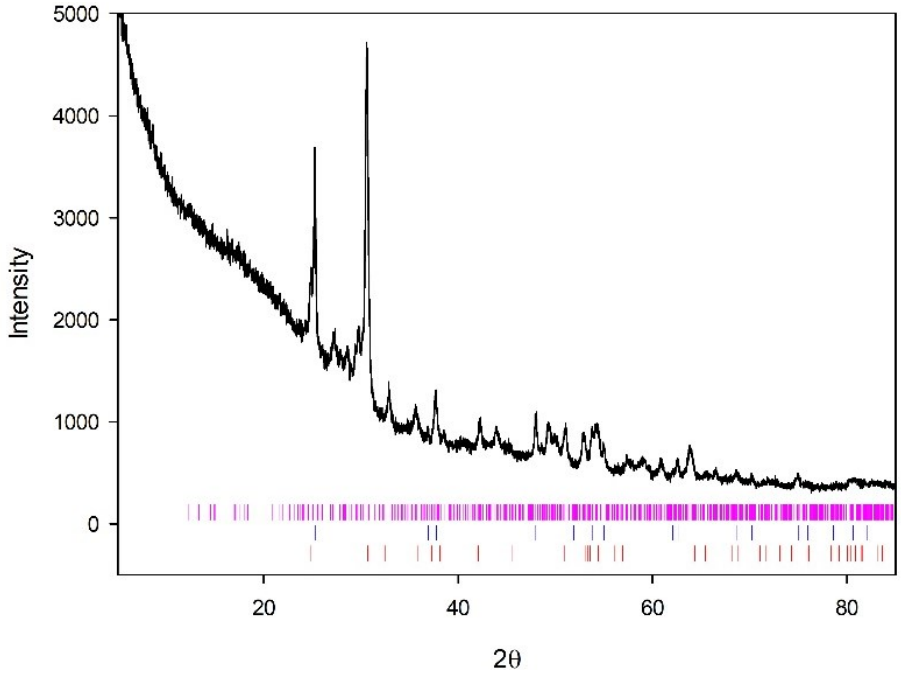

Figure 4.50 *Powder XRD of calcined (900°C) Cs-IONSIV (6wt. %, Cs). Pink ticks: $Cs_2Nb_4O_{11}$, blue ticks: TiO_2 (anatase) and Red ticks: $ZrTiO_4$*

The same three phases, $Cs_2Nb_4O_{11}$, TiO_2 (anatase) and $ZrTiO_4$ were identified (**Figure 4.50**) for the samples calcined at 900°C. As before, Rietveld refinement was not carried out because a number of peaks were not assigned a phase in the search match process.

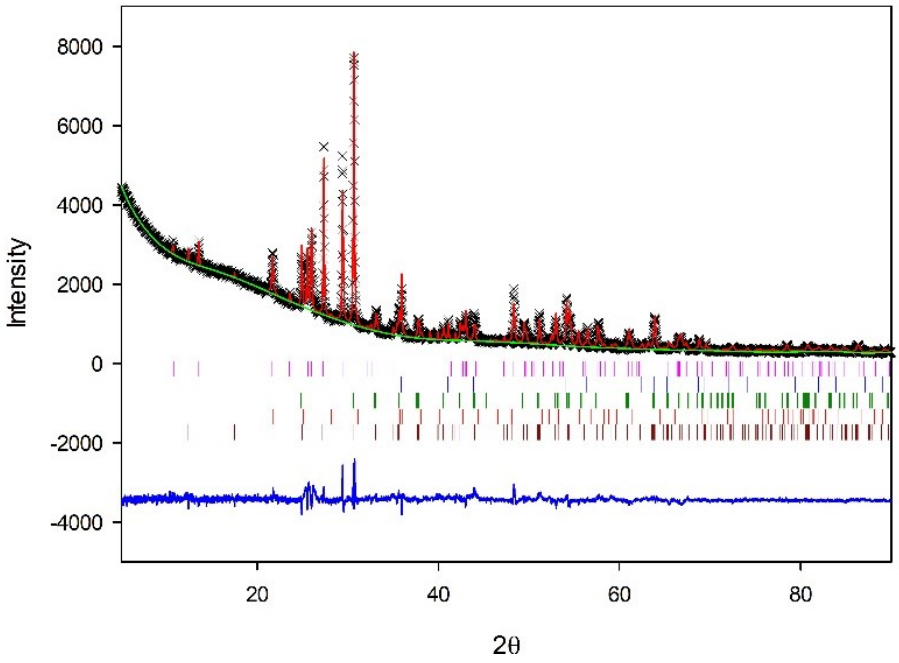

Figure 4.51 *Rietveld refinement plot (GSAS) of calcined (1000°C) Cs-IONSIV (6wt. %, Cs). Pink ticks: $Cs_2TiNb_6O_{18}$, blue Ticks: $(Ti,Nb)O_2$, dark green ticks: $ZrTiO_4$, red ticks: SiO_2 (cristobalite) and brown ticks: $Zr_5Ti_7O_{24}$*

Table 4.35 *Rietveld refinement details for calcined (1000°C) Cs-IONSIV (6wt. %, Cs).*

	Lattice Parameters (Å)			
	a / Å	*b* / Å	*c* / Å	wt. %
$Cs_2TiNb_6O_{18}$	7.52019(26)	/	8.2371(8)	21.40(2)
$Ti_{0.912}Nb_{0.088}O_2$	4.7556(6)	5.3917(7)	5.0273(6)	32.91(4)
$ZrTiO_4$	4.60214(19)	4.60214	2.96779(20)	20.81(3)
SiO_2	5.015(4)	/	7.025(11)	10.29(4)
$Zr_5Ti_7O_{24}$	14.2464(13)	5.4103(5)	5.0233(5)	14.59(4)
Refinement Details				
χ^2	R_{wp}	R_p		
4.068	6.00%	3.98%		

At 6 wt. % Cs loading, decomposition at 1000°C (**Figure 4.51** and **Table 4.35**) and 1100°C (**Figure 4.52** and **Table 4.36**) produce similar phases to what were observed to the 4 wt. % samples and both assemblies are more crystalline than the calcined phase assembly produced at 900°C. The major Cs phase for both was again identified as $Cs_2TINb_6O_{18}$ and as expected, weight fraction analysis from Rietveld showed that more $Cs_2TiNb_6O_{18}$ is present in these samples compared to the lower Cs exchanged 4 wt. % Cs sample. The

sample heated to 1000°C has 21.4 wt. % and the one heated to 1100°C has 24.14 wt. % which is about 5 wt. % more than was observed in the 4 wt. % Cs IOSNIV calcined samples.

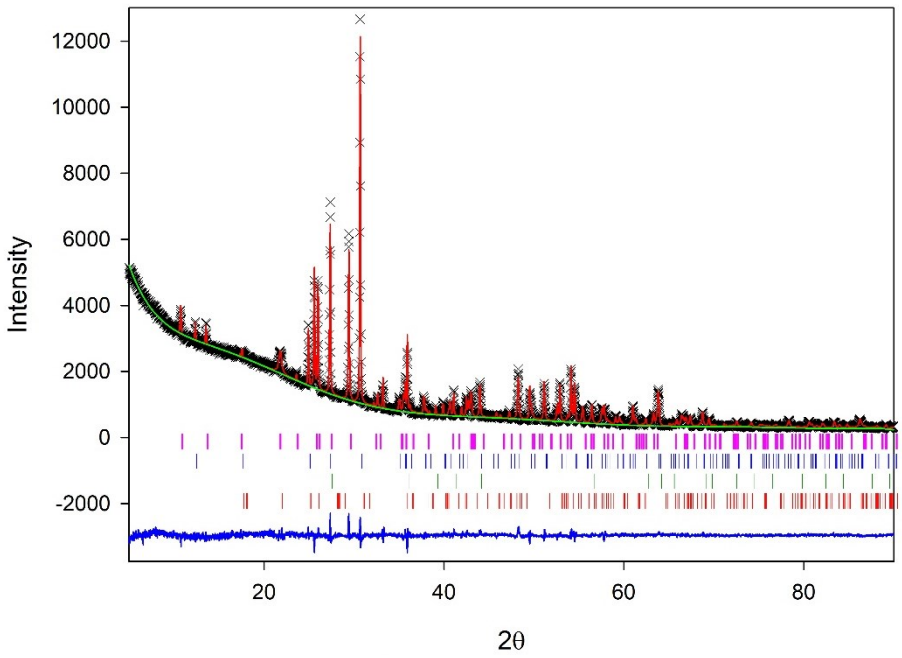

Figure 4.52 *Rietveld refinement plot (GSAS) of calcined (1100°C) Cs-IONSIV (6 wt. %, Cs). Pink ticks: $Cs_2TiNb_6O_{18}$, blue ticks: $Zr_5Ti_7O_{24}$, $(Ti,Nb)O_2$, dark green ticks: $(Ti,Nb)O_2$ and red ticks: SiO_2 (cristobalite)*

Table 4.36 *Rietveld refinement details for calcined (1100°C) Cs-IONSIV (6wt. %, Cs)*

	Lattice Parameters (Å)			
	a / Å	b / Å	c / Å	*wt. %*
$Cs_2TiNb_6O_{18}$	7.53435(16)	/	8.22063(27)	24.13(2)
$Zr_5Ti_7O_{24}$	14.2934(4)	5.38951(15)	5.02975(14)	43.91(2)
$Ti_{0.912}Nb_{0.088}O_2$	4.6060(4)	/	2.9720(4)	22.39(3)
SiO_2	7.113(33)	7.311(33)	6.736(33)	9.57(4)
Refinement Details				
χ^2	R_{wp}	R_p		
2.165	4.14 %	2.98 %		

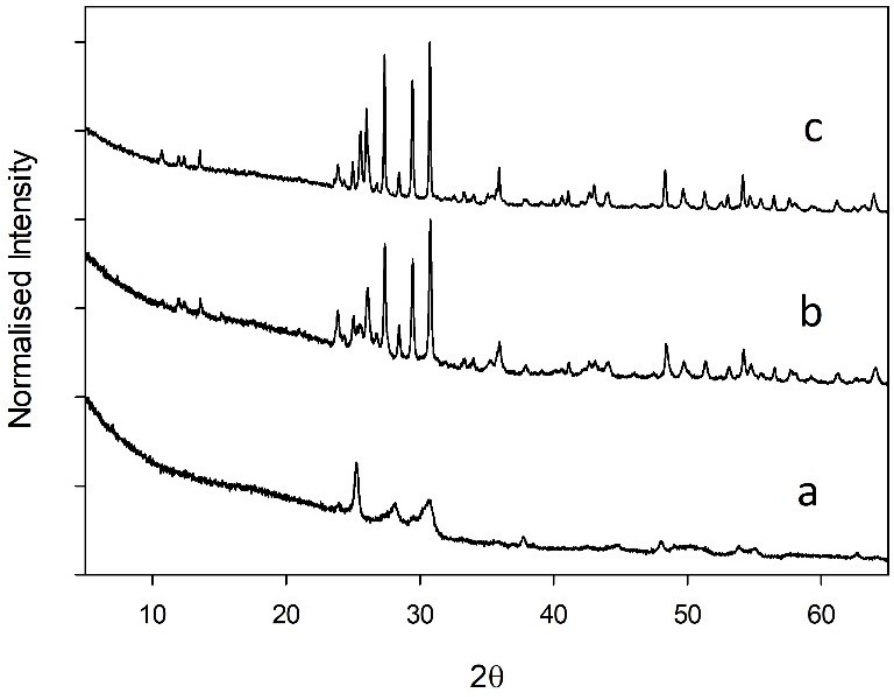

Figure 4.53 *XRD patterns of calcined Cs-IONSIV (12 wt. %, Cs) Stack a: 900°C, b: 1000°C and c: 1100°C*

In comparison to the calcined 4 and 6 wt. % Cs – IONSIV samples (which were quite similar in themselves) the phases formed after calcining 12 wt. % Cs loading are quite different although the pattern of increasing crystallinity with temperature was again observed (***Figure 4.53***).

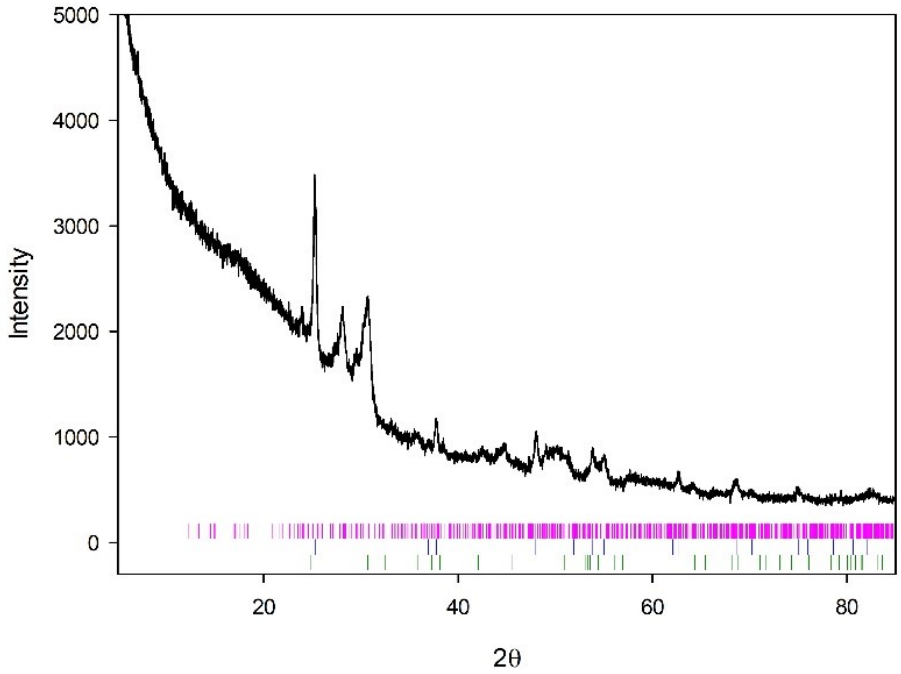

Figure 4.54 *Powder XRD of calcined (900°C) Cs-IONSIV (12wt. %). Pink ticks: $Cs_2Nb_4O_{11}$, blue ticks: TiO_2 (anatase) and Red ticks: $ZrTiO_4$*

At 900°C (**Figure 4.54**) the same phases are observed as before including $Cs_2Nb_4O_{11}$, TiO_2 and $ZrTiO_4$. Again, Rietveld analysis was not carried out on account of poor crystallinity of a number of peaks not being assigned phases.

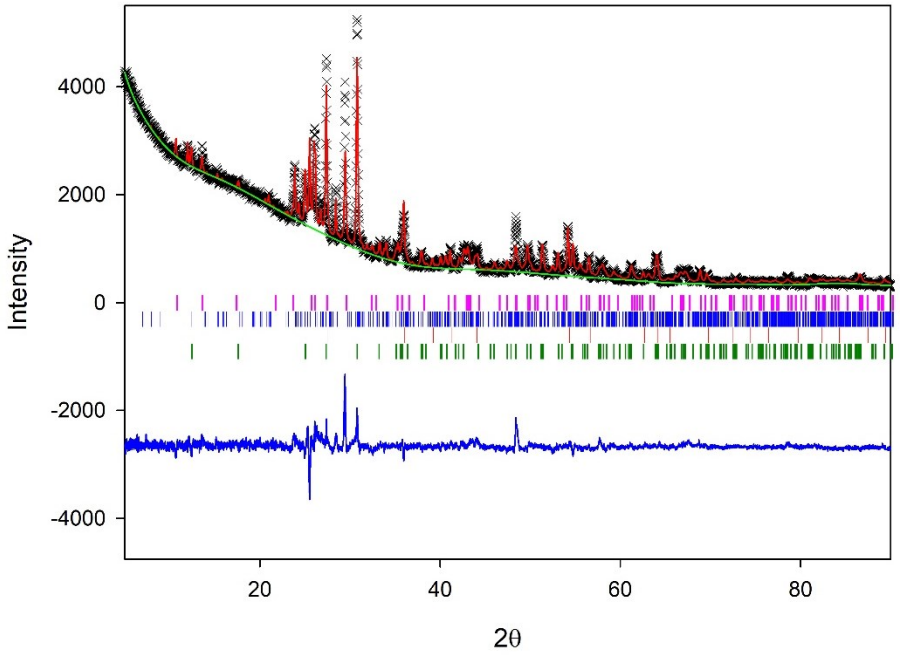

Figure 4.55 *Rietveld refinement plot (GSAS) of calcined (1000°C) Cs-IONSIV (12wt. %, Cs). Pink ticks: $Cs_2TiNb_6O_{18}$, blue ticks: $Cs_2ZrSi_6O_{15}$, red ticks: $(Ti,Nb)O_2$ and green ticks: $Zr_5Ti_7O_{24}$*

Calcining 12 wt. % Cs-IONSIV at 1000°C produces an additional Cs phase which was identified by XRD as $Cs_2ZrSi_6O_{15}$ (**Figure 4.55**). $Cs_2ZrSi_6O_{15}$ is monoclinic and crystallises in the *C*2/m space group. As well as this second Cs phase, $Cs_2TiNb_6O_{18}$, $Zr_5Ti_7O_{24}$ and $Ti_{0.912}Nb_{0.088}O_2$ were also identified. Rietveld refinement (**Table 4.37**) suggested the weight fraction of $Cs_2TiNb_6O_{18}$ to be 21.21 wt. % and 18.63 wt. % of $Cs_2ZrSi_6O_{15}$.

Table 4.37 *Rietveld refinement details for calcined (1000°C) Cs-IONSIV 12wt. %, Cs.*

	Lattice Parameters (Å)				
	a / Å	b / Å	c / Å	*β*/°	*wt. %*
$Cs_2TiNb_6O_{18}$	7.5102(9)	/	8.2489(14)	/	21.21(3)
$Cs_2ZrSi_6O_{15}$	26.748(6)	7.4528(16)	11.6982(30)	107.540(23)	18.63(4)
$Zr_5Ti_7O_{24}$	14.2344(19)	5.3711(7)	5.0131(8)	/	36.44(3)
$Ti_{0.912}Nb_{0.088}O_2$	4.6002(4)	/	2.9672(4)	/	23.72(4)

Refinement Details		
χ^2	R_{wp}	R_p
4.698	6.49 %	4.21 %

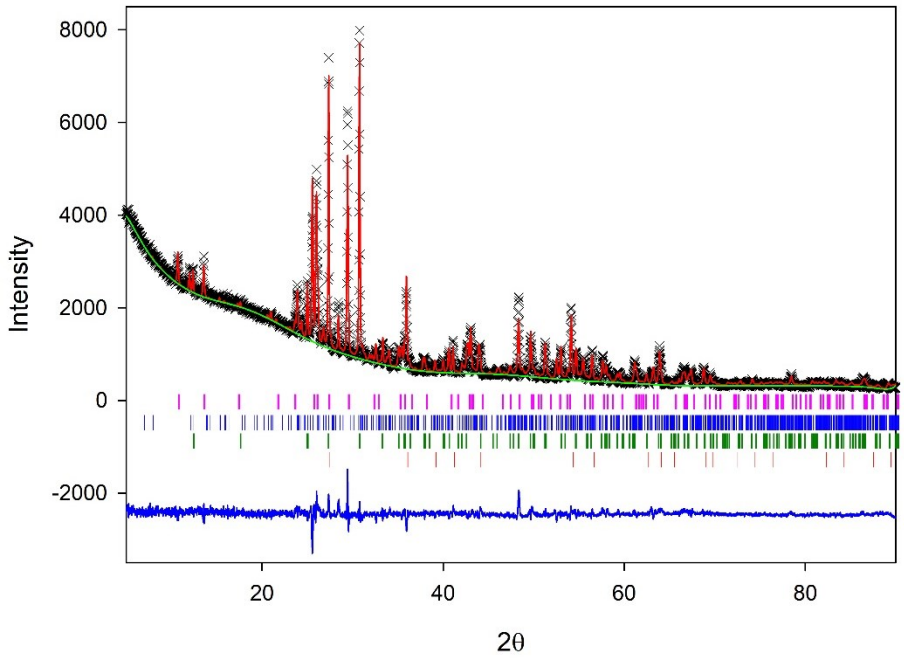

Figure 4.56 *Rietveld refinement plot (GSAS) of calcined (1100°C) Cs-IONSIV (12 wt. %). Pink ticks: $Cs_2TiNb_6O_{18}$, blue ticks: $Cs_2ZrSi_6O_{15}$, red ticks: $(Ti,Nb)O_2$ and green ticks: $Zr_5Ti_7O_{24}$*

At 1100°C, the phases produced from decomposition at 12 wt. % loading (**Figure 4.56** and **Table 4.38**) are identical to those formed at 1000°C. At this higher temperature, more $Cs_2TiNb_6O_{18}$ is formed but there is slightly less $Cs_2ZrSi_6O_{15}$. At 1000°C, there is 21.21 wt. % $Cs_2TiNb_6O_{18}$ and 18.63 wt. % $Cs_2ZrSi_6O_{15}$ and at 1100°C there is 29.77 wt. % $Cs_2TiNb_6O_{18}$ and only 14.10 wt. % $Cs_2ZrSi_6O_{15}$.

Table 4.38 *Rietveld refinement details for Cs-IONSIV (12 wt. %) Calcined at 1100°C in air*

	Lattice Parameters (Å)				
	a / Å	*b* / Å	*c* / Å	*β*/°	wt. %
$Cs_2TiNb_6O_{18}$	7.52411(29)	/	8.2328(4)	/	29.77(2)
$Zr_5Ti_7O_{24}$	14.2646(8)	5.37076(33)	5.01705(32)	/	33.99(3)
$Ti_{0.912}Nb_{0.088}O_2$	4.60413(19)	/	2.97029(15)	/	22.152(2)
$Cs_2ZrSi_6O_{15}$	26.750(4)	7.4544(11)	11.6848(20)	107.484(16)	14.10(26)
Refinement Details					
χ^2	R_{wp}	R_p			
3.385	5.51 %	3.87 %			

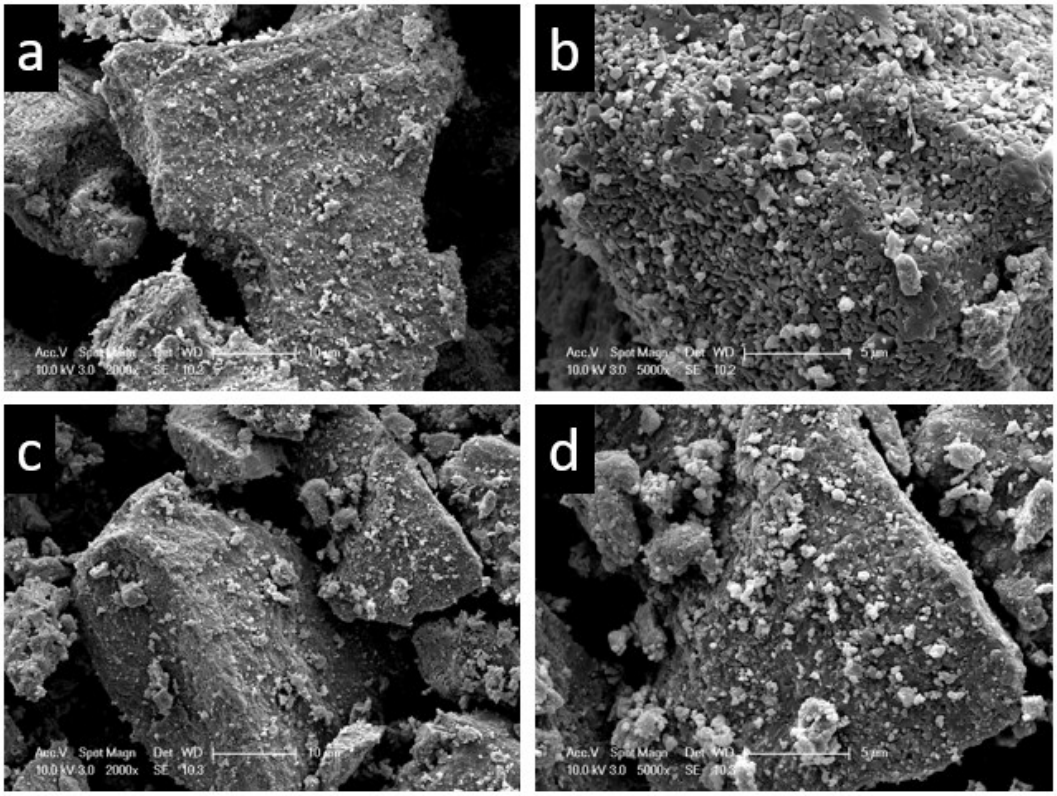

Figure 4.57 *Secondary electron images of calcined (1100°C) Cs-IONSIV samples. a: 6 wt. %, Cs (10 µm), b: 6 wt. %, Cs (5 µm), c: 12 wt. %, Cs (10 µm) and d: 12 wt. %, Cs (5 µm)*

SEM images were taken of the Cs-IONSIV samples at 6 and 12 wt. %. The microstructures are displayed in **Figure 4.57** and appear similar for both the 6 and 12 wt. % sample.

Samples calcined at 1100°C in this work have been directly compared to the HIPed samples produced in a previous study because the processing temperatures being similar. The samples calcined at lower temperatures produce less crystalline phase assemblies which are vastly different to the phases formed through HIPing. For comparison purposes, two additional weight loadings of 8 and 10 wt. % Cs-IONSIV were heated to 1100°C. The phase assembly at 8 wt. % Cs is very similar to the one observed at 6 wt. % and the formation at 10 wt. % is similar to 12 wt. %. The weight fractions for these are found in **Table 4.39** and further details of these refinements can be found in the appendix.

Table 4.39 lists the weight fractions formed from decomposition via calcination at 1100°C and via HIPing at each weight loading of Cs. In terms of Cs phases, the trends in both thermal conversion processes are similar. The main difference is that in the HIPing phase assemblies, $Cs_2ZrSi_6O_{15}$ grows in at 8 wt. % Cs loading but it does not appear until 10 wt. % of Cs in the calcined samples. As far as the other phases are concerned, $(Ti,Nb)O_2$ (rutile) is present in all samples at roughly the same weight percent and SiO_2 is only present in the smaller weight loadings of Cs and disappears altogether as $Cs_2ZrSi_6O_{15}$ grow in at higher Cs weight loading. There is slightly more $(Zr,Ti)O_4$ present in all weight loadings in the calcined samples compared to HIPing but the gradual decrease in weight percent of $(Zr,Ti)O_4$ is consistent with the HIPing formations, which is likely a result of $Cs_2TiNb_6O_{18}$ and $Cs_2ZrSi_6O_{15}$ growing in. $ZrSiO_4$ only forms in the lower weight loadings of the HIP samples and is not observed at all in the calcined samples.

In summary the phases observed from both thermal conversion methods are fairly similar, particularly the Cs containing phases. However, this does not take away the advantage of HIPing these materials. The HIPing process forms an extremely dense material which results in a large volume reduction which is ideal for disposal in a GDF. The HIP process is also carried out in a sealed environment, therefore there is no concern of any volatile radioactive Cs being lost in the process. Furthermore, the mild steel HIP can in a 'real life' scenario will add to the multi-barrier system which will decrease the likelihood of harmful radionuclides leaching into the biosphere.

Table 4.39 *Weight fractions from Rietveld for Cs-IONSIV (4,6,8,10 and 12 wt. %) Calcined at 1100°C (Air) and HIPing taken from previous study* [34,130]

Cs-IONSIV Calcined at 1100°C						
wt. % Cs	$Cs_2TiNb_6O_{18}$	$Cs_2ZrSi_6O_{15}$	ZrSiO4	$Zr_5Ti_7O_{24}$	SiO_2	$(Ti,Nb)O_2$
4	19.48(2)	/	/	47.12(2)	11.56(4)	21.84(3)
6	24.13(2)	/	/	43.91(2)	9.57(4)	22.39(3)
8	30.421(2)	/	/	44.207(3)	/	25.372(3)
10	29.351(2)	10.539(3)	/	36.436(3)	/	23.67(2)
12	29.77(2)	14.10(26)	/	33.99(3)	/	22.152(2)

Cs-IONSIV HIPing						
wt. % Cs	$Cs_2TiNb_6O_{18}$	$Cs_2ZrSi_6O_{15}$	$ZrSiO_4$	$ZrTiO_4$	SiO_2	$(Ti,Nb)O_2$
4	17.56	/	12	37.64	7.05	27.54
6	26.07	/	3.55	41.54	/	28.85
8	25.65	18.65	/	34.66	/	21.04
10	28.39	19.42	/	29.4	/	22.79
12	24.56	31.26	/	19.91	/	24.27

4.3.10 Conclusions of the Thermal Decomposition and HIPing of Cs-IONSIV and Sr-IONSIV

In this chapter a series of Sr and Cs loaded IONSIV phases have been thermally decomposed and the products have been studied using XRD, XRF and microscopy techniques. Two processing methods have been used, including calcination (in air) and HIPing.

Initial studies started with the calcination of Sr loaded Nb-CST and Sr loaded Nb-CST with the addition of $Zr(OH)_4$ at 1000 and 1100°C. On decomposition at these temperatures, it was quickly realised that the temperatures were too high, and the sample melted and fused to the Al_2O_3 crucible. The temperature was then lowered to 900°C and XRD analysis suggested that the major Sr phase produced for Sr-Nb-CST is a $(Na,Sr)(Nb,Ti)O_3$ perovskite. When $Zr(OH)_4$ is added to Sr-Nb-CST (to imitate IONSIV) the phase assembly is more complex and an additional Sr phase, $SrZrO_3$ was identified from XRD after calcination.

Calcined unloaded IONSIV samples were also studied, mainly to help identify new phases formed when Sr-IONSIV was calcined. Sr loaded IONSIV samples at two different Sr loadings (1.5 and 3.0 wt. %) were calcined at 900, 1000 and 1100°C. It became clear that the crystallinity of the phase assemblies greatly improved as the temperature of calcination increased. XRD also indicated that different phase assemblies were formed at the three different temperatures however there was not much difference in the phases produced at the two different Sr loadings. Despite being poorly crystalline the major Sr phase for calcination at 900°C was identified as $Sr_6Nb_{34}O_{91}$, at 1000°C, both $Sr_6Nb_{34}O_{91}$ and $(Na,Sr)NbO_3$ were present and at 1100°C $SrTi_9Nb_4O_{29}$ was identified.

Following the calcination experiments, 3 different Sr-IONSIV samples were HIPed at Sr loadings of 1.5, 3.0 and 4.0 wt. %. For the samples at 1.5 and 3.0 wt. % the phase assemblies are fairly similar. Considering the temperatures, it was thought that HIPing would closely mirror the phase assembly produced from heating Sr-IONSIV to 1100°C, however after HIPing, the phases formed are more similar to the to those formed from calcining at 1000°C where the major Sr phase was $(Na,Sr)NbO_3$. This $(Na,Sr)NbO_3$ perovskite phase was identified using XRD and TEM as the major Sr phase in both the 1.5 and 3.0 wt. % HIPed Sr-IONSIV samples, a small amount of $Na_2SrNb_5O_{15}$ was also identified. The minor differences in the two phases assemblies in the case of these HIP samples was the Sr content on the A site of the perovskite and also that $ZrTiO_4$ was only present in the 1.5 wt. % Sr-IONSIV sample.

HIPing at a higher loading Sr loading IONSIV (4 wt. % Sr) produced a more complex group of phases compared to the lower Sr exchanged samples. EVA search match software identified four different Sr phases including $(Na,Sr)NbO_3$, $SrNb_2O_6$, $SrTi_{11}Nb_4O_{33}$ and $SrTi_{13}Nb_4O_{37}$. Extensive analysis was not carried out on this material on account of there

not being any available solved crystal structures for $SrTi_{11}Nb_4O_{33}$ and $SrTi_{13}Nb_4O_{37}$. To decipher the optimum loading of Sr-IONSIV for HIPing, chemical durability tests were needed to determine the most robust ceramic wasteforms.

Mixed Cs/Sr – IONSIV materials have also been calcined (air) and HIPed at 1100°C. Samples were loaded to approximately 6 wt. % Cs and 1.5 wt. % Sr. Calcination led to $Cs_2TiNb_6O_{18}$ and $SrTi_9Nb_4O_{29}$ plus a number of other background phases. HIPing produced the same Cs containing ceramic, $Cs_2TiNb_6O_{18}$ but a different Sr phase was formed which was identified by XRD as $SrNb_2O_6$. Again, chemical durability tests were needed to gauge the durability of the HIPed Cs/Sr-HIPed IONSIV.

As well as Sr, Cs-IONSIV has also been calcined (1100°C) at loadings of 4, 6, 8, 10 and 12 wt. % to compare to a previous study. The results for the most part agree with what was produced from HIPing from the previous study, particularly the Cs containing phases. [34,70] The differences in calcination to HIPing is some discrepancy in background phases such as no $ZrSiO_4$ was found in any calcined materials and also that $Cs_2ZrSi_6O_{15}$ grows in at 10 wt. % Cs loading in the calcining samples, but it is seen in the 8 wt. % Cs sample for the HIPing formations.

To test of the ceramic wasteforms produced from HIPing a series of MCC-1 static leach tests have been carried out to the procedure described in 'Standard Test Method for Static Leaching of Monolithic Wasteforms for Disposal of Radioactive Wastes' [203] and the results are discussed in the next chapter.

5 AQUEOUS DURABILITY TESTS OF HIPED Sr – IONSIV AND Cs/Sr-IONSIV

5.1 Introduction

The aim of HIPing spent ion exchangers is to create dense wasteforms containing immobilised radionuclides that are suitable for long term disposal in GDF. As a result, the aqueous durability of each HIPed wasteform is an important assessment criterion and has been tested. Shorter term aqueous durability tests of the HIPed material would give a good initial indication of how the wasteform will behave in the long term.

The selection of a testing method is crucial in order to collect meaningful data that can be compared to existing data in the literature. A number of different methods can be used to test wasteforms which is usually dependent on the type of wasteform and the type of release mechanisms exhibited by the wasteform. There are usually two leaching processes that occur with ceramic wasteforms that will affect the integrity of the material which are ion exchange of particular species from the solid and dissolution, which usually effects the entire specimen resulting in a number of species being released into solution.[204]

In general, tests are carried out in two ways which are classed as static and dynamic tests. In this study, tests have been carried out in a static environment to best imitate the environment within a geological disposal facility. The selected method here to test the HIPed materials was the Materials Characterisation centre test (MCC-1) (Matrix B).[203] These tests are designed to provide data to initially rank the chemical durability of a wasteform.[203] The tests were carried out at 90°C for 28 days in pure water at a surface-area-to-volume (S/A) ratio of 10 m^{-1}. This testing method has been selected on account of the procedure being

relatively simple and also as it is a popular method for testing the durability of monoliths allowing straightforward comparison to other studies in the literature.

5.2 Experimental

To carry out MCC-1 chemical durability tests, new PTFE vessels and supports (**Figure 5.1**) were purchased and they were heated and cleaned according to the standard procedure outlined in "Standard Test Method for Static Leaching of Monolithic Wasteforms for disposal of Radioactive Waste". [203]

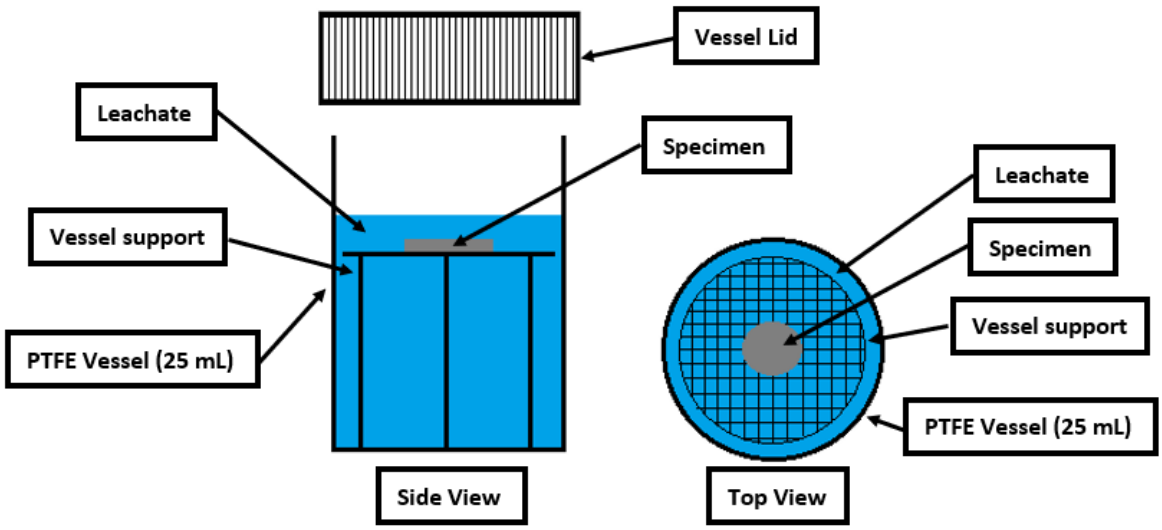

Figure 5.1 *PTFE Leach Testing pots with support and specimen*

Following cleaning and before the actual tests took place, the pH and Fluoride content of water held in the vessel for 16 hours at 90°C were tested to ensure the pH was between 5.0 – 7.0 and the Fluoride content < 0.5 mg cm^{-3}. If this was not the case the cleaning procedure of the vessels was repeated. The HIP samples were cut to approximately 1 mm of thickness using a cutting machine equipped with a Al_2O_3 circular blade. To remove the mild steel HIP cans, the sectioned monoliths were 'pickled' by placing them in 0.1 M HNO_3. Once removed from the HIP can, the monoliths were lightly polished and sonicated for 5 minutes with ethanol followed by five minutes with pure water. The surface area of each

monolith was then measured and the amount of leachant (water) was calculated in order to achieve and S/A ratio of 10 m^{-1}. The specimens were then placed on the supports in the PTFE vessels (**Figure 5.1**) and the appropriate amount of pure water was added. Eight leach tests were required for each HIP sample, one for 3, 7 and 14 days, a further three samples for 28 days and finally two blank solutions which contained no specimens. Once the tests were completed the liquid was filtered through a 75µm filter and then 7 ml of each leachant was taken and a small amount of acid (pure HNO_3) added to preserve the samples. They were then stored at 4°C and sent for ICP-MS analysis (Agilent 7500ce) in the Department of Earth Sciences at the University of Birmingham.

5.3 Data Analysis

The normalised elemental mass loss was calculated using **Equation 5.1** [203];

$$(NR)_j = \frac{(C_{ij} - B_i) \times V_j}{f_i \times SA}$$

Where,

C_{ij} = concentring of element i observed in the leachate from specimen j.

B_i = concentration of element i observed in the leachate from blank leachants

V_j = initial volume of leachate in vessel containing specimen j

f_i = mass fraction of element I in the unleached specimen (obtained from XRF) and

SA = specimen surface area, m^2.

Equation 5.1 *Normalised elemental mass loss* $(NR)_I$ *in* gm^{-2}

The normalised elemental leach rate was calculated using **Equation 5.2** [203];

$$(NR)_i = \frac{(NL)_i}{t}$$

Where,

$(NL)_I$ = Normalised elemental mass loss in $g \cdot m^2$ and,

t = duration of leach test performed, in days.

Equation 5.2 *Normalised elemental leach rate* $(NR)_I$

5.4 Results Leach testing HIPed Sr-IONSIV (1.5, 3.0 and 4.0 wt. %) and Cs/Sr – IOSNIV

The normalised mass loss of each element in the HIPed Sr-IOSNIV (1.5 wt. %), is displayed in **Figure 5.2** and the mass losses are shown in **Table 5.1**. It was found that Na by far leached the most which is represented by the gold line in **Figure 5.2**, which was followed by Si and Sr. The mass loss of Ti, Nb and Zr were almost 5 order of magnitudes less than that of Sr and Si, these values are right on the detection limit of the ICP-MS instrument being used. The normalised leach rate of each element for this material is displayed in **Figure 5.3** and **Table 5.1** and the graph and table show the Na leach rate decreases in the 28 day period. The leach rate for Si and Sr decreased in 14 days and then increased again after 28 days. The leach rates for Ti, Zr and Nb are almost negligible which is a result of these elements being mostly insoluble.

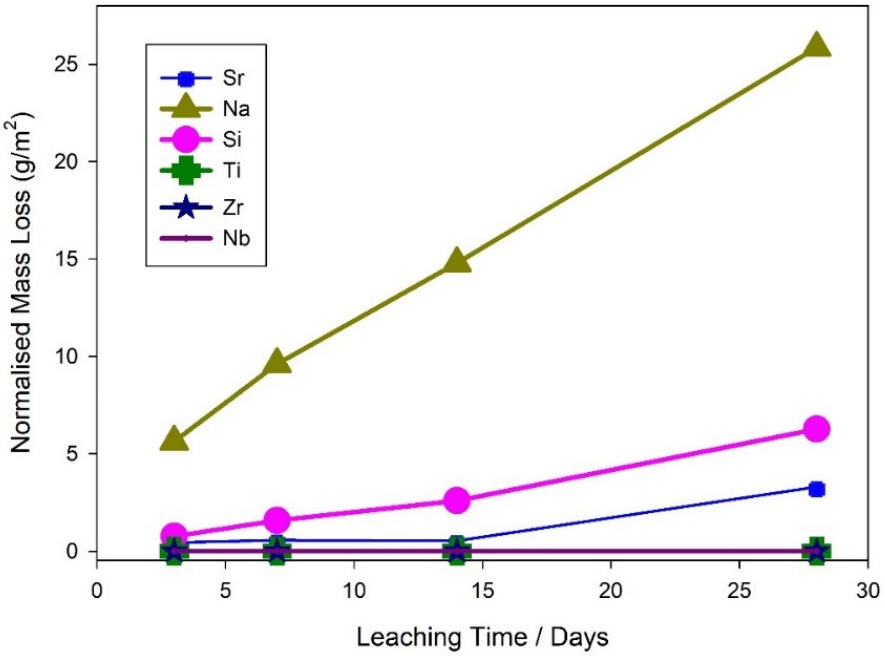

Figure 5.2 *Sr-IONSIV 1.5 wt. % HIPed MCC-1 Leach testing, Normalised mass loss (g/m^2)*

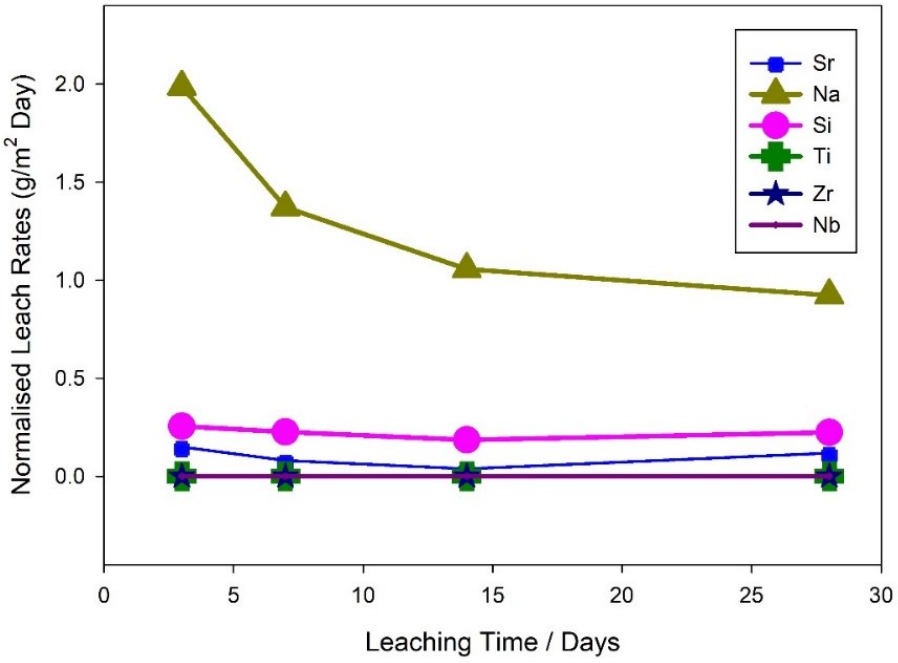

Figure 5.3 *Sr-IONSIV 1.5 wt. % HIPed MCC-1 Leach testing, Normalised leach rate (g/m^2/day)*

Table 5.1 *Sr-IONSIV 1.5 wt. % HIPed MCC-1 Leach testing, Normalised mass loss (g/m^2) and Normalised Leach rates (g/m^2/day)*

Sr-IONSIV HIPed 1.5 wt. % Normalised Mass loss (g/m^2)						
Day	Sr	Na	Si	Ti	Zr	Nb
3	**0.449**	5.629	0.765	1.17E-05	5.82E-04	7.66E-05
7	**0.563**	9.607	1.581	3.97E-07	7.68E-05	1.54E-05
14	**0.535**	14.799	2.590	1.27E-05	3.52E-04	1.36E-04
28	**3.308**	25.849	6.263	3.69E-05	2.61E-04	2.21E-04

Sr-IONSIV HIPed 1.5 wt. % Normalised Leach Rate (g/m^2/day)						
Day	Sr	Na	Si	Ti	Zr	Nb
3	**0.150**	1.988	0.255	3.89E-06	1.94E-04	2.55E-05
7	**0.080**	1.372	0.226	5.67E-08	1.10E-05	2.21E-06
14	**0.038**	1.057	0.185	9.05E-07	2.51E-05	9.73E-06
28	**0.118**	0.923	0.224	1.32E-06	9.34E-06	7.89E-06

Figure 5.4 and **Table 5.2** show the normalised mass loss for each element in HIPed Sr-IONSIV at 3 wt. % Sr loading. The results are much the same as the results found for HIPed Sr-IONSIV (1.5 wt. %) loading. The mass loss for Na was again the highest and was roughly one order of magnitude higher than the other elements. Si and Sr again were the

next two most significant in terms of mass loss. Ti, Zr and Nb up to 14 days were undetectable and were only observed in small amounts at 28 days.

Figure 5.5 and **Table 5.2** reveal the normalised leach rates for each element in HIPed Sr-IONSIV at 3 wt. % Sr loading. The leach rates of Na decrease in the 28 day period and Sr and Si display the same trend as before where the leach rates decrease up to 14 days and increase again after 28 days. As discussed, the other 3 elements, Ti, Zr and Nb are in such low concentrations there are no obvious trends were observed.

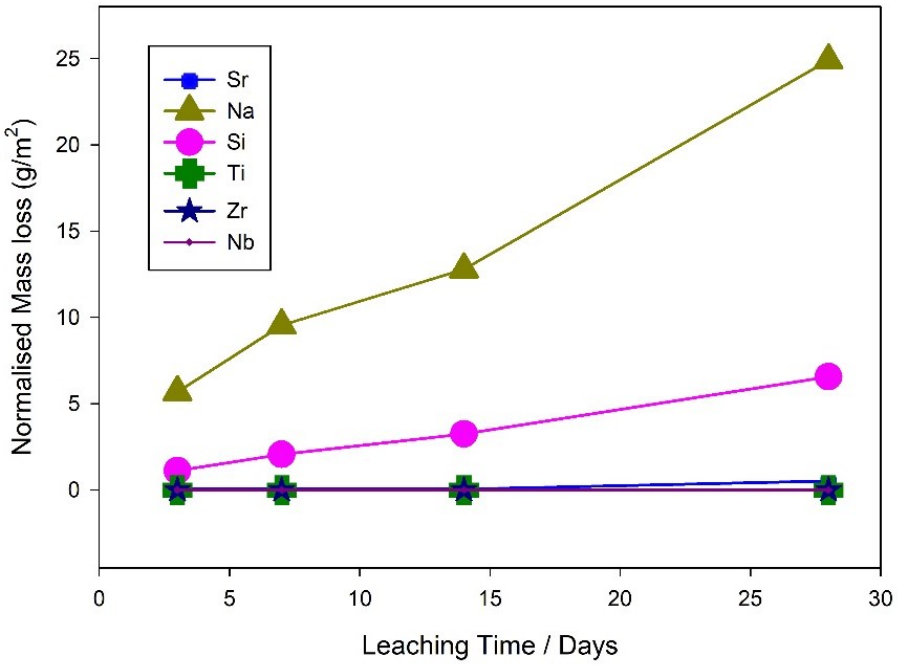

Figure 5.4 *Sr-IONSIV 3.0 wt. % HIPed MCC-1 Leach testing, Normalised mass loss (g/m^2)*

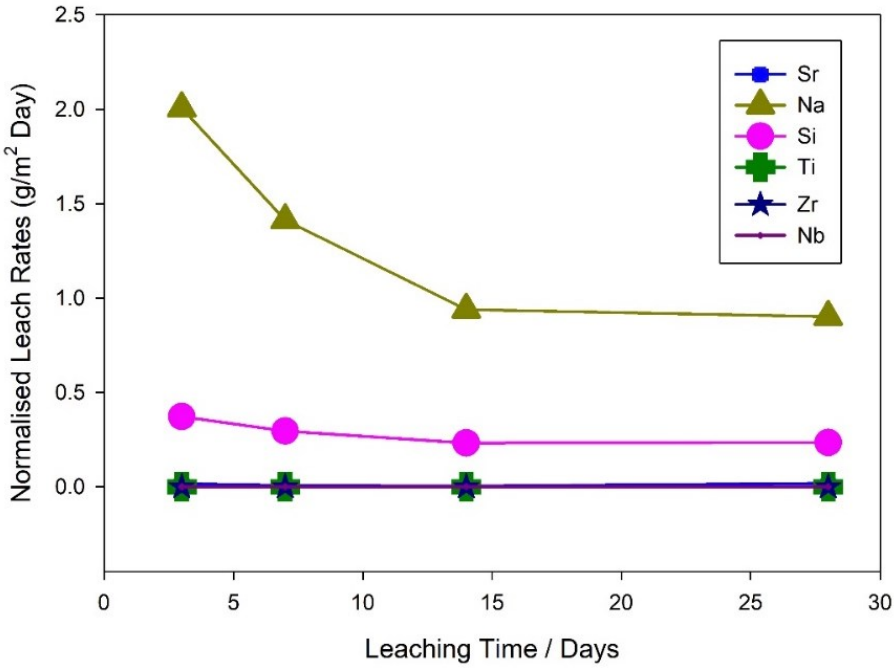

Figure 5.5 *Sr-IONSIV 3.0 wt. % HIPed MCC-1 Leach testing, Normalised Leach rates (g/m^2/day)*

Table 5.2 *Sr-IONSIV 3.0 wt. % HIPed MCC-1 Leach testing, Normalised mass loss (g/m^2) and Normalised Leach rates (g/m^2/day)*

Sr-IONSIV HIPed 3.0 wt. % Normalised Mass loss (g/m^2)						
Day	Sr	Na	Si	Ti	Zr	Nb
3	**0.052**	5.674	1.115	ND	ND	ND
7	**0.049**	9.544	2.064	ND	ND	ND
14	**0.047**	12.800	3.243	ND	ND	ND
28	**0.523**	24.893	6.559	1.27E-04	2.02E-04	6.71E-04

Sr-IONSIV HIPed 3.0 wt. % Normalised Leach Rates (g/m^2/day)						
Day	Sr	Na	Si	Ti	Zr	Nb
3	**0.017**	1.891	0.372	ND	ND	ND
7	**0.007**	1.363	0.295	ND	ND	ND
14	**0.003**	0.914	0.232	ND	ND	ND
28	**0.019**	0.889	0.234	4.53E-06	7.20E-06	2.40E-05

***N.B. ND: Not detectable from ICP-MS**

The MCC-1 leach test results for HIPed Sr-IONSIV at 4.0 wt. % Sr loading are shown in **Figure 5.6** and **Figure 5.7** and the values for normalised mass loss and leach rates for each element are displayed in **Table 5.3**. In this material, the mass loss of Sr is most significant followed by Na and Si which had very similar values. The mass loss for Zr and

Nb are again 5 orders of magnitude less than Sr, Si and Na. Ti was below the detection limit of the ICP-MS instrument.

The normalised leach rates (displayed in **Figure 5.7**) show how Sr, Si and Na all behave in a similar way and decreased as the time progressed from 3 to 28 days. The other three elements were in such low concentrations no trends were observed and Ti was not detected.

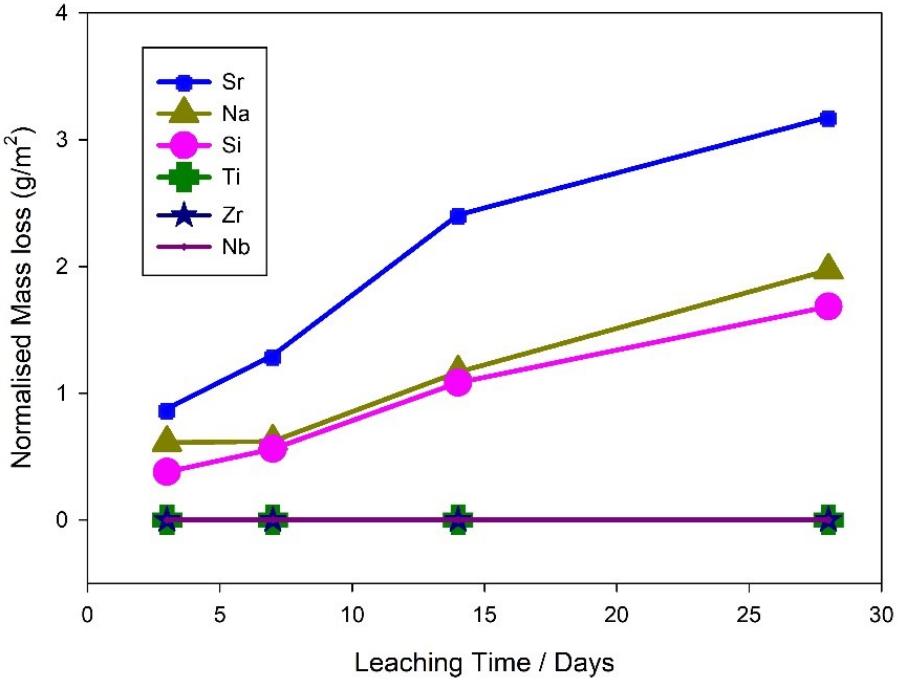

Figure 5.6 *Sr-IONSIV 4.0 wt. % HIPed MCC-1 Leach testing, Normalised mass loss (g/m^2)*

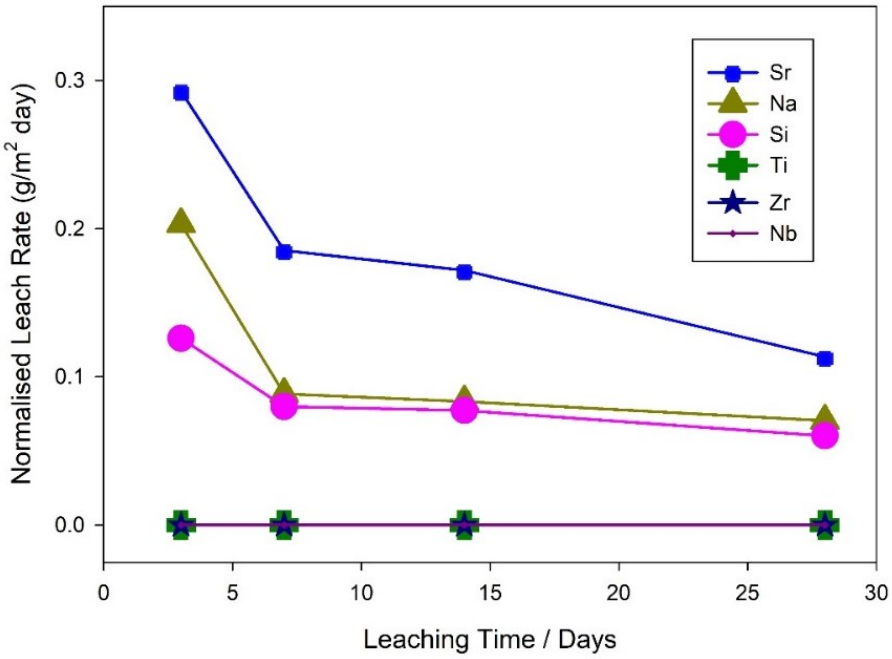

Figure 5.7 *Sr-IONSIV 4.0 wt. % HIPed MCC-1 Leach testing, Normalised Leach rates (g/m^2/day)*

Table 5.3 *Sr-IONSIV 4.0 wt. % HIPed MCC-1 Leach testing, Normalised mass loss (g/m^2) and Normalised Leach rates (g/m^2/day)*

Sr-IONSIV HIPed 4.0 wt. % Normalised Mass loss (g/m^2)						
Day	Sr	Na	Si	Ti	Zr	Nb
3	0.878	0.609	0.378	ND	5.05E-06	6.39E-06
7	1.297	0.620	0.560	ND	ND	4.02E-07
14	2.407	1.166	1.082	ND	2.46E-05	6.96E-05
28	3.179	1.971	1.684	ND	1.47E-04	3.08E-05

Sr-IONSIV HIPed 4.0 wt. % Normalised Leach Rates (g/m^2/day)						
Day	Sr	Na	Si	Ti	Zr	Nb
3	0.293	0.203	0.126	ND	1.68E-06	2.13E-06
7	0.185	0.089	0.080	ND	ND	5.74E-08
14	0.172	0.083	0.077	ND	1.76E-06	4.97E-06
28	0.114	0.070	0.060	ND	5.25E-06	1.10E-06

The normalised mass loss for each element in the HIPed mixed Cs/Sr – IONSIV is displayed in **Figure 5.8** and **Table 5.4**. In this case, Sr leaches the most in terms of mass followed by Si and then Cs and all three of these elements increased in mass loss as the MCC-1 progressed. No Na was detected after 3 days but after 7 days some Na loss is

observed and from 14 days the mass loss increases up to 28 days. The mass of Ti, Zr and Nb mass losses are more or less negligible and no Ti was detected up to 7 days.

The normalised leach rates of the same material are shown in **Figure 5.9** and **Table 5.4**. The trend for Sr, Cs, Si and Na are all similar. There leach rates increase from 3 to 7 days and then steadily decrease at the 14 and 28 day period. No trends were observed on the Ti, Zr and Nb on account of their concentration being so low.

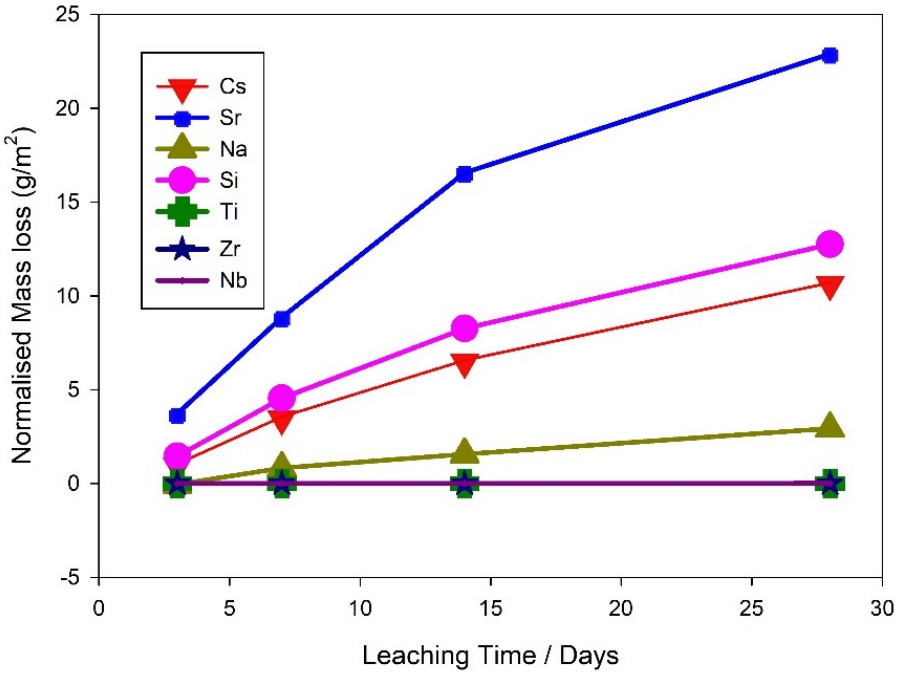

Figure 5.8 *Cs/Sr-IONSIV HIPed MCC-1 Leach testing, Normalised Mass Loss (g/m^2)*

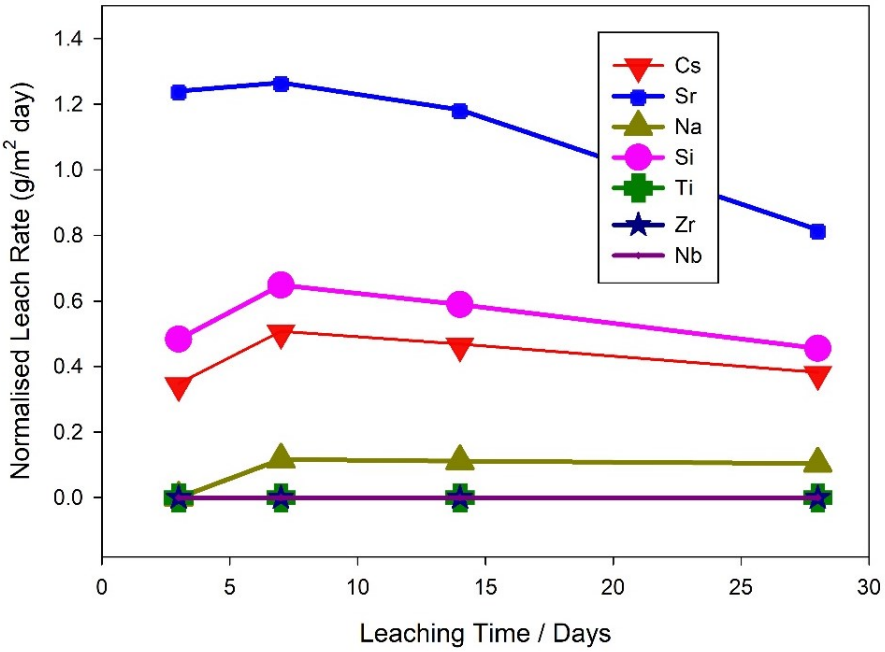

Figure 5.9 *Cs/Sr-IONSIV HIPed MCC-1 Leach testing, Normalised Leach Rates (g/m^2-/day)*

Table 5.4 *Cs/Sr-IONSIV HIPed MCC-1 Leach testing, Normalised mass loss (g/m^2) and Normalised Leach rates (g/m^2/day)*

Cs/Sr-IONSIV HIPed Normalised Mass loss (g/m^2)							
Day	Sr	**Cs**	Na	Si	Ti	Zr	Nb
3	3.719	**1.044**	ND	1.449	ND	5.07E-06	1.18E-05
7	8.857	**3.550**	0.817	4.540	ND	4.32E-05	7.64E-04
14	16.561	**6.560**	1.557	8.253	2.07E-04	8.67E-05	1.93E-03
28	22.892	**10.670**	2.926	12.748	4.07E-04	1.11E-04	4.44E-03

Cs/Sr-IONSIV HIPed Normalised Leach Rates (g/m^2/day)							
Day	Sr	Cs	Na	Si	Ti	Zr	Nb
3	1.240	0.348	ND	0.483	ND	1.69E-06	3.92E-06
7	1.265	0.507	0.117	0.649	ND	6.16E-06	1.09E-04
14	1.183	0.469	0.111	0.590	1.48E-05	6.19E-06	1.38E-04
28	0.818	0.382	0.104	0.455	1.45E-05	3.97E-06	1.59E-04

5.5 Conclusions Leach testing HIPed Sr-IONSIV (1.5, 3.0 and 4.0 wt. %) and Cs/Sr – IOSNIV

For all HIP samples, the mass loss for the soluble elements (Sr, Na, Cs and Si) increased with time. The leach rate trends were less consistent across the HIP samples, it was expected that leach rates would decrease as a function of time, but only the Sr-IONSIV 4.0 wt. % sample demonstrated leach rates (for all soluble elements) that decreased as time

progressed. However, not all elements behaved in the same way for the other HIP samples. The Sr and Si leach rates in both the 1.5 and 3.0 wt. % Sr-IONSIV HIP samples decrease up to the 14 day period and then increase again after 28 days. The Cs, Sr, Na and Si leach rates in the HIPed Cs/Sr-IONSIV sample, all increase from 3 to 7 days but then steadily decrease through 14 to 28 days. These trends were not expected, and it was thought that this behaviour maybe a result of the roughness of the specimen (monolith) surface despite being polished. Surface irregularities (cracks and scratches) may have caused an increase in the amount of element leached at the different time periods causing these trends. The leach rates of the insoluble elements (Ti, Zr and Nb) are not discussed here as the leach rates were so low.

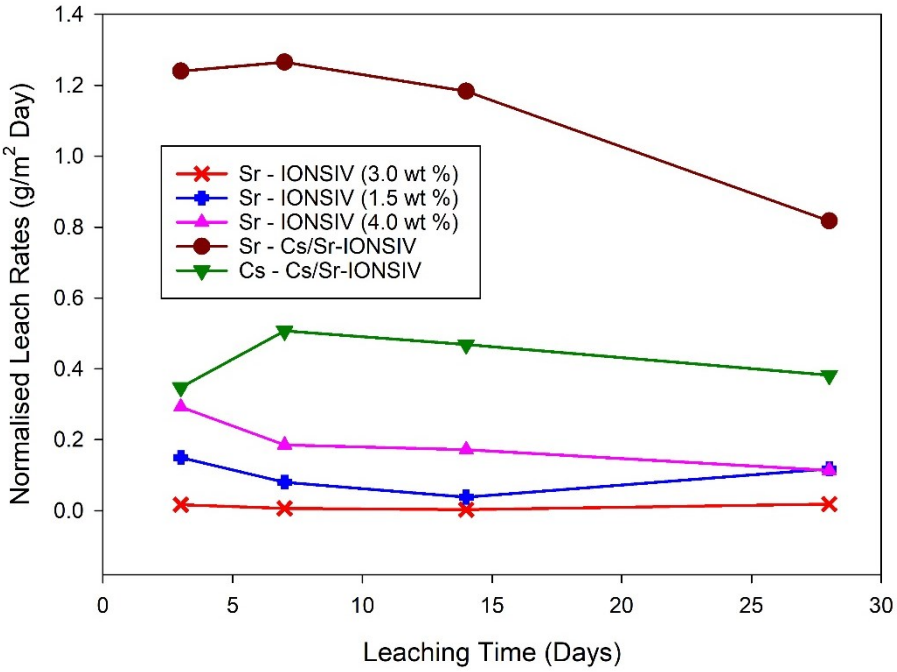

Figure 5.10 *Comparison of Sr and Cs normalised leach rates (g/m^2/day) of HIPed Sr-IONSIV (1.5, 3.0 and 4.0 wt. % Sr) and Cs/Sr-IONSIV*

Figure 5.10 shows the comparison of each of the four HIPed IONSIV materials. The normalised leach rates of Sr and Cs are the focus here as these would be the 'active' species in the wasteform and therefore their chemical durability is of most relevance. In this study the Sr normalised leach rates were by far at their lowest for the 3 wt. % Sr-IONSIV

HIPed sample at 0.019 g/m^2/day (28 days). Interestingly, the Sr leach rates for the 1.5 wt. % Sr-IONSIV HIPed sample were approximately six times higher at 0.118 g/m^2/day (28 days). At 4.0 wt. % Sr loading the Sr leach rates were similar to the 1.5 wt. % Sr sample at 0.114 g/m^2/day (28 days)**.** The normalised leach rate for Sr in the mixed Cs/Sr-IONSIV HIP sample is somewhat higher reaching values of 0.818 g/m^2/day after 28 days.

The low Sr leach rates observed at 3.0 wt. % Sr loading was thought to be on account of the Sr phases present after HIPing. Two Sr phases were identified in this material, the dominant phase being a (Na,Sr)NbO_3 perovskite along with a small amount of $NaSr_2Nb_5O_{15}$. It is understood from previous studies that the Sr-perovskite material (present in SYNROC) is chemically durable hence low Sr leach rates are observed in this study.[48,50,55,56] However, the Sr leach rates in the 1.5 wt. % Sr-IONSIV sample are approximately six times higher than the 3.0 wt. % sample which was a surprise considering the phase assemblies identified and are fairly similar. The only notable differences in these materials is the Sr content in the perovskite phase which was calculated from Rietveld refinement of the XRD beam line data. It may be that the Sr leach rates decrease as a function of increased Sr content in the perovskite phase. Further work is required to understand this and tests to measure Sr leach rates as a function if Sr occupancy in the perovskite phase could prove useful to identify the differences. Microscopy studies could also be useful to identify any irregularities between the specimens as it may be that there are some surface defects on the Sr-IONSIV 1.5 wt. % specimens which have caused the leach rates of Sr to increase.

In the case of the 4.0 wt. % Sr sample, HIPing produced a different phase assembly to the 1.5 and 3.0 wt. % Sr IONSIV HIPed samples. In this sample a number of Sr phases were identified including $SrNb_2O_6$, $SrTi_{11}Nb_4O_{33}$, $SrTi_{13}Nb_4O_{37}$ and (Sr,Na)NbO_3 and the Sr leach rates are higher than that of the 3.0 wt. % Sr- IONSIV sample which is likely on

account of the other Sr phases present being less durable. The Sr leach rates increase significantly in the Cs/Sr-IONSIV HIPed sample, where the Sr leach rates after 28 days are 2 orders of magnitude higher than the 3.0 wt. % Sr- IONSIV sample. The main Sr phase was identified in the mixed Cs/Sr-IONSIV HIP sample was identified as $SrNb_2O_6$, which is clearly not as durable as the other Sr phases in the other HIP formations.

The Cs leach rates in the mixed Cs/Sr-IONSIV material are also displayed in **Figure 5.10**. XRD suggests that Cs resides in the already discussed $Cs_2TiNb_6O_{18}$ phase (**Figure 4.42**). The Cs leach rates observed for this material were discovered to be 0.1542 g/m^2/day after 28 days in a previous study.[34] In this work the Cs leach rates are in a similar range of 0.382 g/m^2/day after 28 days.

Table 5.5 *Comparison of normalised leach rates of Sr and Cs for several different wasteforms*

Wasteforms		Test method and conditions	Normalised leach Rates Sr	Reference
Hollandite	Al-18	MCC-1, (0-28 days)	0.018	Carter et al. 2009 [54]
	Al-12		0.013	
	Mg-18		0.061	
	Mg-12		0.018	
SYNROC-D	Sr in 15 wt. % Perovskite	MCC-1, (0-28 days)	0.28	Campbell et al. 1981 [205]
SYNROC	Polyphase titanate ceramic	MCC-2, (337 days)	0.064	Smith et al. 1992 [206]
Glass Ceramic	GC500	MCC-1, (0-28 days)	0.00097	He et al. 2002 [207]
	GC875		0.00069	
Glass Ceramic	Ceramic + boroaluminosilicate glass	MCC-1 (14 days)	0.5	Raman. 1998 [208]

Wasteforms		Test method and conditions	Normalised leach Rates Cs	Reference
Hollandite	Al-18	MCC-1, (0-28 days)	0.025	Carter et al. 2009 [54]
	Al-12		0.022	
	Mg-18		1	
	Mg-12		2	
SYNROC-D	Cs in 18 wt. % Nepheline	MCC-1, (0-28 days)	0.711	Campbell et al. 1981 [205]
SYNROC	Polyphase titanate ceramic	MCC-2, (337 days)	0.028	Smith et al. 1992 [206]
Thermally Converted CST	Cs-IONSIV (5 wt. %)	MCC-1, (14 days)	0.80 (700°C)	Balmer et al. 1999 [195]
			0.08 (800°C)	
			0.09 (900°C)	
			0.08 (1000°C)	

From analysing the leach test data, it is clear the most robust wasteform is produced when Sr-IONSIV is loaded to 3 wt. % Sr, which demonstrated a normalised leach rate of 0.01 g/m^2/day. This value compared well to many reported Sr- leach rates for other wasteforms, some of which are listed in **Table 5.5**. Four different hollandite formations published by Carter et al. [54] are shown in **Table 5.5** and the Sr leach rates range from 0.01

to 0.06 g/m^2/day which are similar to those reported here. Sr-IONSIV 3.0 wt. % has also outperformed other wasteforms such as SYNROC – D, reported by Campbell et al.[205] For the mixed Cs/Sr-IONSIV HIPed material, the Sr leach rate is somewhat higher than the others reported in **Table 5.5**. Cs leach rates in the mixed sample compare well to the Cs leach rates reported in the previous study [130] and to the other wasteforms listed in **Table 5.5**.

34,70,130

6 CONCLUSIONS AND FURTHER WORK

This work consists of two main studies, the first of which has been based on a Cs ceramic, $Cs_2TiNb_6O_{18}$. This phase was discovered to be the main Cs phase produced after Cs-IONSIV is HIPed. $Cs_2TiNb_6O_{18}$ demonstrated the potential to be an excellent host phase for radioactive Cs as it is extremely durable which was confirmed through a series of chemical durability tests. One key question that remained from this study is would the material be able to retain the decay product of $^{137}Cs^{+}$. $^{137}Ba^{2+}$, is divalent and therefore retention would only be achieved by a reduction mechanism within the material. It was thought that the electron produced in the β^- decay process could reduce either Ti^{4+} or Nb^{5+} to Ti^{3+} and Nb^{4+} respectively allowing Ba to be retained. This process is reported in other ceramic materials including hollandite and pollucite.[55,56,132,133] If Ba could not be retained in $Cs_2TiNb_6O_{18}$, the release of Ba may cause the wasteform to fracture mechanically and increase the likelihood of harmful^{137}Cs being released. As a result, a series of Ba substituted $Cs_2TiNb_6O_{18}$ materials have been synthesised to four co-substituted mechanisms. Firstly with doping excess Ti^{4+} for Nb^{5+} giving the formula $Cs_{2-x}Ba_xTi^{(4+)}_{1+x}Nb^{(5+)}_{6-x}O_{18}$, secondly substituting Nb^{4+} for Nb^{5+} giving the formula $Cs_{2-x}Ba_xNb^{(5+)}_{6-x}Nb^{(4+)}_xTiO_{18}$, thirdly substituting Ti^{3+} for Ti^{4+} giving the formula $Cs_{2-x}Ba_xTi^{(4+)}_{1-x}Ti^{(3+)}_xNb_6O_{18}$ and lastly a mixed sample of Nb^{4+} for Nb^{5+} and Ti^{3+} for Ti^{4+} giving the formula $Cs_{2-x}Ba_xNb^{(5+)}_{6-(x/2)}Ti^{(3+)}_{x/2}Ti^{(4+)}_{1-(x/2)}Nb^{(4+)}_{x/2}O_{18}$. It was thought that successful synthesis of these materials would go a long way to prove Ba can be retained in $Cs_2TiNb_6O_{18}$.

In the early stages of the study, Ba was incorporated into $Cs_2TiNb_6O_{18}$ with the charge balance being achieved through doping excess Ti^{4+} for Nb^{5+}. Despite not being a realistic scenario, doping excess Ti^{4+} for Nb^{5+} was synthetically the easiest method to charge compensate as all species are in their highest oxidation states and conventional solid-state

methods were sufficient to synthesise the products. XRF suggested the expected Ba content but on inspection of the XRD patterns it was quickly realised that Ba incorporation was not successful on account of the presence of several Ba impurities, including $BaTi_3Nb_4O_{17}$, $BaTiNb_4O_{13}$ and $Ba_2Ti_3Nb_4O_{18}$. Subsequent Rietveld refinements suggested that Ba resided entirely in the Ba impurities and not in the target phase. Other synthesis attempts were carried out following the other mechanisms such as substituting Nb^{4+} for Nb^{5+}, Ti^{3+} for Ti^{4+} and a mix of the two (Nb^{4+} for Nb^{5+} and Ti^{3+} for Ti^{4+}) for Ba incorporation. These compounds with formulas $Cs_{2-x}Ba_xNb^{(5+)}_{6-x}Nb^{(4+)}_xTiO_{18}$ and $Cs_{2-x}Ba_xTi^{(4+)}_{1-x}Ti^{(3+)}_xNb_6O_{18}$ were much more challenging to synthesis as both Nb^{4+} and Ti^{3+} are air sensitive and therefore would oxidise at high temperature. As a result, a different synthesis method had to be developed where the reaction conditions were considered more carefully. This new method involved heating samples under vacuum in evacuated sealed tubes to prevent oxidation. However, despite finding a suitable synthesis, Ba impurity phases were still present in the XRD patterns following synthesis, suggesting Ba incorporation is not favourable in the $Cs_2TiNb_6O_{18}$ phase.

Having been not been able to confirm Ba doping experimentally, a series of simulations were carried out. For this work, novel Buckingham potentials were empirically derived using RMC methodology and calculations were performed using the GULP (General Utility Lattice program) code. The energetics of the different co-substitution mechanisms previously studied in the experimental work have been investigated. Initially defects were approximated in the $Cs_2TiNb_6O_{18}$ system at infinite dilution and as clusters in supercells using the Mott-Littleton approach. Although these calculations gave a good initial indication of defect energies, a more robust method was needed to assess the energetics of Ba doping. As a result, Ba was doped into 729 atom supercells using a Markov-Chain Monte-Carlo

(MCMC) method. The solution energies calculated from this more robust method suggested that Ba doping thermodynamically is unfavourable across all schemes which is in agreement with the pervious experimental work.

Despite the experimental and computational studies suggesting that Ba incorporation in the $Cs_2TiNb_6O_{18}$ phase is unfavourable, further synthesis attempts of a Ba doped $Cs_2TINb_6O_{18}$ material could be of interest for this study which were not previously carried out because of time constraints. Further modifying the solid-state synthesis method such as heating under a H_2 (reducing) atmosphere could provide the necessary conditions to drive Ba in the structure. However subtle control of the of the reducing environment would be required to stop cations reducing to metals. As well as this synthesis could also be carried out via Hot Isostatic Pressing. Conditions in a mild steel HIP in the process are slightly reducing and therefore could provide the required conditions to get Ba into the structure.

Another study that was not carried out in this work, mainly because the facilities were not available was to synthesis $Cs_2TiNb_6O_{18}$ with a small amount of short-lived radioactive caesium tracer which would decay to Ba. Any structure changes after transmutation could be analysed by X-ray diffraction and microscopy experiments which could determine if Ba can remain in the target phase.

The second part of this study involved the thermal conversion of Sr, Cs and Cs/Sr loaded IONSIV materials into dense ceramics via calcining in air and HIPing. This work has been based on a previous study which demonstrated that HIPing Cs-IONSIV produces a dense robust ceramic wasteform which is extremely chemically durable and suitable for final disposal.[34,70,130] In this work, the Sr-IONSIV materials converted through calcination in air produced slightly different products to HIPing which was thought to be most likely a result of temperature and pressure differences in the two heating methods. The major Sr phase

produced from HIPing Sr-IONSIV at 1.5 and 3 wt. % Sr loading, was identified as a Sr containing perovskite phase with the formula $(Sr,Na)NbO_3$ along with a small amount of $NaSr_2Nb_5O_{15}$. Interestingly, the Sr-IONSIV at 3.0 wt. % performed better than the 1.5 wt. % sample in terms of Sr leach rates which was surprising considering how similar the phase assemblies are. The Sr leach rates for the 3.0 wt. % Sr-IONSIV HIPed sample were found to be 0.019 g/m^2/day after 28 days and the Sr leach rates for the 1.5 wt. % sample are six times higher at 0.118 g/m^2/day after 28 days. The only notable difference in the two assemblies is the Sr content in the perovskite phase and it was thought this may be the cause in the difference in Sr leach rates. Further work is needed to confirm this relationship between Sr content in the perovskite phase and Sr leach rates.

At higher loading (4 wt. % Sr), a different set of Sr phases were identified which included $SrNb_2O_6$, $(Na,Sr)NbO_3$, $SrTi_{11}Nb_4O_{33}$ and $SrTi_{13}Nb_4O_{37}$**.** The Sr leach rates for this material are 0.114 g/m^2/day (28 days) which is similar to the Sr-IONIV 1.5 wt. % HIPed sample despite the phase assembly being different.

HIPing the mixed Cs/Sr-IONSIV produced the familiar and robust $Cs_2TiNb_6O_{18}$ phase which was reflected in the Cs leach rates as they were similar to the Cs leach rates reported in a previous study.[70] In this case, Sr resides in a orthorhombic $SrNb_2O_6$ phase which proved not be as durable as the other Sr phases in the other HIP formations. The Sr leach rates were forty times higher at 0.818 g/m^2/day after 28 days for the mixed sample compared to the Sr-IONSIV 3.0 wt. % HIPed sample.

The results suggest that in order to get the best performance out of HIPing the Sr-IONSIV material, it must be loaded to 3 wt. % Sr. This results in the majority of Sr residing in the robust perovskite phase which is known from previous work to be chemically robust. The mixed Cs/Sr-IONSIV performed well in terms of Cs leach rates poorly in terms of Sr

leach rates and this material required further work to improve the Sr retention. With the exception of the mixed Cs/Sr-IONSIV sample (more specifically the Sr leach rates), the HIP materials have generally performed well in the static leach tests and the Sr and Cs leach rates compare well to others in the literature (**Table 5.5**).

Additional studies for this HIPing work could involve adding metals such as Fe, Al and Ti before the IONSIV samples are HIPed. It was discovered in previous work that adding these metal altered the phase assemblies produced after HIPing. [34] Therefore it may be possible to influence the Sr phases produced in the examples studied here which my increase the durability of the wasteforms.

In terms of analysis, further TEM studies are required to help understand the difference in Sr leach rates between Sr-IONSIV (1.5 wt. %) and Sr-IONSIV (3.0 wt. %) and to confirm if there is any relationship between Sr occupancy of the perovskite phase and chemical durability. Further microscopy studies are also required to better characterise the phases produced in the 4 wt. % Sr-IONSIV HIPed system. Further to this, it would be useful to carry out product consistency tests (PCT-B) on all the Sr-IONSIV samples calcined in air so the chemical durability can be directly compared to the HIPing materials.

7 APPENDICES

See attached CD

8 REFERENCES

1 N. Chapman and A. Hooper, *Proceedings of the Geologists' Association*, 2012, **123**, 46–63.

2 M. Dittmar, *Energy*, 2012, **37**, 35–40.

3 Y. Kim, M. Kim and W. Kim, *Energy Policy*, 2013, **61**, 822–828.

4 S. Hong, C. J. A. Bradshaw and B. W. Brook, *Energy Policy*, 2013, **56**, 418–424.

5 D. Jahn and S. Korolczuk, *Environmental Politics*, 2012, **21**, 159–164.

6 A. Glaser, *Bulletin of the Atomic Scientists*, 2012, **68**, 10–21.

7 M. M. Abu-Khader, *Progress in Nuclear Energy*, 2009, **51**, 225–235.

8 P. D. Wilson, *The nuclear fuel cycle : From Ore to Wastes*, Oxford University Press, 1996.

9 I. Donald, B. Metacalfe and R. Taylor, *Journal of Materials Science*, 1997, **32**, 5851–5887.

10 I. W. Donald, *Waste Immobilization in Glass and Ceramic Based Hosts: Radioactive, Toxic and Hazardous Wastes*, John Wiley & Sons, 2010.

11 S. Stefanovsky, S. Yudintsev, R. Giere and G. Lumpkin, *Energy, Waste and the Environment: a Geochemical Persspective*, 2004, **236**, 37–63.

12 A. Clearfield, L. Bortun and A. Bortun, *Reactive and Functional Polymers*, 2000, **43**, 85–95.

13 V. Luca, J. Hanna, M. Smith, M. James, D. Mithchell and J. Bartlett, *Microporous and Mesoporous Materials*, 2002, **55**, 1–13.

14 E. Maddrell, *Chemical Engineering Research and Design*, 2013, **91**, 735–741.

15 A. M. El-Kamash, *Journal of Hazardous Materials*, 2008, **151**, 432–445.

16 M. S. Denton and M. J. Manos, in *Phoenix, AZ Conference Proceedings WM2009*, 2009, pp. 1–8.

17 B. Yu, J. Chen and C. Song, *Journal of Materials Science Technology*, 2002, **18**, 206–210.

18 D. W. Evans, J. J. Alberts and R. A. Clark, *Geochimica et Cosmochimica Acta*, 1983, **47**, 1041–1049.

19 J. P. McKinley, J. M. Zachara, S. C. Smith and C. Liu, *Geochimica et Cosmochimica Acta*, 2007, **71**, 305–325.

20 L. Al-Attar, A. Dyer, A. Paajanen and R. Harjula, *Journal of Materials Chemistry*, 2003, **13**, 2969.

21 A. Dyer, A. Chimedtsogzol, L. Campbell and C. Williams, *Microporous and Mesoporous Materials*, 2006, **95**, 172–175.

22 S. G. Baxter and D. C. Berghauser, *Waste management*, 1986, 2, 347–358.

23 T. J. Tranter, R. S. Herbst, T. A. Todd, A. L. Olson and H. B. Eldredge, *Advances in Environmental Research*, 2002, **6**, 107–121.

24 R. Harjula, J. Lehto, A. Paajanen, E. Tusa and P. Yarnell, *Reactive and Functional Polymers*, 2004, **60**, 85–95.

25 A. Merceille, E. Weinzaepfel, Y. Barré and A. Grandjean, *Separation and Purification Technology*, 2012, **96**, 81–88.

26 E. H. Borai, R. Harjula, L. Malinen and A. Paajanen, *Journal of Hazardous Materials*, 2009, **172**, 416–22.

27 A. M. El-Kamash, M. R. El-Naggar and M. I. El-Dessouky, *Journal of Hazardous Materials*, 2006, **136**, 310–316.

28 P. G. Heath, M. W. A. Stewart, S. Moricca and N. C. Hyatt, *Journal of Nuclear Materials*, 2018, **499**, 233–241.

29 B. Gu, L. Wang, S. Wang, D. Zhao, V. H. Rotberg and R. C. Ewing, *Journal of Materials Chemistry*, 2000, **10**, 2610–2616.

30 Z. Zheng, C. V. Philip and R. G. Anthony, *Industrial & Engineering Chemistry Research*, 1996, **35**, 4246–4256.

31 L. M. Wang, J. Chen and R. C. Ewing, *Current Opinion in Solid State and Materials Science*, 2004, **8**, 405–418.

32 M. Petersková, C. Valderrama, O. Gibert and J. L. Cortina, *Desalination*, 2012, **286**, 316–323.

33 R. Koivula, R. Harjula and J. Lehto, in *Combined and Hybrid Adsorbents Fundamentals and Applications*, eds. J. Loureiro and K. Mykola, Springer Science & Business Media, 2006, Illustrate., 2006, pp. 37–47.

34 T.-Y. Chen, J. A. Hriljac, A. S. Gandy, M. C. Stennett, N. C. Hyatt and E. R. Maddrell, in *Scientific Basis for Nuclear Waste Management XXXVI, MRS Symp*, 2013, pp. 67–72.

35 J. Van R. Smit, J. J. Jacobs and W. Robb, *Journal of Inorganic and Nuclear Chemistry*, 1959, **12**, 95–103.

36 A. Nilchi, R. Saberi, M. Moradi, H. Azizpour and R. Zarghami, *Journal of Radioanalytical and Nuclear Chemistry*, 2011, **292**, 609–617.

37 S. F. Yates and P. Sylvester, *Separation Science and Technology*, 2001, **36**, 867–883.

38 E. A. Behrens, P. Sylvester and A. Clearfield, *Environmental Science & Technology*, 1998, **32**, 101–107.

39 J. Lehto, L. Brodkin and R. Harjula, in *Proceedings of the Sixth International Conference on Radioactive Waste Management and Environmental Remedition*, Singapore, 1997, pp. 245–258.

40 National-Research-Council, in *Alternatives for High-Level Waste Salt Processing at*

the Savannah River Site, National Academies Press, Washington DC, 2000, pp. 55–65.

41 R. G. Anthony, R. G. Dosch, D. Gu and C. V. Philip, *Industrial & Engineering Chemistry Research*, 1994, **33**, 2702–2705.

42 S. Chitra, R. Sudha, S. Kalavathi, A. G. S. Mani, S. V. S. Rao and P. K. Sinha, *Journal of Radioanalytical and Nuclear Chemistry*, 2012, **295**, 607–613.

43 A. J. Celestian, D. G. Medvedev, A. Tripathi, J. B. Parise and A. Clearfield, *Nuclear Instruments & Methods in Physics Research. Section B, Beam Interactions with Materials and Atoms*, 2005, **238**, 61–69.

44 D. C. Grant, M. C. Skriba and A. K. Saha, *Environmental Progress*, 1987, **6**, 104–109.

45 A. J. Celestian, J. D. Kubicki, J. Hanson, A. Clearfield and J. B. Parise, *Journal of the American Chemical Society*, 2008, **130**, 11689–11694.

46 G. J. Thorogood, B. J. Kennedy, C. S. Griffith, M. M. Elcombe, M. Avdeev, J. V. Hanna, S. K. Thorogood and V. Luca, *Chemistry of Materials*, 2010, **22**, 4222–4231.

47 P. Riley, *Nuclear Energy*, 2004, **43**, 323–329.

48 A. Ringwood, *Mineralocial Magazine*, 1985, **49**, 159–176.

49 W. E. Lee, M. I. Ojovan, M. C. Stennett and N. C. Hyatt, *Advances in Applied Ceramics*, 2006, **105**, 3–12.

50 A. E. Ringwood, S. E. Kesson, N. G. Ware, W. Hibberson and A. Major, *Nature*, 1979, **278**, 219–223.

51 Y. Xu, Y. Wen, R. Grote, J. Amoroso, L. Shuller Nickles and K. S. Brinkman, *Scientific Reports*, 2016, **6**, 27412.

52 S. Ching, P. F. Driscoll, K. S. Kieltyka, M. R. Marvel and S. L. Suib, *Chemical Communications*, 2001, **0**, 2486–2487.

53 Y. Xu, M. Feygenson, K. Page, L. S. Nickles and K. S. Brinkman, *Journal of the American Ceramic Society*, 2016, **99**, 4100–4106.

54 M. L. Carter, A. L. Gillen, K. Olufson and E. R. Vance, *Journal of the American Ceramic Society*, 2009, **92**, 1112–1117.

55 A. Y. Leinekugel-le-Cocq, P. Deniard, S. Jobic, R. Cerny, F. Bart and H. Emerich, *Journal of Solid State Chemistry*, 2006, **179**, 3196–3208.

56 A. Y. Leinekugel-le-Cocq-Errien, P. Deniard, S. Jobic, E. Gautier, M. Evain, V. Aubin and F. Bart, *Journal of Solid State Chemistry*, 2007, **180**, 322–330.

57 E. R. Vance, S. Moricca, B. D. Begg, M. W. A. Stewart, Y. Zhang and M. L. Carter, *Advances in Science and Technology*, 2010, **73**, 130–135.

58 E. R. Vance, B. D. Begg, R. A. Day and C. J. Ball, *MRS Proceedings*, 1994, **353**, 767.

59 C. L. Corkhill, N. J. Cassingham, P. G. Heath and N. C. Hyatt, *International Journal of Applied Glass Science*, 2013, **4**, 341–356.

60 P. D. Soper, D. D. Walker and M. J. Plodinec, *American Ceramic Society Bulletin*, 1983, **62**, 1013–1018.

61 W. H. Sutton, in *Microwave Processesing of Materials III, MRS Symp*, eds. R. L. Beatty, W. H. Sutton and M. F. Iskander, Cambridge University Press, San Francisco, 1992, vol. 269, pp. 3–20.

62 T. White, *Oak Ridge National Laboratory Review*, 1990, **22**, 40–44.

63 H. Li, Y. Zhang, P. J. McGlinn, S. Moricca, B. D. Begg and E. R. Vance, *Journal of Nuclear Materials*, 2006, **355**, 136–141.

64 R. M. German, *Sintering Theory and Practice*, Wiley, Illustrate., 1996.

65 B. E. Scheetz, D. K. Agrawal, E. Breval and R. Roy, *Waste Management*, 1994, **14**, 489–505.

66 T. Basak, S. K. Samanta and A. Jindamwar, *Chemical Engineering Science*, 2008, **63**, 3292–3308.

67 M. C. Stennett, I. J. Pinnock and N. C. Hyatt, *Journal of Nuclear Materials*, 2011, **414**, 352–359.

68 A. H. Naik, S. B. Deb, A. B. Chalke, M. K. Saexena, K. L. Ramakumar, V. Venugopal and S. R. Dharwadkar, *Journal of Chemical Sciences*, 2010, **122**, 71–82.

69 A. K. Mandal, S. Sen, S. Mandal, C. Guha and R. Sen, *International Journal of Green Energy*, 2015, **12**, 1280–1287.

70 T.-Y. Chen, E. R. Maddrell, N. C. Hyatt, A. S. Gandy, M. C. Stennett and J. A. Hriljac, *Journal of Nuclear Materials*, 2017, **498**, 33–43.

71 S. Thornber, P. Heath, E. Maddrell, M. C. Stennett and N. C. Hyatt, *MRS Advances*, 2016, **1**, 4269–4274.

72 S. M. Thornber, P. G. Heath, G. P. Da Costa, M. C. Stennett and N. C. Hyatt, *Journal of Nuclear Materials*, 2017, **485**, 253–261.

73 M. W. A. Stewart, S. A. Moricca, B. D. Begg, R. A. Day, C. R. Scales, E. R. Maddrell and A. B. Eilbeck, in *The 11th International Conference on Environmental Remediation and Radioactive Waste Management*, Bruges, 2007, pp. 1453–1460.

74 M. L. Carter, H. Li, Y. Zhang, E. R. Vance and D. R. G. Mitchell, *Journal of Nuclear Materials*, 2009, **384**, 322–326.

75 A. R. West, *Solid State Chemistry and Its Applications*, Wiley, 1987.

76 C. J. Brinker and G. W. Scherer, *Sol-Gel Science: The Physics and Chemistry of Sol-Gel Processing*, Elsevier Science, Revised., 2013.

77 K. H. Stern, *Journal of Physical and Chemical Reference Data*, 1972, **1**, 747–772.

78 C. Giacovazzo, *Fundamentals of Crystallography*, Oxford University Press, 2002.

79 W. H. Bragg and W. L. Bragg, *Proceedings of the Royal Society A: Mathematical, Physical and Engineering Sciences*, 1913, **88**, 428–438.

80 R. A. Young, *The Rietveld Method*, Oxford University Press, Oxford, 1993.

81 H. Rietveld, *Journal of Applied Crystallography*, 1969, **2**, 65–71.

82 B. H. Toby, *Powder Diffraction*, 2006, **21**, 67–70.

83 D. B. Wiles and R. A. Young, *Journal of Applied Crystallography*, 1981, 14, 149–151.

84 G. Desgardin, C. Robert, D. Groult and B. Raveau, *Journal of Solid State Chemistry*, 1977, **22**, 101–111.

85 M. Gasperin, *Acta Crystallographica Section C Crystal Structure Communications*, 1984, **40**, 9–11.

86 D. Groult, J. M. Chailleux, J. Choisnet and B. Raveau, *Journal of Solid State Chemistry*, 1976, **19**, 235–244.

87 D. Mezaoui, C. Michel, D. Groult and B. Raveau, *Materials Research Bulletin*, 1986, **21**, 1039–1044.

88 A. A. Awadalla and B. M. Gatehouse, *Journal of Solid State Chemistry*, 1978, **24**, 183–187.

89 R. B. Von Dreele and A. K. Cheetham, *Proceedings of the Royal Society of London A: Mathematical, Physical and Engineering Sciences*, 1974, **338**, 311–326.

90 F. Galasso, G. Layden and G. Ganung, *Materials Research Bulletin*, 1968, **3**, 397–408.

91 S. P. Sirotinkin, V. P. Sirotinkin and V. K. Trunov, *Zhurnal Neorganicheskoj Khimii*, 1990, **35**, 1609–1611.

92 T. A. Vanderah, T. R. Collins, W. Wong-Ng, R. S. Roth and L. Farber, *Journal of Alloys and Compounds*, 2002, **346**, 116–128.

93 V. Aubin-Chevaldonnet, D. Philippe, E. Michel, L.-L.-C.-E. A. Ysoline, J. Stéphane, C. Daniel, P. Václav and A. Thierry, *Zeitschrift für Kristallographie*, 2007, 222, 383–390.

94 R. W. Cheary, *Acta Crystallographica Section B Structural Science*, 1987, **43**, 28–34.

95 J. A. Kaduk, B. H. Toby, W. Wong-Ng and W. Greenwood, *Powder Diffraction*, 1998, **13**, 178–184.

96 A. Tripathi, D. G. Medvedev, M. Nyman and A. Clearfield, *Journal of Solid State Chemistry*, 2003, **175**, 72–83.

97 W. H. Baur and A. A. Khan, *Acta Crystallographica Section B Structural Crystallography and Crystal Chemistry*, 1971, **27**, 2133–2139.

98 H. T. Chung and H. G. Kim, *Journal of the Korean Ceramic Society*, 1995, **32**, 582–586.

99 U. Troitzsch, A. G. Christy and D. J. Ellis, *Physics and Chemistry of Minerals*, 2005, **32**, 504–514.

100 P. Bordet, A. McHale, A. Santoro and R. S. Roth, *Journal of Solid State Chemistry*, 1986, **64**, 30–46.

101 A. Ahtee, M. Ahtee, A. M. Glazer and A. W. Hewat, *Acta Crystallographica Section B Structural Crystallography and Crystal Chemistry*, 1976, **32**, 3243–3246.

102 Y.-I. Kim, S.-H. Nahm, W. Bin Im, D. Y. Jeon and D. H. Gregory, *Journal of Luminescence*, 2005, **115**, 1–6.

103 K. Kihara, *European Journal of Mineralogy*, 1990, **2**, 63–77.

104 T. F. W. Barth, *American Journal of Science*, 1932, **24**, 97–110.

105 D. C. Craig and N. C. Stephenson, *Solid State Chemistry*, 1971, **3**, 89–100.

106 M. D. Peel, S. P. Thompson, A. Daoud-Aladine, S. E. Ashbrook and P. Lightfoot, *Inorganic chemistry*, 2012, **51**, 6876–6889.

107 A. W. Hewat, *Ferroelectrics*, 1974, **7**, 83–85.

108 M. C. F. Horn, C. F. Schwebdtfeger and E. P. Meagher, *Zeitschrift für Kristallographie - Crystalline Materials*, 1972, **136**, 273–281.

109 M. Okrusch, R. Hock, U. Schüssler and A. Brummer, *American Mineralogist*, 2003, **88**, 986–995.

110 K. Schueckel and H. Mueller Buschbaum, *Revue de Chimie Minerale*, 1986, **23**, 154–161.

111 S. Y. Istomin, G. Svensson and J. Köhler, *Journal of Solid State Chemistry*, 2002, **167**, 7–16.

112 S. Lanfredi, D. H. M. Gênova, I. A. O. Brito, A. R. F. Lima and M. A. L. Nobre, *Journal of Solid State Chemistry*, 2011, **184**, 990–1000.

113 W. L. Finger, *Carnegie Inst. Wash. Year Book*, 1974, **73**, 544–547.

114 B. O. Marinder, P.-L. Wang and P. E. Werner, *Acta Chemica Scandinavica, Series A*, 1986, **40**, 467–475.

115 G. Jolicart, M. Leblanc, B. Morel, P. Dehaudt and S. Dubois, *European Journal of Solid State and Inorganic Chemistry*, 1996, **33**, 647–657.

116 M. H. Bocanegra-Bernal, *Journal of Materials Science*, 2004, **39**, 6399–6420.

117 J. D. Gale and A. L. Rohl, *Molecular Simulation*, 2003, **29**, 291–341.

118 G. Cutts (2017), *Radiation Damage in Xenotime: An Atomistic Modelling and X-ray Total Scattering Study (Doctoral Thesis, Univeristy of Birmingham, Birmingham, United Kingdom)*, .

119 M. P. Tosi, *Solid State Physics - Advances in Research and Applications*, 1964, **16**, 1–120.

120 J. D. Gale, *GULP. User Manual, Royal Institution and Imperial College, London*,

1998.

121 P. P. Ewald, *Annalen der Physik*, 1921, **369**, 253–287.

122 J. D. Gale, *Journal of the Chemical Society, Faraday Transactions*, 1997, **93**, 629–637.

123 J. W. Perram, H. G. Petersen and S. W. De Leeuw, *Molecular Physics*, 1988, **65**, 875–893.

124 R. A. Jackson and C. R. A. Catlow, *Molecular Simulation*, 1988, **1**, 207–224.

125 R. A. Buckingham, *Proceedings of the Royal Society A: Mathematical, Physical and Engineering Sciences*, 1938, **168**, 264–283.

126 N. F. Mott and M. J. Littleton, *Transactions of the Faraday Society*, 1938, **34**, 485.

127 T. Möller, R. Harjula and J. Lehto, *Separation and Purification Technology*, 2002, **28**, 13–23.

128 A. Jenni and N. C. Hyatt, *Cement and Concrete Research*, 2010, **40**, 1271–1277.

129 L. L. Hamm, T. Hang, D. J. McCabe and W. D. King, *Preliminary Ion Exchange Modeling for Removal of Cesium from Hanford Waste Using Hydrous Crystalline Silicotitanate Material*, Aiken, SC, 2004, vol. WSRC-TR-20.

130 T.-Y. Chen, E. R. Maddrell, N. C. Hyatt and J. A. Hriljac, *Inorganic Chemistry*, 2016, **55**, 12686–12695.

131 J. Namiesnik and P. Szefer, *Analytical Measurements in Aquatic Environments*, CRC Press, Illustrate., 2009.

132 T.-J. Park, T. J. Garino, T. M. Nenoff, D. Rademacher and A. Navrotsky, *Journal of the American Ceramic Society*, 2011, **94**, 3053–3059.

133 W. Jiang, L. Kovarik, Z. Zhu, T. Varga, M. H. Engelhard, M. E. Bowden, T. M. Nenoff and T. J. Garino, *The Journal of Physical Chemistry C*, 2014, **118**, 18160–18169.

134 I. Yanase, H. Kobayashi, Y. Shibasaki and T. Mitamura, *Journal of the American Ceramic Society*, 2005, **80**, 2693–2695.

135 M. Lou Balmer, Y. Su, H. Xu, E. Bitten, D. McCready and A. Navrotsky, *Journal of the American Ceramic Society*, 2001, **84**, 153–160.

136 H. Xu, G. C. C. Costa, C. R. Stanek and A. Navrotsky, *Journal of the American Ceramic Society*, 2015, **98**, 255–262.

137 G. C. C. Costa, H. Xu and A. Navrotsky, *Journal of the American Ceramic Society*, 2013, **96**, 1554–1561.

138 B. H. Toby, *Journal of Applied Crystallography*, 2001, **34**, 210–213.

139 A. C. Larson and R. B. Von Dreele, *General structure analysis system (GSAS)*, Los Alamos National Laboratory, Los Alamos, 1994.

140 L. Bursill, *Journal of Solid State Chemistry*, 1987, **69**, 355–359.

141 R. D. Shannon, *Acta Crystallograpica Section A: Foundations and Advances*, 1976, **32**, 751–767.

142 G. L. Roberts, R. J. Cava, W. F. Peck and J. J. Krajewski, *Journal of Materials Research*, 1997, **12**, 526–530.

143 J. A. Bearden, *Review of Modern Physics*, 1967, **39**, 86–99.

144 G. Day, G. L. Cutts, T.-Y. Chen, J. A. Hriljac and Y. Guo, in *MRS Advances*, Cambridge Core, 2017, vol. 2, pp. 723–728.

145 W. A. Dollase, *Journal of Applied Crystallography*, 1986, **19**, 267–272.

146 E. Zolotoyabko, *Journal of Applied Crystallography*, 2009, **42**, 513–518.

147 R. L. McGreevy and L. Pusztai, *Molecular Simulation*, 1988, **1**, 359–367.

148 T. Strutz, *Data Fitting and Uncertainty: A practical introduction to weighted least squares and beyond*, Springer Vieweg, 2011.

149 S. M. Woodley, P. D. Battle, J. D. Gale and R. Catlow, *Physical Chemistry Chemical Physics*, 1999, **1**, 2535–2542.

150 T. S. Bush, J. D. Gale, R. Catlow and P. D. Battle, *Journal of Materials Chemistry*, 1994, **4**, 831–837.

151 R. A. Jackson, P. A. Meenan, G. D. Price, K. J. Roberts, G. B. Telfer and P. J. Wilde, *Mineralogical Magazine*, 1995, **59**, 617–622.

152 M. J. Sanders, M. Leslie and C. R. A. Catlow, *Journal of the Chemical Society, Chemical Communications*, 1984, **0**, 1271–1273.

153 P. S. Baram and S. C. Parker, *Philosophical Magazine Part B*, 1996, **73**, 49–58.

154 S. Girard, J. D. Gale, A. Caroline Mellot-Draznieks and G. Férey*, *Chemistry of Materials*, 2001, **13**, 1732–1738.

155 D. Lewis, C. Catlow, G. Sankar and S. Carr, *The Journal of Physical Chemistry*, 1995, **99**, 2377–283.

156 W. Gerlach, *Zeitschrift for Physik*, 1922, **9**, 184–192.

157 S. T. Weir, Y. K. Vohra and A. L. Ruoff, *Physical Review B*, 1986, **33**, 4221–4226.

158 P. E. A. Turchi, *Complex Inorganic Solids : Structural, Stability, and MagneticProperties of Alloys*, Springer, 2005.

159 E. P. Meagher and G. A. Lager, *The Canadian Mineralogist*, 1979, **17**, 77–85.

160 R. H. Buttner and E. N. Maslen, *Acta Crystallographica Section B: Structural Science*, 1992, **48**, 764–769.

161 S. Piskunov, E. Heifets, R. I. Eglitis and G. Borstel, *Computational Materials Science*, 2004, **29**, 165–178.

162 T. S. Ercit, *Mineralogy and Petrology*, 1991, **43**, 217–223.

163 C. Valencia-Balvín, S. Pérez-Walton, G. M. Dalpian and J. M. Osorio-Guillén,

Computational Materials Science, 2014, **81**, 133–140.

164 D. Mezaoui, C. Michel, D. Groult and B. Raveau, *Materials Research Bulletin*, 1986, **21**, 1039–1044.

165 K. Kato, *Acta Crystallographica Section B Structural Crystallography and Crystal Chemistry*, 1976, **32**, 764–767.

166 K.-R. Tsai, P. M. Harris and E. N. Lassettre, *The Journal of Physical Chemistry*, 1956, **60**, 338–344.

167 A. K. Cheetham and C. N. R. Rao, *Acta Crystallographica Section B Structural Crystallography and Crystal Chemistry*, 1976, **32**, 1579–1580.

168 S. S. Batsanov, *Effects of Explosions on Materials: Modification and Synthesis Under High-Pressure Shock Compression*, Springer-Verlag, New York, 1994.

169 G. Meyer and R. Hoppe, *Zeitschrift for anorganische und allgemeine Chemie*, 1977, **436**, 75–86.

170 C. E. Rice and W. R. Robinson, *Journal of Solid State Chemistry*, 1977, **21**, 145–154.

171 D. Nishio-Hamane, M. Katagiri and K. Niwa, *High Pressure Research*, 2009, **29**, 379–388.

172 S. Naray-Szabo, *Zeitschrift für Kristallographie-Crystalline Materials*, 1938, **99**, 277–282.

173 S. Kondo, K. Tateishi and N. Ishizawa, *Japanese Journal of Applied*, 2008, **47**, 616.

174 S. Ovsyannikov, D. Trots and A. Kurnosov, *Journal of Physics:*, 2013, **25**, 385–401.

175 R. Cheary, *Acta Crystallographica Section B: Structural Science*, 1986, **42**, 229–236.

176 T. Araki and T. Zoltai, *Zeitschrift fur Kristallographie Kristallgeometrie Kristallphysik Kristallchemie*, 1969, **129**, 381.

177 A. Wadsley, *Acta Crystallographica*, 1961, **14**, 664–670.

178 V. P. Suritinkin and S. P. Sirotinkin, *Russian Journal of Inorganic Chemistry*, 1990, **35**, 1246–1248.

179 M. Okrusch, R. Hock, U. Schüssler, A. Brummer, M. Baier and H. Theisinger, *American Mineralogist*, 2003, **88**, 986–995.

180 A. Knyazev, M. Mączka and I. Ladenkov, *Journal of Solid State Chemistry*, 2012, **196**, 110–118.

181 M. Marezio and J. Remeika, *The Journal of Chemical Physics*, 1967, **46**, 1862–1865.

182 H. Saalfeld, *Neues Jahrbuch fur Mineralogie*, 1960, **95**, 1–87.

183 R. Blake and R. Hessevick, *American Mineralogist*, 1966, **51**, 123.

184 G. Langlet, *Comptes Rendus Hebdomadaires des Seances De L'Academie des Sciences*, 1964, **259**, 3769.

185 C. DoDinh and E. Bertaut, *Bulletin De La Societe Francaise Mineralogie et De Cristallographie*, 1965, **88**, 413.

186 F. A. Kröger and H. J. Vink, *Solid State Physics*, 1956, **3**, 307–435.

187 W. K. Hastings, *Biometrika*, 1970, **57**, 97–109.

188 B. A. Berg and A. Billoire, in *Wiley Encyclopedia of Computer Science and Engineering*, John Wiley & Sons, Inc., Hoboken, NJ, USA, 2007.

189 J. C. Walter and G. T. Barkema, *Physica A: Statistical Mechanics and its Applications*, 2015, **418**, 78–87.

190 D. C. Young, *Computational chemistry : A Practical Guide for Applying Techniques to Real World Problems*, Wiley, 2001.

191 R. W. Cheary, *Acta Crystallographica Section B Structural Science*, 1986, **42**, 229–236.

192 H. Faghihian, M. Ghannadi Marageh and H. Kazemian, *Applied Radiation and Isotopes*, 1999, **50**, 655–660.

193 I. Smičiklas, S. Dimović and I. Plećaš, *Applied Clay Science*, 2007, **35**, 139–144.

194 N. R. Mann and T. A. Todd, *Separation Science and Technology*, 2005, **39**, 2351–2371.

195 T. M. Nenoff, M. L. Balmer, A. Navrotsky, S. G. Thoma, J. L. Krumhansl and J. Miller, *Abstracts of Papers of the Ameican Chemical Society*, 1998, **215**, U688–U688.

196 A. Dyer, J. Newton, L. O'Brien and S. Owens, *Microporous and Mesoporous Materials*, 2009, **120**, 272–277.

197 A. Tripathi, D. G. Medvedev and A. Clearfield, *Journal of Solid State Chemistry*, 2005, **178**, 253–261.

198 S. Chitra, A. G. Shanmugamani, R. Sudha, S. Kalavathi and B. Paul, *Journal of Radioanalytical and Nuclear Chemistry*, 2017, **312**, 507–515.

199 M. K. Andrews and P. J. Workman, in *Environmental issues and Waste Management Technologies in the Ceramic and Nuclear Industries IV*, ed. G. Marra, JC and Chandler, American Ceramic Society, Cincinnati, 1999, vol. 93, pp. 171–177.

200 F. J. Torres, M. A. Tena and J. Alarcón, *Journal of the European Ceramic Society*, 2002, **22**, 1991–1994.

201 D. M. Poojary, R. A. Cahill and A. Clearfield, *Chemistry of Materials*, 1994, **6**, 2364–2368.

202 J. M. Loezos, T. A. Vanderah, A. R. Drews and R. S. Roth, *Powder Diffraction*, 2013, **12**, 117–125.

203 ASTM International, *Standard Test Method for Monolithic Waste Forms for Disposal of Radioactive Waste*, 1998.

204 O. P. Shrivastava and R. Srivastava, *Progress in Crystal Growth and Characterization of Materials*, 2002, **45**, 103–106.

205 J. Campbell, C. Hoenig, F. Bazan, F. Ryerson, M. Guinan, R. Van Konynenburg and R. Razsa, *Properties of Synroc-D Nuclear Waste Form: A State-of-the-Art Review, Review No. UCRL-53 240*, 1982.

206 K. L. Smith, G. R. Lumpkin, M. G. Blackford, R. A. Day and K. P. Hart, *Journal of Nuclear Materials*, 1992, **190**, 287–294.

207 Y. He, W. Bao and C. Song, *Journal of Nuclear Materials*, 2002, **305**, 202–208.

208 S. V Raman, *Journal of Materials Science*, 1998, **33**, 1887–1895.

The Immobilisation of Caesium and Strontium from Nuclear Waste Captured by IONSIV

Chapter 7 Appendices

George Day

Contents

Appendix 1

Chapter 3 Rietveld Refinements

Rietveld Refinement $Cs_2TiNb_6O_{18}$ (Solid-state method)

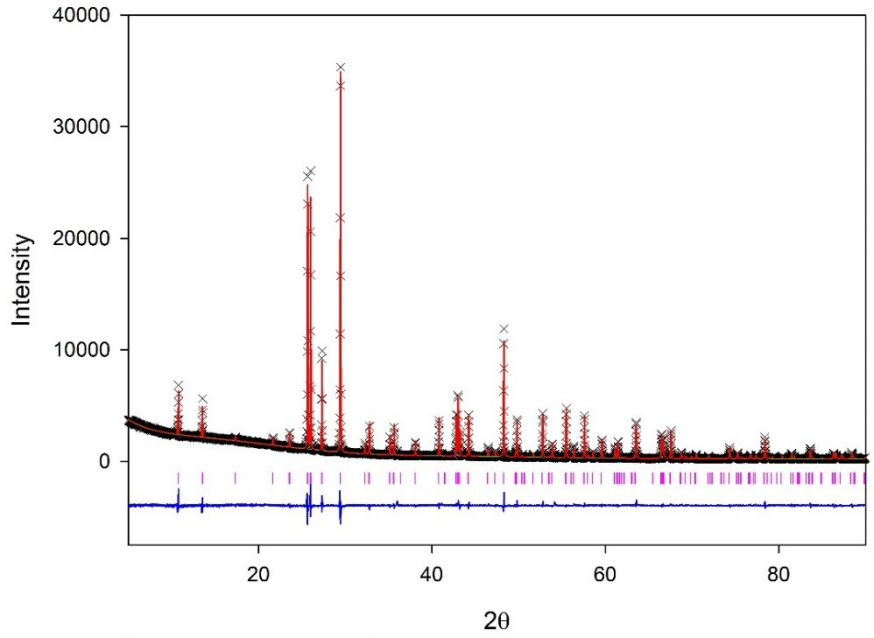

Figure 7.1 *Rietveld Refinement (GSAS Liveplot) for $Cs_2TiNb_6O_{18}$ (solid-state). Red line: calculated pattern, black crosses: experimental pattern, green line: background, blue line: difference curve. Pink ricks: $Cs_2TiNb_6O_{18}$*

Table 7.1 *Rietveld Refinement (GSAS) details for $Cs_2TiNb_6O_{18}$ (solid-state)*

χ^2	wRp	Rp
3.481	5.85 %	3.91 %
Phase	**Symmetry Setting**	**Space Group**
$Cs_2TiNb_6O_{18}$	Trigonal	*P*-3*m*1

Phase Information	***a***	***b***	***c***	***V***	
	7.52862(5)	7.52862	8.18147(7)	401.599(7)	
	α	***β***	***γ***		
	90	90	120		
Atom	***x***	***y***	***z***	**Occupancy**	**U_{iso}**
Cs	0.3333	0.6667	0.63257(35)	1	0.0308(7)
Nb1	0	0	0.5	0.787(5)	0.0137(19)
Ti1	0	0	0.5	0.073(5)	0.0137(19)
Nb2	0.16957(12)	-0.16957(12)	0.14717(24)	0.8688(8)	0.0107(5)
Ti2	0.16957(12)	-0.16957(12)	0.14717(24)	0.1546(8)	0.0107(5)
O1	0.447	-0.447	0.16	1	0.01
O2	0.861	0.861	0.11	1	0.01
O3	0.12	-0.12	0.37	1	0.01

Rietveld Refinement $Cs_2TiNb_6O_{18}$ (Sol-gel method)

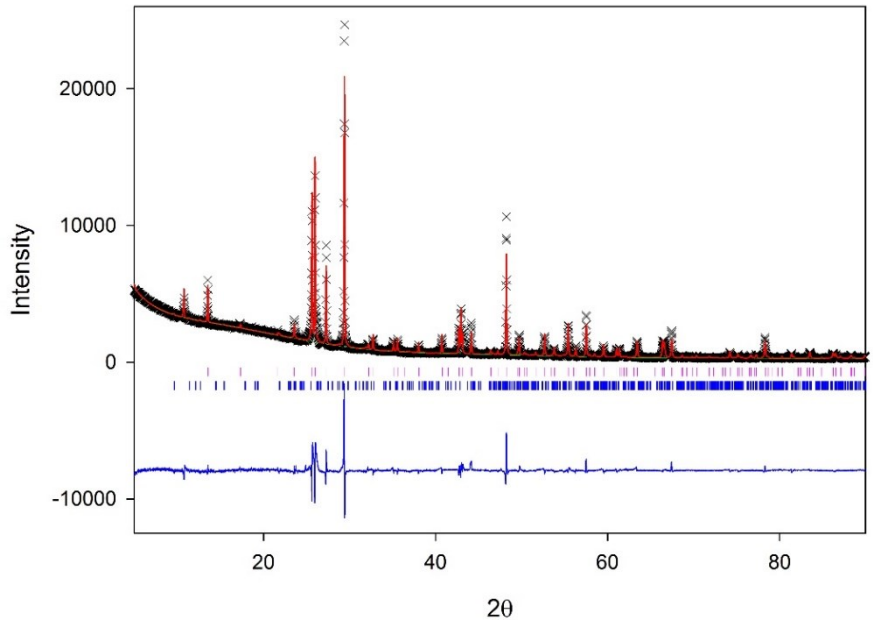

Figure 7.2 *Rietveld Refinement (GSAS Liveplot) for $Cs_2TiNb_6O_{18}$ (sol-gel). Pink ticks: $Cs_2TiNb_6O_{18}$ and blue ticks: $Ti_2Nb_{10}O_{29}$*

Table 7.2 *Rietveld Refinement (GSAS) details for $Cs_2TiNb_6O_{18}$ (sol-gel)*

χ^2	wRp	Rp
12.78	9.93 %	6.01 %

Phase	Symmetry Setting	Space Group
$Cs_2TiNb_6O_{18}$	Trigonal	*P*-3*m*1

Phase Information	***a***	***b***	***c***	***V***	
	7.53707(16)	7.53707	8.19577(25)	403.204(22)	
	α	***β***	***γ***		
	90	90	120		
Atom	***x***	***y***	***z***	**Occupancy**	**Uiso**
Cs	0.3333	0.6667	0.6307(11)	1	0.0322(19)
Nb1	0	0	0.5	0.790(12)	0.020(6)
Ti1	0	0	0.5	0.076(12)	0.020(6)
Nb2	0.16867(31)	-0.16867(31)	0.1420(7)	0.8681(21)	-0.0014(11)
Ti2	0.16867(31)	-0.16867(31)	0.1420(7)	0.1541(21)	-0.0014(11)
O1	0.447	-0.447	0.16	1	0.01
O2	0.861	0.861	0.11	1	0.01
O3	0.12	-0.12	0.37	1	0.01

Phase	Symmetry Setting	Space Group
$Ti_2Nb_{10}O_{29}$	Monoclinic	*C*2/*m*

Phase Information	*a*	*b*	*c*	*V*	
	15.615(24)	3.9056(32)	20.392(14)	1112.4(13)	
	α	***β***	***γ***		
	90	116.56(14)	90		
Atom	***x***	***y***	***z***	**Occupancy**	**U_{iso}**
Nb1	0.099	0	0.068	0.833	0.01
Nb2	0.096	0	0.697	0.833	0.01
Nb3	0.097	0	0.881	0.833	0.01
Nb4	0.367	0	0.149	0.833	0.01
Nb5	0.366	0	0.779	0.833	0.01
Nb6	0.366	0	0.964	0.833	0.01
Ti1	0.099	0	0.068	0.167	0.01
Ti2	0.096	0	0.697	0.167	0.01
Ti3	0.097	0	0.881	0.167	0.01
Ti4	0.367	0	0.149	0.167	0.01
Ti5	0.366	0	0.779	0.167	0.01
Ti6	0.3666	0	0.964	0.167	0.01
O1	0.5	0	0	1	0.01
O2	0.066	0	0.166	1	0.01
O3	0.038	0	0.358	1	0.01
O4	0.086	0	0.602	1	0.01
O5	0.09	0	0.784	1	0.01
O6	0.074	0	0.971	1	0.01
O7	0.22	0	0.106	1	0.01
O8	0.228	0	0.73	1	0.01
O9	0.222	0	0.92	1	0.01
O10	0.362	0	0.055	1	0.01
O11	0.364	0	0.247	1	0.01
O12	0.364	0	0.463	1	0.01
O13	0.364	0	0.678	1	0.01
O14	0.364	0	0.869	1	0.01
O15	0.5	0	0.188	1	0.01

Weight Fractions	
Phase	wt%
$Cs_2TiNb_6O_{18}$	**86.232(12)**
$Ti_2Nb_{10}O_{29}$	**13.77(12)**

Rietveld Refinement $BaTi_2Nb_5O_{18}$ (Solid-state method)

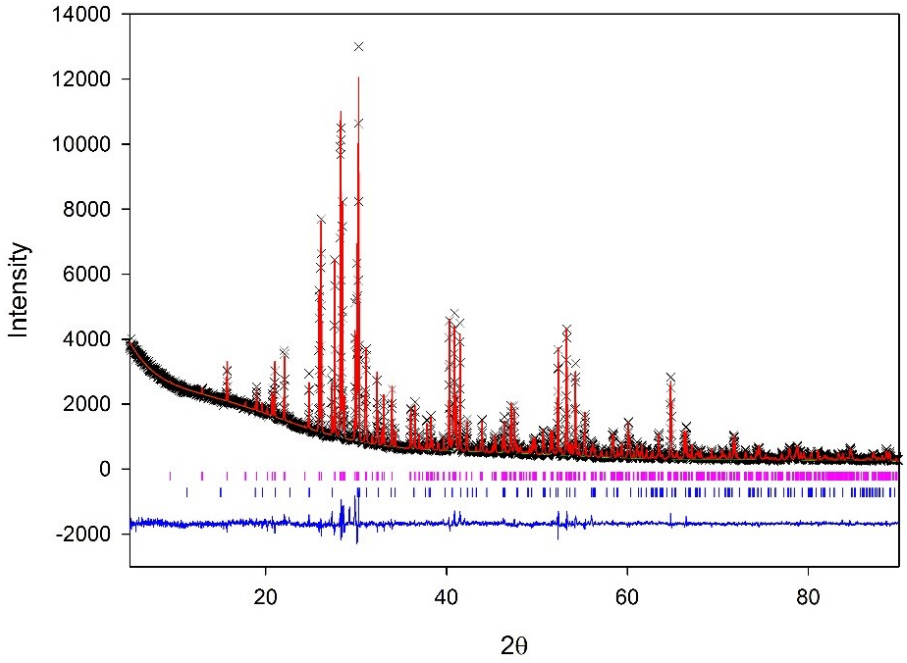

Figure 7.3 *Rietveld Refinement (GSAS Liveplot) for $Ba_2Ti_3Nb_4O_{18}$ (solid-state) Pink ticks: $Ba_2Ti_3Nb_4O_{18}$ and blue ticks: $Ba_3Nb_4Ti_4O_{21}$*

Table 7.3 *Rietveld Refinement details for $Ba_2Ti_3Nb_4O_{18}$ (solid-state)*

χ^2	wRp	Rp
3.006	5.28 %	3.66 %

Phase	Symmetry Setting	Space Group
$Ba_2Ti_3Nb_4O_{18}$	Monoclinic	$P2_1/c$

Phase Information	*a*	*b*	*c*	*V*	
	10.00113(11)	9.96209(11)	7.31243(8)	678.784(17)	
	α	*β*	*γ*		
	90	111.3007(7)	90		
Atom	***x***	***y***	***z***	**Occupancy**	**U_{iso}**
Ba	0.20456(33)	0.08988(22)	0.0631(4)	1	0.0153(8)
Nb1	0.1049(4)	0.7471(4)	0.3504(6)	1	0.0248(14)
Ti1	0	0.5	0	1	-0.0257(28)
Nb2	0.5194(4)	0.2719(5)	0.5091(6)	0.484(4)	0.0031(23)
Ti2	0.5194(4)	0.2719(5)	0.5091(6)	0.484(4)	0.0031(23)
Nb3	0.3803(5)	0.0148(4)	0.6071(7)	0.516(4)	0.0164(23)
Ti3	0.3803(5)	0.0148(4)	0.6071(7)	0.516(4)	0.0164(23)
O1	0.4047	0.0907	0.8515	1	0.01
O2	0.5814	0.084	0.6211	1	0.01
O3	0.8074	0.0709	0.4761	1	0.01
O4	0.9843	0.0883	0.2516	1	0.01
O5	0.0697	0.1617	0.6458	1	0.01
O6	0.3237	0.1719	0.4633	1	0.01

O7	0.5096	0.1626	0.2545	1	0.01
O8	0.7001	0.174	0.0459	1	0.01
O9	0.899	0.1688	0.8755	1	0.01

Phase	**Symmetry Setting**	**Space Group**
$Ba_3Nb_4Ti_4O_{21}$	Hexagonal	$P6_3/mcm$

Phase Information	***a***	***b***	***c***	***V***	
	9.03753(19)	9.03753(19)	11.7716(4)	832.659(34)	
	α	***β***	***γ***		
	90	90	120		
Atom	***x***	***y***	***z***	**Occupancy**	**U_{iso}**
Ba	0.596	0	0.25	1	0.01
Nb1	0.244	0	0.093	0.5	0.01
Ti1	0.244	0	0.093	0.5	0.01
Nb2	0.3333	0.6667	0	0.5	0.01
Ti2	0.3333	0.6667	0	0.5	0.01
O1	0.238	0	0.25	1	0.01
O2	0.795	0	0.086	1	0.01
O3	0.173	0.507	0.107	1	0.01

Weight fractions	
Phase	wt. %
$Ba_2Ti_3Nb_4O_{18}$	**89.838(5)**
$Ba_3Nb_4Ti_4O_{21}$	**10.162(2)**

Rietveld Refinement $CsBaTi_2Nb_5O_{18}$ (Solid-state method)

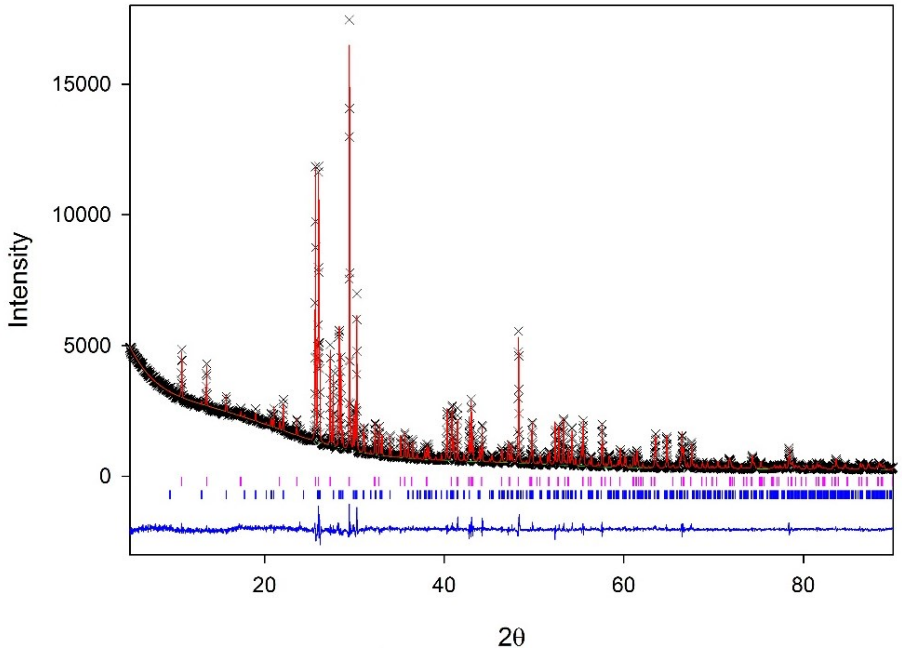

Figure 7.4 *Rietveld Refinement (GSAS Liveplot) for $CsBaTi_2Nb_5O_{18}$ (solid-state). Pink ticks: $Cs_2TiNb_6O_{18}$ and blue ticks: $Ba_2Ti_3Nb_4O_{18}$*

Table 7.4 *Rietveld Refinement details for $CsBaTi_2Nb_5O_{18}$ (solid-state)*

χ^2	wRp	Rp
3.264	5.15 %	3.58 %

Phase	Symmetry Setting	Space Group
$Cs_2TiNb_6O_{18}$	Trigonal	*P*-3*m*1

Phase Information	***a***	***b***	***c***	***V***	
	7.52798(8)	7.52798(8)	8.18296(12)	401.604(11)	
	α	***β***	***γ***		
	90	90	120		
Atom	***x***	***y***	***z***	**Occupancy**	**U_{iso}**
Cs	0.3333	0.6667	0.6326(7)	1	0.0326(13)
Nb1	0	0	0.5	0.795(9)	0.015(4)
Ti1	0	0	0.5	0.081(9)	0.015(4)
Nb2	0.17026(22)	-0.17026(22)	0.1475(4)	0.8674(14)	0.0080(8)
Ti2	0.17026(22)	-0.17026(22)	0.1475(4)	0.1534(14)	0.0080(8)
O1	0.447	-0.447	0.16	1	0.01
O2	0.861	0.861	0.11	1	0.01
O3	0.12	-0.12	0.37	1	0.01

Phase	Symmetry Setting	Space Group
$Ba_2Ti_3Nb_4O_{18}$	Monoclinic	$P2_1/c$

Phase Information	***a***	***b***	***c***	***V***	
	10.00074(15)	9.96186(16)	7.31464(12)	678.930(19)	
	α	β	γ		
	90	111.3042(12)	90		
Atom	***x***	***y***	***z***	**Occupancy**	**Uiso**
Ba	0.20448	0.08876	0.06374	1	0.01
Nb1	0.10467	0.75127	0.35107	1	0.01
Ti1	0	0.5	0	1	0.01
Nb2	0.5182	0.2697	0.5095	0.5	0.01
Ti2	0.5182	0.2697	0.5095	0.5	0.01
Nb3	0.3795	0.0151	0.6055	0.5	0.01
Ti3	0.3795	0.0151	0.6055	0.5	0.01
O1	0.4047	0.0907	0.8515	1	0.01
O2	0.5814	0.084	0.6211	1	0.01
O3	0.8074	0.0709	0.4761	1	0.01
O4	0.9843	0.0883	0.2516	1	0.01
O5	0.0697	0.1617	0.6458	1	0.01
O6	0.3237	0.1719	0.4633	1	0.01
O7	0.5096	0.1626	0.2545	1	0.01
O8	0.7001	0.174	0.0459	1	0.01
O9	0.899	0.1688	0.8755	1	0.01

Weight fraction	
Phase	Wt. %
$Cs_2TiNb_6O_{18}$	**50.953(2)**
$Ba_2Ti_3Nb_4O_{18}$	**49.047(2)**

Rietveld Refinement $Cs_{1.4}Ba_{0.6}Ti_{1.6}Nb_{5.4}O_{18}$ (Solid-state method)

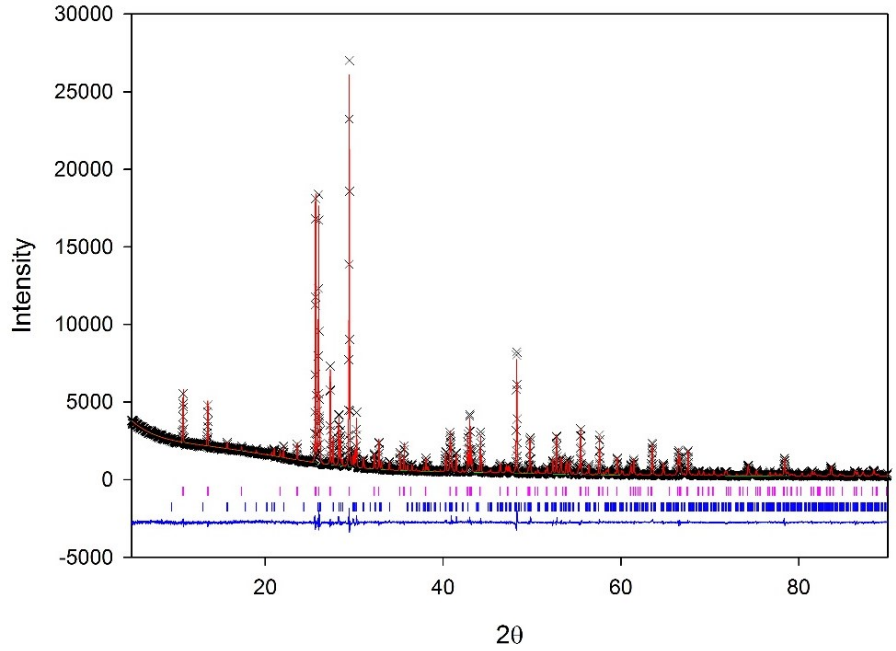

Figure 7.5 *Rietveld Refinement (GSAS Liveplot) for $Cs_{1.4}Ba_{0.6}Ti_{1.6}Nb_{5.4}O_{18}$ (solid-state) Pink ticks: $Cs_2TiNb_6O_{18}$ and blue ticks: $Ba_2Ti_3Nb_4O_{18}$*

Table 7.5 *Rietveld Refinement details for $Cs_{1.4}Ba_{0.6}Ti_{1.6}Nb_{5.4}O_{18}$ (solid-state)*

χ^2	wRp	Rp
2.756	5.13 %	3.60 %

Phase	Symmetry Setting	Space Group
$Cs_2TiNb_6O_{18}$	Trigonal	*P*-3*m*1

Phase Information	***a***	***b***	***c***	***V***	
	7.52921(6)	7.52921(6)	8.18432(8)	401.802(7)	
	α	***β***	***γ***		
	90	90	120		
Atom	***x***	***y***	***z***	**Occupancy**	**U_{iso}**
Cs	0.3333	0.6667	0.6339(4)	1	0.0345(8)
Nb1	0	0	0.5	0.805(5)	0.0188(21)
Ti1	0	0	0.5	0.091(5)	0.0188(21)
Nb2	0.16955(13)	-0.16955(13)	0.14642(26)	0.8657(9)	0.0105(5)
Ti2	0.16955(13)	-0.16955(13)	0.14642(26)	0.1517(9)	0.0105(5)
O1	0.447	-0.447	0.16	1	0.01
O2	0.861	0.861	0.11	1	0.01
O3	0.12	-0.12	0.37	1	0.01

Phase	Symmetry Setting	Space Group
$Ba_2Ti_3Nb_4O_{18}$	Monoclinic	$P2_1/c$

Phase Information	***a***	***b***	***c***	***V***	
	10.00397(18)	9.96445(19)	7.31424(14)	679.286(18)	
	α	***β***	***γ***		
	90	111.3049(16)	90		
Atom	***x***	***y***	***z***	**Occupancy**	**U_{iso}**
Ba	0.20448	0.08876	0.06374	1	0.01
Nb1	0.10467	0.75127	0.35107	1	0.01
Ti1	0	0.5	0	1	0.01
Nb2	0.5182	0.2697	0.5095	0.5	0.01
Ti2	0.5182	0.2697	0.5095	0.5	0.01
Nb3	0.3795	0.0151	0.6055	0.5	0.01
Ti3	0.3795	0.0151	0.6055	0.5	0.01
O1	0.4047	0.0907	0.8515	1	0.01
O2	0.5814	0.084	0.6211	1	0.01
O3	0.8074	0.0709	0.4761	1	0.01
O4	0.9843	0.0883	0.2516	1	0.01
O5	0.0697	0.1617	0.6458	1	0.01
O6	0.3237	0.1719	0.4633	1	0.01
O7	0.5096	0.1626	0.2545	1	0.01
O8	0.7001	0.174	0.0459	1	0.01
O9	0.899	0.1688	0.8755	1	0.01

Weight Fraction	
Phase	Wt. %
$Cs_2TiNb_6O_{18}$	**71.61(09)**
$Ba_2Ti_3Nb_4O_{18}$	**28.39(2)**

Rietveld Refinement $Cs_{1.5}Ba_{0.5}Ti_{1.6}Nb_{5.5}O_{18}$ (Solid-state method)

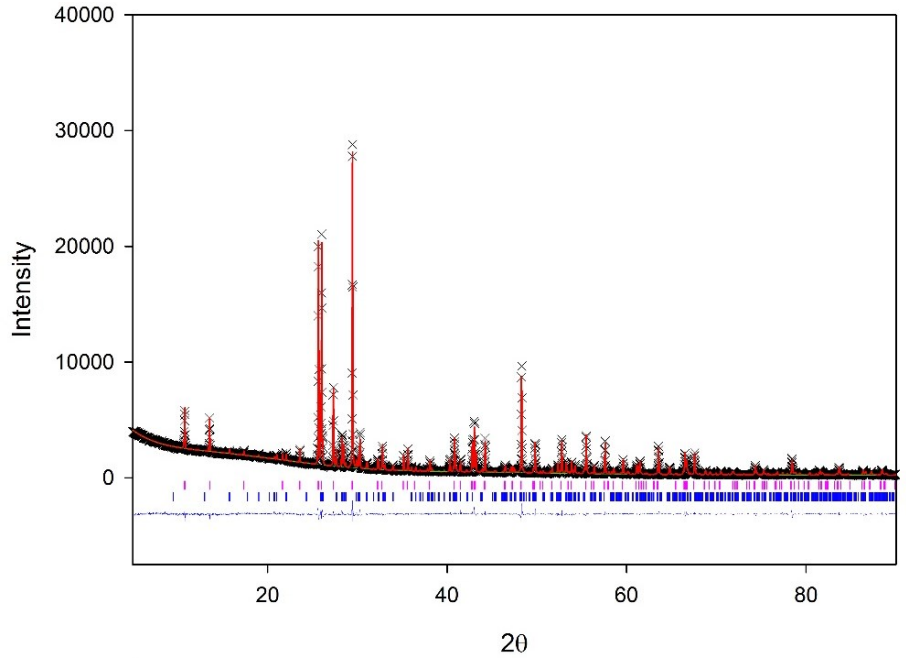

Figure 7.6 *Rietveld Refinement (GSAS Liveplot) for $Cs_{1.5}Ba_{0.5}Ti_{1.6}Nb_{5.5}O_{18}$ (solid-state). Pink ticks: $Cs_2TiNb_6O_{18}$ and blue ticks: $Ba_2Ti_3Nb_4O_{18}$*

Table 7.6 *Rietveld Refinement details for $Cs_{1.5}Ba_{0.5}Ti_{1.6}Nb_{5.5}O_{18}$ (solid-state)*

χ^2	wRp	Rp
2.959	5.2 %	3.63 %

Phase	Symmetry Setting	Space Group
$Cs_2TiNb_6O_{18}$	Trigonal	*P*-3*m*1

Phase Information	***a***	***b***	***c***	***V***	
	7.52622(5)	7.52622	8.18054(7)	401.297(7)	
	α	***β***	***γ***		
	90	90	120		
Atom	***x***	***y***	***z***	**Occupancy**	**U_{iso}**
Cs	0.3333	0.6667	0.6338(4)	1	0.0344(8)
Nb1	0	0	0.5	0.791(5)	0.0153(20)
Ti1	0	0	0.5	0.077(5)	0.0153(20)
Nb2	0.16958(13)	-0.16958(13)	0.14656(26)	0.8680(8)	0.0111(5)
Ti2	0.16958(13)	-0.16958(13)	0.14656(26)	0.1540(8)	0.0111(5)
O1	0.447	-0.447	0.16	1	0.01
O2	0.861	0.861	0.11	1	0.01
O3	0.12	-0.12	0.37	1	0.01

Phase	Symmetry Setting	Space Group
$Ba_2Ti_3Nb_4O_{18}$	Monoclinic	$P2_1/c$

Phase Information	***a***	***b***	***c***	***V***	
	10.00037(21)	9.96140(22)	7.31017(17)	679.395(34)	
	α	***β***	***γ***		
	90	111.3038(19)	90		
Atom	***x***	***y***	***z***	**Occupancy**	**U_{iso}**
Ba	0.20448	0.08876	0.06374	1	0.01
Nb1	0.10467	0.75127	0.35107	1	0.01
Ti1	0	0.5	0	1	0.01
Nb2	0.5182	0.2697	0.5095	0.5	0.01
Ti2	0.5182	0.2697	0.5095	0.5	0.01
Nb3	0.3795	0.0151	0.6055	0.5	0.01
Ti3	0.3795	0.0151	0.6055	0.5	0.01
O1	0.4047	0.0907	0.8515	1	0.01
O2	0.5814	0.084	0.6211	1	0.01
O3	0.8074	0.0709	0.4761	1	0.01
O4	0.9843	0.0883	0.2516	1	0.01
O5	0.0697	0.1617	0.6458	1	0.01
O6	0.3237	0.1719	0.4633	1	0.01
O7	0.5096	0.1626	0.2545	1	0.01
O8	0.7001	0.174	0.0459	1	0.01
O9	0.899	0.1688	0.8755	1	0.01

Weight Fraction	
Phase	Wt. %
$Cs_2TiNb_6O_{18}$	**76.724(7)**
$Ba_2Ti_3Nb_4O_{18}$	**23.28(2)**

Rietveld Refinement $Cs_{1.6}Ba_{0.4}Ti_{1.4}Nb_{5.6}O_{18}$ (Solid-state method)

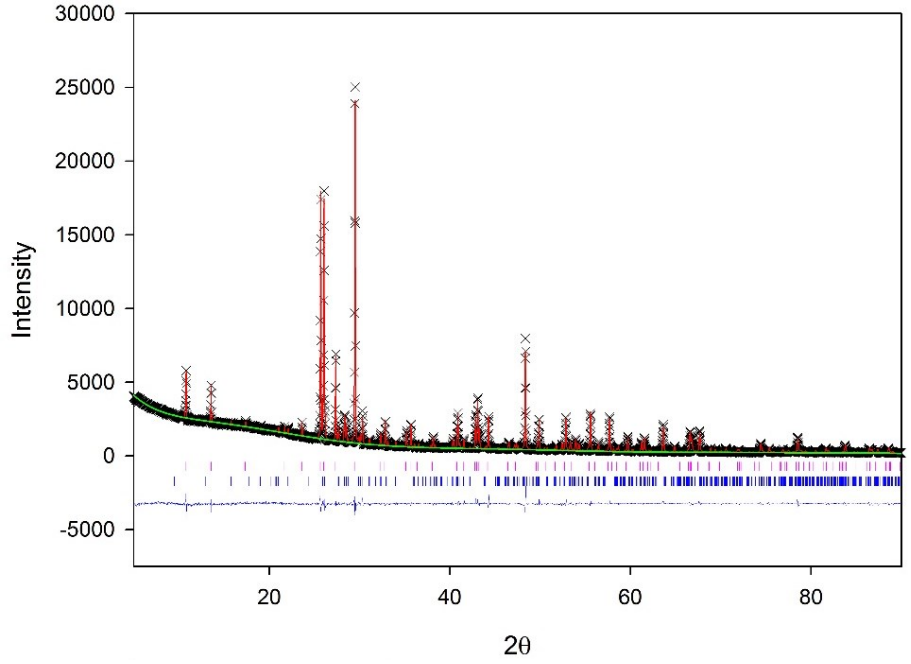

Figure 7.7 *Rietveld Refinement (GSAS Liveplot) for $Cs_{1.6}Ba_{0.4}Ti_{1.4}Nb_{5.6}O_{18}$ (solid-state) Pink ticks: $Cs_2TiNb_6O_{18}$ and blue ticks: $Ba_2Ti_3Nb_4O_{18}$*

Table 7.7 *Rietveld Refinement details for $Cs_{1.6}Ba_{0.4}Ti_{1.4}Nb_{5.6}O_{18}$ (solid-state)*

χ^2	wRp	Rp
3.066	5.36 %	3.57 %

Phase	Symmetry Setting	Space Group
$Cs_2TiNb_6O_{18}$	Trigonal	*P*-3*m*1

Phase Information	*a*	*b*	*c*	*V*	
	7.51870(7)	7.51870(7)	8.17232(10)	400.094(9)	
	α	*β*	*γ*		
	90	90	120		
Atom	***x***	***y***	***z***	**Occupancy**	**U_{iso}**
Cs	0.3333	0.6667	0.6338(4)	1	0.0375(9)
Nb1	0	0	0.5	0.788(5)	0.0157(22)
Ti1	0	0	0.5	0.074(5)	0.0157(22)
Nb2	0.16963(14)	-0.16963(14)	0.14689(29)	0.8684(9)	0.0143(6)
Ti2	0.16963(14)	-0.16963(14)	0.14689(29)	0.1544(9)	0.0143(6)
O1	0.447	-0.447	0.16	1	0.01
O2	0.861	0.861	0.11	1	0.01
O3	0.12	-0.12	0.37	1	0.01

Phase	Symmetry Setting	Space Group
$Ba_2Ti_3Nb_4O_{18}$	Monoclinic	$P2_1/c$

Phase Information	***a***	***b***	***c***	***V***	
	9.98936(33)	9.9508(4)	7.30418(26)	676.438(29)	
	α	***β***	***γ***		
	90	111.3043(31)	90		
Atom	***x***	***y***	***z***	**Occupancy**	**U_{iso}**
Ba	0.20448	0.08876	0.06374	1	0.01
Nb1	0.10467	0.75127	0.35107	1	0.01
Ti1	0	0.5	0	1	0.01
Nb2	0.5182	0.2697	0.5095	0.5	0.01
Ti2	0.5182	0.2697	0.5095	0.5	0.01
Nb3	0.3795	0.0151	0.6055	0.5	0.01
Ti3	0.3795	0.0151	0.6055	0.5	0.01
O1	0.4047	0.0907	0.8515	1	0.01
O2	0.5814	0.084	0.6211	1	0.01
O3	0.8074	0.0709	0.4761	1	0.01
O4	0.9843	0.0883	0.2516	1	0.01
O5	0.0697	0.1617	0.6458	1	0.01
O6	0.3237	0.1719	0.4633	1	0.01
O7	0.5096	0.1626	0.2545	1	0.01
O8	0.7001	0.174	0.0459	1	0.01
O9	0.899	0.1688	0.8755	1	0.01

Weight Fractions	
Phase	Wt. %
$Cs_2TiNb_6O_{18}$	**80.181(7)**
$Ba_2Ti_3Nb_4O_{18}$	**19.82(2)**

Rietveld Refinement $Cs_{1.7}Ba_{0.3}Ti_{1.3}Nb_{5.7}O_{18}$ (Solid-state method)

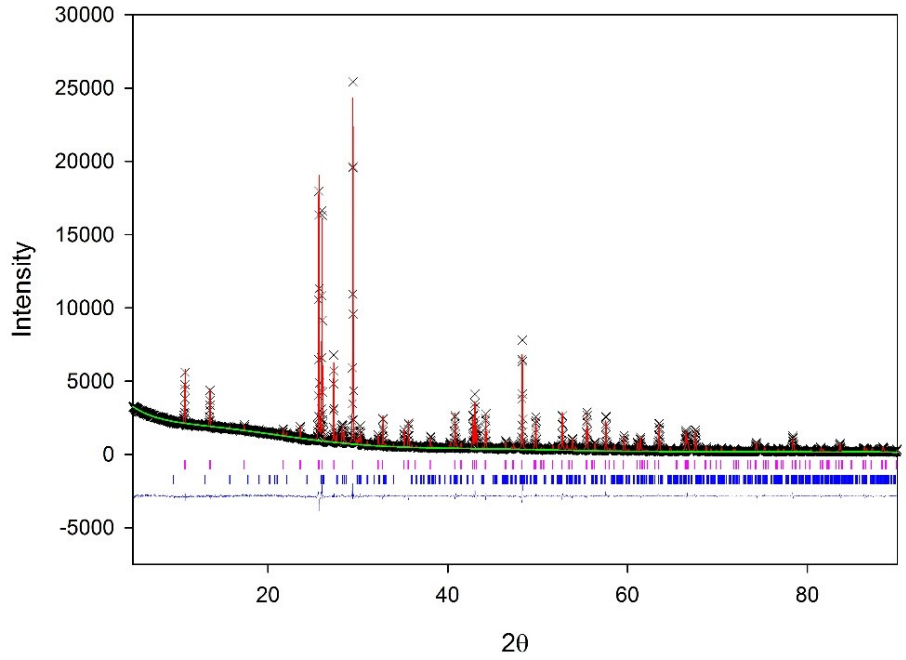

Figure 7.8 *Rietveld Refinement (GSAS Liveplot) for $Cs_{1.7}Ba_{0.3}Ti_{1.3}Nb_{5.7}O_{18}$ (solid-state) Pink ticks: $Cs_2TiNb_6O_{18}$ and blue ticks: $Ba_2Ti_3Nb_4O_{18}$*

Table 7.8 *Rietveld Refinement details for $Cs_{1.7}Ba_{0.3}Ti_{1.3}Nb_{5.7}O_{18}$ (solid-state)*

χ^2	wRp	Rp
2.438	5.29 %	3.74 %

Phase	Symmetry Setting	Space Group
$Cs_2TiNb_6O_{18}$	Trigonal	P -3 m 1

Phase Information	*a*	*b*	*c*	*V*	
	7.52815(5)	7.52815(5)	8.18430(7)	401.688(7)	
	α	*β*	*γ*		
	90	90	120		
Atom	**x**	**y**	**z**	**Occupancy**	**Uiso**
Cs	0.3333	0.6667	0.6326(4)	1	0.0375(8)
Nb1	0	0	0.5	0.783(5)	0.0148(19)
Ti1	0	0	0.5	0.069(5)	0.0148(19)
Nb2	0.16957(12)	-0.16957(12)	0.14717(24)	0.8693(8)	0.0146(5)
Ti2	0.16957(12)	-0.16957(12)	0.14717(24)	0.1553(8)	0.0146(5)
O1	0.447	-0.447	0.16	1	0.01
O2	0.861	0.861	0.11	1	0.01
O3	0.12	-0.12	0.37	1	0.01

Phase	Symmetry Setting	Space Group
$Ba_2Ti_3Nb_4O_{18}$	Monoclinic	$P2_1/c$

Phase Information	***a***	***b***	***c***	***V***	
	10.0053(4)	9.9655(5)	7.31398(33)	679.395(34)	
	α	***β***	***γ***		
	90	111.311(4)	90		
Atom	***x***	***y***	***z***	**Occupancy**	**U_{iso}**
Ba	0.20448	0.08876	0.06374	1	0.01
Nb1	0.10467	0.75127	0.35107	1	0.01
Ti1	0	0.5	0	1	0.01
Nb2	0.5182	0.2697	0.5095	0.5	0.01
Ti2	0.5182	0.2697	0.5095	0.5	0.01
Nb3	0.3795	0.0151	0.6055	0.5	0.01
Ti3	0.3795	0.0151	0.6055	0.5	0.01
O1	0.4047	0.0907	0.8515	1	0.01
O2	0.5814	0.084	0.6211	1	0.01
O3	0.8074	0.0709	0.4761	1	0.01
O4	0.9843	0.0883	0.2516	1	0.01
O5	0.0697	0.1617	0.6458	1	0.01
O6	0.3237	0.1719	0.4633	1	0.01
O7	0.5096	0.1626	0.2545	1	0.01
O8	0.7001	0.174	0.0459	1	0.01
O9	0.899	0.1688	0.8755	1	0.01

Weight Fraction	
Phases	Wt. %
$Cs_2TiNb_6O_{18}$	**85.530(5)**
$Ba_2Ti_3Nb_4O_{18}$	**14.47(2)**

Rietveld Refinement $Cs_{1.85}Ba_{0.15}Ti_{1.15}Nb_{5.85}O_{18}$ (Solid-state method)

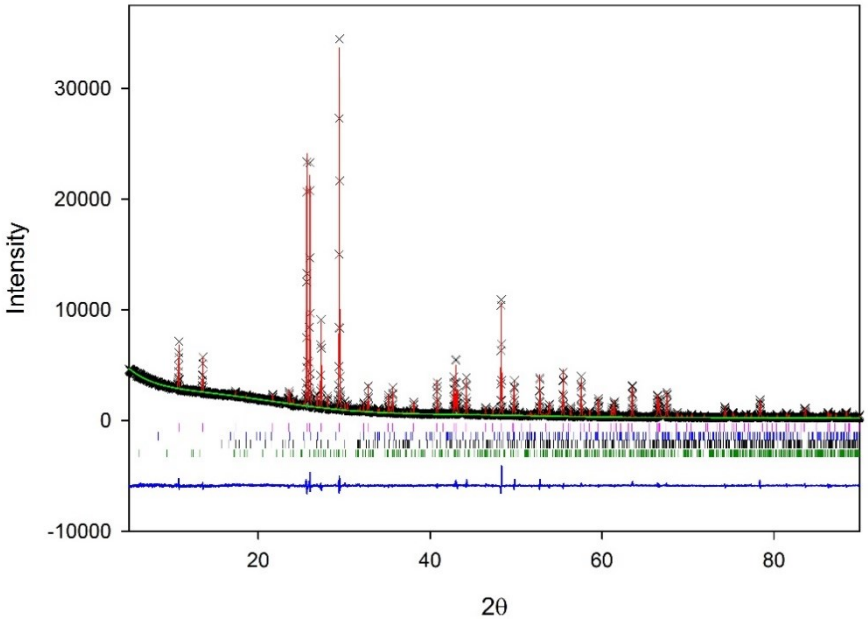

Figure 7.9 *Rietveld Refinement (GSAS Liveplot) $Cs_{1.85}Ba_{0.15}Ti_{1.15}Nb_{5.85}O_{18}$ (solid-state). Pink ticks: $Cs_2TiNb_6O_{18}$, blue ticks: $BaTi_3Nb_4O_{17}$, dark red ticks: $BaTiNb_4O_{13}$ and green ticks: $Ti_2Nb_{10}O_{29}$*

Table 7.9 *Rietveld Refinement details for $Cs_{1.85}Ba_{0.15}Ti_{1.15}Nb_{5.85}O_{18}$ (solid-state)*

χ^2	wRp	Rp
2.977	4.99 %	3.35 %

Phase	Symmetry Setting	Space Group
$Cs_2TiNb_6O_{18}$	Trigonal	*P*-3*m*1

Phase Information	***a***	***b***	***c***	***V***	
	7.52979(4)	7.52979(4)	8.18412(6)	401.854(6)	
	α	***β***	***γ***		
	90	90	120		
Atom	***x***	***y***	***z***	**Occupancy**	**U_{iso}**
Cs	0.3333	0.6667	0.6336(4)	1	0.0344(7)
Nb1	0	0	0.5	0.788(5)	0.0109(18)
Ti1	0	0	0.5	0.074(5)	0.0109(18)
Nb2	0.16944(12)	-0.16944(12)	0.14657(24)	0.8685(8)	0.0105(5)
Ti2	0.16944(12)	-0.16944(12)	0.14657(24)	0.1545(8)	0.0105(5)
O1	0.447	-0.447	0.16	1	0.01
O2	0.861	0.861	0.11	1	0.01
O3	0.12	-0.12	0.37	1	0.01

Phase	Symmetry Setting	Space Group
$BaTi_3Nb_4O_{17}$	Orthorhombic	*Cmcm*

Phase Information	***a***	***b***	***c***	***V***	
	6.63262(31)	8.9647(7)	21.1380(14)	1256.85(11)	
	α	***β***	***γ***		
	90	90	90		
Atom	***x***	***y***	***z***	**Occupancy**	**Uiso**
Ba	0	0.9807	0.25	1	0.01
Nb1	0	0.1026	0.0568	0.6	0.01
Ti1	0	0.1026	0.0568	0.4	0.01
Nb2	0	0.3446	0.3404	0.225	0.01
Ti2	0	0.3446	0.3404	0.775	0.01
Nb3	0	0.7359	0.3878	0.3	0.01
Ti3	0	0.7359	0.3878	0.7	0.01
Nb4	0	0.5	0.5	0.75	0.01
Ti4	0	0.5	0.5	0.25	0.01
O1	0	0.546	0.3365	1	0.01
O2	0	0.304	0.25	1	0.01
O3	0	0.315	0.4549	1	0.01
O4	0	0.889	0.4539	1	0.01
O5	0	0.12	0.357	1	0.01
O6	0.195	0.197	0.6571	1	0.01
O7	0.28	0.096	0.4562	1	0.01

Phase	Symmetry Setting	Space Group
$BaTiNb_4O_{13}$	Orthorhombic	*Pbcm*

Phase Information	***a***	***b***	***c***	***V***	
	5.6306(5)	10.7171(8)	16.4567(11)	993.05(8)	
	α	***β***	***γ***		
	90	90	90		
Atom	***x***	***y***	***z***	**Occupancy**	**U_{iso}**
Ba	0.2056	0.8256	0.25	1	0.01
Nb1	0.1615	0.4378	0.0765	0.8	0.01
Ti1	0.1615	0.4378	0.0765	0.2	0.01
Nb2	0.3431	0.1341	0.137	0.8	0.01
Ti2	0.3431	0.1341	0.137	0.2	0.01
Nb3	0.6651	0.25	0	0.8	0.01

Ti3	0.6651	0.25	0	0.2	0.01
O1	0.09	0.016	0.138	1	0.01
O2	0.127	0.282	0.126	1	0.01
O3	0.124	0.604	0.004	1	0.01
O4	0.369	0.154	0.25	1	0.01
O5	0.366	0.127	0.012	1	0.01
O6	0.592	0.004	0.136	1	0.01
O7	0.606	0.251	0.111	1	0.01

Phase	**Symmetry Setting**	**Space Group**
$Ti_2Nb_{10}O_{29}$	Monoclinic	*A*12/*m*1

Phase Information	***a***	***b***	***c***	***V***	
	15.557(4)	3.8109(8)	20.519(5)	1115.38(32)	
	α	***β***	***γ***		
	90	113.526(23)	90		
Atom	***x***	***y***	***z***	**Occupancy**	**Uiso**
Nb1	0.099	0	0.068	0.833	0.01
Ti1	0.099	0	0.068	0.167	0.01
Nb2	0.096	0	0.697	0.833	0.01
Ti2	0.096	0	0.697	0.167	0.01
Nb3	0.097	0	0.881	0.833	0.01
Ti3	0.097	0	0.881	0.167	0.01
Nb4	0.367	0	0.149	0.833	0.01
Ti4	0.367	0	0.149	0.167	0.01
Nb5	0.366	0	0.779	0.833	0.01
Ti5	0.366	0	0.779	0.167	0.01
Nb5	0.366	0	0.964	0.833	0.01
Ti5	0.366	0	0.964	0.167	0.01
O1	0.5	0	0	1	0.01
O2	0.066	0	0.166	1	0.01
O3	0.038	0	0.358	1	0.01
O4	0.086	0	0.602	1	0.01
O5	0.09	0	0.784	1	0.01
O6	0.074	0	0.971	1	0.01
O7	0.22	0	0.106	1	0.01
O8	0.228	0	0.73	1	0.01
O9	0.222	0	0.92	1	0.01
O10	0.362	0	0.055	1	0.01
O11	0.364	0	0.247	1	0.01

O12	0.364	0	0.463	1	0.01
O13	0.364	0	0.678	1	0.01
O14	0.364	0	0.869	1	0.01
O15	0.5	0	0.188	1	0.01

Weight Fraction	
Phases	**Wt. %**
$Cs_2TiNb_6O_{18}$	**88.831(4)**
$BaTi_3Nb_4O_{17}$	**4.98(2)**
$BaTiNb_4O_{13}$	**5.28(2)**
$Ti_2Nb_{10}O_{29}$	**0.92(1)**

Rietveld Refinement $Cs_{1.9}Ba_{0.1}Ti_{1.1}Nb_{5.9}O_{18}$(Solid-state method)

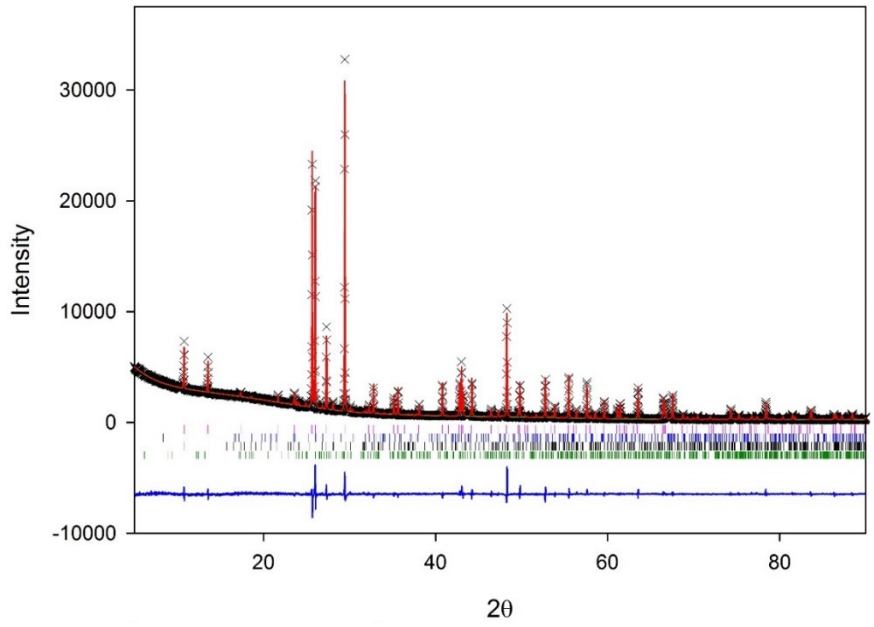

Figure 7.10 *Rietveld Refinement (GSAS Liveplot) for $Cs_{1.9}Ba_{0.1}Ti_{1.1}Nb_{5.9}O_{18}$ (solid-state Pink ticks: $Cs_2TiNb_6O_{18}$, blue ticks: $BaTi_3Nb_4O_{17}$, dark red ticks: $BaTiNb_4O_{13}$ and green ticks: $Ti_2Nb_{10}O_{29}$*

Table 7.10 *Rietveld Refinement details for $Cs_{1.9}Ba_{0.1}Ti_{1.1}Nb_{5.9}O_{18}$ (solid-state)*

χ2	**wRp**	**Rp**
4.113	5.8 %	3.87 %

Phase	**Symmetry Setting**	**Space Group**
$Cs_2TiNb_6O_{18}$	trigonal	*P*-3*m*1

Phase Information	***a***	***b***	***c***	***V***	
	7.529004(29)	7.529004(29)	8.18402(5)	401.7660(30)	
	α	***β***	***γ***		
	90	90	120		
Atom	***x***	***y***	***z***	**Occupancy**	**Uiso**
Cs	0.3333	0.6667	0.6333(4)	1	0.0320(9)
Nb1	0	0	0.5	0.788(5)	0.0094(22)
Ti1	0	0	0.5	0.074(5)	0.0094(22)
Nb2	0.16920(14)	-0.16920(14)	0.14726(28)	0.8685(10)	0.0087(6)
Ti2	0.16920(14)	-0.16920(14)	0.14726(28)	0.1545(10)	0.0087(6)
O1	0.447	-0.447	0.16	1	0.01
O2	0.861	0.861	0.11	1	0.01
O3	0.12	-0.12	0.37	1	0.01

Phase	Symmetry Setting	Space Group
$BaTi_3Nb_4O_{17}$	Orthorhombic	*Cmcm*

Phase Information	***a***	***b***	***c***	***V***	
	6.6323(10)	8.9685(19)	21.138(4)	1257.34(31)	
	α	***β***	***γ***		
	90	90	90		
Atom	***x***	***y***	***z***	**Occupancy**	**Uiso**
Ba	0	0.9807	0.25	1	0.01
Nb1	0	0.1026	0.0568	0.6	0.01
Ti1	0	0.1026	0.0568	0.4	0.01
Nb2	0	0.3446	0.3404	0.225	0.01
Ti2	0	0.3446	0.3404	0.775	0.01
Nb3	0	0.7359	0.3878	0.3	0.01
Ti3	0	0.7359	0.3878	0.7	0.01
Nb4	0	0.5	0.5	0.75	0.01
Ti4	0	0.5	0.5	0.25	0.01
O1	0	0.546	0.3365	1	0.01
O2	0	0.304	0.25	1	0.01
O3	0	0.315	0.4549	1	0.01
O4	0	0.889	0.4539	1	0.01
O5	0	0.12	0.357	1	0.01
O6	0.195	0.197	0.6571	1	0.01
O7	0.28	0.096	0.4562	1	0.01

Phase	Symmetry Setting	Space Group
$BaTiNb_4O_{13}$	Orthorhombic	*Pbcm*

Phase Information	***a***	***b***	***c***	***V***	
	5.6299(8)	10.7187(13)	16.4553(19)	993.00(14)	
	α	***β***	***γ***		
	90	90	90		
Atom	***x***	***y***	***z***	**Occupancy**	**U_{iso}**
Ba	0.2056	0.8256	0.25	1	0.01
Nb1	0.1615	0.4378	0.0765	0.8	0.01
Ti1	0.1615	0.4378	0.0765	0.2	0.01
Nb2	0.3431	0.1341	0.137	0.8	0.01
Ti2	0.3431	0.1341	0.137	0.2	0.01
Nb3	0.6651	0.25	0	0.8	0.01

Ti3	0.6651	0.25	0	0.2	0.01
O1	0.09	0.016	0.138	1	0.01
O2	0.127	0.282	0.126	1	0.01
O3	0.124	0.604	0.004	1	0.01
O4	0.369	0.154	0.25	1	0.01
O5	0.366	0.127	0.012	1	0.01
O6	0.592	0.004	0.136	1	0.01
O7	0.606	0.251	0.111	1	0.01

Phase	**Symmetry Setting**	**Space Group**
$Ti_2Nb_{10}O_{29}$	monoclinic	*A*12/*m*1

Phase Information	***a***	***b***	***c***	***V***	
	15.571(4)	3.8088(6)	20.543(4)	1115.96(27)	
	α	***β***	***γ***		
	90	113.649(22)	90		
Atom	***x***	***y***	***z***	**Occupancy**	**Uiso**
Nb1	0.099	0	0.068	0.833	0.01
Ti1	0.099	0	0.068	0.167	0.01
Nb2	0.096	0	0.697	0.833	0.01
Ti2	0.096	0	0.697	0.167	0.01
Nb3	0.097	0	0.881	0.833	0.01
Ti3	0.097	0	0.881	0.167	0.01
Nb4	0.367	0	0.149	0.833	0.01
Ti4	0.367	0	0.149	0.167	0.01
Nb5	0.366	0	0.779	0.833	0.01
Ti5	0.366	0	0.779	0.167	0.01
Nb5	0.366	0	0.964	0.833	0.01
Ti5	0.366	0	0.964	0.167	0.01
O1	0.5	0	0	1	0.01
O2	0.066	0	0.166	1	0.01
O3	0.038	0	0.358	1	0.01
O4	0.086	0	0.602	1	0.01
O5	0.09	0	0.784	1	0.01
O6	0.074	0	0.971	1	0.01
O7	0.22	0	0.106	1	0.01
O8	0.228	0	0.73	1	0.01
O9	0.222	0	0.92	1	0.01
O10	0.362	0	0.055	1	0.01
O11	0.364	0	0.247	1	0.01

O12	0.364	0	0.463	1	0.01
O13	0.364	0	0.678	1	0.01
O14	0.364	0	0.869	1	0.01
O15	0.5	0	0.188	1	0.01

Weight Fractions	
Phase	Wt. %
$Cs_2TiNb_6O_{18}$	**91.462(4)**
$BaTi_3Nb_4O_{17}$	**1.74(2)**
$BaTiNb_4O_{13}$	**4.03(2)**
$Ti_2Nb_{10}O_{29}$	**2.77(2)**

Rietveld Refinement $Cs_{1.95}Ba_{0.05}Ti_{1.05}Nb_{5.95}O_{18}$ (Solid-state method)

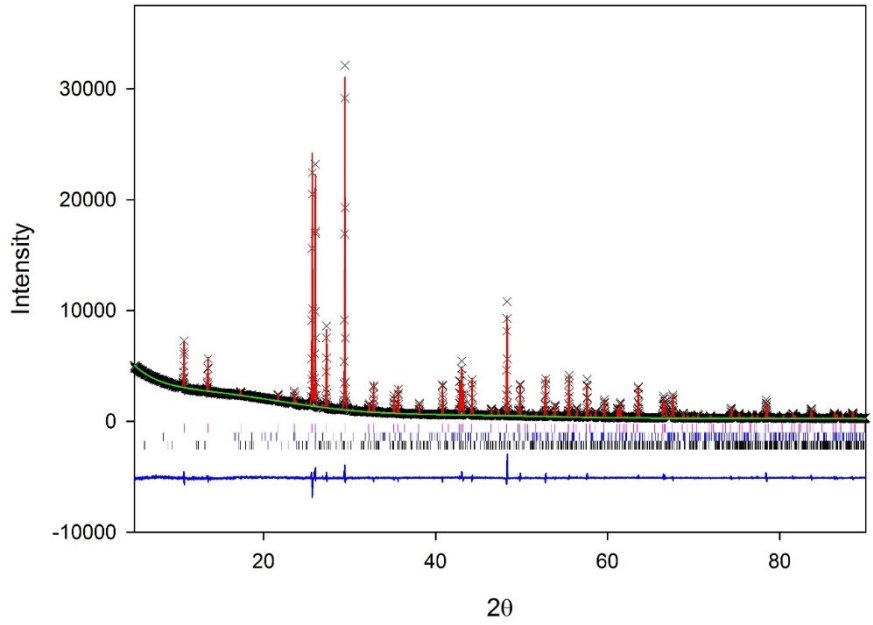

Figure 7.11 *Rietveld Refinement (GSAS Liveplot) for $Cs_{1.95}Ba_{0.05}Ti_{1.05}Nb_{5.95}O_{18}$ (solid-state). state Pink ticks: $Cs_2TiNb_6O_{18}$, blue ticks: $BaTi_3Nb_4O_{17}$ and black ticks: $Ti_2Nb_{10}O_{29}$*

Table 7.11 *Rietveld Refinement details for $Cs_{1.95}Ba_{0.05}Ti_{1.05}Nb_{5.95}O_{18}$ (solid-state)*

χ^2	wRp	Rp
3.118	5.05 %	3.43 %

Phase	Symmetry Setting	Space Group
$Cs_2TiNb_6O_{18}$	Trigonal	*P*-3*m*1

Phase Information	*a*	*b*	*c*	*V*
	7.52469(5)	7.52469(5)	8.17920(7)	401.069(6)
	α	*β*	*γ*	
	90	90	120	

Atom	*x*	*y*	*z*	Occupancy	U_{iso}
Cs	0.3333	0.6667	0.6329(4)	1	0.0324(8)
Nb1	0	0	0.5	0.788(5)	0.0094(18)
Ti1	0	0	0.5	0.074(5)	0.0094(18)
Nb2	0.16918(12)	-0.16918(12)	0.14718(24)	0.8685(8)	0.0079(5)
Ti2	0.16918(12)	-0.16918(12)	0.14718(24)	0.1545(8)	0.0079(5)
O1	0.447	-0.447	0.16	1	0.01
O2	0.861	0.861	0.11	1	0.01
O3	0.12	-0.12	0.37	1	0.01

Phase	Symmetry Setting	Space Group
$BaTi_3Nb_4O_{17}$	Orthorhombic	*Cmcm*

Phase Information	***a***	***b***	***c***	***V***	
	6.6286(15)	8.9585(31)	21.122(6)	1254.2(5)	
	α	***β***	***γ***		
	90	90	90		
Atom	***x***	***y***	***z***	**Occupancy**	**U_{iso}**
Ba	0	0.9807	0.25	1	0.01
Nb1	0	0.1026	0.0568	0.6	0.01
Ti1	0	0.1026	0.0568	0.4	0.01
Nb2	0	0.3446	0.3404	0.225	0.01
Ti2	0	0.3446	0.3404	0.775	0.01
Nb3	0	0.7359	0.3878	0.3	0.01
Ti3	0	0.7359	0.3878	0.7	0.01
Nb4	0	0.5	0.5	0.75	0.01
Ti4	0	0.5	0.5	0.25	0.01
O1	0	0.546	0.3365	1	0.01
O2	0	0.304	0.25	1	0.01
O3	0	0.315	0.4549	1	0.01
O4	0	0.889	0.4539	1	0.01
O5	0	0.12	0.357	1	0.01
O6	0.195	0.197	0.6571	1	0.01
O7	0.28	0.096	0.4562	1	0.01

Phase	Symmetry Setting	Space Group
$Ti_2Nb_{10}O_{29}$	Monoclinic	*A*12/*m*1

Phase Information	***a***	***b***	***c***	***V***	
	15.547(5)	3.8065(8)	20.512(5)	1112.7(4)	
	α	***β***	***γ***		
	90	113.552(28)	90		
Atom	***x***	***y***	***z***	**Occupancy**	**U_{iso}**
Nb1	0.099	0	0.068	0.833	0.01
Ti1	0.099	0	0.068	0.167	0.01
Nb2	0.096	0	0.697	0.833	0.01
Ti2	0.096	0	0.697	0.167	0.01
Nb3	0.097	0	0.881	0.833	0.01
Ti3	0.097	0	0.881	0.167	0.01

Nb4	0.367	0	0.149	0.833	0.01
Ti4	0.367	0	0.149	0.167	0.01
Nb5	0.366	0	0.779	0.833	0.01
Ti5	0.366	0	0.779	0.167	0.01
Nb5	0.366	0	0.964	0.833	0.01
Ti5	0.366	0	0.964	0.167	0.01
O1	0.5	0	0	1	0.01
O2	0.066	0	0.166	1	0.01
O3	0.038	0	0.358	1	0.01
O4	0.086	0	0.602	1	0.01
O5	0.09	0	0.784	1	0.01
O6	0.074	0	0.971	1	0.01
O7	0.22	0	0.106	1	0.01
O8	0.228	0	0.73	1	0.01
O9	0.222	0	0.92	1	0.01
O10	0.362	0	0.055	1	0.01
O11	0.364	0	0.247	1	0.01
O12	0.364	0	0.463	1	0.01
O13	0.364	0	0.678	1	0.01
O14	0.364	0	0.869	1	0.01
O15	0.5	0	0.188	1	0.01

Weight Fractions	
Phase	Wt. %
$Cs_2TiNb_6O_{18}$	**95.637(2)**
$BaTi_3Nb_4O_{17}$	**2.16(2)**
$Ti_2Nb_{10}O_{29}$	**2.21(2)**

Rietveld Refinement $BaNb_2O_6$ (Starting Material)

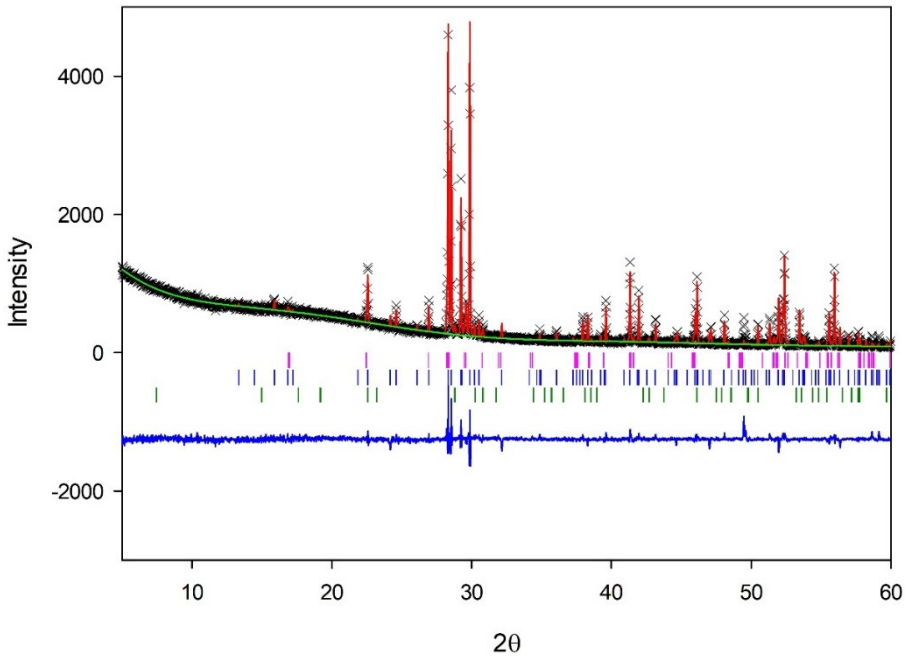

Figure 7.12 *Rietveld refinement (GSAS Liveplot) $BaNb_2O_6$. Pink ticks: $BaNb_2O_6$ (Monoclinic), blue ticks: $BaNb_2O_6$ (Orthorhombic) and green ticks: $Ba_4Nb_5O_{15}$*

Table 7.12 *Refinement details for $BaNb_2O_6$ (Test Bottle)*

χ^2	wRp	Rp
2.405	12.23 %	5.09%

Phase	Symmetry Setting	Space Group
$BaNb_2O_6$	Monoclinic	$P2_1/c$

Phase Information	*a*	*b*	*c*	*V*	
	3.9461(4)	6.0369(7)	10.4157(9)	248.23(4)	
	α	*β*	*γ*		
	90	89.636(10)	90		
Atom	***x***	***y***	***z***	**Occupancy**	**U_{iso}**
Ba1	0	0.5	0.5	1	0.01381
Nb1	0.531	0.0465	0.6504	1	0.00874
O1	0.499	0.198	0.464	1	0.01647
O2	0.501	0.384	0.697	1.0	0.01013
O3	0.007	0.084	0.65	1.0	0.0152

Phase	Symmetry Setting	Space Group
$BaNb_2O_6$	Orthorhombic	$C222_1$

Phase Information	***a***	***b***	***c***	***V***	
	7.85631(14)	12.18796(26)	10.26735(21)	983.12(5)	
	α	***β***	***γ***		
	90	90	90		
Atom	**x**	**y**	**z**	**Occupancy**	**U_{iso}**
Ba1	0	0.5742	0.25	1.0	0.01064
Ba2	0.5	0.6245	0.25	1.0	0.01013
Nb1	0.2781	0.3599	0.4259	1.0	0.00988
Nb2	0.7735	0.6418	0.5755	1.0	0.00659
O1	0.288	0.418	0.257	1.0	0.0076
O2	0.025	0.341	0.386	1.0	-0.01266
O3	0.209	0.298	0.614	1.0	0.0038
O4	0.508	0.38	0.466	1.0	-0.00507
O5	0.186	0.5	0.5	1.0	0.02533
O6	0.796	0.5	0.5	1.0	0.03166
O7	0.257	0.204	0.401	1.0	0.03166

Phase	Symmetry Setting	Space Group
$Ba_4Nb_5O_{15}$	Trigonal	$P\text{-}3m1$

Phase Information	***a***	***b***	***c***	***V***	
	5.7887(12)	5.7887	11.782(4)	341.92(12)	
	α	***β***	***γ***		
	90	90	120		
Atom	***x***	***y***	***z***	**Occupancy**	**U_{iso}**
Ba1	0	0	0	1.0	0.00032
Ba2	0.333	0.6667	0.42828	1.0	0.00032
Ba3	0.667	0.333	0.20795	1.0	0.00032
Nb1	0	0	0.31709	1.0	0.00032
Nb2	0.3333	0.6667	0.10539	1.0	0.00032
O1	0.3272	0.1636	0.3873	1.0	0.00009
O2	0.661	0.8305	0.1918	1.0	0.00009
O3	0.5	0	0	1.0	0.00009

Weight Fraction:	Wt %
$BaNb_2O_6$ (Monoclinic)	**10.58(3)**
$BaNb_2O_6$ (Orthorhombic)	**87.24(7)**
$Ba_4Nb_5O_{15}$	**2.17(2)**

Rietveld Refinement $Cs_{1.8}Ba_{0.2}Ti^{(4+)}_{0.8}Ti^{(3+)}_{0.2}Nb_6O_{18}$ (Solid-state method, quartz tube with pre-decomposition step)

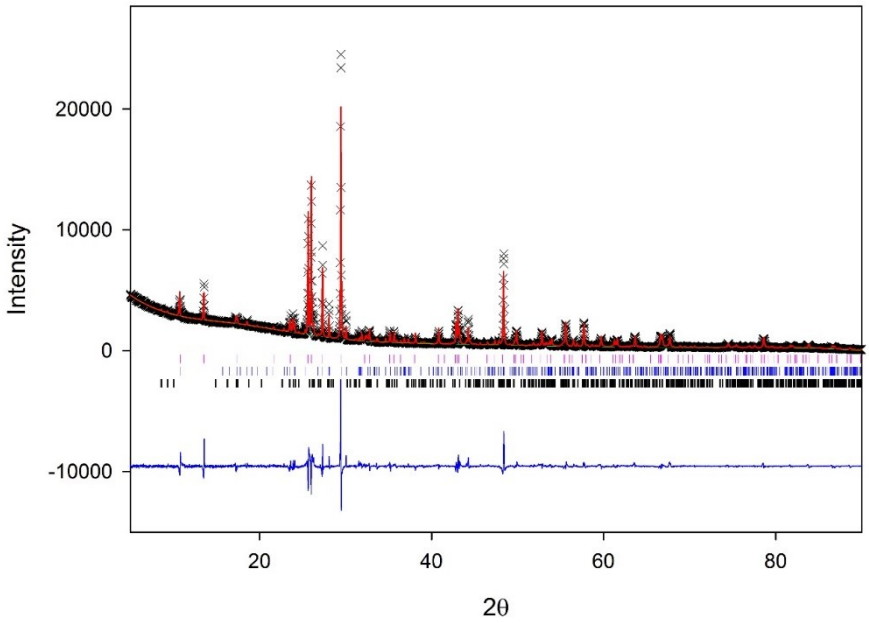

Figure 7.13 *Rietveld Refinement (GSAS Liveplot) for $Cs_{1.8}Ba_{0.2}Ti^{(4+)}_{0.8}Ti^{(3+)}_{0.2}Nb_6O_{18}$. Pink ticks: $Cs_2TiNb_6O_{18}$, blue ticks: $BaTiNb_4O_{13}$ and black ticks: $BaTi_3Nb_4O_{17}$.*

Table 7.13 *Refinement details for $Cs_{1.8}Ba_{0.2}Ti^{(4+)}_{0.8}Ti^{(3+)}_{0.2}Nb_6O_{18}$*

χ^2	wRp	Rp
12.77	10.39 %	6.2 %

Phase	Symmetry Setting	Space Group
$Cs_2TiNb_6O_{18}$	Trigonal	*P*-3*m*1

Phase Information	***a***	***b***	***c***	***V***	
	7.50619(19)	7.50619	8.16354(31)	401.873(10)	
	α	β	γ		
	90	90	120		
Atom	***x***	***y***	***z***	**Occupancy**	**U_{iso}**
Cs	0.3333	0.6667	0.6313(12)	1	0.0353(11)
Nb1	0	0	0.5	0.790(13)	0.032(7)
Ti1	0	0	0.5	0.076(13)	0.032(7)
Nb2	0.1702(4)	-0.1702(4)	0.1447(8)	0.8681(22)	0.0094(13)
Ti2	0.1702(4)	-0.1702(4)	0.1447(8)	0.1541(22)	0.0094(13)
O1	0.447	-0.447	0.16	1	0.01
O2	0.861	0.861	0.11	1	0.01
O3	0.12	-0.12	0.37	1	0.01

Phase	Symmetry Setting	Space Group
$BaTiNb_4O_{13}$	Orthorhombic	*Pbcm*

Phase Information	*a*	*b*	*c*	*V*	
	5.6346(4)	10.7248(7)	16.4530(10	994.24(8)	
	α	*β*	*γ*		
	90	90	90		
Atom	***x***	***y***	***z***	**Occupancy**	**U_{iso}**
Ba	0.2056	0.8256	0.25	1	0.01
Nb1	0.1615	0.4378	0.0765	0.8	0.01
Ti1	0.1615	0.4378	0.0765	0.2	0.01
Nb2	0.3431	0.1341	0.137	0.8	0.01
Ti2	0.3431	0.1341	0.137	0.2	0.01
Nb3	0.6651	0.25	0	0.8	0.01
Ti3	0.6651	0.25	0	0.2	0.01
O1	0.09	0.016	0.138	1	0.01
O2	0.127	0.282	0.126	1	0.01
O3	0.124	0.604	0.004	1	0.01
O4	0.369	0.154	0.25	1	0.01
O5	0.366	0.127	0.012	1	0.01
O6	0.592	0.004	0.136	1	0.01
O7	0.606	0.251	0.111	1	0.01

Phase	Symmetry Setting	Space Group
$BaTi_3Nb_4O_{17}$	Orthorhombic	*Cmcm*

Phase Information	*a*	*b*	*c*	*V*	
	6.6406(4)	8.9688(7)	21.1200(16)	1257.86(12)	
	α	*β*	*γ*		
	90	90	90		
Atom	***x***	***y***	***z***	**Occupancy**	**U_{iso}**
Nb1	0	0	0	0.909	0.01
Ti1	0	0	0	0.091	0.01
Nb2	0.18528	0	0.17993	0.798	0.01
Ti2	0.18528	0	0.17993	0.202	0.01
Nb3	0.07842	0	-0.55844	0.643	0.01
Ti3	0.07842	0	-0.55844	0.357	0.01
Nb4	0.88938	0	0.25857	0.727	0.01

Ti4	0.88938	0	0.25857	0.273	0.01
Nb5	0.29286	0	-0.07479	0.376	0.01
Ti5	0.29286	0	-0.07479	0.624	0.01
O1	0.1735	0	-0.4233	1	0.01
O2	0.37287	0	-0.2069	1	0.01
O3	0.59702	0	-0.0252	1	0.01
O4	0.79131	0	0.1744	1	0.01
O5	0.24932	0	0.054	1	0.01
O6	0.70916	0	0.7059	1	0.01
O7	0.89988	0	-0.0851	1	0.01
O8	0.02523	0	-0.392	1	0.01
O9	0.87451	0	0.6853	1	0.01
O10	0.5	0	0.5	1	0.01
O11	0.04964	0	-0.1479	1	0.01

Weight Fractions	
Phase	Wt. %
$Cs_2TiNb_6O_{18}$	**74.8(2)**
$BaTiNb_4O_{13}$	**11.4(4)**
$TiNb_2O_7$	**13.8(6)**

Rietveld Refinement $Cs_{1.8}Ba_{0.2}Nb^{(5+)}_{5.8}Nb^{(4+)}_{0.2}TiO_{18}$ (Solid-state method, quartz tube with pre-decomposition step)

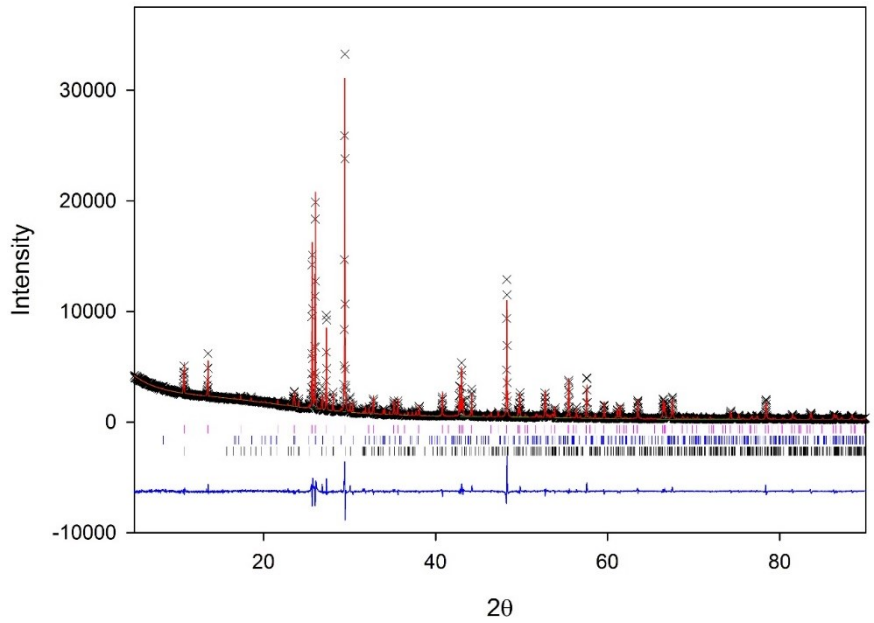

Figure 7.14 *Rietveld Refinement (GSAS Liveplot) for $Cs_{1.8}Ba_{0.2}Nb^{(5+)}_{5.8}Nb^{(4+)}_{0.2}TiO_{18}$*

Table 7.14 *Rietveld Refinement details for $Cs_{1.8}Ba_{0.2}Nb^{(5+)}_{5.8}Nb^{(4+)}_{0.2}TiO_{18}$*

χ^2	wRp	Rp
6.075	7.41 %	4.8 %

Phase	Symmetry Setting	Space Group
$Cs_2TiNb_6O_{18}$	Trigonal	*P*-3*m*1

Phase Information	*a*	*b*	*c*	*V*	
	7.52859(8)	7.52859	8.18712(12)	401.873(10)	
	α	*β*	*γ*		
	90	90	120		
Atom	***x***	***y***	***z***	**Occupancy**	**Uiso**
Cs	0.3333	0.6667	0.6340(6)	1	0.0353(11)
Nb1	0	0	0.5	0.781(7)	0.0176(31)
Ti1	0	0	0.5	0.067(7)	0.0176(31)
Nb2	0.16868(18)	-0.16868(18)	0.1457(4)	0.8697(12)	0.0078(7)
Ti2	0.16868(18)	-0.16868(18)	0.1457(4)	0.1557(12)	0.0078(7)
O1	0.447	-0.447	0.16	1	0.01
O2	0.861	0.861	0.11	1	0.01
O3	0.12	-0.12	0.37	1	0.01

Phase	Symmetry Setting	Space Group
$BaTiNb_4O_{13}$	Orthorhombic	*Pbcm*

Phase Information	***a***	***b***	***c***	***V***	
	5.6346(4)	10.7248(7)	16.4530(10	994.24(8)	
	α	***β***	***γ***		
	90	90	90		
Atom	***x***	***y***	***z***	**Occupancy**	**U_{iso}**
Ba	0.2056	0.8256	0.25	1	0.01
Nb1	0.1615	0.4378	0.0765	0.8	0.01
Ti1	0.1615	0.4378	0.0765	0.2	0.01
Nb2	0.3431	0.1341	0.137	0.8	0.01
Ti2	0.3431	0.1341	0.137	0.2	0.01
Nb3	0.6651	0.25	0	0.8	0.01
Ti3	0.6651	0.25	0	0.2	0.01
O1	0.09	0.016	0.138	1	0.01
O2	0.127	0.282	0.126	1	0.01
O3	0.124	0.604	0.004	1	0.01
O4	0.369	0.154	0.25	1	0.01
O5	0.366	0.127	0.012	1	0.01
O6	0.592	0.004	0.136	1	0.01
O7	0.606	0.251	0.111	1	0.01

Phase	Symmetry Setting	Space Group
$BaTi_3Nb_4O_{17}$	Orthorhombic	*Cmcm*

Phase Information	***a***	***b***	***c***	***V***	
	6.6406(4)	8.9688(7)	21.1200(16)	1257.86(12)	
	α	***β***	***γ***		
	90	90	90		
Atom	***x***	***y***	***z***	**Occupancy**	**U_{iso}**
Ba	0	0.9807	0.25	1	0.01
Nb1	0	0.1026	0.0568	0.6	0.01
Ti1	0	0.1026	0.0568	0.4	0.01
Nb2	0	0.3446	0.3404	0.225	0.01
Ti2	0	0.3446	0.3404	0.775	0.01
Nb3	0	0.7359	0.3878	0.3	0.01
Ti3	0	0.7359	0.3878	0.7	0.01
Nb4	0	0.5	0.5	0.75	0.01

Ti4	0	0.5	0.5	0.25	0.01
O1	0	0.546	0.3365	1	0.01
O2	0	0.304	0.25	1	0.01
O3	0	0.315	0.4549	1	0.01
O4	0	0.889	0.4539	1	0.01
O5	0	0.12	0.357	1	0.01
O6	0.195	0.197	0.6571	1	0.01
O7	0.28	0.096	0.4562	1	0.01

Weight Fractions	
Phase	Wt. %
$Cs_2TiNb_6O_{18}$	**84.73(8)**
$BaTiNb_4O_{13}$	**7.6(2)**
$BaTi_3Nb_4O_{17}$	**7.6(3)**

Rietveld Refinement $Cs_{1.8}Ba_{0.2}Nb^{(5+)}_{5.9}Ti^{(3+)}_{0.1}Ti^{(4+)}_{0.9}Nb^{(4+)}_{0.1}O_{18}$ (Solid-state method, quartz tube with pre-decomposition step)

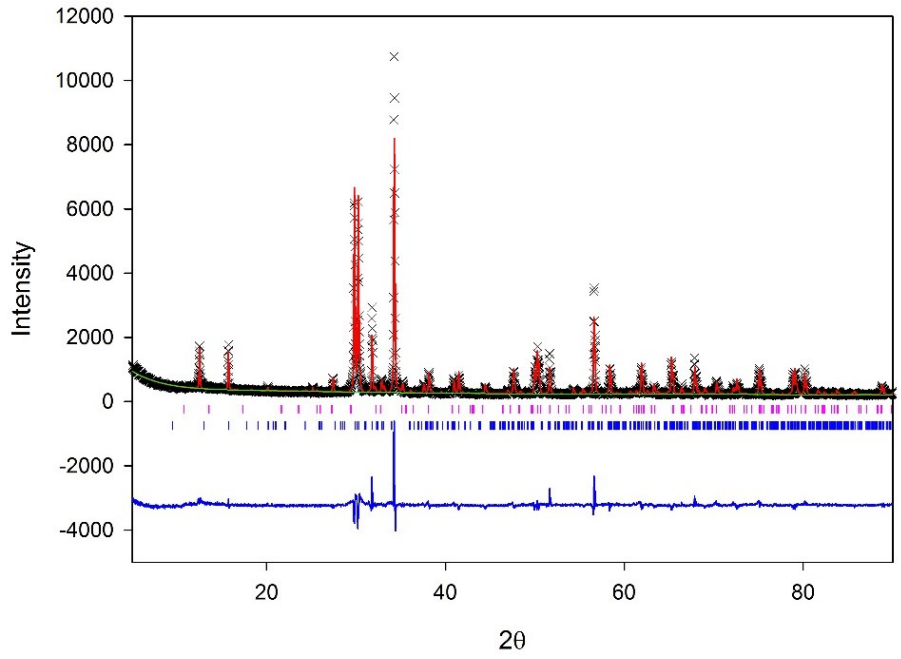

Figure 7.15 *Rietveld refinement (GSAS Liveplot) for $Cs_{1.8}Ba_{0.2}Nb^{(5+)}_{5.9}Ti^{(3+)}_{0.1}Ti^{(4+)}_{0.9}Nb^{(4+)}_{0.1}O_{18}$. Pink ticks: $Cs_2TiNb_6O_{18}$ and blue ticks: $Ba_2Ti_3Nb_4O_{18}$*

Table 7.15 *Rietveld refinement details for $Cs_{1.8}Ba_{0.2}Nb^{(5+)}_{5.9}Ti^{(3+)}_{0.1}Ti^{(4+)}_{0.9}Nb^{(4+)}_{0.1}O_{18}$*

χ^2	wRp	Rp
4.054	9.99%	7.55%

Phase	Symmetry Setting	Space Group
$Cs_2TiNb_6O_{18}$	Trigonal	*P*-3*m*1

Phase Information	***a***	***b***	***c***	***V***	
	7.54249(21)	7.54249	8.21052	404.511(28)	
	α	***β***	***γ***		
	90	90	120		
Atom	***x***	***y***	***z***	**Occupancy**	**U_{iso}**
Cs	0.3333	0.6667	0.6330(7)	1	0.0325(19)
Nb1	0	0	0.5	0.831(6)	0.033(4)
Ti1	0	0	0.5	0.1473(10)	0.033(4)
Nb2	0.16955(21)	-0.16955(21)	0.1437(4)	0.883(6)	0.0026(12)
Ti2	0.16955(21)	-0.16955(21)	0.1437(4)	0.1387(10)	0.0026(12)
O1	0.447	-0.447	0.16	1	0.01
O2	0.861	0.861	0.11	1	0.01
O3	0.12	-0.12	0.37	1	0.01

Phase	Symmetry Setting	Space Group
$Ba_2Ti_3Nb_4O_{18}$	Monoclinic	$P2_1/c$

Phase Information	***a***	***b***	***c***	***V***	
	10.0414(22)	9.9931(21)	7.3318(17)	685.30(25)	
	α	***β***	***γ***		
	90	111.332(23)	90		
Atom	***x***	***y***	***z***	**Occupancy**	**Uiso**
Ba	0.20448	0.08876	0.06374	1	0.01
Nb1	0.10467	0.75127	0.35107	1	0.01
Ti1	0	0.5	0	1	0.01
Nb2	0.5182	0.2697	0.5095	0.5	0.01
Ti2	0.5182	0.2697	0.5095	0.5	0.01
Nb3	0.3795	0.0151	0.6055	0.5	0.01
Ti3	0.3795	0.0151	0.6055	0.5	0.01
O1	0.4047	0.0907	0.8515	1	0.01
O2	0.5814	0.084	0.6211	1	0.01
O3	0.8074	0.0709	0.4761	1	0.01
O4	0.9843	0.0883	0.2516	1	0.01
O5	0.0697	0.1617	0.6458	1	0.01
O6	0.3237	0.1719	0.4633	1	0.01
O7	0.5096	0.1626	0.2545	1	0.01
O8	0.7001	0.174	0.0459	1	0.01
O9	0.899	0.1688	0.8755	1	0.01

Weight Fraction	
Phase	Wt, %
$Cs_2TiNb_6O_{18}$	**88.882(9)**
$Ba_2Ti_3Nb_4O_{18}$	**11.11(3)**

Rietveld Refinement $Cs_{1.9}Ba_{0.1}Ti^{(4+)}_{0.9}Ga^{(3+)}_{0.1}Nb^{(5+)}_{6}O_{18}$ (Solid-state method)

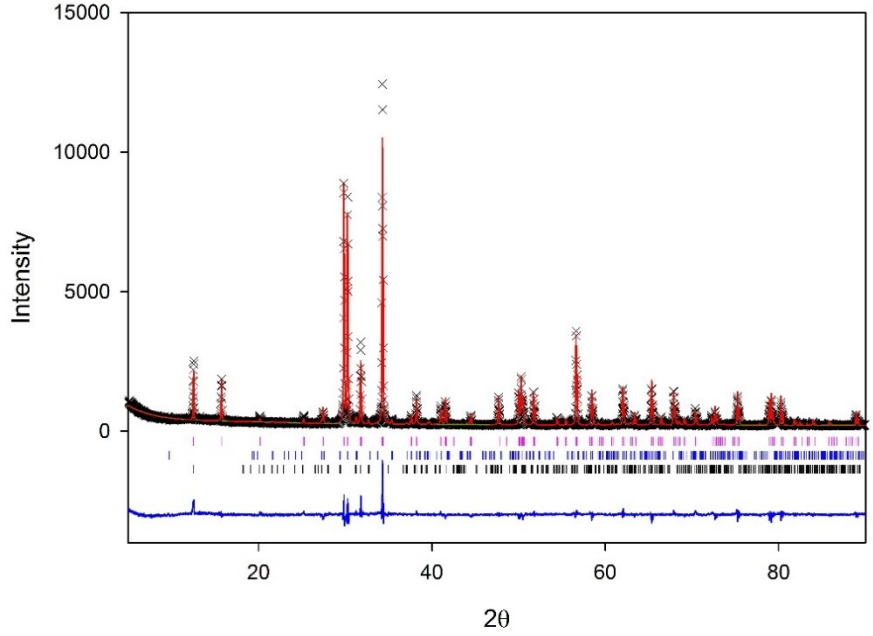

Figure 7.16 *Rietveld Refinement (GSAS Liveplot) for $Cs_{1.9}Ba_{0.1}Ti^{(4+)}_{0.9}Ga^{(3+)}_{0.1}Nb^{(5+)}_{6}O_{18}$. Pink ticks: $Cs_2TiNb_6O_{18}$, blue ticks: $BaTi_3Nb_4O_{17}$ and black ticks: $BaTiNb_4O_{13}$*

Table 7.16 *Rietveld Refinement details for $Cs_{1.9}Ba_{0.1}Ti^{(4+)}_{0.9}Ga^{(3+)}_{0.1}Nb^{(5+)}_{6}O_{18}$*

χ^2	wRp	Rp
3.294	9.14 %	7.21 %

Phase	Symmetry Setting	Space Group
$Cs_2TiNb_6O_{18}$	Trigonal	*P*-3*m*1

Phase Information	*a*	*b*	*c*	*V*
	7.54182(5)	7.54182	8.19872(8)	403.858(5)
	α	***β***	***γ***	
	90	90	120	
Atom	**x**	**y**	**z**	**Occupancy**	**U_{iso}**
Cs	0.3333	0.6667	0.632	1	0.01
Nb1	0	0	0.5	0.857	0.01
Ti1	0	0	0.5	0.143	0.01
Nb2	0.17	-0.17	0.1457	0.857	0.01
Ti2	0.17	-0.17	0.1457	0.143	0.01
O1	0.447	-0.447	0.16	1	0.01
O2	0.861	0.861	0.11	1	0.01
O3	0.12	-0.12	0.37	1	0.01

Phase	Symmetry Setting	Space Group
$BaTi_3Nb_4O_{17}$	Orthorhombic	*Cmcm*

Phase Information	***a***	***b***	***c***	***V***	
	6.6429(16)	8.9926(28)	21.182(6)	1265.3(6)	
	α	***β***	***γ***		
	90	90	90		
Atom	**x**	**y**	**z**	**Occupancy**	**Uiso**
Ba	0	0.9807	0.25	1	0.01
Nb1	0	0.1026	0.0568	0.6	0.01
Ti1	0	0.1026	0.0568	0.4	0.01
Nb2	0	0.3446	0.3404	0.225	0.01
Ti2	0	0.3446	0.3404	0.775	0.01
Nb3	0	0.7359	0.3878	0.3	0.01
Ti3	0	0.7359	0.3878	0.7	0.01
Nb4	0	0.5	0.5	0.75	0.01
Ti4	0	0.5	0.5	0.25	0.01
O1	0	0.546	0.3365	1	0.01
O2	0	0.304	0.25	1	0.01
O3	0	0.315	0.4549	1	0.01
O4	0	0.889	0.4539	1	0.01
O5	0	0.12	0.357	1	0.01
O6	0.195	0.197	0.6571	1	0.01
O7	0.28	0.096	0.4562	1	0.01

Phase	Symmetry Setting	Space Group
$BaTiNb_4O_{13}$	Orthorhombic	*Pbcm*

Phase Information	***a***	***b***	***c***	***V***	
	5.6503(32)	10.790(5)	16.487(8)	1005.2(9)	
	α	***β***	***γ***		
	90	90	90		
Atom	***x***	***y***	***z***	**Occupancy**	**U_{iso}**
Ba	0.2056	0.8256	0.25	1	0.01
Nb1	0.1615	0.4378	0.0765	0.8	0.01
Ti1	0.1615	0.4378	0.0765	0.2	0.01
Nb2	0.3431	0.1341	0.137	0.8	0.01
Ti2	0.3431	0.1341	0.137	0.2	0.01
Nb3	0.6651	0.25	0	0.8	0.01

Ti3	0.6651	0.25	0	0.2	0.01
O1	0.09	0.016	0.138	1	0.01
O2	0.127	0.282	0.126	1	0.01
O3	0.124	0.604	0.004	1	0.01
O4	0.369	0.154	0.25	1	0.01
O5	0.366	0.127	0.012	1	0.01
O6	0.592	0.004	0.136	1	0.01
O7	0.606	0.251	0.111	1	0.01

Weight Fractions	
Phases	Wt. %
$Cs_2TiNb_6O_{18}$	**92.508(2)**
$BaTi_3Nb_4O_{17}$	**4.71(2)**
$BaTiNb_4O_{13}$	**2.78(2)**

Rietveld Refinement $Cs_{1.9}Ba_{0.1}Ti^{(4+)}_{0.9}Al^{(3+)}_{0.1}Nb^{(5+)}_{6}O_{18}$ (Solid-state method)

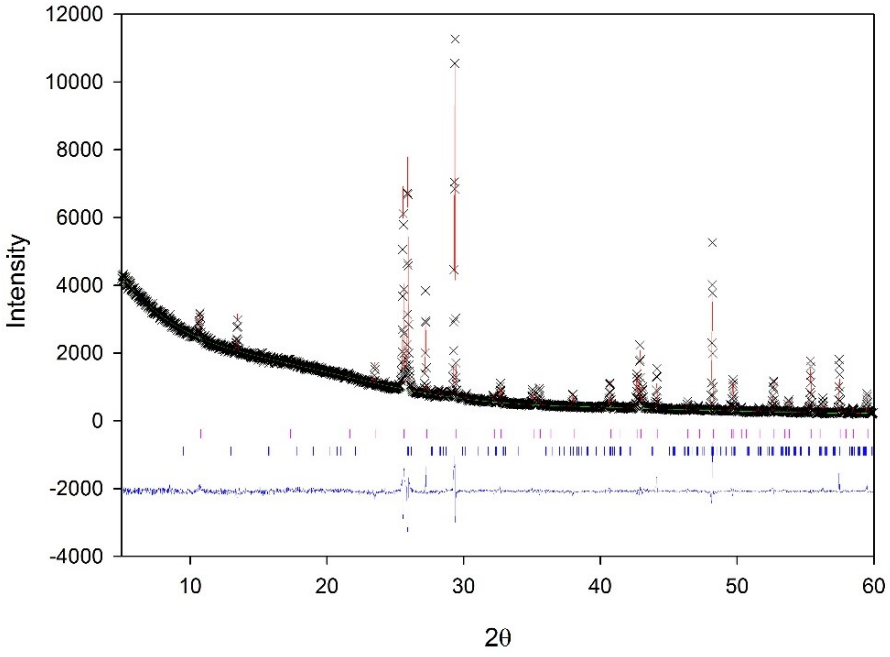

Figure 7.17 *Rietveld Refinement (GSAS Liveplot) for $Cs_{1.9}Ba_{0.1}Ti^{(4+)}_{0.9}Ga^{(3+)}_{0.1}Nb^{(5+)}_{6}O_{18}$. Pink ticks: $Ba_2Ti_3Nb_4O_{18}$ and blue ticks: $Cs_2TiNb_6O_{18}$*

Table 7.17 *Rietveld Refinement details for $Cs_{1.9}Ba_{0.1}Ti^{(4+)}_{0.9}Ga^{(3+)}_{0.1}Nb^{(5+)}_{6}O_{18}$*

χ^2	wR_p	R_p
3.205	5.33%	3.43%

Phase	Symmetry Setting	Space Group
$Cs_2TiNb_6O_{18}$	Trigonal	*P*-3*m*1

Phase Information	*a*	*b*	*c*	*V*	
	7.53236(12)	7.53236	8.18269(18)	402.058(17)	
	α	*β*	*γ*		
	90	90	120		
Atom	***x***	***y***	***z***	**Occupancy**	U_{iso}
Cs	0.3333	0.6667	0.632	1	0.01
Nb1	0	0	0.5	0.857	0.01
Ti1	0	0	0.5	0.143	0.01
Nb2	0.17	-0.17	0.1457	0.857	0.01
Ti2	0.17	-0.17	0.1457	0.143	0.01
O1	0.447	-0.447	0.16	1	0.01
O2	0.861	0.861	0.11	1	0.01
O3	0.12	-0.12	0.37	1	0.01

Phase	Symmetry Setting	Space Group
$Ba_2Ti_3Nb_4O_{18}$	Monoclinic	$P2_1/c$

Phase Information	***a***	***b***	***c***	***V***	
	10.0094(30)	9.965(4)	7.3143(24)	679.77(26)	
	α	β	γ		
	90	111.291(31)	90		
Atom	**x**	**y**	**z**	**Occupancy**	**U_{iso}**
Ba	0.20448	0.08876	0.06374	1	0.01
Nb1	0.10467	0.75127	0.35107	1	0.01
Ti1	0	0.5	0	1	0.01
Nb2	0.5182	0.2697	0.5095	0.5	0.01
Ti2	0.5182	0.2697	0.5095	0.5	0.01
Nb3	0.3795	0.0151	0.6055	0.5	0.01
Ti3	0.3795	0.0151	0.6055	0.5	0.01
O1	0.4047	0.0907	0.8515	1	0.01
O2	0.5814	0.084	0.6211	1	0.01
O3	0.8074	0.0709	0.4761	1	0.01
O4	0.9843	0.0883	0.2516	1	0.01
O5	0.0697	0.1617	0.6458	1	0.01
O6	0.3237	0.1719	0.4633	1	0.01
O7	0.5096	0.1626	0.2545	1	0.01
O8	0.7001	0.174	0.0459	1	0.01
O9	0.899	0.1688	0.8755	1	0.01

Weight Fractions	
Phases	Wt. %
$Cs_2TiNb_6O_{18}$	**94.129(3)**
$Ba_2Ti_3Nb_4O_{18}$	**5.87(44)**

Rietveld Refinement $BaAl_2Ti_6O_{16}$ (Ba-Hollandite) (Citrate combustion synthesis)

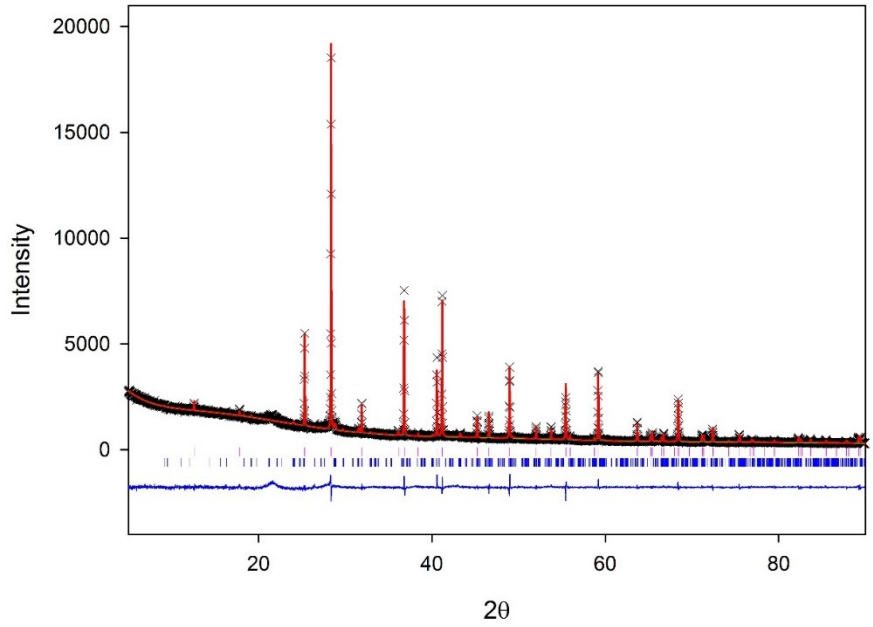

Figure 7.18 Rietveld Refinement (GSAS Liveplot) for $BaAl_2Ti_6O_{16}$ (Ba-Hollandite). Pink ticks: $Ba_{1.24}Al_{2.48}Ti_{5.52}O_{16}$ and blue ticks: $Ba_4Al_2Ti_{10}O_{27}$

Table 7.18 *Rietveld Refinement details for $BaAl_2Ti_6O_{16}$ (Ba-Hollandite).*

χ2	**wRp**	**Rp**
2.367	5.14%	3.71%

Phase	**Symmetry Setting**	**Space Group**
$BaAl_2Ti_6O_{16}$	Tetragonal	*I*4/*m*

Phase Information	***a***	***b***	***c***	***V***	
	9.93202(11)	9.93202(11)	2.919097(33)	287.955(9)	
	α	***β***	***γ***		
	90	90	90		
Atom	***x***	***y***	***z***	**Occupancy**	**U_{iso}**
Ba	0	0	0.296(4)	0.1831(21)	0.0117(25)
Ba	0	0	0.5	0.3113(11)	0.041(4)
Ti1	0.3518(4)	0.1664(4)	0	0.074(5)	0.0159(10)
Al1	0.3518(4)	0.1664(4)	0	0.074(5)	0.0159(10)
O1	0.15491	0.20152	0	1	0.01
O2	0.53998	0.16555	0	1	0.01

Phase	Symmetry Setting	Space Group
$Ba_4Al_2Ti_{10}O_{27}$	Monoclinic	*C*2/*m*

Phase Information	*a*	*b*	*c*	*V*	
	19.671(5)	11.3355(26)	9.8122(24)	2065.8(5)	
	α	*β*	*γ*		
	90	109.241(16)	90		
Atom	***x***	***y***	***z***	**Occupancy**	U_{iso}
Ba1	0.0655	0.2749	0.2159	1	0.01
Ba2	0.2028	0	0.1284	1	0.01
Ba3	0.4252	0.5	0.2883	1	0.01
Ti1	0.3771	0.259	0.0794	0.833	0.01
Al1	0.3771	0.259	0.0794	0.167	0.01
Ti2	0.3872	0	0.0796	0.833	0.01
Al2	0.3872	0	0.0796	0.167	0.01
Ti3	0	0	0	0.833	0.01
Al3	0	0	0	0.167	0.01
Ti4	0	0.5	0.5	0.833	0.01
Al4	0	0.5	0.5	0.167	0.01
Ti5	0.2349	0.5	0.4831	0.833	0.01
Al5	0.2349	0.5	0.4831	0.167	0.01
Ti6	0.248	0.6346	0.2176	0.833	0.01
Al6	0.248	0.6346	0.2176	0.167	0.01
Ti7	0	0.227	0.5	0.833	0.01
Al7	0	0.227	0.5	0.167	0.01
Ti8	0.1129	0	0.3947	0.833	0.01
Al8	0.1129	0	0.3947	0.167	0.01
Ti9	0.3684	0.8619	0.3435	0.833	0.01
Al9	0.3684	0.8619	0.3435	0.167	0.01
Ti10	0.25	0.25	0.5	0.833	0.01
Al10	0.25	0.25	0.5	0.167	0.01
O1	0.302	0.755	0.363	1	0.01
O2	0.179	0.253	0.114	1	0.01
O3	0.059	0.631	0.47	1	0.01
O4	0.318	0	0.384	1	0.01
O5	0.298	0.5	0.351	1	0.01
O6	0.438	0.129	0.056	1	0.01
O7	0.434	0.254	0.303	1	0.01
O8	0.441	0.376	0.052	1	0.01
O9	0.056	0.119	0.442	1	0.01

O10	0.433	0	0.307	1	0.01
O11	0.193	0.633	0.372	1	0.01
O12	0.328	0.124	0.141	1	0.01
O13	0.187	0.5	0.115	1	0.01
O14	0.069	0	0.202	1	0.01
O15	0.313	0.369	0.125	1	0.01
O16	0.191	0.114	0.4	1	0.01

Weight Fractions	
Phases	Wt. %
$BaAl_2Ti_6O_{16}$	**96.861(3)**
$Ba_4Al_2Ti_{10}O_{27}$	**3.14(2)**

Rietveld Refinement $BaCsAlTi_7O_{16}$ (Cs/Ba-Hollandite) Citrate combustion synthesis

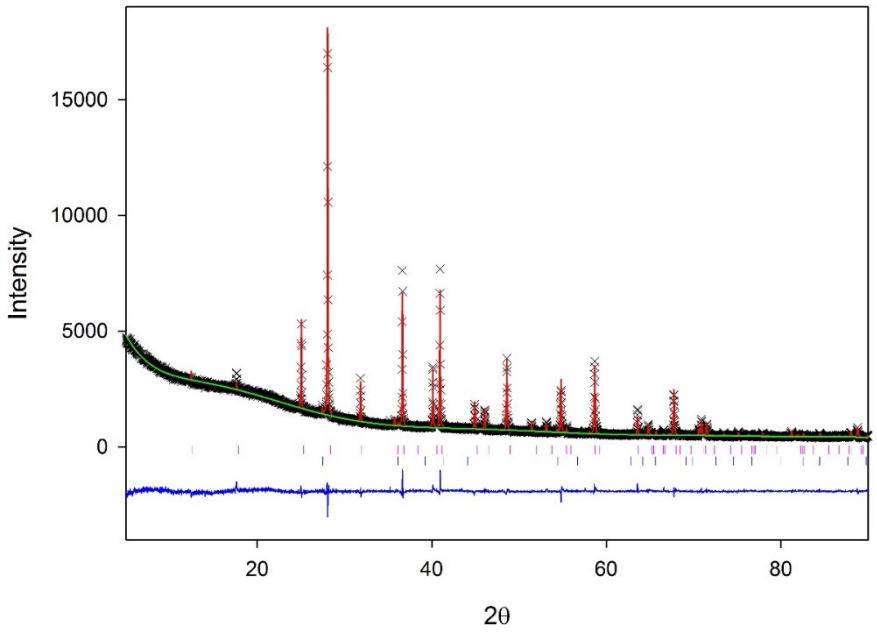

Figure 7.19 *Rietveld Refinement (GSAS Liveplot) for $CsBaAlTi_7O_{16}$ (Cs/Ba-Hollandite). Pink ticks: $Ba_{1.24}Al_{2.48}Ti_{5.52}O_{16}$ and blue ticks: TiO_2*

Table 7.19 *Rietveld Refinement details for $Ba_{0.62}Cs_{0.62}Al_{1.86}Ti_{6.14}O_{16}$ GSAS*

χ2	**wRp**	**Rp**
2.144	4.04 %	2.97 %

Phase	**Symmetry Setting**	**Space Group**
$Ba_{0.62}Cs_{0.62}Al_{1.86}Ti_{6.14}O_{16}$	Tetragonal	*I*4/*m*

Phase Information	***a***	***b***	***c***	***V***	
	10.03715(13)	10.03715(13)	2.92299(4)	294.475(10)	
	α	***β***	***γ***		
	90	90	90		
Atom	***x***	***y***	***z***	**Occupancy**	**U_{iso}**
Ba	0	0	0.5742(23)	0.228(15)	0.0614(23)
Cs	0	0	0.5742(23)	0.112(15)	0.0614(23)
Ti1	0.35207(29)	0.1664(4)	0	0.712(15)	0.0094(10)
Al1	0.35207(29)	0.1664(4)	0	0.288(15)	0.0094(10)
O1	0.154	0.201	0	1	0.01
O2	0.538	0.167	0	1	0.01

Phase	Symmetry Setting	Space Group
TiO_2	Tetragonal	$P4_2/mnm$

Phase Information	*a*	*b*	*c*	*V*	
	4.5842(9)	4.5842(9)	2.9537(11)	62.072(24)	
	α	***β***	***γ***		
	90	90	90		
Atom	***x***	***y***	***z***	**Occupancy**	**U_{iso}**
Ti	0	0	0	1	0.01
O	0.3057	0.3057	0	1	0.01

Weight Fractions	
Phases	Wt. %
$Ba_{0.62}Cs_{0.62}Al_{1.86}Ti_{6.14}O_{16}$	**98.645(1)**
TiO_2	**1.36(1)**

Appendix 2

Chapter 3 - Computational Section Ba-doped $Cs_2TiNb_6O_{18}$

MCMC Energy Distributions

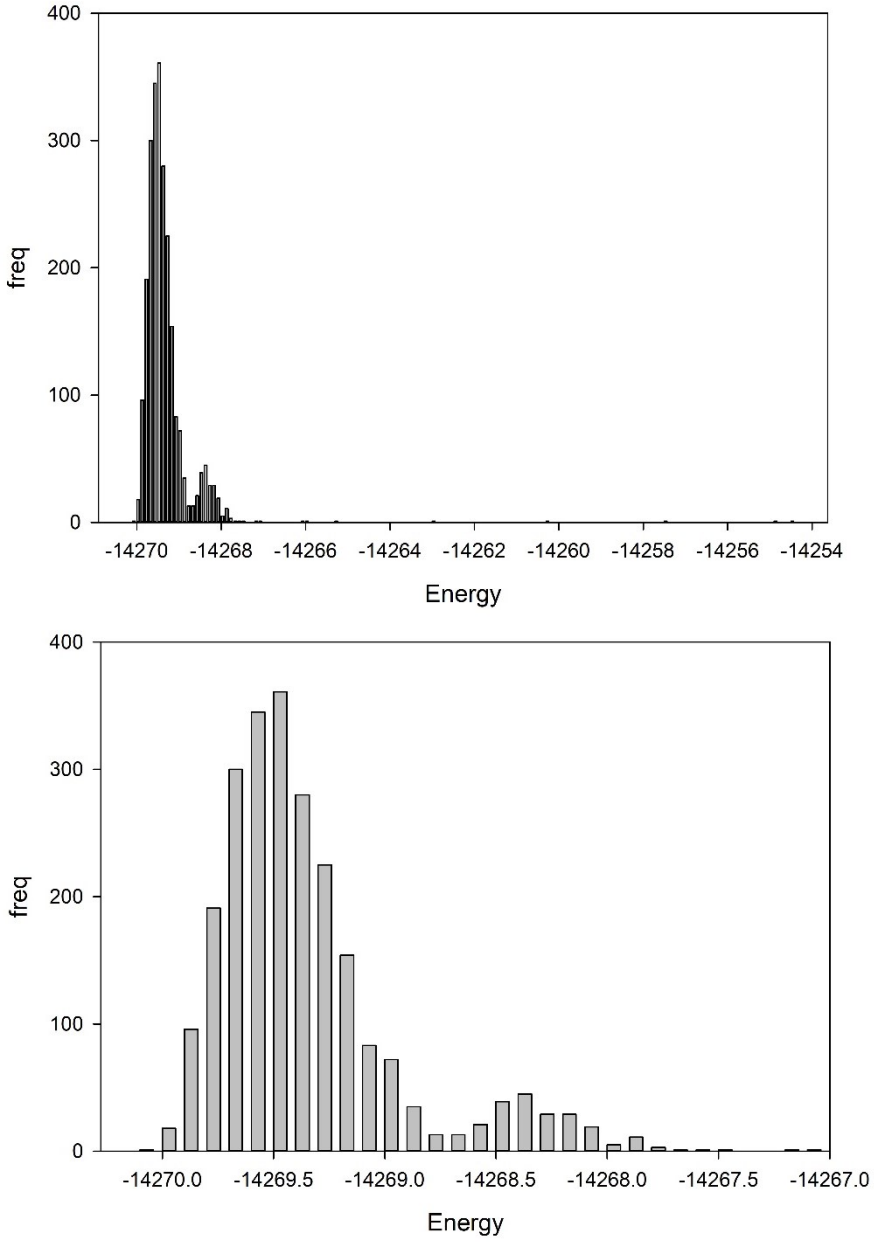

Figure 7.20 *MCMC Energy distributions (KeV), histograms $Cs_2TiNb_6O_{18}$, Ba 20% - doping Ti^{4+} substituted for Nb^{5+}*

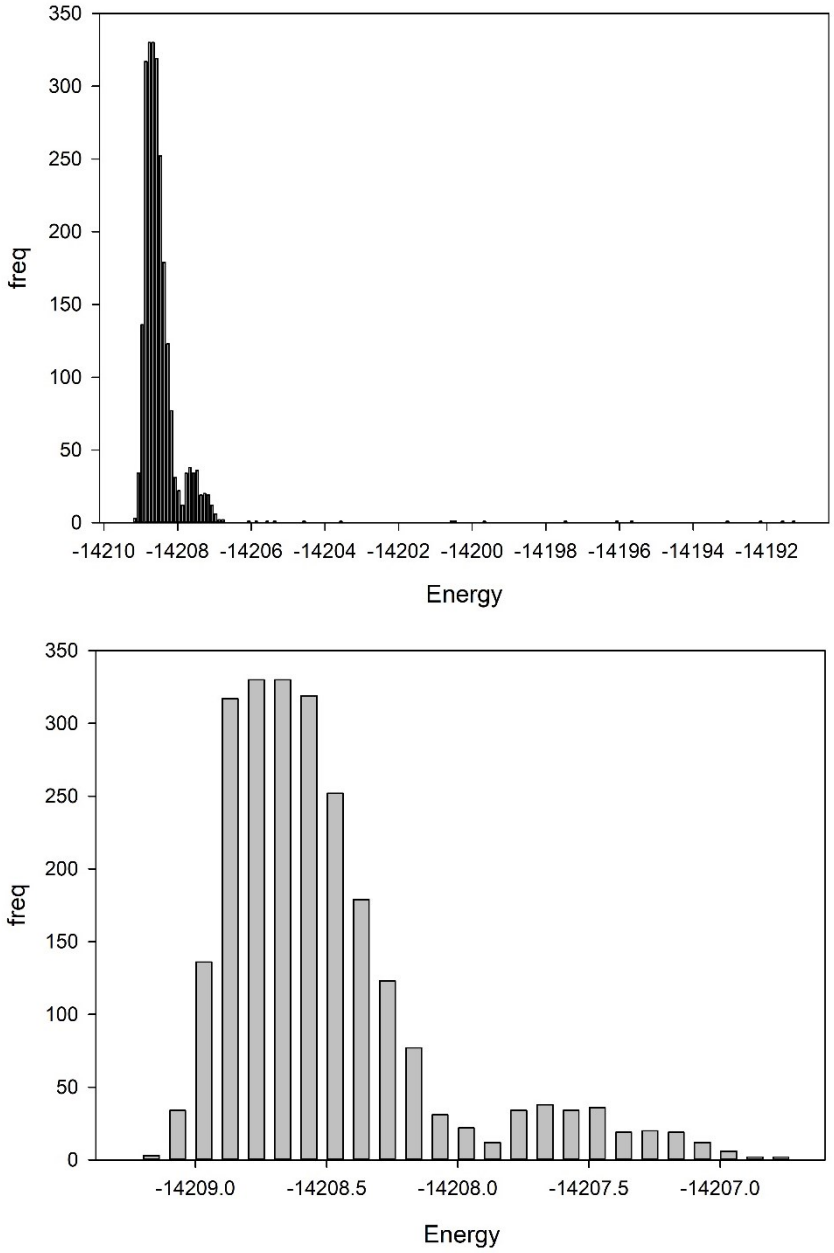

Figure 7.21 *MCMC Energy distributions (KeV), histograms $Cs_2TiNb_6O_{18}$, Ba 30% - doping Ti^{4+} substituted for Nb^{5+}*

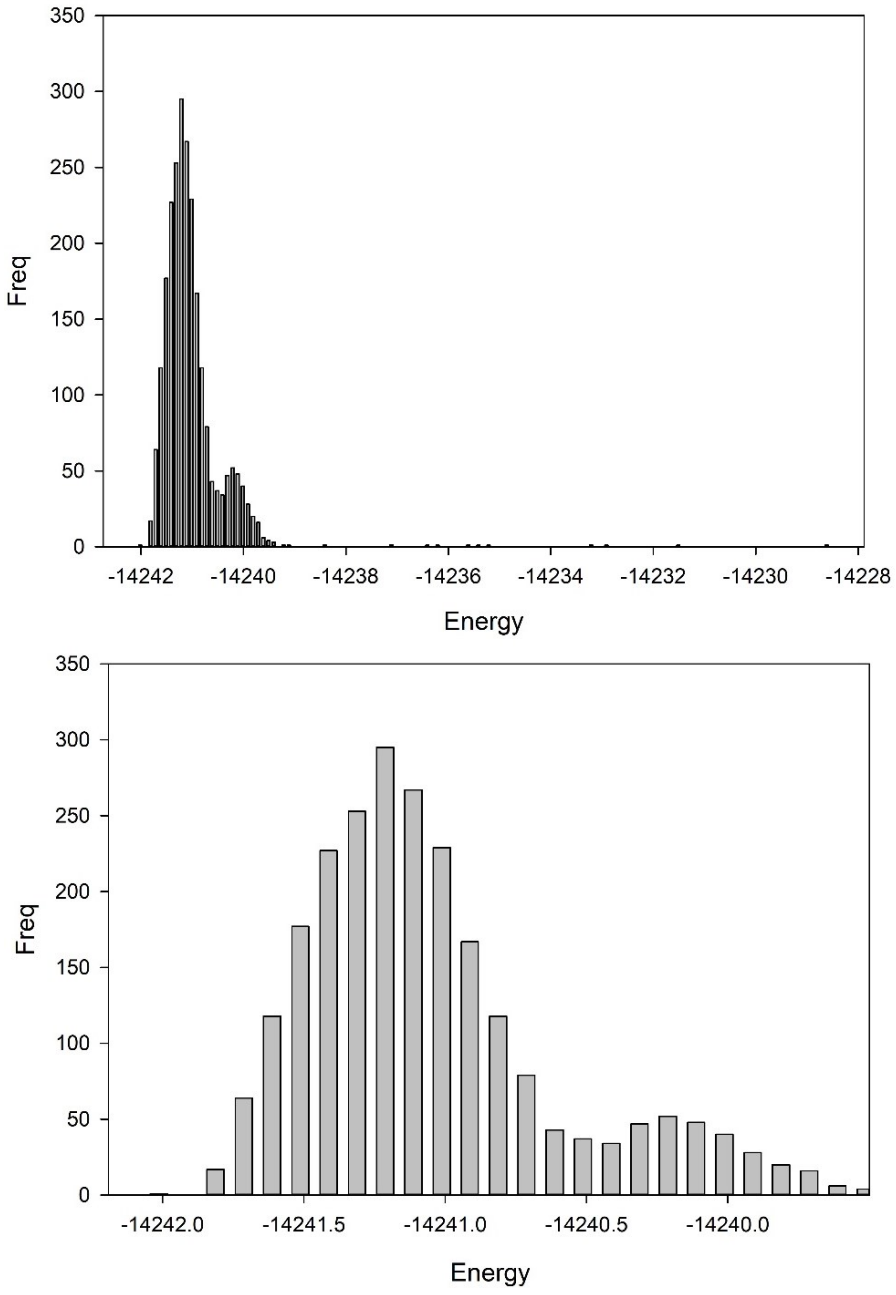

Figure 7.22 *MCMC Energy distributions (KeV), histograms $Cs_2TiNb_6O_{18}$, Ba 20% - doping Nb^{4+} substituted for Nb^{5+}*

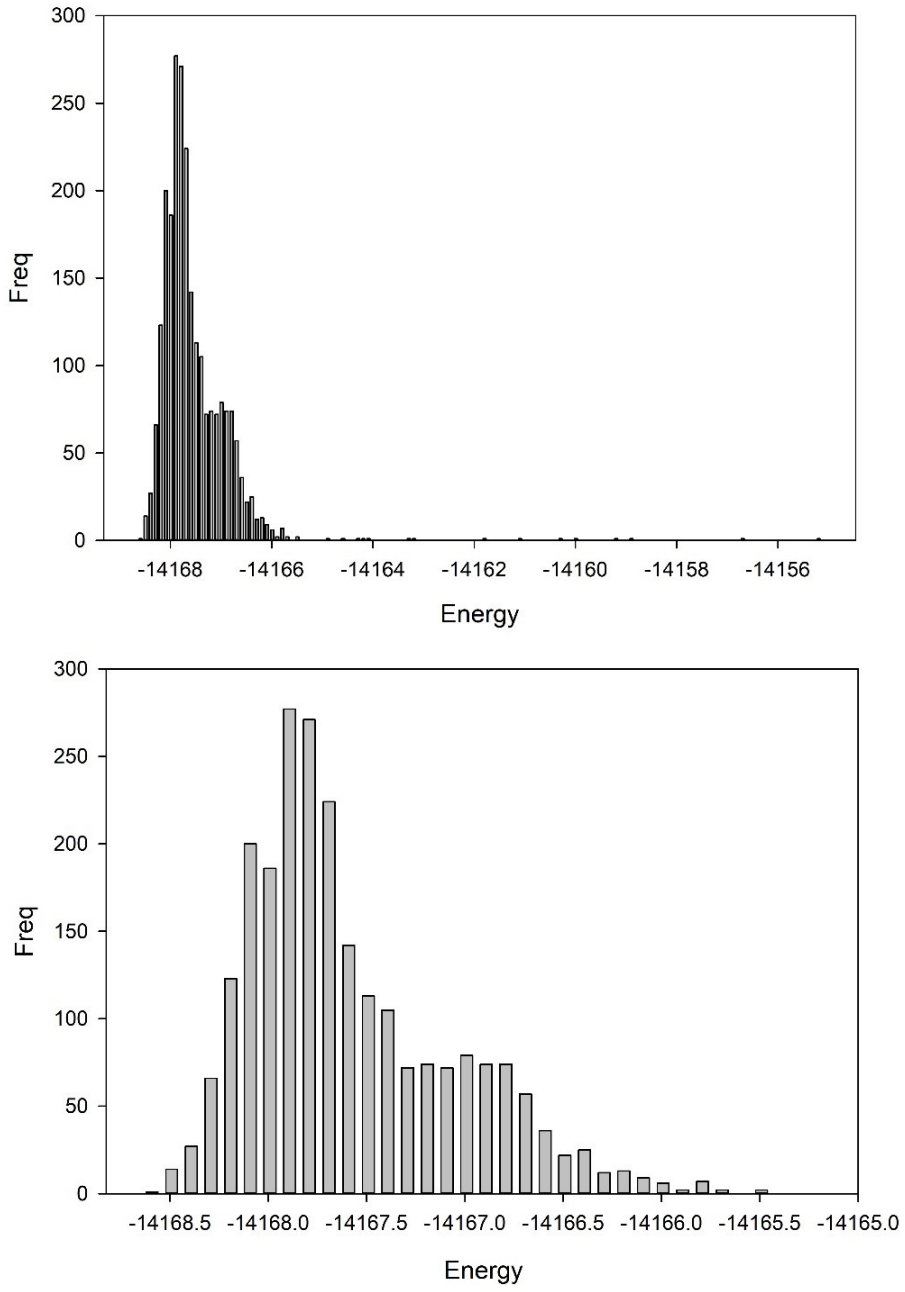

Figure 7.23 *MCMC Energy distributions (KeV), histograms $Cs_2TiNb_6O_{18}$, Ba 30% - doping Nb^{4+} substituted for Nb^{5+}*

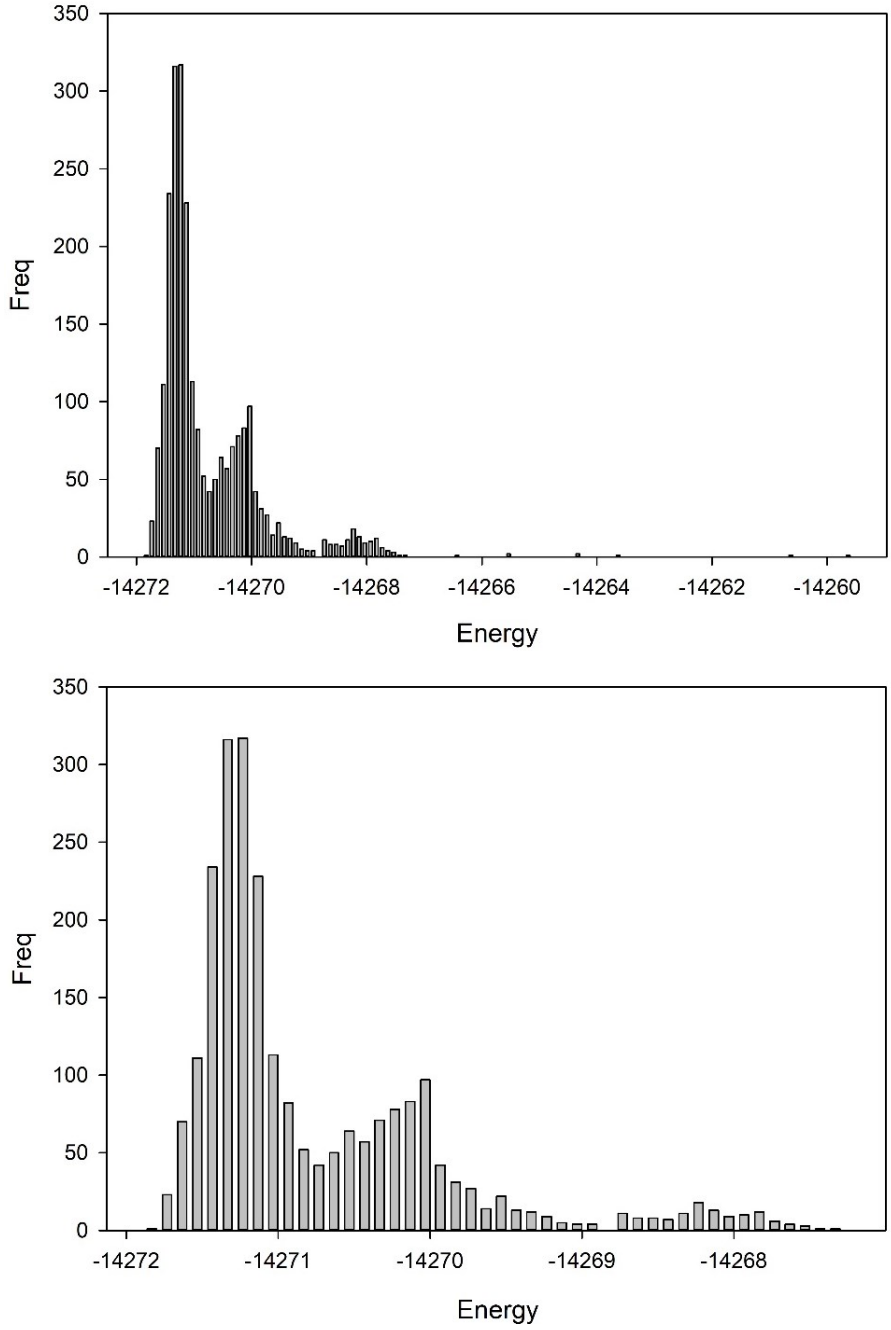

Figure 7.24 *MCMC Energy distributions (KeV), histograms $Cs_2TiNb_6O_{18}$, Ba 20% - doping Ti^{3+} substituted for Ti^{4+}*

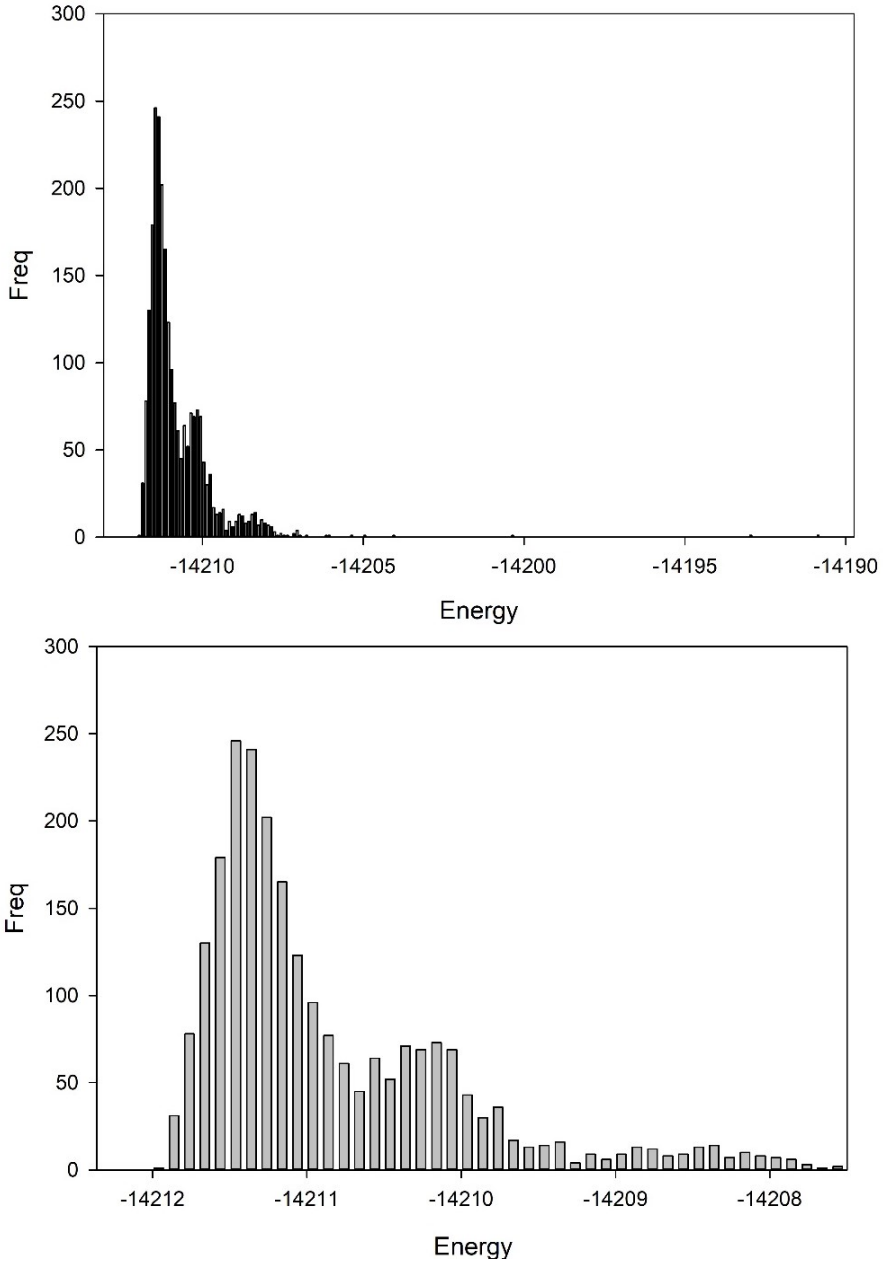

Figure 7.25 *MCMC Energy distributions (KeV), histograms $Cs_2TiNb_6O_{18}$, Ba 30% - doping Ti^{3+} substituted for Ti^{4+}*

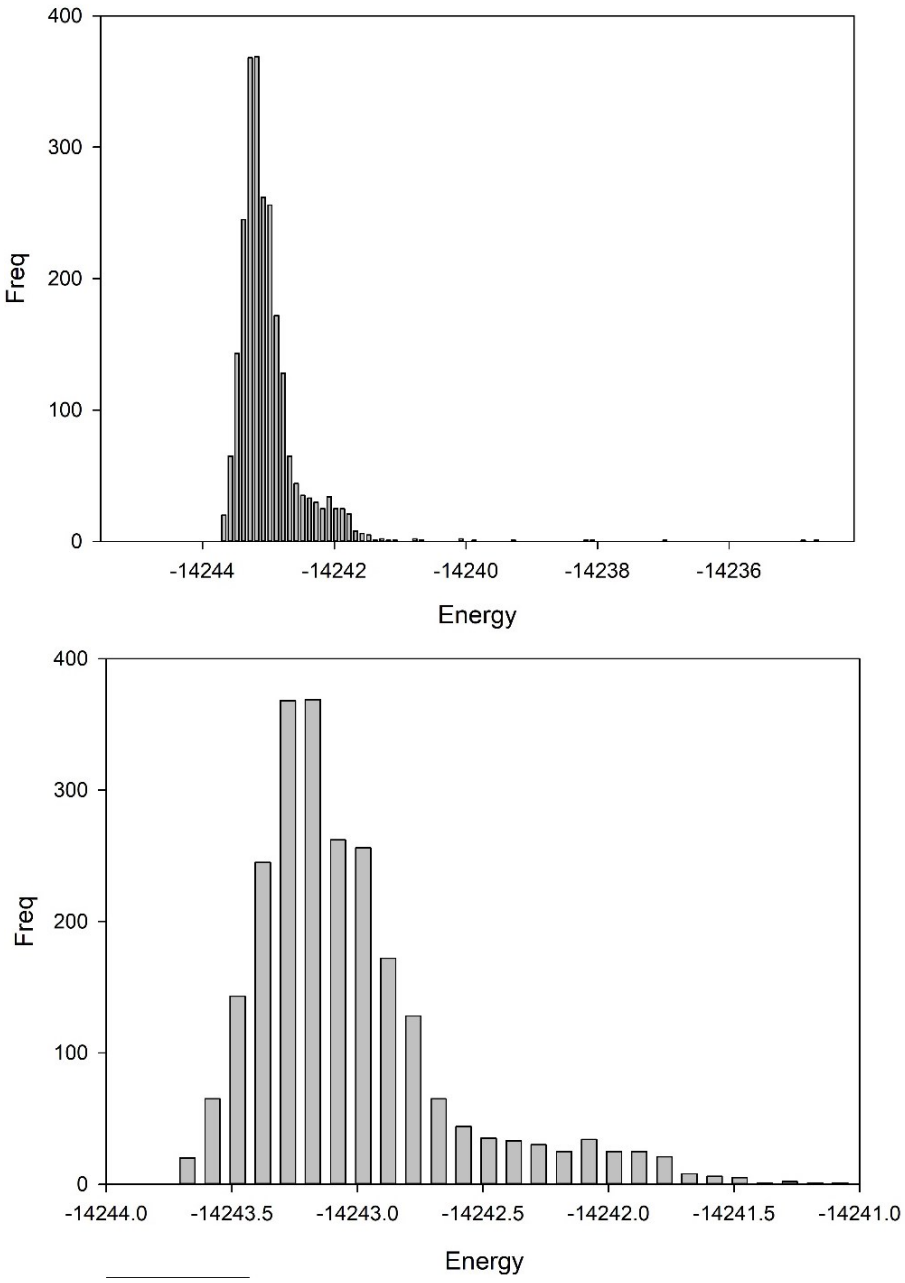

Figure 7.26 *MCMC Energy distributions (KeV), histograms $Cs_2TiNb_6O_{18}$, Ba 20% - doping $Ti^{3+}$and Nb^{4+} substituted for Ti^{4+} and Nb^{5+}*

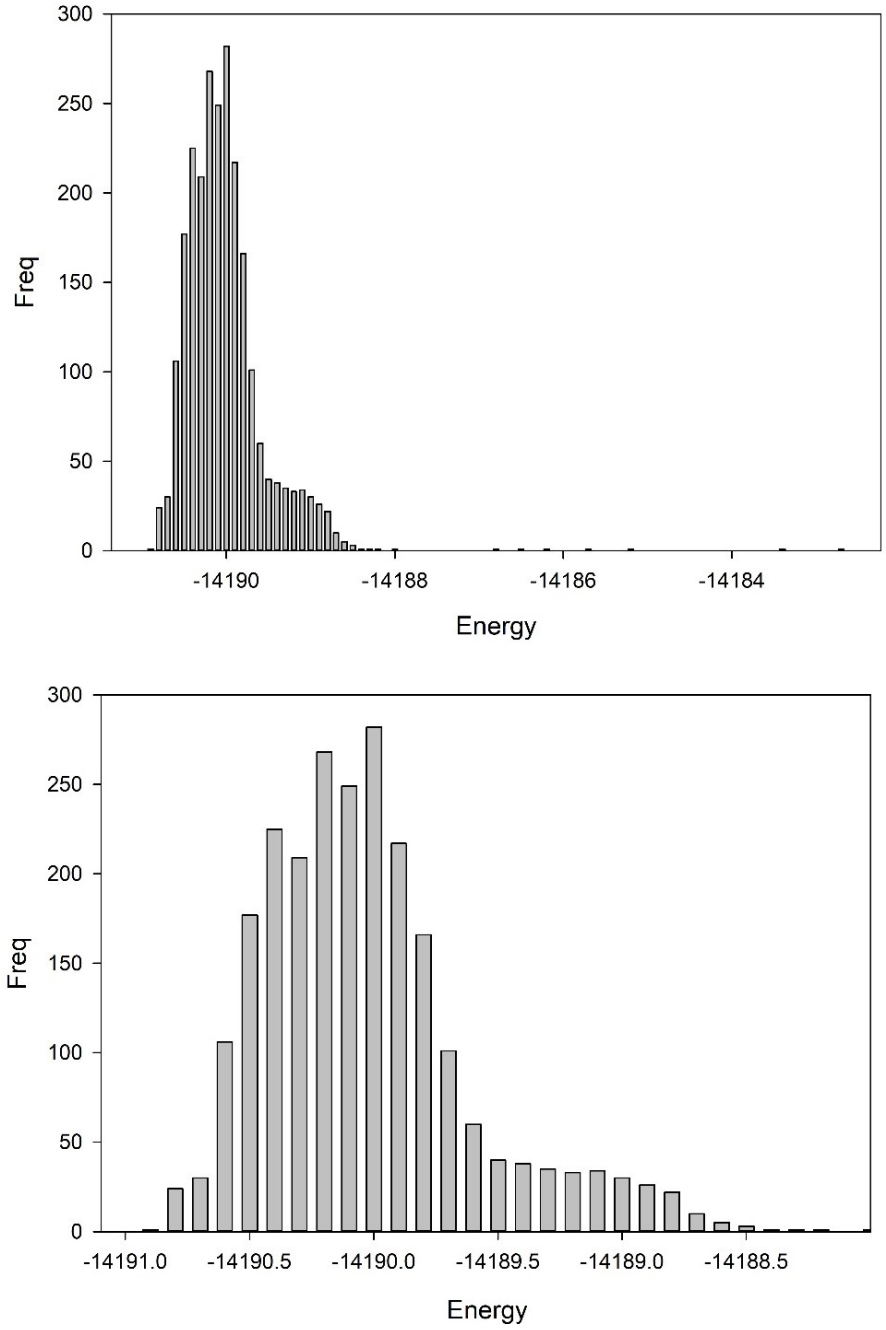

Figure 7.27 *MCMC Energy distributions (KeV), histograms $Cs_2TiNb_6O_{18}$, Ba 30% - doping $Ti^{3+}$and Nb^{4+} substituted for Ti^{4+} and Nb^{5+}*

Appendix 3

Elemental Analysis (X-ray Florescence, (XRF)) Chapter 3

XRF $Cs_2TiNb_6O_{18}$ (Sol-gel)

Table 7.20 *XRF details for $Cs_2TiNb_6O_{18}$ Sol-gel*

Formula	Z	Concentration	Status
Nb2O5	41	63.67	XRF 3
Cs2O	55	24.59	XRF 2
TiO2	22	5.77	XRF 1
SiO2	14	0.38	XRF 1
I	53	0.315	XRF 1
Cl	17	0.21	XRF 1
SO3	16	0.11	XRF 1
CuO	29	0.0723	XRF 1
Fe2O3	26	0.062	XRF 1
CaO	20	0.054	XRF 1
ZnO	30	0.0426	XRF 1
NiO	28	0.015	XRF 1

Line 1	Net int.	Used intensity	Calc. conc	Crystal	Collimator	Stat. error	LLD	Analyzed layer
Nb KA1-HR-Tr	6981	14027	73.28	LiF200	0.23	0.04%	272.4 PPM	6.4 mm
Cs KA1-HR-Tr	159.6	303.7	35.19	LiF200	0.23	0.29%	0.17%	13.1 mm
Ti KA1-HR-Tr	17.64	42.32	5.77	LiF200	0.23	0.80%	336.1 PPM	211 um
Si KA1-HR-Tr	0.1882	0.6697	0.38	PET	0.23	9.91%	676.6 PPM	19.9 um
I KA1-HR-Tr	4.013	4.575	0.315	LiF200	0.23	5.09%	0.12%	10.5 mm
Cl KA1-HR-Tr	0.3143	1.26	0.21	PET	0.23	7.43%	251.9 PPM	48 um
S KA1-HR-Tr	0.4542	0.4902	0.11	PET	0.23	14.80%	657.2 PPM	44 um
Cu KA1-HR-Tr	2.392	5.577	0.0723	LiF200	0.23	3.94%	82.8 PPM	0.80 mm
Fe KA1-HR-Tr	0.7583	1.783	0.062	LiF200	0.23	7.40%	135.0 PPM	0.42 mm
Ca KA1-HR-Tr	0.1452	0.3476	0.054	LiF200	0.23	17.20%	272.4 PPM	120 um
Zn KA1-HR-Tr	1.817	4.238	0.0426	LiF200	0.23	5.44%	71.4 PPM	0.98 mm
Ni KA1-HR-Tr	0.3696	0.8618	0.015	LiF200	0.23	19.20%	92.5 PPM	0.65 mm

Line 2	Net int.	Used intensity	Calc. conc	Crystal	Collimator	Stat. error	LLD	Analyzed layer
Nb KB1-HR-Tr	1370	2753	74.21	LiF200	0.23	0.09%	0.14%	8.9 mm
Cs LA1-HR-Tr	30.95	74.24	24.59	LiF200	0.23	0.59%	739.9 PPM	183 um
Ti KB1-HR-Tr	10.02	24.04	21.3	LiF200	0.23	1.08%	0.23%	271 um
Si KB1-HR-Tr/Ox	-0.00096	-0.00342	-0.096	PET	0.23		3.32%	22.9 um
I KB1-HR-Tr	0.4895	0.9627	0.068	LiF200	0.23	96.50%	978.2 PPM	14.7 mm
Cu KB1-HR-Tr	0.2641	0.6158	0.042	LiF200	0.23	88.20%	498.4 PPM	1.06 mm
Fe KB1-HR-Tr	0.2355	0.5538	0.1	LiF200	0.23	26.80%	900.6 PPM	0.55 mm
Ca KB1-HR-Tr	-0.00372	-0.01521	-0.019	LiF200	0.23		0.26%	152 um
Zn KB1-HR-Tr	-0.09854	-0.2298	-0.013	LiF200	0.23		465.8 PPM	1.31 mm

Ni KB1-HR-Tr	33.4	61.48	5.53	LiF200	0.23	1.54%	0.12%	0.86 mm

Line 3	Net int.	Used intensity	Calc. conc	Crystal	Collimator	Stat. error	LLD	Analyzed layer
Nb LA1-HR	33.07	132.6	63.67	PET	0.23	0.57%	752.9 PPM	36 um
Cs LB1-HR-Tr	19.83	47.55	23.8	LiF200	0.23	0.75%	0.14%	226 um
I LA1-HR-Tr	0.4022	0.963	0.28	LiF200	0.23	7.83%	559.4 PPM	144 um
Cu LA1-HR	0.05938	0.1496	0.76	XS-55	0.23	27.70%	0.62%	3.9 um
Zn LA1-HR-Tr	0.01373	0.03424	0.084	XS-55	0.23	285%	0.32%	4.7 um
Ni LA1-HR	-0.00779	-0.01985	-0.23	XS-55	0.23		1.35%	3.1 um

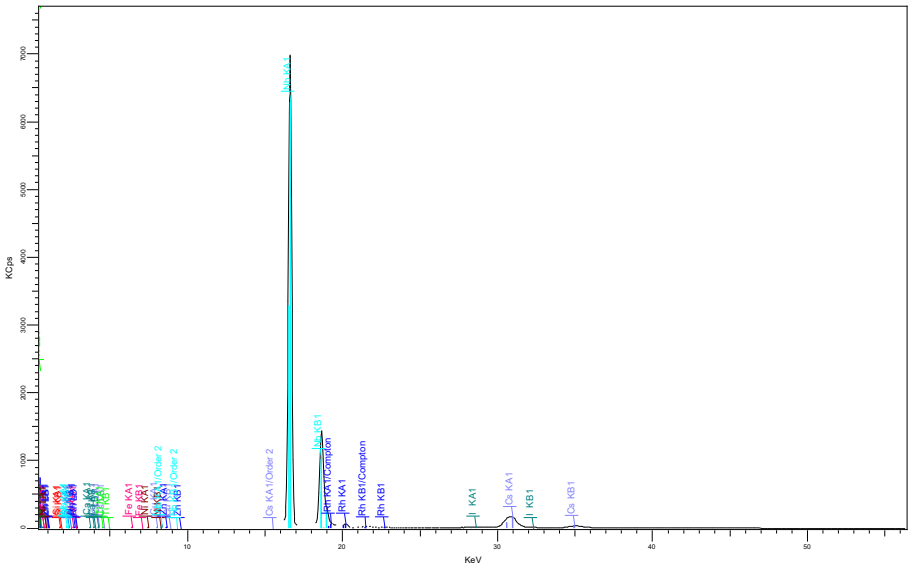

Figure 7.28 *XRF Spectrum $Cs_2TiNb_6O_{18}$ sol-gel*

XRF $Cs_2TiNb_6O_{18}$ (Solid-state)

Table 7.21 *XRF details for $Cs_2TiNb_6O_{18}$ Solid-state*

Formula	Z	Concentration	Status
Nb2O5	41	60.9	XRF 3
Cs2O	55	23.8	XRF 2
TiO2	22	8.82	XRF 1
MoO3	42	1.84	XRF 2
SO3	16	0.153	XRF 1
Al2O3	13	0.15	XRF 1
CaO	20	0.1	XRF 1
CuO	29	0.0751	XRF 1
Fe2O3	26	0.068	XRF 1
ZnO	30	0.0387	XRF 1
SrO	38	0.008	XRF 1

Line 1	Net int.	Used intensity	Calc. conc	Crystal	Collimator	Stat. error	LLD	Analyzed layer
Nb KA1-HR-Tr	6679	13419	69.45	LiF200	0.23	0.04%	279.5 PPM	6.4 mm
Cs KA1-HR-Tr	154.5	293.9	33.64	LiF200	0.23	0.29%	0.17%	13.2 mm
Ti KA1-HR-Tr	27.17	65.15	8.82	LiF200	0.23	0.64%	336.1 PPM	213 um
Mo KA1-HR-Tr	17.88	24.25	0.126	LiF200	0.23	3.69%	118.2 PPM	7.4 mm
S KA1-HR-Tr	0.5496	0.708	0.153	PET	0.23	5.25%	678.7 PPM	44 um
Al KA1-HR-Tr	0.07262	0.231	0.15	PET	0.23	18.70%	630.2 PPM	12.9 um
Ca KA1-HR-Tr	0.2857	0.6841	0.1	LiF200	0.23	9.65%	266.1 PPM	121 um
Cu KA1-HR-Tr	2.493	5.813	0.0751	LiF200	0.23	3.76%	81.4 PPM	0.80 mm
Fe KA1-HR-Tr	0.8344	1.962	0.068	LiF200	0.23	6.80%	134.6 PPM	0.42 mm
Zn KA1-HR-Tr	1.658	3.866	0.0387	LiF200	0.23	5.88%	70.8 PPM	0.98 mm
Sr KA1-HR-Tr	1.362	2.805	0.008	LiF200	0.23	14.30%	42.8 PPM	4.0 mm

Line 2	Net int.	Used intensity	Calc. conc	Crystal	Collimator	Stat. error	LLD	Analyzed layer
Nb KB1-HR-Tr	1313	2639	70.43	LiF200	0.23	0.09%	0.14%	8.9 mm
Cs LA1-HR-Tr	30.21	72.46	23.8	LiF200	0.23	0.60%	732.3 PPM	184 um
Ti KB1-HR-Tr	11.43	27.42	24.1	LiF200	0.23	1.01%	0.23%	274 um
Mo KB1-HR-Tr	22.02	44.24	1.84	LiF200	0.23	2.93%	647.2 PPM	3.9 mm

Al KB1-HR-Tr/Ox	0.17	0.5408	30	PET	0.23	9.66%	4.93%	14.5 um
Ca KB1-HR-Tr	-0.00141	-0.00994	-0.012	LiF200	0.23		0.26%	153 um
Cu KB1-HR-Tr	0.4516	1.053	0.071	LiF200	0.23	20.90%	498.3 PPM	1.07 mm
Fe KB1-HR-Tr	0.2341	0.5504	0.1	LiF200	0.23	26.80%	894.7 PPM	0.55 mm
Zn KB1-HR-Tr	0.08454	0.1971	0.011	LiF200	0.23	304%	464.6 PPM	1.31 mm
Sr KB1-HR-Tr	47.69	95.94	1.19	LiF200	0.23	1.64%	201.0 PPM	5.6 mm

Line 3	Net int.	Used intensity	Calc. conc	Crystal	Collimator	Stat. error	LLD	Analyzed layer
Nb LA1-HR	31.78	127.4	60.9	PET	0.23	0.58%	765.4 PPM	37 um
Cs LB1-HR-Tr	19.76	47.37	23.5	LiF200	0.23	0.75%	0.14%	228 um
Mo LA1-HR-Tr	0.1276	-0.4557	-0.19	PET	0.23	38.30%	0.12%	43 um
Cu LA1-HR	0.08754	0.2208	1.1	XS-55	0.23	20.00%	0.62%	3.9 um
Zn LA1-HR-Tr	0.04415	0.111	0.27	XS-55	0.23	38.50%	0.33%	4.7 um
Sr LA1-HR	-0.00715	-0.02543	-0.021	PET	0.23		964.9 PPM	22.0 um

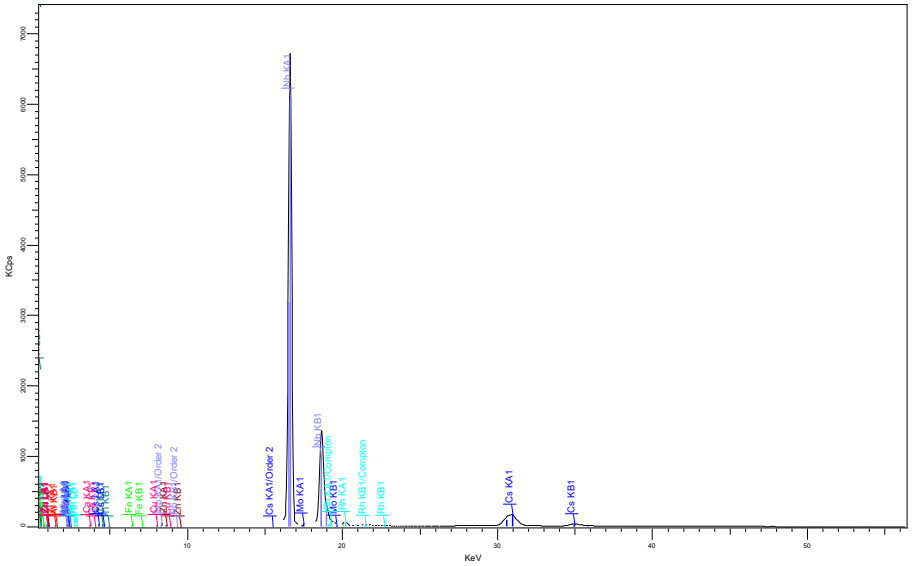

Figure 7.29 *XRF Spectrum $Cs_2TiNb_6O_{18}$ solid-state*

XRF $Ba_2Ti_3Nb_6O_{18}$ (Solid-state)

Table 7.22 *XRF details for $Ba_2Ti_3Nb_6O_{18}$ Solid-state*

Formula	Z	Concentration	Status
Nb2O5	41	45.4	XRF 3
BaO	56	28.7	XRF 2
TiO2	22	21.33	XRF 1
Na2O	11	0.48	XRF 1
SiO2	14	0.26	XRF 1
SO3	16	0.11	XRF 1
Fe2O3	26	0.071	XRF 1
CuO	29	0.0665	XRF 1
ZnO	30	0.0409	XRF 1
SrO	38	0.02	XRF 1

Line 1	Net int.	Used intensity	Calc. conc	Crystal	Collimator	Stat. error	LLD	Analyzed layer
Nb KA1-HR-Tr	5146	10339	51.15	LiF200	0.23	0.05%	251.5 PPM	6.1 mm
Ba LA1-HR-Tr	44.18	105.3	30.33	LiF200	0.23	0.50%	0.11%	222 um
Ti KA1-HR-Tr	69.42	166.1	21.33	LiF200	0.23	0.39%	431.1 PPM	229 um
Na KA1-HR-Tr	0.1441	0.3564	0.48	XS-55	0.23	14.00%	0.20%	5.1 um
Si KA1-HR-Tr	0.1284	0.4569	0.26	PET	0.23	12.80%	645.6 PPM	19.6 um
S KA1-HR-Tr	0.363	0.4952	0.11	PET	0.23	6.86%	598.4 PPM	43 um
Fe KA1-HR-Tr	0.8266	1.943	0.071	LiF200	0.23	6.58%	133.6 PPM	0.40 mm
Cu KA1-HR-Tr	2.073	4.834	0.0665	LiF200	0.23	4.26%	82.7 PPM	0.76 mm
Zn KA1-HR-Tr	1.636	3.814	0.0409	LiF200	0.23	5.71%	72.0 PPM	0.93 mm
Sr KA1-HR-Tr	2.991	6.159	0.02	LiF200	0.23	6.27%	43.5 PPM	3.8 mm

Line 2	Net int.	Used intensity	Calc. conc	Crystal	Collimator	Stat. error	LLD	Analyzed layer
Nb KB1-HR-Tr	1032	2073	52.14	LiF200	0.23	0.10%	0.13%	8.4 mm
Ba LB1-HR-Tr	29.64	70.85	28.7	LiF200	0.23	0.61%	0.14%	278 um
Ti KB1-HR-Tr	16.27	25.39	21.2	LiF200	0.23	0.84%	0.71%	295 um
Si KB1-HR-Tr/Ox	-0.0015	-0.0052	-0.15	PET	0.23		3.38%	22.7 um
Fe KB1-HR-Tr	0.1076	0.2529	0.049	LiF200	0.23	54.50%	894.9 PPM	0.53 mm
Cu KB1-HR-Tr	0.4004	0.9336	0.067	LiF200	0.23	22.40%	505.8 PPM	1.01 mm
Zn KB1-HR-Tr	-0.0375	-0.08733	-0.005	LiF200	0.23		469.0 PPM	1.25 mm
Sr KB1-HR-Tr	34.78	57.21	0.762	LiF200	0.23	2.04%	288.7 PPM	5.3 mm

Line 3	Net int.	Used intensity	Calc. conc	Crystal	Collimator	Stat. error	LLD	Analyzed layer
Nb LA1-HR	23.9	95.83	45.4	PET	0.23	0.67%	718.0 PPM	36 um
Ba KA1-HR-Tr	176.8	336.4	27.36	LiF200	0.23	0.27%	0.12%	17.7 mm
Cu LA1-HR	-0.0188	-0.04736	-0.24	XS-55	0.23		0.63%	3.8 um
Zn LA1-HR-Tr	0.0186	0.01912	0.047	XS-55	0.23	218%	0.39%	4.7 um
Sr LA1-HR	-0.0087	-0.03151	-0.026	PET	0.23		990.7 PPM	21.8 um

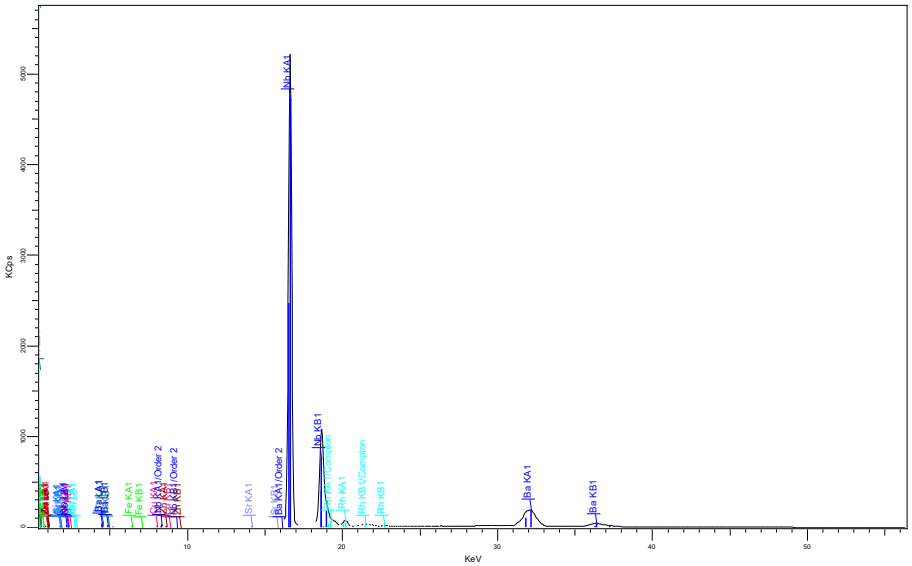

Figure 7.30 *XRF spectrum for $Ba_2Ti_3Nb_6O_{18}$ Solid-state*

XRF $BaCsTi_2Nb_5O_{18}$ Solid-state

Table 7.23 *XRF details for $BaCsTi_2Nb_5O_{18}$ Solid-state*

Formula	Z	Concentration	Status
Nb2O5	41	54.9	XRF 3
TiO2	22	14.22	XRF 1
BaO	56	13.9	XRF 1
Cs2O	55	12.2	XRF 3
MoO3	42	2.03	XRF 2
Na2O	11	0.32	XRF 1
SO3	16	0.0908	XRF 1
CuO	29	0.0711	XRF 1
K2O	19	0.052	XRF 1
Fe2O3	26	0.052	XRF 1
ZnO	30	0.0441	XRF 1
SrO	38	0.008	XRF 1

Line 1	Net int.	Used intensity	Calc. conc	Crystal	Collimator	Stat. error	LLD	Analyzed layer
Nb KA1-HR-Tr	6082	12219	62.83	LiF200	0.23	0.04%	273.9 PPM	6.2 mm
Ti KA1-HR-Tr	44.62	106.9	14.22	LiF200	0.23	0.49%	442.4 PPM	217 um
Ba LA1-HR-Tr	19.65	46.68	13.9	LiF200	0.23	0.76%	0.11%	211 um
Cs KA1-HR-Tr	89.87	168.2	18.21	LiF200	0.23	0.42%	0.20%	13.9 mm
Mo KA1-HR-Tr	15.61	20.78	0.107	LiF200	0.23	4.11%	114.7 PPM	7.2 mm
Na KA1-HR-Tr	0.09805	0.2399	0.32	XS-55	0.23	19.10%	0.20%	5.1 um
S KA1-HR-Tr	0.452	0.4211	0.0908	PET	0.23	5.84%	643.4 PPM	43 um
Cu KA1-HR-Tr	2.285	5.328	0.0711	LiF200	0.23	4.06%	84.6 PPM	0.78 mm
K KA1-HR-Tr	0.1501	0.3603	0.052	LiF200	0.23	15.80%	237.0 PPM	91 um
Fe KA1-HR-Tr	0.6205	1.459	0.052	LiF200	0.23	8.72%	136.8 PPM	0.41 mm
Zn KA1-HR-Tr	1.825	4.256	0.0441	LiF200	0.23	5.34%	72.7 PPM	0.95 mm
Sr KA1-HR-Tr	1.229	2.53	0.008	LiF200	0.23	15.50%	43.8 PPM	3.9 mm

Line 2	Net int.	Used intensity	Calc. conc	Crystal	Collimator	Stat. error	LLD	Analyzed layer
Nb KB1-HR-Tr	1213	2438	64.3	LiF200	0.23	0.10%	0.14%	8.6 mm
Ti KB1-HR-Tr	12.33	23.2	20.1	LiF200	0.23	0.97%	0.58%	280 um
Ba LB1-HR-Tr	13.5	32.24	13.4	LiF200	0.23	0.92%	0.14%	263 um
Cs LA1-HR-Tr	15.98	38.33	12.3	LiF200	0.23	0.84%	773.5 PPM	188 um
Mo KB1-HR-Tr	25.35	50.94	2.03	LiF200	0.23	2.61%	615.7 PPM	4.1 mm
Cu KB1-HR-Tr	0.313	0.7299	0.051	LiF200	0.23	73.30%	506.2 PPM	1.03 mm
K KB1-HR-Tr	-0.0013	-0.00311	-0.004	LiF200	0.23		0.22%	114 um
Fe KB1-HR-Tr	0.1172	0.2755	0.052	LiF200	0.23	129%	901.8 PPM	0.54 mm
Zn KB1-HR-Tr	0.02001	0.04667	0.003	LiF200	0.23	1228%	462.4 PPM	1.27 mm
Sr KB1-HR-Tr	42.06	78.81	1.01	LiF200	0.23	1.79%	258.7 PPM	5.4 mm

Line 3	Net int.	Used intensity	Calc. conc	Crystal	Collimator	Stat. error	LLD	Analyzed layer
Nb LA1-HR	28.8	115.5	54.9	PET	0.23	0.61%	717.5 PPM	36 um
Ba KA1-HR-Tr	80.18	152.6	13.18	LiF200	0.23	0.44%	0.13%	15.5 mm
Cs LB1-HR-Tr	10.47	25.06	12.2	LiF200	0.23	1.06%	0.15%	232 um
Mo LA1-HR-Tr	0.09079	-0.504	-0.21	PET	0.23	48.60%	0.11%	43 um
Cu LA1-HR	0.00502	0.01266	0.064	XS-55	0.23	750%	0.64%	3.9 um
Zn LA1-HR-Tr	0.02019	0.03212	0.079	XS-55	0.23	201%	0.38%	4.7 um
Sr LA1-HR	0.01521	0.05413	0.044	PET	0.23	81.80%	963.8 PPM	21.9 um

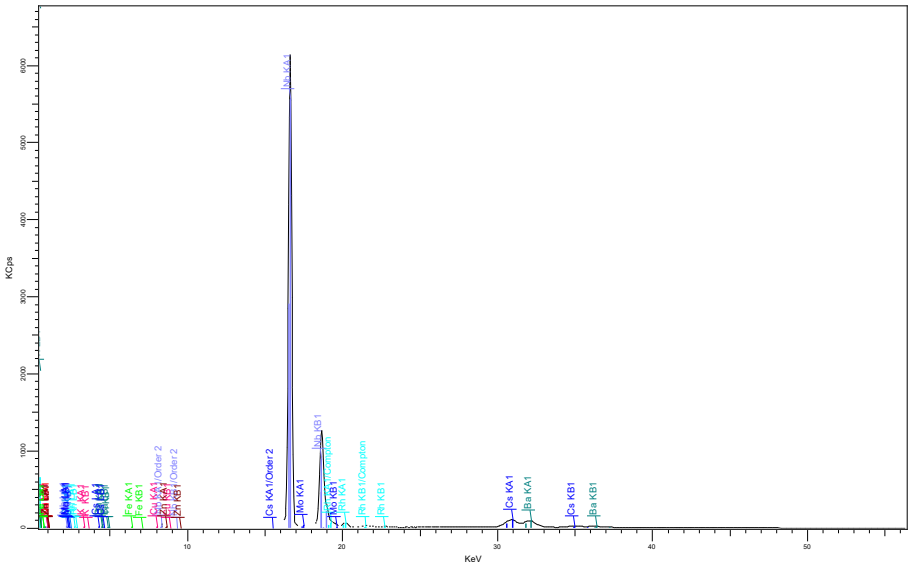

Figure 7.31 *XRF Spectrum for* $CsBaTi_2Nb_5O_{18}$

XRF $Cs_{2-x}Ba_xTi^{(4+)}_{1+x}Nb^{(5+)}_{6-x}O_{18}$ (x=0.6)

Table 7.24 *XRF details for $Cs_{2-x}Ba_xTi^{(4+)}_{1+x}Nb^{(5+)}_{6-x}O_{18}$ (x=0.6)*

Formula	Z	Concentration	Status
Nb2O5	41	59.66	XRF 3
Cs2O	55	17.9	XRF 2
TiO2	22	11.4	XRF 1
BaO	56	8.37	XRF 1
MoO3	42	1.86	XRF 2
Na2O	11	0.37	XRF 1
SiO2	14	0.2	XRF 1
SO3	16	0.167	XRF 1
CeO2	58	0.139	XRF 1
CuO	29	0.0745	XRF 1
Fe2O3	26	0.061	XRF 1
ZnO	30	0.0462	XRF 1
K2O	19	0.039	XRF 1

Line 1	Net int.	Used intensity	Calc. conc	Crystal	Collimator	Stat. error	LLD	Analyzed layer
Nb KA1-HR-Tr	6369	12688	67.1	LiF200	0.23	0.04%	280.4 PPM	6.1 mm
Cs KA1-HR-Tr	123.8	234	26.64	LiF200	0.23	0.34%	0.20%	13.1 mm
Ti KA1-HR-Tr	34.91	84.1	11.4	LiF200	0.23	0.56%	420.8 PPM	211 um
Ba LA1-HR-Tr	11.71	27.88	8.37	LiF200	0.23	0.99%	0.11%	205 um
Mo KA1-HR-Tr	16.39	21.48	0.114	LiF200	0.23	3.94%	118.7 PPM	7.1 mm
Na KA1-HR-Tr	0.1121	0.2746	0.37	XS-55	0.23	17.90%	0.21%	5.0 um
Si KA1-HR-Tr	0.09948	0.3529	0.2	PET	0.23	15.60%	650.7 PPM	19.6 um
S KA1-HR-Tr	0.5536	0.7711	0.167	PET	0.23	5.19%	673.3 PPM	43 um
Ce LA1-HR-Tr	3.75	0.4617	0.139	LiF200	0.23	4.77%	0.22%	257 um
Cu KA1-HR-Tr	2.373	5.56	0.0745	LiF200	0.23	3.88%	83.9 PPM	0.76 mm
Fe KA1-HR-Tr	0.7451	1.718	0.061	LiF200	0.23	7.37%	135.5 PPM	0.40 mm
Zn KA1-HR-Tr	1.895	4.439	0.0462	LiF200	0.23	5.11%	72.3 PPM	0.93 mm
K KA1-HR-Tr	0.1089	0.2619	0.039	LiF200	0.23	21.00%	244.0 PPM	89 um

Line 2	Net int.	Used intensity	Calc. conc	Crystal	Collimator	Stat. error	LLD	Analyzed layer
Nb KB1-HR-Tr	1250	2491	67.77	LiF200	0.23	0.09%	0.14%	8.5 mm
Cs LA1-HR-Tr	22.83	55.06	17.9	LiF200	0.23	0.70%	809.8 PPM	182 um
Ti KB1-HR-Tr	11.77	24.63	21.7	LiF200	0.23	0.99%	0.51%	272 um
Ba LB1-HR-Tr	8.152	19.35	8.15	LiF200	0.23	1.22%	0.15%	256 um
Mo KB1-HR-Tr	22.35	44.53	1.86	LiF200	0.23	2.88%	641.8 PPM	3.8 mm
Si KB1-HR-Tr/Ox	0.00156	0.00555	0.16	PET	0.23	2000%	3.50%	22.6 um
Ce LB1-HR-Tr	0.2402	0.5642	0.3	LiF200	0.23	37.40%	0.14%	263 um
Cu KB1-HR-Tr	0.3757	0.8802	0.062	LiF200	0.23	60.90%	508.0 PPM	1.02 mm
Fe KB1-HR-Tr	0.08845	0.204	0.038	LiF200	0.23	170%	903.1 PPM	0.53 mm
Zn KB1-HR-Tr	0.1052	0.2465	0.014	LiF200	0.23	95.80%	477.2 PPM	1.25 mm

K KB1-HR-Tr	-0.00928	-0.02232	-0.029	LiF200	0.23		0.22%	111 um

Line 3	Net int.	Used intensity	Calc. conc	Crystal	Collimator	Stat. error	LLD	Analysed layer
Nb LA1-HR	31.11	125.2	59.66	PET	0.23	0.59%	748.3 PPM	36 um
Cs LB1-HR-Tr	15.08	36.33	17.9	LiF200	0.23	0.87%	0.15%	226 um
Ba KA1-HR-Tr	47.74	90.89	8.12	LiF200	0.23	0.63%	0.13%	14.6 mm
Mo LA1-HR-Tr	0.1252	-0.4356	-0.18	PET	0.23	38.30%	0.12%	42 um
Cu LA1-HR	0.0242	0.06095	0.31	XS-55	0.23	165%	0.65%	3.8 um
Zn LA1-HR-Tr	0.01097	0.00617	0.015	XS-55	0.23	381%	0.40%	4.7 um

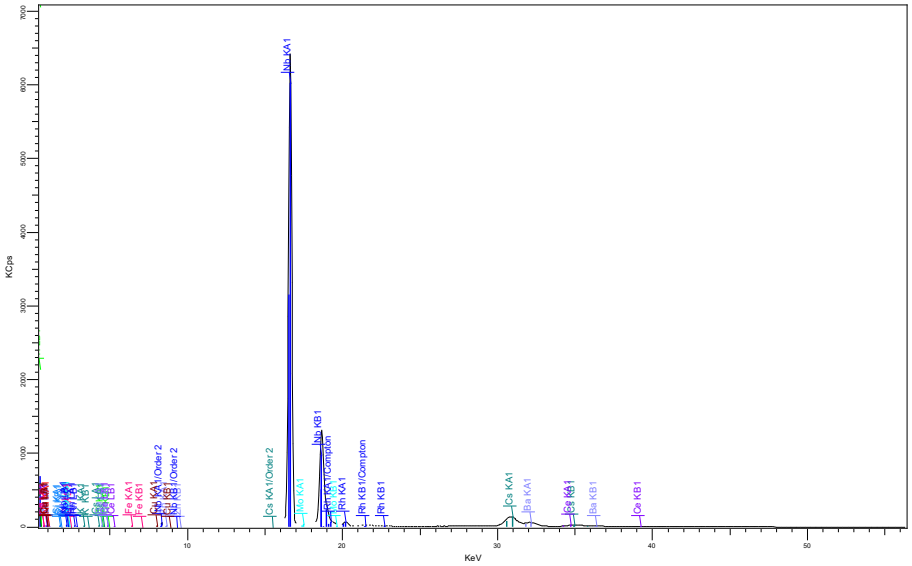

Figure 7.32 *XRF spectrum for* $Cs_{2-x}Ba_xTi^{(4+)}{}_{1+x}Nb^{(5+)}{}_{6-x}O_{18}$ *(x=0.6)*

XRF $Cs_{2-x}Ba_xTi^{(4+)}_{1+x}Nb^{(5+)}_{6-x}O_{18}$ (x=0.5)

Table 7.25 *XRF details for $Cs_{2-x}Ba_xTi^{(4+)}_{1+x}Nb^{(5+)}_{6-x}O_{18}$ (x=0.5)*

Formula	Z	Concentration	Status
Nb2O5	41	59.26	XRF 3
Cs2O	55	19.1	XRF 2
TiO2	22	10.62	XRF 1
BaO	56	6.95	XRF 1
MoO3	42	1.94	XRF 2
CuO	29	0.0796	XRF 1
Fe2O3	26	0.062	XRF 1
SO3	16	0.048	XRF 1
CaO	20	0.045	XRF 1
ZnO	30	0.038	XRF 1
Y2O3	39	0.017	XRF 1
NiO	28	0.016	XRF 1
CeO2	58	0.0042	XRF 1

Line 1	Net int.	Used intensity	Calc. conc	Crystal	Collimator	Stat. error	LLD	Analyzed layer
Nb KA1-HR-Tr	6395	12739	66.83	LiF200	0.23	0.04%	279.8 PPM	6.2 mm
Cs KA1-HR-Tr	126.1	238.6	27.09	LiF200	0.23	0.33%	0.19%	13.3 mm
Ti KA1-HR-Tr	32.56	78.44	10.62	LiF200	0.23	0.58%	415.2 PPM	213 um
Ba LA1-HR-Tr	9.712	23.09	6.95	LiF200	0.23	1.10%	0.11%	207 um
Mo KA1-HR-Tr	16.82	22.3	0.117	LiF200	0.23	3.85%	117.6 PPM	7.2 mm
Cu KA1-HR-Tr	2.557	5.991	0.0797	LiF200	0.23	3.65%	83.3 PPM	0.78 mm
Fe KA1-HR-Tr	0.7532	1.737	0.062	LiF200	0.23	7.32%	134.3 PPM	0.41 mm
S KA1-HR-Tr	0.4191	0.2219	0.048	PET	0.23	15.60%	675.5 PPM	43 um
Ca KA1-HR-Tr	0.1233	0.2951	0.045	LiF200	0.23	19.60%	265.9 PPM	121 um
Zn KA1-HR-Tr	1.569	3.677	0.038	LiF200	0.23	6.11%	72.4 PPM	0.95 mm
Y KA1-HR-Tr	1.92	3.831	0.017	LiF200	0.23	27.00%	67.6 PPM	4.6 mm
Ni KA1-HR-Tr	0.4095	0.9498	0.016	LiF200	0.23	17.00%	96.0 PPM	0.63 mm
Ce LA1-HR-Tr	2.972	-0.02541	0	LiF200	0.23	5.50%	0.21%	260 um

Line 2	Net int.	Used intensity	Calc. conc	Crystal	Collimator	Stat. error	LLD	Analyzed layer
Nb KB1-HR-Tr	1259	2508	67.69	LiF200	0.23	0.09%	0.14%	8.6 mm
Cs LA1-HR-Tr	24.21	58.39	19.1	LiF200	0.23	0.67%	760.9 PPM	184 um
Ti KB1-HR-Tr	11.57	24.76	21.8	LiF200	0.23	1.00%	0.48%	274 um
Ba LB1-HR-Tr	6.528	15.63	6.6	LiF200	0.23	1.38%	0.14%	258 um
Mo KB1-HR-Tr	23.43	46.67	1.94	LiF200	0.23	2.76%	634.5 PPM	3.9 mm
Cu KB1-HR-Tr	0.3851	0.9021	0.063	LiF200	0.23	59.50%	502.4 PPM	1.03 mm
Fe KB1-HR-Tr	0.155	0.3575	0.067	LiF200	0.23	97.40%	885.9 PPM	0.54 mm
Ca KB1-HR-Tr	0.02957	0.06402	0.078	LiF200	0.23	206%	0.25%	153 um
Zn KB1-HR-Tr	-0.1094	-0.2564	-0.015	LiF200	0.23		468.3 PPM	1.27 mm
Y KB1-HR-Tr	2130	359	8.067	LiF200	0.23	0.18%	0.36%	6.3 mm

Ni KB1-HR-Tr	25.57	44.73	4.13	LiF200	0.23	1.80%	0.12%	0.84 mm
Ce LB1-HR-Tr	0.2348	0.5514	0.29	LiF200	0.23	38.10%	0.14%	266 um

Line 3	Net int.	Used intensity	Calc. conc	Crystal	Collimator	Stat. error	LLD	Analyzed layer
Nb LA1-HR	30.84	124.1	59.26	PET	0.23	0.59%	749.4 PPM	36 um
Cs LB1-HR-Tr	15.37	37.03	18.3	LiF200	0.23	0.86%	0.15%	228 um
Ba KA1-HR-Tr	39.02	74.29	6.6	LiF200	0.23	0.72%	0.13%	14.8 mm
Mo LA1-HR-Tr	0.0896	-0.5671	-0.24	PET	0.23	51.10%	0.12%	43 um
Cu LA1-HR	0.06073	0.1528	0.78	XS-55	0.23	27.70%	0.65%	3.9 um
Zn LA1-HR-Tr	0.01613	0.04022	0.099	XS-55	0.23	252%	0.34%	4.7 um
Y LA1-HR	0.08322	0.1275	0.094	PET	0.23	19.20%	0.14%	26.0 um
Ni LA1-HR	0.0058	0.01436	0.17	XS-55	0.23	243%	1.39%	3.1 um

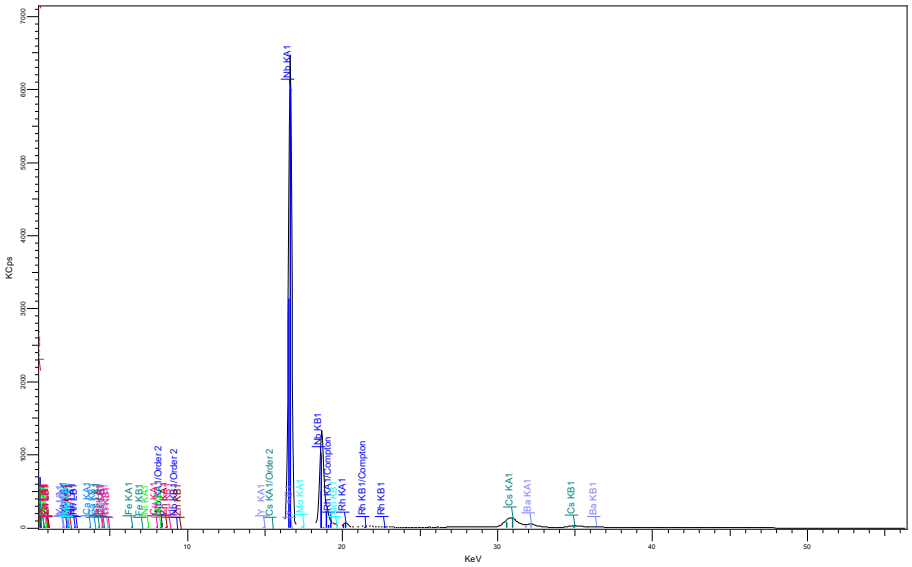

Figure 7.33 *XRF spectrum of* $Cs_{2-x}Ba_xTi^{(4+)}{}_{1+x}Nb^{(5+)}{}_{6-x}O_{18}$ *(x=0.5)*

XRF $Cs_{2-x}Ba_xTi^{(4+)}_{1+x}Nb^{(5+)}_{6-x}O_{18}$ (x=0.4)

Table 7.26 *XRF details for $Cs_{2-x}Ba_xTi^{(4+)}_{1+x}Nb^{(5+)}_{6-x}O_{18}$ (x=0.4)*

Formula	Z	Concentration	Status
Nb2O5	41	61.97	XRF 3
Cs2O	55	20.1	XRF 2
TiO2	22	10.13	XRF 1
BaO	56	5.67	XRF 1
MoO3	42	1.85	XRF 2
ZrO2	40	0.343	XRF 1
SO3	16	0.181	XRF 1
SiO2	14	0.13	XRF 1
CeO2	58	0.12	XRF 1
Cl	17	0.084	XRF 1
CuO	29	0.0701	XRF 1
Fe2O3	26	0.068	XRF 1
ZnO	30	0.0444	XRF 1
K2O	19	0.041	XRF 1
NiO	28	0.016	XRF 1

Line 1	Net int.	Used intensity	Calc. conc	Crystal	Collimator	Stat. error	LLD	Analyzed layer
Nb KA1-HR-Tr	6470	12888	68.87	LiF200	0.23	0.04%	285.4 PPM	6.1 mm
Cs KA1-HR-Tr	135.7	257.3	29.9	LiF200	0.23	0.32%	0.20%	12.7 mm
Ti KA1-HR-Tr	30.77	74.16	10.13	LiF200	0.23	0.60%	410.2 PPM	207 um
Ba LA1-HR-Tr	7.915	18.77	5.67	LiF200	0.23	1.23%	0.11%	201 um
Mo KA1-HR-Tr	16.08	17.77	0.0954	LiF200	0.23	4.02%	124.5 PPM	7.0 mm
Zr KA1-HR-Tr	46.48	79.64	0.343	LiF200	0.23	0.67%	97.0 PPM	5.2 mm
S KA1-HR-Tr	0.5804	0.8348	0.181	PET	0.23	5.01%	674.6 PPM	43 um
Si KA1-HR-Tr	0.06493	0.2303	0.13	PET	0.23	22.30%	664.5 PPM	19.5 um
Ce LA1-HR-Tr	2.566	0.3879	0.12	LiF200	0.23	5.99%	0.20%	253 um
Cl KA1-HR-Tr	0.1348	0.508	0.084	PET	0.23	13.50%	277.0 PPM	48 um
Cu KA1-HR-Tr	2.243	5.254	0.0701	LiF200	0.23	4.10%	84.3 PPM	0.76 mm
Fe KA1-HR-Tr	0.8261	1.905	0.068	LiF200	0.23	6.74%	135.1 PPM	0.40 mm
Zn KA1-HR-Tr	1.83	4.287	0.0444	LiF200	0.23	5.29%	72.4 PPM	0.93 mm
K KA1-HR-Tr	0.1153	0.2773	0.041	LiF200	0.23	20.00%	247.8 PPM	87 um
Ni KA1-HR-Tr	0.3869	0.9065	0.016	LiF200	0.23	18.10%	94.9 PPM	0.62 mm

Line 2	Net int.	Used intensity	Calc. conc	Crystal	Collimator	Stat. error	LLD	Analyzed layer
Nb KB1-HR-Tr	1277	2543	70.27	LiF200	0.23	0.09%	0.14%	8.4 mm
Cs LA1-HR-Tr	25.42	61.31	20.1	LiF200	0.23	0.66%	827.6 PPM	179 um
Ti KB1-HR-Tr	11.61	25.46	22.6	LiF200	0.23	1.00%	0.46%	267 um
Ba LB1-HR-Tr	5.423	12.81	5.43	LiF200	0.23	1.52%	0.15%	251 um
Mo KB1-HR-Tr	21.72	43.26	1.85	LiF200	0.23	2.95%	659.8 PPM	3.7 mm
Zr KB1-HR-Tr	20.1	-14.07	-0.354	LiF200	0.23	3.32%	740.3 PPM	7.3 mm

Si KB1-HR-Tr/Ox	-0.00066	-0.00233	-0.066	PET	0.23		3.41%	22.5 um
Ce LB1-HR-Tr	0.3127	0.7345	0.38	LiF200	0.23	29.50%	0.14%	261 um
Cu KB1-HR-Tr	0.5778	1.354	0.094	LiF200	0.23	16.00%	505.0 PPM	1.01 mm
Fe KB1-HR-Tr	0.1764	0.4069	0.076	LiF200	0.23	34.60%	900.9 PPM	0.53 mm
Zn KB1-HR-Tr	0.2428	0.5688	0.033	LiF200	0.23	104%	473.8 PPM	1.25 mm
K KB1-HR-Tr	0.00431	0.01037	0.013	LiF200	0.23	489%	0.22%	109 um
Ni KB1-HR-Tr	26.68	46.97	4.35	LiF200	0.23	1.75%	0.12%	0.82 mm

Line 3	Net int.	Used intensity	Calc. conc	Crystal	Collimator	Stat. error	LLD	Analyzed layer
Nb LA1-HR	32.29	129.9	61.97	PET	0.23	0.58%	808.6 PPM	36 um
Cs LB1-HR-Tr	16.99	40.95	20.3	LiF200	0.23	0.82%	0.15%	222 um
Ba KA1-HR-Tr	31.63	60.22	5.45	LiF200	0.23	0.85%	0.13%	14.1 mm
Mo LA1-HR-Tr	0.1161	-0.5063	-0.21	PET	0.23	40.40%	0.12%	42 um
Zr LA1-HR	-0.00113	-0.00453	-0.003	PET	0.23		974.5 PPM	30 um
Cu LA1-HR	0.02746	0.06901	0.35	XS-55	0.23	142%	0.64%	3.8 um
Zn LA1-HR-Tr	0.00951	0.0236	0.058	XS-55	0.23	425%	0.34%	4.6 um
Ni LA1-HR	-0.00774	-0.01969	-0.23	XS-55	0.23		1.36%	3.1 um

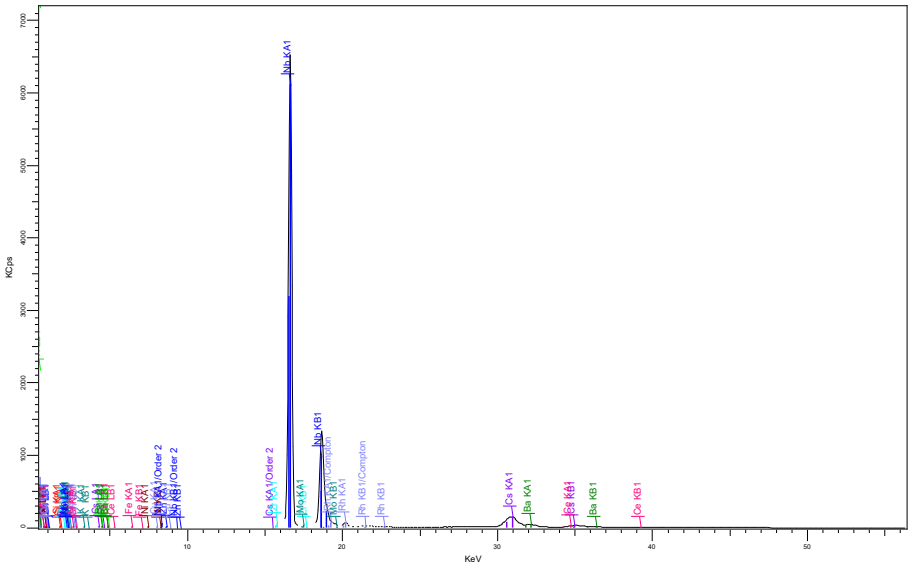

Figure 7.34 *XRF spectrum for* $Cs_{2-x}Ba_xTi^{(4+)}{}_{1+x}Nb^{(5+)}{}_{6-x}O_{18}$ *(x=0.4)*

XRF $Cs_{2-x}Ba_xTi^{(4+)}_{1+x}Nb^{(5+)}_{6-x}O_{18}$ (x=0.3)

Table 7.27 *XRF details for $Cs_{2-x}Ba_xTi^{(4+)}_{1+x}Nb^{(5+)}_{6-x}O_{18}$ (x=0.3)*

Formula	Z	Concentration	Status
Nb2O5	41	62.51	XRF 3
Cs2O	55	20.8	XRF 3
TiO2	22	9.16	XRF 1
BaO	56	4.26	XRF 1
MoO3	42	1.86	XRF 2
SiO2	14	0.55	XRF 1
SO3	16	0.11	XRF 1
Fe2O3	26	0.076	XRF 1
CuO	29	0.0761	XRF 1
ZnO	30	0.0441	XRF 1

Line 1	Net int.	Used intensity	Calc. conc	Crystal	Collimator	Stat. error	LLD	Analyzed layer
Nb KA1-HR-Tr	6515	12977	68.75	LiF200	0.23	0.04%	283.1 PPM	6.2 mm
Cs KA1-HR-Tr	139.1	264	30.62	LiF200	0.23	0.31%	0.19%	12.8 mm
Ti KA1-HR-Tr	27.86	67.15	9.16	LiF200	0.23	0.63%	403.6 PPM	208 um
Ba LA1-HR-Tr	5.954	14.07	4.26	LiF200	0.23	1.44%	0.10%	202 um
Mo KA1-HR-Tr	17.28	22.74	0.121	LiF200	0.23	3.78%	120.3 PPM	7.2 mm
Si KA1-HR-Tr	0.2786	0.9883	0.55	PET	0.23	7.53%	668.7 PPM	19.6 um
S KA1-HR-Tr	0.5026	0.5062	0.11	PET	0.23	5.50%	675.3 PPM	43 um
Fe KA1-HR-Tr	0.9437	2.176	0.076	LiF200	0.23	6.03%	133.5 PPM	0.41 mm
Cu KA1-HR-Tr	2.467	5.778	0.0761	LiF200	0.23	3.76%	82.4 PPM	0.77 mm
Zn KA1-HR-Tr	1.84	4.311	0.0441	LiF200	0.23	5.26%	71.3 PPM	0.95 mm

Line 2	Net int.	Used intensity	Calc. conc	Crystal	Collimator	Stat. error	LLD	Analyzed layer
Nb KB1-HR-Tr	1273	2537	69.31	LiF200	0.23	0.09%	0.14%	8.6 mm
Cs LA1-HR-Tr	27.46	66.22	21.7	LiF200	0.23	0.63%	783.7 PPM	180 um
Ti KB1-HR-Tr	10.96	24.53	21.7	LiF200	0.23	1.03%	0.43%	268 um
Ba LB1-HR-Tr	3.993	9.542	4.05	LiF200	0.23	1.84%	0.14%	253 um
Mo KB1-HR-Tr	21.92	43.67	1.86	LiF200	0.23	2.94%	658.8 PPM	3.7 mm
Si KB1-HR-Tr/Ox	-0.01741	-0.06177	-1.7	PET	0.23		3.35%	22.6 um
Fe KB1-HR-Tr	0.1702	0.3925	0.073	LiF200	0.23	35.90%	889.4 PPM	0.54 mm
Cu KB1-HR-Tr	0.469	1.099	0.076	LiF200	0.23	19.90%	504.4 PPM	1.03 mm
Zn KB1-HR-Tr	-0.1469	-0.3441	-0.02	LiF200	0.23		465.9 PPM	1.27 mm

Line 3	Net int.	Used intensity	Calc. conc	Crystal	Collimator	Stat. error	LLD	Analyzed layer
Nb LA1-HR	32.53	130.9	62.51	PET	0.23	0.57%	757.2 PPM	36 um
Cs LB1-HR-Tr	17.4	41.93	20.8	LiF200	0.23	0.81%	0.15%	223 um
Ba KA1-HR-Tr	22.62	43.07	3.88	LiF200	0.23	1.10%	0.13%	14.2 mm
Mo LA1-HR-Tr	0.1609	-0.3315	-0.14	PET	0.23	12.40%	0.12%	42 um
Cu LA1-HR	0.03189	0.08033	0.41	XS-55	0.23	50%	0.63%	3.8 um

Zn LA1-HR-Tr	0.0387	0.09708	0.24	XS-55	0.23	111%	0.34%	4.7 um

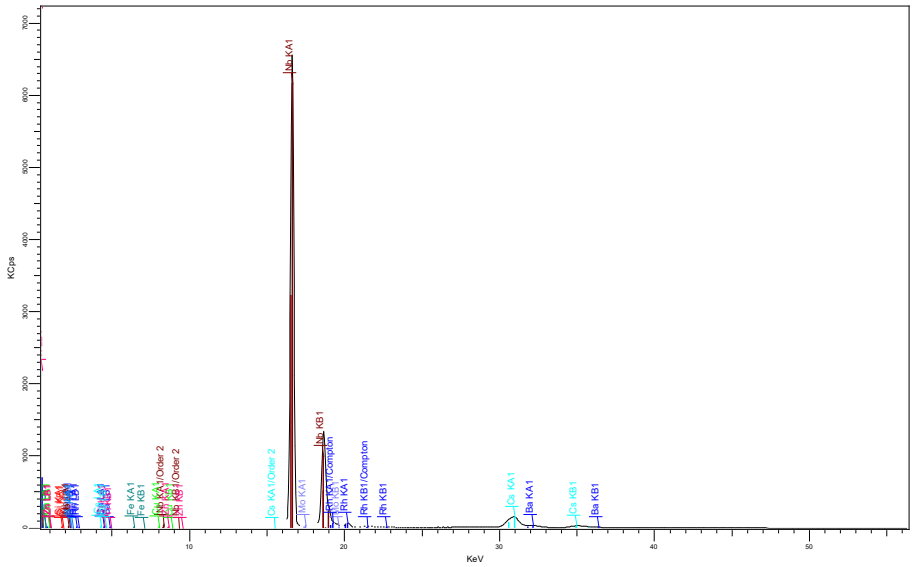

Figure 7.35 *XRF spectrum for* $Cs_{2-x}Ba_xTi^{(4+)}{}_{1+x}Nb^{(5+)}{}_{6-x}O_{18}$ *(x=0.3)*

XRF $Cs_{2-x}Ba_xTi^{(4+)}_{1+x}Nb^{(5+)}_{6-x}O_{18}$ (x=0.15)

Table 7.28 *XRF details for $Cs_{2-x}Ba_xTi^{(4+)}_{1+x}Nb^{(5+)}_{6-x}O_{18}$ (x=0.15)*

Formula	Z	Concentration	Status
Nb2O5	41	62.29	XRF 3
Cs2O	55	21.6	XRF 2
TiO2	22	8.04	XRF 1
BaO	56	1.86	XRF 1
Cl	17	0.814	XRF 1
Na2O	11	0.47	XRF 1
SiO2	14	0.36	XRF 1
SO3	16	0.226	XRF 1
K2O	19	0.15	XRF 1
I	53	0.099	XRF 1
CeO2	58	0.082	XRF 1
CaO	20	0.082	XRF 1
CuO	29	0.0736	XRF 1
Fe2O3	26	0.069	XRF 1
ZnO	30	0.0455	XRF 1
SeO2	34	0.02	XRF 1
NiO	28	0.015	XRF 1

Line 1	Net int.	Used intensity	Calc. conc	Crystal	Collimator	Stat. error	LLD	Analyzed layer
Nb KA1-HR-Tr	6824	13594	70.13	LiF200	0.23	0.04%	268.9 PPM	6.4 mm
Cs KA1-HR-Tr	143.7	273.3	30.99	LiF200	0.23	0.31%	0.18%	13.3 mm
Ti KA1-HR-Tr	24.61	59.34	8.04	LiF200	0.23	0.67%	377.3 PPM	212 um
Ba LA1-HR-Tr	2.653	6.142	1.86	LiF200	0.23	2.32%	999.0 PPM	206 um
Cl KA1-HR-Tr	1.233	4.961	0.814	PET	0.23	3.18%	256.7 PPM	49 um
Na KA1-HR-Tr	0.1429	0.3522	0.47	XS-55	0.23	14.30%	0.20%	5.1 um
Si KA1-HR-Tr	0.1813	0.6432	0.36	PET	0.23	10.30%	686.9 PPM	19.9 um
S KA1-HR-Tr	0.5842	1.045	0.226	PET	0.23	5.04%	656.2 PPM	44 um
K KA1-HR-Tr	0.4137	0.995	0.15	LiF200	0.23	7.04%	243.5 PPM	89 um
I KA1-HR-Tr	2.258	1.457	0.099	LiF200	0.23	8.78%	0.12%	10.7 mm
Ce LA1-HR-Tr	0.9457	0.2718	0.082	LiF200	0.23	12.00%	0.15%	259 um
Ca KA1-HR-Tr	0.2231	0.5329	0.082	LiF200	0.23	12.00%	281.8 PPM	121 um
Cu KA1-HR-Tr	2.444	5.725	0.0736	LiF200	0.23	3.83%	81.2 PPM	0.80 mm
Fe KA1-HR-Tr	0.865	1.995	0.069	LiF200	0.23	6.53%	130.8 PPM	0.42 mm
Zn KA1-HR-Tr	1.949	4.566	0.0455	LiF200	0.23	5.02%	69.6 PPM	0.98 mm
Se KA1-HR-Tr	0.8961	2.077	0.02	LiF200	0.23	15.10%	102.7 PPM	2.07 mm
Ni KA1-HR-Tr	0.3706	0.8683	0.015	LiF200	0.23	18.90%	91.2 PPM	0.65 mm

Line 2	Net int.	Used intensity	Calc. conc	Crystal	Collimator	Stat. error	LLD	Analyzed layer
Nb KB1-HR-Tr	1334	2658	70.71	LiF200	0.23	0.09%	0.14%	9.0 mm
Cs LA1-HR-Tr	27.21	65.62	21.6	LiF200	0.23	0.64%	802.0 PPM	184 um

Ti KB1-HR-Tr	10.5	24.48	21.5	LiF200	0.23	1.05%	0.36%	273 um
Ba LB1-HR-Tr	1.934	4.467	1.89	LiF200	0.23	2.89%	0.14%	257 um
Si KB1-HR Tr/Ox	-0.00005	-0.00017	-0.005	PET	0.23		3.49%	22.9 um
K KB1-HR-Tr	0.08818	0.2121	0.27	LiF200	0.23	26.40%	0.22%	111 um
I KB1-HR-Tr	10.18	19.97	1.39	LiF200	0.23	5.29%	967.4 PPM	14.9 mm
Ce LB1-HR-Tr	0.3919	0.9203	0.47	LiF200	0.23	24.70%	0.14%	272 um
Ca KB1-HR-Tr	0.02159	0.04519	0.056	LiF200	0.23	289%	0.26%	152 um
Cu KB1-HR-Tr	0.6038	1.415	0.095	LiF200	0.23	15.50%	488.5 PPM	1.07 mm
Fe KB1-HR-Tr	0.1827	0.4214	0.076	LiF200	0.23	33.70%	870.0 PPM	0.56 mm
Zn KB1-HR-Tr	0.07753	0.1816	0.01	LiF200	0.23	325%	454.6 PPM	1.32 mm
Se KB1-HR-Tr	0.5761	1.335	0.044	LiF200	0.23	27.50%	410.3 PPM	2.83 mm
Ni KB1-HR-Tr	29.93	53.88	4.81	LiF200	0.23	1.64%	0.12%	0.87 mm

Line 3	Net int.	Used intensity	Calc. conc	Crystal	Collimator	Stat. error	LLD	Analyzed layer
Nb LA1-HR	32.41	130.4	62.29	PET	0.23	0.58%	757.2 PPM	37 um
Cs LB1-HR-Tr	17.77	42.84	21.3	LiF200	0.23	0.80%	0.14%	227 um
Ba KA1-HR-Tr	11.13	21.19	1.86	LiF200	0.23	4.90%	0.12%	14.8 mm
I LA1-HR-Tr	0.2254	0.5394	0.16	LiF200	0.23	12.70%	564.4 PPM	144 um
Cu LA1-HR	0.00845	0.02114	0.11	XS-55	0.23	462%	0.66%	3.9 um
Zn LA1-HR-Tr	0.02715	0.04094	0.1	XS-55	0.23	157%	0.40%	4.7 um
Ni LA1-HR	-0.00387	-0.00996	-0.12	XS-55	0.23		1.43%	3.1 um

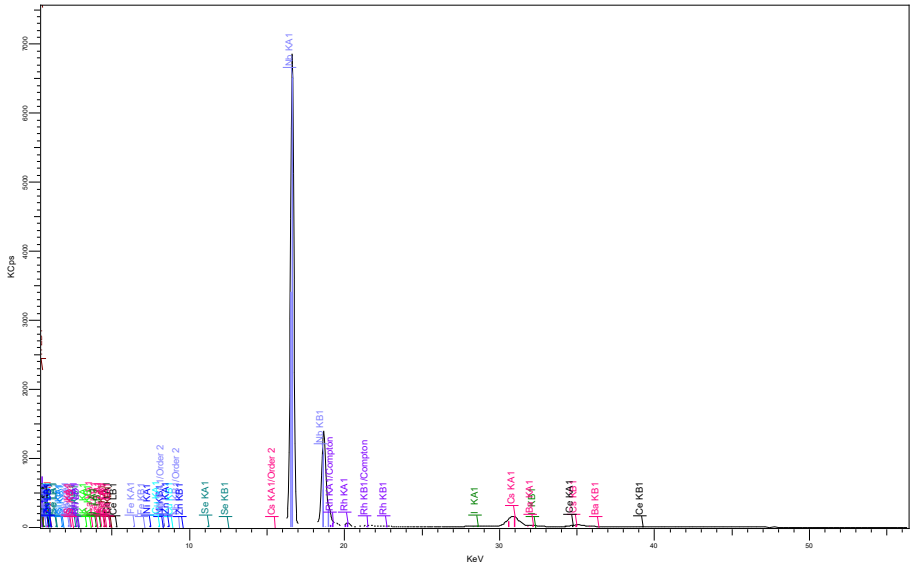

Figure 7.36 *XRF spectrum for* $Cs_{2-x}Ba_xTi^{(4+)}{}_{1+x}Nb^{(5+)}{}_{6-x}O_{18}$ *(x=0.15)*

XRF $Cs_{2-x}Ba_xTi^{(4+)}{}_{1+x}Nb^{(5+)}{}_{6-x}O_{18}$ (x=0.10)

Table 7.29 *XRF details for $Cs_{2-x}Ba_xTi^{(4+)}{}_{1+x}Nb^{(5+)}{}_{6-x}O_{18}$ (x=0.10)*

Formula	Z	Concentration	Status
Nb2O5	41	65.01	XRF 3
Cs2O	55	22.5	XRF 2
TiO2	22	7.54	XRF 1
MoO3	42	1.75	XRF 2
BaO	56	1.21	XRF 1
I	53	0.472	XRF 1
Na2O	11	0.3	XRF 1
SiO2	14	0.17	XRF 1
CuO	29	0.0759	XRF 1
Fe2O3	26	0.069	XRF 1
ZnO	30	0.0432	XRF 1
SO3	16	0.035	XRF 1
CeO2	58	0.024	XRF 1

Line 1	Net int.	Used intensity	Calc. conc	Crystal	Collimator	Stat. error	LLD	Analyzed layer
Nb KA1-HR-Tr	6779	13503	71.9	LiF200	0.23	0.04%	281.4 PPM	6.2 mm
Cs KA1-HR-Tr	145.7	277.2	32.73	LiF200	0.23	0.30%	0.18%	12.5 mm
Ti KA1-HR-Tr	22.78	54.93	7.54	LiF200	0.23	0.70%	380.0 PPM	206 um
Mo KA1-HR-Tr	18.16	24.08	0.129	LiF200	0.23	3.59%	120.4 PPM	7.2 mm
Ba LA1-HR-Tr	1.745	3.971	1.21	LiF200	0.23	3.05%	0.10%	199 um
I KA1-HR-Tr	4.912	6.661	0.471	LiF200	0.23	4.19%	0.12%	10.0 mm
Na KA1-HR-Tr	0.09104	0.222	0.3	XS-55	0.23	20.70%	0.20%	5.0 um
Si KA1-HR-Tr	0.08717	0.3092	0.17	PET	0.23	18.00%	691.9 PPM	19.5 um
Cu KA1-HR-Tr	2.488	5.829	0.0759	LiF200	0.23	3.72%	81.2 PPM	0.78 mm
Fe KA1-HR-Tr	0.8593	1.982	0.069	LiF200	0.23	6.55%	132.8 PPM	0.41 mm
Zn KA1-HR-Tr	1.827	4.281	0.0432	LiF200	0.23	5.28%	70.2 PPM	0.95 mm
S KA1-HR-Tr	0.426	0.1591	0.035	PET	0.23	15.50%	689.0 PPM	43 um
Ce LA1-HR-Tr	0.5749	0.07336	0.022	LiF200	0.23	17.70%	0.14%	250 um

Line 2	Net int.	Used intensity	Calc. conc	Crystal	Collimator	Stat. error	LLD	Analyzed layer
Nb KB1-HR-Tr	1327	2644	72.75	LiF200	0.23	0.09%	0.14%	8.7 mm
Cs LA1-HR-Tr	28.28	68.2	22.5	LiF200	0.23	0.62%	798.2 PPM	178 um
Ti KB1-HR-Tr	10.38	24.5	21.9	LiF200	0.23	1.06%	0.34%	263 um
Mo KB1-HR-Tr	20.22	40.29	1.75	LiF200	0.23	3.09%	656.5 PPM	3.6 mm
Ba LB1-HR-Tr	1.322	3.082	1.32	LiF200	0.23	3.75%	0.14%	248 um
I KB1-HR-Tr	6.882	13.5	0.98	LiF200	0.23	7.46%	997.3 PPM	14.0 mm
Si KB1-HR-Tr/Ox	0.02132	0.07565	2.1	PET	0.23	58.90%	3.26%	22.5 um
Cu KB1-HR-Tr	0.2929	0.6862	0.047	LiF200	0.23	78.40%	496.6 PPM	1.04 mm
Fe KB1-HR-Tr	0.2811	0.6483	0.12	LiF200	0.23	21.90%	873.7 PPM	0.54 mm
Zn KB1-HR-Tr	-0.1236	-0.2895	-0.016	LiF200	0.23		461.5 PPM	1.27 mm

Ce LB1-HR-Tr	0.4628	1.087	0.56	LiF200	0.23	20.80%	0.13%	264 um

Line 3	Net int.	Used intensity	Calc. conc	Crystal	Collimator	Stat. error	LLD	Analyzed layer
Nb LA1-HR	33.8	136	65.01	PET	0.23	0.56%	771.9 PPM	36 um
Cs LB1-HR-Tr	18.19	43.85	22	LiF200	0.23	0.79%	0.14%	219 um
Mo LA1-HR-Tr	0.1132	-0.556	-0.23	PET	0.23	42.00%	0.12%	42 um
Ba KA1-HR-Tr	7.383	14.06	1.3	LiF200	0.23	7.00%	0.12%	13.9 mm
I LA1-HR-Tr	0.6012	1.438	0.42	LiF200	0.23	5.75%	564.3 PPM	140 um
Cu LA1-HR	0.0404	0.1018	0.52	XS-55	0.23	100%	0.63%	3.8 um
Zn LA1-HR-Tr	0.02117	0.03589	0.088	XS-55	0.23	194%	0.38%	4.6 um

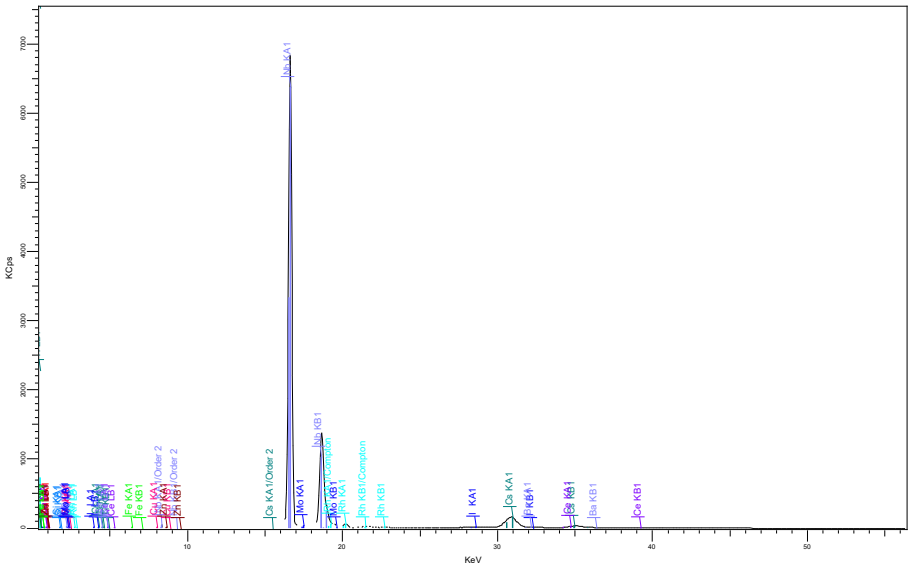

Figure 7.37 *XRF spectrum for* $Cs_{2-x}Ba_xTi^{(4+)}{}_{1+x}Nb^{(5+)}{}_{6-x}O_{18}$ *(x=0.10)*

XRF $Cs_{2-x}Ba_xTi^{(4+)}_{1+x}Nb^{(5+)}_{6-x}O_{18}$ (x=0.05)

Table 7.30 *XRF details for $Cs_{2-x}Ba_xTi^{(4+)}_{1+x}Nb^{(5+)}_{6-x}O_{18}$ (x=0.05)*

Formula	Z	Concentration	Status
Nb2O5	41	66.71	XRF 3
Cs2O	55	24.2	XRF 2
TiO2	22	7.68	XRF 1
MoO3	42	1.83	XRF 2
BaO	56	0.701	XRF 1
SiO2	14	0.18	XRF 1
CuO	29	0.0779	XRF 1
SO3	16	0.0766	XRF 1
Fe2O3	26	0.068	XRF 1
ZnO	30	0.0407	XRF 1

Line 1	Net int.	Used intensity	Calc. conc	Crystal	Collimator	Stat. error	LLD	Analyzed layer
Nb KA1-HR-Tr	6908	13761	74.6	LiF200	0.23	0.04%	288.8 PPM	6.1 mm
Cs KA1-HR-Tr	154.2	293.5	35.29	LiF200	0.23	0.29%	0.18%	12.1 mm
Ti KA1-HR-Tr	23.04	55.56	7.68	LiF200	0.23	0.69%	373.1 PPM	202 um
Mo KA1-HR-Tr	17.82	23.32	0.127	LiF200	0.23	3.67%	123.5 PPM	7.0 mm
Ba LA1-HR-Tr	1.052	2.298	0.701	LiF200	0.23	4.31%	0.10%	196 um
Si KA1-HR-Tr	0.09155	0.3248	0.18	PET	0.23	17.30%	694.8 PPM	19.3 um
Cu KA1-HR-Tr	2.522	5.909	0.0779	LiF200	0.23	3.74%	84.6 PPM	0.76 mm
S KA1-HR-Tr	0.4823	0.3521	0.0767	PET	0.23	5.74%	704.8 PPM	42 um
Fe KA1-HR-Tr	0.843	1.944	0.068	LiF200	0.23	6.75%	137.5 PPM	0.40 mm
Zn KA1-HR-Tr	1.698	3.978	0.0407	LiF200	0.23	5.74%	72.9 PPM	0.93 mm

Line 2	Net int.	Used intensity	Calc. conc	Crystal	Collimator	Stat. error	LLD	Analyzed layer
Nb KB1-HR-Tr	1352	2694	75.48	LiF200	0.23	0.09%	0.14%	8.5 mm
Cs LA1-HR-Tr	30.25	72.95	24.2	LiF200	0.23	0.60%	784.2 PPM	175 um
Ti KB1-HR-Tr	10.63	25.32	22.7	LiF200	0.23	1.05%	0.32%	260 um
Mo KB1-HR-Tr	20.63	41.1	1.83	LiF200	0.23	3.05%	675.6 PPM	3.5 mm
Ba LB1-HR-Tr	0.718	1.658	0.71	LiF200	0.23	5.96%	0.13%	245 um
Si KB1-HR-Tr/Ox	-0.0265	-0.09403	-2.6	PET	0.23		3.66%	22.3 um
Cu KB1-HR-Tr	0.3968	0.9296	0.064	LiF200	0.23	58.50%	507.7 PPM	1.01 mm
Fe KB1-HR-Tr	0.1647	0.3797	0.071	LiF200	0.23	92.60%	894.7 PPM	0.53 mm
Zn KB1-HR-Tr	-0.1579	-0.37	-0.021	LiF200	0.23		471.7 PPM	1.24 mm

Line 3	Net int.	Used intensity	Calc. conc	Crystal	Collimator	Stat. error	LLD	Analyzed layer
Nb LA1-HR	34.7	139.7	66.71	PET	0.23	0.56%	790.1 PPM	35 um
Cs LB1-HR-Tr	19.38	46.72	23.4	LiF200	0.23	0.76%	0.15%	216 um
Mo LA1-HR-Tr	0.1082	-0.5993	-0.25	PET	0.23	44.30%	0.12%	42 um
Ba KA1-HR-Tr	3.298	6.279	0.58	LiF200	0.23	14.90%	0.13%	13.4 mm
Cu LA1-HR	0.02192	0.05521	0.28	XS-55	0.23	176%	0.63%	3.8 um

Zn LA1-HR-Tr	0.02209	0.05524	0.14	XS-55	0.23	185%	0.33%	4.6 um

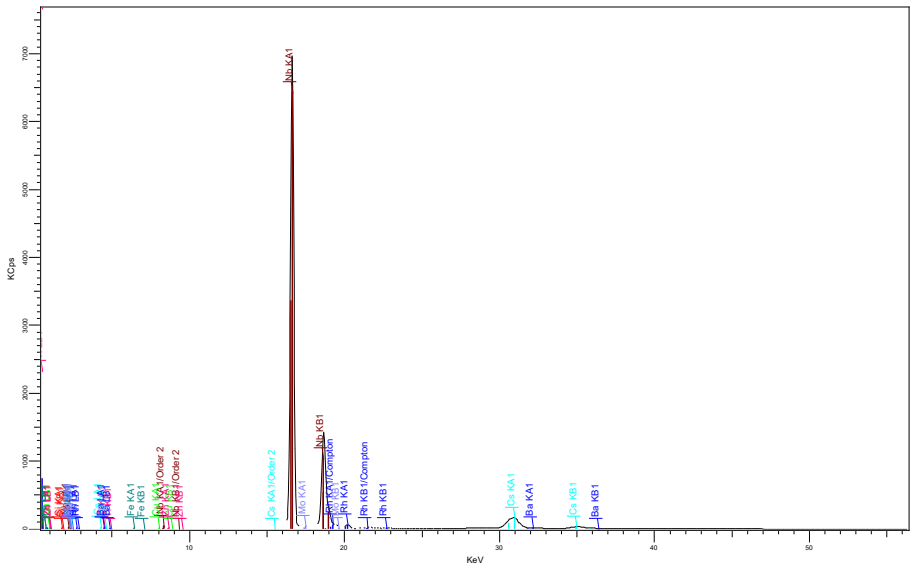

Figure 7.38 *XRF spectrum for* $Cs_{2-x}Ba_xTi^{(4+)}{}_{1+x}Nb^{(5+)}{}_{6-x}O_{18}$ *(x=0.05)*

XRF $Cs_{2-x}Ba_xTi^{(4+)}{}_{1-x}Ti^{(3+)}xNb_6O_{18}$ (x=0.2)

Table 7.31 *XRF details for $Cs_{2-x}Ba_xTi^{(4+)}{}_{1-x}Ti^{(3+)}xNb_6O_{18}$ (x=0.2)*

Formula	Z	Concentration	Status
Nb2O5	41	72.94	XRF 2
Cs2O	55	17.8	XRF 3
TiO2	22	6.81	XRF 1
BaO	56	2.42	XRF 1
SiO2	14	0.18	XRF 1
WO3	74	0.143	XRF 1
Fe2O3	26	0.0918	XRF 1
CuO	29	0.0724	XRF 1
SO3	16	0.053	XRF 1
ZnO	30	0.038	XRF 1
CeO2	58	0.019	XRF 1

Line 1	Net int.	Used intensity	Calc. conc	Crystal	Collimator	Stat. error	LLD	Analyzed layer
Nb KA1-HR-Tr	6728	13518	72.67	LiF200	0.23	0.04%	291.8 PPM	6.3 mm
Cs KA1-HR-Tr	115.6	219.5	26.17	LiF200	0.23	0.35%	0.19%	11.6 mm
Ti KA1-HR-Tr	20.58	49.34	6.81	LiF200	0.23	0.74%	385.2 PPM	196 um
Ba LA1-HR-Tr	3.395	7.931	2.42	LiF200	0.23	1.98%	989.4 PPM	191 um
Si KA1-HR-Tr	0.08949	0.3176	0.18	PET	0.23	17.40%	699.2 PPM	19.2 um
W LA1-HR-Tr	2.044	4.758	0.143	LiF200	0.23	4.92%	222.6 PPM	0.88 mm
Fe KA1-HR-Tr	1.159	2.725	0.0918	LiF200	0.23	5.16%	132.8 PPM	0.41 mm
Cu KA1-HR-Tr	2.473	5.767	0.0724	LiF200	0.23	3.93%	84.0 PPM	0.78 mm
S KA1-HR-Tr	0.4374	0.2422	0.053	PET	0.23	15.10%	680.5 PPM	42 um
Zn KA1-HR-Tr	1.666	3.886	0.038	LiF200	0.23	6.08%	72.5 PPM	0.95 mm
Ce LA1-HR-Tr	1.066	0.0602	0.018	LiF200	0.23	11.00%	0.16%	239 um

Line 2	Net int.	Used intensity	Calc. conc	Crystal	Collimator	Stat. error	LLD	Analyzed layer
Nb KB1-HR-Tr	1300	2611	72.94	LiF200	0.23	0.09%	0.15%	8.7 mm
Cs LA1-HR-Tr	22.56	54.1	17.9	LiF200	0.23	0.70%	784.7 PPM	170 um
Ti KB1-HR-Tr	8.837	20.13	18	LiF200	0.23	1.16%	0.39%	253 um
Ba LB1-HR-Tr	2.383	5.619	2.41	LiF200	0.23	2.52%	0.14%	238 um
Si KB1-HR-Tr/Ox	-0.00106	-0.06686	-1.9	PET	0.23		4.29%	22.1 um
W LB1-HR-Tr	2.329	5.384	0.178	LiF200	0.23	5.10%	294.4 PPM	1.32 mm
Fe KB1-HR-Tr	0.1238	0.2911	0.052	LiF200	0.23	126%	890.8 PPM	0.54 mm
Cu KB1-HR-Tr	0.4838	1.128	0.074	LiF200	0.23	50.10%	500.9 PPM	1.04 mm
Zn KB1-HR-Tr	-0.04551	-0.4084	-0.022	LiF200	0.23		519.6 PPM	1.28 mm
Ce LB1-HR-Tr	0.3168	0.7435	0.38	LiF200	0.23	29.70%	0.14%	260 um

Line 3	Net int.	Used intensity	Calc. conc	Crystal	Collimator	Stat. error	LLD	Analyzed layer
Nb LA1-HR	30.92	124	59.09	PET	0.23	0.59%	740.4 PPM	35 um
Cs LB1-HR-Tr	14.78	35.44	17.8	LiF200	0.23	0.88%	0.14%	210 um

Ba KA1-HR-Tr	13.21	25.14	2.32	LiF200	0.23	1.75%	0.13%	12.9 mm
W MA1,2-HR-Tr	0.01592	0.05643	0.073	PET	0.23	197%	0.16%	20.3 um
Cu LA1-HR	0.03631	0.09067	0.46	XS-55	0.23	109%	0.65%	3.7 um
Zn LA1-HR-Tr	0.01431	0.03572	0.088	XS-55	0.23	274%	0.32%	4.5 um

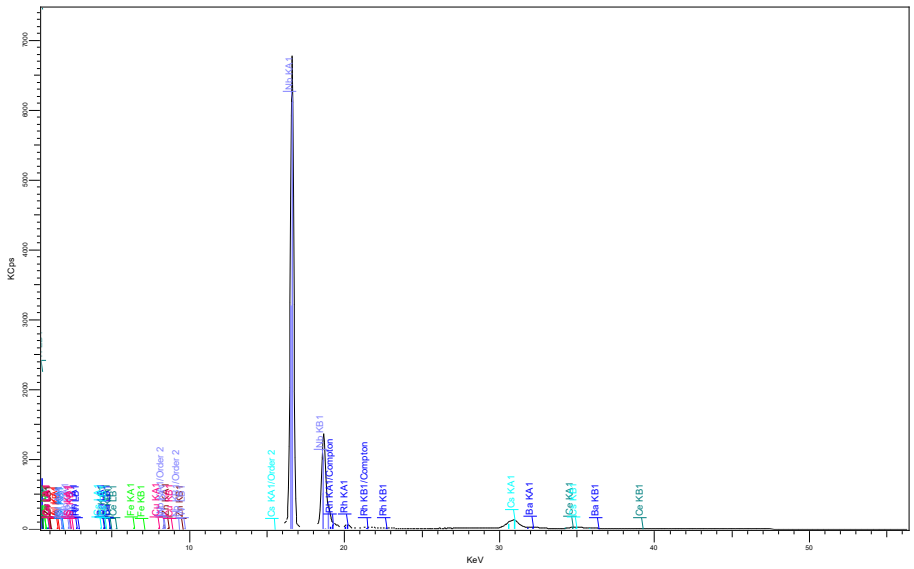

Figure 7.39 *XRF spectrum for* $Cs_{2-x}Ba_xTi^{(4+)}{}_{1-x}Ti^{(3+)}xNb_6O_{18}$ *(x=0.2)*

XRF $Cs_{2-x}Ba_xNb^{(5+)}_{6-x}Nb^{(4+)}_xTiO_{18}$ (x=0.2)

Table 7.32 *XRF details for $Cs_{2-x}Ba_xNb^{(5+)}_{6-x}Nb^{(4+)}_xTiO_{18}$ (x=0.2)*

Formula	Z	Concentration	Status
Nb2O5	41	63.24	XRF 3
Cs2O	55	20	XRF 2
TiO2	22	6.96	XRF 1
BaO	56	2.87	XRF 1
MoO3	42	1.76	XRF 2
Na2O	11	0.36	XRF 1
Al2O3	13	0.31	XRF 1
WO3	74	0.172	XRF 1
SiO2	14	0.17	XRF 1
SO3	16	0.124	XRF 1
Fe2O3	26	0.0924	XRF 1
CuO	29	0.077	XRF 1
ZnO	30	0.047	XRF 1

Line 1	Net int.	Used intensity	Calc. conc	Crystal	Collimator	Stat. error	LLD	Analyzed layer
Nb KA1-HR-Tr	6853	13769	71.65	LiF200	0.23	0.04%	283.1 PPM	6.4 mm
Cs KA1-HR-Tr	130.9	248.4	28.52	LiF200	0.23	0.33%	0.19%	12.9 mm
Ti KA1-HR-Tr	21.38	51.26	6.96	LiF200	0.23	0.72%	380.2 PPM	210 um
Ba LA1-HR-Tr	4.03	9.443	2.87	LiF200	0.23	1.79%	972.0 PPM	203 um
Mo KA1-HR-Tr	18.22	24.54	0.128	LiF200	0.23	3.65%	120.1 PPM	7.5 mm
Na KA1-HR-Tr	0.1101	0.2698	0.36	XS-55	0.23	17.50%	0.20%	5.1 um
Al KA1-HR-Tr	0.149	0.4737	0.31	PET	0.23	11.20%	662.6 PPM	12.9 um
W LA1-HR-Tr	2.397	5.577	0.172	LiF200	0.23	4.19%	219.9 PPM	0.91 mm
Si KA1-HR-Tr	0.08488	0.301	0.17	PET	0.23	18.40%	712.5 PPM	19.8 um
S KA1-HR-Tr	0.524	0.5706	0.124	PET	0.23	5.26%	648.8 PPM	43 um
Fe KA1-HR-Tr	1.151	2.707	0.0924	LiF200	0.23	5.23%	134.8 PPM	0.42 mm
Cu KA1-HR-Tr	2.59	6.04	0.077	LiF200	0.23	3.69%	82.1 PPM	0.80 mm
Zn KA1-HR-Tr	2.039	4.755	0.047	LiF200	0.23	4.97%	71.6 PPM	0.98 mm

Line 2	Net int.	Used intensity	Calc. conc	Crystal	Collimator	Stat. error	LLD	Analyzed layer
Nb KB1-HR-Tr	1338	2688	72.26	LiF200	0.23	0.09%	0.14%	9.0 mm
Cs LA1-HR-Tr	25.36	60.83	20	LiF200	0.23	0.66%	764.2 PPM	181 um
Ti KB1-HR-Tr	9.405	21.26	18.7	LiF200	0.23	1.12%	0.39%	270 um
Ba LB1-HR-Tr	2.59	6.139	2.61	LiF200	0.23	2.38%	0.13%	254 um
Mo KB1-HR-Tr	20.58	41.35	1.76	LiF200	0.23	3.11%	663.4 PPM	3.8 mm
Al KB1-HR-Tr/Ox	0.1401	0.4455	25	PET	0.23	28.60%	5.42%	14.5 um
W LB1-HR-Tr	1.932	4.461	0.15	LiF200	0.23	6.00%	295.4 PPM	1.35 mm
Si KB1-HR-Tr/Ox	0.02859	0.02537	0.71	PET	0.23	46.00%	4.33%	22.8 um
Fe KB1-HR-Tr	0.2547	0.5988	0.11	LiF200	0.23	24.90%	890.3 PPM	0.56 mm
Cu KB1-HR-Tr	0.3979	0.9277	0.062	LiF200	0.23	23.80%	495.8 PPM	1.07 mm

Zn KB1-HR-Tr	0.08895	-0.1519	-0.008	LiF200	0.23	296%	523.3 PPM	1.32 mm

Line 3	Net int.	Used intensity	Calc. conc	Crystal	Collimator	Stat. error	LLD	Analyzed layer
Nb LA1-HR	32.95	132.1	63.24	PET	0.23	0.57%	712.3 PPM	36 um
Cs LB1-HR-Tr	16.1	38.6	19.2	LiF200	0.23	0.84%	0.14%	224 um
Ba KA1-HR-Tr	16.18	30.78	2.74	LiF200	0.23	1.45%	0.13%	14.3 mm
Mo LA1-HR-Tr	0.1356	-0.4551	-0.19	PET	0.23	34.30%	0.11%	43 um
W MA1,2-HR-Tr	0.04544	0.1615	0.21	PET	0.23	30.20%	0.16%	20.9 um
Cu LA1-HR	0.07795	0.1955	0.99	XS-55	0.23	22.40%	0.66%	3.9 um
Zn LA1-HR-Tr	0.03187	0.05923	0.15	XS-55	0.23	132%	0.38%	4.7 um

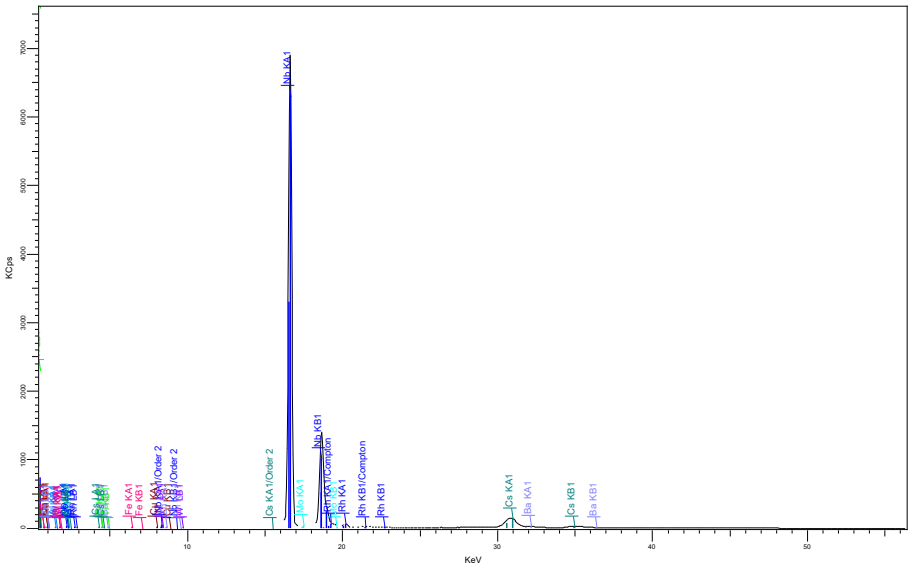

Figure 7.40 *XRF spectrum for* $Cs_{2-x}Ba_xNb^{(5+)}{}_{6-x}Nb^{(4+)}{}_xTiO_{18}$ *(x=0.2)*

XRF $Cs_{2-x}Ba_xNb^{(5+)}_{6-(x/2)}Ti^{(3+)}_{x/2}Ti^{(4+)}_{1-(x/2)}Nb^{(4+)}_{x/2}O_{18}$ (x=0.2)

Table 7.33 *XRF details for $Cs_{2-x}Ba_xNb^{(5+)}_{6-(x/2)}Ti^{(3+)}_{x/2}Ti^{(4+)}_{1-(x/2)}Nb^{(4+)}_{x/2}O_{18}$ (x=0.2)*

Formula	Z	Concentration	Status
Nb2O5	41	61.82	XRF 3
Cs2O	55	22.2	XRF 2
TiO2	22	6.66	XRF 1
BaO	56	2.6	XRF 1
MoO3	42	1.53	XRF 2
Na2O	11	0.95	XRF 1
SO3	16	0.206	XRF 1
Cl	17	0.13	XRF 1
CuO	29	0.0699	XRF 1
Fe2O3	26	0.061	XRF 1
ZnO	30	0.038	XRF 1
CeO2	58	0.023	XRF 1

Line 1	Net int.	Used intensity	Calc. conc	Crystal	Collimator	Stat. error	LLD	Analyzed layer
Nb KA1-HR-Tr	6495	13050	68.06	LiF200	0.23	0.04%	274.9 PPM	6.4 mm
Cs KA1-HR-Tr	134	254.5	29.25	LiF200	0.23	0.32%	0.18%	13.1 mm
Ti KA1-HR-Tr	20.42	48.95	6.66	LiF200	0.23	0.74%	372.7 PPM	212 um
Ba LA1-HR-Tr	3.655	8.555	2.6	LiF200	0.23	1.89%	955.7 PPM	205 um
Mo KA1-HR-Tr	16.67	21.73	0.114	LiF200	0.23	3.86%	117.2 PPM	7.4 mm
Na KA1-HR-Tr	0.2838	0.7091	0.95	XS-55	0.23	8.42%	0.20%	5.1 um
S KA1-HR-Tr	0.6034	0.947	0.206	PET	0.23	4.95%	679.7 PPM	43 um
Cl KA1-HR-Tr	0.1971	0.7613	0.13	PET	0.23	10.50%	291.2 PPM	49 um
Cu KA1-HR-Tr	2.307	5.379	0.0699	LiF200	0.23	4.00%	81.2 PPM	0.80 mm
Fe KA1-HR-Tr	0.7532	1.771	0.061	LiF200	0.23	7.41%	134.5 PPM	0.42 mm
Zn KA1-HR-Tr	1.622	3.783	0.038	LiF200	0.23	5.93%	70.2 PPM	0.97 mm
Ce LA1-HR-Tr	1.169	0.07532	0.023	LiF200	0.23	10.10%	0.16%	258 um

Line 2	Net int.	Used intensity	Calc. conc	Crystal	Collimator	Stat. error	LLD	Analyzed layer
Nb KB1-HR-Tr	1269	2551	68.62	LiF200	0.23	0.09%	0.14%	8.9 mm
Cs LA1-HR-Tr	28.05	67.27	22.2	LiF200	0.23	0.63%	770.0 PPM	183 um
Ti KB1-HR-Tr	9.92	22.62	20	LiF200	0.23	1.08%	0.37%	272 um
Ba LB1-HR-Tr	2.601	6.139	2.61	LiF200	0.23	2.35%	0.13%	256 um
Mo KB1-HR-Tr	18.11	36.39	1.53	LiF200	0.23	3.41%	642.1 PPM	3.8 mm
Cu KB1-HR-Tr	0.6081	1.418	0.096	LiF200	0.23	15.30%	489.6 PPM	1.06 mm
Fe KB1-HR-Tr	0.1358	0.3193	0.058	LiF200	0.23	45.40%	894.3 PPM	0.55 mm
Zn KB1-HR-Tr	-0.0524	-0.1222	-0.007	LiF200	0.23		459.3 PPM	1.30 mm
Ce LB1-HR-Tr	0.3621	0.8498	0.44	LiF200	0.23	26.70%	0.14%	272 um

Line 3	Net int.	Used intensity	Calc. conc	Crystal	Collimator	Stat. error	LLD	Analyzed layer
Nb LA1-HR	32.17	129	61.82	PET	0.23	0.58%	768.0 PPM	36 um

Cs LB1-HR-Tr	18.1	43.4	21.6	LiF200	0.23	0.79%	0.14%	226 um
Ba KA1-HR-Tr	13.79	26.23	2.34	LiF200	0.23	1.63%	0.12%	14.6 mm
Mo LA1-HR-Tr	0.1295	-0.4634	-0.2	PET	0.23	37.90%	0.12%	43 um
Cu LA1-HR	0.06766	0.1706	0.86	XS-55	0.23	25.50%	0.64%	3.9 um
Zn LA1-HR-Tr	0.05504	0.08396	0.21	XS-55	0.23	81.00%	0.42%	4.7 um

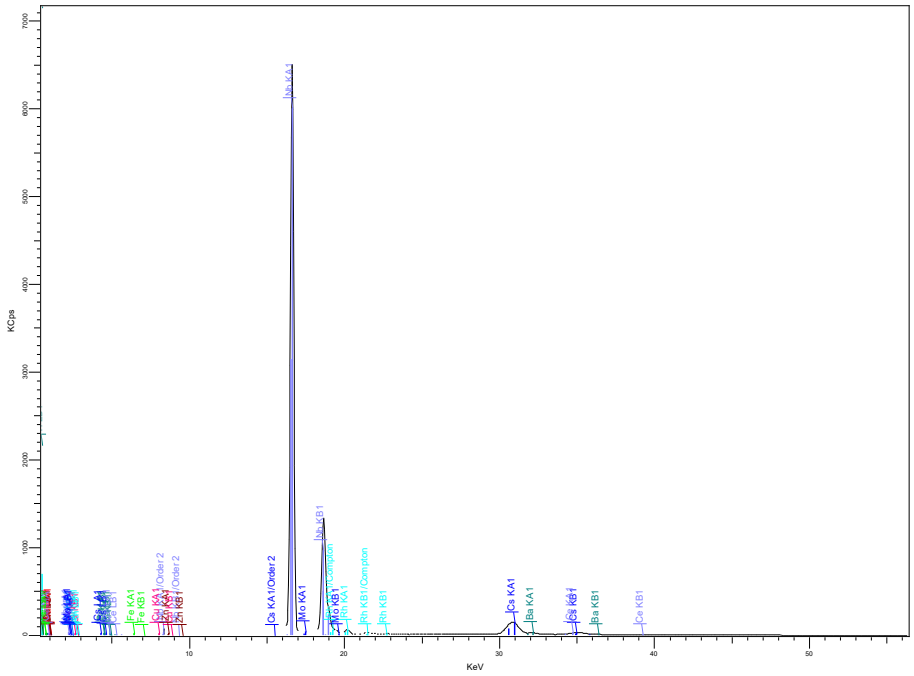

Figure 7.41 *XRF spectrum for* $Cs_{2-x}Ba_xNb^{(5+)}_{6-(x/2)}Ti^{(3+)}_{x/2}Ti^{(4+)}_{1-(x/2)}Nb^{(4+)}_{x/2}O_{18}$ *(x=0.2)*

XRF $Cs_{1.9}Ba_{0.1}Ga^{(3+)}_{0.1}Ti^{(4+)}_{0.9}Nb^{(5+)}_{6}O_{18}$

Table 7.34 *XRF details $Cs_{1.9}Ba_{0.1}Ga^{(3+)}_{0.1}Ti^{(4+)}_{0.9}Nb^{(5+)}_{6}O_{18}$*

Formula	Z	Concentration	Status
Nb2O5	41	64.34	XRF 1
orig-g		0.5	Input
Cs2O	55	22	XRF 2
added-g		0.1	Input
TiO2	22	5.74	XRF 1
BaO	56	0.97	XRF 3
Ga2O3	31	0.782	XRF 1
SO3	16	0.12	XRF 1
CuO	29	0.057	XRF 1
Fe2O3	26	0.053	XRF 1
ZnO	30	0.033	XRF 1
ZrO2	40	0.0317	XRF 1

Line 1	Net int.	Used intensity	Calc. conc	Crystal	Collimator	Stat. error	LLD	Analyzed layer
Nb KA1-HR-Tr	991.6	15855	64.34	LiF200	0.23	0.10%	154.8 PPM	228 um
Cs KA1-HR-Tr	37.37	343.6	31.1	LiF200	0.23	0.55%	710.9 PPM	0.36 mm
Ti KA1-HR-Tr	3.735	84.43	5.74	LiF200	0.23	1.71%	180.1 PPM	11.6 um
Ba LA1-HR-Tr	0.3308	7.104	1.1	LiF200	0.23	6.49%	424.9 PPM	11.3 um
Ga KA1-HR-Tr	6.18	133.7	0.782	LiF200	0.23	1.39%	38.0 PPM	46 um
S KA1-HR-Tr	0.1826	2.018	0.12	PET	0.23	8.35%	166.9 PPM	5.7 um
Cu KA1-HR-Tr	0.3186	6.892	0.057	LiF200	0.23	9.37%	45.7 PPM	32 um
Fe KA1-HR-Tr	0.115	2.495	0.053	LiF200	0.23	16.00%	74.9 PPM	17.4 um
Zn KA1-HR-Tr	0.2377	5.143	0.033	LiF200	0.23	12.90%	39.8 PPM	39 um
Zr KA1-HR-Tr	1.522	10.26	0.0317	LiF200	0.23	4.57%	44.2 PPM	198 um

Line 2	Net int.	Used intensity	Calc. conc	Crystal	Collimator	Stat. error	LLD	Analyzed layer
Nb KB1-HR-Tr	203.9	3260	68.88	LiF200	0.23	0.23%	770.0 PPM	0.31 mm
Cs LA1-HR-Tr	5.866	132.6	22	LiF200	0.23	1.36%	362.1 PPM	10.2 um
Ti KB1-HR-Tr	1.931	42.78	19.4	LiF200	0.23	2.41%	0.14%	14.7 um
Ba LB1-HR-Tr	0.2171	4.796	1.1	LiF200	0.23	8.58%	595.0 PPM	13.9 um
Ga KB1-HR-Tr				LiF220	0.23			61 um
Cu KB1-HR-Tr	-0.02045	-0.4425	-0.019	LiF200	0.23		275.5 PPM	42 um
Fe KB1-HR-Tr	-0.02443	-0.5299	-0.061	LiF200	0.23		495.8 PPM	22.5 um
Zn KB1-HR-Tr	-0.04668	-1.01	-0.037	LiF200	0.23		240.0 PPM	51 um
Zr KB1-HR-Tr	1.159	10.31	0.19	LiF200	0.23	14.80%	260.0 PPM	271 um

Line 3	Net int.	Used intensity	Calc. conc	Crystal	Collimator	Stat. error	LLD	Analyzed layer
Nb LA1-HR	10.01	394.4	50.6	PET	0.23	1.03%	248.1 PPM	4.9 um
Cs LB1-HR-Tr	3.7	83.53	21.3	LiF200	0.23	1.72%	698.6 PPM	12.4 um
Ba KA1-HR-Tr	1.542	14.19	0.97	LiF200	0.23	9.69%	473.5 PPM	0.40 mm

Ga LA1-HR	0.05901	2.327	0.58	XS-55	0.23	16.40%	447.1 PPM	0.96 um
Cu LA1-HR	0.00271	0.1067	0.075	XS-55	0.23	383%	873.9 PPM	0.77 um
Zn LA1-HR-Tr	0.0092	0.3607	0.14	XS-55	0.23	153%	609.1 PPM	0.81 um
Zr LA1-HR	0.00081	0.03185	0.005	PET	0.23	1812%	297.3 PPM	4.2 um

XRF $Cs_{1.9}Ba_{0.1}Al^{(3+)}_{0.1}Ti^{(4+)}_{0.9}Nb^{(5+)}_{6}O_{18}$

Table 7.35 *XRF details of $Cs_{1.9}Ba_{0.1}Al^{(3+)}_{0.1}Ti^{(4+)}_{0.9}Nb^{(5+)}_{6}O_{18}$*

Formula	Z	Concentration	Status
Nb2O5	41	65.44	XRF 1
orig-g		0.5	Input
Cs2O	55	23.6	XRF 2
added-g		0.1	Input
TiO2	22	6.03	XRF 1
BaO	56	1.1	XRF 3
Al2O3	13	0.48	XRF 1
SO3	16	0.13	XRF 1
CeO2	58	0.11	XRF 1
CuO	29	0.055	XRF 1
ZnO	30	0.033	XRF 1

Line 1	Net int.	Used intensity	Calc. conc	Crystal	Collimator	Stat. error	LLD	Analyzed layer
Nb KA1-HR-Tr	999.9	15988	65.44	LiF200	0.23	0.10%	158.2 PPM	224 um
Cs KA1-HR-Tr	38.96	358.3	33.1	LiF200	0.23	0.54%	728.9 PPM	0.35 mm
Ti KA1-HR-Tr	3.871	87.5	6.03	LiF200	0.23	1.68%	175.0 PPM	11.5 um
Ba LA1-HR-Tr	0.4026	8.721	1.34	LiF200	0.23	5.69%	416.1 PPM	11.2 um
Al KA1-HR-Tr	0.1087	3.703	0.48	PET	0.23	10.90%	199.5 PPM	1.87 um
S KA1-HR-Tr	0.1829	2.098	0.13	PET	0.23	8.36%	172.7 PPM	5.6 um
Ce LA1-HR-Tr	0.1329	0.6792	0.11	LiF200	0.23	29.10%	497.7 PPM	13.8 um
Cu KA1-HR-Tr	0.3004	6.5	0.055	LiF200	0.23	9.68%	46.8 PPM	31 um
Zn KA1-HR-Tr	0.2296	4.967	0.033	LiF200	0.23	12.80%	39.7 PPM	37 um

Line 2	Net int.	Used intensity	Calc. conc	Crystal	Collimator	Stat. error	LLD	Analyzed layer
Nb KB1-HR-Tr	206	3294	70.27	LiF200	0.23	0.23%	792.0 PPM	0.31 mm
Cs LA1-HR-Tr	6.303	142.5	23.6	LiF200	0.23	1.31%	370.0 PPM	10.0 um
Ti KB1-HR-Tr	2.09	46.29	21.3	LiF200	0.23	2.30%	0.13%	14.5 um
Ba LB1-HR-Tr	0.3333	7.117	1.6	LiF200	0.23	6.39%	603.0 PPM	13.7 um
Al KB1-HR-Tr/Ox	0.00934	0.3184	3.6	PET	0.23	146%	1.56%	2.07 um
Ce LB1-HR-Tr	0.0701	1.534	0.46	LiF200	0.23	49.90%	800.5 PPM	12.1 um
Cu KB1-HR-Tr	0.062	1.341	0.06	LiF200	0.23	109%	277.5 PPM	40 um
Zn KB1-HR-Tr	-0.01186	-0.2566	-0.01	LiF200	0.23		259.1 PPM	49 um

Line 3	Net int.	Used intensity	Calc. conc	Crystal	Collimator	Stat. error	LLD	Analyzed layer
Nb LA1-HR	10.95	431.5	55.2	PET	0.23	0.99%	259.7 PPM	4.7 um
Cs LB1-HR-Tr	3.969	89.71	22.9	LiF200	0.23	1.66%	654.4 PPM	12.2 um
Ba KA1-HR-Tr	1.684	15.5	1.1	LiF200	0.23	9.11%	492.1 PPM	0.39 mm
Cu LA1-HR	0.01655	0.6529	0.47	XS-55	0.23	86.70%	933.8 PPM	0.75 um
Zn LA1-HR-Tr	0.0017	0.06495	0.026	XS-55	0.23	666%	581.1 PPM	0.78 um

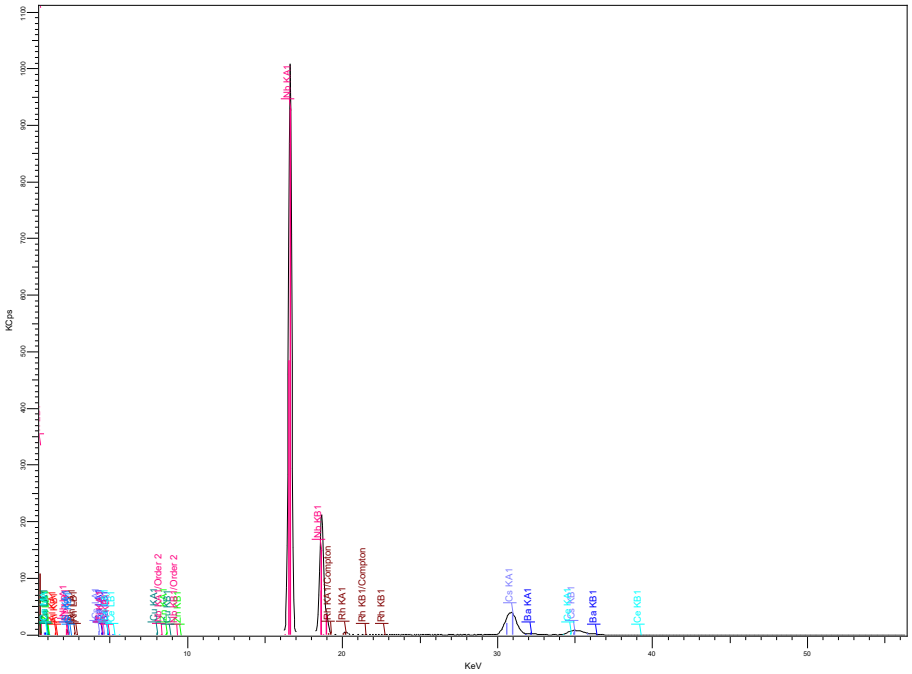

Figure 7.42 *XRF spectrum* $Cs_{1.9}Ba_{0.1}Ga^{(3+)}_{0.1}Ti^{(4+)}_{0.9}Nb^{(5+)}_{6}O_{18}$

XRF $Ba_{1.24}Al_{2.48}Ti_{5.52}O_{16}$ (Ba – Hollandite)

Table 7.36 *XRF details for $Ba_{1.24}Al_{2.48}Ti_{5.52}O_{16}$ (Ba – Hollandite)*

Formula	Z	Concentration	Status
TiO2	22	54.8	XRF 1
BaO	56	25.6	XRF 2
Al2O3	13	13.6	XRF 1
P2O5	15	0.25	XRF 1
WO3	74	0.15	XRF 1
CaO	20	0.084	XRF 1
Fe2O3	26	0.036	XRF 1
CuO	29	0.023	XRF 1
Nb2O5	41	0.021	XRF 1
SrO	38	0.018	XRF 1

Line 1	Net int.	Used intensity	Calc. conc	Crystal	Collimator	Stat. error	LLD	Analyzed layer
Ti KA1-HR-Tr	63.27	1461	54.8	LiF200	0.23	0.41%	136.6 PPM	42 um
Ba LA1-HR-Tr	14.09	319.1	27.1	LiF200	0.23	0.88%	357.9 PPM	41 um
Al KA1-HR-Tr	1.952	122.6	13.6	PET	0.23	2.34%		2.67 um
P KA1-HR-Tr	0.06095	3.233	0.25	PET	0.23	15.70%	149.5 PPM	5.0 um
W LA1-HR-Tr	0.2885	6.273	0.15	LiF200	0.23	8.33%	91.5 PPM	47 um
Ca KA1-HR-Tr	0.1276	2.891	0.084	LiF200	0.23	10.20%	41.6 PPM	24.4 um
Fe KA1-HR-Tr	0.07184	1.562	0.036	LiF200	0.23	18.80%	56.7 PPM	23.1 um
Cu KA1-HR-Tr	0.1137	2.473	0.023	LiF200	0.23	16.50%	33.7 PPM	42 um
Nb KA1-HR-Tr	0.5375	8.606	0.021	LiF200	0.23	7.82%	17.5 PPM	0.30 mm
Sr KA1-HR-Tr	0.3912	7.347	0.018	LiF200	0.23	9.11%	15.6 PPM	194 um

Line 2	Net int.	Used intensity	Calc. conc	Crystal	Collimator	Stat. error	LLD	Analyzed layer
Ti KB1-HR-Tr	10.96	207.8	53.8	LiF200	0.23	0.99%	0.16%	53 um
Ba LB1-HR-Tr	9.135	208.4	25.6	LiF200	0.23	1.09%	429.1 PPM	50 um
Al KB1-HR-Tr/Ox	0.02385	1.417	14	PET	0.23	52.90%		2.97 um
W LB1-HR-Tr	0.2072	4.355	0.12	LiF200	0.23	11.80%	123.7 PPM	68 um
Ca KB1-HR-Tr	0.02717	0.6047	0.15	LiF200	0.23	81.90%	427.3 PPM	30 um
Fe KB1-HR-Tr	0.02357	0.5117	0.063	LiF200	0.23	55.10%	363.8 PPM	29.8 um
Cu KB1-HR-Tr	0.00508	0.1103	0.005	LiF200	0.23	356%	215.9 PPM	55 um
Nb KB1-HR-Tr	0.6912	11.07	0.13	LiF200	0.23	18.00%	103.7 PPM	0.42 mm
Sr KB1-HR-Tr	0.1956	-30.74	-0.3	LiF200	0.23	18.30%	103.0 PPM	265 um

Line 3	Net int.	Used intensity	Calc. conc	Crystal	Collimator	Stat. error	LLD	Analyzed layer
Ba KA1-HR-Tr	95.79	873.4	24.19	LiF200	0.23	0.34%	254.9 PPM	2.01 mm
W MA1,2-HR-Tr	0.00907	0.4905	0.13	PET	0.23	85.70%		3.7 um
Cu LA1-HR	0.00487	1.282	0.89	XS-55	0.23	117%		1.01 um
Nb LA1-HR	0.01645	0.8388	0.083	PET	0.23	43.10%	205.3 PPM	6.0 um
Sr LA1-HR	0.01548	0.8161	0.13	PET	0.23	26.20%		3.8 um

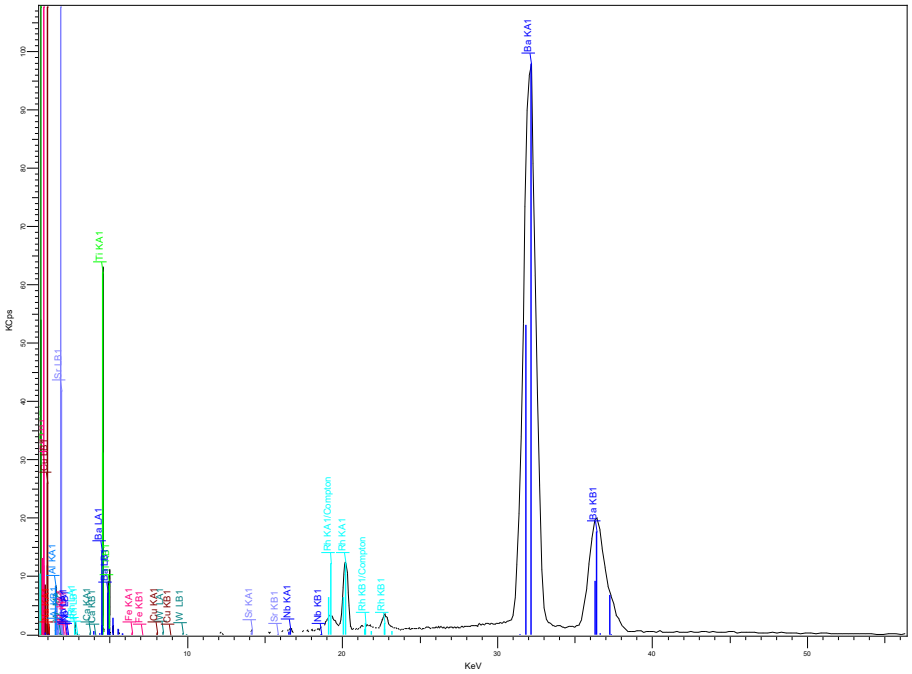

Figure 7.43 *XRF Spectrum for* $Ba_{1.24}Al_{2.48}Ti_{5.52}O_{16}$ *(Ba – Hollandite)*

XRF $Ba_{0.62}Cs_{0.62}Al_{1.86}Ti_{6.14}O_{16}$ (Cs/Ba – Hollandite)

Table 7.37 *XRF details for $Ba_{0.62}Cs_{0.62}Al_{1.86}Ti_{6.14}O_{16}$ (Cs/Ba – Hollandite)*

Formula	Z	Concentration	Status
TiO2	22	65.3	XRF 2
BaO	56	13.1	XRF 2
Al2O3	13	12.1	XRF 1
Cs2O	55	8.24	XRF 2
P2O5	15	0.21	XRF 1
Nb2O5	41	0.0554	XRF 1
Fe2O3	26	0.035	XRF 1
SrO	38	0.009	XRF 1

Line 1	Net int.	Used intensity	Calc. conc	Crystal	Collimator	Stat. error	LLD	Analyzed layer
Ti KA1-HR-Tr	73.49	1698	60.49	LiF200	0.23	0.38%	140.4 PPM	46 um
Ba LA1-HR-Tr	8.077	178.7	13.6	LiF200	0.23	1.16%	376.5 PPM	45 um
Al KA1-HR-Tr	1.787	112.2	12.1	PET	0.23	2.44%		2.80 um
Cs KA1-HR-Tr	32.16	284	8.62	LiF200	0.23	0.60%	324.8 PPM	1.92 mm
P KA1-HR-Tr	0.05451	2.895	0.21	PET	0.23	17.50%	158.8 PPM	5.4 um
Nb KA1-HR-Tr	1.464	23.45	0.0554	LiF200	0.23	3.56%	17.0 PPM	0.32 mm
Fe KA1-HR-Tr	0.07125	1.549	0.035	LiF200	0.23	19.00%	57.0 PPM	24.2 um
Sr KA1-HR-Tr	0.2188	4.109	0.009	LiF200	0.23	14.90%	15.2 PPM	206 um

Line 2	Net int.	Used intensity	Calc. conc	Crystal	Collimator	Stat. error	LLD	Analyzed layer
Ti KB1-HR-Tr	12.53	264.9	65.3	LiF200	0.23	0.93%	0.13%	58 um
Ba LB1-HR-Tr	5.27	119	13.1	LiF200	0.23	1.44%	433.4 PPM	55 um
Al KB1-HR-Tr/Ox	0.02069	1.229	12	PET	0.23	56.80%		3.1 um
Cs LA1-HR-Tr	4.337	100.5	8.24	LiF200	0.23	1.59%	249.3 PPM	40 um
Nb KB1-HR-Tr	0.8234	13.18	0.15	LiF200	0.23	15.20%	96.3 PPM	0.45 mm
Fe KB1-HR-Tr	-0.00898	-0.195	-0.023	LiF200	0.23		371.4 PPM	31 um
Sr KB1-HR-Tr	-0.02793	-19.32	-0.18	LiF200	0.23		90.2 PPM	281 um

Line 3	Net int.	Used intensity	Calc. conc	Crystal	Collimator	Stat. error	LLD	Analyzed layer
Ba KA1-HR-Tr	41.41	377.6	9.516	LiF200	0.23	0.52%	206.0 PPM	2.15 mm
Cs LB1-HR-Tr	2.817	64.25	8.22	LiF200	0.23	2.01%	510.3 PPM	49 um
Nb LA1-HR	0.01918	0.9783	0.088	PET	0.23	38.40%	197.1 PPM	6.5 um
Sr LA1-HR	0.00028	0.01487	0.002	PET	0.23	4681%	308.3 PPM	4.1 um

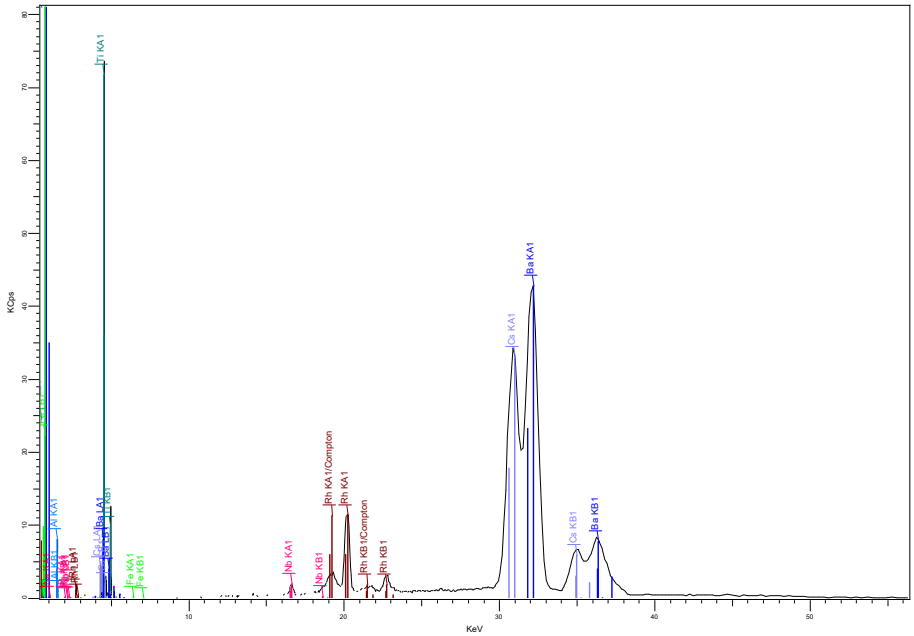

Figure 7.44 *XRF spectrum for Cs/Ba – Hollandite*

Appendix 4

Chapter 4 Rietveld Refinements

Rietveld Refinement Nb-CST

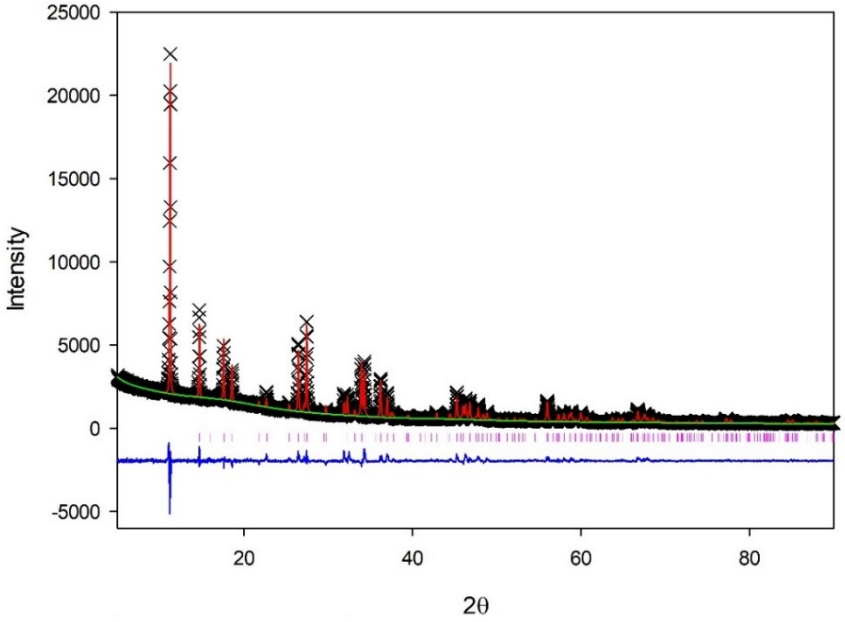

Figure 7.45 *Rietveld Refinement (GSAS Liveplot) Red Ticks: Nb-CST* $(H_{0.5}Na(Nb_{0.5}Ti_{1.5})O_3(SiO_4)(H_2O)_2)$

Table 7.38 *Refinement details for Nb-CST* $(H_{0.5}Na(Nb_{0.5}Ti_{1.5})O_3(SiO_4)(H_2O)_2)$

χ^2	wRp	Rp
5.306	7.41 %	4.97 %

Phase	Symmetry Setting	Space Group
$H_{0.5}Na(Nb_{0.5}Ti_{1.5})O_3(SiO_4)(H_2O)_2$	Tetragonal	$P4_2/mcm$

Phase Information	a	b	c	V	
	7.83604(15)	7.83604	12.00876(29)	737.380(29)	
	α	β	γ		
	90	90	90		
Atom	**x**	**y**	**z**	**Occupancy**	**U_{iso}**
Ti1	0.14302(27)	0.14302(27)	0.15278(26)	0.826(7)	0.01
Nb1	0.14302(27)	0.14302(27)	0.15278(26)	0.174(7)	0.01
Si	0	0.5	0.5	1	0.01
O1	0.1195	0.3876	0.171	1	0.01
O2	0.1126	0.1126	0.3295	1	0.01
O3	0.1445	0.1445	0	1	0.01
Na	0	0.5	0.5	0.848(14)	0.01
O4	0.2965	0.2965	0	1	0.01
O5	0.4479	0.4479	0.117	0.5	0.01

Rietveld Refinement IONSIV

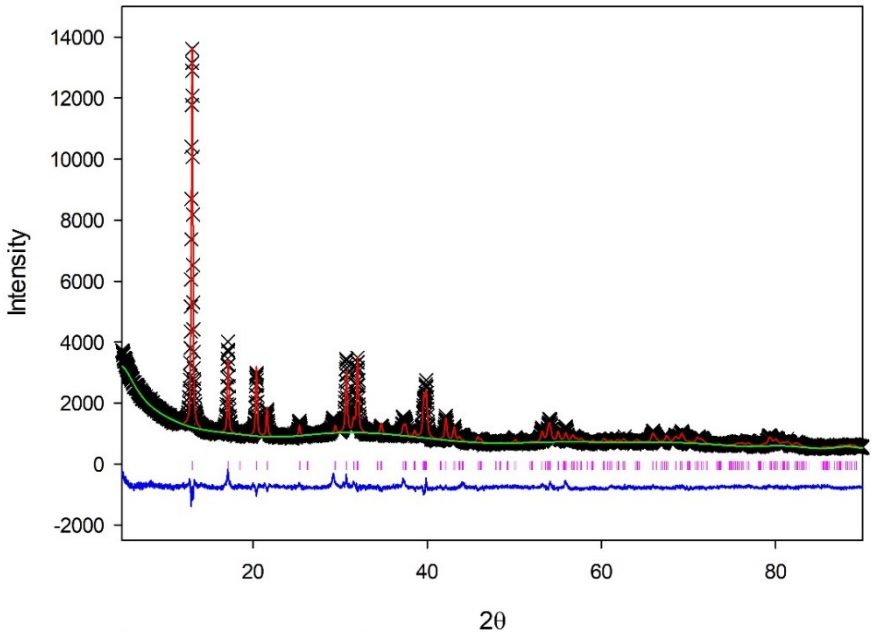

Figure 7.46 *Rietveld Refinement (GSAS Liveplot) Red Ticks: IONSIV* $(H_{0.5}Na(Nb_{0.5}Ti_{1.5})O_3(SiO_4)(H_2O)_2)$

Table 7.39 *Rietveld Refinement details for IONSIV* $(H_{0.5}Na(Nb_{0.5}Ti_{1.5})O_3(SiO_4)(H_2O)_2)$

χ^2	wRp	Rp
3.104	5.46%	4.17%

Phase	Symmetry Setting	Space Group
IONSIV	Tetragonal	P 42/*mcm*

Phase Information	***a***	***b***	***c***	***V***	
	7.8716(5)	7.8715	11.9910(8)	742.99(12)	
	α	***β***	***γ***		
	90	90	90		
Atom	***x***	***y***	***z***	**Occupancy**	**U_{iso}**
Ti1	0.14725(28)	0.14725(28)	0.15301(23)	0.587(17)	0.0181(12)
Nb1	0.14725(28)	0.14725(28)	0.15301(23)	0.413(17)	0.0181(12)
Si	0.0	0.5	0.25	1.0	-0.001(4)
O1	0.1195	0.3876	0.171	1.0	0.01
O2	0.1126	0.1126	0.3295	1.0	0.01
O3	0.1445	0.1445	0.0	1.0	0.01
Na	0	0.5	0.5	0.781(34)	0.80(6)
O4	0.2744	0.2744	0.5	1.0	0.01
O5	0.4479	0.4479	0.1117	0.5	0.01

Rietveld Refinement Sr-Nb-CST

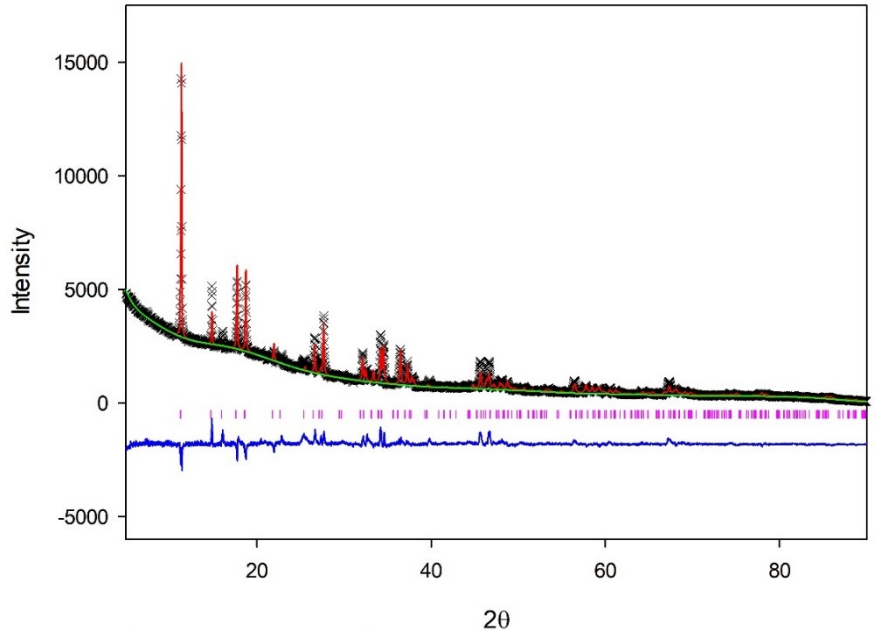

Figure 7.47 *Rietveld Refinement (GSAS Liveplot) Red Ticks: Sr-Nb-CST* $(H_{0.5}Na(Nb_{0.5}Ti_{1.5})O_3(SiO_4)(H_2O)_2)$

Table 7.40 *Rietveld Refinement details for Sr-Nb-CST* $(H_{0.5}Na(Nb_{0.5}Ti_{1.5})O_3(SiO_4)(H_2O)_2)$

χ^2	wRp	Rp
6.184	7.14%	4.56 %

Phase	Symmetry Setting	Space Group
Sr-Nb-CST	Tetragonal	$P4_2/mcm$

Phase Information	***a***	***b***	***c***	***V***	
	7.7804(4)	7.7804(4)	11.9096(7)	720.93(10)	
	α	***β***	***γ***		
	90	90	90		
Atom	***x***	***y***	***z***	**Occupancy**	**U_{iso}**
Ti1	0.1456(4)	0.1456(4)	0.1560(4)	0.738(21)	0.01
Nb1	0.1456(4)	0.1456(4)	0.1560(4)	0.262(21)	0.01
Si	0	0.5	0.5	1	0.01
O1	0.1256	0.3978	0.1663	1	0.01
O2	0.119	0.119	0.3234	1	0.01
O3	0.1559	0.1559	0	1	0.01
Na	0	0.5	0.5	0.572(6)	0.01
Sr	0.4016(12)	0.4016(12)	0	0.362(6)	0.01
O4	0.2683	0.2683	0.5	1	0.01

Rietveld Refinement Sr-Nb-CST Calcination 900°C

Table 7.41 *Rietveld Refinement details for Sr-Nb-CST Calcination 900°C*

χ^2	wRp	Rp
2.368	4.67%	3.35%

Phase	Symmetry Setting	Space Group
TiO_2	Tetragonal	*$P4_2/mnm$*

Phase Information	*a*	*b*	*c*	*V*	
	4.59111(5)	4.59111(5)	2.95641(6)	62.3160(10)	
	α	*β*	*γ*		
	90	90	90		
Atom	***x***	***y***	***z***	**Occupancy**	**U_{iso}**
Ti1	0	0	0	1	0.01
O1	0.3057	0.3057	0	1	0.01

Phase	Symmetry Setting	Space Group
(Sr,Na)(Nb,Ti)O_3	Cubic	*Pm*-3*m*

Phase Information	*a*	*b*	*c*	*V*	
	3.914483(22)	3.914483	3.914483	59.9820(10)	
	α	*β*	*γ*		
	90	90	90		
Atom	***x***	***y***	***z***	**Occupancy**	**U_{iso}**
Sr	0.5	0.5	0.5	0.736	0.01
Na	0.14302(27)	0.14302(27)	0.15278(26)	0.027	0.01
Ti	0	0.5	0.5	0.5	0.01
Nb	0.1195	0.3876	0.171	0.5	0.01
O1	0.1126	0.1126	0.3295	1	0.01

Weight Fractions	
Phases	Wt. %
(Sr,Na)NbO_3	**40.67(2)**
TiO_2	**59.33(1)**

Rietveld Refinement Sr-Nb-CST + 20 wt% $Zr(OH)_4$ Calcination 900°C

Table 7.42 *Rietveld Refinement details for Sr-Nb-CST + 20 wt% $Zr(OH)_4$ Calcination 900°C*

χ2	**wRp**	**Rp**
3.678	5.91 %	3.93 %

Phase	**Symmetry Setting**	**Space Group**
(Sr,Na)NbO_3	Cubic	*Pm*-3*m*

Phase Information	***a***	***b***	***c***	***V***	
	3.91448(7)	3.91448(7)	3.91448(7)	59.9820(30)	
	α	***β***	***γ***		
	90	90	90		
Atom	**x**	**y**	**z**	**Occupancy**	**U_{iso}**
Sr	0.5	0.5	0.5	0.5	0.01
Na	0.5	0.5	0.5	0.5	0.01
Ti	0	0	0	0.5	0.01
Nb	0	0	0	0.5	0.01
O1	0.5	0	0	1	0.01

Phase	**Symmetry Setting**	**Space Group**
TiO_2	Tetragonal	$P4_2/mnm$

Phase Information	***a***	***b***	***c***	***V***	
	4.59609(11)	4.59609	2.96316(13)	62.5940(30)	
	α	*β*	*γ*		
	90	90	90		
Atom	***x***	***y***	***z***	**Occupancy**	**U_{iso}**
Ti1	0	0	0	1	0.01
O1	0.3057	0.3057	0	1	0.01

Phase	**Symmetry Setting**	**Space Group**
$ZrTiO_4$	Orthorhombic	*Pbcn*

Phase Information	**a**	**b**	**c**	**V**	
	4.8013(23)	5.5083(30)	5.0824(25)	134.41(5)	
	α	***β***	***γ***		
	90	90	90		
Atom	***x***	***y***	***z***	**Occupancy**	**U_{iso}**
Zr1	0	0.1992	0.25	0.5	0.01
Ti1	0	0.1992	0.25	0.5	0.01
O1	0.271	0.398	0.432	1	0.01

Phase	Symmetry Setting	Space Group
$SrZrO_3$	Orthorhombic	*Pbnm*

Phase Information	***a***	***b***	***c***	***V***	
	5.773(9)	5.887(11)	8.151(10)	277.0(4)	
	α	***β***	***γ***		
	90	90	90		
Atom	***x***	***y***	***z***	**Occupancy**	**U_{iso}**
Sr	0.003	0.526	0.25	1	0.01
Zr1	0	0	0	1	0.01
O1	-0.073	-0.018	0.25	1	0.01
O2	0.217	0.284	0.035	1	0.01

Phase	Symmetry Setting	Space Group
SiO_2	Tetragonal	$P4_12_12$

Phase Information	***a***	***b***	***c***	***V***	
	5.07	5.07	7.085	182.11923	
	α	***β***	***γ***		
	90	90	90		
Atom	**x**	**y**	**z**	**Occupancy**	**U_{iso}**
Si	0.3047	0.3047	0	1	0.01
O1	0.2381	0.1109	0.1826	1	0.01

Weight Fractions	
Phases	Wt. %
$NaSrNbTiO_3$	**49.062(2)**
TiO_2 (rutile)	**34.549(2)**
$Zr_{0.5}Ti_{0.5}O_2$	**13.820(3)**
$SrZrO_3$	**1.270(2)**
SiO_2 (92)	**1.290(2)**

Unloaded IONSIV Calcination 900°C

Table 7.43 *Refinement details IONSIV (Unloaded) Calcination 900°C*

χ2	wRp	Rp
4.824	6.28%	4.11%

Phase	Symmetry Setting	Space Group
$Na_{13}Nb_{35}O_{91}$	Orthorhombic	*Pba*2

Phase Information	*a*	*b*	*c*	*V*	
	12.406(6)	37.089(16)	3.9033(10)	1796.0(10)	
	α	*β*	*γ*		
	90	90	90		
Atom	***x***	***y***	***z***	**Occupancy**	**U_{iso}**
Na1	0	0	0.0092	1	0.01
Na2	0.0061	0.333	0.0069	1	0.01
Na3	0.3333	0.0553	0.0102	1	0.01
Na4	0.1843	0.2261	-0.0051	0.75	0.01
Nb1	0.07993	0	0.5	1	0.01
Nb2	0.02141	0.07091	0.5315	1	0.01
Nb3	0.21835	0.17327	0.502	1	0.01
Nb4	0.075	0.30877	0.5131	1	0.01
Nb5	0.29842	0.40313	0.5189	1	0.01
Nb6	0.42699	0.1314	0.5012	1	0.01
Nb7	0.29553	0.23379	0.4917	1	0.01
Nb8	0.33769	0.47814	0.5285	1	0.01
Nb9	0.291	0.39054	0.4318	1	0.01
Nb10	0.0861	0.191	-0.0053	0.125	0.01
Nb11	0.0861	0.266	-0.0009	0.125	0.01
O1	0.11002	0.01893	0.5113	1	0.01
O2	0.22175	0.09106	0.4929	1	0.01
O3	0.00288	0.118	0.4813	1	0.01
O4	0.16783	0.165	0.4732	1	0.01
O5	0.02142	0.22341	0.4806	1	0.01
O6	0.34026	0.00307	0.4947	1	0.01
O7	0.44762	0.12411	0.4973	1	0.01
O8	0.35678	0.18945	0.4922	1	0.01
O9	0.29241	0.26259	0.4885	1	0.01
O10	0.0709	0.2934	0.4687	1	0.01
O11	0.3645	0.33481	0.492	1	0.01
O12	0.18622	0.36325	0.4752	1	0.01
O13	0.2192	0.42935	0.4875	1	0.01
O14	0.00106	0.44776	0.4573	1	0.01

O15	0.4171	0.44088	0.5028	1	0.01
O16	0	0.5	-0.021	1	0.01
O17	0.08318	0.06973	-0.0064	1	0.01
O18	0.02819	0.1762	-0.0126	1	0.01
O19	0.21431	0.30788	-0.0208	1	0.01
O20	0.07566	0.4026	0.0036	1	0.01
O21	0.30313	0.14759	-0.0211	1	0.01
O22	0.43238	0.23397	-0.0168	1	0.01
O23	0.3005	0.47944	-0.011	1	0.01
O24	0.33867	0.39005	-0.0297	1	0.01

Phase	**Symmetry Setting**	**Space Group**
$NaNbO_3$	Orthorhombic	*Pbma*

Phase Information	***a***	***b***	***c***	***V***	
	7.7661(22)	7.8796(22)	15.659(4)	958.2(4)	
	α	***β***	***γ***		
	90	90	90		
Atom	**x**	**y**	**z**	**Occupancy**	**U_{iso}**
Nb1	0.2705	0.1231	0.247	1	0.01
Na1	0.75	0	0.257	1	0.01
Na2	0.781	0.25	0.254	1	0.01
O1	0.25	0	0.304	1	0.01
O2	0.232	0.25	0.18	1	0.01
O3	0.025	0.141	0.533	1	0.01
O4	0.456	0.109	-0.036	1	0.01

Phase	**Symmetry Setting**	**Space Group**
TiO_2	Tetragonal	$P4_2/mnm$

Phase Information	***a***	***b***	***c***	***V***	
	4.60044(14)	4.60044(14)	2.96823(17)	62.820(4)	
	α	***β***	***γ***		
	90	90	90		
Atom	***x***	***y***	***z***	**Occupancy**	**U_{iso}**
Ti1	0	0	0	1	0.01
O	0.3057	0.3057	0	1	0.01

Phase	Symmetry Setting	Space Group
$Zr_5Ti_7O_{24}$	Orthorhombic	*Pbcn*

Phase Information	***a***	***b***	***c***	***V***	
	14.2698(14)	5.4113(5)	5.0278(5)	388.24(4)	
	α	***β***	***γ***		
	90	90	90		
Atom	***x***	***y***	***z***	**Occupancy**	**U_{iso}**
Zr1	0	0.2629	0.25	0.968	0.01
Ti1	0	0.2629	0.25	0.032	0.01
Zr2	0.3324	0.3335	0.1798	0.111	0.01
Ti2	0.3324	0.3335	0.1798	0.889	0.01
O1	0.0873	0.0668	-0.0234	1	0.01
O2	0.4194	0.0824	0.0599	1	0.01
O3	0.76	0.1226	0.1402	1	0.01

Phase	Symmetry Setting	Space Group
$ZrTiO_4$	Orthorhombic	*Pbcn*

Phase Information	***a***	***b***	***c***	***V***	
	4.7501(5)	5.3967(5)	5.0267(5)	128.859(15)	
	α	***β***	***γ***		
	90	90	90		
Atom	***x***	***y***	***z***	**Occupancy**	**U_{iso}**
Zr1	0	0.1915	0.25	0.333	0.01
Ti1	0	0.1915	0.25	0.666	0.01
O1	0.27	0.27	0.389	1	0.01

Phase	Symmetry Setting	Space Group
TiO_2 (Anatase)	Tetragonal	$I4_1/amd$

Phase Information	***a***	***b***	***c***	***V***	
	3.7828(8)	3.7828	9.5386(28)	136.49(6)	
	α	***β***	***γ***		
	90	90	90		
Atom	***x***	***y***	***z***	**Occupancy**	**U_{iso}**
Ti1	0	0	0	1	0.01
O	0	0	0.2081	1	0.01

Phase	Symmetry Setting	Space Group
SiO_2	Orthorhombic	$P2_12_12_1$

Phase Information	***a***	***b***	***c***	***V***	
	7.184(13)	7.021(13)	6.973(15)	351.73(15)	
	α	***β***	***γ***		
	90	90	90		
Atom	***x***	***y***	***z***	**Occupancy**	**U_{iso}**
Si1	0.25	0.33	0.25	1	0.01
Si1	0.08	0	0	1	0.01
O1	0.67	0.65	0.14	1	0.01
O2	0.06	0.64	0.58	1	0.01
O3	0.625	0.06	0.625	1	0.01
O4	0.125	0.21	0.125	1	0.01

Weight Fraction	
Phases	Wt. %
$Na_{13}Nb_{35}O_{94}$	**3.42(4)**
$NaNbO_3$	**4.85(3)**
TiO_2 (R)	**7.76(5)**
$Zr_5Ti_7O_{24}$	**19.2(1)**
$ZrTiO_4$	**42.39(8)**
TiO_2 (A)	**4.70(3)**
SiO_2	**17.69(6)**

Unloaded IONSIV Calcination 1000°C

Table 7.44 *Refinement details for IONSIV (Unloaded) Calcination 1000°C*

χ^2	wRp	Rp
3.678	5.69%	3.66%

Phase	Symmetry Setting	Space Group
$Na_{13}Nb_{35}O_{91}$	Orthorhombic	*Pba*2

Phase Information	*a*	*b*	*c*	*V*	
	12.4116(18)	37.156(5)	3.93621(29)	1815.23(28)	
	α	*β*	*γ*		
	90	90	90		
Atom	***x***	***y***	***z***	**Occupancy**	**U_{iso}**
Na1	0	0	0.0092	1	0.01
Na2	0.0061	0.333	0.0069	1	0.01
Na3	0.3333	0.0553	0.0102	1	0.01
Na4	0.1843	0.2261	-0.0051	0.75	0.01
Nb1	0.07993	0	0.5	1	0.01
Nb2	0.02141	0.07091	0.5315	1	0.01
Nb3	0.21835	0.17327	0.502	1	0.01
Nb4	0.075	0.30877	0.5131	1	0.01
Nb5	0.29842	0.40313	0.5189	1	0.01
Nb6	0.42699	0.1314	0.5012	1	0.01
Nb7	0.29553	0.23379	0.4917	1	0.01
Nb8	0.33769	0.47814	0.5285	1	0.01
Nb9	0.291	0.39054	0.4318	1	0.01
Nb10	0.0861	0.191	-0.0053	0.125	0.01
Nb11	0.0861	0.266	-0.0009	0.125	0.01
O1	0.11002	0.01893	0.5113	1	0.01
O2	0.22175	0.09106	0.4929	1	0.01
O3	0.00288	0.118	0.4813	1	0.01
O4	0.16783	0.165	0.4732	1	0.01
O5	0.02142	0.22341	0.4806	1	0.01
O6	0.34026	0.00307	0.4947	1	0.01
O7	0.44762	0.12411	0.4973	1	0.01
O8	0.35678	0.18945	0.4922	1	0.01
O9	0.29241	0.26259	0.4885	1	0.01
O10	0.0709	0.2934	0.4687	1	0.01
O11	0.3645	0.33481	0.492	1	0.01
O12	0.18622	0.36325	0.4752	1	0.01
O13	0.2192	0.42935	0.4875	1	0.01
O14	0.00106	0.44776	0.4573	1	0.01
O15	0.4171	0.44088	0.5028	1	0.01

O16	0	0.5	-0.021	1	0.01
O17	0.08318	0.06973	-0.0064	1	0.01
O18	0.02819	0.1762	-0.0126	1	0.01
O19	0.21431	0.30788	-0.0208	1	0.01
O20	0.07566	0.4026	0.0036	1	0.01
O21	0.30313	0.14759	-0.0211	1	0.01
O22	0.43238	0.23397	-0.0168	1	0.01
O23	0.3005	0.47944	-0.011	1	0.01
O24	0.33867	0.39005	-0.0297	1	0.01

Phase	**Symmetry Setting**	**Space Group**
$NaNbO_3$	Orthorhombic	*Pbma*

Phase Information	***a***	***b***	***c***	***V***	
	5.5446(7)	15.5553(13)	15.5553(13)	474.69(5)	
	α	***β***	***γ***		
	90	90	90		
Atom	***x***	***y***	***z***	**Occupancy**	**U_{iso}**
Nb1	0.2705	0.1231	0.247	1	0.01
Na1	0.75	0	0.257	1	0.01
Na2	0.781	0.25	0.254	1	0.01
O1	0.25	0	0.304	1	0.01
O2	0.232	0.25	0.18	1	0.01
O3	0.025	0.141	0.533	1	0.01
O4	0.456	0.109	-0.036	1	0.01

Phase	**Symmetry Setting**	**Space Group**
TiO_2	Tetragonal	*$P4_2/mnm$*

Phase Information	***a***	***b***	***c***	***V***	
	4.60044(14)	4.60044(14)	2.96823(17)	62.820(4)	
	α	***β***	***γ***		
	90	90	90		
Atom	***x***	***y***	***z***	**Occupancy**	**U_{iso}**
Ti1	0	0	0	1	0.01
O	0.3057	0.3057	0	1	0.01

Phase	Symmetry Setting	Space Group
$Zr_5Ti_7O_{24}$	Orthorhombic	*Pbcn*

Phase Information	*a*	*b*	*c*	*V*	
	14.2698(14)	5.4113(5)	5.0278(5)	388.24(4)	
	α	*β*	*γ*		
	90	90	90		
Atom	***x***	***y***	***z***	**Occupancy**	**U_{iso}**
Zr1	0	0.2629	0.25	0.968	0.01
Ti1	0	0.2629	0.25	0.032	0.01
Zr2	0.3324	0.3335	0.1798	0.111	0.01
Ti2	0.3324	0.3335	0.1798	0.889	0.01
O1	0.0873	0.0668	-0.0234	1	0.01
O2	0.4194	0.0824	0.0599	1	0.01
O3	0.76	0.1226	0.1402	1	0.01

Phase	Symmetry Setting	Space Group
$ZrTiO_4$	Orthorhombic	*Pbcn*

Phase Information	*a*	*b*	*c*	*V*	
	4.7501(5)	5.3967(5)	5.0267(5)	128.859(15)	
	α	*β*	*γ*		
	90	90	90		
Atom	***x***	***y***	***z***	**Occupancy**	**U_{iso}**
Zr1	0	0.1915	0.25	0.333	0.01
Ti1	0	0.1915	0.25	0.666	0.01
O1	0.27	0.27	0.389	1	0.01

Phase	Symmetry Setting	Space Group
SiO_2	Orthorhombic	$P2_12_12_1$

Phase Information	*a*	*b*	*c*	*V*	
	7.184(13)	7.021(13)	6.973(15)	351.73(15)	
	α	*β*	*γ*		
	90	90	90		
Atom	**x**	**y**	**z**	**Occupancy**	**U_{iso}**
Si1	0.25	0.33	0.25	1	0.01
Si1	0.08	0	0	1	0.01
O1	0.67	0.65	0.14	1	0.01
O2	0.06	0.64	0.58	1	0.01
O3	0.625	0.06	0.625	1	0.01
O4	0.125	0.21	0.125	1	0.01

Weight Fractions	
Phases	Wt. %
$Na_{13}Nb_{35}O_{94}$	**7.07(2)**
$NaNbO_3$	**9.45(1)**
TiO_2(R)	**21.00(2)**
$Zr_5Ti_7O_{24}$	**26.63(5)**
$Zr_{0.33}Ti_{0.67}O_4$	**19.47(5)**
SiO_2	**16.38(3)**
$Na_{13}Nb_{35}O_{94}$	**7.07(2)**
$NaNbO_3$	**9.45(1)**

Unloaded IONSIV Calcination 1100°C

Table 7.45 *Refinement details for IONSIV (Unloaded) Calcination 1100°C*

χ^2	wRp	Rp
4.003	5.83%	4.04%

Phase	Symmetry Setting	Space Group
$Na_{13}Nb_{35}O_{91}$	Orthorhombic	*Pba2*

Phase Information	*a*	*b*	*c*	*V*	
	12.3960(15)	37.101(4)	3.93759(22)	1810.92(21)	
	α	*β*	*γ*		
	90	90	90		
Atom	***x***	***y***	***z***	**Occupancy**	U_{iso}
Na1	0	0	0.0092	1	0.01
Na2	0.0061	0.333	0.0069	1	0.01
Na3	0.3333	0.0553	0.0102	1	0.01
Na4	0.1843	0.2261	-0.0051	0.75	0.01
Nb1	0.07993	0	0.5	1	0.01
Nb2	0.02141	0.07091	0.5315	1	0.01
Nb3	0.21835	0.17327	0.502	1	0.01
Nb4	0.075	0.30877	0.5131	1	0.01
Nb5	0.29842	0.40313	0.5189	1	0.01
Nb6	0.42699	0.1314	0.5012	1	0.01
Nb7	0.29553	0.23379	0.4917	1	0.01
Nb8	0.33769	0.47814	0.5285	1	0.01
Nb9	0.291	0.39054	0.4318	1	0.01
Nb10	0.0861	0.191	-0.0053	0.125	0.01
Nb11	0.0861	0.266	-0.0009	0.125	0.01
O1	0.11002	0.01893	0.5113	1	0.01
O2	0.22175	0.09106	0.4929	1	0.01
O3	0.00288	0.118	0.4813	1	0.01
O4	0.16783	0.165	0.4732	1	0.01
O5	0.02142	0.22341	0.4806	1	0.01
O6	0.34026	0.00307	0.4947	1	0.01
O7	0.44762	0.12411	0.4973	1	0.01
O8	0.35678	0.18945	0.4922	1	0.01
O9	0.29241	0.26259	0.4885	1	0.01
O10	0.0709	0.2934	0.4687	1	0.01
O11	0.3645	0.33481	0.492	1	0.01
O12	0.18622	0.36325	0.4752	1	0.01
O13	0.2192	0.42935	0.4875	1	0.01
O14	0.00106	0.44776	0.4573	1	0.01
O15	0.4171	0.44088	0.5028	1	0.01
O16	0	0.5	-0.021	1	0.01

O17	0.08318	0.06973	-0.0064	1	0.01
O18	0.02819	0.1762	-0.0126	1	0.01
O19	0.21431	0.30788	-0.0208	1	0.01
O20	0.07566	0.4026	0.0036	1	0.01
O21	0.30313	0.14759	-0.0211	1	0.01
O22	0.43238	0.23397	-0.0168	1	0.01
O23	0.3005	0.47944	-0.011	1	0.01
O24	0.33867	0.39005	-0.0297	1	0.01

Phase	**Symmetry Setting**	**Space Group**
$Zr_5Ti_7O_{24}$	Orthorhombic	*Pbcn*

Phase Information	***a***	***b***	***c***	***V***	
	14.2965(6)	5.41248(22)	5.03822(21)	389.855(18)	
	α	***β***	***γ***		
	90	90	90		
Atom	***x***	***y***	***z***	**Occupancy**	**U_{iso}**
Zr1	0	0.2629	0.25	0.968	0.01
Ti1	0	0.2629	0.25	0.032	0.01
Zr2	0.3324	0.3335	0.1798	0.111	0.01
Ti2	0.3324	0.3335	0.1798	0.889	0.01
O1	0.0873	0.0668	-0.0234	1	0.01
O2	0.4194	0.0824	0.0599	1	0.01
O3	0.76	0.1226	0.1402	1	0.01

Phase	**Symmetry Setting**	**Space Group**
$Ti_{0.912}Nb_{0.088}O_2$	Tetragonal	$P4_2/mnm$

Phase Information	***a***	***b***	***c***	***V***	
	4.60757(11)	4.60757(11)	2.97427(12)	63.1430(30)	
	α	***β***	***γ***		
	90	90	90		
Atom	***x***	***y***	***z***	**Occupancy**	**U_{iso}**
Ti1	0	0	0	0.912	0.1
Nb1	0	0	0	0.088	0.1
O	0.2965	0.2965	0	1	0.1

Phase	**Symmetry Setting**	**Space Group**
SiO_2	Orthorhombic	$P2_12_12_1$

Phase Information	***a***	***b***	***c***	***V***
	7.457(20)	7.072(19)	6.681(17)	352.33(27)
	α	***β***	***γ***	
	90	90	90	

Atom	***x***	***y***	***z***	**Occupancy**	**Uiso**
Si1	0.25	0.33	0.25	1	0.01
Si1	0.08	0	0	1	0.01
O1	0.67	0.65	0.14	1	0.01
O2	0.06	0.64	0.58	1	0.01
O3	0.625	0.06	0.625	1	0.01
O4	0.125	0.21	0.125	1	0.01

Phase	**Symmetry Setting**	**Space Group**
$ZrTiO_4$	Orthorhombic	*Pbcn*

Phase Information	***a***	***b***	***c***	***V***	
	4.75975(35)	5.42305(33)	5.03850(30)	130.056(10)	
	α	***β***	***γ***		
	90	90	90		
Atom	***x***	***y***	***z***	**Occupancy**	**Uiso**
Zr1	0.1915	0.25	0.333	0.333	0.01
Ti1	0.1915	0.25	0.666	0.666	0.01
O1	0.27	0.389	0.43	1	0.01

Weight Fractions	
Phases	Wt. %
$Na_{13}Nb_{35}O_{94}$	**13.66(2)**
$Zr_5Ti_7O_{24}$	**30.94(3)**
$Ti_{0.912}Nb_{0.088}O_2$	**23.29(2)**
SiO_2	**15.29(4)**
$ZrTiO_4$	**16.82(4)**

Rietveld Refinement Sr-IONSIV (1.5 wt %)

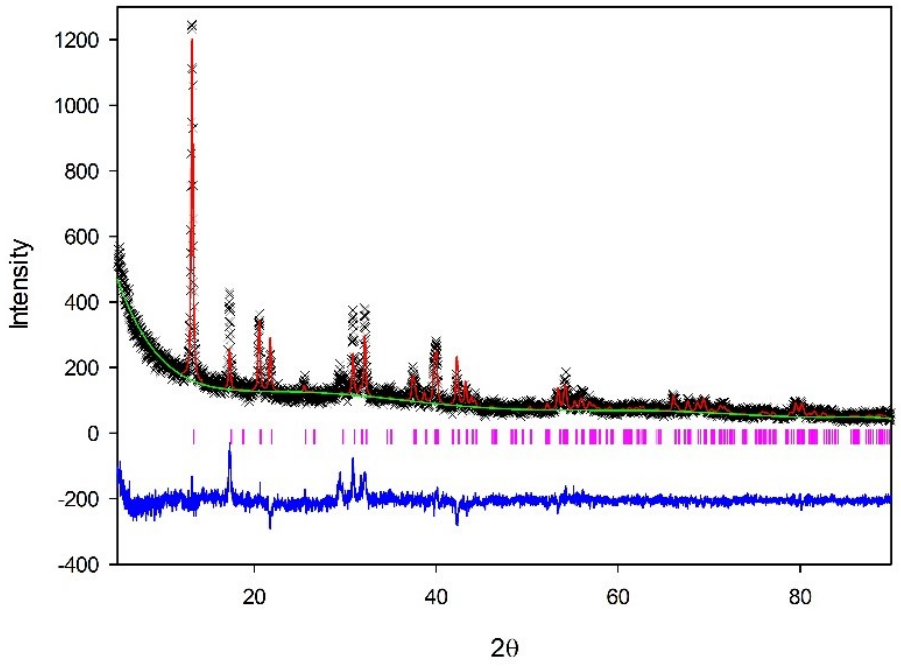

Figure 7.48 *Rietveld Refinement (GSAS Liveplot) for Sr-IONSIV (1.5 wt. %). Pink ticks: Sr-Nb-CST ($H_{0.5}Na(Nb_{0.5}Ti_{1.5})O_3(SiO_4)(H_2O)_2$)*

Table 7.46 *Rietveld Refinement details for Sr-IONSIV (1.5 wt. %)*

χ^2	wRp	Rp
1.904	12.69%	9.66%

Phase	**Symmetry Setting**	**Space Group**
Sr-Nb-CST	Tetragonal	P 4_2/mcm

Phase Information	***a***	***b***	***c***	***V***	
	7.8694(14)	7.8694	11.9765(25)	741.7(4)	
	α	***β***	***γ***		
	90	90	90		
Atom	***x***	***y***	***z***	**Occupancy**	**U_{iso}**
Ti1	0.1435	0.1435	0.1548	0.75	0.01
Nb1	0.1435	0.1435	0.1548	0.25	0.01
Si	0.0	0.5	0.25	1	0.01
O1	0.1256	0.3978	0.1663	1	0.01
O2	0.119	0.119	0	1	0.01
O3	0.1559	0.1559	0	1	0.01
Na	0.0	0.5	0.5	0.737	0.01
Sr	0.3696	0.3969	0	0.197	0.01
O4	0.2683	0.2683	0.5	1	0.01

Rietveld Refinement Sr-IONSIV (3.0 wt %)

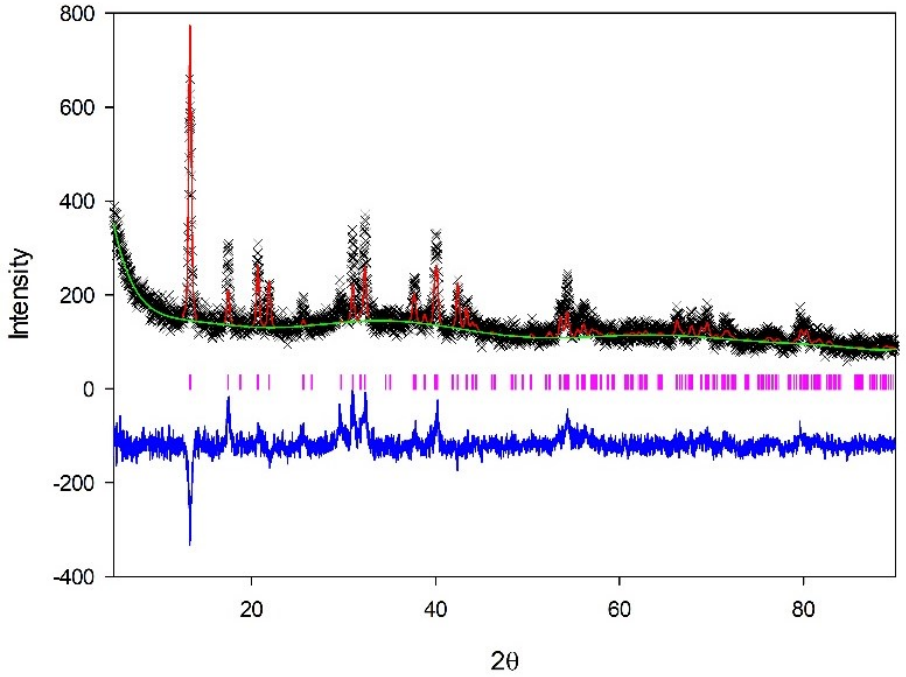

Figure 7.49 *Rietveld Refinement (GSAS Liveplot) for Sr-IONSIV (3.0 wt. %). Pink ticks: Sr-Nb-CST ($H_{0.5}Na(Nb_{0.5}Ti_{1.5})O_3(SiO_4)(H_2O)_2$)*

Table 7.47 *Rietveld Refinement details for Sr-IONSIV (3.0 wt. %)*

χ^2	wRp	Rp
2.036	12.02%	9.45%

Phase	Symmetry Setting	Space Group
Sr-Nb-CST	tetragonal	$P4_2/mcm$

Phase Information	***a***	***b***	***c***	***V***	
	7.8694(14)	7.8694	11.9765(25)	741.7(4)	
	α	***β***	***γ***		
	90	90	90		
Atom	***x***	***y***	***z***	**Occupancy**	**U_{iso}**
Ti1	0.1435	0.1435	0.1548	0.75	0.01
Nb1	0.1435	0.1435	0.1548	0.25	0.01
Si	0.0	0.5	0.25	1	0.01
O1	0.1256	0.3978	0.1663	1	0.01
O2	0.119	0.119	0	1	0.01
O3	0.1559	0.1559	0	1	0.01
Na	0.0	0.5	0.5	0.737	0.01
Sr	0.3696	0.3969	0	0.197	0.01
O4	0.2683	0.2683	0.5	1	0.01

Rietveld Refinement Sr-IONSIV (1.5 wt %, Calcination 900°C)

Table 7.48 *Rietveld Refinement details for Sr-IONSIV (1.5 wt%, Sr) Calcination 900°C*

χ^2	wRp	Rp
4.436	6.26%	4.22%

Phase	Symmetry Setting	Space Group
TiO_2	Tetragonal	$P4_2/mnm$

Phase Information	*a*	*b*	*c*	*V*	
	4.6014(6)	4.6014(6)	2.9656(7)	62.792(17)	
	α	***β***	***γ***		
	90	90	90		
Atom	***x***	***y***	***z***	**Occupancy**	**U_{iso}**
Ti1	0	0	0	1	0.01
O1	0.3057	0.3057	0	1	0.01

Phase	Symmetry Setting	Space Group
TiO_2	Tetragonal	$I4_1/amd$

Phase Information	*a*	*b*	*c*	*V*	
	3.7809(7)	3.7809(7)	9.5267(25)	136.18(5)	
	α	***β***	***γ***		
	90	90	90		
Atom	***x***	***y***	***z***	**Occupancy**	**U_{iso}**
Ti1	0	0	0	1	0.01
O1	0	0	0.2081	1	0.01

Phase	Symmetry Setting	Space Group
$ZrTiO_4$	Orthorhombic	*Pbcn*

Phase Information	*a*	*b*	*c*	*V*	
	4.7512(8)	5.4188(9)	5.0344(8)	129.614(18)	
	α	***β***	***γ***		
	90	90	90		
Atom	***x***	***y***	***z***	**Occupancy**	**U_{iso}**
Zr	0	0.1915	0.25	0.333	0.01
Ti1	0	0.1915	0.25	0.666	0.01
O1	0.27	0.389	0.43	1	0.01

Phase	Symmetry Setting	Space Group
$Sr_6Nb_{34}O_{91}$	Tetragonal	*P4bm*

Phase Information	*a*	*b*	*c*	*V*	
	37.0663(26)	37.0663(26)	3.9269(5)	5395.2(9)	
	α	*β*	*γ*		
	90	90	90		
Atom	***x***	***y***	***z***	**Occupancy**	**U_{iso}**
Nb1	0.5	0	0.583	1	0.01
Nb2	0.5673	0.477	0.401	1	0.01
Nb3	0.1412	0.0991	0.4	1	0.01
Nb4	0.0953	0.1931	0.463	1	0.01
Nb5	0.1882	0.2371	0.501	1	0.01
Nb6	0.2328	0.1426	0.482	1	0.01
Nb7	0.9956	0.1702	0.461	1	0.01
Nb8	0.0693	0.3611	0.507	1	0.01
Nb9	0.4015	0.0233	0.501	1	0.01
Nb10	0.0202	0.2663	0.431	1	0.01
Nb11	0.3067	0.0731	0.547	1	0.01
Nb12	0.1094	0.278	0.583	1	0.01
Nb13	0.3246	0.1754	0.378	1	0.01
Nb14	0.1667	0.3333	0.558	1	0.01
Nb15	0.3894	0.1106	0.498	1	0.01
Sr1	0	0	0.96	1	0.01
Sr2	0.2191	0.0664	0.96	1	0.01
Sr3	0.2724	0.2276	0.969	1	0.01
Sr4	0.0559	0.4441	0.974	1	0.01
O1	0.5	0	0.06	0.9681	0.01
O2	0.073	0.025	0.93	0.9681	0.01
O3	0.137	0.107	0.92	0.9681	0.01
O4	0.094	0.199	0.01	0.9681	0.01
O5	0.244	0.807	0.99	0.9681	0.01
O6	0.233	0.133	0.96	0.9681	0.01
O7	0.179	0.004	0.01	0.9681	0.01
O8	0.077	0.353	0.98	0.9681	0.01
O9	0.397	0.024	0.02	0.9681	0.01
O10	0.266	0.985	0.96	0.9681	0.01
O11	0.312	0.072	0.97	0.9681	0.01
O12	0.115	0.27	0.05	0.9681	0.01
O13	0.324	0.176	0.92	0.9681	0.01
O14	0.17	0.33	0.01	0.9681	0.01
O15	0.39	0.11	0.98	0.9681	0.01
O16	0.051	0.307	0.4	0.9681	0.01
O17	0.621	0.024	0.55	0.9681	0.01
O18	0.551	0.003	0.49	0.9681	0.01

O19	0.055	0.164	0.56	0.9681	0.01
O20	0.382	0.175	0.47	0.9681	0.01
O21	0.121	0.151	0.42	0.9681	0.01
O22	0.141	0.222	0.55	0.9681	0.01
O23	0.005	0.122	0.46	0.9681	0.01
O24	0.161	0.725	0.53	0.9681	0.01
O25	0.224	0.008	0.5	0.9681	0.01
O26	0.38	0.833	0.47	0.9681	0.01
O27	0.163	0.054	0.43	0.9681	0.01
O28	0.41	0.241	0.43	0.9681	0.01
O29	0.571	0.26	0.45	0.9681	0.01
O30	0.093	0.079	0.42	0.9681	0.01
O31	0.186	0.123	0.49	0.9681	0.01
O32	0.218	0.192	0.41	0.9681	0.01
O33	0.302	0.029	0.48	0.9681	0.01
O34	0.283	0.835	0.49	0.9681	0.01
O35	0.028	0.054	0.41	0.9681	0.01
O36	0.362	0.061	0.47	0.9681	0.01
O37	0.236	0.264	0.51	0.9681	0.01
O38	0.091	0.409	0.49	0.9681	0.01
O39	0.426	0.074	0.46	0.9681	0.01

SiO_2	**Symmetry Setting**	**Space Group**
	Orthorhombic	$P2_12_12_1$

Phase Information	***a***	***b***	***c***	***V***	
	7.07	7.07	7.07	353.39325	
	α	***β***	***γ***		
	90	90	90		
Atom	***x***	***y***	***z***	**Occupancy**	**U_{iso}**
Si	0.25	0.33	0.25	1	0.01
Si	0.08	0	0	1	0.01
O1	0.67	0.65	0.14	1	0.01
O2	0.06	0.64	0.58	1	0.01
O3	0.625	0.06	0.625	1	0.01
O4	0.125	0.21	0.125	1	0.01

Weight Fraction	
Phases	Wt. %
TiO_2 (rutile)	**19.52(4)**
TiO_2(anatase)	**3.86(3)**
$ZrTiO_4$	**57.78(3)**
$Sr_6Nb_{34}O_{91}$	**16.27(3)**
SiO_2(ortho)	**2.57(49)**

Rietveld Refinement Sr-IONSIV (1.5 wt %, Calcination 1000°C)

Table 7.49 *Rietveld Refinement details Sr-IONSIV (1.5 wt%, Sr) Calcination 1000°C*

χ^2	wRp	Rp
4.554	6.21 %	4.11 %

Phase	Symmetry Setting	Space Group
TiO_2	Tetragonal	*$P4_2/mnm$*

Phase Information	*a*	*b*	*c*	*V*
	4.59917(11)	4.59917(11)	2.96786(13)	62.7770(30)
	α	***β***	***γ***	
	90	90	90	

Atom	*x*	*y*	*z*	Occupancy	U_{iso}
Ti1	0	0	0	1	0.01
O1	0.3057	0.3057	0	1	0.01

Phase	Symmetry Setting	Space Group
$Zr_5Ti_7O_{24}$	Orthorhombic	*Pbcn*

Phase Information	*a*	*b*	*c*	*V*	
	14.2665(9)	5.38519(34)	5.02545(33)	386.094(27)	
	α	***β***	***γ***		
	90	90	90		
Atom	***x***	***y***	***z***	**Occupancy**	**U_{iso}**
Zr1	0	0.2629	0.25	0.968	0.01
Ti1	0	0.2629	0.25	0.032	0.01
Zr2	0.3324	0.3335	0.1798	0.111	0.01
Ti2	0.3324	0.3335	0.1798	0.889	0.01
O1	0.0873	0.0668	-0.0234	1	0.01
O2	0.4194	0.0824	0.0599	1	0.01
O3	0.76	0.1226	0.1402	1	0.01

Phase	Symmetry Setting	Space Group
$Sr_6Nb_{34}O_{91}$	Tetragonal	*P4bm*

Phase Information	*a*	*b*	*c*	*V*	
	37.1125(24)	37.1125	3.9338(5)	5418.2(8)	
	α	***β***	***γ***		
	90	90	90		
Atom	**x**	**y**	**z**	**Occupancy**	**U_{iso}**
Nb1	0.5	0	0.583	1	0.01
Nb2	0.5673	0.477	0.401	1	0.01
Nb3	0.1412	0.0991	0.4	1	0.01

Nb4	0.0953	0.1931	0.463	1	0.01
Nb5	0.1882	0.2371	0.501	1	0.01
Nb6	0.2328	0.1426	0.482	1	0.01
Nb7	0.9956	0.1702	0.461	1	0.01
Nb8	0.0693	0.3611	0.507	1	0.01
Nb9	0.4015	0.0233	0.501	1	0.01
Nb10	0.0202	0.2663	0.431	1	0.01
Nb11	0.3067	0.0731	0.547	1	0.01
Nb12	0.1094	0.278	0.583	1	0.01
Nb13	0.3246	0.1754	0.378	1	0.01
Nb14	0.1667	0.3333	0.558	1	0.01
Nb15	0.3894	0.1106	0.498	1	0.01
Sr1	0	0	0.96	1	0.01
Sr2	0.2191	0.0664	0.96	1	0.01
Sr3	0.2724	0.2276	0.969	1	0.01
Sr4	0.0559	0.4441	0.974	1	0.01
O1	0.5	0	0.06	0.9681	0.01
O2	0.073	0.025	0.93	0.9681	0.01
O3	0.137	0.107	0.92	0.9681	0.01
O4	0.094	0.199	0.01	0.9681	0.01
O5	0.244	0.807	0.99	0.9681	0.01
O6	0.233	0.133	0.96	0.9681	0.01
O7	0.179	0.004	0.01	0.9681	0.01
O8	0.077	0.353	0.98	0.9681	0.01
O9	0.397	0.024	0.02	0.9681	0.01
O10	0.266	0.985	0.96	0.9681	0.01
O11	0.312	0.072	0.97	0.9681	0.01
O12	0.115	0.27	0.05	0.9681	0.01
O13	0.324	0.176	0.92	0.9681	0.01
O14	0.17	0.33	0.01	0.9681	0.01
O15	0.39	0.11	0.98	0.9681	0.01
O16	0.051	0.307	0.4	0.9681	0.01
O17	0.621	0.024	0.55	0.9681	0.01
O18	0.551	0.003	0.49	0.9681	0.01
O19	0.055	0.164	0.56	0.9681	0.01
O20	0.382	0.175	0.47	0.9681	0.01
O21	0.121	0.151	0.42	0.9681	0.01
O22	0.141	0.222	0.55	0.9681	0.01
O23	0.005	0.122	0.46	0.9681	0.01
O24	0.161	0.725	0.53	0.9681	0.01
O25	0.224	0.008	0.5	0.9681	0.01
O26	0.38	0.833	0.47	0.9681	0.01
O27	0.163	0.054	0.43	0.9681	0.01
O28	0.41	0.241	0.43	0.9681	0.01
O29	0.571	0.26	0.45	0.9681	0.01

O30	0.093	0.079	0.42	0.9681	0.01
O31	0.186	0.123	0.49	0.9681	0.01
O32	0.218	0.192	0.41	0.9681	0.01
O33	0.302	0.029	0.48	0.9681	0.01
O34	0.283	0.835	0.49	0.9681	0.01
O35	0.028	0.054	0.41	0.9681	0.01
O36	0.362	0.061	0.47	0.9681	0.01
O37	0.236	0.264	0.51	0.9681	0.01
O38	0.091	0.409	0.49	0.9681	0.01
O39	0.426	0.074	0.46	0.9681	0.01

Phase	**Symmetry Setting**	**Space Group**
$ZrTiO_4$	Orthorhombic	*Pbcn*

Phase Information	***a***	***b***	***c***	***V***	
	4.7488(5)	5.3985(4)	5.0233(4)	128.777(13)	
	α	***β***	***γ***		
	90	90	90		
Atom	***x***	***y***	***z***	**Occupancy**	**U_{iso}**
Zr	0	0.1915	0.25	0.333	0.01
Ti1	0	0.1915	0.25	0.666	0.01
O1	0.27	0.389	0.43	1	0.01

Phase	**Symmetry Setting**	**Space Group**
SiO_2	Orthorhombic	$P2_12_12_1$

Phase Information	***a***	***b***	***c***	***V***	
	8.163(18)	6.026(7)	7.525(16)	370.16(33)	
	α	***β***	***γ***		
	90	90	90		
Atom	***x***	***y***	***z***	**Occupancy**	**U_{iso}**
Si	0.25	0.33	0.25	1	0.01
Si	0.08	0	0	1	0.01
O1	0.67	0.65	0.14	1	0.01
O2	0.06	0.64	0.58	1	0.01
O3	0.625	0.06	0.625	1	0.01
O4	0.125	0.21	0.125	1	0.01

Phase	Symmetry Setting	Space Group
$(Sr,Na)NbO_3$	Orthorhombic	*Pm*-3*m*

Phase Information	***a***	***b***	***c***	***V***
	3.91703(16)	3.91703	3.91703	60.100(7)
	α	***β***	***γ***	
	90	90	90	

Atom	***x***	***y***	***z***	Occupancy	U_{iso}
Sr	0.5	0.5	0.5	0.25	0.01
Na	0.5	0.5	0.5	0.5	0.01
Nb	0	0	0	1	0.01
O1	0.5	0	0	1	0.01

Weight Fractions	
Phases	Wt. %
TiO_2 (R)	**21.04(2)**
$Zr_5Ti_7O_{24}$	**29.09(5)**
$Sr_6Nb_{34}O_{91}$	**10.55(3)**
$ZrTiO_4$	**17.00(5)**
SiO_2(ortho)	**15.64(4)**
$(Sr,Na)NbO_3$	**6.69(2)**

Rietveld Refinement Sr-IONSIV (3.0 wt %, Calcination (Calcination in air, 900°C)

Table 7.50 *Refinement Details for Sr-IONSIV (3.0 wt%, Sr) Calcination (900°C)*

χ^2	wRp	Rp
4.499	5.97%	3.85%

Phase	Symmetry Setting	Space Group
TiO_2 (Rutile)	Tetragonal	$P4_2/mnm$

Phase Information	*a*	*b*	*c*	*V*	
	4.6044(6)	4.6044(6)	2.9663(7)	62.888(15)	
	α	*β*	*γ*		
	90	90	90		
Atom	***x***	***y***	***z***	**Occupancy**	**U_{iso}**
Ti1	0	0	0	1	0.01
O1	0.3057	0.3057	0	1	0.01

Phase	Symmetry Setting	Space Group
TiO_2 (Anatase)	Tetragonal	$I4_1/amd$

Phase Information	*a*	*b*	*c*	*V*	
	3.7837(11)	3.7837(11)	9.524(4)	136.35(9)	
	α	*β*	*γ*		
	90	90	90		
Atom	***x***	***y***	***z***	**Occupancy**	**U_{iso}**
Ti1	0	0	0	1	0.01
O1	0	0	0.2081	1	0.01

Phase	Symmetry Setting	Space Group			
$ZrTiO_4$	Orthorhombic	*Pbcn*			
Phase Information	***a***	***b***	***c***	***V***	
	4.7570(9)	5.4148(11)	5.0338(9)	129.661(21)	
	α	*β*	*γ*		
	90	90	90		
Atom	***x***	***y***	***z***	**Occupancy**	**U_{iso}**
Zr	0	0.1915	0.25	0.333	0.01
Ti1	0	0.1915	0.25	0.666	0.01
O1	0.27	0.389	0.43	1	0.01

Phase	Symmetry Setting	Space Group
$Sr_6Nb_{34}O_{91}$	Tetragonal	*P*4*bm*

Phase Information	*a*	*b*	*c*	*V*	
	37.0499(31)	37.0499	3.9272(5)	5390.9(11)	
	α	*β*	*γ*		
	90	90	90		
Atom	***x***	***y***	***z***	**Occupancy**	U_{iso}
Nb1	0.5	0	0.583	1	0.01
Nb2	0.5673	0.477	0.401	1	0.01
Nb3	0.1412	0.0991	0.4	1	0.01
Nb4	0.0953	0.1931	0.463	1	0.01
Nb5	0.1882	0.2371	0.501	1	0.01
Nb6	0.2328	0.1426	0.482	1	0.01
Nb7	0.9956	0.1702	0.461	1	0.01
Nb8	0.0693	0.3611	0.507	1	0.01
Nb9	0.4015	0.0233	0.501	1	0.01
Nb10	0.0202	0.2663	0.431	1	0.01
Nb11	0.3067	0.0731	0.547	1	0.01
Nb12	0.1094	0.278	0.583	1	0.01
Nb13	0.3246	0.1754	0.378	1	0.01
Nb14	0.1667	0.3333	0.558	1	0.01
Nb15	0.3894	0.1106	0.498	1	0.01
Sr1	0	0	0.96	1	0.01
Sr2	0.2191	0.0664	0.96	1	0.01
Sr3	0.2724	0.2276	0.969	1	0.01
Sr4	0.0559	0.4441	0.974	1	0.01
O1	0.5	0	0.06	0.9681	0.01
O2	0.073	0.025	0.93	0.9681	0.01
O3	0.137	0.107	0.92	0.9681	0.01
O4	0.094	0.199	0.01	0.9681	0.01
O5	0.244	0.807	0.99	0.9681	0.01
O6	0.233	0.133	0.96	0.9681	0.01
O7	0.179	0.004	0.01	0.9681	0.01
O8	0.077	0.353	0.98	0.9681	0.01
O9	0.397	0.024	0.02	0.9681	0.01
O10	0.266	0.985	0.96	0.9681	0.01
O11	0.312	0.072	0.97	0.9681	0.01
O12	0.115	0.27	0.05	0.9681	0.01
O13	0.324	0.176	0.92	0.9681	0.01
O14	0.17	0.33	0.01	0.9681	0.01
O15	0.39	0.11	0.98	0.9681	0.01
O16	0.051	0.307	0.4	0.9681	0.01
O17	0.621	0.024	0.55	0.9681	0.01

O18	0.551	0.003	0.49	0.9681	0.01
O19	0.055	0.164	0.56	0.9681	0.01
O20	0.382	0.175	0.47	0.9681	0.01
O21	0.121	0.151	0.42	0.9681	0.01
O22	0.141	0.222	0.55	0.9681	0.01
O23	0.005	0.122	0.46	0.9681	0.01
O24	0.161	0.725	0.53	0.9681	0.01
O25	0.224	0.008	0.5	0.9681	0.01
O26	0.38	0.833	0.47	0.9681	0.01
O27	0.163	0.054	0.43	0.9681	0.01
O28	0.41	0.241	0.43	0.9681	0.01
O29	0.571	0.26	0.45	0.9681	0.01
O30	0.093	0.079	0.42	0.9681	0.01
O31	0.186	0.123	0.49	0.9681	0.01
O32	0.218	0.192	0.41	0.9681	0.01
O33	0.302	0.029	0.48	0.9681	0.01
O34	0.283	0.835	0.49	0.9681	0.01
O35	0.028	0.054	0.41	0.9681	0.01
O36	0.362	0.061	0.47	0.9681	0.01
O37	0.236	0.264	0.51	0.9681	0.01
O38	0.091	0.409	0.49	0.9681	0.01
O39	0.426	0.074	0.46	0.9681	0.01

Weight Fractions	
Phase	Wt. %
TiO_2 (R)	**23.51(4)**
TiO_2(A)	**2.93(3)**
$ZrTiO_4$	**55.53(3)**
$Sr_6Nb_{34}O_{91}$	**18.03(3)**

Rietveld Refinement Sr-IONSIV (3.0 wt %, Calcination 1000°C)

Table 7.51 *Refinement Details for Sr-IONSIV (3.0 wt %, Calcination 1000°C)*

χ^2	wRp	Rp
7.298	8.58%	5.97%

Phase	Symmetry Setting	Space Group
TiO_2	Tetragonal	*$P4_2/mnm$*

Phase Information	*a*	*b*	*c*	*V*
	4.59999(12)	4.59999(12)	2.96873(14)	62.8180(30)
	α	*β*	*γ*	
	90	90	90	

Atom	*x*	*y*	*z*	Occupancy	U_{iso}
Ti1	0	0	0	1	0.01
O1	0.3057	0.3057	0	1	0.01

Phase	Symmetry Setting	Space Group
$Zr_5Ti_7O_{24}$	Orthorhombic	*Pbcn*

Phase Information	*a*	*b*	*c*	*V*	
	14.2662(10)	5.3867(4)	5.0224(4)	385.960(33)	
	α	*β*	*γ*		
	90	90	90		
Atom	***x***	***y***	***z***	**Occupancy**	**U_{iso}**
Zr1	0	0.2629	0.25	0.968	0.01
Ti1	0	0.2629	0.25	0.032	0.01
Zr2	0.3324	0.3335	0.1798	0.111	0.01
Ti2	0.3324	0.3335	0.1798	0.889	0.01
O1	0.0873	0.0668	-0.0234	1	0.01
O2	0.4194	0.0824	0.0599	1	0.01
O3	0.76	0.1226	0.1402	1	0.01

Phase	Symmetry Setting	Space Group
$Sr_6Nb_{34}O_{91}$	Tetragonal	*P4bm*

Phase Information	*a*	*b*	*c*	*V*
	37.0622(26)	37.0622(26)	3.9301(5)	5398.4(9)
	α	*β*	*γ*	
	90	90	90	

Atom	*x*	*y*	*z*	Occupancy	U_{iso}
Nb1	0.5	0	0.583	1	0.01
Nb2	0.5673	0.477	0.401	1	0.01
Nb3	0.1412	0.0991	0.4	1	0.01
Nb4	0.0953	0.1931	0.463	1	0.01
Nb5	0.1882	0.2371	0.501	1	0.01
Nb6	0.2328	0.1426	0.482	1	0.01
Nb7	0.9956	0.1702	0.461	1	0.01
Nb8	0.0693	0.3611	0.507	1	0.01
Nb9	0.4015	0.0233	0.501	1	0.01
Nb10	0.0202	0.2663	0.431	1	0.01
Nb11	0.3067	0.0731	0.547	1	0.01
Nb12	0.1094	0.278	0.583	1	0.01
Nb13	0.3246	0.1754	0.378	1	0.01
Nb14	0.1667	0.3333	0.558	1	0.01
Nb15	0.3894	0.1106	0.498	1	0.01
Sr1	0	0	0.96	1	0.01
Sr2	0.2191	0.0664	0.96	1	0.01
Sr3	0.2724	0.2276	0.969	1	0.01
Sr4	0.0559	0.4441	0.974	1	0.01
O1	0.5	0	0.06	0.9681	0.01
O2	0.073	0.025	0.93	0.9681	0.01
O3	0.137	0.107	0.92	0.9681	0.01
O4	0.094	0.199	0.01	0.9681	0.01
O5	0.244	0.807	0.99	0.9681	0.01
O6	0.233	0.133	0.96	0.9681	0.01
O7	0.179	0.004	0.01	0.9681	0.01
O8	0.077	0.353	0.98	0.9681	0.01
O9	0.397	0.024	0.02	0.9681	0.01
O10	0.266	0.985	0.96	0.9681	0.01
O11	0.312	0.072	0.97	0.9681	0.01
O12	0.115	0.27	0.05	0.9681	0.01
O13	0.324	0.176	0.92	0.9681	0.01
O14	0.17	0.33	0.01	0.9681	0.01
O15	0.39	0.11	0.98	0.9681	0.01
O16	0.051	0.307	0.4	0.9681	0.01
O17	0.621	0.024	0.55	0.9681	0.01
O18	0.551	0.003	0.49	0.9681	0.01
O19	0.055	0.164	0.56	0.9681	0.01
O20	0.382	0.175	0.47	0.9681	0.01
O21	0.121	0.151	0.42	0.9681	0.01
O22	0.141	0.222	0.55	0.9681	0.01
O23	0.005	0.122	0.46	0.9681	0.01
O24	0.161	0.725	0.53	0.9681	0.01
O25	0.224	0.008	0.5	0.9681	0.01

O26	0.38	0.833	0.47	0.9681	0.01
O27	0.163	0.054	0.43	0.9681	0.01
O28	0.41	0.241	0.43	0.9681	0.01
O29	0.571	0.26	0.45	0.9681	0.01
O30	0.093	0.079	0.42	0.9681	0.01
O31	0.186	0.123	0.49	0.9681	0.01
O32	0.218	0.192	0.41	0.9681	0.01
O33	0.302	0.029	0.48	0.9681	0.01
O34	0.283	0.835	0.49	0.9681	0.01
O35	0.028	0.054	0.41	0.9681	0.01
O36	0.362	0.061	0.47	0.9681	0.01
O37	0.236	0.264	0.51	0.9681	0.01
O38	0.091	0.409	0.49	0.9681	0.01
O39	0.426	0.074	0.46	0.9681	0.01

Phase	**Symmetry Setting**	**Space Group**
$ZrTiO_4$	Orthorhombic	*Pbcn*

Phase Information	***a***	***b***	***c***	***V***	
	4.7478(6)	5.3791(5)	5.0228(5)	128.276(18)	
	α	***β***	***γ***		
	90	90	90		
Atom	***x***	***y***	***z***	**Occupancy**	**U_{iso}**
Zr	0	0.1915	0.25	0.333	0.01
Ti1	0	0.1915	0.25	0.666	0.01
O1	0.27	0.389	0.43	1	0.01

Phase	**Symmetry Setting**	**Space Group**
SiO_2	Orthorhombic	$P2_12_12_1$

Phase Information	***a***	***b***	***c***	***V***	
	7.07	7.07	7.07	353.39325	
	α	***β***	***γ***		
	90	90	90		
Atom	**x**	**y**	**z**	**Occupancy**	**U_{iso}**
Si	0.25	0.33	0.25	1	0.01
Si	0.08	0	0	1	0.01
O1	0.67	0.65	0.14	1	0.01
O2	0.06	0.64	0.58	1	0.01
O3	0.625	0.06	0.625	1	0.01
O4	0.125	0.21	0.125	1	0.01

Phase	Symmetry Setting	Space Group
(Sr,Na)NbO_3	Orthorhombic	*Pm*-3*m*

Phase Information	***a***	***b***	***c***	***V***	
	3.92306(19)	3.92306(19)	3.92306(19)	60.378(9)	
	α	***β***	***γ***		
	90	90	90		
Atom	***x***	***y***	***z***	**Occupancy**	**U_{iso}**
Sr	0.5	0.5	0.5	0.25	0.01
Na	0.5	0.5	0.5	0.5	0.01
Nb	0	0	0	1	0.01
O1	0.5	0	0	1	0.01

Weight Fractions	
Phase	Wt. %
TiO_2 (R)	**20.74(2)**
$Zr_5Ti_7O_{24}$	**31.82(5)**
$Sr_6Nb_{34}O_{91}$	**13.12(3)**
$ZrTiO_4$	**14.38(6)**
SiO_2(ortho)	**15.69(4)**
(Sr,Na)NbO_3	**4.21(1)**

Rietveld Refinement Sr-IONSIV (1.5 wt %, HIPing) (D8)

Table 7.52 *Refinement Details for Sr-IONSIV (1.5 wt %) HIPing (1100°C, 2 hours) (D8)*

χ^2	wRp	Rp
3.754	5.5%	3.88%

Phase	Symmetry Setting	Space Group
$ZrSiO_4$	Tetragonal	*$I4_1/amd$*

Phase Information	*a*	*b*	*c*	*V*	
	6.58817(24)	6.58817(24)	5.96861(26)	259.062(22)	
	α	*β*	*γ*		
	90	90	120		
Atom	***x***	***y***	***z***	**Occupancy**	**Uiso**
Zr	0	0.75	0.125	1	0.01
Si	0	0.75	0.125	1	0.01
O	0	0.066	0.1941	1	0.01

Phase	Symmetry Setting	Space Group
$ZrTiO_4$	Orthorhombic	*Pbcn*

Phase Information	*a*	*b*	*c*	*V*
	4.6944(14)	5.5290(20)	5.0373(15)	130.744(31)
	α	*β*	*γ*	
	90	90	90	

Atom	*x*	*y*	*z*	Occupancy	U_{iso}
Zr1	0	0.1915	0.25	0.333	0.01
Ti1	0	0.1915	0.25	0.666	0.01
O1	0.27	0.389	0.43	1	0.01

Phase	Symmetry Setting	Space Group
$Ti_{0.912}Nb_{0.088}O_2$	Tetragonal	*$P4_2/mnm$*

Phase Information	*a*	*b*	*c*	*V*
	4.62220(15)	4.62220(15)	2.98259(12)	63.722(5)
	α	*β*	*γ*	
	90	90	90	

Atom	*x*	*y*	*z*	Occupancy	U_{iso}
Ti1	0	0	0	0.912	0.01
Nb1	0	0	0	0.088	0.01
O	0.2965	0.2965	0	1	0.01

Phase	Symmetry Setting	Space Group
$Ti_{0.69}Nb_{0.24}O_2$	tetragonal	$P4_2/mnm$

Phase Information	*a*	*b*	*c*	*V*
	4.66034(35)	4.66034(35)	3.00588(28)	65.284(9)
	α	*β*	*γ*	
	90	90	90	

Atom	*x*	*y*	*z*	Occupancy	U_{iso}
Ti1	0	0	0	0.69	0.01
Nb1	0	0	0	0.24	0.01
O	0.307	0.307	0	1	0.01

Phase	Symmetry Setting	Space Group
$(Sr,Na)NbO_3$	cubic	$Pm\text{-}3m$

Phase Information	*a*	*b*	*c*	*V*
	3.91561(17)	3.91561(17)	3.91561(17)	60.034(8)
	α	*β*	*γ*	
	90	90	90	
Atom	**x**	**y**	**z**	**Occupancy**	**U_{iso}**
Sr	0.5	0.5	0.5	0.055(13)	0.01
Na	0.5	0.5	0.5	0.890(26)	0.01
Nb	0	0	0	1	0.01
O	0.5	0	0	1	0.01

Phase	Symmetry Setting	Space Group
SiO_2	trigonal	$P3_221$

Phase Information	*a*	*b*	*c*	*V*
	4.9169(10)	4.9169(10)	5.4084(18)	113.235(23)
	α	*β*	*γ*	
	90	90	120	
Atom	***x***	***y***	***z***	**Occupancy**	**U_{iso}**
Si	0.4697	0	0.1667	1	0.01
O	0.4133	0.2672	0.2855	1	0.01

Phase	Symmetry Setting	Space Group
$NaSr_2Nb_5O_{15}$	Tetragonal	*P*4/*mbm*

Phase Information	***a***	***b***	***c***	***V***	
	12.3279(23)	12.3279(23)	3.9302(11)	597.30(23)	
	α	***β***	***γ***		
	90	90	90		
Atom	***x***	***y***	***z***	**Occupancy**	**U_{iso}**
Sr1	0	0	0	0.6667	0.01
Na1	0	0	0	0.33333	0.01
Sr2	0.17064	0.67064	0	0.6667	0.01
Na2	0.17064	0.67064	0	0.33333	0.01
Nb1	0	0.5	0.5	1	0.01
Nb2	0.07663	0.21335	0.5	1	0.01
O1	0	0.5	0	1	0.01
O2	0.2815	0.78152	0.5	1	0.01
O3	0.0759	0.2095	0	1	0.01
O4	0.3442	0.0074	0.5	1	0.01
O5	0.1395	0.0699	0.5	1	0.01

Weight fraction	
Phases	Wt. %
$ZrSiO_4$	**25.35(2)**
$ZrTiO_4$	**4.47(2)**
$Ti_{0.912}Nb_{0.088}O_2$	**33.98(2)**
$Ti_{0.69}Nb_{0.24}O2$	**9.87(2)**
$(Sr,Na)NbO_3$	**11.03(2)**
SiO_2	**11.19(3)**
$NaSr_2Nb_5O_{15}$	**4.11(2)**

Rietveld Refinement Sr-IONSIV (1.5 wt %, HIPing) (I11)

Table 7.53 *Refinement Details Sr-IONSIV (1.5 wt %) HIPing (1100°C, 2 hours) (I11)*

χ^2	wRp	Rp
8.592	13.08%	9.81%

Phase	Symmetry Setting	Space Group
$ZrSiO_4$	Tetragonal	$I4_1/amd$

Phase Information	*a*	*b*	*c*	*V*	
	6.59804(7)	6.59804	5.97785(8)	260.241(6)	
	α	*β*	*γ*		
	90	90	90		
Atom	***x***	***y***	***z***	**Occupancy**	**U_{iso}**
Zr1	0	0.75	0.125	1	0.00416(34)
Si1	0	0.75	0.625	1	-0.0041(7)
O1	0	0.066	0.1941	1	0.01

Phase	Symmetry Setting	Space Group
$ZrTiO_4$	Orthorhombic	*Pbcn*

Phase Information	*a*	*b*	*c*	*V*	
	4.79036(29)	5.40470(23)	5.04478(30)	130.612(6)	
	α	*β*	*γ*		
	90	90	90		
Atom	***x***	***y***	***z***	**Occupancy**	**Uiso**
Zr1	0	0.75	0.125	1	0.00024(31)
Si1	0	0.75	0.625	1	-0.0179(6)
O1	0	0.066	0.1941	1	0.01

Phase	Symmetry Setting	Space Group
$Ti_{0.69}Nb_{0.24}O_2$	Tetragonal	$P4_2/mnm$

Phase Information	*a*	*b*	*c*	*V*	
	4.66632(11)	4.66632	3.01087(7)	65.5600(30)	
	α	*β*	*γ*		
	90	90	90		
Atom	***x***	***y***	***z***	**Occupancy**	**U_{iso}**
Ti1	0	0	0	0.794(8)	0.0065(8)
Nb1	0	0	0	0.206(8)	0.0065(8)
O1	0.307	0.307	0	1	0.01

Phase	Symmetry Setting	Space Group
$Ti_{0.912}Nb_{0.088}O_2$	Tetragonal	$P4_2/mnm$

Phase Information	*a*	*b*	*c*	*V*	
	4.62884(4)	4.62884	2.987492(32)	64.0100(10)	
	α	*β*	*γ*		
	90	90	90		
Atom	***x***	***y***	***z***	**Occupancy**	**U_{iso}**
Ti1	0	0	0	0.965(4)	0.00211(30)
Nb1	0	0	0	0.035(4)	0.00211(30)
O	0.2965	0.2965	0	1	0.1

Phase	Symmetry Setting	Space Group
SiO_2 (1)	trigonal	$P3_221$

Phase Information	*a*	*b*	*c*	*V*	
	4.91530(17)	4.9153	5.4078(4)	113.150(6)	
	α	*β*	*γ*		
	90	90	120		
Atom	***x***	***y***	***z***	**Occupancy**	**U_{iso}**
Si1	0.4996(28)	0	0.6667	1	0.0165(35)
O1	0.408	0.265	0.786	1	0.01

Phase	Symmetry Setting	Space Group
SiO_2 (2)	trigonal	$P3_221$

Phase Information	*a*	*b*	*c*	*V*
	4.9380(6)	4.938	5.4145(10)	114.338(30)
	α	*β*	*γ*	
	90	90	120	

Atom	***x***	***y***	***z***	**Occupancy**	**U_{iso}**
Si1	0.4883(25)	0	0.6667	1	0.050(4)
O1	0.4136	0.2676	0.7857	1	0.01

Phase	Symmetry Setting	Space Group
(Sr,Na)NbO_3	Cubic	*Pm*-3*m*

Phase Information	***a***	***b***	***c***	***V***	
	3.92215(6)	3.92215	3.92215	60.3350(30)	
	α	***β***	***γ***		
	90	90	90		
Atom	***x***	***y***	***z***	**Occupancy**	**U_{iso}**
Sr1	0.5	0.5	0.5	0.148(7)	0.0157(16)
Na1	0.5	0.5	0.5	0.705(14)	0.0157(16)
Nb1	0	0	0	0.0191(7)	0.01
O1	0.5	0	0	1	0.01

Phase	Symmetry Setting	Space Group
(Sr_2,Na)Nb_5O_{15}	Tetragonal	*P*4*bm*

Phase Information	***a***	***b***	***c***	***V***	
	12.33919(31)	12.33919	3.93579(19)	599.25(4)	
	α	***β***	***γ***		
	90	90	90		
Atom	***x***	***y***	***z***	**Occupancy**	**U_{iso}**
Sr1	0	0	-0.021(13)	1	0.038(8)
Na1	0.1885(14)	0.6885(14)	0.198(14)	0.5	0.122(10)
Sr2	0.1885(14)	0.6885(14)	0.198(14)	0.5	0.122(10)
Nb1	0	0.5	0.476(11)	1	0.035(4)
Nb2	0.0839(6)	0.2099(7)	0.410(10)	1	0.0442(34)
O1	0.1327	0.06722	0.37197	1	0.01
O2	0.34232	0.00469	0.38305	1	0.01
O3	0.08883	0.19947	-0.07274	1	0.01
O4	0.28409	0.78409	0.4352	1	0.01
O5	0	0.5	0.027	1	0.01

Weight fractions	
Phases	Wt. %
$ZrSiO_4$	**20.422(8)**
$ZrTiO_4$	**5.161(7)**
$Ti_{0.69}Nb_{0.24}O_2$	**13.73(2)**
$Ti_{0.912}Nb_{0.088}O_2$	**35.97(1)**
SiO_2 (1)	**4.11(3)**
SiO_2 (2)	**6.55(3)**
(Sr,Na)NbO_3	**10.505(4)**
(Sr_2,Na)Nb_5O_{15}	**3.554(7)**

Rietveld Refinement Sr-IONSIV (3.0 wt %, HIPing) (D8)

Table 7.54 *Refinement Details Sr-IONSIV (3.0 wt %) HIPing (1100°C, 2 hours) (D8)*

χ^2	wRp	Rp
3.451	5.33%	3.80%

Phase	Symmetry Setting	Space Group
$ZrSiO_4$	Tetragonal	$I4_1/amd$

Phase Information	*a*	*b*	*c*	*V*	
	6.58689(18)	6.58689(18)	5.96935(19)	258.993(17)	
	α	*β*	*γ*		
	90	90	120		
Atom	***x***	***y***	***z***	**Occupancy**	**U_{iso}**
Zr	0	0.75	0.125	1	0.01
Si	0	0.75	0.125	1	0.01
O	0	0.066	0.1941	1	0.01

Phase	Symmetry Setting	Space Group
$Ti_{0.912}Nb_{0.088}O_2$	Tetragonal	$P4_2/mnm$

Phase Information	*a*	*b*	*c*	*V*	
	4.62055(13)	4.62055(13)	2.97856(11)	63.591(4)	
	α	*β*	*γ*		
	90	90	90		
Atom	***x***	***y***	***z***	**Occupancy**	**Uiso**
Ti1	0	0	0	0.912	0.01
Nb1	0	0	0	0.088	0.01
O	0.2965	0.2965	0	1	0.01

Phase	Symmetry Setting	Space Group
$Ti_{0.69}Nb_{0.24}O2$	Tetragonal	$P4_2/mnm$

Phase Information	*a*	*b*	*c*	*V*	
	4.66018(24)	4.66018(24)	3.00486(18)	65.258(6)	
	α	*β*	*γ*		
	90	90	90		
Atom	***x***	***y***	***z***	**Occupancy**	**U_{iso}**
Ti1	0	0	0	0.69	0.01
Nb1	0	0	0	0.24	0.01
O	0.307	0.307	0	1	0.01

Phase	Symmetry Setting	Space Group
(Sr,Na)NbO_3	cubic	Pm-3m

Phase Information	*a*	*b*	*c*	*V*	
	3.92280(13)	3.92280(13)	3.92280(13)	60.366(6)	
	α	*β*	*γ*		
	90	90	90		
Atom	***x***	***y***	***z***	**Occupancy**	**U_{iso}**
Sr	0.5	0.5	0.5	0.132(20)	0.003(5)
Na	0.5	0.5	0.5	0.74(4)	0.003(5)
Nb	0	0	0	1	0.01
O	0.5	0	0	1	0.01

Phase	Symmetry Setting	Space Group
SiO_2	Trigonal	$P3_221$

Phase Information	*a*	*b*	*c*	*V*	
	4.9203(14)	4.9203(14)	5.4064(26)	113.350(23)	
	α	*β*	*γ*		
	90	90	120		
Atom	***x***	***y***	***z***	**Occupancy**	**U_{iso}**
Si	0.4697	0	0.1667	1	0.01
O	0.4133	0.2672	0.2855	1	0.01

Phase	Symmetry Setting	Space Group
$NaSr_2Nb_5O_{15}$	Tetragonal	*P*4/*mbm*

Phase Information	*a*	*b*	*c*	*V*	
	12.3200(19)	12.3200(19)	3.9297(10)	596.47(21)	
	α	*β*	*γ*		
	90	90	90		
Atom	***x***	***y***	***z***	**Occupancy**	**Uiso**
Sr1	0	0	0	0.6667	0.01
Na1	0	0	0	0.33333	0.01
Sr2	0.17064	0.67064	0	0.6667	0.01
Na2	0.17064	0.67064	0	0.33333	0.01
Nb1	0	0.5	0.5	1	0.01
Nb2	0.07663	0.21335	0.5	1	0.01
O1	0	0.5	0	1	0.01
O2	0.2815	0.78152	0.5	1	0.01
O3	0.0759	0.2095	0	1	0.01
O4	0.3442	0.0074	0.5	1	0.01
O5	0.1395	0.0699	0.5	1	0.01

Weight Fraction	
Phases	Wt. %
$ZrSiO_4$	**30.34(2)**
$Ti_{0.912}Nb_{0.088}O_2$	**31.77(2)**
$Ti_{0.69}Nb_{0.24}O_2$	**14.27(3)**
$(Sr,Na)NbO_3$	**10.25(1)**
SiO_2	**8.98(2)**
$NaSr_2Nb_5O_{15}$	**4.38(2)**

Rietveld Refinement Sr-IONSIV (3.0 wt %, HIPing) (I11)

Table 7.55 *Refinement Details Sr-IONSIV (3.0 wt %) HIPing (1100°C, 2 hours) (I11)*

χ^2	wRp	Rp
7.196	15.38%	11.67%

Phase	Symmetry Setting	Space Group
$ZrSiO_4$	Tetragonal	$I4_1/amd$

Phase Information	*a*	*b*	*c*	*V*	
	6.59779(4)	6.59779	5.97961(6)	260.244(6)	
	α	***β***	***γ***		
	90	90	90		
Atom	***x***	***y***	***z***	**Occupancy**	**U_{iso}**
Zr1	0	0.75	0.125	1	0.00024(31)
Si1	0	0.75	0.625	1	-0.0179(6)
O1	0	0.066	0.1941	1	0.01

Phase	Symmetry Setting	Space Group
$Ti_{0.912}Nb_{0.088}O_2$	Tetragonal	$P4_2/mnm$

Phase Information	*a*	*b*	*c*	*V*	
	4.66843(7)	4.66843(7)	3.01041(5)	65.6100(20)	
	α	***β***	***γ***		
	90	90	90		
Atom	***x***	***y***	***z***	**Occupancy**	**U_{iso}**
Ti1	0	0	0	0.83(9)	0.0155(9)
Nb1	0	0	0	0.170(9)	0.0155(9)
O1	0.2965	0.2965	0	1	0.01

Phase	Symmetry Setting	Space Group
$Ti_{0.69}Nb_{0.24}O_2$	Tetragonal	$P4_2/mnm$

Phase Information	*a*	*b*	*c*	*V*	
	4.627923(29)	4.627923	2.98350(4)	63.9000(10)	
	α	***β***	***γ***		
	90	90	90		
Atom	***x***	***y***	***z***	**Occupancy**	**Uiso**
Ti1	0	0	0	0.911(4)	-0.0008(4)
Nb1	0	0	0	0.019(4)	-0.0008(4)
O	0.307	0.307	0	1	0.1

Phase	Symmetry Setting	Space Group
SiO_2 (1)	Trigonal	$P3_221$

Phase Information	*a*	*b*	*c*	*V*	
	4.91910(21)	4.9191	5.4105(4)	113.380(8)	
	α	*β*	*γ*		
	90	90	120		
Atom	***x***	***y***	***z***	**Occupancy**	**U_{iso}**
Si1	0.4754(28)	0	0.6667	1	0.014(4)
O1	0.408	0.265	0.786	1	0.01

Phase	Symmetry Setting	Space Group
SiO_2 (2)	Trigonal	$P3_221$

Phase Information	*a*	*b*	*c*	*V*	
	4.94234(31)	4.94234(31)	5.4241(7)	114.742(12)	
	α	*β*	*γ*		
	90	90	120		
Atom	***x***	***y***	***z***	**Occupancy**	**U_{iso}**
Si1	0.4764(27)	0	0.6667	1	0.043(4)
O1	0.4136	0.2676	0.7857	1	0.01

Phase	Symmetry Setting	Space Group
(Sr,Na)NbO_3	Cubic	*Pm*-3*m*

Phase Information	*a*	*b*	*c*	*V*	
	3.92997(4)	3.92997	3.92997	60.6970(20)	
	α	*β*	*γ*		
	90	90	90		
Atom	***x***	***y***	***z***	**Occupancy**	**U_{iso}**
Sr1	0.5	0.5	0.5	0.189(9)	0.0143(21)
Na1	0.5	0.5	0.5	0.622(9)	0.0143(21)
Nb1	0	0	0	0.0191(7)	0.0191(7)
O1	0.5	0	0	1	0.01

Phase	Symmetry Setting	Space Group
$(Sr_2,Na)Nb_5O_{15}$	Tetragonal	*P4bm*

Phase Information	***a***	***b***	***c***	***V***	
	12.3429(6)	12.3429	3.9340(4)	599.33(7)	
	α	***β***	***γ***		
	90	90	90		
Atom	***x***	***y***	***z***	**Occupancy**	**U_{iso}**
Sr1	0	0	-0.007(21)	1	0.101(9)
Na1	0.1868(16)	0.6868(16)	-0.231(20)	0.5	0.031(13)
Sr2	0.1868(16)	0.6868(16)	-0.231(20)	0.5	0.031(13)
Nb1	0	0.5	0.532(16)	1	-0.045(8)
Nb2	0.0854(8)	0.2008(9)	0.418(14)	1	0.043(4)
O1	0.1327	0.06722	0.37197	1	0.01
O2	0.34232	0.00469	0.38305	1	0.01
O3	0.08883	0.19947	-0.07274	1	0.01
O4	0.28409	0.78409	0.4352	1	0.01
O5	0	0.5	0.027	1	0.01

Weight fractions	
Phases	Wt%
$ZrSiO_4$	**26.480(8)**
$Ti_{0.912}Nb_{0.088}O_2$	**15.58(2)**
$Ti_{0.69}Nb0.24O_2$	**35.58(2)**
SiO_2 (1)	**2.865(10)**
SiO_2 (2)	**5.33(1)**
$(Sr,Na)NbO_3$	**9.839(7)**
$(Sr_2,Na)Nb_5O_{15}$	**4.327(9)**

Rietveld Refinement Cs/Sr-IONSIV HIPing (D8)

Table 7.56 *Refinement details for HIPed Cs/Sr-IONSIV (D8)*

χ^2	wRp	Rp
2.857	4.8 %	3.35 %

Phase	Symmetry Setting	Space Group
$Ti_{0.912}Nb_{0.088}O_2$	Tetragonal	$P4_2/mnm$

Phase Information	*a*	*b*	*c*	*V*
	4.62059(11)	4.62059(11)	2.98206(12)	63.6670(30)
	α	*β*	*γ*	
	90	90	90	

Atom	*x*	*y*	*z*	Occupancy	U_{iso}
Ti1	0	0	0	0.912	0.01
Nb1	0	0	0	0.088	0.01
O	0.2965	0.2965	0	1	0.01

Phase	Symmetry Setting	Space Group
$Cs_2TiNb_6O_{18}$	trigonal	*P*-3*m*1

Phase Information	*a*	*b*	*c*	*V*
	7.52927(33)	7.52927(33)	8.2399(6)	404.539(32)
	α	*β*	*γ*	
	90	90	120	

Atom	*x*	*y*	*z*	Occupancy	U_{iso}
Cs	0.3333	0.6667	0.632	1	0.01
Nb1	0	0	0.5	0.857	0.01
Ti1	0	0	0.5	0.143	0.01
Nb2	0.17	-0.17	0.1457	0.857	0.01
Ti2	0.17	-0.17	0.1457	0.143	0.01
O	0.447	-0.447	0.16	1	0.01
O	0.861	-0.861	0.11	1	0.01
O	0.12	-0.12	0.37	1	0.01

Phase	Symmetry Setting	Space Group
$SrNb_2O_6$	Monoclinic	$P2_1/c$

Phase Information	*a*	*b*	*c*	*V*	
	7.6788(14)	5.6027(11)	10.9783(19)	472.30(12)	
	α	*β*	*γ*		
	90	90.228(23)	90		
Atom	***x***	***y***	***z***	**Occupancy**	**U_{iso}**
Sr	0.2523	0.536	0.0393	1	0.01
Nb	0.0143	0.0294	0.1448	1	0.01
Nb	0.5232	0.4698	0.6428	1	0.01
O1	0.044	0.228	0.975	1	0.01
O2	0.456	0.262	0.467	1	0.01
O3	0.07	0.376	0.206	1	0.01
O4	0.454	0.129	0.701	1	0.01
O5	0.258	0.963	0.149	1	0.01
O6	0.758	0.149	0.116	1	0.01

Phase	Symmetry Setting	Space Group
SiO_2	Tetragonal	$P4_12_12$

Phase Information	*a*	*b*	*c*	*V*	
	5.080(5)	5.080(5)	6.812(13)	175.78(15)	
	α	*β*	*γ*		
	90	90	90		
Atom	***x***	***y***	***z***	**Occupancy**	**U_{iso}**
Si	0.3047	0.3047	0	1	0.01
O	0.2381	0.1109	0.1826	1	0.01

Phase	Symmetry Setting	Space Group
$Zr_5Ti_7O_{24}$	Orthorhombic	*Pbcn*

Phase Information	*a*	*b*	*c*	*V*	
	14.3399(8)	5.39018(31)	5.03037(31)	388.822(20)	
	α	*β*	*γ*		
	90	90	90		
Atom	***x***	***y***	***z***	**Occupancy**	**U_{iso}**
Zr1	0	0.2629	0.25	0.968	0.01
Ti1	0	0.2629	0.25	0.032	0.01
Zr2	0.3324	0.3335	0.1798	0.111	0.01
Ti2	0.3324	0.3335	0.1798	0.889	0.01
O1	0.0873	0.0668	-0.0234	1	0.01
O2	0.4194	0.0825	0.0599	1	0.01

O3	0.76	0.1226	0.1402	1	0.01

Phase	**Symmetry Setting**	**Space Group**
$Ti_{0.912}Nb_{0.088}O_2$	Tetragonal	$P4_2/mnm$

Phase Information	***a***	***b***	***c***	***V***	
	4.6668(6)	4.6668(6)	2.9873(9)	65.060(22)	
	α	***β***	***γ***		
	90	90	90		
Atom	***x***	***y***	***z***	**Occupancy**	**U_{iso}**
Ti1	0	0	0	0.712	0.01
Nb1	0	0	0	0.288	0.01
O	0.307	0.307	0	1	0.01

Weight Fraction	
Phases	Wt. %
$Ti_{0.912}Nb_{0.088}O_2$	**29.138(2)**
$Cs_2TiNb_6O_{18}$	**15.749(2)**
$SrNb_2O_6$	**5.809(2)**
SiO_2	**7.366(4)**
$Zr_5Ti_7O_{24}$	**37.17(2)**
$Ti_{0.69}Nb_{0.24}O_2$	**4.769(3)**

Rietveld Refinement Cs-IONSIV (4 wt. %) Calcination 1000ºC

Table 7.57 *Rietveld Refinement details for Cs-IONSIV (4 wt. %) Calcination 1000ºC*

χ^2	wRp	Rp
3.33	5.15%	3.38%

Phase	**Symmetry Setting**	**Space Group**
$Cs_2TiNb_6O_{18}$	Trigonal	*P*-3*m*1

Phase Information	***a***	***b***	***c***	***V***	
	7.5153(4)	7.5153(4)	8.2201(6)	402.07(5)	
	α	***β***	***γ***		
	90	90	120		
Atom	***x***	***y***	***z***	**Occupancy**	**U_{iso}**
Cs	0.3333	0.6667	0.632	1	0.01
Nb1	0	0	0.5	0.857	0.01
Ti1	0	0	0.5	0.143	0.01
Nb2	0.17	-0.17	0.1457	0.857	0.01
Ti2	0.17	-0.17	0.1457	0.143	0.01
O1	0.447	-0.447	0.16	1	0.01
O2	0.861	0.861	0.11	1	0.01
O3	0.12	-0.12	0.37	1	0.01

Phase	**Symmetry Setting**	**Space Group**
$(Ti,Nb)O_2$	Tetragonal	$P4_2/mnm$

Phase Information	***a***	***b***	***c***	***V***	
	4.59925(25)	4.59925(25)	2.96636(20)	62.748(8)	
	α	***β***	***γ***		
	90	90	90		
Atom	***x***	***y***	***z***	**Occupancy**	**U_{iso}**
Ti1	0	0	0	0.912	0.01
Nb1	0	0	0	0.088	0.01
O	0.2965	0.2965	0	1	0.01

Phase	**Symmetry Setting**	**Space Group**
$ZrTiO_4$	Orthorhombic	*Pbcn*

Phase Information	***a***	***b***	***c***	***V***
	4.7534(8)	5.4250(8)	5.0312(7)	129.742(24)
	α	*β*	*γ*	

	90	90	90		

Atom	*x*	*y*	*z*	Occupancy	U_{iso}
Zr1	0.1915	0.25	0.333	0.826(9)	0.01
Ti1	0.1915	0.25	0.666	0.174(9)	0.01
O1	0.27	0.389	0.43	1	0.01

Phase	Symmetry Setting	Space Group
SiO_2	Tetragonal	$P4_12_12$

Phase Information	*a*	*b*	*c*	*V*	
	5.0116(28)	5.0116	6.996(7)	175.70(9)	
	α	*β*	*γ*		
	90	90	90		
Atom	***x***	***y***	***z***	**Occupancy**	**U_{iso}**
Si1	0.3047	0.3047	0	1	0.01
O1	0.2381	0.1109	0.1826	1	0.01

Phase	Symmetry Setting	Space Group
$Zr_5Ti_7O_{24}$	Orthorhombic	*Pbcn*

Phase Information	*a*	*b*	*c*	*V*	
	14.2618(21)	5.4108(7)	5.0312(7)	388.24(7)	
	α	*β*	*γ*		
	90	90	90		
Atom	***x***	***y***	***z***	**Occupancy**	**U_{iso}**
Zr1	0	0.2629	0.25	0.968	0.01
Ti1	0	0.2629	0.25	0.032	0.01
Zr2	0.3324	0.3335	0.1798	0.111	0.01
Ti2	0.3324	0.3335	0.1798	0.889	0.01
O1	0.0873	0.0668	-0.0234	1	0.01
O2	0.4194	0.0824	0.0599	1	0.01
O3	0.76	0.1226	0.1402	1	0.01

Phase	Symmetry Setting	Space Group
$NaNbO_3$	Orthorhombic	*Pbma*

Phase Information	*a*	*b*	*c*	*V*
	5.84(10)	15.65(9)	5.27(6)	481(5)
	α	*β*	*γ*	
	90	90	90	

Atom	***x***	***y***	***z***	**Occupancy**	**U_{iso}**
Nb1	0.2705	0.1231	0.247	1	0.01
Na1	0.75	0	0.247	1	0.01
Na2	0.781	0.25	0.254	1	0.01
O1	0.25	0	0.304	1	0.01
O2	0.232	0.25	0.18	1	0.01
O3	0.025	0.141	0.533	1	0.01
O4	0.456	0.109	-0.036	1	0.01

Weight Fraction	
Phases	wt %
$Cs_2TiNb_6O_{18}$	**15.514(2)**
$TiNbO_2$	**18.907(2)**
$ZrTiO_4$	**19.887(7)**
SiO_2	**14.677(4)**
$Zr_5Ti_7O_{24}$	**30.66(6)**
NaNbO3	**0.362(3)**

Rietveld Refinement Cs-IONSIV (4 wt. %) Calcination 1100ºC

Table 7.58 *Rietveld Refinement details for Cs-IONSIV (4 wt. %) Calcination 1100ºC*

χ^2	wRp	Rp
2.373	4.53%	3.27%

Phase	**Symmetry Setting**	**Space Group**
$Cs_2TiNb_6O_{18}$	Trigonal	*P*-3*m*1

Phase Information	***a***	***b***	***c***	***V***	
	7.52785(21)	7.52785(21)	8.20863(34)	402.850(26)	
	α	***β***	***γ***		
	90	90	120		
Atom	***x***	***y***	***z***	**Occupancy**	**U_{iso}**
Cs	0.3333	0.6667	0.6308(13)	1	0.0387(30)
Nb1	0	0	0.5	0.755(16)	0.000(7)
Ti1	0	0	0.5	0.041(16)	0.000(7)
Nb2	0.1685(4)	-0.1685(4)	0.1463(8)	0.8740(27)	0.0081(17)
Ti2	0.1685(4)	-0.1685(4)	0.1463(8)	0.1600(27)	0.0081(17)
O1	0.447	-0.447	0.16	1	0.01
O2	0.861	0.861	0.11	1	0.01
O3	0.12	-0.12	0.37	1	0.01

Phase	**Symmetry Setting**	**Space Group**
$Zr_5Ti_7O_{24}$	Orthorhombic	*Pbcn*

Phase Information	***a***	***b***	***c***	***V***	
	14.2940(5)	5.40375(17)	5.03624(16)	389.005(23)	
	α	***β***	***γ***		
	90	90	90		
Atom	*x*	*y*	*z*	Occupancy	Uiso
Zr1	0	0.2705(9)	0.25	0.826(9)	0.0119(14)
Ti1	0	0.2705(9)	0.25	0.174(9)	0.0119(14)
Zr2	0.33228(32)	0.3151(6)	0.1928(6)	0.253(9)	0.0087(17)
Ti2	0.33228(32)	0.3151(6)	0.1928(6)	0.747(9)	0.0087(17)
O1	0.0873	0.0668	-0.0234	1	0.01
O2	0.4194	0.0825	0.0599	1	0.01
O3	0.76	0.1226	0.1402	1	0.01

Phase	Symmetry Setting	Space Group
$Ti_{0.8}Nb_{0.2}O_2$	Tetragonal	$P4_2/mnm$

Phase Information	*a*	*b*	*c*	*V*	
	4.60635(12)	4.60635(12)	2.97211(10)	63.064(4)	
	α	*β*	*γ*		
	90	90	120		
Atom	**x**	**y**	**z**	**Occupancy**	**U_{iso}**
Ti1	0	0	0	0.8	0.0168(15)
Nb1	0	0	0	0.2	0.0168(15)
O	0.33228(32)	0.3151(6)	0.1928(6)	1	0.1

Phase	Symmetry Setting	Space Group
SiO_2	Orthorhombic	$P2_12_12_1$

Phase Information	*a*	*b*	*c*	*V*	
	7.150(24)	7.046(23)	6.908(16)	348.01(22)	
	α	*β*	*γ*		
	90	90	120		
Atom	***x***	***y***	***z***	**Occupancy**	**U_{iso}**
Si1	0.25	0.33	0.25	1	0.01
Si1	0.08	0	0	1	0.01
O1	0.67	0.65	0.14	1	0.01
O2	0.06	0.64	0.58	1	0.01
O3	0.625	0.06	0.625	1	0.01
O4	0.125	0.21	0.125	1	0.01

Weight Fraction	
Phases	*wt%*
$Cs_2TiNb_6O_{18}$	**19.48(2)**
$Zr_5Ti_7O_{24}$	**47.12(2)**
$Ti_{0.8}Nb_{0.2}O_2$	**21.84(3)**
SiO_2	**11.56(4)**

Rietveld Refinement Cs-IONSIV (6 wt. %) Calcination 1000ºC

Table 7.59 *Rietveld Refinement details for Cs-IONSIV (6 wt. %) Calcination 1000ºC*

χ^2	wRp	Rp
4.068	6.00 %	3.98 %

Phase	Symmetry Setting	Space Group
$Cs_2TiNb_6O_{18}$	Trigonal	*P*-3*m*1

Phase Information	*a*	*b*	*c*	*V*	
	7.52019(26)	7.52019(26)	8.2371(8)	403.43(4)	
	α	*β*	*γ*		
	90	**90**	**120**		
Atom	***x***	***y***	***z***	**Occupancy**	**U_{iso}**
Cs	0.3333	0.6667	0.632	1	0.01
Nb1	0	0	0.5	0.857	0.01
Ti1	0	0	0.5	0.143	0.01
Nb2	0.17	-0.17	0.1457	0.857	0.01
Ti2	0.17	-0.17	0.1457	0.143	0.01
O1	0.447	-0.447	0.16	1	0.01
O2	0.861	0.861	0.11	1	0.01
O3	0.12	-0.12	0.37	1	0.01

Phase	Symmetry Setting	Space Group
$Ti_{0.912}Nb_{0.088}O_2$	Tetragonal	$P4_2/mnm$

Phase Information	*a*	*b*	*c*	*V*	
	4.60214(19)	4.60214(19)	2.96779(19)	62.857(5)	
	α	***β***	***γ***		
	90	90	90		
Atom	***x***	***y***	***z***	**Occupancy**	**U_{iso}**
Ti1	0	0	0	0.912	0.01
Nb1	0	0	0	0.088	0.01
O	0.2965	0.2965	0	1	0.01

Phase	Symmetry Setting	Space Group
$ZrTiO_4$	Orthorhombic	*Pbcn*

Phase Information	*a*	*b*	*c*	*V*
	4.7556(6)	5.3917(7)	5.0273(6)	128.902(15)
	α	***β***	***γ***	
	90	90	90	

Atom	*x*	*y*	*z*	Occupancy	U_{iso}
Zr1	0.1915	0.25	0.333	0.826(9)	0.01
Ti1	0.1915	0.25	0.666	0.174(9)	0.01
O1	0.27	0.389	0.43	1	0.01

Phase	Symmetry Setting	Space Group
SiO_2	Tetragonal	$P4_12_12$

Phase Information	*a*	*b*	*c*	*V*	
	5.015(4)	5.015(4)	7.025(11)	176.70(12)	
	α	*β*	*γ*		
	90	90	90		
Atom	***x***	***y***	***z***	**Occupancy**	**U_{iso}**
Si1	0.3047	0.3047	0	1	0.01
O1	0.2381	0.1109	0.1826	1	0.01

Phase	Symmetry Setting	Space Group
$Zr_5Ti_7O_{24}$	Orthorhombic	*Pbcn*

Phase Information	*a*	*b*	*c*	*V*	
	14.2464(13)	5.4103(5)	5.0233(5)	387.18(4)	
	α	*β*	*γ*		
	90	90	90		
Atom	***x***	***y***	***z***	**Occupancy**	**U_{iso}**
Zr1	0	0.2629	0.25	0.968	0.01
Ti1	0	0.2629	0.25	0.032	0.01
Zr2	0.3324	0.3335	0.1798	0.111	0.01
Ti2	0.3324	0.3335	0.1798	0.889	0.01
O1	0.0873	0.0668	-0.0234	1	0.01
O2	0.4194	0.0824	0.0599	1	0.01
O3	0.76	0.1226	0.1402	1	0.01

Weight Fractions	
Phases	Wt. %
$Cs_2TiNb_6O_{18}$	**21.40(2)**
$TiNbO_2$	**32.91(4)**
$ZrTiO_4$	**20.81(3)**
SiO_2	**10.29(4)**
$Zr_5Ti_7O_{24}$	**14.59(4)**

Rietveld Refinement Cs-IONSIV (6 wt. %) Calcination 1100ºC

Table 7.60 *Rietveld Refinement details for Cs-IONSIV (6 wt. %) Calcination 1100ºC*

χ^2	wRp	Rp
2.165	4.14%	2.98%

Phase	Symmetry Setting	Space Group
$Cs_2TiNb_6O_{18}$	Trigonal	*P*-3*m*1

Phase Information	*a*	*b*	*c*	*V*	
	7.53435(16)	7.53435(16)	8.22063(27)	404.135(18)	
	α	*β*	*γ*		
	90	90	120		
Atom	***x***	***y***	***z***	**Occupancy**	**Uiso**
Cs	0.3333	0.6667	0.6346(12)	1	0.0396(25)
Nb1	0	0	0.5	0.801(14)	0.008(5)
Ti1	0	0	0.5	0.087(14)	0.008(5)
Nb2	0.1686(4)	-0.1686(4)	0.1443(7)	0.8664(24)	0.0081(17)
Ti2	0.1686(4)	-0.1686(4)	0.1443(7)	0.1524(24)	0.0081(17)
O1	0.447	-0.447	0.16	1	0.01
O2	0.861	0.861	0.11	1	0.01
O3	0.12	-0.12	0.37	1	0.01

Phase	Symmetry Setting	Space Group
$Zr_5Ti_7O_{24}$	Orthorhombic	*Pbcn*

Phase Information	*a*	*b*	*c*	*V*	
	14.2934(4)	5.38951(15)	5.02975(14)	387.464(15)	
	α	*β*	*γ*		
	90	90	90		
Atom	***x***	***y***	***z***	**Occupancy**	**Ui_{so}**
Zr1	0	0.2666(9)	0.25	0.845(10)	0.0122(15)
Ti1	0	0.2666(9)	0.25	0.155(10)	0.0122(15)
Zr2	0.3331(4)	0.3183(6)	0.1919(7)	0.234(10)	0.0172(21)
Ti2	0.3331(4)	0.3183(6)	0.1919(7)	0.766(10)	0.0172(21)
O1	0.0873	0.0668	-0.0234	1	0.01
O2	0.4194	0.0825	0.0599	1	0.01
O3	0.76	0.1226	0.1402	1	0.01

Phase	Symmetry Setting	Space Group
$Ti_{0.912}Nb_{0.088}O_2$	Tetragonal	$P4_2/mnm$

Phase Information	*a*	*b*	*c*	*V*	
	4.6060(4)	4.6060(4)	2.9720(4)	63.383(10)	
	α	*β*	*γ*		
	90	90	120		
Atom	***x***	***y***	***z***	**Occupancy**	**U_{iso}**
Ti1	0	0	0	0.912	0.0144(15)
Nb1	0	0	0	0.088	0.0144(15)
O	0.2965	0.2965	0	1	0.01

Phase	Symmetry Setting	Space Group
SiO_2	orthorhombic	$P2_12_12_1$

Phase Information	*a*	*b*	*c*	*V*	
	7.113(33)	7.311(33)	6.736(33)	350.3(4)	
	α	*β*	*γ*		
	90	90	90		
Atom	***x***	***y***	***z***	**Occupancy**	**U_{iso}**
Si1	0.25	0.33	0.25	1	0.01
Si1	0.08	0	0	1	0.01
O1	0.67	0.65	0.14	1	0.01
O2	0.06	0.64	0.58	1	0.01
O3	0.625	0.06	0.625	1	0.01
O4	0.125	0.21	0.125	1	0.01

Weight Fractions	
Phases	*Wt. %*
$Cs_2TiNb_6O_{18}$	**24.13(2)**
$Zr_5Ti_7O_{24}$	**43.91(2)**
$Ti_{0.912}Nb_{0.088}O_2$	**22.39(3)**
SiO_2	**9.57(4)**

Rietveld Refinement Cs-IONSIV (12 wt. %) Calcination 1000ºC

Table 7.61 *Refinement Details for* Cs-IONSIV (12wt%) Calcination 1000°C

χ^2	wRp	Rp
4.698	6.49%	4.21%

Phase	Symmetry Setting	Space Group
$Cs_2TiNb_6O_{18}$	Trigonal	*P*-3*m*1

Phase Information	*a*	*b*	*c*	*V*	
	7.5102(9)	7.5102(14)	8.2483(14)	402.90(11)	
	α	*β*	*γ*		
	90	90	120		
Atom	***x***	***y***	***z***	**Occupancy**	**U_{iso}**
Cs	0.3333	0.6667	0.632	1	0.0304
Nb1	0	0	0.5	0.849(16)	0.152
Ti1	0	0	0.5	0.135(16)	0.152
Nb2	0.17	-0.17	0.1457	0.8583(26)	0.0038
Ti2	0.17	-0.17	0.1457	0.1443(26)	0.0038
O1	0.447	-0.447	0.16	1	0.01
O2	0.861	0.861	0.11	1	0.01
O3	0.12	-0.12	0.37	1	0.01

Phase	Symmetry Setting	Space Group
$Cs_2ZrSi_6O_{15}$	Monoclinic	*C*2/*m*

Phase Information	*a*	*b*	*c*	*V*	
	26.748(6)	7.4528(16)	11.6982(30)	2223.6(8)	
	α	*β*	*γ*		
	90	107.540(23)	90		
Atom	***x***	***y***	***z***	**Occupancy**	**U_{iso}**
Cs1	0.57556	0	0.01298	1	0.01
Cs2	0.897	0	0.37209	1	0.01
Cs3	0.75285	0	0.36099	1	0.01
Zr1	0	0	0	1	0.01
Zr2	0.32034	0	0.35804	1	0.01
Si1	0.62801	0.1981	0.3709	1	0.01
Si2	0.3062	0.1978	0.092	1	0.01
Si3	0.458	0	0.3674	1	0.01
Si4	0.13668	0	-0.0027	1	0.01
Si5	0.18322	0	0.2678	1	0.01
Si6	0.51238	0.3033	0.2679	1	0.01
O1	0.6649	0.1972	0.5069	1	0.01

O2	0.3996	0	0.3704	1	0.01
O3	0.25	0.25	0	1	0.01
O4	0	0.5	0.5	1	0.01
O5	0.8055	0.297	0.2297	1	0.01
O6	0.6514	0.324	0.2859	1	0.01
O7	0.5692	0.2596	0.3642	1	0.01
O8	0.6256	0	0.3096	1	0.01
O9	0.1813	0.00E+00	0.1279	1	0.01
O10	0.3526	3.26E-01	0.074	1	0.01
O11	0.5135	3.00E-01	0.1313	1	0.01
O12	0.3215	0.00E+00	0.055	1	0.01
O13	0.2414	0.00E+00	0.3555	1	0.01

Phase	**Symmetry Setting**	**Space Group**
$Zr_5Ti_7O_{24}$	Orthorhombic	*Pbcn*

Phase Information	***a***	***b***	***c***	***V***	
	14.2344(19)	5.3711(7)	5.0131(8)	383.27(9)	
	α	***β***	***γ***		
	90	90	90		
Atom	***x***	***y***	***z***	**Occupancy**	**U_{iso}**
Zr1	0	0.2629	0.25	0.968	0.00811
Ti1	0	0.2629	0.25	0.032	0.00811
Zr2	0.3324	0.3335	0.1798	0.111	0.0152
Ti2	0.3324	0.3335	0.1798	0.889	0.0152
O1	0.0873	0.0668	-0.0234	1	0.01
O2	0.4194	0.0825	0.0599	1	0.01
O3	0.76	0.1226	0.1402	1	0.01

Phase	**Symmetry Setting**	**Space Group**
$(Ti,Nb)O_2$	Tetragonal	*$P4_2/mnm$*

Phase Information	***a***	***b***	***c***	***V***	
	4.6002(4)	4.6002	2.9672(4)	62.792(14)	
	α	***β***	***γ***		
	90	90	120		
Atom	***x***	***y***	***z***	**Occupancy**	**U_{iso}**
Ti1	0	0	0	0.912	0.1
Nb1	0	0	0	0.088	0.1
O	0.2965	0.2965	0	1	0.1

Weight Fractions	
Phases	wt%
$Cs_2TiNb_6O_{18}$	**21.21(3)**
$Cs_2ZrSi_6O_{15}$	**18.63(4)**
Zr_5Ti7O_{24}	**36.44(3)**
$TiNbO_2$	**23.72(4)**

Rietveld Refinement Cs-IONSIV (12 wt. %) Calcination 1100ºC

Table 7.62 *Refinement Details for* Cs-IONSIV (12wt%) Calcination 1100°C

χ^2	wRp	Rp
3.385	5.51 %	3.87 %

Phase	Symmetry Setting	Space Group
$Cs_2TiNb_6O_{18}$	Trigonal	*P*-3*m*1

Phase Information	*a*	*b*	*c*	*V*	
	7.52411(29)	7.52411(29)	8.2328(4)	403.63(4)	
	α	*β*	*γ*		
	90	90	120		
Atom	***x***	***y***	***z***	**Occupancy**	**U_{iso}**
Cs	0.3333	0.6667	0.6340(13)	1	0.0509(30)
Nb1	0	0	0.5	0.849(16)	0.041(7)
Ti1	0	0	0.5	0.135(16)	0.041(7)
Nb2	0.1665(4)	-0.1665(4)	0.1448(8)	0.8583(26)	0.0187(17)
Ti2	0.1665(4)	-0.1665(4)	0.1448(8)	0.1443(26)	0.0187(17)
O1	0.447	-0.447	0.16	1	0.01
O2	0.861	0.861	0.11	1	0.01
O3	0.12	-0.12	0.37	1	0.01

Phase	Symmetry Setting	Space Group
$Zr_5Ti_7O_{24}$	Orthorhombic	*Pbcn*

Phase Information	*a*	*b*	*c*	*V*	
	14.2646(8)	5.37076(33)	5.01705(32)	384.36(4)	
	α	*β*	*γ*		
	90	90	90		
Atom	***x***	***y***	***z***	**Occupancy**	**Uiso**
Zr1	0	0.2683(14)	0.25	0.893(14)	0.0190(23)
Ti1	0	0.2683(14)	0.25	0.107(14)	0.0190(23)
Zr2	0.3343(5)	0.3177(11)	0.1885(12)	0.186(14)	0.0210(32)
Ti2	0.3343(5)	0.3177(11)	0.1885(12)	0.814(14)	0.0210(32)
O1	0.0873	0.0668	-0.0234	1	0.01
O2	0.4194	0.0825	0.0599	1	0.01
O3	0.76	0.1226	0.1402	1	0.01

Phase	Symmetry Setting	Space Group
(Ti,Nb)O_2	Tetragonal	*P*4$_2$/*mnm*

Phase Information	***a***	***b***	***c***	***V***	
	4.60413(19)	4.60413	2.97029(15)	62.964(6)	
	α	***β***	***γ***		
	90	90	120		
Atom	***x***	***y***	***z***	**Occupancy**	**U_{iso}**
Ti1	0	0	0	0.912	0.0147(17)
Nb1	0	0	0	0.088	0.0147(17)
O	0.2965	0.2965	0	1	0.1

Phase	Symmetry Setting	Space Group
$Cs_2ZrSi_6O_{15}$	Monoclinic	*C*2/*m*

Phase Information	***a***	***b***	***c***	***V***	
	26.750(4)	7.4544(11)	11.6848(20)	2222.4(5)	
	α	***β***	***γ***		
	90	107.484(16)	90		
Atom	***x***	***y***	***z***	**Occupancy**	**U_{iso}**
Cs1	0.57556	0	0.01298	1	0.01
Cs2	0.897	0	0.37209	1	0.01
Cs3	0.75285	0	0.36099	1	0.01
Zr1	0	0	0	1	0.01
Zr2	0.32034	0	0.35804	1	0.01
Si1	0.62801	0.1981	0.3709	1	0.01
Si2	0.3062	0.1978	0.092	1	0.01
Si3	0.458	0	0.3674	1	0.01
Si4	0.13668	0	-0.0027	1	0.01
Si5	0.18322	0	0.2678	1	0.01
Si6	0.51238	0.3033	0.2679	1	0.01
O1	0.6649	0.1972	0.5069	1	0.01
O2	0.3996	0	0.3704	1	0.01
O3	0.25	0.25	0	1	0.01
O4	0	0.5	0.5	1	0.01
O5	0.8055	0.297	0.2297	1	0.01
O6	0.6514	0.324	0.2859	1	0.01
O7	0.5692	0.2596	0.3642	1	0.01
O8	0.6256	0	0.3096	1	0.01
O9	0.1813	0	0.1279	1	0.01
O10	0.3526	0.3257	0.074	1	0.01
O11	0.5135	0.2995	0.1313	1	0.01
O12	0.3215	0	0.055	1	0.01

O13	0.2414	0	0.3555	1	0.01
O14	0.9966	0	0.3048	1	0.01
O15	0.4687	0.171	0.2937	1	0.01
O16	0.0784	0	0.0052	1	0.01

Weight Fraction	
Phases	Wt. %
$Cs_2TiNb_6O_{18}$	**29.77(2)**
$Zr_5Ti_7O_{24}$	**33.99(3)**
$TiNbO_2$	**22.152(2)**
$Cs_2ZrSi_6O_{15}$	**14.10(26)**

Rietveld Refinement Cs-IONSIV (8 wt. %) Calcination 1100ºC

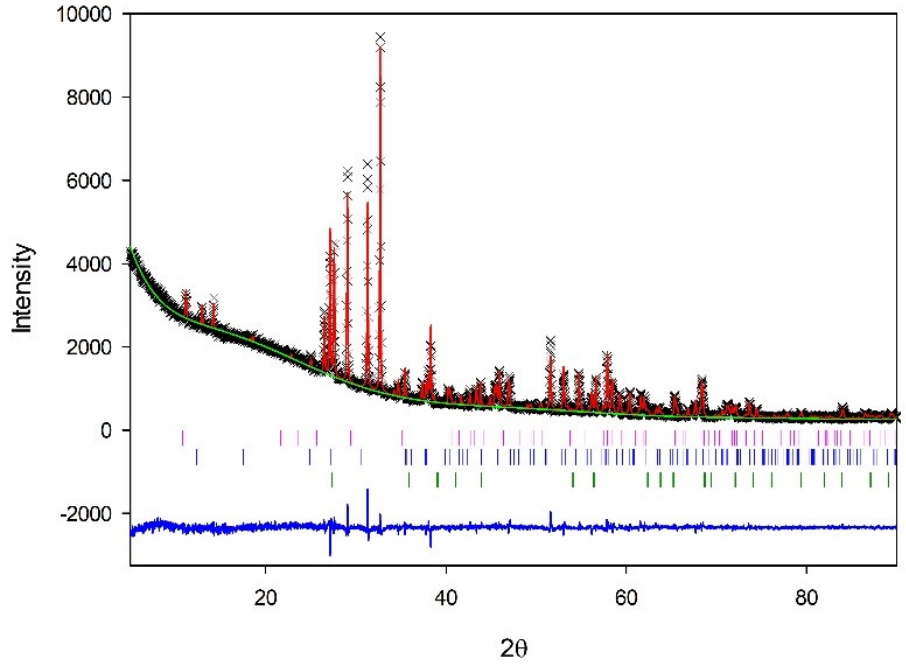

Figure 7.50 *Rietveld Refinement (GSAS Liveplot) Cs-IONSIV (8 wt. %) Calcination 1100ºC*

Table 7.63 Rietveld Refinement Cs-IONSIV (8 wt. %) Calcination 1100ºC

χ^2	wRp	Rp
2.329	4.56%	3.24%

Phase	Symmetry Setting	Space Group
$Cs_2TiNb_6O_{18}$	trigonal	*P*-3*m*1

Phase Information	*a*	*b*	*c*	*V*	
	7.52708(20)	7.52708(20)	8.22593(30)	403.617(25)	
	α	*β*	*γ*		
	90	90	120		
Atom	***x***	***y***	***z***	**Occupancy**	U_{iso}
Cs	0.3333	0.6667	0.6352(12)	1	0.0358(25)
Nb1	0	0	0.5	0.823(14)	0.008(5)
Ti1	0	0	0.5	0.109(14)	0.008(5)
Nb2	0.1680(4)	-0.1680(4)	0.1461(7)	0.8626(24)	0.0053(15)
Ti2	0.1680(4)	-0.1680(4)	0.1461(7)	0.1486(24)	0.0053(15)
O1	0.447	-0.447	0.16	1	0.01
O2	0.861	0.861	0.11	1	0.01
O3	0.12	-0.12	0.37	1	0.01

Phase	Symmetry Setting	Space Group
$Zr_5Ti_7O_{24}$	Orthorhombic	*Pbcn*

Phase Information	*a*	*b*	*c*	*V*	
	14.2708(5)	5.37558(20)	5.01953(19)	385.068(25)	
	α	*β*	*γ*		
	90	90	90		
Atom	***x***	***y***	***z***	**Occupancy**	**U_{iso}**
Zr1	0	0.2699(11)	0.25	0.884(12)	0.0101(18)
Ti1	0	0.2699(11)	0.25	0.174(9)	0.0101(18)
Zr2	0.3326(4)	0.3172(8)	0.1906(9)	0.227(12)	0.0177(26)
Ti2	0.3326(4)	0.3172(8)	0.1906(9)	0.773(12)	0.0177(26)
O1	0.0873	0.0668	-0.0234	1	0.01
O2	0.4194	0.0825	0.0599	1	0.01
O3	0.76	0.1226	0.1402	1	0.01

Phase	Symmetry Setting	Space Group
$(Ti_{0.912}Nb_{0.088})O_2$	Tetragonal	$P4_2/mnm$

Phase Information	a	b	c	V	
	4.60255(13)	4.60255(13)	2.96926(11)	62.899(4)	
	α	*β*	*γ*		
	90	90	120		
Atom	**x**	**y**	**z**	**Occupancy**	**U_{iso}**
Ti1	0	0	0	0.912	0.0147(17)
Nb1	0	0	0	0.088	0.0147(17)
O	0.2965	0.2965	0	1	0.1

Weight Fractions	
Phases	Wt %
$Cs_2TiNb_6O_{18}$	**30.421(2)**
$Zr_5Ti_7O_{24}$	**44.207(3)**
$TiNbO_2$	**25.372(3)**

Rietveld Refinement Cs-IONSIV (10 wt. %) Calcination 1100ºC

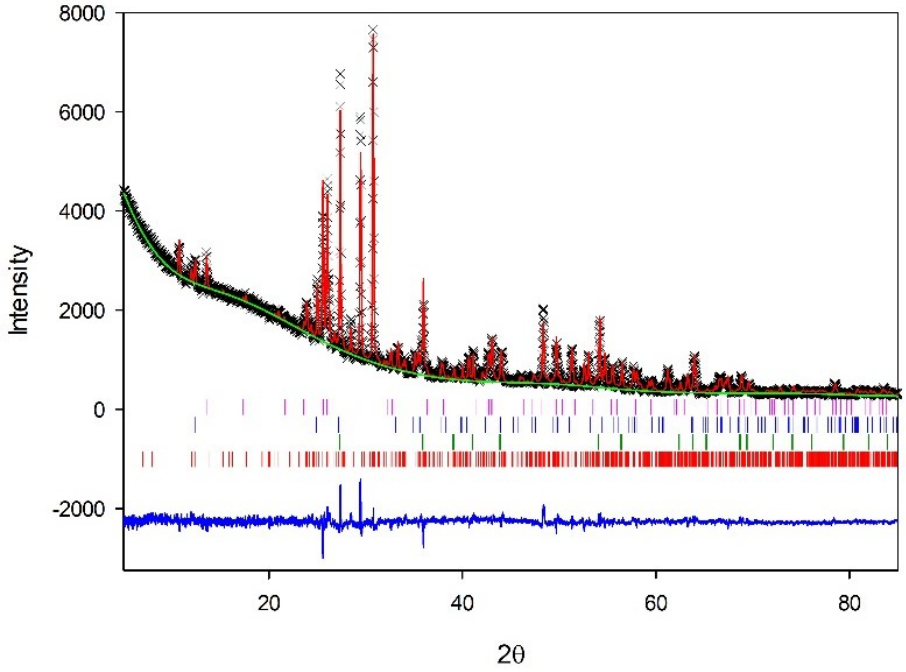

Figure 7.51 *Rietveld Refinement (GSAS Liveplot) Cs-IONSIV (10 wt. %) Calcination 1100ºC*

Table 7.64 Rietveld Refinement for Cs-IONSIV (10 wt. %) Calcination 1100ºC

χ^2	wRp	Rp
2.98	5.01%	3.49%

Phase	Symmetry Setting	Space Group
$Cs_2TiNb_6O_{18}$	Trigonal	*P*-3*m*1

Phase Information	*a*	*b*	*c*	*V*	
	7.51921(27)	7.51921(27)	8.2248(4)	402.716(34)	
	α	*β*	*γ*		
	90	90	120		
Atom	***x***	***y***	***z***	**Occupancy**	**U_{iso}**
Cs	0.3333	0.6667	0.6350(13)	1	0.0449(28)
Nb1	0	0	0.5	0.824(15)	0.018(6)
Ti1	0	0	0.5	0.110(15)	0.018(6)
Nb2	0.1664(4)	-0.1664(4)	0.1445(8)	0.8625(25)	0.0103(15)
Ti2	0.1664(4)	-0.1664(4)	0.1445(8)	0.1485(25)	0.0103(15)
O1	0.447	-0.447	0.16	1	0.01
O2	0.861	0.861	0.11	1	0.01
O3	0.12	-0.12	0.37	1	0.01

Phase	Symmetry Setting	Space Group
$Zr_5Ti_7O_{24}$	Orthorhombic	P b c n

Phase Information	*a*	*b*	*c*	*V*	
	14.2568(7)	5.36873(30)	5.01431(29)	383.800(35)	
	α	*β*	*γ*		
	90	90	90		
Atom	***x***	***y***	***z***	**Occupancy**	**U_{iso}**
Zr1	0	0.2683(14)	0.25	0.893(14)	0.0190(23)
Ti1	0	0.2683(14)	0.25	0.107(14)	0.0190(23)
Zr2	0.3343(5)	0.3177(11)	0.1885(12)	0.186(14)	0.0210(32)
Ti2	0.3343(5)	0.3177(11)	0.1885(12)	0.814(14)	0.0210(32)
O1	0.0873	0.0668	-0.0234	1	0.01
O2	0.4194	0.0825	0.0599	1	0.01
O3	0.76	0.1226	0.1402	1	0.01

Phase	Symmetry Setting	Space Group
$(Ti_{0.912}Nb_{0.088})O_2$	Tetragonal	$P4_2/mnm$

Phase Information	*a*	*b*	*c*	*V*	
	4.60011(17)	4.60011(17)	2.96728(14)	62.791(6)	
	α	*β*	*γ*		
	90	90	120		
Atom	***x***	***y***	***z***	**Occupancy**	**U_{iso}**
Ti1	0	0	0	0.912	0.0147(17)
Nb1	0	0	0	0.088	0.0147(17)
O	0.2965	0.2965	0	1	0.1

Phase	Symmetry Setting	Space Group
$Cs_2ZrSi_6O_{15}$	Monoclinic	*C*2/*m*

Phase Information	*a*	*b*	*c*	*V*	
	26.731(5)	7.4511(12)	11.6823(24)	2218.5(5)	
	α	*β*	*γ*		
	90	107.551(19)	90		
Atom	***x***	***y***	***z***	**Occupancy**	**U_{iso}**
Cs1	0.57556	0	0.01298	1	0.01
Cs2	0.897	0	0.37209	1	0.01
Cs3	0.75285	0	0.36099	1	0.01
Zr1	0	0	0	1	0.01
Zr2	0.32034	0	0.35804	1	0.01
Si1	0.62801	0.1981	0.3709	1	0.01
Si2	0.3062	0.1978	0.092	1	0.01

Si3	0.458	0	0.3674	1	0.01
Si4	0.13668	0	-0.0027	1	0.01
Si5	0.18322	0	0.2678	1	0.01
Si6	0.51238	0.3033	0.2679	1	0.01
O1	0.6649	0.1972	0.5069	1	0.01
O2	0.3996	0	0.3704	1	0.01
O3	0.25	0.25	0	1	0.01
O4	0	0.5	0.5	1	0.01
O5	0.8055	0.297	0.2297	1	0.01
O6	0.6514	0.324	0.2859	1	0.01
O7	0.5692	0.2596	0.3642	1	0.01
O8	0.6256	0	0.3096	1	0.01
O9	0.1813	0	0.1279	1	0.01
O10	0.3526	0.3257	0.074	1	0.01
O11	0.5135	0.2995	0.1313	1	0.01
O12	0.3215	0	0.055	1	0.01
O13	0.2414	0	0.3555	1	0.01
O14	0.9966	0	0.3048	1	0.01
O15	0.4687	0.171	0.2937	1	0.01
O16	0.0784	0	0.0052	1	0.01

Weight Fractions	
Phases	Wt. %
$Cs_2TiNb_6O_{18}$	**29.351(2)**
$Zr_5Ti_7O_{24}$	**36.436(3)**
$(Ti,Nb)O_2$	**23.67(2)**
$Cs_2ZrSi_6O_{15}$	**10.539(3)**

Appendix 5

Elemental Analysis (X-ray Florescence, (XRF)) Chapter 4

XRF Nb-CST

Table 7.65 *XRF details Nb-CST*

Formula	Z	Concentration	Status
TiO2	22	43.92	XRF 1
SiO2	14	21	XRF 1
Na2O	11	20.2	XRF 1
Nb2O5	41	18.9	XRF 3
SO3	16	0.061	XRF 1
Fe2O3	26	0.046	XRF 1
CuO	29	0.0352	XRF 1
K2O	19	0.03	XRF 1
ZnO	30	0.013	XRF 1
SrO	38	0.008	XRF 1

Line 1	Net int.	Used intensity	Calc. conc	Crystal	Collimator	Stat. error	LLD	Analyzed layer
Ti KA1-HR-Tr	176	422.1	43.92	LiF200	0.23	0.25%	256.5 PPM	272 um
Si KA1-HR-Tr	11.15	39.69	21	PET	0.23	0.98%	643.6 PPM	20.4 um
Na KA1-HR-Tr	6.212	15.66	20.2	XS-55	0.23	1.34%	0.19%	5.3 um
Nb KA1-HR-Tr	3445	6922	21.26	LiF200	0.23	0.06%	179.0 PPM	9.5 mm
S KA1-HR-Tr	0.1807	0.306	0.061	PET	0.23	10.80%	456.7 PPM	43 um
Fe KA1-HR-Tr	0.7654	1.8	0.046	LiF200	0.23	7.36%	102.4 PPM	0.57 mm
Cu KA1-HR-Tr	1.565	3.65	0.0352	LiF200	0.23	5.70%	62.2 PPM	1.09 mm
K KA1-HR-Tr	0.1081	0.2596	0.03	LiF200	0.23	20.00%	179.6 PPM	111 um
Zn KA1-HR-Tr	0.7485	1.745	0.013	LiF200	0.23	12.50%	54.2 PPM	1.34 mm
Sr KA1-HR-Tr	1.698	3.495	0.008	LiF200	0.23	12.00%	33.8 PPM	5.8 mm

Line 2	Net int.	Used intensity	Calc. conc	Crystal	Collimator	Stat. error	LLD	Analyzed layer
Ti KB1-HR-Tr	27.05	64.87	43.5	LiF200	0.23	0.64%	0.17%	0.35 mm
Si KB1-HR-Tr/Ox	0.204	0.7261	19	PET	0.23	9.39%	3.23%	23.6 um
Nb KB1-HR-Tr	731.6	1470	22.94	LiF200	0.23	0.13%	959.9 PPM	13.4 mm
Fe KB1-HR-Tr	0.07406	0.1741	0.024	LiF200	0.23	210%	679.9 PPM	0.75 mm
Cu KB1-HR-Tr	0.1683	0.3924	0.02	LiF200	0.23	139%	378.6 PPM	1.47 mm
K KB1-HR-Tr	-0.01969	-0.04727	-0.047	LiF200	0.23		0.16%	140 um
Zn KB1-HR-Tr	0.2128	0.4962	0.021	LiF200	0.23	123%	353.4 PPM	1.82 mm
Sr KB1-HR-Tr	33.77	67.94	0.624	LiF200	0.23	2.23%	162.3 PPM	8.2 mm

Line 3	Net int.	Used intensity	Calc. conc	Crystal	Collimator	Stat. error	LLD	Analyzed layer
Nb LA1-HR	10.62	42.6	18.9	PET	0.23	1.01%	633.8 PPM	36 um
Cu LA1-HR	0.01887	0.04759	0.23	XS-55	0.23	208%	0.63%	4.0 um
Zn LA1-HR-Tr	0.4771	0.00257	0.006	XS-55	0.23	14.60%	0.73%	4.9 um

Sr LA1-HR	0.00459	-0.02139	-0.016	PET	0.23	677%	0.11%	22.7 um

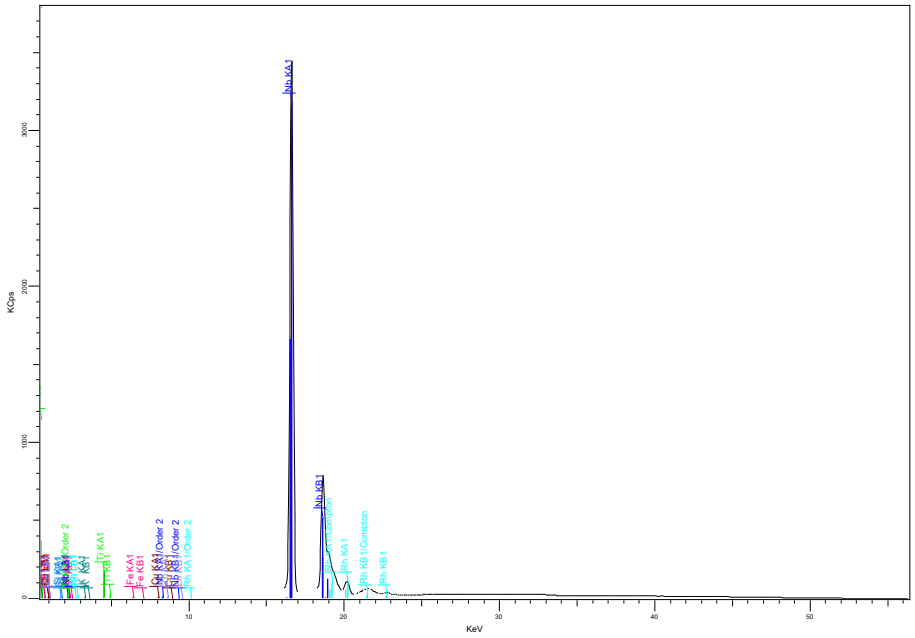

Figure 7.52 *XRF spectrum Nb-CST*

XRF IONSIV

Table 7.66 *XRF details Unloaded IONSIV*

	Z	Concentration	Status
TiO2	22	35.92	XRF 1
Nb2O5	41	22.4	XRF 3
ZrO2	40	19.4	XRF 3
SiO2	14	19.1	XRF 1
Na2O	11	3.42	XRF 1
MoO3	42	0.2578	XRF 1
HfO2	72	0.235	XRF 2
CaO	20	0.208	XRF 1
SO3	16	0.21	XRF 1
K2O	19	0.193	XRF 1
Al2O3	13	0.15	XRF 1
Fe2O3	26	0.11	XRF 1
CuO	29	0.0552	XRF 1
Cl	17	0.055	XRF 1
ZnO	30	0.0394	XRF 1
As2O3	33	0.005	XRF 1
Ta2O5	73	0.001	XRF 1

Line 1	Net int.	Used intensity	Calc. conc	Crystal	Collimator	Stat. error	LLD	Analyzed layer
Ti KA1-HR-Tr	129.9	311.5	35.92	LiF200	0.23	0.29%	296.7 PPM	242 um
Nb KA1-HR-Tr	3330	6686	25.45	LiF200	0.23	0.06%	226.4 PPM	8.7 mm
Zr KA1-HR-Tr	2815	7464	24.43	LiF200	0.23	0.06%	191.1 PPM	7.5 mm
Si KA1-HR-Tr	10.17	36.21	19.1	PET	0.23	1.03%	717.5 PPM	20.8 um
Na KA1-HR-Tr	1.048	2.636	3.42	XS-55	0.23	3.54%	0.19%	5.2 um
Mo KA1-HR-Tr	138.8	67.47	0.258	LiF200	0.23	0.82%	312.4 PPM	10.2 mm
Hf LA1-HR-Tr	18.33	30.51	0.907	LiF200	0.23	0.88%	359.6 PPM	0.98 mm
Ca KA1-HR-Tr	0.658	1.574	0.208	LiF200	0.23	5.19%	242.6 PPM	136 um
S KA1-HR-Tr	0.3891	0.9458	0.21	PET	0.23	6.43%	544.3 PPM	41 um
K KA1-HR-Tr	0.6241	1.498	0.193	LiF200	0.23	5.24%	213.1 PPM	100 um
Al KA1-HR-Tr	0.07618	0.2423	0.15	PET	0.23	18.50%	631.5 PPM	13.5 um
Fe KA1-HR-Tr	1.749	4.111	0.11	LiF200	0.23	3.76%	108.5 PPM	0.54 mm
Cu KA1-HR-Tr	2.385	5.561	0.0552	LiF200	0.23	4.03%	66.5 PPM	1.03 mm
Cl KA1-HR-Tr	0.09365	0.3701	0.055	PET	0.23	19.00%	246.1 PPM	53 um
Zn KA1-HR-Tr	2.199	5.128	0.0394	LiF200	0.23	4.74%	57.5 PPM	1.27 mm
As KA1-HR-Tr	1.325	0.9552	0.005	LiF200	0.23	9.94%	59.4 PPM	2.27 mm
Ta LA1-HR-Tr	0.5928	0.04509	0.001	LiF200	0.23	14.70%	237.6 PPM	1.07 mm

Line 2	Net int.	Used intensity	Calc. conc	Crystal	Collimator	Stat. error	LLD	Analyzed layer
Ti KB1-HR-Tr	20.33	48.75	36.2	LiF200	0.23	0.74%	0.18%	0.31 mm
Nb KB1-HR-Tr	528.9	1063	26.37	LiF200	0.23	0.15%	0.14%	7.1 mm

Zr KB1-HR-Tr	550.9	1096	21.1	LiF200	0.23	0.15%	0.12%	10.5 mm
Si KB1-HR-Tr/Ox	0.1368	0.4869	13	PET	0.23	12.90%	3.42%	24.1 um
Mo KB1-HR-Tr	32.28	64.85	1.93	LiF200	0.23	2.26%	502.8 PPM	5.5 mm
Hf LB1-HR-Tr	4.596	7.316	0.235	LiF200	0.23	2.66%	358.4 PPM	1.44 mm
Ca KB1-HR-Tr	0.1335	0.3134	0.33	LiF200	0.23	19.80%	0.22%	173 um
K KB1-HR-Tr	0.1176	0.2823	0.31	LiF200	0.23	20.30%	0.19%	126 um
Al KB1-HR-Tr/Ox	0.04892	0.1556	8.2	PET	0.23	66.60%	5.43%	15.2 um
Fe KB1-HR-Tr	0.2285	0.5372	0.076	LiF200	0.23	28.60%	729.8 PPM	0.71 mm
Cu KB1-HR-Tr	0.8855	1.025	0.053	LiF200	0.23	11.70%	497.5 PPM	1.38 mm
Zn KB1-HR-Tr	-0.03043	-0.07254	-0.003	LiF200	0.23		378.7 PPM	1.71 mm
As KB1-HR-Tr	-0.2021	-0.4684	-0.011	LiF200	0.23		289.2 PPM	3.1 mm
Ta LB1-HR-Tr	2.607	1.757	0.0513	LiF200	0.23	4.50%	347.0 PPM	1.59 mm

Line 3	Net int.	Used intensity	Calc. conc	Crystal	Collimator	Stat. error	LLD	Analyzed layer
Nb LA1-HR	12.42	49.51	22.4	PET	0.23	0.93%	0.10%	37 um
Zr LA1-HR	7.967	31.95	19.4	PET	0.23	1.17%	901.6 PPM	31 um
Mo LA1-HR-Tr	0.0385	-0.2142	-0.088	PET	0.23	103%	945.5 PPM	41 um
Cu LA1-HR	-0.00972	-0.02452	-0.12	XS-55	0.23		0.61%	3.9 um
Zn LA1-HR-Tr	0.04948	-0.07768	-0.18	XS-55	0.23	87.70%	0.48%	4.8 um
As LA1-HR	0.08258	0.143	0.26	XS-55	0.23	24.80%	0.33%	9.0 um
Ta MA1,2-HR-Tr	-0.01273	-0.0528	-0.074	PET	0.23		0.21%	19.8 um

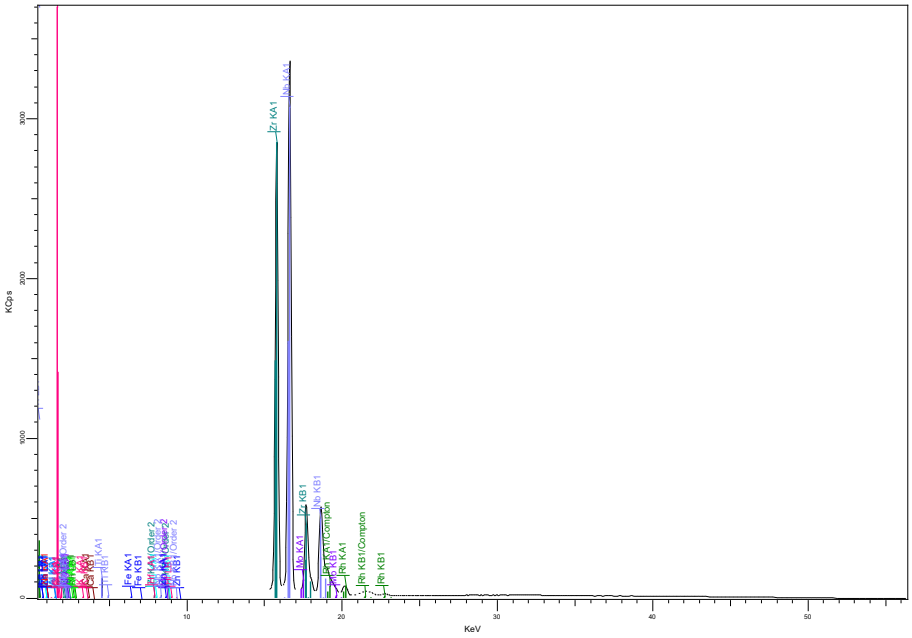

Figure 7.53 *XRF spectrum Unloaded IONSIV*

XRF Sr-Nb-CST

Table 7.67 *XRF details of Sr-Nb-CST*

Formula	Z	Concentration	Status
TiO2	22	45.55	XRF 1
SiO2	14	20	XRF 1
SrO	38	13.7	XRF 2
Nb2O5	41	12.8	XRF 3
Na2O	11	9.26	XRF 1
SO3	16	0.2	XRF 1
ZrO2	40	0.11	XRF 2
CaO	20	0.071	XRF 1
Cl	17	0.068	XRF 1
K2O	19	0.063	XRF 1
CuO	29	0.0553	XRF 1
Fe2O3	26	0.053	XRF 1
MnO	25	0.051	XRF 1
ZnO	30	0.0326	XRF 1
Rb2O	37	0.0142	XRF 1
NiO	28	0.012	XRF 1

Line 1	Net int.	Used intensity	Calc. conc	Crystal	Collimator	Stat. error	LLD	Analyzed layer
Ti KA1-HR-Tr	175.6	423.5	45.55	LiF200	0.23	0.25%	268.4 PPM	264 um
Si KA1-HR-Tr	10.74	38.1	20	PET	0.23	1.00%	696.2 PPM	20.8 um
Sr KA1-HR-Tr	2935	6086	16.6	LiF200	0.23	0.06%	132.1 PPM	5.6 mm
Nb KA1-HR-Tr	1501	2991	12.53	LiF200	0.23	0.09%	216.7 PPM	6.0 mm
Na KA1-HR-Tr	2.846	7.163	9.26	XS-55	0.23	2.03%	0.20%	5.2 um
S KA1-HR-Tr	0.3005	0.9379	0.2	PET	0.23	7.60%	454.3 PPM	41 um
Zr KA1-HR-Tr	611.4	479.4	1.413	LiF200	0.23	0.14%	297.5 PPM	7.7 mm
Ca KA1-HR-Tr	0.2428	0.5804	0.071	LiF200	0.23	10.90%	215.1 PPM	147 um
Cl KA1-HR-Tr	0.1219	0.4907	0.068	PET	0.23	14.50%	201.3 PPM	56 um
K KA1-HR-Tr	0.2184	0.5253	0.063	LiF200	0.23	11.40%	193.2 PPM	108 um
Cu KA1-HR-Tr	2.385	5.586	0.0553	LiF200	0.23	3.93%	63.7 PPM	1.05 mm
Fe KA1-HR-Tr	0.8633	1.991	0.053	LiF200	0.23	6.63%	104.1 PPM	0.55 mm
Mn KA1-HR-Tr	0.6292	1.478	0.051	LiF200	0.23	7.24%	106.3 PPM	0.43 mm
Zn KA1-HR-Tr	1.812	4.245	0.0326	LiF200	0.23	5.45%	55.3 PPM	1.29 mm
Rb KA1-HR-Tr	9.987	5.198	0.0141	LiF200	0.23	5.36%	57.0 PPM	4.7 mm
Ni KA1-HR-Tr	0.3814	0.8934	0.012	LiF200	0.23	18.70%	72.0 PPM	0.85 mm

Line 2	Net int.	Used intensity	Calc. conc	Crystal	Collimator	Stat. error	LLD	Analyzed layer
Ti KB1-HR-Tr	27.75	66.92	46.4	LiF200	0.23	0.63%	0.18%	0.34 mm
Si KB1-HR-Tr/Ox	0.2102	0.7458	20	PET	0.23	9.59%	3.55%	24.0 um
Sr KB1-HR-Tr	611.4	1200	13.7	LiF200	0.23	0.14%	672.5 PPM	7.8 mm
Nb KB1-HR-Tr	346.2	689.7	14.36	LiF200	0.23	0.19%	0.11%	8.3 mm

Zr KB1-HR-Tr	3.486	5.195	0.11	LiF200	0.23	16.50%	397.0 PPM	7.1 mm
Ca KB1-HR-Tr	-0.0041	-0.01611	-0.016	LiF200	0.23		0.20%	188 um
K KB1-HR-Tr	0.01692	0.04069	0.042	LiF200	0.23	303%	0.17%	136 um
Cu KB1-HR-Tr	0.4566	1.07	0.055	LiF200	0.23	20.80%	386.4 PPM	1.41 mm
Fe KB1-HR-Tr	11.78	27.17	3.79	LiF200	0.23	1.08%	681.7 PPM	0.72 mm
Mn KB1-HR-Tr	0.08261	0.1902	0.034	LiF200	0.23	154%	747.5 PPM	0.57 mm
Zn KB1-HR-Tr	-0.1418	-0.3321	-0.014	LiF200	0.23		362.6 PPM	1.75 mm
Rb KB1-HR-Tr	5.811	12.05	0.17	LiF200	0.23	9.66%	220.8 PPM	6.6 mm
Ni KB1-HR-Tr	2.041	0.6877	0.047	LiF200	0.23	11.60%	683.5 PPM	1.14 mm

Line 3	Net int.	Used intensity	Calc. conc	Crystal	Collimator	Stat. error	LLD	Analyzed layer
Sr LA1-HR	6.236	22.09	16.9	PET	0.23	1.33%	0.12%	23.0 um
Nb LA1-HR	6.859	27.6	12.8	PET	0.23	1.26%	694.3 PPM	35 um
Zr LA1-HR	0.04132	0.1663	0.1	PET	0.23	87.30%	857.5 PPM	29.6 um
Cu LA1-HR	0.01382	0.03468	0.17	XS-55	0.23	276%	0.63%	3.9 um
Zn LA1-HR-Tr	0.1792	-0.09843	-0.23	XS-55	0.23	29.90%	0.60%	4.9 um
Rb LA1-HR				PET	0.23			19.3 um
Ni LA1-HR	0.00886	0.02216	0.25	XS-55	0.23	152%	1.29%	3.2 um

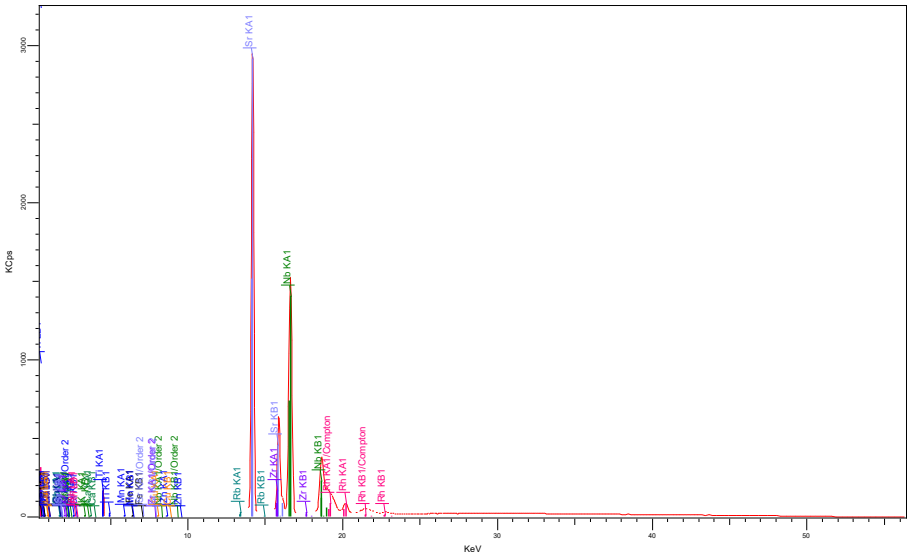

Figure 7.54 *XRF spectrum of Sr-Nb-CST*

XRF Sr-IONSIV (1.5 Wt. %)

Table 7.68 *XRF details of Sr-IONSIV (1.5 wt. %)*

Formula	Z	Concentration	Status
TiO2	22	35.16	XRF 1
Nb2O5	41	21.2	XRF 3
ZrO2	40	18.5	XRF 3
SiO2	14	17.5	XRF 1
Na2O	11	2.5	XRF 1
MoO3	42	1.98	XRF 2
SrO	38	1.422	XRF 1
SO3	16	0.22	XRF 1
K2O	19	0.21	XRF 1
HfO2	72	0.2	XRF 2
CaO	20	0.13	XRF 1
Fe2O3	26	0.127	XRF 1
Y2O3	39	0.122	XRF 1
Cl	17	0.11	XRF 1
CuO	29	0.05	XRF 1
ZnO	30	0.035	XRF 1
As2O3	33	0.008	XRF 1

Line 1	Net int.	Used intensity	Calc. conc	Crystal	Collimator	Stat. error	LLD	Analyzed layer
Ti KA1-HR-Tr	128.1	303.5	35.16	LiF200	0.23	0.50%	511.8 PPM	242 um
Nb KA1-HR-Tr	3151	6289	24.55	LiF200	0.23	0.10%	419.3 PPM	8.3 mm
Zr KA1-HR-Tr	2696	6989	22.98	LiF200	0.23	0.11%	414.6 PPM	7.5 mm
Si KA1-HR-Tr	10.08	33.14	17.5	PET	0.23	1.79%	0.10%	20.9 um
Na KA1-HR-Tr	0.7811	1.897	2.5	XS-55	0.23	7.14%	0.29%	5.2 um
Mo KA1-HR-Tr	111.1	25.68	0.101	LiF200	0.23	1.64%	290.7 PPM	9.7 mm
Sr KA1-HR-Tr	265.6	543.8	1.422	LiF200	0.23	0.37%	226.1 PPM	5.4 mm
S KA1-HR-Tr	0.4956	1.033	0.22	PET	0.23	9.19%	914.7 PPM	41 um
K KA1-HR-Tr	0.6792	1.61	0.21	LiF200	0.23	8.58%	368.4 PPM	100 um
Hf LA1-HR-Tr	13.4	19.87	0.593	LiF200	0.23	1.84%	610.6 PPM	0.98 mm
Ca KA1-HR-Tr	0.4167	0.9842	0.13	LiF200	0.23	12.70%	429.4 PPM	136 um
Fe KA1-HR-Tr	2.018	4.734	0.127	LiF200	0.23	5.75%	182.1 PPM	0.54 mm
Y KA1-HR-Tr	20.38	36.55	0.122	LiF200	0.23	2.28%	118.0 PPM	6.4 mm
Cl KA1-HR-Tr	0.2123	0.7398	0.11	PET	0.23	16.30%	409.5 PPM	53 um
Cu KA1-HR-Tr	2.158	5.086	0.05	LiF200	0.23	7.56%	113.3 PPM	1.04 mm
Zn KA1-HR-Tr	1.959	4.616	0.035	LiF200	0.23	9.07%	99.2 PPM	1.27 mm
As KA1-HR-Tr	1.506	1.692	0.008	LiF200	0.23	14.90%	98.8 PPM	2.28 mm

Line 2	Net int.	Used intensity	Calc. conc	Crystal	Collimator	Stat. error	LLD	Analyzed layer
Ti KB1-HR-Tr	19.29	45.69	34.1	LiF200	0.23	1.32%	0.32%	0.31 mm
Nb KB1-HR-Tr	496.6	992.2	24.88	LiF200	0.23	0.27%	0.25%	7.1 mm

Zr KB1-HR-Tr	523.1	979.9	19.4	LiF200	0.23	0.26%	0.25%	10.0 mm
Si KB1-HR-Tr/Ox	0.2856	0.9389	25	PET	0.23	13.10%	5.57%	24.1 um
Mo KB1-HR-Tr	33.34	66.61	1.98	LiF200	0.23	3.85%	878.4 PPM	5.6 mm
Sr KB1-HR-Tr	2696	2389	26.21	LiF200	0.23	0.11%	0.29%	7.6 mm
K KB1-HR-Tr	0.06919	0.164	0.18	LiF200	0.23	145%	0.34%	126 um
Hf LB1-HR-Tr	4.004	6.19	0.2	LiF200	0.23	5.09%	604.0 PPM	1.44 mm
Ca KB1-HR-Tr	0.00451	0.00496	0.005	LiF200	0.23	2377%	0.39%	173 um
Fe KB1-HR-Tr	0.4236	0.994	0.14	LiF200	0.23	26.50%	0.12%	0.71 mm
Y KB1-HR-Tr	1079	299.6	5.157	LiF200	0.23	0.44%	0.40%	8.5 mm
Cu KB1-HR-Tr	0.5083	0.3117	0.016	LiF200	0.23	84.50%	936.9 PPM	1.39 mm
Zn KB1-HR-Tr	0.2268	0.5345	0.023	LiF200	0.23	80.70%	639.6 PPM	1.72 mm
As KB1-HR-Tr	-0.5929	-1.376	-0.032	LiF200	0.23		489.5 PPM	3.1 mm

Line 3	Net int.	Used intensity	Calc. conc	Crystal	Collimator	Stat. error	LLD	Analyzed layer
Nb LA1-HR	12.73	46.58	21.2	PET	0.23	1.60%	0.16%	37 um
Zr LA1-HR	8.227	30.28	18.5	PET	0.23	1.99%	0.14%	31 um
Mo LA1-HR-Tr	0.1033	0.02805	0.012	PET	0.23	69.50%	0.15%	41 um
Sr LA1-HR	0.6177	1.886	1.5	PET	0.23	8.00%	0.23%	23.2 um
Y LA1-HR	0.00786	-0.04858	-0.034	PET	0.23	736%	0.21%	26.7 um
Cu LA1-HR	0.03206	0.0781	0.39	XS-55	0.23	170%	0.80%	3.9 um
Zn LA1-HR-Tr	0.06347	0.00874	0.021	XS-55	0.23	106%	0.70%	4.8 um
As LA1-HR	0.0328	0.03239	0.058	XS-55	0.23	286%	0.69%	9.1 um

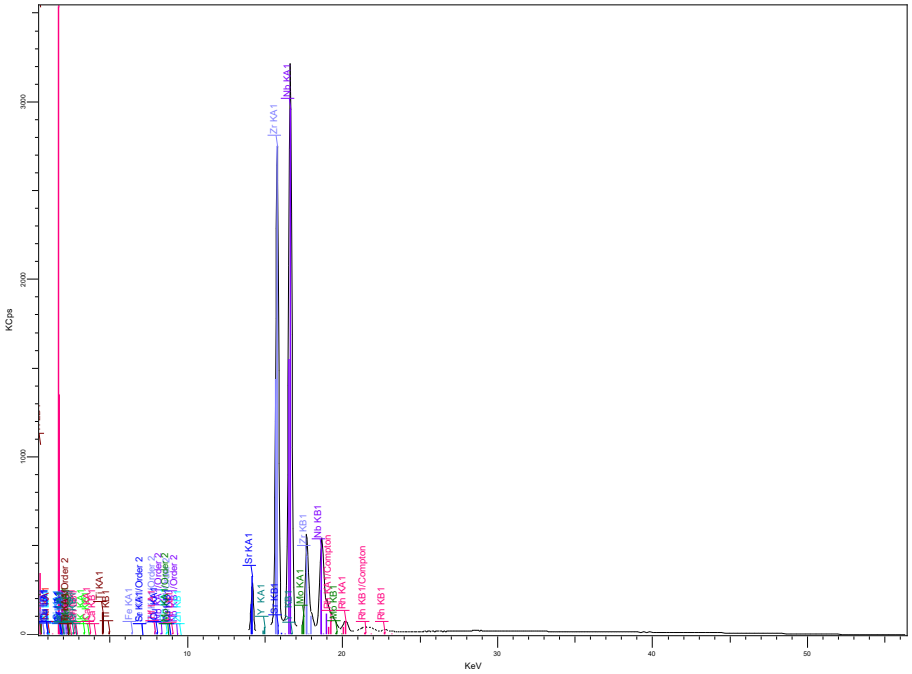

Figure 7.55 *XRF spectrum for Sr-IONSIV (1.5 wt. %)*

XRF Sr-IONSIV (3.0 Wt. %)

Table 7.69 *XRF details of Sr-IONSIV (3.0 wt. %)*

Formula	Z	Concentration	Status
TiO2	22	35.71	XRF 1
Nb2O5	41	21.5	XRF 3
ZrO2	40	18.7	XRF 3
SiO2	14	18.3	XRF 1
Na2O	11	2.4	XRF 1
SrO	38	2.117	XRF 1
MoO3	42	2	XRF 2
SO3	16	0.28	XRF 1
HfO2	72	0.206	XRF 2
K2O	19	0.17	XRF 1
Fe2O3	26	0.11	XRF 1
CuO	29	0.058	XRF 1
ZnO	30	0.031	XRF 1

Line 1	Net int.	Used intensity	Calc. conc	Crystal	Collimator	Stat. error	LLD	Analyzed layer
Ti KA1-HR-Tr	129.8	307.4	35.71	LiF200	0.23	0.50%	522.0 PPM	240 um
Nb KA1-HR-Tr	3119	6228	24.87	LiF200	0.23	0.10%	424.2 PPM	8.1 mm
Zr KA1-HR-Tr	2710	6991	23.26	LiF200	0.23	0.11%	441.3 PPM	7.4 mm
Si KA1-HR-Tr	10.51	34.55	18.3	PET	0.23	1.76%	0.12%	20.8 um
Na KA1-HR-Tr	0.7576	1.84	2.4	XS-55	0.23	7.25%	0.29%	5.2 um
Sr KA1-HR-Tr	390	798.7	2.117	LiF200	0.23	0.30%	229.7 PPM	5.4 mm
Mo KA1-HR-Tr	113.4	32.49	0.131	LiF200	0.23	1.62%	296.6 PPM	9.4 mm
S KA1-HR-Tr	0.5627	1.276	0.28	PET	0.23	8.41%	899.1 PPM	41 um
Hf LA1-HR-Tr	13.02	18.99	0.567	LiF200	0.23	1.87%	614.4 PPM	0.97 mm
K KA1-HR-Tr	0.5625	1.333	0.17	LiF200	0.23	9.97%	389.7 PPM	99 um
Fe KA1-HR-Tr	1.775	4.164	0.11	LiF200	0.23	6.37%	185.3 PPM	0.53 mm
Cu KA1-HR-Tr	2.489	5.865	0.058	LiF200	0.23	6.63%	112.9 PPM	1.03 mm
Zn KA1-HR-Tr	1.728	4.072	0.031	LiF200	0.23	10.10%	98.7 PPM	1.26 mm

Line 2	Net int.	Used intensity	Calc. conc	Crystal	Collimator	Stat. error	LLD	Analyzed layer
Ti KB1-HR-Tr	19.81	46.94	35.1	LiF200	0.23	1.30%	0.32%	0.31 mm
Nb KB1-HR-Tr	503.4	1006	25.68	LiF200	0.23	0.27%	0.25%	6.9 mm
Zr KB1-HR-Tr	504.2	942.8	19.06	LiF200	0.23	0.27%	0.26%	9.7 mm
Si KB1-HR-Tr/Ox	0.2495	0.8203	22	PET	0.23	14.20%	5.42%	24.1 um
Sr KB1-HR-Tr	2710	2424	26.99	LiF200	0.23	0.11%	0.29%	7.5 mm
Mo KB1-HR-Tr	33.13	66.19	2	LiF200	0.23	3.87%	896.6 PPM	5.5 mm
Hf LB1-HR-Tr	4.08	6.368	0.206	LiF200	0.23	5.04%	613.2 PPM	1.43 mm
K KB1-HR-Tr	0.0419	0.09928	0.11	LiF200	0.23	224%	0.33%	125 um
Fe KB1-HR-Tr	0.3622	0.8499	0.12	LiF200	0.23	77.50%	0.12%	0.71 mm
Cu KB1-HR-Tr	0.7714	0.9119	0.047	LiF200	0.23	22.70%	942.3 PPM	1.38 mm

Zn KB1-HR-Tr	-0.152	-0.3582	-0.016	LiF200	0.23		647.8 PPM	1.70 mm

Line 3	Net int.	Used intensity	Calc. conc	Crystal	Collimator	Stat. error	LLD	Analyzed layer
Nb LA1-HR	12.9	47.21	21.5	PET	0.23	1.58%	0.15%	37 um
Zr LA1-HR	8.309	30.58	18.7	PET	0.23	1.98%	0.13%	31 um
Sr LA1-HR	0.8266	2.571	2	PET	0.23	6.74%	0.23%	23.1 um
Mo LA1-HR-Tr	0.02735	-0.2579	-0.11	PET	0.23	211%	0.15%	41 um
Cu LA1-HR	0.05407	0.1317	0.66	XS-55	0.23	108%	0.80%	3.9 um
Zn LA1-HR-Tr	0.08962	0.07686	0.18	XS-55	0.23	79.80%	0.70%	4.8 um

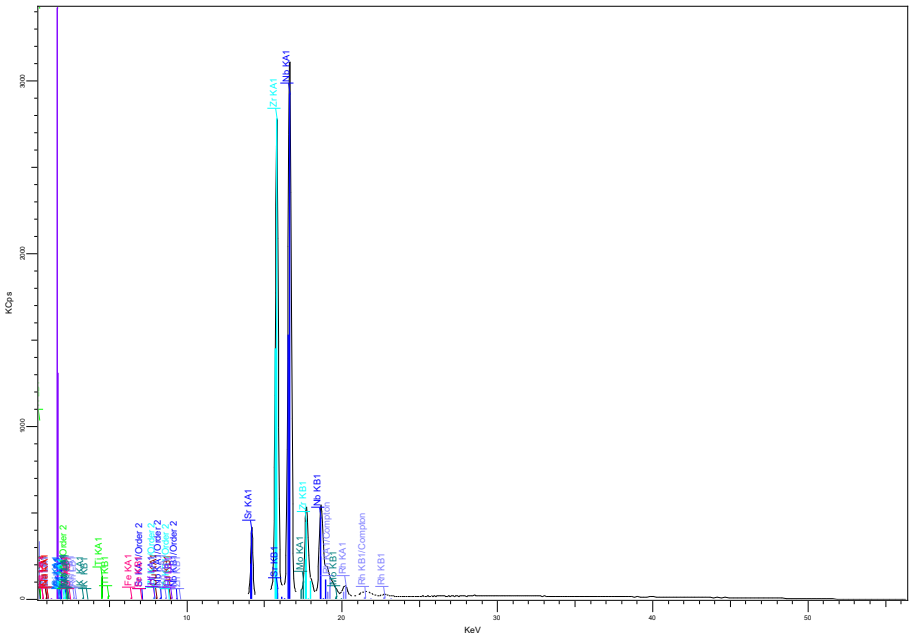

Figure 7.56 *XRF spectrum of Sr-IONSIV (3.0 wt. %)*

XRF Sr-IONSIV (4.0 Wt. %)

Table 7.70 *XRF details Sr-IONSIV (4.0 wt. %)*

Formula	Z	Concentration	Status
TiO2	22	35.42	XRF 1
Nb2O5	41	21.5	XRF 3
SiO2	14	18.7	XRF 1
ZrO2	40	18.7	XRF 3
SrO	38	4.008	XRF 1
MoO3	42	2.05	XRF 2
Na2O	11	0.91	XRF 1
HfO2	72	0.208	XRF 2
K2O	19	0.182	XRF 1
SO3	16	0.16	XRF 1
Al2O3	13	0.14	XRF 1
Fe2O3	26	0.117	XRF 1
CuO	29	0.0628	XRF 1
ZnO	30	0.0361	XRF 1
As2O3	33	0.006	XRF 1

Line 1	Net int.	Used intensity	Calc. conc	Crystal	Collimator	Stat. error	LLD	Analyzed layer
Ti KA1-HR-Tr	125.5	302.7	35.42	LiF200	0.23	0.29%	307.1 PPM	238 um
Nb KA1-HR-Tr	2905	5813	24.26	LiF200	0.23	0.06%	259.3 PPM	7.5 mm
Si KA1-HR-Tr	10.27	35.41	18.7	PET	0.23	1.03%	704.3 PPM	20.9 um
Zr KA1-HR-Tr	2672	6801	23.03	LiF200	0.23	0.06%	286.3 PPM	7.4 mm
Sr KA1-HR-Tr	713.5	1474	4.008	LiF200	0.23	0.13%	139.1 PPM	5.3 mm
Mo KA1-HR-Tr	104.2	23.55	0.0988	LiF200	0.23	0.99%	177.3 PPM	8.8 mm
Na KA1-HR-Tr	0.2858	0.7004	0.91	XS-55	0.23	8.22%	0.19%	5.2 um
Hf LA1-HR-Tr	13.69	20.61	0.617	LiF200	0.23	1.05%	356.6 PPM	0.96 mm
K KA1-HR-Tr	0.5806	1.393	0.182	LiF200	0.23	5.54%	220.3 PPM	99 um
S KA1-HR-Tr	0.3921	0.723	0.16	PET	0.23	6.59%	608.3 PPM	40 um
Al KA1-HR-Tr	0.07337	0.2291	0.14	PET	0.23	19.50%	650.6 PPM	13.5 um
Fe KA1-HR-Tr	1.857	4.307	0.117	LiF200	0.23	3.56%	107.2 PPM	0.53 mm
Cu KA1-HR-Tr	2.671	6.273	0.0628	LiF200	0.23	3.61%	65.7 PPM	1.02 mm
Zn KA1-HR-Tr	1.986	4.665	0.0361	LiF200	0.23	5.11%	57.1 PPM	1.25 mm
As KA1-HR-Tr	1.371	1.308	0.006	LiF200	0.23	9.49%	58.3 PPM	2.24 mm

Line 2	Net int.	Used intensity	Calc. conc	Crystal	Collimator	Stat. error	LLD	Analyzed layer
Ti KB1-HR-Tr	19.1	46.1	34.8	LiF200	0.23	0.77%	0.19%	0.31 mm
Nb KB1-HR-Tr	478	957.4	25.28	LiF200	0.23	0.16%	0.15%	6.6 mm
Si KB1-HR-Tr/Ox	0.1717	0.5916	16	PET	0.23	11.10%	3.49%	24.1 um
Zr KB1-HR-Tr	479.1	898.4	18.98	LiF200	0.23	0.16%	0.16%	9.0 mm
Sr KB1-HR-Tr	2672	2437	27.9	LiF200	0.23	0.06%	0.17%	7.5 mm
Mo KB1-HR-Tr	32.99	66.08	2.05	LiF200	0.23	2.24%	532.0 PPM	5.3 mm

Hf LB1-HR-Tr	4.092	6.408	0.208	LiF200	0.23	2.91%	355.8 PPM	1.42 mm
K KB1-HR-Tr	0.07722	0.1853	0.21	LiF200	0.23	73.20%	0.20%	124 um
Al KB1-HR-Tr/Ox	0.05474	0.1709	9	PET	0.23	63.70%	5.79%	15.2 um
Fe KB1-HR-Tr	1.086	2.519	0.36	LiF200	0.23	6.46%	711.3 PPM	0.70 mm
Cu KB1-HR-Tr	0.9933	1.423	0.074	LiF200	0.23	10.30%	552.1 PPM	1.37 mm
Zn KB1-HR-Tr	-0.00359	-0.00844	0	LiF200	0.23		379.6 PPM	1.69 mm
As KB1-HR-Tr	-0.1232	-0.2836	-0.007	LiF200	0.23		288.7 PPM	3.1 mm

Line 3	Net int.	Used intensity	Calc. conc	Crystal	Collimator	Stat. error	LLD	Analyzed layer
Nb LA1-HR	12.2	46.92	21.5	PET	0.23	0.94%	0.11%	36 um
Zr LA1-HR	7.835	30.3	18.7	PET	0.23	1.18%	952.2 PPM	31 um
Sr LA1-HR	1.569	5.259	4.05	PET	0.23	2.74%	0.14%	23.2 um
Mo LA1-HR-Tr	0.0666	-0.08818	-0.037	PET	0.23	26.90%	0.10%	41 um
Cu LA1-HR	0.01356	0.03354	0.17	XS-55	0.23	272%	0.60%	3.9 um
Zn LA1-HR-Tr	0.05351	0.07828	0.19	XS-55	0.23	80.00%	0.39%	4.8 um
As LA1-HR	0.01921	0.00129	0.002	XS-55	0.23	267%	0.39%	9.1 um

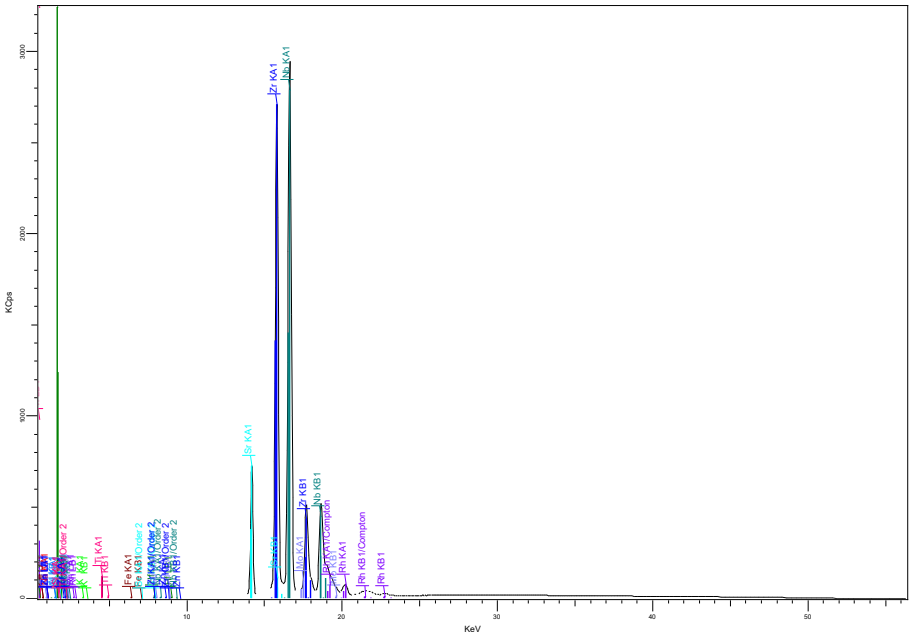

Figure 7.57 *XRF spectrum of Sr-IONSIV (4.0 wt. %)*

XRF Cs/Sr-IONSIV

Table 7.71 *XRF details for Cs/Sr-IONSIV*

Formula	Z	Concentration	Status
TiO2	22	32.86	XRF 1
Nb2O5	41	19.9	XRF 3
ZrO2	40	17.4	XRF 3
SiO2	14	16.6	XRF 1
Cs2O	55	6.85	XRF 3
MoO3	42	2.17	XRF 2
SrO	38	1.368	XRF 1
Na2O	11	0.69	XRF 1
HfO2	72	0.189	XRF 2
K2O	19	0.14	XRF 1
Al2O3	13	0.14	XRF 1
Fe2O3	26	0.104	XRF 1
SO3	16	0.097	XRF 1
Cl	17	0.062	XRF 1
CuO	29	0.0584	XRF 1
ZnO	30	0.0362	XRF 1
NiO	28	0.017	XRF 1
CeO2	58	0.013	XRF 1
As2O3	33	0.005	XRF 1

Line 1	Net int.	Used intensity	Calc. conc	Crystal	Collimator	Stat. error	LLD	Analyzed layer
Ti KA1-HR-Tr	116.3	278.8	32.86	LiF200	0.23	0.30%	319.5 PPM	242 um
Nb KA1-HR-Tr	2769	5569	22.71	LiF200	0.23	0.06%	244.4 PPM	7.6 mm
Zr KA1-HR-Tr	2382	6058	20.98	LiF200	0.23	0.07%	244.7 PPM	6.8 mm
Si KA1-HR-Tr	9.005	31.1	16.6	PET	0.23	1.10%	665.3 PPM	20.6 um
Cs KA1-HR-Tr	61.15	116.3	9.844	LiF200	0.23	0.56%	0.14%	19.2 mm
Mo KA1-HR-Tr	102.7	30.29	0.124	LiF200	0.23	1.00%	167.5 PPM	8.9 mm
Sr KA1-HR-Tr	235.8	481.5	1.367	LiF200	0.23	0.23%	139.1 PPM	5.0 mm
Na KA1-HR-Tr	0.214	0.5233	0.69	XS-55	0.23	10.20%	0.19%	5.2 um
Hf LA1-HR-Tr	12.81	19.76	0.644	LiF200	0.23	1.09%	368.5 PPM	0.91 mm
K KA1-HR-Tr	0.4579	1.095	0.14	LiF200	0.23	6.37%	202.0 PPM	100 um
Al KA1-HR-Tr	0.07145	0.2224	0.14	PET	0.23	18.40%	570.7 PPM	13.4 um
Fe KA1-HR-Tr	1.535	3.58	0.104	LiF200	0.23	4.11%	113.5 PPM	0.50 mm
S KA1-HR-Tr	0.3144	0.4454	0.097	PET	0.23	7.47%	573.6 PPM	41 um
Cl KA1-HR-Tr	0.1187	0.4153	0.062	PET	0.23	15.60%	269.0 PPM	53 um
Cu KA1-HR-Tr	2.307	5.403	0.0584	LiF200	0.23	4.07%	69.8 PPM	0.96 mm
Zn KA1-HR-Tr	1.841	4.312	0.0361	LiF200	0.23	5.44%	60.9 PPM	1.18 mm
Ni KA1-HR-Tr	0.5045	1.182	0.017	LiF200	0.23	14.30%	78.2 PPM	0.78 mm
Ce LA1-HR-Tr	0.2602	0.05182	0.014	LiF200	0.23	35.00%	0.10%	296 um
As KA1-HR-Tr	1.089	0.9866	0.005	LiF200	0.23	11.70%	61.7 PPM	2.09 mm

Line 2	Net int.	Used intensity	Calc. conc	Crystal	Collimator	Stat. error	LLD	Analyzed layer
Ti KB1-HR-Tr	19.81	47.5	36.2	LiF200	0.23	0.75%	0.20%	0.31 mm
Nb KB1-HR-Tr	467.9	941.6	24.01	LiF200	0.23	0.16%	0.14%	6.8 mm
Zr KB1-HR-Tr	458.5	853.7	17.63	LiF200	0.23	0.16%	0.15%	9.1 mm
Si KB1-HR-Tr/Ox	0.1012	0.3494	9.3	PET	0.23	41.30%	3.43%	23.8 um
Cs LA1-HR-Tr	10.21	24.48	6.97	LiF200	0.23	1.06%	666.3 PPM	209 um
Mo KB1-HR-Tr	36.12	72.7	2.17	LiF200	0.23	2.09%	511.9 PPM	5.6 mm
Sr KB1-HR-Tr	2382	2126	25.25	LiF200	0.23	0.07%	0.17%	6.9 mm
Hf LB1-HR-Tr	3.499	5.351	0.189	LiF200	0.23	3.28%	372.5 PPM	1.33 mm
K KB1-HR-Tr	0.07712	0.1845	0.21	LiF200	0.23	72.30%	0.19%	126 um
Al KB1-HR-Tr/Ox	0.08785	0.2734	15	PET	0.23	15.40%	4.72%	15.1 um
Fe KB1-HR-Tr	0.5233	1.22	0.19	LiF200	0.23	12.40%	747.4 PPM	0.66 mm
Cu KB1-HR-Tr	0.8252	1.165	0.066	LiF200	0.23	12.10%	512.3 PPM	1.28 mm
Zn KB1-HR-Tr	0.06328	0.1482	0.007	LiF200	0.23	411%	394.7 PPM	1.58 mm
Ni KB1-HR-Tr	5.553	6.455	0.484	LiF200	0.23	5.10%	811.1 PPM	1.03 mm
Ce LB1-HR-Tr	0.2286	0.5339	0.25	LiF200	0.23	37.60%	0.12%	294 um
As KB1-HR-Tr	-0.1659	-0.388	-0.01	LiF200	0.23		305.4 PPM	2.85 mm

Line 3	Net int.	Used intensity	Calc. conc	Crystal	Collimator	Stat. error	LLD	Analyzed layer
Nb LA1-HR	11.22	43.28	19.9	PET	0.23	0.98%	986.3 PPM	37 um
Zr LA1-HR	7.238	28.08	17.4	PET	0.23	1.23%	896.1 PPM	31 um
Cs LB1-HR-Tr	6.72	16	6.85	LiF200	0.23	1.35%	0.14%	259 um
Mo LA1-HR-Tr	0.07355	-0.03424	-0.014	PET	0.23	58.40%	929.2 PPM	41 um
Sr LA1-HR	0.539	1.727	1.35	PET	0.23	5.06%	0.14%	22.9 um
Cu LA1-HR	0.01496	0.03684	0.18	XS-55	0.23	103%	0.63%	3.9 um
Zn LA1-HR-Tr	0.00518	-0.02766	-0.066	XS-55	0.23	761%	0.39%	4.8 um
Ni LA1-HR	-0.01176	-0.02927	-0.34	XS-55	0.23		1.37%	3.2 um
As LA1-HR	0.03256	0.03561	0.064	XS-55	0.23	157%	0.34%	9.0 um

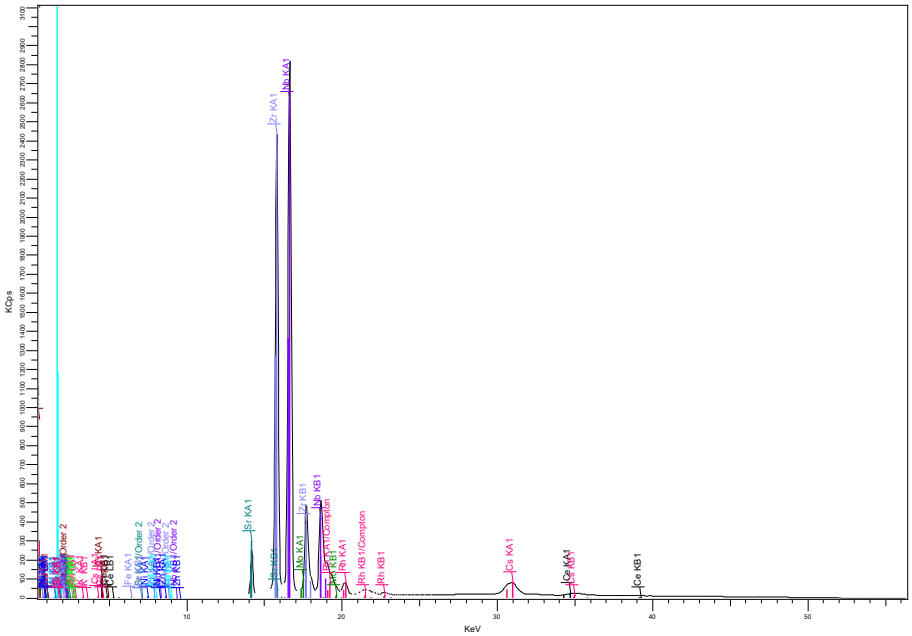

Figure 7.58 *XRF spectrum Cs/Sr-IONSIV*

XRF Cs-IONSIV (4.0 Wt. %)

Table 7.72 *XRF details for Cs-IONSIV (4 wt. %)*

Formula	Z	Concentration	Status
TiO2	22	34.13	XRF 1
Nb2O5	41	21.3	XRF 3
ZrO2	40	17.7	XRF 3
SiO2	14	17.6	XRF 1
Cs2O	55	5.37	XRF 3
Na2O	11	1.98	XRF 1
MoO3	42	0.2587	XRF 1
HfO2	72	0.222	XRF 2
K2O	19	0.17	XRF 1
CaO	20	0.17	XRF 1
SO3	16	0.16	XRF 1
Fe2O3	26	0.126	XRF 1
Cl	17	0.069	XRF 1
CuO	29	0.0613	XRF 1
P2O5	15	0.04	XRF 1
ZnO	30	0.0379	XRF 1
CeO2	58	0.018	XRF 1
As2O3	33	0.007	XRF 1
Rb2O	37	0.006	XRF 1

Line 1	Net int.	Used intensity	Calc. conc	Crystal	Collimator	Stat. error	LLD	Analyzed layer
Ti KA1-HR-Tr	122	292.6	34.13	LiF200	0.23	0.30%	314.8 PPM	244 um
Nb KA1-HR-Tr	3034	6092	23.85	LiF200	0.23	0.06%	229.6 PPM	8.1 mm
Zr KA1-HR-Tr	2502	6457	21.84	LiF200	0.23	0.07%	194.5 PPM	7.0 mm
Si KA1-HR-Tr	9.309	33.13	17.6	PET	0.23	1.08%	724.3 PPM	20.7 um
Cs KA1-HR-Tr	49.48	94.14	7.76	LiF200	0.23	0.64%	0.13%	19.9 mm
Na KA1-HR-Tr	0.6045	1.518	1.98	XS-55	0.23	4.94%	0.19%	5.2 um
Mo KA1-HR-Tr	126.4	66.01	0.2589	LiF200	0.23	0.87%	313.0 PPM	9.5 mm
Hf LA1-HR-Tr	14.5	23.17	0.74	LiF200	0.23	1.01%	368.0 PPM	0.92 mm
K KA1-HR-Tr	0.5492	1.318	0.17	LiF200	0.23	5.56%	196.3 PPM	101 um
Ca KA1-HR-Tr	0.5347	1.279	0.17	LiF200	0.23	5.93%	234.3 PPM	137 um
S KA1-HR-Tr	0.3271	0.7289	0.16	PET	0.23	7.36%	552.6 PPM	41 um
Fe KA1-HR-Tr	1.883	4.428	0.126	LiF200	0.23	3.51%	112.2 PPM	0.51 mm
Cl KA1-HR-Tr	0.1174	0.4654	0.069	PET	0.23	15.60%	240.5 PPM	53 um
Cu KA1-HR-Tr	2.476	5.774	0.0613	LiF200	0.23	3.86%	69.4 PPM	0.98 mm
P KA1-HR-Tr	0.07473	0.1096	0.04	PET	0.23	22.10%	734.9 PPM	30 um
Zn KA1-HR-Tr	1.974	4.603	0.0379	LiF200	0.23	5.15%	60.4 PPM	1.20 mm
Ce LA1-HR-Tr	0.2787	0.06893	0.018	LiF200	0.23	32.20%	980.9 PPM	298 um
As KA1-HR-Tr	1.361	1.297	0.007	LiF200	0.23	9.47%	61.7 PPM	2.13 mm
Rb KA1-HR-Tr	1.141	2.349	0.006	LiF200	0.23	16.10%	34.3 PPM	4.3 mm

Line 2	Net int.	Used intensity	Calc. conc	Crystal	Collimator	Stat. error	LLD	Analyzed layer
Ti KB1-HR-Tr	20.16	48.35	36.4	LiF200	0.23	0.74%	0.19%	0.32 mm
Nb KB1-HR-Tr	497.6	999.8	24.79	LiF200	0.23	0.15%	0.14%	7.1 mm
Zr KB1-HR-Tr	498.1	989.9	19.58	LiF200	0.23	0.15%	0.12%	9.8 mm
Si KB1-HR-Tr/Ox	0.2074	0.738	20	PET	0.23	9.23%	3.20%	23.9 um
Cs LA1-HR-Tr	8.132	19.5	5.49	LiF200	0.23	1.20%	669.0 PPM	210 um
Mo KB1-HR-Tr	32.72	65.75	1.93	LiF200	0.23	2.25%	500.2 PPM	5.6 mm
Hf LB1-HR-Tr	4.01	6.392	0.222	LiF200	0.23	2.94%	370.3 PPM	1.36 mm
K KB1-HR-Tr	0.01935	0.04646	0.052	LiF200	0.23	274%	0.19%	127 um
Ca KB1-HR-Tr	0.1179	0.2758	0.29	LiF200	0.23	21.90%	0.22%	174 um
Fe KB1-HR-Tr	0.2729	0.6417	0.096	LiF200	0.23	58.00%	742.0 PPM	0.67 mm
Cu KB1-HR-Tr	0.8164	0.9895	0.055	LiF200	0.23	12.40%	515.4 PPM	1.31 mm
Zn KB1-HR-Tr	-0.07447	-0.1737	-0.008	LiF200	0.23		395.8 PPM	1.61 mm
Ce LB1-HR-Tr	0.2476	0.5811	0.27	LiF200	0.23	35.00%	0.11%	296 um
As KB1-HR-Tr	-0.2309	-0.5351	-0.014	LiF200	0.23		300.5 PPM	2.91 mm
Rb KB1-HR-Tr	16.83	34.65	0.438	LiF200	0.23	3.77%	206.3 PPM	6.0 mm

Line 3	Net int.	Used intensity	Calc. conc	Crystal	Collimator	Stat. error	LLD	Analyzed layer
Nb LA1-HR	11.71	46.71	21.3	PET	0.23	0.96%	0.10%	37 um
Zr LA1-HR	7.192	28.84	17.7	PET	0.23	1.23%	922.1 PPM	31 um
Cs LB1-HR-Tr	5.345	12.7	5.37	LiF200	0.23	1.53%	0.13%	261 um
Mo LA1-HR-Tr	0.00297	-0.3366	-0.14	PET	0.23	1289%	963.4 PPM	41 um
Cu LA1-HR	0.01944	0.04904	0.24	XS-55	0.23	191%	0.60%	3.9 um
Zn LA1-HR-Tr	0.04575	-0.00147	-0.004	XS-55	0.23	91.90%	0.44%	4.8 um
As LA1-HR	0.03546	0.03684	0.066	XS-55	0.23	56.70%	0.34%	9.0 um
Rb LA1-HR				PET	0.23			19.2 um

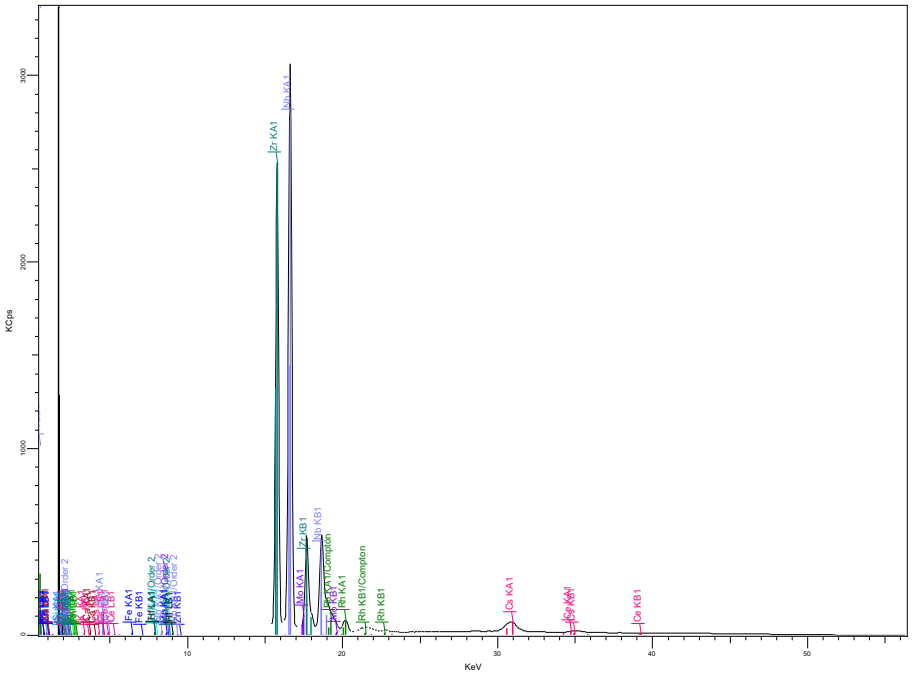

Figure 7.59 *XRF spectrum for Cs-IONSIV (4 wt. %)*

XRF Cs-IONSIV (6 wt. %)

Table 7.73 *XRF details for Cs-IONSIV (6 wt. %)*

Formula	Z	Concentration	Status
TiO2	22	32.93	XRF 1
Nb2O5	41	20.7	XRF 3
ZrO2	40	17.3	XRF 3
SiO2	14	17	XRF 1
Cs2O	55	8.38	XRF 3
Na2O	11	1.2	XRF 1
MoO3	42	0.2255	XRF 1
HfO2	72	0.202	XRF 2
SO3	16	0.17	XRF 1
CaO	20	0.15	XRF 1
Al2O3	13	0.15	XRF 1
Fe2O3	26	0.11	XRF 1
CuO	29	0.0595	XRF 1
ZnO	30	0.0392	XRF 1
Rb2O	37	0.008	XRF 1
As2O3	33	0.006	XRF 1
Ta2O5	73	0.002	XRF 1

Line 1	Net int.	Used intensity	Calc. conc	Crystal	Collimator	Stat. error	LLD	Analyzed layer
Ti KA1-HR-Tr	116.9	280.4	32.93	LiF200	0.23	0.30%	322.7 PPM	244 um
Nb KA1-HR-Tr	2881	5786	23.07	LiF200	0.23	0.06%	232.0 PPM	7.8 mm
Zr KA1-HR-Tr	2382	6080	21.01	LiF200	0.23	0.07%	196.6 PPM	6.7 mm
Si KA1-HR-Tr	8.935	31.8	17	PET	0.23	1.10%	699.2 PPM	20.6 um
Cs KA1-HR-Tr	75.26	143.2	12.02	LiF200	0.23	0.48%	0.14%	19.9 mm
Na KA1-HR-Tr	0.371	0.929	1.2	XS-55	0.23	6.89%	0.19%	5.2 um
Mo KA1-HR-Tr	118	56.56	0.2257	LiF200	0.23	0.90%	315.5 PPM	9.1 mm
Hf LA1-HR-Tr	13.59	21.57	0.715	LiF200	0.23	1.05%	375.6 PPM	0.90 mm
S KA1-HR-Tr	0.334	0.7769	0.17	PET	0.23	7.22%	546.1 PPM	41 um
Ca KA1-HR-Tr	0.47	1.125	0.15	LiF200	0.23	6.64%	236.6 PPM	137 um
Al KA1-HR-Tr	0.0752	0.2392	0.15	PET	0.23	18.60%	629.8 PPM	13.3 um
Fe KA1-HR-Tr	1.586	3.728	0.11	LiF200	0.23	3.99%	114.8 PPM	0.50 mm
Cu KA1-HR-Tr	2.323	5.414	0.0595	LiF200	0.23	4.05%	71.8 PPM	0.95 mm
Zn KA1-HR-Tr	1.97	4.594	0.0392	LiF200	0.23	5.09%	61.4 PPM	1.16 mm
Rb KA1-HR-Tr	1.419	2.921	0.008	LiF200	0.23	13.00%	35.5 PPM	4.2 mm
As KA1-HR-Tr	1.157	1.048	0.006	LiF200	0.23	10.90%	62.5 PPM	2.06 mm
Ta LA1-HR-Tr	0.5246	0.0819	0.002	LiF200	0.23	16.20%	252.7 PPM	0.98 mm

Line 2	Net int.	Used intensity	Calc. conc	Crystal	Collimator	Stat. error	LLD	Analyzed layer
Ti KB1-HR-Tr	20.66	49.55	37.6	LiF200	0.23	0.73%	0.20%	0.32 mm
Nb KB1-HR-Tr	483.5	971.5	24.31	LiF200	0.23	0.16%	0.14%	7.0 mm

Zr KB1-HR-Tr	476.7	948.3	19.11	LiF200	0.23	0.16%	0.12%	9.4 mm
Si KB1-HR-Tr/Ox	0.1752	0.6234	17	PET	0.23	10.80%	3.52%	23.7 um
Cs LA1-HR-Tr	12.61	30.24	8.57	LiF200	0.23	0.95%	666.4 PPM	211 um
Mo KB1-HR-Tr	33.99	68.29	2.01	LiF200	0.23	2.19%	502.5 PPM	5.6 mm
Hf LB1-HR-Tr	3.614	5.609	0.202	LiF200	0.23	3.19%	378.5 PPM	1.31 mm
Ca KB1-HR-Tr	0.00213	-0.00102	-0.001	LiF200	0.23	2814%	0.22%	174 um
Al KB1-HR-Tr/Ox	0.04478	0.1424	7.6	PET	0.23	68.10%	5.07%	15.0 um
Fe KB1-HR-Tr	0.2408	0.5663	0.088	LiF200	0.23	65.60%	766.7 PPM	0.65 mm
Cu KB1-HR-Tr	0.7017	0.8323	0.048	LiF200	0.23	35.30%	521.5 PPM	1.27 mm
Zn KB1-HR-Tr	-0.0539	-0.1286	-0.006	LiF200	0.23		406.7 PPM	1.56 mm
Rb KB1-HR-Tr	15.24	31.38	0.412	LiF200	0.23	4.07%	211.7 PPM	5.7 mm
As KB1-HR-Tr	-0.0949	-0.2199	-0.006	LiF200	0.23		309.8 PPM	2.81 mm
Ta LB1-HR-Tr	2.111	1.414	0.0463	LiF200	0.23	5.31%	365.9 PPM	1.45 mm

Line 3	Net int.	Used intensity	Calc. conc	Crystal	Collimator	Stat. error	LLD	Analyzed layer
Nb LA1-HR	11.32	45.14	20.7	PET	0.23	0.98%	0.10%	37 um
Zr LA1-HR	7.001	28.07	17.3	PET	0.23	1.25%	917.3 PPM	31 um
Cs LB1-HR-Tr	8.244	19.66	8.38	LiF200	0.23	1.20%	0.14%	261 um
Mo LA1-HR-Tr	0.0248	-0.2397	-0.099	PET	0.23	160%	954.2 PPM	41 um
Cu LA1-HR	0.01821	0.04593	0.23	XS-55	0.23	204%	0.60%	3.9 um
Zn LA1-HR-Tr	0.01535	-0.03293	-0.079	XS-55	0.23	262%	0.42%	4.8 um
Rb LA1-HR				PET	0.23			19.1 um
As LA1-HR	0.02195	0.00971	0.018	XS-55	0.23	223%	0.34%	9.0 um
Ta MA1,2-HR-Tr	0.00958	0.0277	0.039	PET	0.23	140%	0.20%	19.6 um

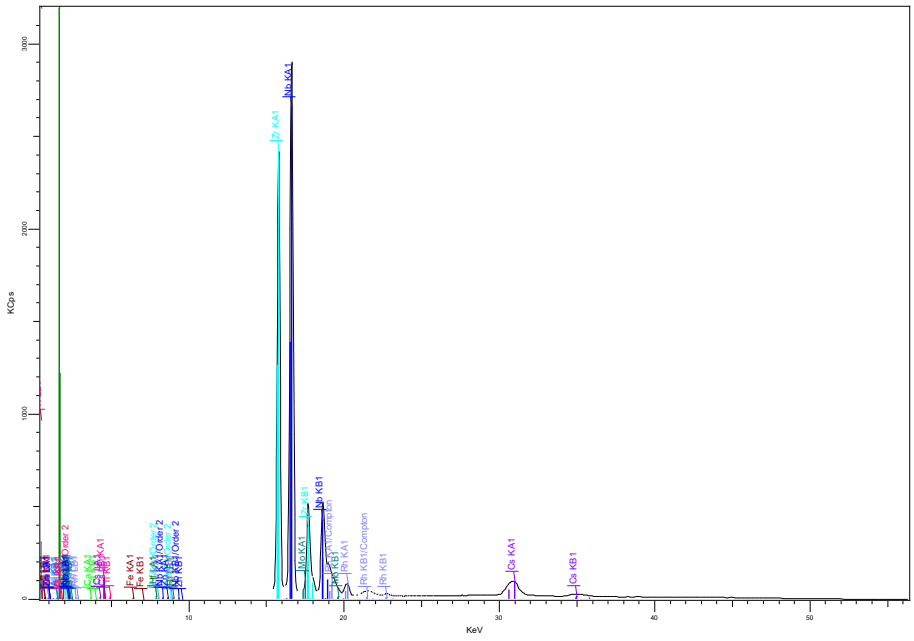

Figure 7.60 *XRF spectrum of Cs-IONSIV (6 wt. %)*

XRF Cs-IONSIV (8 wt. %)

Table 7.74 *XRF details for Cs-IONSIV (8 wt. %)*

Formula	Z	Concentration	Status
TiO2	22	31.96	XRF 1
Nb2O5	41	19.4	XRF 3
ZrO2	40	17.1	XRF 3
SiO2	14	16.4	XRF 1
Cs2O	55	10.7	XRF 3
MoO3	42	2.04	XRF 2
Na2O	11	0.87	XRF 1
HfO2	72	0.183	XRF 2
CaO	20	0.12	XRF 1
K2O	19	0.12	XRF 1
Fe2O3	26	0.0976	XRF 1
CuO	29	0.0616	XRF 1
Cl	17	0.05	XRF 1
ZnO	30	0.0438	XRF 1
SO3	16	0.042	XRF 1
CeO2	58	0.035	XRF 1
Rb2O	37	0.01	XRF 1

Line 1	Net int.	Used intensity	Calc. conc	Crystal	Collimator	Stat. error	LLD	Analyzed layer
Ti KA1-HR-Tr	112.3	269.2	31.96	LiF200	0.23	0.31%	319.6 PPM	242 um
Nb KA1-HR-Tr	2758	5538	22.56	LiF200	0.23	0.06%	236.6 PPM	7.6 mm
Zr KA1-HR-Tr	2299	5826	20.63	LiF200	0.23	0.07%	199.7 PPM	6.5 mm
Si KA1-HR-Tr	8.587	30.56	16.4	PET	0.23	1.13%	713.5 PPM	20.5 um
Cs KA1-HR-Tr	94.24	179.3	15.4	LiF200	0.23	0.41%	0.14%	19.5 mm
Mo KA1-HR-Tr	110.4	48.04	0.196	LiF200	0.23	0.94%	164.6 PPM	8.8 mm
Na KA1-HR-Tr	0.2639	0.6582	0.87	XS-55	0.23	8.66%	0.19%	5.1 um
Hf LA1-HR-Tr	13.18	21.02	0.717	LiF200	0.23	1.07%	382.2 PPM	0.87 mm
Ca KA1-HR-Tr	0.3772	0.9021	0.12	LiF200	0.23	7.75%	239.8 PPM	136 um
K KA1-HR-Tr	0.3864	0.9277	0.12	LiF200	0.23	7.32%	209.5 PPM	100 um
Fe KA1-HR-Tr	1.373	3.229	0.0976	LiF200	0.23	4.47%	117.9 PPM	0.48 mm
Cu KA1-HR-Tr	2.334	5.442	0.0616	LiF200	0.23	4.02%	72.6 PPM	0.92 mm
Cl KA1-HR-Tr	0.09504	0.3384	0.05	PET	0.23	18.50%	264.4 PPM	53 um
Zn KA1-HR-Tr	2.136	4.982	0.0438	LiF200	0.23	4.71%	62.9 PPM	1.13 mm
S KA1-HR-Tr	0.2335	0.1909	0.042	PET	0.23	9.18%	566.6 PPM	41 um
Ce LA1-HR-Tr	0.2851	0.133	0.035	LiF200	0.23	12.70%	989.0 PPM	297 um
Rb KA1-HR-Tr	1.829	3.765	0.01	LiF200	0.23	9.96%	36.0 PPM	4.0 mm

Line 2	Net int.	Used intensity	Calc. conc	Crystal	Collimator	Stat. error	LLD	Analyzed layer
Ti KB1-HR-Tr	20.82	49.94	38.4	LiF200	0.23	0.73%	0.20%	0.31 mm
Nb KB1-HR-Tr	471.6	947.5	24.03	LiF200	0.23	0.16%	0.14%	6.9 mm

Zr KB1-HR-Tr	457.7	849.3	17.52	LiF200	0.23	0.16%	0.15%	9.1 mm
Si KB1-HR-Tr/Ox	0.1908	0.679	18	PET	0.23	10.20%	3.55%	23.6 um
Cs LA1-HR-Tr	15.79	37.87	10.8	LiF200	0.23	0.84%	680.1 PPM	209 um
Mo KB1-HR-Tr	34.37	69.06	2.04	LiF200	0.23	2.16%	502.7 PPM	5.6 mm
Hf LB1-HR-Tr	3.278	4.939	0.183	LiF200	0.23	3.45%	386.7 PPM	1.28 mm
Ca KB1-HR-Tr	0.07171	0.1656	0.18	LiF200	0.23	86.40%	0.22%	173 um
K KB1-HR-Tr	0.07278	0.1747	0.2	LiF200	0.23	30.00%	0.18%	126 um
Fe KB1-HR-Tr	0.1564	0.3678	0.059	LiF200	0.23	99.20%	784.5 PPM	0.63 mm
Cu KB1-HR-Tr	0.7222	0.9774	0.058	LiF200	0.23	13.60%	528.8 PPM	1.23 mm
Zn KB1-HR-Tr	-0.08962	-0.209	-0.01	LiF200	0.23		412.6 PPM	1.51 mm
Ce LB1-HR-Tr	0.2943	0.6909	0.33	LiF200	0.23	30.20%	0.12%	289 um
Rb KB1-HR-Tr	14.77	30.41	0.413	LiF200	0.23	4.16%	217.0 PPM	5.6 mm

Line 3	Net int.	Used intensity	Calc. conc	Crystal	Collimator	Stat. error	LLD	Analyzed layer
Nb LA1-HR	10.55	42.08	19.4	PET	0.23	1.01%	988.5 PPM	36 um
Zr LA1-HR	6.887	27.62	17.1	PET	0.23	1.26%	915.0 PPM	31 um
Cs LB1-HR-Tr	10.36	24.74	10.7	LiF200	0.23	1.06%	0.14%	259 um
Mo LA1-HR-Tr	0.00429	-0.2891	-0.12	PET	0.23	858%	921.6 PPM	41 um
Cu LA1-HR	0.04963	0.1252	0.63	XS-55	0.23	32.40%	0.61%	3.9 um
Zn LA1-HR-Tr	0.01173	-0.02126	-0.051	XS-55	0.23	334%	0.40%	4.8 um
Rb LA1-HR				PET	0.23			19.0 um

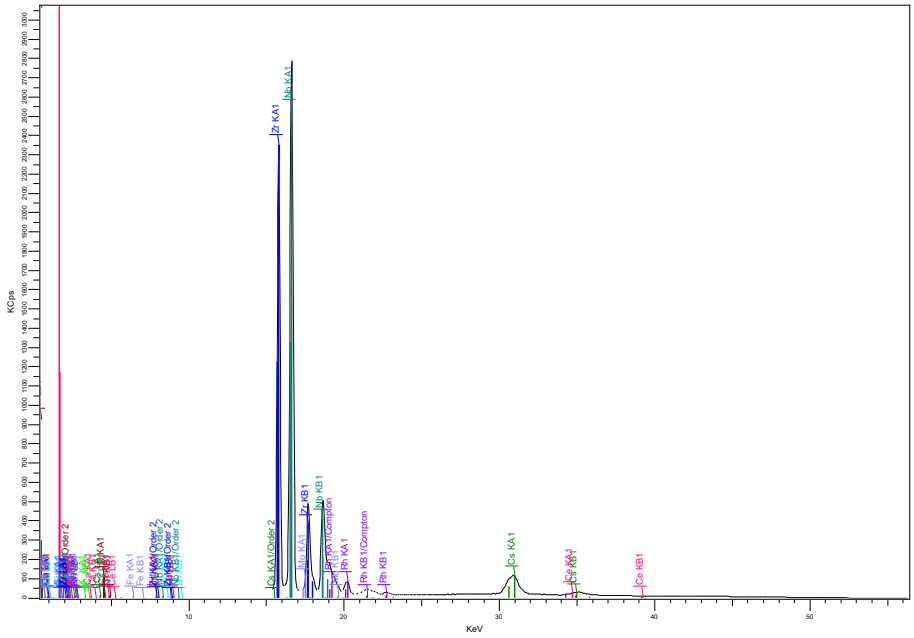

Figure 7.61 *XRF spectrum of Cs-IONSIV (8 wt. %)*

XRF Cs-IONSIV (10 wt. %)

Table 7.75 *XRF details for Cs-IONSIV (10 wt. %)*

Formula	Z	Concentration	Status
TiO2	22	32.53	XRF 1
Nb2O5	41	19.9	XRF 3
ZrO2	40	17.6	XRF 3
SiO2	14	16.8	XRF 1
Cs2O	55	13.2	XRF 3
MoO3	42	2	XRF 2
Na2O	11	0.41	XRF 1
HfO2	72	0.188	XRF 2
Al2O3	13	0.14	XRF 1
CaO	20	0.12	XRF 1
Fe2O3	26	0.105	XRF 1
SO3	16	0.067	XRF 1
CuO	29	0.0668	XRF 1
ZnO	30	0.0433	XRF 1
CeO2	58	0.043	XRF 1
Cl	17	0.041	XRF 1
Rb2O	37	0.01	XRF 1
Ta2O5	73	0.004	XRF 1

Line 1	Net int.	Used intensity	Calc. conc	Crystal	Collimator	Stat. error	LLD	Analyzed layer
Ti KA1-HR-Tr	112.8	270.5	32.53	LiF200	0.23	0.31%	336.3 PPM	238 um
Nb KA1-HR-Tr	2724	5469	23.17	LiF200	0.23	0.06%	242.8 PPM	7.2 mm
Zr KA1-HR-Tr	2251	5680	20.94	LiF200	0.23	0.07%	204.9 PPM	6.2 mm
Si KA1-HR-Tr	8.707	30.99	16.8	PET	0.23	1.12%	741.0 PPM	20.2 um
Cs KA1-HR-Tr	111.2	211.5	18.79	LiF200	0.23	0.37%	0.14%	18.7 mm
Mo KA1-HR-Tr	111	51.08	0.217	LiF200	0.23	0.93%	169.9 PPM	8.3 mm
Na KA1-HR-Tr	0.1265	0.3118	0.41	XS-55	0.23	15.50%	0.20%	5.1 um
Hf LA1-HR-Tr	12.92	20.54	0.723	LiF200	0.23	1.08%	395.6 PPM	0.83 mm
Al KA1-HR-Tr	0.07162	0.2278	0.14	PET	0.23	18.70%	605.0 PPM	13.2 um
Ca KA1-HR-Tr	0.3696	0.8848	0.12	LiF200	0.23	7.90%	239.0 PPM	134 um
Fe KA1-HR-Tr	1.429	3.359	0.105	LiF200	0.23	4.30%	121.4 PPM	0.46 mm
S KA1-HR-Tr	0.2621	0.3065	0.067	PET	0.23	8.56%	584.8 PPM	40 um
Cu KA1-HR-Tr	2.434	5.672	0.0668	LiF200	0.23	3.84%	76.2 PPM	0.88 mm
Zn KA1-HR-Tr	2.028	4.73	0.0433	LiF200	0.23	4.88%	64.9 PPM	1.08 mm
Ce LA1-HR-Tr	0.2966	0.1635	0.043	LiF200	0.23	12.40%	0.10%	292 um
Cl KA1-HR-Tr	0.07833	0.2728	0.041	PET	0.23	22.00%	271.2 PPM	52 um
Rb KA1-HR-Tr	1.785	3.676	0.01	LiF200	0.23	10.10%	37.5 PPM	3.8 mm
Ta LA1-HR-Tr	0.4924	0.1278	0.004	LiF200	0.23	16.90%	265.9 PPM	0.91 mm

Line 2	Net int.	Used intensity	Calc. conc	Crystal	Collimator	Stat. error	LLD	Analyzed layer

Ti KB1-HR-Tr	21.25	50.96	39.7	LiF200	0.23	0.72%	0.20%	0.31 mm
Nb KB1-HR-Tr	462.9	930.2	24.47	LiF200	0.23	0.16%	0.14%	6.5 mm
Zr KB1-HR-Tr	446.1	830	17.81	LiF200	0.23	0.16%	0.15%	8.6 mm
Si KB1-HR-Tr/Ox	0.1841	0.6552	18	PET	0.23	10.40%	3.53%	23.4 um
Cs LA1-HR-Tr	19.13	45.88	13.2	LiF200	0.23	0.76%	725.0 PPM	206 um
Mo KB1-HR-Tr	32.62	65.54	2	LiF200	0.23	2.24%	514.5 PPM	5.4 mm
Hf LB1-HR-Tr	3.239	4.884	0.188	LiF200	0.23	3.44%	398.7 PPM	1.22 mm
Al KB1-HR-Tr/Ox	0.0558	0.1775	9.6	PET	0.23	55.40%	4.95%	14.8 um
Ca KB1-HR-Tr	0.09258	0.2153	0.23	LiF200	0.23	66.60%	0.22%	170 um
Fe KB1-HR-Tr	0.2059	0.484	0.08	LiF200	0.23	29.90%	808.0 PPM	0.61 mm
Cu KB1-HR-Tr	0.6269	0.7715	0.047	LiF200	0.23	38.40%	545.7 PPM	1.17 mm
Zn KB1-HR-Tr	0.1082	0.2477	0.013	LiF200	0.23	236%	431.3 PPM	1.44 mm
Ce LB1-HR-Tr	0.3819	0.8964	0.43	LiF200	0.23	23.80%	0.12%	280 um
Rb KB1-HR-Tr	13.76	28.32	0.402	LiF200	0.23	4.36%	223.6 PPM	5.3 mm
Ta LB1-HR-Tr	1.661	0.8036	0.028	LiF200	0.23	16.20%	382.6 PPM	1.35 mm

Line 3	Net int.	Used intensity	Calc. conc	Crystal	Collimator	Stat. error	LLD	Analyzed layer
Nb LA1-HR	10.83	43.16	19.9	PET	0.23	1.00%	0.10%	36 um
Zr LA1-HR	7.098	28.46	17.6	PET	0.23	1.24%	904.4 PPM	31 um
Cs LB1-HR-Tr	12.75	30.46	13.2	LiF200	0.23	0.95%	0.14%	255 um
Mo LA1-HR-Tr	0.03852	-0.1576	-0.066	PET	0.23	106%	955.0 PPM	40 um
Cu LA1-HR	0.06422	0.1619	0.81	XS-55	0.23	26.20%	0.62%	3.9 um
Zn LA1-HR-Tr	0.00139	-0.02075	-0.05	XS-55	0.23	2817%	0.38%	4.7 um
Rb LA1-HR				PET	0.23			18.8 um
Ta MA1,2-HR-Tr	-0.01597	-0.06266	-0.089	PET	0.23		0.21%	19.3 um

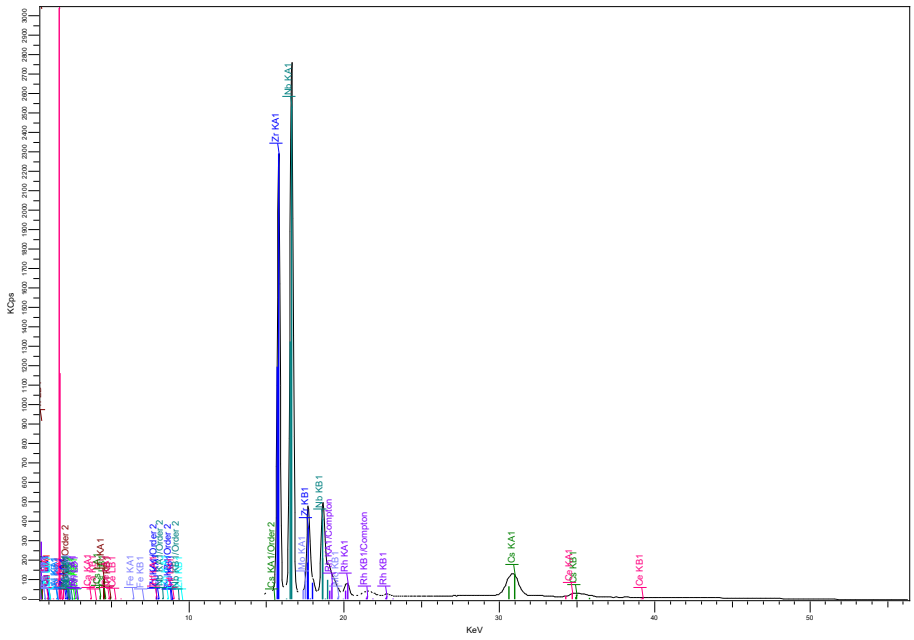

Figure 7.62 *XRF spectrum for Cs-IONSIV (10 wt. %)*

XRF Cs-IONSIV (12 wt. %)

Table 7.76 *XRF details for Cs-IONSIV (12 wt. %)*

Formula	Z	Concentration	Status
TiO2	22	31.12	XRF 1
Nb2O5	41	19.1	XRF 3
ZrO2	40	16.1	XRF 3
SiO2	14	16.1	XRF 1
Cs2O	55	13.6	XRF 3
MoO3	42	2.07	XRF 2
HfO2	72	0.176	XRF 2
CaO	20	0.14	XRF 1
Fe2O3	26	0.103	XRF 1
K2O	19	0.078	XRF 1
CuO	29	0.0637	XRF 1
SO3	16	0.063	XRF 1
Cl	17	0.058	XRF 1
ZnO	30	0.0366	XRF 1
NiO	28	0.015	XRF 1
Rb2O	37	0.014	XRF 1
As2O3	33	0.004	XRF 1

Line 1	Net int.	Used intensity	Calc. conc	Crystal	Collimator	Stat. error	LLD	Analyzed layer
Ti KA1-HR-Tr	108.5	260.2	31.12	LiF200	0.23	0.32%	326.9 PPM	242 um
Nb KA1-HR-Tr	2676	5373	22.29	LiF200	0.23	0.06%	238.7 PPM	7.3 mm
Zr KA1-HR-Tr	2161	5410	19.55	LiF200	0.23	0.07%	201.6 PPM	6.3 mm
Si KA1-HR-Tr	8.402	29.9	16.1	PET	0.23	1.14%	719.4 PPM	20.4 um
Cs KA1-HR-Tr	117.6	223.8	19.54	LiF200	0.23	0.36%	0.14%	19.5 mm
Mo KA1-HR-Tr	107.6	54.7	0.227	LiF200	0.23	0.96%	163.6 PPM	8.5 mm
Hf LA1-HR-Tr	11.87	18.73	0.661	LiF200	0.23	1.14%	386.0 PPM	0.85 mm
Ca KA1-HR-Tr	0.426	1.019	0.14	LiF200	0.23	7.12%	242.6 PPM	136 um
Fe KA1-HR-Tr	1.401	3.294	0.103	LiF200	0.23	4.34%	118.8 PPM	0.47 mm
K KA1-HR-Tr	0.2487	0.597	0.078	LiF200	0.23	10.10%	204.8 PPM	100 um
Cu KA1-HR-Tr	2.335	5.444	0.0637	LiF200	0.23	4.00%	74.7 PPM	0.89 mm
S KA1-HR-Tr	0.2555	0.2871	0.063	PET	0.23	8.69%	573.3 PPM	41 um
Cl KA1-HR-Tr	0.108	0.3896	0.058	PET	0.23	16.70%	265.3 PPM	53 um
Zn KA1-HR-Tr	1.726	4.026	0.0366	LiF200	0.23	5.70%	65.0 PPM	1.09 mm
Ni KA1-HR-Tr	0.4222	0.9846	0.015	LiF200	0.23	16.80%	83.4 PPM	0.73 mm
Rb KA1-HR-Tr	2.455	5.055	0.014	LiF200	0.23	7.43%	37.1 PPM	3.9 mm
As KA1-HR-Tr	0.8786	0.702	0.004	LiF200	0.23	14.10%	65.3 PPM	1.94 mm

Line 2	Net int.	Used intensity	Calc. conc	Crystal	Collimator	Stat. error	LLD	Analyzed layer
Ti KB1-HR-Tr	21.06	50.51	39.1	LiF200	0.23	0.73%	0.20%	0.31 mm
Nb KB1-HR-Tr	448.4	901	22.92	LiF200	0.23	0.16%	0.14%	6.8 mm

Zr KB1-HR-Tr	436.5	807	16.94	LiF200	0.23	0.17%	0.15%	8.8 mm
Si KB1-HR-Tr/Ox	0.1877	0.6681	18	PET	0.23	10.00%	3.35%	23.5 um
Cs LA1-HR-Tr	20.51	49.18	14.2	LiF200	0.23	0.74%	674.6 PPM	209 um
Mo KB1-HR-Tr	34.87	70.06	2.07	LiF200	0.23	2.14%	502.2 PPM	5.6 mm
Hf LB1-HR-Tr	3.036	4.588	0.176	LiF200	0.23	3.64%	391.2 PPM	1.24 mm
Ca KB1-HR-Tr	0.0773	0.1789	0.19	LiF200	0.23	32.60%	0.22%	173 um
Fe KB1-HR-Tr	0.1837	0.4319	0.071	LiF200	0.23	33.40%	796.3 PPM	0.62 mm
K KB1-HR-Tr	0.02444	0.05866	0.066	LiF200	0.23	85.90%	0.19%	126 um
Cu KB1-HR-Tr	0.7019	0.98	0.06	LiF200	0.23	13.90%	539.1 PPM	1.19 mm
Zn KB1-HR-Tr	0.0516	0.1203	0.006	LiF200	0.23	495%	421.0 PPM	1.47 mm
Ni KB1-HR-Tr	6.181	8.217	0.666	LiF200	0.23	4.68%	862.9 PPM	0.96 mm
Rb KB1-HR-Tr	13.03	26.83	0.378	LiF200	0.23	4.60%	222.8 PPM	5.4 mm
As KB1-HR-Tr	-0.2427	-0.5623	-0.016	LiF200	0.23		325.2 PPM	2.63 mm

Line 3	Net int.	Used intensity	Calc. conc	Crystal	Collimator	Stat. error	LLD	Analyzed layer
Nb LA1-HR	10.39	41.43	19.1	PET	0.23	1.02%	989.1 PPM	36 um
Zr LA1-HR	6.48	25.98	16.1	PET	0.23	1.30%	914.5 PPM	31 um
Cs LB1-HR-Tr	13.06	31.23	13.6	LiF200	0.23	0.94%	0.14%	259 um
Mo LA1-HR-Tr	0.02985	-0.1844	-0.077	PET	0.23	133%	935.5 PPM	41 um
Cu LA1-HR	0.05248	0.1322	0.66	XS-55	0.23	30.20%	0.60%	3.9 um
Zn LA1-HR-Tr	0.03329	0.08362	0.2	XS-55	0.23	119%	0.31%	4.8 um
Ni LA1-HR	-0.00755	-0.01922	-0.22	XS-55	0.23		1.31%	3.1 um
Rb LA1-HR				PET	0.23			18.9 um
As LA1-HR	0.06429	0.1133	0.21	XS-55	0.23	75.00%	0.31%	8.9 um

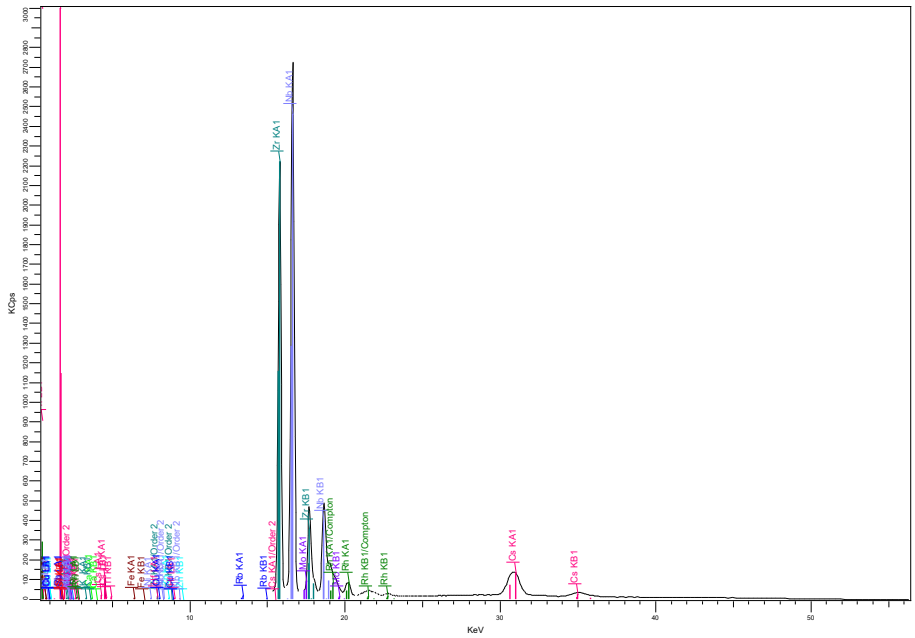

Figure 7.63 *XRF spectrum for Cs-IONSIV (12 wt. %)*